Les échanges entre liquide céphalo-rachidien et parenchyme cérébral : observation in-vivo par imagerie par résonance magnétique et implications dans le développement, le vieillissement et la pathologie

Audrey Chagnot

▶ To cite this version:

Audrey Chagnot. Les échanges entre liquide céphalo-rachidien et parenchyme cérébral : observation in-vivo par imagerie par résonance magnétique et implications dans le développement, le vieillissement et la pathologie. Médecine humaine et pathologie. Normandie Université, 2021. Français. NNT : 2021NORMC415 . tel-03517072

HAL Id: tel-03517072

https://theses.hal.science/tel-03517072v1

Submitted on 7 Jan 2022

THÈSE

Pour obtenir le diplôme de doctorat

Spécialité SCIENCES DE LA VIE ET DE LA SANTE

Préparée au sein de l'Université de Caen Normandie

Les échanges entre liquide céphalo-rachidien et parenchyme cérébral - observation in-vivo par imagerie par résonance magnétique et implications dans le développement, le vieillissement et la pathologie

Présentée et soutenue par
AUDREY CHAGNOT

Thèse soutenue le 16/12/2021 devant le jury composé de		
MME ROXANA CARARE	Professeur, Université de Southampton - UK	Rapporteur du jury
M. JEAN-PHILIPPE RANJEVA	Professeur des universités, Aix-Marseille Université	Rapporteur du jury
M. PIERRE GRESSENS	Professeur des universités, UFR MED PARIS 7 DENIS DIDEROT	Membre du jury
M. AXEL MONTAGNE	Directeur de recherche, Université Edinbourg	Membre du jury
MME GAELLE CHETELAT	Professeur des universités, Université Caen Normandie	Président du jury
M. DENIS VIVIEN	Professeur des universités PraticienHosp, Université Caen Normandie	Directeur de thèse
MME MARINA RUBIO	Ingénieur HDR, Université Caen Normandie	Co-directeur de thèse

Thèse dirigée par DENIS VIVIEN et MARINA RUBIO, Physiopathologie et imagerie des troubles neurologiques

Remerciements

En premier lieu, je remercie vivement le professeur Denis Vivien pour m'avoir accueillie dans son laboratoire et pour avoir supervisé ma thèse. Merci Denis pour le temps que tu as consacré à mes projets malgré ton emploi du temps plus que chargé, merci pour ton écoute et ta bienveillance et merci pour la confiance que tu m'as accordée tout au long de ces quatre ans.

Je remercie le professeur Gaël Chételat et le docteur Marina Rubio pour avoir été l'une après l'autre mes codirectrices de thèses. Merci à toutes les deux pour vos conseils avisés et vos relectures.

I would like to thank the professor Roxana Carare for sharing her expertise in the field of brain waste clearance as rapporteur.

Je remercie le professeur Jean-Philippe Ranjeva pour avoir accepté de nous faire part de son expertise en neuroimagerie en tant que rapporteur.

Je remercie le professeur Pierre Gressens pour avoir accepté de prendre part au jury et de nous partager son expérience du neurodéveloppement.

Je remercie le docteur Axel Montagne pour sa participation au jury et le partage de son expertise du vieillissement de la barrière hémato-encéphalique. Merci aussi Axel pour ta chouette collaboration sur cette revue dans Neuroscience.

Je remercie spécialement le docteur Mikaël Naveau pour avoir substantiellement contribué à ma formation et à mon encadrement. Merci Mika d'avoir réveillé ma passion pour la physique des champs magnétiques, l'algèbre linéaire appliquée à la biologie, et les langages de programmation de haut niveau.

Un énorme merci à JF, Jennifer, Marine, Max, Clément, Thomas et tous nos amis cliniciens pour m'avoir fait part avec passion de leurs aventures de CHU. Merci pour toutes les opportunités que vous m'avez offertes d'élargir mon champ de recherches et pour m'avoir montré à quoi serviraient toutes mes heures passées à maniper, analyser, biblioter, etc etc. La clinique c'est fantastique.

Merci à Zaza, Anna et Pauline pour avoir été là quand je n'allais pas. Merci à toi Juju pour la main que tu m'as tendue. Merci au Bureau où j'ai fini mes jours de thésarde vétérane, Célia et Fanny les biches, Barbara la discrète, Damien et Florent les bellâtres, Manu l'Espagnol et Alex l'invisible. Et merci, merci à toi Carine pour ta bienveillance, ton écoute discrète mais attentive, et tes coups de pieds au cul. On devrait tous avoir une Carine dans notre vie.

Un grand merci à l'ensemble des équipes et personnels du labo pour leur accueil et leur gentillesse. C'est grâce à vous tous et toutes que ces travaux ont pu être menés.

Merci à toi Florian d'exister, tout simplement. Tu es la preuve que la Vie existe quelque part ailleurs dans l'Univers.

Merci à ma Maman, mon Papa, Pierre et Fred, et toute la famille. Mon Poupi et ma Nini. Je vous aime et sans vous je ne serais pas là.

Résumé

Le liquide céphalo-rachidien (LCR) baigne l'ensemble du système nerveux central. En plus de son rôle protecteur, le LCR transporte des nutriments, des facteurs trophiques et des déchets qu'il échange avec le fluide interstitiel cérébral (FISC). Situés en périphérie des vaisseaux, les espaces périvasculaires offrent un accès au LCR vers la profondeur du tissu cérébral. Depuis une décennie, l'hypothèse d'un flux de liquide emportant les déchets du métabolisme vers ces espaces est avancée sous le nom de système glymphatique. Bien que ce modèle reste controversé, l'altération des échanges LCR-FISC a été montrée dans diverses pathologies dont la maladie d'Alzheimer, une démence liée à l'accumulation de plaques amyloïdes.

L'imagerie par résonance magnétique (IRM) permet d'observer in vivo la circulation du LCR et a montré chez l'être humain les échanges LCR-FISC. Cependant, l'utilisation d'agents de contraste restreint son exploitation clinique. Moins invasive, l'IRM de diffusion se base sur le mouvement des molécules d'eau et pourrait remplacer l'IRM rehaussée par agent de contraste pour l'exploration des échanges LCR-FISC.

Au cours de ma thèse, j'ai exploité deux techniques d'IRM (diffusion ou agent de contraste) pour explorer les échanges LCR-FISC chez la souris. Mes travaux soulignent la complémentarité de ces techniques et l'importance des traceurs utilisés dans des modèles de développement, de pathologie et de vieillissement.

Mots-clés : IRM | liquide céphalo-rachidien | glymphatique | développement | maladie d'Alzheimer

Abstract

The central nervous system is bathed in the cerebrospinal fluid (CSF). In addition to its protective role, the CSF carries nutrients, trophic factors and metabolic waste that are exchanged with the interstitial fluid of the brain (bISF). Around the vessels, the perivascular spaces give to the CSF an access toward the deep brain tissues. Since a decade, the 'glymphatic system' hypothesis has been advanced as a convective flow draining the metabolic waste to the perivascular spaces. While this model remains disputed, the CSF-bISF exchanges dysfunctions in a variety of pathologies including the Alzheimer's disease, a dementia related to the accumulation of amyloid plaques.

Magnetic resonance imaging (MRI) allows in vivo observations of the CSF circulation and shown the CSF-bISF exchnages in humans. However, the necessity of contrast agents restricts its clinical use. Diffusion-weighted MRI is a alternative, contrast agent-free technique exploiting the motion of water molecules and could replace contrast-enhanced MRI to investigate the CSF-bISF exchanges.

During my thesis, I used two MRI techniques (diffusion-weighted or contrast agent enhanced) to explore the CSF-bISF exchanges in mouse. My works emphasize the complementarity of these techniques and the importance of tracers in several models of development, pathology and aging.

Keywords : MRI | cerebrospinal fluid | glymphatic | development | Alzheimer's disease

"All models are wrong, but some are useful."

"Tous les modèles sont faux, mais certains sont utiles."

Georges EP Box, 1976

TABLE DES MATIÈRES

LISTE DES ABREVIATIONS (FR/EN)

α-syn : Alpha-synucléine / *Synuclein alpha*

AAC : Angiopathie amyloïde cérébrale / *Cerebral amyloid angiopathy*

ADC : Coefficient de diffusion apparent / *Apparent diffusion coefficient*

APOE ε4 : Allèle ε4 de l'apolipoprotéine E / *ε4 allele for the apolipoprotein E*

APP : Protéine précurseure de l'amyloïde / *Amyloid precursor protein*

AQP1 : Aquaporine de type I / *Type I aquaporin*

AQP4 : Aquaporine de type IV / *Type IV aquaporin*

AQP9 : Aquaporine de type IX / *Type IX aquaporin*

ASL : Marquage des spins artériels / *Arterial spin labelling*

ATP : Adénosine triphosphate / *Adenosine triphosphate*

Aβ : Bêta-amyloïde / *Amyloid beta*

BAM : Macrophage associé aux bordures / *Border-associated macrophage*

BDNF : Facteur neurotrophique dérivé du cerveau / *Brain-derived neurotrophic factor*

BHE : Barrière hémato-encéphalique / *Blood-brain barrier*

BOLD : Dépendant du taux d'oxygène dans le sang / *Blood-oxygen-level-dependent*

CBF : Flux sanguin cerebral / *Cerebral blood flow*

EAE : Encéphalite auto-immune expérimentale / *Experimental autoimmune encephalitis*

EHPAD : Etablissement d'hospitalisation pour personne agée dépendante / *Accomodation establishment for dependent elderly persons*

eLCR : LCR embryonnaire / *Embryonic cerebrospinal fluid*

EOP : Ensemble orthogonal de particules / *Orthogonal array of particles*

EPC : Epithélium des plexus choroïdes / *Choroid plexus epithelium*

EPV : Espace périvasculaire / *Perivascular space*

FA : Anisotropie fractionnelle / *Fractional anisotropy*

FAIR : — / *Flow-sensitive alternating inversion recovery*

FDA : Agence américaine du médicament / *Food and drug administration*

FISC : Fluide interstitiel cérébral / *Brain interstitial fluid*

IPAD : Drainage intramural périartériel / *Intramural periarterial drainage*

IRGRE : Gradient d'écho avec récupération d'inversion / *Inversion recovery gradient echo*

IRM : Imagerie par résonance magnétique / *Magnetic resonance imaging*

IRM-RCD : IRM rehaussée par contraste dynamique / *Dynamic contrast-enhanced MRI*

LCR : Liquide céphalo-rachidien / *Cerebrospinal fluid*

LRP-1 : Récepteur aux lipoprotéines de basse densité 1 / *Low-density lipoprotein receptor-related protein 1*

MA : Maladie d'Alzheimer / *Alzheimer's disease*

MCI : Déficit cognitif léger / *Mild cognitive impairment*

MLC : Leucodystrophie mégalencéphalique avec kystes sous-corticaux (maladie de Van der Knaap) / *Megalencephalic leukoencephalopathy with subcortical cysts (Van der Knaap's disease)*

MMP : Métalloprotéinase matricielle / *Matrix metalloproteinase*

MPIO : Microparticules d'oxide de fer / *Micro-sized particles of iron oxide*

MPV : Macrophages périvasculaires / *Perivascular macrophages*

NFT : Neurofibrilles tau / *Neurofibrillary tangles*

p75NTR : Récepteur p75 aux neurotrophines / *p75 neurotrophins receptor*

PaCO$_2$: Pression partielle sanguine du CO$_2$ / *CO$_2$ partial pressure in blood*

PAM : Pression artérielle moyenne / *Mean arterial blood pressure*

PaO$_2$: Pression partielle sanguine de l'O$_2$ / *O$_2$ partial pressure in blood*

PART : Tauopathie primaire liée à l'âge / *Primary age-related tauopathy*

PIC : Pression intracrânienne / *Intracranial pressure*

PrP : Protéine prion / *Prion protein*

p-tau : Protéine tau hyperphosphorylée / *Hyperphosphorylated tau protein*

RAGE : Récepteur aux produits finaux de la glycation avancée / *Receptor for advanced glycation end products*

RARE : Imagerie rapide avec échos refocalisés / *Rapid imaging with refocused echoes*

RLM : Réseau lymphatique méningé / *Meningeal lymphatics*

ROS : Espèces réactives de l'oxygène / *Reactive oxygen species*

SANS : Syndrome neuro-oculaire associé au vol spatial / *Spaceflight-associated neuro-ocular syndrome*

SB : Substance blanche / *White matter*

SEP : Sclérose en plaques / *Multiple sclerosis*

SG : Substance grise / *Grey matter*

SLA : Sclérose latérale amyotrophique (maladie de Charcot) / *Amyotrophic lateral sclerosis (Charcot's disease)*

SNC : Système nerveux central / *Central nervous system*

SPGR : — / *Spoiled Gradient Recalled*

TDP-43 : — / *TAR DNA-binding protein 43*

TEP : Tomographie par émission de positons / *Positon emission tomography*

TGN-020 : 2-nicotinamide-1,3,4-thiadiazole

tPA : Activateur tissulaire du plasminogène / *Tissue plasminogen activator*

TSA : Trouble du spectre autistique / *Autistic spectrum disorder*

USPIO : Nanoparticules d'oxide de fer / *Ultra-small particles of iron oxide*

VFA : Angle de bascule variable / *Variable flip angle*

INDEX DES FIGURES

INDEX DES TABLEAUX

AVANT PROPOS

En 2018, pour la première fois dans l'histoire de l'Humanité, le nombre de personnes âgées (plus de 65 ans) a dépassé celui des enfants de moins de cinq ans. La classe des seniors est le groupe démographique qui enregistre la croissance la plus rapide et, selon l'Organisation des Nations Unies, elle dépassera la classe des adolescents et des jeunes (15-24 ans) d'ici à 2050. Ce phénomène mondial, lié à l'augmentation de l'espérance de vie et au contrôle de la fécondité, affecte plus spécifiquement les nations industrialisées. En France en 2020, les personnes âgées représentaient 20% de la population.

Ce vieillissement démographique sous-tend l'augmentation de la prévalence de pathologies liées à l'âge. Les patients âgés, qui présentent souvent plusieurs comorbidités, forment ainsi une part croissante de la demande de soin. Malgré l'existence de structures dédiées tels les établissements d'hébergement pour personnes âgées dépendantes (EHPAD) qui accueillaient 600 000 résidents en France en 2020, les systèmes de santé peinent à s'adapter. Ce manque de préparation a pu avoir des conséquences tragiques, comme lors de la pandémie de Covid-19 qui affecte plus sévèrement les personnes âgées et aura causé plus de 110 000 décès en France.

Fortement corrélée à l'âge, la maladie d'Alzheimer est la démence la plus fréquente et concerne près d'un million de personnes en France. Ce nombre devrait doubler d'ici vingt ans. Cette maladie cause une dégradation progressive et irréversible des capacités cognitives, notamment de la mémoire. La perte d'autonomie des patients pèse lourdement sur leur entourage et les systèmes de santé, jusqu'au décès qui survient en moyenne six ans après le diagnostic. Bien que des facteurs protecteurs aient été identifiés, il n'existe pas encore de traitement.

Parmi les agents impliqués dans la maladie d'Alzheimer, le peptide bêta-amyloïde a bénéficié d'une attention considérable. En effet, ce déchet toxique du métabolisme cérébral est retrouvé en quantité anormalement élevée dans le cerveau des patients. Les plaques amyloïdes sont une des signatures de la maladie d'Alzheimer, mais se retrouvent aussi dans des pathologies apparentées comme l'angiopathie amyloïde cérébrale. La présence de déchets toxiques est d'ailleurs retrouvée dans d'autres conditions neurodégénératives telles que la maladie de Parkinson ou la maladie de Creutzfeld-Jakob.

Le peptide bêta-amyloïde bénéficie de multiples voies d'élimination, mais leur défaillance lors du vieillissement pourrait expliquer son accumulation. Héritière d'une longue lignée de travaux, une équipe a récemment suggéré que le liquide céphalorachidien serait un acteur majeur de l'élimination de ce peptide (Iliff et al., 2012). Cette voie a été baptisée 'système glymphatique', en référence aux cellules gliales qui y joueraient un rôle similaire à celui du système lymphatique dans le reste du corps. Bien que de nombreuses équipes se soient depuis emparées de la théorie, cette dernière reste le sujet de débats parmi la communauté scientifique.

Au cours de ma thèse, j'ai exploité plusieurs méthodes d'imagerie par résonance magnétique (IRM) pour étudier ce 'système glymphatique' chez la souris (*mus musculus*). Mon objectif a été de déterminer si l'imagerie de diffusion, une technique réalisable en clinique, pouvait remplacer les méthodes utilisant des agents de contraste. Mes travaux ont contribué à plusieurs articles publiés ou en soumission dont les résultats sont présentés et discutés dans ce manuscrit.

INTRODUCTION

"Si l'on souhaite faire une théorie sur la formation de la lymphe et les forces agissant sur sa locomotion, cela demande en tant que base indispensable une idée précise des tenants anatomiques aux racines du système."

"If one wants to make a theory about the formation of the lymph and of the forces acting on its locomotion, which one desires, this, as an indispensable basis, demands a precise idea of the anatomical behaviour of the first roots of the system."

Wilhelm His, 1863

Bases anatomiques : un crâne, quatre humeurs

Sang, lymphe, bile et atrabile. Héritées de l'Antiquité, ces quatre fluides, ou humeurs, ont formé le cadre théorique de la médecine occidentale jusque vers la fin de la Renaissance. La théorie des humeurs prétendait associer les quatre éléments (eau, air, terre et feu) à la santé et à la psychologie humaine. Selon elle, toute pathologie dérivait d'une perturbation de l'équilibre entre ces quatre fluides. Complètement discréditée de nos jours, elle a néanmoins laissé une empreinte durable dans le vocabulaire médical.

Le tissu nerveux humain est constitué d'eau à 73% (Mitchell et al., 1945), dont 80% est intracellulaire (Quirk et al., 2003). Parmi les fluides extracellulaires figurent le sang, la lymphe et le fluide interstitiel. Cas particulier, le système nerveux central (SNC) n'est pas desservi directement par le système lymphatique mais baigne dans un fluide spécifique, le liquide céphalo-rachidien (LCR).

Les échanges d'eau, de solutés et de cellules sont finement régulés au travers de routes et de barrières. Comme anticipé par la théorie archaïque des humeurs, des échanges déséquilibrés entre ces fluides sont retrouvés dans diverses pathologies.

Dans la première partie de cette introduction, nous considèrerons les bases anatomiques et les interactions entre quatre compartiments au sein du SNC : le **sang**, la **lymphe**, le **LCR** et le **fluide interstitiel cérébral (FISC)**.

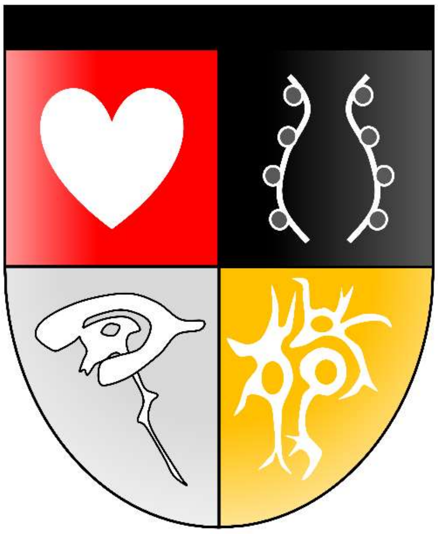

Figure 1 : Un crâne, quatre humeurs

Les quatre compartiments extracellulaires liés au système nerveux central : le sang, la lymphe, le liquide céphalo-rachidien et le fluide interstitiel

Rappels anatomiques

Définitions et généralités sur le système nerveux central

Généralités

Le **système nerveux central (SNC)** est un tissu nerveux spécialisé dans le traitement de l'information, par opposition au système nerveux périphérique chargé de la transmettre. Chez l'être humain, le SNC est subdivisé en l'**encéphale**, situé dans la cavité crânienne, et la **moelle épinière**, protégée par la colonne vertébrale.

La fonction nerveuse du SNC est assurée par un type cellulaire dédié, les **neurones**, qui forment un réseau communiquant à l'aide de courants électriques (potentiels d'action) et de messagers chimiques (neurotransmetteurs). Le cerveau humain contient environ 80 milliards de neurones (von Bartheld et al., 2016) et la moelle épinière près de 50 millions (BAHNEY and VON BARTHELD, 2018).

Extrêmement vulnérables, les neurones sont entretenus et protégés par les **cellules gliales** (du grec γλια, glue) : les **astrocytes**, qui maintiennent l'homéostasie du tissu nerveux ; les **oligodendrocytes**, dont les prolongements forment une gaine de myéline autour des axones pour accélérer la transmission du signal ; et la **microglie**, des macrophages résidents chargés de la surveillance immunitaire. Les cellules gliales sont un peu moins nombreuses que les neurones dans le cerveau mais 5 à 7 fois plus fréquentes dans la moelle épinière (Bahney et von Bartheld, 2018).

Le tissu nerveux est classiquement divisé en deux tissus, nommés d'après leur aspect à la dissection : la **substance grise (SG)**, riche en corps cellulaires de neurones, et la **substance blanche (SB)** qui contient leurs prolongements. Très gourmand en énergie, le SNC bénéficie d'une abondante vascularisation mais ne dispose pas de vaisseaux lymphatiques. En revanche, il est baigné dans le LCR, qui assure diverses fonctions en plus de sa protection physique.

Encéphale

L'encéphale est composé du **cerveau**, du **cervelet** et du **tronc cérébral**. La SG couvre la superficie du cerveau (le cortex) et forme plusieurs **noyaux** au centre, le tout étant connecté par la SB. Chez certaines espèces dont les êtres humains, le cortex présente un aspect plissé qui augmente sa superficie (gyrencéphalie). Le cerveau et le cervelet sont divisés en deux hémisphères, connectés par des tractus de fibres comme le corps calleux. Chaque hémisphère est subdivisé en six lobes, quatre internes (frontal, temporal, pariétal et occipital) et deux internes (limbique et insulaire). Au cœur du cerveau se trouve un réseau de citernes produisant le LCR ; le **système ventriculaire**.

La fonctionnalité du cerveau est basée sur une division en **régions spécialisées**. Par exemple, l'aire de Broca, située dans le lobe temporal, intervient dans la compréhension du langage. Ces régions sont connectées par les tractus de fibres dans la SB, et c'est grâce à leur **synchronisation** que sont assurées les fonctions exécutives et certaines fonctions autonomes.

Moelle épinière

La moelle épinière est spécialisée dans la **transmission** de l'information sensorielle et motrice. Elle se présente sous la forme d'un long cylindre contenu dans le canal spinal formé par les vertèbres. Contrairement au cerveau, la SB est périphérique et la SG centrale. Cette dernière est traversée par un canal courant tout le long de la moelle et communiquant avec le système ventriculaire, le **canal de l'épendyme**.

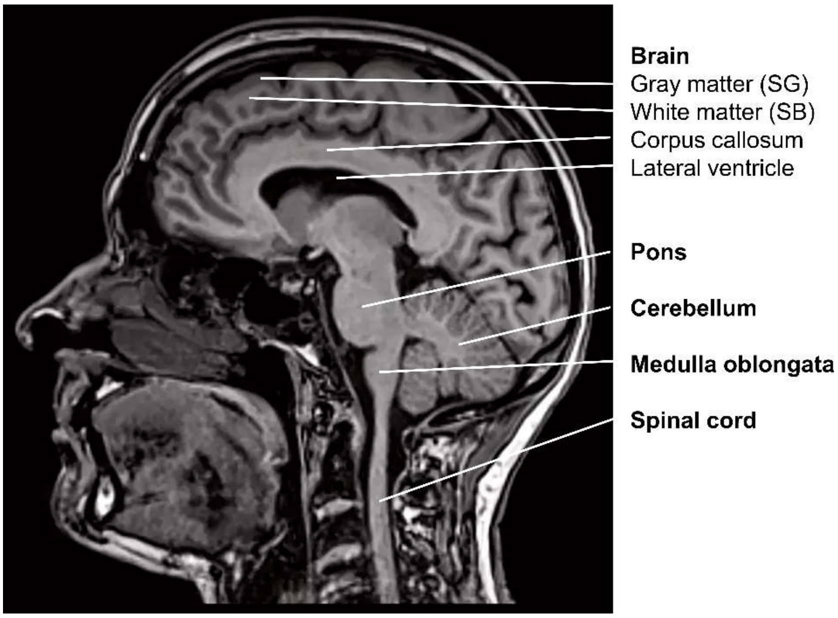

Figure 2 : Système nerveux central vu en imagerie par résonance magnétique

Coupe sagittale d'une tête humaine sur laquelle sont visible l'encéphale et le départ de la moelle épinière. Le contraste utilisé (T1) permet de distinguer la SG, plus sombre, de la SB.

Barrières physiques du SNC

La protection du SNC, tissu mou et extrêmement fragile, passe en premier lieu par l'établissement de remparts physiques. L'émergence de ces structures dans le règne animal il y a environ 500 millions d'années marque l'apparition des **vertébrés** (Xian-guang et al., 2002).

Crâne

Le **crâne** est la barrière du SNC la plus robuste chez les vertébrés. La cavité crânienne, qui ceint l'encéphale, est composée de huit os chez les êtres humains (ethmoïde, frontal, occipital, pariétaux droit et gauche, sphénoïde et temporaux droit et gauche). L'accès à l'intérieur du crâne est restreint au travers d'orifices dont le plus important est le ***foramen magnum*** (Anderson et al., 2021). Ce milieu clôt et rigide appose son lot de contraintes sur l'encéphale. En particulier, toute variation de volume d'un de ses compartiments (tissu cérébral, sang ou LCR) doit se faire aux dépends des autres, sous peine de modifier la pression générale. Georges Monro et Alexander Kellie ont été les premiers à formaliser cette relation par le 'dogme' qui porte leurs noms (Schaller and Graf, 2005). La **trépanation** en est une application. Cette procédure consiste à forer un trou dans le crâne pour évacuer les fluides et abaisser la pression intracrânienne, par exemple suite à une hémorragie. Il pourrait s'agir d'une des plus anciennes pratiques chirurgicales de l'Humanité, comme l'attestent des crânes trépanés datant de la préhistoire (Alt et al., 1997).

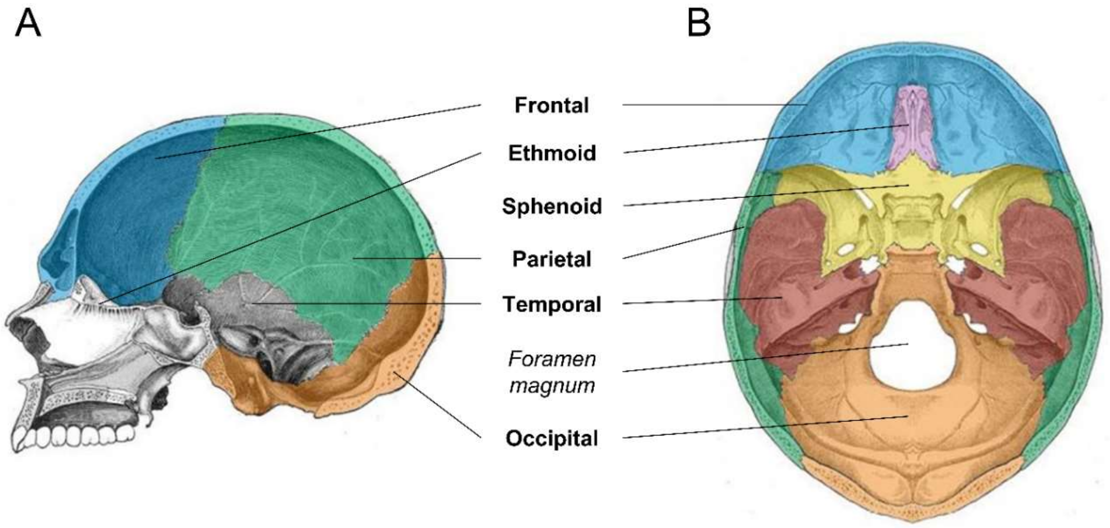

Figure 3 : Os de la cavité crânienne

Représentation en vue latérale gauche (A) et vue de dessus (B) des huit os de la cavité crânienne. Illustrations tirées de teachmeanatomy.info.

Colonne vertébrale

La moelle épinière bénéficie de sa propre protection osseuse sous la forme des **vertèbres**. La colonne vertébrale, trait distinctif des vertébrés, assure un rôle structurel majeur en plus de la protection du SNC. Chez les êtres humains, elle supporte le poids de l'individu tout en gardant une certaine mobilité. La moelle épinière est rendue virtuellement inaccessible par l'enchevêtrement des vertèbres. Les interstices restants sont couverts par le **ligament jaune**.

Dure-mère

Le SNC est enveloppé de membranes robustes qui complémentent la protection offerte par les os, les **méninges**. La plus externe et épaisse est la **dure-mère**. Elle tapisse l'intérieur de la cavité crânienne et forme quatre **cloisons** qui contribuent à délimiter les parties de l'encéphale : la faux du cerveau qui sépare les deux hémisphères cérébraux ; la tente du cervelet qui sépare le cervelet du cerveau ; la faux du cervelet qui délimite les hémisphères cérébelleux ; et la tente de l'hypophyse qui couvre la selle turcique, loge de l'hypophyse (Adeeb et al., 2012). La dure-mère bénéficie de sa propre vascularisation mais supporte également les vaisseaux qui desservent l'encéphale. En particulier, elle comporte des **sinus veineux** dont le plus imposant est le sinus sagittal supérieur, qui court au-dessus de la délimitation entre les hémisphères cérébraux. Malgré les observations de précurseurs comme Paolo Mascagni dès le XVIIIème siècle (Bucchieri et al., 2015), la dure-mère a longtemps été décrite comme dépourvue de **système lymphatique**. Des études récentes ont permis de redécouvrir ce réseau (Aspelund et al., 2015; Louveau et al., 2015), qui pourrait jouer un rôle majeur dans la clairance des déchets du métabolisme cérébral (Ahn et al., 2019; Zou et al., 2019).

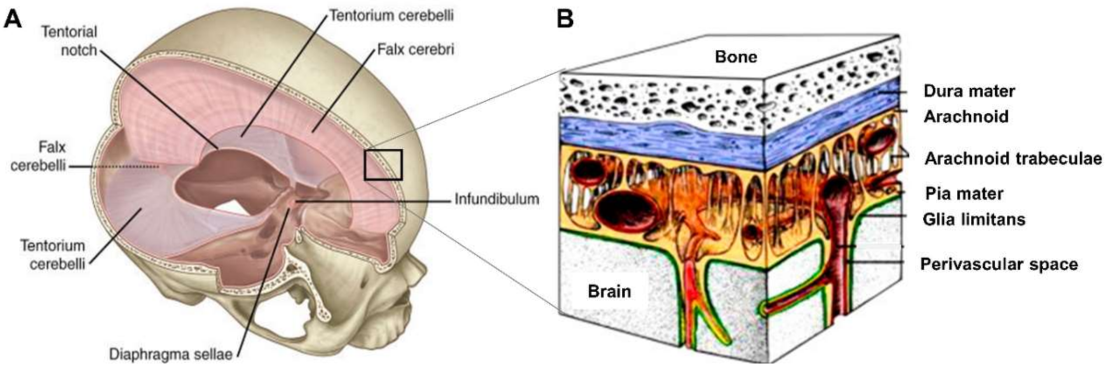

Figure 4 : Méninges

Représentation des feuillets de la dure-mère (A) et détail de l'organisation des méninges : dure-mère, arachnoïde et pie-mère (B). Illustration provenant de medicine.en-academic.com et d'après Saboori et Sadegh, 2011.

Leptoméninges

Les deux autres méninges, beaucoup plus fines, sont parfois groupées sous le terme de **leptoméninges**.

L'**arachnoïde** est la couche externe de cet ensemble. Il se constitue d'un feuillet accolé à la dure-mère, formé de plusieurs couches de cellules mésothéliales unies par des jonctions serrées. Ce feuillet enveloppe les vaisseaux qui pénètrent la cavité crânienne et contribue à la **barrière leptoméningée**. Sous l'arachnoïde se trouve l'**espace sous-arachnoïdien**, lequel contient la majeure partie du LCR, un fluide biologique incolore qui baigne également le système ventriculaire (Adeeb et al., 2013a). Le LCR assure une part importante dans la protection du SNC en amortissant les chocs et en le gardant en quasi-impesanteur grâce à la poussée d'Archimède (Spector et al., 2015b).

L'espace sous-arachnoïdien est traversé de piliers, ou **trabécules**, qui relient le feuillet externe de l'arachnoïde à la méninge sous-jacente, la pie-mère. Les trabécules arachnoïdiens possèdent un cœur constitué d'une matrice viscoélastique recouverte de cellules. Ils existent en une variété de formes allant du pilier simple aux feuillets, et permettent de suspendre le SNC dans le bain de LCR. Leur réseau compartimente l'espace sous-arachnoïdien pour favoriser la circulation du LCR (Saboori, 2021). Au niveau des gros sinus veineux qui courent entre l'arachnoïde et la dure-mère, l'espace sous-arachnoïdien forme des protrusions nommées **villosités arachnoïdiennes**.

La plus interne des méninges est la **pie-mère**. C'est une membrane fine (une à deux couches de cellules), délicate et très vascularisée qui tapisse la surface du SNC. Au bas de la moelle épinière, la pie-mère se prolonge pour constituer une part importante du **filum terminal**. Les cellules de la pie-mère sont connectées par des desmosomes et des jonctions *gap* (Adeeb et al., 2013b).

Glie limitante superficielle

Sous la pie-mère se trouve la **glie limitante superficielle**, une couche du SNC formée par des **extensions (pieds) astrocytaires**. Chez le rongeur, cette barrière n'est formée que d'une couche, au contraire des primates (dont les êtres humains) où elle est constituée de plusieurs épaisseurs (Liu et al., 2013). La glie limitante superficielle recouvre l'ensemble du SNC à l'exception du système ventriculaire où elle est remplacée par l'**épendyme**. Elle est continue avec la **glie limitante périvasculaire** qui enveloppe les vaisseaux perfusant le tissu cérébral. Entre la glie limitante superficielle et la pie-mère il existe un espace virtuel, l'**espace sous-pial** (Engelhardt et al., 2016).

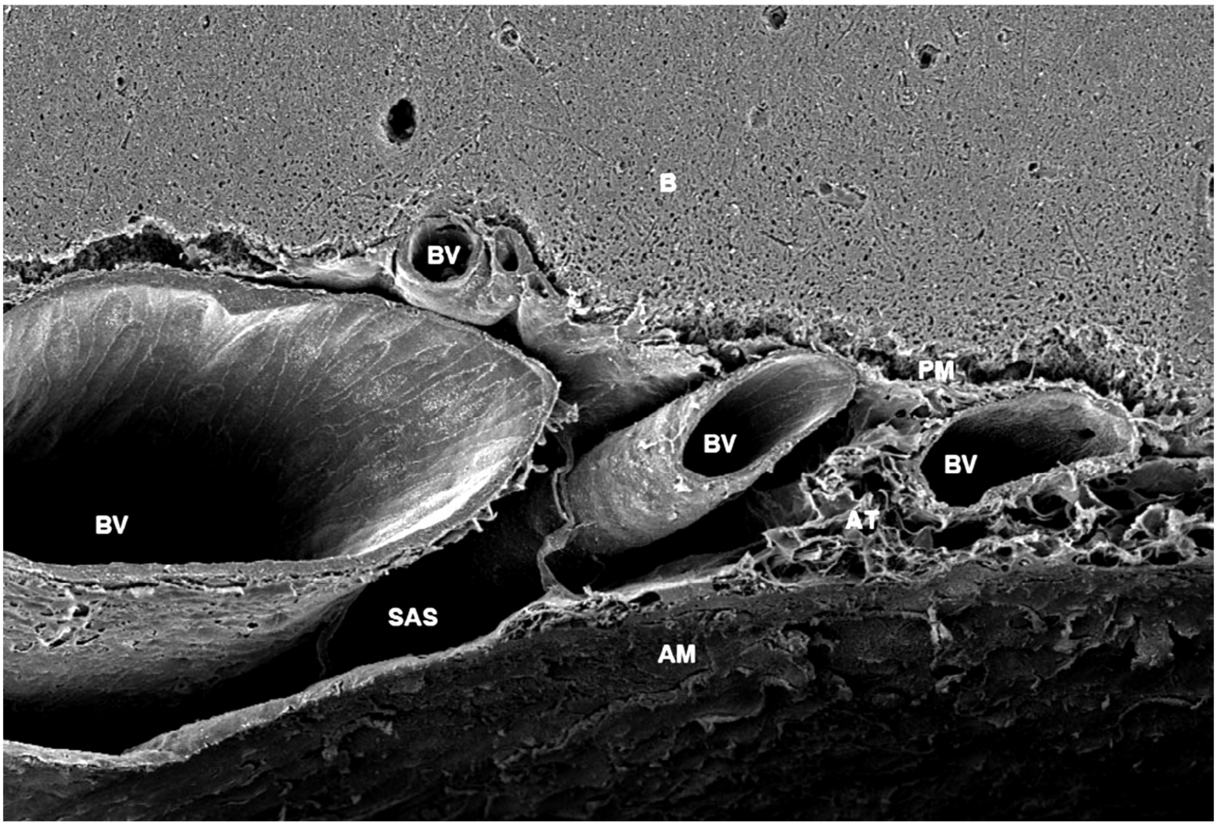

Figure 5 : Leptoméninges et espace sous-arachnoïdien observés en microscopie électronique à balayage

Plusieurs vaisseaux (BV) sont présents à la surface du cerveau (B), compris dans l'espace sous-arachnoïdien (SAS) entre la pie-mère (PM) et l'arachnoïde (AM). Les deux méninges sont unies par des trabécules arachnoïdiens (AT). La dure-mère et le crâne ont été retirés lors de la préparation de l'échantillon. D'après Saboori, 2021

Privilège immunitaire

Le SNC se distingue par une faible réactivité aux agressions extérieures (*e.g.* greffes, injections de composés immunogènes). Cette observation, qui a amené à la notion de "**privilège immunitaire**", est liée à la fragilité du tissu nerveux. En effet, la réaction inflammatoire observée dans les autres tissus se traduit par des altérations (œdème, cytotoxicité, infiltration leucocytaire, …) dont l'irruption dans le SNC aurait des conséquences catastrophiques. Le SNC est donc protégé du système immunitaire périphérique par des barrières telles que la **barrière hémato-encéphalique** (**BHE)** qui le sépare du sang (Engelhardt et al., 2017). En revanche, le SNC dispose de son propre système de défense sous la forme de **macrophages résidents**. Les cellules microgliales, localisées dans le parenchyme, forment la catégorie la plus abondante, alors qu'en périphérie du SNC se trouvent les macrophages associés aux bordures (BAM) qui incluent les macrophages périvasculaires (PVM) et les cellules de l'épiplexus. L'ensemble de ces cellules représente 10% des cellules du SNC (Prinz et al., 2021).

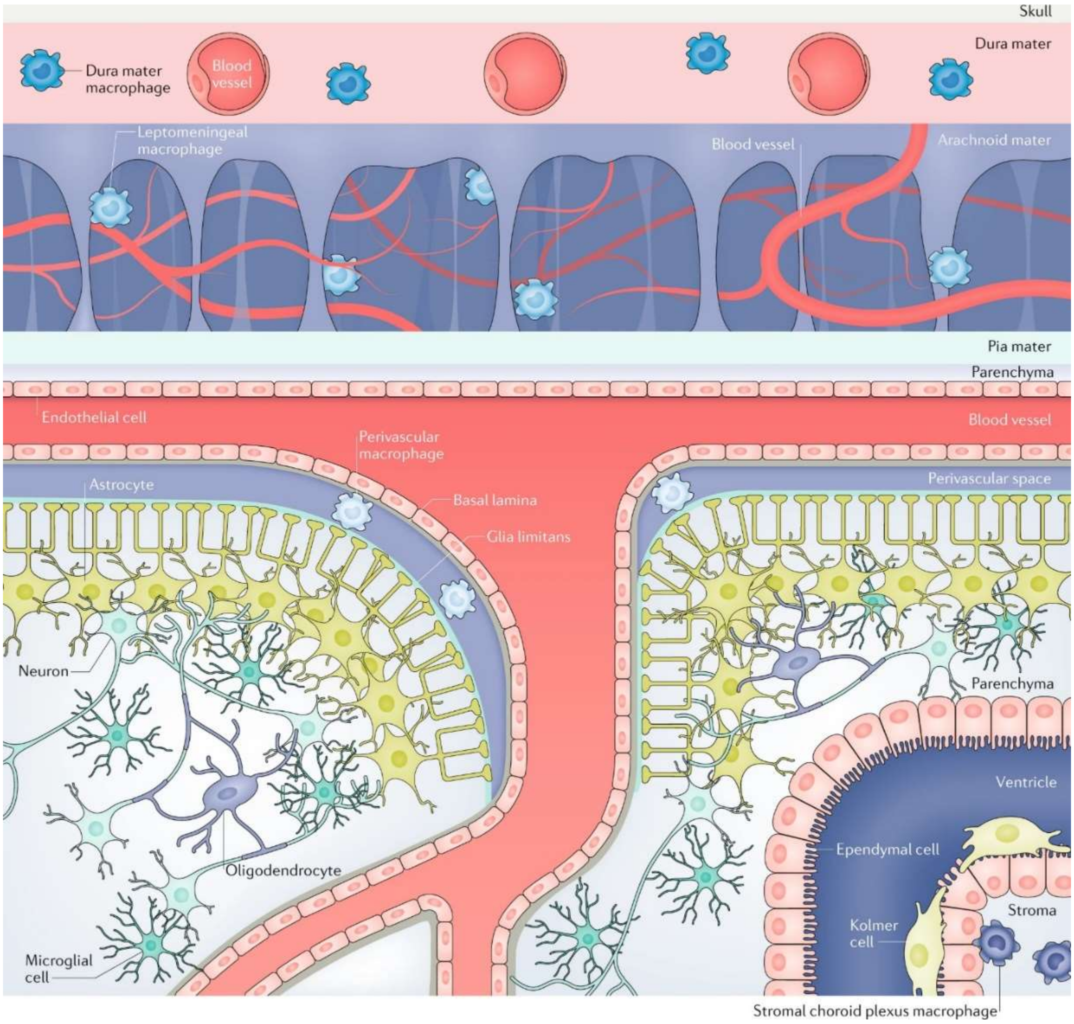

Figure 6 : Macrophages du système nerveux central

Illustration représentant les macrophages du SNC : macrophages de la dure-mère, macrophages des leptoméninges, macrophages périvasculaires, macrophages du stroma des plexus choroïdes, macrophages de l'épiplexus et cellules microgliales. D'après Kierdorf et al., 2019.

Microglie

Le terme ‘microglie’ est dérivé du mot ‘glie’ (du grec γλία, glue) qui désigne les cellules non nerveuses du SNC. Cependant, et contrairement aux autres cellules gliales (astrocytes, oligodendrocytes) d’origine neurectodermique, les cellules microgliales proviennent du **sac vitellin** (Prinz et al., 2019).

Les cellules microgliales présentent des morphologies variables en fonction de leur **état d’activation**. Globalement, elles se constituent d’un corps cellulaire de petite taille (7-10 µm) d’où partent plusieurs **prolongements**. Ces derniers, très motiles, couvrent une aire importante et permettent à la cellule de scruter son environnement (Prinz et al., 2021).

En plus de leur rôle de surveillance du SNC, les cellules microgliales contribuent à le nettoyer en phagocytant les cellules apoptotiques (**efferocytose**). Elles interviennent aussi dans le remodelage synaptique, la régulation de l’activité neuronale et sécrètent des **facteurs trophiques** comme le facteur neurotrophique dérivé du cerveau (BDNF, *Brain-derived neurotrophic factor*) (Prinz et al., 2021).

Macrophages périvasculaires

Distincts des cellules microgliales, ces BAM de forme allongée se situent sous la **membrane basale vasculaire**. À l'instar du SNC, de nombreux tissus disposent de leurs propres macrophages périvasculaires (PVM) où ils interviennent dans la régulation de la **perméabilité vasculaire** et de l’**inflammation**. Dans les organes circumventriculaires (OCV), des régions du SNC dépourvues de BHE, les PVM suppléent cette barrière. Entre autres, ils régulent le **couplage neurovasculaire** et permettent le passage de cellules immunitaires en cas d’infection (méningite) (Faraco et al., 2017). Expérimentalement, la déplétion des PVM est obtenue à l’aide de liposomes chargés en clodronate (une molécule cytotoxique) et injectés dans le LCR. Les PVM réapparaissent après deux semaines, ce qui suggère leur renouvellement par des sources périphériques (Levard et al., 2021).

Les PVM contribuent à la clairance du peptide Aβ, mais perdent leur capacité à l’internaliser chez les patients atteints de la maladie d'Alzheimer (Prinz and Priller, 2014). Cependant, ils pourraient aussi être acteurs de la pathologie : les effets toxiques du peptide Aβ sur les vaisseaux passent par la dysfonction de ces cellules (Faraco et al., 2016).

Macrophages des plexus choroïdes

Il en existe deux populations à la localisation anatomique distincte. Les **cellules de l'épiplexus**, ou cellules de Kolmer, sont situées à la surface des plexus au contact direct du LCR. Dans le stroma des plexus (tissu conjonctif très vascularisé qui les supporte), se trouve une autre population, en contact étroit avec les capillaires fenêtrés et les cellules dendritiques. Les **macrophages du stroma** auscultent leur environnement par de nombreux processus très motiles, mais ne semblent pas capables de se déplacer. Au contraire, les cellules de l'épiplexus présentent une grande mobilité, pouvant atteindre plusieurs centaines de micromètres par heure. Les deux populations, sensibles aux cytokines et chémokines, interviennent dans la **régulation de la réponse immunitaire du SNC** et sont capables de recruter d'autres types cellulaires (Cui et al., 2021).

Connexions avec le système immunitaire périphérique

En conditions physiologiques, les cellules immunitaires circulantes sont restreintes hors du SNC par la BHE. Cependant, une fraction des **monocytes circulants** peut infiltrer le SNC pour renouveler les cellules résidentes. Des expériences chez la souris suggèrent que les monocytes pourraient contribuer à l'élimination du peptide Aβ des veines cérébrales (Prinz and Priller, 2014).

Les méninges, desservies par le système lymphatique, ne sont pas isolées du système immunitaire périphérique. Les **cellules immunitaires des méninges** sont un intermédiaire privilégié entre le SNC et le reste de l'organisme (Norris and Kipnis, 2019), avec un réservoir possible dans la **moelle osseuse du crâne et des vertèbres** (Cugurra et al., 2021; Engelhardt, 2021). La communication entre moelle osseuse et vaisseaux méningés y serait permise grâce à des canaux au travers de l'os (Herisson et al., 2018).

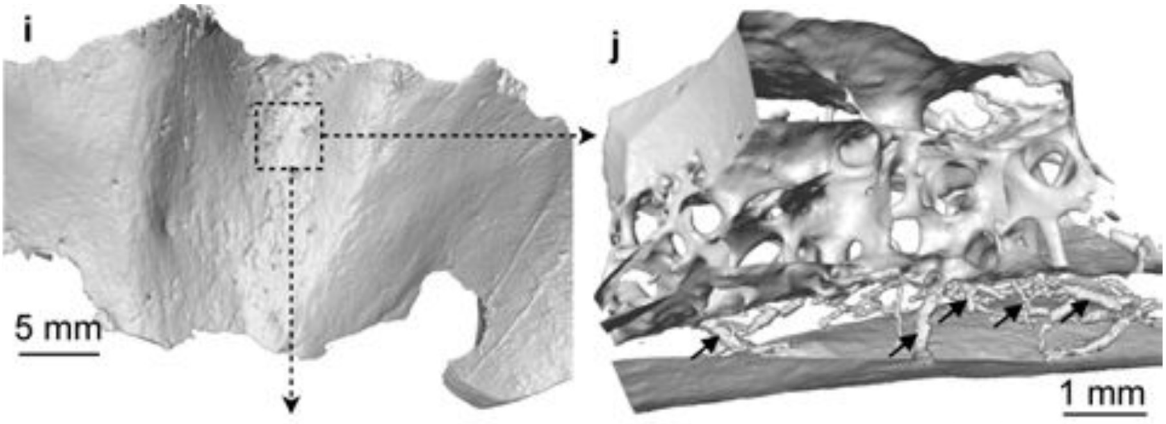

Figure 7 : Canaux du crâne

Canaux microscopiques permettant la communication entre la moelle osseuse et la vascularisation des méninges au travers du crâne. Microtomodensitométrie sur fragment d'os occipital humain. D'après Herisson et al., 2018.

Bases moléculaires du transport de l'eau : les aquaporines du SNC

Les aquaporines sont une famille de **canaux protéiques transmembranaires perméables à l'eau** exprimées dans l'ensemble du vivant. Leur découverte en 1992 par Peter Agre et son équipe dans la membrane des globules rouges a été récompensée par le prix Nobel de chimie en 2003.

Chez les mammifères, il existe 13 types d'aquaporines, principalement dédiées à faciliter le transport de l'eau au travers des membranes. Le cerveau humain exprime les **types I, IV et IX** (Verkman, 2012).

Elles se caractérisent par une structure en **six hélices α**, arrangées autour d'un pore au travers de la membrane. Les aquaporines peuvent s'assembler en **homotétramères**, l'interstice central formant alors un pore supplémentaire.

Les aquaporines ne se limitent pas au transport de l'eau. Le sous-groupe des aquaglycéroporines (types III, VII, IX et X) est perméable aux petites molécules polaires (glycérol, urée, lactate), et le pore central des tétramères formés par les types I, IV et V est perméable aux gaz (Badaut et al., 2014; Nagelhus and Ottersen, 2013).

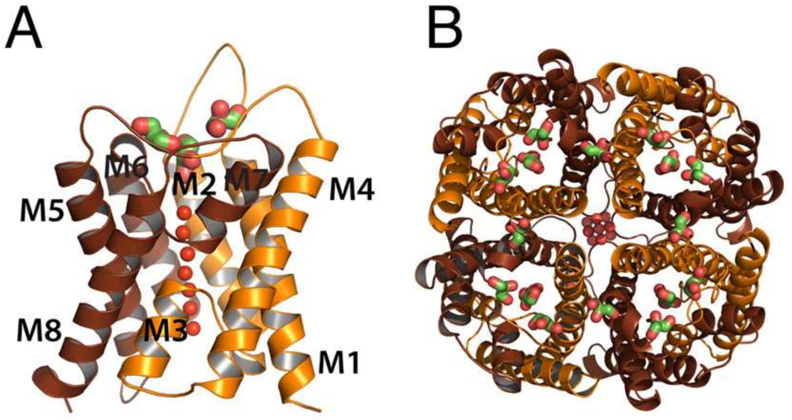

Figure 8 : Structure moléculaire de l'auaporine de type IV

Monomère en vue latérale (A) et homotétramère en vue supérieure (B). Des molécules d'eau sont représentées à l'emplacement des pores. Reconstruction à partir de données cristallographiques, d'après Ho et al., 2009.

Aquaporine de type IV

Dans le SNC, l'**aquaporine de type IV (AQP4)** est exprimée par les épendymocytes et les **astrocytes**. Chez ces derniers, elle se localise surtout au niveau de leurs pieds (projections) en bordure des vaisseaux (glie limitante vasculaire) et du SNC (glie limitante superficielle). L'AQP4 est aussi retrouvée en périphérie des synapses.

En plus de l'assemblage en tétramères, les AQP4 peuvent former des **ensembles orthogonaux de particules (EOP)** rassemblant plusieurs centaines d'unités, au travers desquels la diffusion de l'eau est amplifiée. La constitution de ces EOP est régulée par deux isoformes produites par épissage alternatif : M1-AQP4 et M23-AQP4. Les deux participent à la formation des EOP, M23-AQP4 étant la plus favorable. Le ratio d'expression de ces deux formes définit la taille des EOP (de Bellis et al., 2021).

L’AQP4 intervient dans la régulation des volumes d’eau du SNC en créant au travers des astrocytes des routes entre les synapses et les espaces liquidiens. La présence de canaux potassique Kir près des AQP4 suggère l'implication de ces dernières dans l’**homéostasie ionique** (Nagelhus and Ottersen, 2013).

En conditions pathologiques, l’AQP4 est impliquée dans la **formation et la résorption des œdèmes** (Papadopoulos et al., 2004). Ainsi, dans les modèles d’AVC transitoires, l’expression de l’AQP4 sur les pieds astrocytaires augmente dans la phase aigüe de l’ischémie et est corrélée au gonflement tissulaire. En parallèle, le degré d’expression d’AQP4 est inversement corrélé au temps nécessaire à la résolution de l’œdème (Badaut et al., 2014).

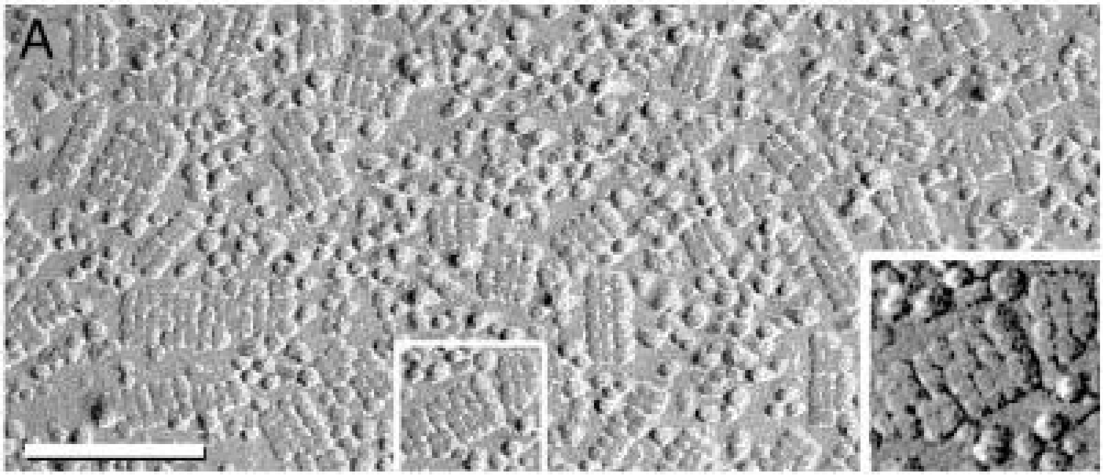

Figure 9 : Ensembles orthogonaux de particules formés par l'AQP4

Miscroscopie électronique à balayage de la face extracellulaire des pieds astrocytaires (glie limitante). Les tétramères d'AQP4 s'arrangent en ensembles orthogonaux. Barre d'échelle : 100nm. D'après Furman et al., 2003.

Plusieurs molécules peuvent **inhiber** les AQP4. En particulier, le **2-(nicotinamide)-1,3,4-thiadiazole (TGN-020)** est capable de se fixer réversiblement dans les pores de l'isoforme M23, obstruant ainsi le passage de l'eau (Huber et al., 2009). Le TGN-020 ne présente pas d'autres effets biologiques notables et son utilisation permet de réduire la formation de l'œdème cérébral après un AVC chez la souris (Abir-Awan et al., 2019).

La **neuromyélite optique** est une maladie auto-immune dirigée contre les AQP4. Elle se traduit par des atteintes de la moelle épinière et du nerf optique, qui causent une paralysie, des troubles de la vision et des vomissements (Huda et al., 2019).

Aquaporines de type I et IX

Dans le SNC, l’**aquaporine de type I (AQP1)** est principalement exprimée par l’EPC où elle contribue à la **formation du LCR**.

L’**aquaporine de type IX (AQP9)** est une aquaglycéroporine présente chez les astrocytes, les cellules endothéliales et les neurones catécholaminergiques. Elle est impliquée dans la régulation du **métabolisme énergétique** en permettant le passage de nutriments au travers des membranes (Badaut et al., 2014).

Résumé / *Abstract*

- La protection physique du SNC est assurée par les **os crâniens**, la **colonne vertébrale** et les **méninges**.
- La **boîte rigide** formée par le crâne crée un environnement très sensible aux variations de volume et de pression.
- Les **méninges** compartimentent la cavité crânienne, supportent les vaisseaux cérébraux et sont desservies par le système lymphatique.
- Le SNC est suspendu dans le **bain de LCR** par les trabécules arachnoïdiens
- Les **aquaporines** sont à la base du transport de l'eau dans le SNC, en particulier l'AQP4
- Le SNC bénéficie d'un "**privilège immunitaire**". Son entretien et sa surveillance sont assurés par des **macrophages** résidents spécialisés.

- The **cranial bones**, the **spine** and the **meninx** protect the central nervous system against physical trauma.
- Within the **rigid box** of the skull, changes of volume are related to intracranial pressure changes.
- The **meninx** creates compartiments within the cranial cavity and support the cerebral vascularization. They benefit from lymphatic drainage.
- The arachnoid trabeculae suspend the central nervous system within the **bath of cerebrospinal fluid**.
- **Aquaporins**, and more specifically aquaporin type IV, are the molecular bases of water transport within the central nervous system.
- The central nervous system is an **immune-privileged organ** whose protection is ensured by specialized, resident **macrophages**.

Liquide céphalo-rachidien

Les premières mentions du LCR sont attribuées à Imhotep, un célèbre savant Egyptien qui aurait vécu il y a plus de 4000 ans. De la théorie du *spiritus animalis*, chère à Galien et Descartes, à la 'troisième circulation' décrite par Harvey Cushing, la compréhension de ce fluide est passée par l'élaboration d'une multitude de modèles.

Loin d'être passif, le LCR est un acteur majeur dans une variété de conditions physiopathologiques telles que les hydrocéphalies ou les œdèmes cérébraux. C'est aussi un axe de circulation pour diverses substances dès le développement embryonnaire. La sécrétion, la circulation et l'excrétion du LCR sont coordonnées avec précision et varient selon la posture, l'activité physique, le sommeil et l'âge.

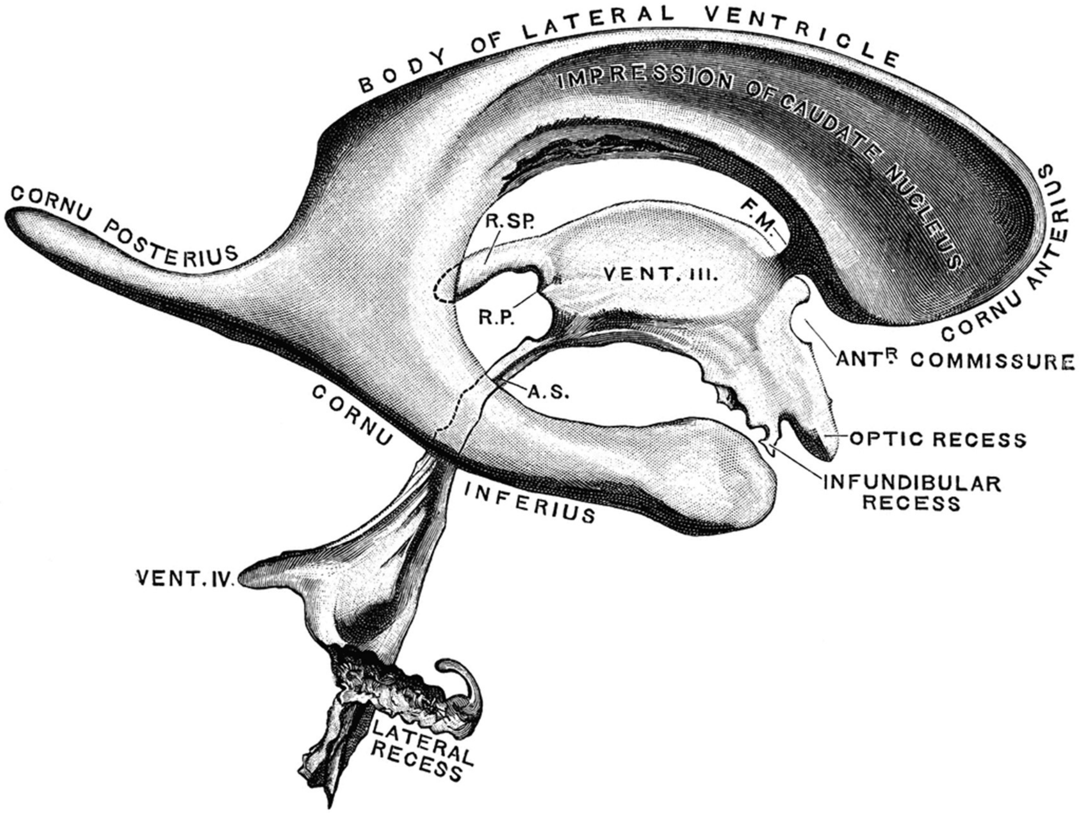

Figure 10 : Système ventriculaire

Vue latérale droite. D'après Florida Center for Instructional Technology

Historique

Les premières traces du liquide céphalo-rachidien nous viennent des sables d'Egypte. Le **papyrus de Smith**, datant de 1600 av. J.-C., relate plusieurs cas médicaux, notamment une fracture du crâne où est décrite la fuite d'un fluide suite à la rupture des méninges. Le papyrus étant lui-même une copie de textes plus anciens attribués à **Imhotep**, la découverte de ce qui deviendra le LCR remonterait à plus de 4000 ans (Herbowski, 2013). De plus, la présence de **crânes trépanés** datant de plusieurs millénaires sur tous les continents suggère que nos ancêtres avaient notion de l'hypertension intracrânienne dès la fin du **paléolithique** (Alt et al., 1997).

La **médecine gréco-romaine** empruntera beaucoup aux textes égyptiens, mais la notion de liquide s'éclipsera pour un temps. En effet, Hérophile de Chalcédoine, qui évoque le système ventriculaire vers 300 av. J.-C., semble **ignorer la présence de LCR**. Vers l'an 200, Galien décrit avec précision les méninges, le système ventriculaire et les plexus choroïdes. Le médecin perse soutiendra l'idée de ***spiritus animalis***, une vapeur emplissant les ventricules cérébraux et censée véhiculer l'énergie du corps. Les dissections étant prohibées pendant le Moyen-Âge, cette théorie restera pour un temps la vision officielle (Herbowski, 2013).

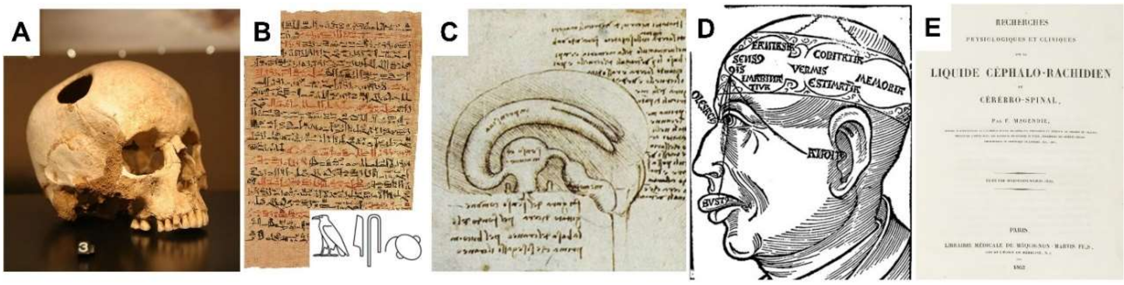

Figure 11 : Histoire de la découverte du LCR

Crâne trépané préhistorique (-7000) (A) ; Papyrus de Smith dans lequel se trouve la première description connue du LCR (-1600) et hiéroglyphes associés au cerveau (B) ; Croquis de Léonard de Vinci représentant le système ventriculaire d'après un moulage à la cire (1504) (C) ; Schéma présentant la théorie du spiritus animalis (1525) (D) ; Première mention du terme 'liquide céphalorachidien' dans un rapport d'expériences de François Magendie (1842) (E).

Avec la **Renaissance**, les dissections sont à nouveau autorisées. Léonard de Vinci, par des **injections de cire dans le système ventriculaire**, parviendra à en saisir la forme qu'il reproduira sur le papier. À mesure des observations, il devient apparent que le modèle du *spiritus animalis* est faux et que les ventricules sont emplis de liquide. Nicolo Massa en 1536 est l'un des premiers à défendre cette idée. En revanche, la théorie d'un fluide vital apporté au corps par les nerfs reste prégnante et défendue notamment par Marcello Malpighi en 1665. Peu à peu, **la thèse d'une substance fluide est acceptée**. En 1764 Domenico Felice Cotugno décrira cette ***aqua ventriculorum***, dont il proposera qu'elle circule dans les ventricules. Deux sites majeurs d'excrétion du LCR, les granulations arachnoïdiennes et les vaisseaux lymphatiques méningés, seront décrits respectivement en 1705 par Pacchioni et en 1787 par Mascagni, qui en ignorent le rôle (Herbowski, 2013).

Dès la fin du XVIII^{ème} siècle, l'existence d'un fluide en circulation dans le système ventriculaire est globalement acceptée. En 1783, Alexander Monro et George Kellie décrivent **le crâne comme un système fermé**, dont les contenus (sang, cerveau et LCR) doivent s'ajuster en permanence sous peine d'altérer la pression intracrânienne, une idée fondatrice de la neurochirurgie. François Magendie proposera le terme **'liquide céphalo-rachidien'** dès 1842, démontrant la communication entre les ventricules et l'espace sous-arachnoïdien et introduisant des techniques permettant d'en mesurer la pression. En 1876, Key et Retzius, observant qu'un colorant injecté dans l'espace sous-arachnoïdien fuyait par les **granulations arachnoïdiennes** dans le sang veineux, proposent ces structures comme site d'excrétion du LCR, soutenus par Weed en 1914. Quincke développe la **ponction lombaire** en 1891, qui permettra des études poussées sur du LCR prélevé sur ses patients. Les expériences de Paul Ehrlich et d'Edwin Goldman au début du XXème siècle montrent qu'une teinture injectée dans la circulation générale n'atteint pas le cerveau. Inversement, une teinture injectée dans le LCR ne passe pas dans la circulation générale. Ces résultats mèneront à la découverte de la **barrière hémato-encéphalique**. En 1919, Walter Dandy, observant un effondrement du ventricule latéral suite à une plexectomie, soutiendra que les **plexus choroïdes** sont le seul organe à sécréter du LCR. En compilant les résultats de ses contemporains, Harvey Cushing décrira en 1925 la **'troisième circulation'**, de la production du LCR par les plexus choroïdes jusqu'à son absorption par les villosités arachnoïdiennes, ce qui restera le modèle dominant jusqu'à aujourd'hui (Herbowski, 2013).

Maintenant que les grandes lignes du système du LCR sont tracées, la recherche se focalisera sur la compréhension de ses mécanismes. Michael Földi observe dès 1968 que des teintures injectées dans le LCR se retrouvaient dans les nœuds lymphatiques cervicaux, suggérant une **communication entre LCR et système lymphatique** dont il suggèrera que les **espaces périvasculaires** sont le chaînon manquant (Földi et al., 1968). Cette hypothèse est reprise par Helen Cserr dès 1977, avec l'hypothèse de flux liquidiens le long des **voies de moindre résistance**, incluant les espaces périvasculaires mais aussi les faisceaux de substance blanche (Cserr et al., 1977). En 1992, Peter Agre et son équipe découvrent les **aquaporines**, canaux protéiques spécifiques à l'eau, ce qui lui vaudra le prix Nobel de chimie en 2003 (Agre, 2004). Dans les années 2000, le groupe de Roxana Carare reprend l'idée des voies de moindre résistance dans le SNC et suggère que le FISC est drainé dans la **membrane basale des artères** (Carare et al., 2008). De son côté, le groupe de Maiken Nedergaard propose le terme de "**système glymphatique**" en 2012 pour évoquer la circulation périvasculaire et intra-parenchymateuse du LCR (Iliff et al., 2012). Les groupes de Jonathan Kipnis et Kari Alitalo redécouvrent simultanément en 2015 les **canaux lymphatiques méningés** (Aspelund et al., 2015; Louveau et al., 2015).

Le système ventriculaire

Anatomie

Chez les êtres humains et la plupart des mammifères, le cerveau contient **quatre ventricules** remplis de LCR qui communiquent entre eux et avec l'espace sous-arachnoïdien par des foramens et des aqueducs. Les deux ventricules latéraux décrivent une large boucle dont l'ouverture est orientée vers l'avant. Ils abouchent par leur extrémité antéro-supérieure dans le troisième ventricule qui se trouve en position centrale. Ce troisième ventricule communique avec le quatrième ventricule, qui se trouve dans le pont, par l'**aqueduc de Sylvius**.

Les **plexus choroïdes**, principaux producteurs du LCR, se retrouvent dans chacun des ventricules sous la forme de structures très vascularisées. L'ensemble du système ventriculaire est tapissé par l'**épendyme**.

Le LCR quitte le système ventriculaire pour se jeter dans l'espace sous-arachnoïdien par les **foramens de Luschka et de Magendie**, présents au niveau du quatrième ventricule.

A la suite du quatrième ventricule et courant tout le long de la moelle épinière se trouve le **canal de l'épendyme**, un reliquat du tube neural. L'extrémité caudale de ce canal présente parfois un cinquième ventricule sous la forme d'un léger renflement (Spector et al., 2015b).

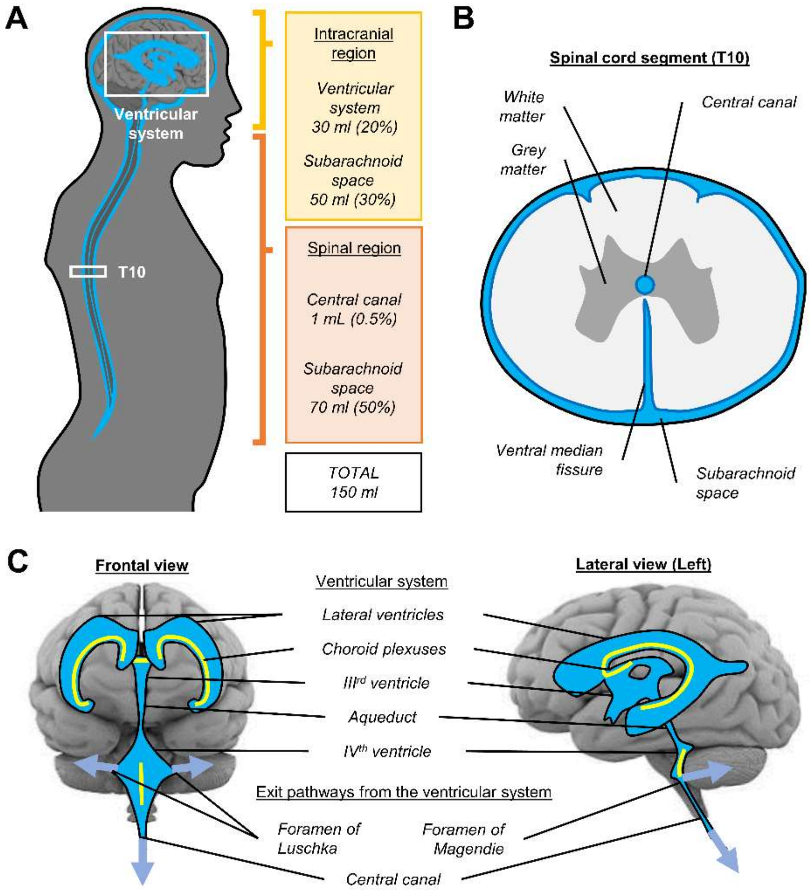

Figure 12 : Structures du LCR

Compartiments contenant le LCR (en bleu) dans l'organisme (A), au niveau de la moelle épinière (B) et de l'encéphale (C).

Embryogenèse

La formation du SNC débute dès les premiers stades embryonnaires. Lors de la neurulation primaire (semaines 3-4 post-conception), une portion dorsale de l'ectoderme se spécialise en neurectoderme, lequel formera un canal parcourant l'embryon sur toute sa longueur, le **tube neural**. Vers la fin de la neurulation, la partie antérieure du tube neural va se développer et se scinder en vésicules pour former l'encéphale, alors que la partie dorsale deviendra la moelle épinière (Bueno et al., 2020).

Le contenu du tube neural est une **forme embryonnaire du LCR (eLCR)** enrichie de **facteurs trophiques** chargés de guider le développement de l'organisme. Dès la fermeture du tube neural, la pression de l'eLCR augmente et crée une **force expansive** qui stimule la division cellulaire (Bueno et al., 2020).

La production de l'eLCR reste à élucider, notamment pour les stades précédant l'apparition des plexus choroïdes (7ème semaine). L'**interface sang-eLCR** est déjà régulée, et pourrait impliquer des cellules situées à l'avant du tube neural, distinctes des futurs plexus choroïdes (Bueno et al., 2020).

Ces derniers ont une double origine, mésenchymateuse et neurectodermique. De la première dérivent les cellules stromales et de la seconde l'épithélium sécréteur. Les cellules épithéliales maturent au travers de 4 stades développementaux au cours desquels elles acquièrent leur polarisation, leurs cils et leurs microvillosités (Lun et al., 2015).

Aux stades fœtaux (à partir de la 11ème semaine post-conception), le LCR conserve son rôle trophique, mais **sa concentration en protéines va progressivement décliner jusqu'à la naissance** (Bueno et al., 2020).

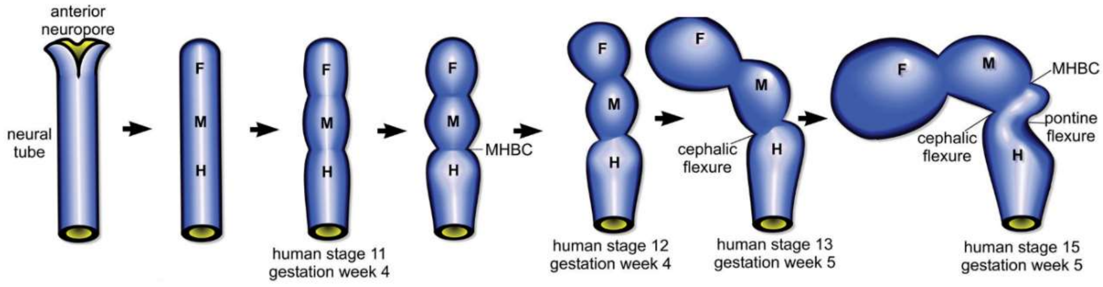

Figure 13 : Embryologie de l'encéphale

Vue latérale gauche des transformations du tube neural aboutissant à la formation de l'encéphale. Le système ventriculaire correspond à la lumière du tube, conservée dans les vésicules cérébrales du prosencéphale (F), du mésencéphale (M) et du rhombencéphale (H). D'après Lowery et SIve, 2009.

Anomalies du développement

Plus d'un enfant sur 1000 est atteint d'**hydrocéphalie** à la naissance. Les étiologies sont variées (sténoses, tumeurs, kystes, ciliopathies, hémorragies) et se traduisent souvent par une obstruction du circuit du LCR (Kahle et al., 2016).

Les **défauts du tube neural** regroupent des troubles sévères causés par une absence de fermeture du tube neural. Ils se traduisent par des hernies du SNC hors du corps (moelle épinière : spina bifida ; encéphale : exencéphalie) voire une absence totale ou partielle de l'encéphale (anencéphalie, craniorachischisis). L'acide folique (Vitamine B9) est un facteur protecteur (Greene and Copp, 2014).

Les **troubles du spectre autistique (TSA)** sont un ensemble de conditions caractérisées par des déficits dans la communication sociale et des comportements stéréotypés. Des travaux récents ont mis en évidence un lien entre un surplus de LCR hors du système ventriculaire et les TSA (Shen et al., 2017, p. 201).

Épendyme

Le système ventriculaire et le canal de l'épendyme disposent de leur propre revêtement : l'épendyme. Cette membrane consiste en une couche unique de cellules ciliées, les **épendymocytes**. La surface des cellules, au contact du LCR, présente des microvillosités ainsi qu'un cluster central de **cils**. Des jonctions serrées et des jonctions gap unissent les épendymocytes, les premières limitant les passages paracellulaires et les secondes facilitant leur coordination. Sous l'épendyme se trouve une fine membrane basale, traversée par des processus astrocytaires qui contactent le pôle basal des épendymocytes (Del Bigio, 2010). L'**AQP4**, canal perméable à l'eau, est exprimée aux pôles basolatéraux des épendymocytes où elle joue également un rôle structurel (Li et al., 2009).

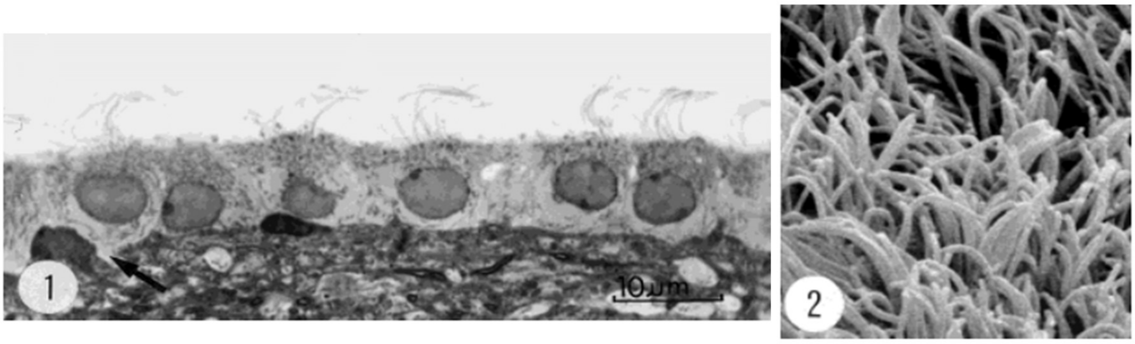

Figure 14 : Ependymocytes vus en microscopie électronique

Vue en coupe montrant la couche unicellulaire (1) et vue en microscopie électronique à balayage du tapis formé par les cils (2). D'après Bruni, 1998.

Les cils des épendymocytes sont animés d'un **battement synchronisé** qui balaie le LCR dans son sens d'écoulement. Cette motilité ciliaire est particulièrement importante au cours du développement embryonnaire, où elle permet la définition des axes de symétrie du corps. Les dyskinésies ciliaires peuvent ainsi avoir pour conséquence un *situs inversus* cérébral (Jiménez et al., 2014). D'autres cellules de l'épendyme possèdent des **mécanorécepteurs** sensibles aux flux du LCR et contribuent à la régulation de sa production (Ludwig et al., 2021).

L'épendyme bénéficie d'une **innervation** double : un réseau d'axones glutamatergiques à sa surface et des axones dopaminergiques à sa base. Ces deux systèmes sont supposés réguler le métabolisme des épendymocytes ainsi qu'aider à la synchronisation du battement des cils (Del Bigio, 2010). Des terminaisons nerveuses ciliées traversent régulièrement l'épendyme, notamment au niveau du canal central. Ces **cils sensitifs** permettent de détecter la torsion de la colonne vertébrale et sont impliqués dans le contrôle de la locomotion (Böhm et al., 2016). D'autres terminaisons nerveuses sont impliquées dans la **transmission de messagers *via* le LCR** (Jalalvand et al., 2018; Song et al., 2020).

Fonctionnelle au cours du développement embryonnaire, **la barrière formée par l'épendyme perd en efficacité avec l'âge** (Whish et al., 2015). Malgré la présence de **cellules neuroépithéliales** dans la zone sous-ventriculaire qui contribuent à le régénérer (Jiménez et al., 2014), l'épendyme perd peu à peu en superficie, les plages perdues se trouvant remplacées par des cellules gliales non ciliées. Dépourvu de cette barrière, le tissu périventriculaire devient œdémateux alors que les ventricules gagnent en volume du fait de l'accumulation de LCR (Shook et al., 2014).

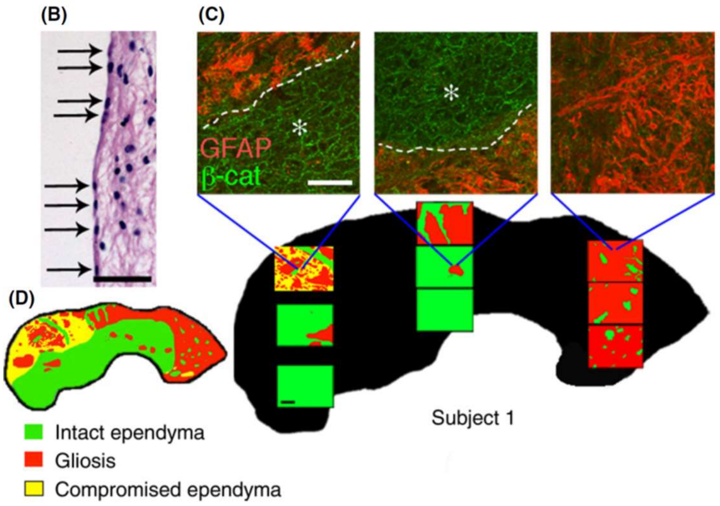

Figure 15 : Perte d'intégrité de la barrière épendymaire avec l'âge

Observations post-mortem de la paroi du ventricule latéral chez une femme de 82 ans. L'épendyme présente des régions où les épendymocytes (marquage β-caténine, en vert) ont été remplacés par des prolongements atrocytaires inflammatoires (marquage GFAP, en rouge).

Organes circumventriculaires

En périphérie du système ventriculaire se trouvent des structures spécialisées, les organes circumventriculaires (OCV) dont le trait commun est une **absence de la BHE**. Au contraire, les capillaires qui les irriguent sont très perméables (**fenestrés**). Les OCV sont habituellement divisés entre **structures sécrétrices** (dont font partie les plexus choroïdes) et **structures sensorielles**.

Parmi les structures sécrétrices se trouve la **glande pinéale**. Elle se trouve dans le troisième ventricule et joue un rôle clé dans la régulation du rythme circadien en fonction de la luminosité par la production de mélatonine. La glande pinéale est un vestige du troisième œil présent chez les ancêtres des vertébrés. La **neurohypophyse**, qui forme la glande pituitaire avec l'adénohypophyse, est un autre OCV sécréteur. La neurohypophyse secrète l'ocytocine, impliquée dans les processus liés à l'attachement et à la parentalité, et la vasopressine, intervenant dans la régulation de la tension artérielle (Kiecker, 2018).

L'**organe subfornical**, l'**organe vasculaire de la lame terminale** et l'**organe subcommissural** font partie des structures sensorielles. Ils sont situés en périphérie du troisième ventricule et interviennent dans la perception et la régulation de la natrémie (taux de sodium dans le sang). L'**éminence médiane**, autre structure sensorielle, se trouve sur le plancher du troisième ventricule et le sépare de l'espace sous-arachnoïdien. Les **tanycytes**, des épendymocytes particuliers, y joignent capillaires fenestrés et troisième ventricule. L'éminence médiane interviendrait entre autres dans la régulation de l'appétit. Enfin, l'**area postrema** se situe sur le bord inférieur du quatrième ventricule et permet le vomissement en réponse à la détection de composés inhabituels dans le LCR (Kiecker, 2018).

Durant le développement, l'organe subcomissural sécrète la **fibre de Reissner**, un filament qui s'étend jusqu'à la citerne lombaire et guide la croissance de l'organisme (Aboitiz and Montiel, 2021).

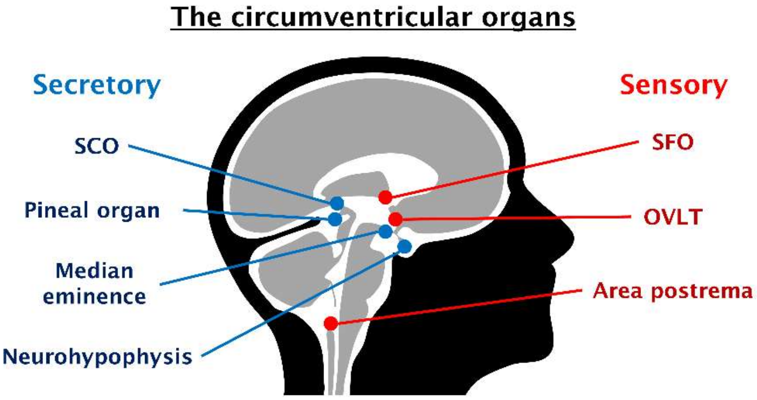

Figure 16 : Organes circumventriculaires

Localisation des organes circumventriculaires sécréteurs et sensoriels. SCO : organe sous-commissural, SFO : organe subfornical, OVLT : organe vasculaire de la lame terminale.

Plexus choroïdes

Les plus conséquents des OCV sont les plexus choroïdes. Il s'agit de formations intraventriculaires présentant un aspect de dentelle flottante dans le LCR. À l'échelle macroscopique, les quatre plexus choroïdes présentent des aspects distincts : un voile fin et ondulé dans les ventricules latéraux, une structure complexe et lobulaire dans le quatrième ventricule, et une forme intermédiaire dans le troisième ventricule (Strazielle and Ghersi-Egea, 2000).

Ces différences s'estompent au niveau microscopique, les plexus choroïdes partageant une structure similaire. Ils sont revêtus d'un épithélium cubique spécialisé, doté de **microvillosités** et de cils motiles au pôle luminal (en contact avec le LCR). Les microvillosités présentes au pôle luminal des cellules de l'épithélium des plexus choroïdes créent une surface d'échange conséquente avec le LCR, entre 2 et 5 m² chez les êtres humains (Spector et al., 2015a). Les cellules contiennent de nombreuses mitochondries et sont unies par des jonctions serrées. L'épithélium des plexus choroïdes (EPC) constitue la **barrière sang-LCR**, responsable de la formation de la majeure partie du LCR. L'EPC repose sur un stroma conjonctif irrigué par des **capillaires fenestrés**. Dans ce stroma sont présents des macrophages et des cellules dendritiques, tandis qu'à la surface des plexus se trouvent des macrophages spécialisés, les cellules de l'épiplexus (Kaur et al., 2016).

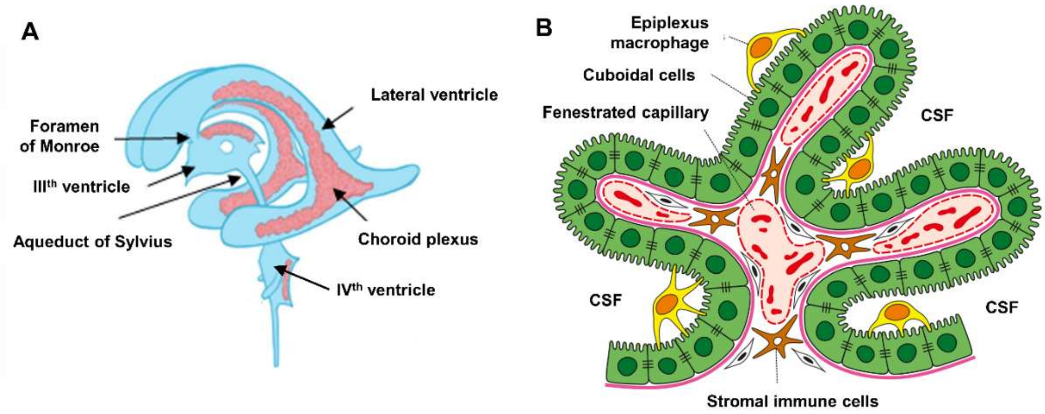

Figure 17 : Plexus choroïdes

Localisation des plexus choroïdes dans le système ventriculaire, un par ventricule (A), et détail de leur structure (B). Adapté d'après Oreskovic et al., 2017 ; et Solar et al., 2020.

L'alimentation des plexus choroïdes provient à la fois des artères carotides internes et des artères vertébrales. Les plexus des ventricules latéraux sont irrigués par les artères choroïdales antérieures (issues de l'artère cérébrale moyenne) et postérieures (issue de l'artère cérébrale postérieure). Les artères choroïdales postérieures alimentent aussi le plexus du troisième ventricule, tandis que celui du quatrième ventricule est desservi par les artères cérébelleuses antéro- et postéro-inférieures (Damkier et al., 2013). Plusieurs types de fibres nerveuses affèrent aux plexus choroïdes, notamment des fibres parasympathiques dont la stimulation ralentit la production de LCR (Ellis et al., 2000). D'autres transmetteurs comme la sérotonine stimulent la sécrétion (Shipley et al., 2020).

Les plexus choroïdes ne se limitent pas à leur rôle sécrétoire et contribuent à la **clairance** de certains composés présents dans le LCR en les excrétant dans le sang (Spector et al., 2015a, 2015b). La présence des capillaires fenêtrés permet le passage des leucocytes dans le LCR (Kivisäkk et al., 2003), mais aussi de divers pathogènes (Schwerk et al., 2015). Les plexus choroïdes sont ainsi impliqués dans la réaction du SNC face à de nombreuses pathologies (Solár et al., 2020).

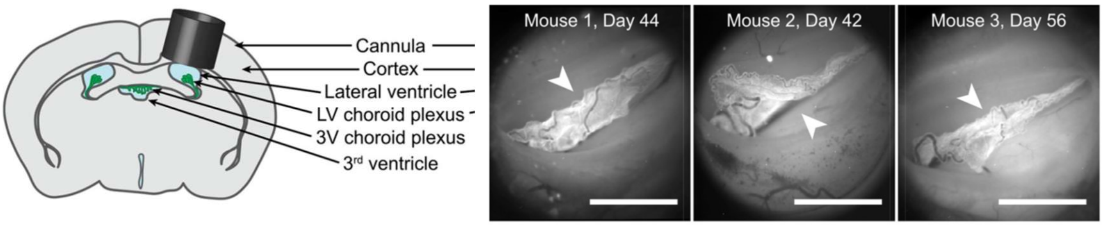

Figure 18 : Plexus choroides observés in vivo chez la souris

Une fenêtre donne accès au ventricule latéral et permet l'observation des plexus choroïdes chez une souris vigile (l'animal est maintenu sur une plate-forme mobile). Cette étude a permis de montrer l'existence de vagues calciques dans le plexus qui augmentent sa sécrétion et dépendent de la sérotonine. D'après Shipley et al., 2020.

Composition et production du LCR

L'EPC est considéré comme l'**acteur principal de la production du LCR**. Malgré les controverses avancées par certaines équipes (Oresković and Klarica, 2010), ce modèle est soutenu par un corpus majoritaire dans la littérature (Brinker et al., 2014; Spector et al., 2015a, 2015b). Les cellules épithéliales des plexus choroïdes (cEPC) sont fortement polarisées et expriment une variété de **transporteurs**, actifs et passifs, à leurs pôles basolatéraux et luminal. La compréhension des mécanismes impliqués dans la sécrétion du LCR est passée par l'élaboration de nombreux modèles et reste incomplète à ce jour (Damkier et al., 2013).

Composition comparée du sang et du LCR			
		LCR	**SANG**
Aspect		Clair	Rouge
Volume (ml)		90 – 250	4500 – 5700
pH		7,28 – 7,32	7,35 – 7,45
Pression (mmHg)		0 *(haut)* 30 *(bas)*	120 *(systole)* 80 *(diastole)*
Ions ($mmol.l^{-1}$)	Na^+	140	142
	K^+	3	5
	Mg^{2+}	4	1.5
	Ca^{2+}	2,5	2,5
	Cl^-	120	103
	HCO_3^-	20	27
Glucose (mg/dl)		45 – 80 (2:3 sang)	80 – 110 (à jeun)
Protéines et peptides	*Total (g/l)*	0,2 – 0,5	60 – 80
	Albumine (g/l)	0,12 – 0,3	35 – 55
	IgG (g/l)	< 0,04	7 – 16
Cellules (ç/µl)	*Leucocytes*	>5	4 500 – 11 000
	Hématies	0	4,2 M – 6 M

Tableau 1 : Composition comparée du sang et du LCR

Composition

Le LCR est un fluide biologique incolore produit par le système ventriculaire. Chez les êtres humains, un volume de **150 ml de LCR** est souvent cité (Spector et al., 2015a) mais des études plus récentes en IRM trouvent une quantité supérieure (~250 ml) (Chazen et al., 2017). Ce volume est **renouvelé quatre à cinq fois par jour**. La composition du LCR est semblable à celle du plasma à l'exception des protéines et des cellules, beaucoup moins nombreuses (Spector et al., 2015b).

Production du LCR

La force motrice de la production du LCR est fournie par la **pompe Na^+/K^+ ATPase**, fortement exprimée au pôle luminal des cEPC. En revanche, le transport des ions Na^+ au travers de la membrane basolatérale reste mal connu. Il pourrait dépendre de pompes Na^+/HCO_3^- de type NCBE ou NCBn2 (Damkier et al., 2013).

L'**ion bicarbonate HCO_3^-** est un acteur essentiel de la sécrétion du LCR par les plexus. L'**anhydrase carbonique** est une enzyme catalysant la production d'HCO_3^- à partir d'H_2O et de CO_2. En plus de son isoforme cytosolique ubiquitaire CAII, les cEPC expriment ses isoformes membranaires CAXII et CAIX. En clinique, les inhibiteurs de cette enzyme, tel que l'acétazolamide, diminuent la production de LCR et sont utilisés dans le traitement du glaucome ou du mal des montagnes (Damkier et al., 2013).

Le passage de l'eau est facilité au travers des cEPC par la présence d'**AQP1** au pôle basolatéral et surtout au pôle luminal. Le transfert préférentiel du sang au LCR serait, quant à lui, conduit par une légère différence d'osmolalité (5 mosM) de part et d'autre de l'EPC. Bien que l'AQP1 joue un rôle certain dans la sécrétion de l'eau du LCR, une partie de l'eau pourrait perméer par les espaces entre cellules (Damkier et al., 2013).

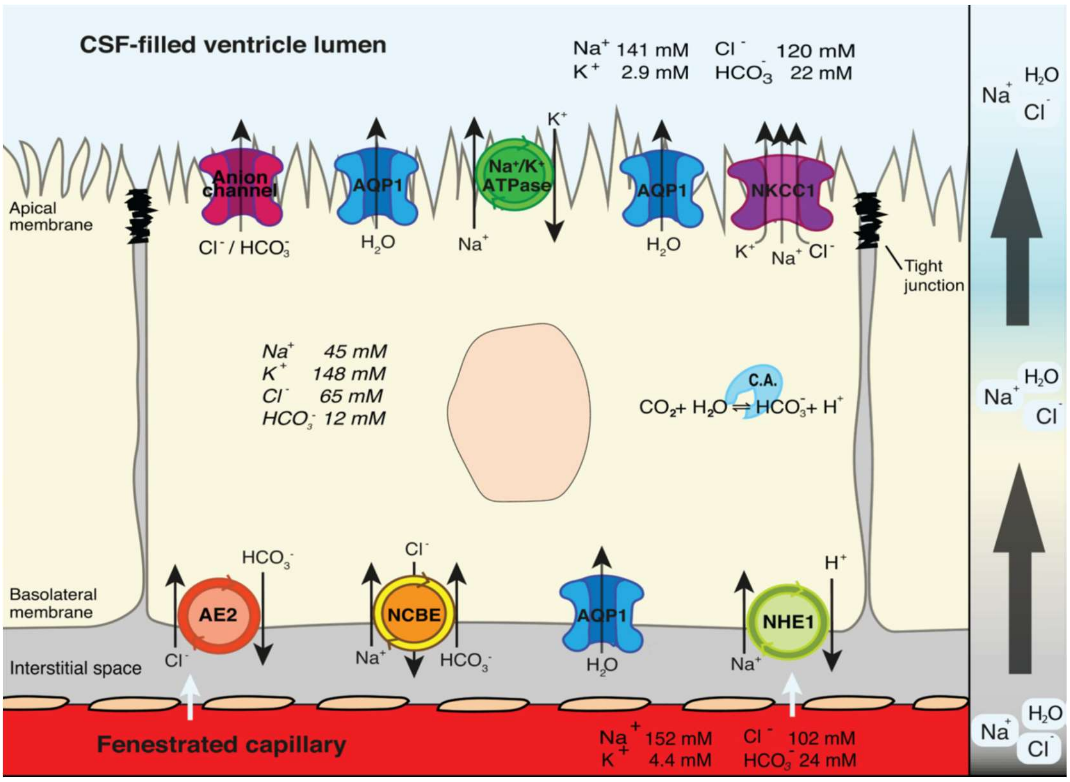

Figure 19: Production du LCR par les plexus choroïdes

Schéma simplifié représentant les transporteurs impliqués dans la production du LCR. La force motrice est assurée par la Na^+/K^+ ATPase, le Na^+ nécessaire à son fonctionnement étant apporté par des échangeurs dépendants de HCO_3^-, ce dernier pouvant être produit sur place par l'anhydrase carbonique. Le gradient osmotique entraîne le déplacement de l'eau, facilité par les aquaporines de type I. D'après Jessen et al., 2015.

Autres molécules

L'EPC **enrichit** le LCR d'une grande variété de substances et intervient dans l'extraction d'autres (Spector et al., 2015a). Quelques exemples sont présentés dans le **tableau 2** ci-dessous.

Exemples de substances secrétées ou extraites du LCR par l'EPC			
	Nom	**Concentration dans le LCR**	**Fonctions**
Substances sécrétées	Ascorbate (Vit. C)	240 µmol/l	Antioxydant, synthèse de la dopamine
	Folate (Vit. B9)	10 ng/ml	Synthèse des nucléotides
	Transthyrétine	7.5 mg/l	Neurogenèse
	Transferrine	1.5 mg/l	Homéostasie du fer
	ApoE	7 µg/ml	Transporteur de lipides
	VEGF	2.7 pg/ml	Angiogenèse
	BDNF-pp	420 pg/ml	Précurseur du BDNF (facteur trophique)
	IGF-2	35 ng/ml	Facteur trophique, neuroprotection
	Leptine	290 pg/ml (F) 140 pg/ml (M)	Régulation de l'appétit, Homéostasie énergétique
Substances extraites	Aβ40 Aβ42	1420 pmol/l 190 pmol/l	Déchets métaboliques Impliqués dans la maladie d'Alzheimer
	HVA	250 pmol/ml	Métabolite de la dopamine
	5-HIAA	100 pmol/ml	Métabolite de la sérotonine
	Pénicilline	N/A	Médicament anti-inflammatoire

Tableau 2 : Exemples de molécules sécrétées ou réabsorbées par les plexus choroïdes dans le LCR

Élimination du LCR

Villosités arachnoïdiennes

Ce sont des invaginations de l'**espace sous-arachnoïdien** dans le **sinus sagittal supérieur**. Les observations des villosités en microscopie révèlent la présence de canaux ne s'ouvrant sur le sang veineux que si la pression du LCR lui est supérieure (équivalents à une **valve anti-retour**). Absentes chez le nourrisson et les petits mammifères (*e.g.* les rongeurs), le nombre et la taille des villosités augmentent avec l'âge (le Gros Clark, 1920). Historiquement considérées comme le seul site d'excrétion du LCR, leur importance a depuis été tempérée, notamment avec la redécouverte des lymphatiques méningés mais aussi des voies périnerveuses. Les villosités sous-arachnoïdiennes sont par ailleurs absentes de la colonne vertébrale (Proulx, 2021).

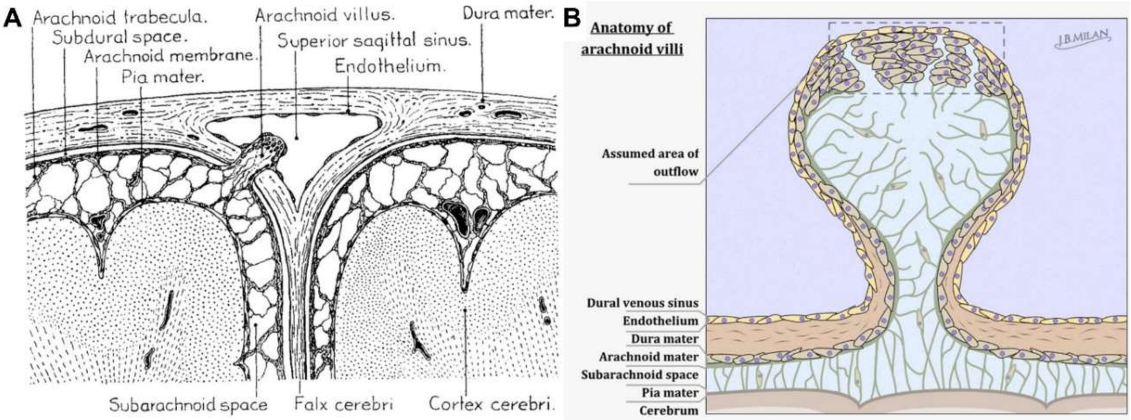

Figure 20 : Villosités arachnoïdiennes

Localisation (A) et structure (B) des villosités arachnoïdiennes. Adapté de Proulx 2021, dessins de Weed et Milan, respectivement.

Lame criblée de l'ethmoïde

La lame criblée est une portion de l'os ethmoïde qui sépare la cavité crânienne des **fosses nasales**. Comme son nom l'indique, elle présente des perforations de la taille d'un trou d'aiguille dont le nombre (40 en moyenne) et la position varient d'une personne à l'autre (Vasvári et al., 2005). Ces orifices permettent le passage des **nerfs olfactifs (I)** vers la muqueuse nasale. À cet endroit, les méninges sont plus fines voire absente dans le cas de la dure mère et remplacées par le périnèvre (feuillet de tissu conjonctif). Un récessus de l'espace sous-arachnoïdien accompagne les nerfs dans les perforations. Bien que des solutés macroscopiques puissent être drainés du LCR au réseau lymphatique, les tenants anatomiques de cette communication restent mal caractérisés (Proulx, 2021). Les canaux lymphatiques de la muqueuse olfactive se drainent ensuite dans les **nœuds cervicaux** le long de la voie jugulaire (Koroulakis et al., 2021). Chez le rongeur, la lame criblée est une zone majeure d'évacuation du LCR vers la lymphe (Ma et al., 2017), mais son importance reste **modeste chez l'être humain** (Proulx, 2021).

Autres voies périnerveuses

De même que pour les nerfs olfactifs, un récessus de l'espace sous-arachnoïdien accompagne le **nerf optique (II)** sur une partie de son trajet. Cependant, le LCR ne semble pas être directement pris en charge par un réseau lymphatique et passerait par l'interstitium du tissu conjonctif de l'orbite avant de rejoindre les canaux lymphatiques de la conjonctive et la voie submandibulaire (Proulx, 2021).

La cochlée (siège de l'appareil auditif situé dans l'oreille interne) est remplie de périlymphe, un liquide en communication avec le LCR *via* le périnèvre du **nerf auditif (VIII)**. La périlymphe est drainée par le réseau lymphatique de l'oreille moyenne, lui-même aboutissant à la voie jugulaire (Koroulakis et al., 2021; Proulx, 2021).

Le foramen jugulaire (trou déchiré postérieur) laisse passage à la veine jugulaire interne, mais aussi à trois nerfs crâniens : le **glossopharyngien (IX)**, le **vague (X)** et l'**accessoire (XI)**. Des expériences utilisant des traceurs suggèrent une communication avec les nœuds lymphatiques cervicaux profonds. Le foramen jugulaire est une des voies transcrâniennes pour le RLM (Proulx, 2021).

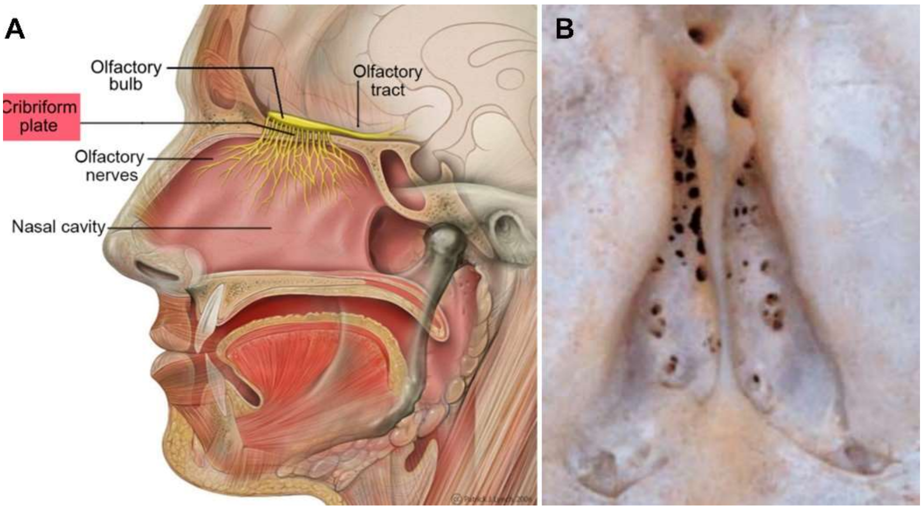

Figure 21 : Lame criblée de l'ethmoïde

Localisation de la lame criblée juste au-dessus des fosses nasales, perforée par les terminaisons olfactives (A). Vue supérieure de la lame criblée montrant les perforations (B). Illustration de PJ Lynch et d'après Vasvari et al., 2005.

Drainage du LCR le long de la moelle épinière

Plusieurs expériences avec injection de traceurs suggèrent que le LCR présent dans l'espace sous-arachnoïdien spinal se draine différentiellement dans le réseau lymphatique. La région cervicale rejoindrait les **nœuds lymphatiques cervicaux**, et la portion lombo-sacrale communiquerait avec les **nœuds abdominaux**. Le passage se ferait par les récessus de l'espace sous-arachnoïdien entourant le départ des **nerfs spinaux**, le long desquels ont été identifiés des **vaisseaux lymphatiques méningés** (Antila et al., 2017; Ma et al., 2019).

Circulation

Système ventriculaire

500 ml de LCR sont produits quotidiennement par les plexus choroïdes. Bien que le système ventriculaire soit en communication avec l'espace sous-arachnoïdien via l'aqueduc, le flux net de LCR implique l'existence d'un gradient de pression entre ces deux compartiments. Ce gradient reste extrêmement faible (0.01-0.03 mmHg) et **les flux de LCR sont principalement influencés par le rythme cardiaque et la respiration** (Vinje et al., 2019). Négligeable par rapport aux autres moteurs, le battement des cils des épendymocytes permet cependant d'éviter la formation de turbulences au contact des parois des ventricules et ainsi de faciliter l'écoulement du LCR (Siyahhan et al., 2014).

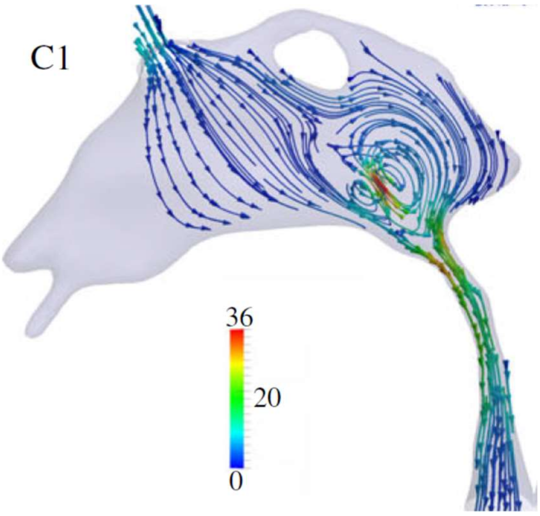

Figure 22 : Modélisation du flux de LCR dans le IIIème ventricule

Flux instantané du LCR à un instant du cycle cardiaque. Le LCR provient des ventricules latéraux depuis le haut et s'échappe par l'aqueduc de Sylvius où il atteint sa vitesse maximale. Le courant forme un vortex permanent à l'entrée de l'aqueduc. Données issues d'une simulation. La vitesse est en mm.s^{-1}. D'après Siyahhan et al., 2014.

Hydrocéphalie : une question de pression ?

La plupart des hydrocéphalies se traduisent par une augmentation de la taille des ventricules. Pourtant, les mécanismes aboutissant à cette distension ne sont pas toujours clairs, en particulier lorsque la circulation du LCR n'est *a priori* pas obstruée (hydrocéphalie communicante) ou que la pression intracrânienne reste dans la norme (hydrocéphalie à pression normale). Ces observations ont amené certaines équipes à reconsidérer le rôle de l'EPC dans la production du LCR (Oresković and Klarica, 2010), mais sont plus vraisemblablement causées par des modifications du **tonus osmotique** dans le tissu cérébral (WILKIE et al., 2012).

Rythmes cardiaque et respiratoire

Le dogme de Monroe-Kellie implique que, dans le compartiment rigide formé par l'encéphale, toute variation du volume d'un de ses constituant (sang, tissu cérébral ou LCR) doit se' faire aux dépends des autres sous peine de modifier la pression intracrânienne (PIC). Animé par les **battements cardiaques**, le flux sanguin artériel est pulsatile, oscillant entre systole (contraction) et diastole (relaxation). Cela se traduit par des **ondes de pression** supersoniques qui parcourent le tissu nerveux et le LCR, amorties par la compliance (élasticité) des veines et de la citerne lombaire. Malgré leur grande vitesse (qui signifient que les oscillations sont quasi-simultanées dans l'organisme), ces ondes de pression ne correspondent pas à un flux net de fluide (Wagshul et al., 2011). En plus de l'activité cardiaque, la **mécanique ventilatoire** est un contributeur essentiel à ces oscillations (Dreha-Kulaczewski et al., 2015, p.).

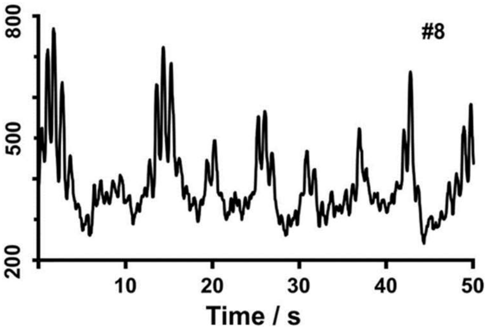

Figure 23 : Oscillations du LCR

Oscillations du LCR mesurées en IRM au niveau de l'aqueduc (unités arbitraires). Les pulsations d'origine cardiaque (périodicité courte) sont superposées aux pulsations d'origine ventilatoire (périodicité longue). D'après Dreha-Kulaczewski et al., 2015.

Sommeil

Plusieurs études ont montré un lien entre sommeil et circulation du LCR. Lors du **sommeil lent profond**, des ondes de grande amplitude apparaissent, possiblement grâce au couplage neurovasculaire (Fultz et al., 2019). La production de LCR est plus importante penant la nuit (Nilsson et al., 1992) et les plexus choroïdes disposeraient d'oscillateurs moléculaires sensibles au rythme circadien (Quintela et al., 2018). Selon certaines équipes, ces flux permettraient d'éliminer les déchets accumulés dans le tissu cérébral au cours des périodes d'activité (Cai et al., 2020; Eide and Ringstad, 2021; Xie et al., 2013).

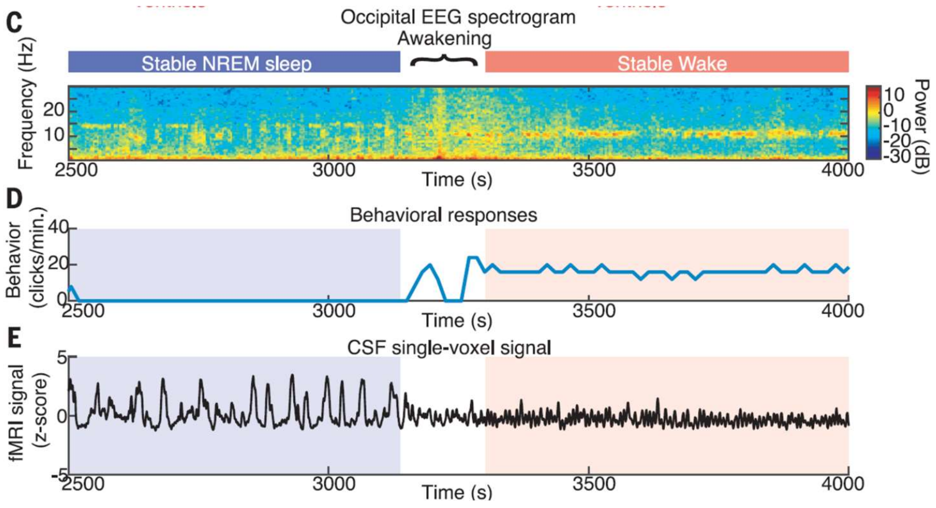

Figure 24 : Oscillations du LCR lors du sommeil lent profond

La vitesse du LCR dans l'aqueduc de Sylvius (E), mesurée en IRM, est corrélée au sommeil lent profond (C) détecté par électroencéphalographie. Les oscillations du flux de LCR deviennent plus lentes et amples pendant cette phase du sommeil. Acquisitions réalisées chez un volontaire sain. D'après Fultz et al., 2019.

Influence de la pesanteur

Chez les êtres humains, la posture bipède a fait des espaces du LCR une **colonne de liquide**.

La pression moyenne dans le LCR dépend de la hauteur à laquelle est faite la mesure. Quasi-nulle au sommet du crâne, elle atteint 30 mmHg au niveau de la citerne lombaire en position debout (Magnaes, 1976).

La pression locale du LCR varie selon la disposition du corps. En position debout, la pression du LCR à la sortie du système ventriculaire est de 3 à 4 mmHg, mais passe à environ 8 mmHg en position allongée (décubitus). La pression du LCR est hétérogène jusque dans la cavité crânienne ; ainsi en décubitus dorsal la pression près du lobe frontal est quasi-nulle tandis qu'elle s'élève à 12 mmHg près du lobe occipital (Bradley, 1970).

Dans les situations d'**impesanteur** telles que les vols spatiaux, le rôle joué par la gravité dans l'homéostasie du LCR devient flagrant. Les astronautes, dont les missions en microgravité peuvent durer plusieurs mois, sont exposés au **syndrome neuro-oculaire associé au vol spatial (SANS)**. Le SANS se traduit par une augmentation de la PIC et une baisse de l'acuité visuelle liée à un glaucome. De nombreux mécanismes liés à l'impesanteur sont à l'origine du SANS, dont l'augmentation du volume de LCR intracrânien, mais aussi du volume sanguin et du taux de CO_2 présent dans le sang ($PaCO_2$) (Marshall-Goebel et al., 2019).

Au sol, l'effet de la microgravité sur le LCR peut être modélisé par un décubitus de la tête légèrement en contrebas suivant un angle de -6° (Marshall-Goebel et al., 2019).

Voies cliniques d'accès au LCR

De par son rôle de filtre, la BHE est souvent un obstacle au passage de médicaments vers le cerveau. En regard, les barrières entre le LCR et le SNC, représentées par la pie-mère, la glie limitante superficielle et l'épendyme, sont beaucoup plus perméables. L'interstitium cérébral est quant à lui dépourvu de barrières, la seule limitation étant liée à la vitesse de diffusion des composés. Ces accès *a priori* plus aisés sont abordés par une variété d'applications cliniques.

L'**injection intrathécale** est faite directement dans le LCR. Chez les êtres humains, elle est réalisée au niveau lombaire pour éviter de piquer dans la moelle. L'**injection épidurale (ou péridurale)** vise à administrer le médicament dans l'espace épidural (entre le ligament jaune et la dure-mère) grâce à un cathéter. Dans ce dernier cas, la distribution du médicament dans le LCR est ralentie par les méninges. Ces voies sont utilisées pour l'analgésie, notamment lors de l'accouchement ou pour le traitement de douleurs chroniques (Farquhar-Smith and Chapman, 2012). La voie intrathécale permet de plus l'administration d'agents de contraste pour l'imagerie des compartiments de LCR (cisternographie) et la détection de fuites (Algin and Turkbey, 2013).

L'**injection intracisternale** est analogue à l'injection intrathécale mais se réalise au niveau de la nuque dans la *cisterna magna* (citerne cérébromédullaire). Plus risquée du fait de la proximité du tissu nerveux, elle est surtout utilisée en préclinique (Zamboni et al., 2020).

L'**injection intraventriculaire (ou intracérébroventriculaire)** est réalisée dans le système ventriculaire grâce à un cathéter. Elle permet d'obtenir une meilleure distribution du médicament dans le LCR qu'une injection intrathécale et est utilisée pour délivrer des agents antinéoplastiques (anticancéreux) et antibiotiques (Atkinson, 2017).

L'**injection facilitée par transport convectif** (CED) est réalisée au moyen d'une aiguille implantée dans le tissu cérébral. Le médicament est administré à de faibles débits (0.1-10 µl/min) afin de se diffuser au travers des espaces interstitiels. Cette technique est utilisée en chimiothérapie (Mehta et al., 2017).

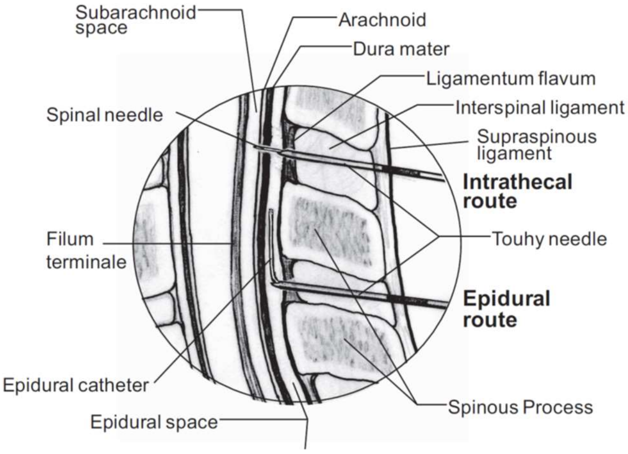

Figure 25 : Voies intrathécale et péridurale

La voie intrathécale est la plus utilisée pour accéder au LCR, par exemple pour une ponction lombaire (prélèvement). Elle est réalisée au niveau de la citerne lombaire, après la terminaison de la moelle épinière. La voie péridurale ne perce pas les méninges et est notamment utilisée pour délivrer les anesthésiques et analgésiques lors de l'accouchement. D'après Farquhar-Smith et Chapman, 2012.

Résumé / *Abstract*

- Le LCR baigne l'ensemble du SNC. Sa **composition est semblale à celle du plasma**, mais plus **pauvre en protéine** et **quasiment exempte de cellules**. Il contient plusieurs **facteurs trophiques** ainsi que des **déchets du métabolisme**.
- Le LCR est principalement produit par les **plexus choroïdes**, des organes spécialisés présent dans le **système ventriculaire.**
- La production du LCR est complexe et dépend notamment des **AQP1** et de l'ion HCO_3^- produit par **l'anhydrase carbonique**.
- La circulation du LCR est **oscillatoire**, parcourue par des ondes de pression d'origine **cardiaque et respiratoire**.
- Le LCR est drainé par le **réseau lymphatique des méninges**, les **voies périnerveuses** et les **villosités sous-arachnoïdiennes**.

- The central nervous system is bathed in cerebrospinal fluid, whose composition is **similar to plasma but poor in proteins and cells**. The cerebrospinal fluid contains both **trophic factors** and **metabolic waste**.
- The cerebrospinal fluid is mostly produced by the **choroid plexus**, specialized structures within the **ventricular system**.
- The production of the cerebrospinal fluid depends notably on **aquaporin type I** and **carbonic anhydrase**, which produces HCO_3^-.
- The circulation of cerbrospinal fluid is **oscillatory** and mostly influenced by **cardiac and respiratory rythms**.
- The cerebrospinal fluid is drained by the **meningeal lymphatics**, the **arachnoid villi** and the **perinervous pathways**.

Sang

Fluide vital par excellence, le sang est une voie de circulation incontournable pour l'ensemble de l'organisme. Le SNC nécessite un apport constant en oxygène pour alimenter son métabolisme, et une ischémie de quelques minutes suffit à endommager irrémédiablement le tissu nerveux (Moskowitz et al., 2010). Cependant, le sang peut aussi être vecteur de toxines et de pathogènes et doit être isolé du SNC par des barrières sélectives.

À tout moment, 100 à 130 ml de sang se trouvent dans la cavité crânienne, dont 15% dans la circulation artérielle, 40% dans la circulation veineuse et le reste (45%) dans la microcirculation. Bien qu'il ne représente que 2% du poids du corps, le SNC reçoit 14% du sang sortant du cœur au repos, soit un débit d'environ 700 ml par minute (Wilson, 2016). Cet afflux massif est finement régulé pour maintenir constante la PIC tout en s'adaptant aux besoins locaux (Cipolla, 2009).

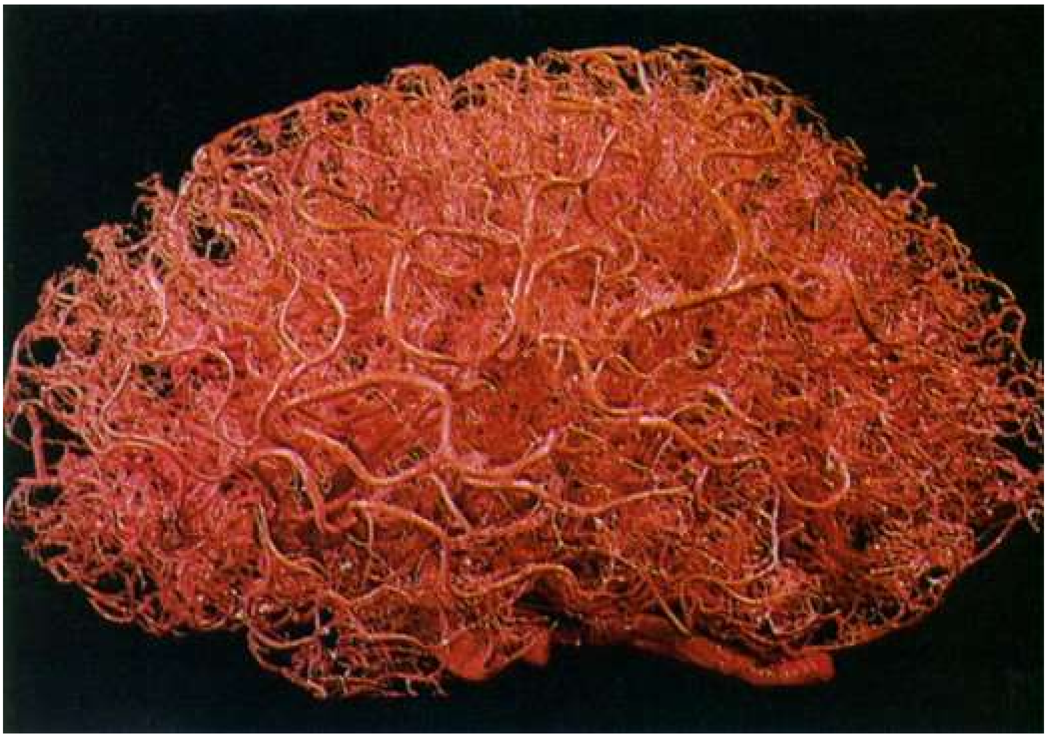

Figure 26 : Moulage des vaisseaux sanguins cérébraux

D'après Zlokovic et al., 1998

Vascularisation du SNC

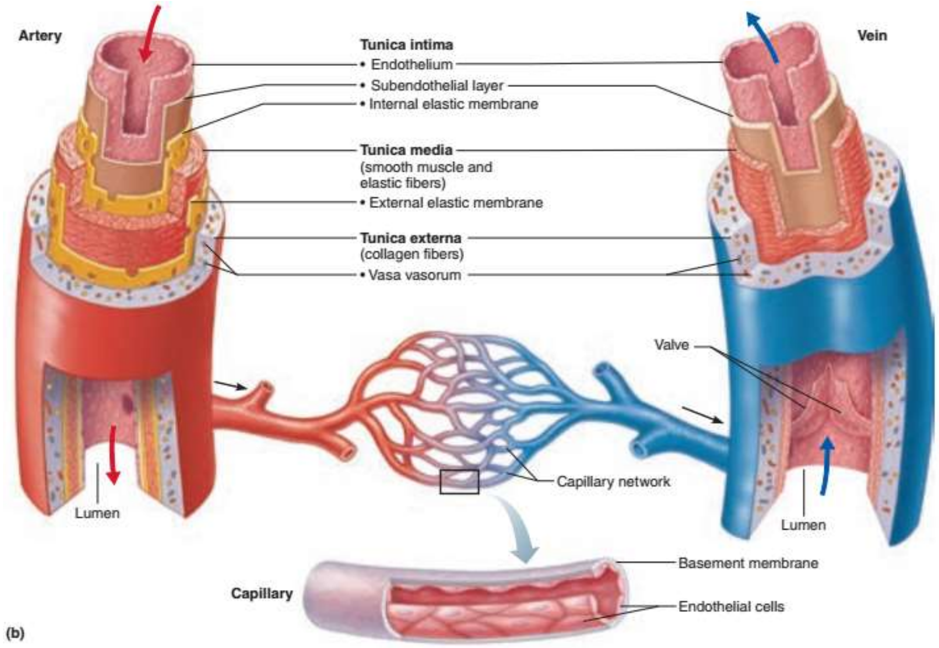

Figure 27 : Anatomie vasculaire générale

Schéma représentant la structure générale des artères, circulation à haute pression, et celle des veines, circulation à basse pression. À noter que, contrairement au reste de l'organisme, les veines cérébrales ne possèdent pas de valves.

Anatomie - artères

Les artères et artérioles sont les vaisseaux spécialisés dans l'**apport du sang du cœur vers les tissus**. Elles sont pourvues d'une importante **tunique musculaire** (la media) qui amortit les pulsations cardiaques et régule le flux sanguin cérébral.

L'encéphale reçoit sa vascularisation de deux sources : les artères carotides internes, dérivées des artères carotides communes, et les artères vertébrales, qui fusionnent au niveau du pont pour former l'artère basilaire. Les artères carotides internes et l'artère basilaire forment un anneau anastomotique à la base du cerveau, le **polygone de Willis** (Rosner et al., 2021). La vascularisation de la moelle épinière est issue quant à elle des artères vertébrales, suppléées par les artères médullaires issues des branches segmentales de l'aorte (Purves et al., 2001).

La cartographie des régions desservies par les artères permet de définir des territoires artériels (Tatu et al., 2012). Les **artères cérébrales antérieure et moyenne** sont issues des carotides internes et alimentent le cerveau antérieur, *i.e.* le cortex et les structures profondes (thalamus, noyaux gris centraux et capsule interne). La circulation postérieure est issue des **artères cérébrales postérieures, basilaire et vertébrales**. Elle dessert le cortex postérieur, le mésencéphale et le tronc cérébral (Cipolla, 2009). Le cervelet est alimenté par trois artères issues du système vertébro-basilaire : l'artère cérébelleuse supérieure, l'artère cérébelleuse inféro-antérieure et l'artère cérébelleuse inféro-postérieure (Delion et al., 2017).

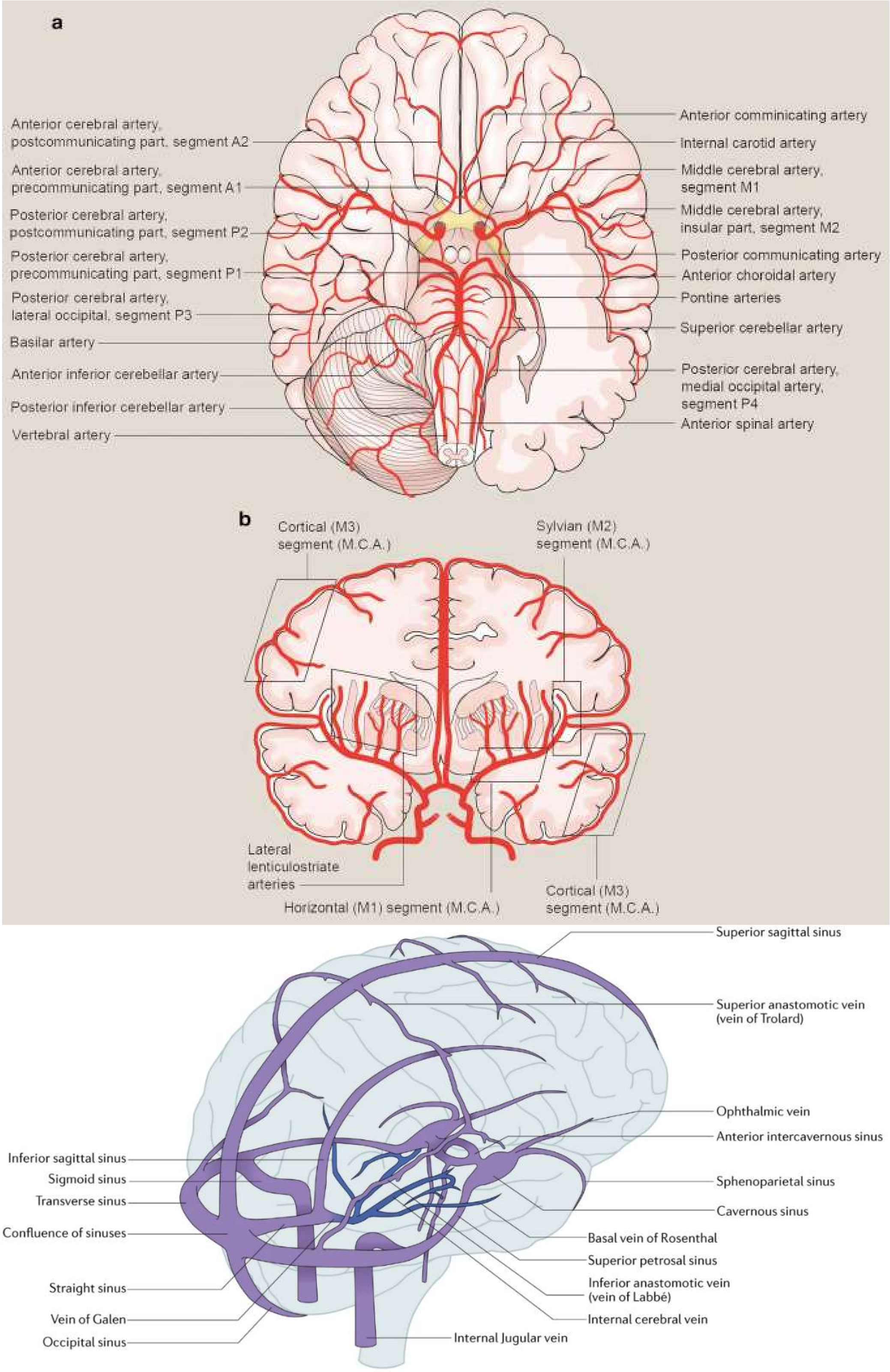

Nature Reviews | Neurology

Figure 28 : Vascularisation du SNC.

Artères (haut) et veines (bas) principales desservant l'encéphale. D'après Hart et al., 2018 ; et Silvis et al., 2017.

La surface du cerveau est sillonnée par des ramifications des artères cérébrales antérieures, moyennes et postérieures : les **artérioles piales**. Elles forment des anastomoses qui unissent les territoires artériels. Ces communications permettent de suppléer dans une certaine mesure à la défaillance d'une des artères majeures (Brozici et al., 2003). Ainsi, lors d'une ischémie cérébrale, les régions en bordure du territoire lésé peuvent survivre un peu plus longtemps que celles au cœur de la lésion. Ce territoire correspond à la pénombre ischémique et peut être en partie sauvé par une désobstruction du vaisseau dans les premières heures de l'ischémie (Heiss and Graf, 1994).

Les **artérioles pénétrantes** sont issues des artérioles piales. Comme leur nom l'indique, elles pénètrent dans l'épaisseur du tissu cérébral où elles se ramifient en **capillaires**.

Anatomie - veines

Le **retour du sang** est assuré par la circulation veineuse. Les veines et veinules sont plus **élastiques** que les artères et leur tunique musculaire est beaucoup plus fine voire absente. Dans le reste de l'organisme, l'endothélium des veines forme des valvules pour favoriser le retour du sang, mais ces structures sont absentes des veines cérébrales. Alors que la vascularisation cérébrale artérielle est ascendante et tend à pénétrer dans le tissu cérébral par le bas, celle veineuse est descendante. Les veinules émergent du cortex pour rejoindre les sinus veineux. Le **sinus sagittal supérieur** court le long du sillon interhémisphérique à la naissance de la faux du cerveau. L'ensemble de la vascularisation cérébrale est drainé hors du crâne par les **veines jugulaires internes droite et gauche** (Kiliç and Akakin, 2008).

Microcirculation

La perfusion du sang au travers des tissus est assurée par les **capillaires**. Ces vaisseaux extrêmement fins ne sont constitués que de la couche unique de cellules endothéliales à laquelle sont associés des **péricytes**, des cellules contractiles qui régulent leur perméabilité et le flux sanguin local.

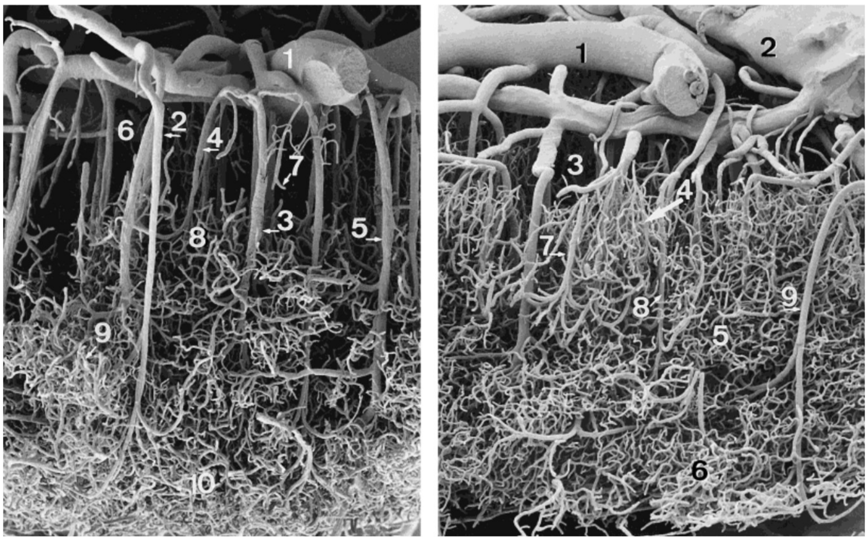

Figure 29 : Structure vasculaire du cortex

Distribution des vaisseaux corticaux observée en microcopie électronique à balayage, à gauche dans le lobe temporal et à droite dans le lobe occipital. D'après Reina-De la Torre et al., 1998.

Vascularisation de la moelle épinière

La moelle épinière est desservie par des artères qui la suivent sur toute sa longueur. L'**artère spinale antérieure**, accolée à la fissure spinale antérieure, irrigue la SG ventrale via l'**artère sulcale** et émet des collatérales piales qui ceignent la moelle. Les **artères spinales postérieures droite et gauche** émettent également des collatérales autour de la moelle et alimentent la SG dorsale. Les collatérales piales des artères spinales postérieures et antérieures forment des **anastomoses** (Purves et al., 2001; Rojas et al., 2021).

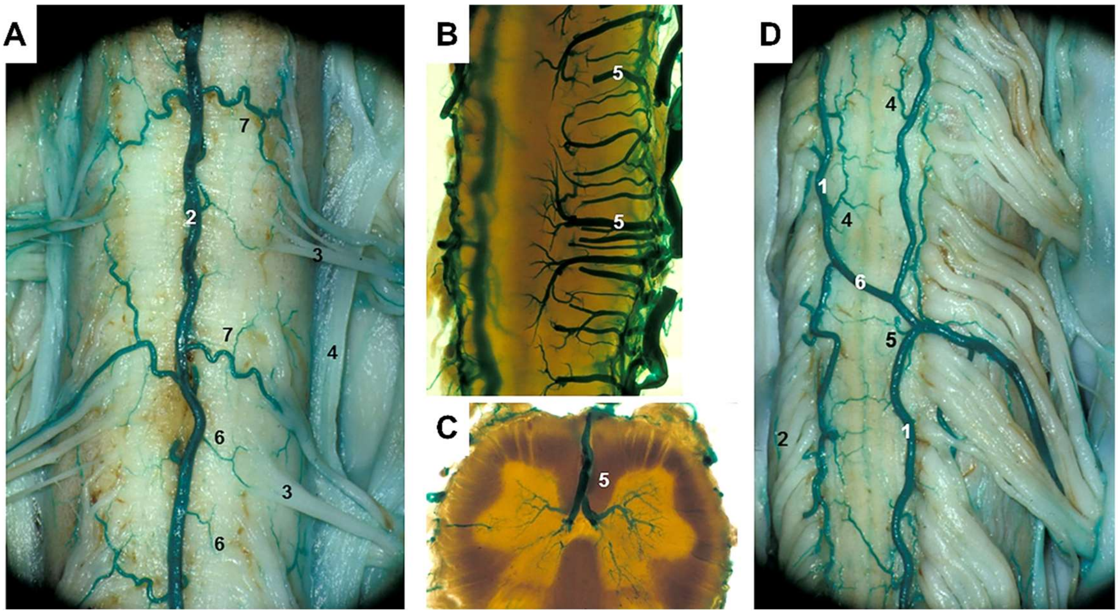

Figure 30 : Vascularisation artérielle de la moelle épinière

Vue antérieure de la moelle épinière montrant l'artère spinale antérieure après injection de teinture bleue (A). Coupe sagittale montrant les artères sulcales qui joignent la SG (B) Coupe coronale montrant l'arbre vasculaire d'une des artères sulcales (C). Vue postérieure de la moelle épinière montrant les artères spinales postérieures droite et gauche, unies par des collatérales (D). D'après Rojas et al., 2021.

Circulation

Autorégulation cérébrale

Le **flux sanguin cérébral (CBF)** est capable de se maintenir à un débit global **constant** (50-60 ml/100g/min) malgré les variations de la pression artérielle moyenne (PAM) systémique (Cipolla, 2009). Ce phénomène, nommé **autorégulation cérébrale**, repose en premier lieu sur des **barorécepteurs** (organes sensibles à la pression) situés aux bifurcations carotidiennes. Les barorécepteurs affèrent au noyau du tractus solitaire, lequel agit sur le cœur et les muscles des artères *via* le **nerf vague (X)** pour ajuster la PAM (Ogoh and Tarumi, 2019). Les **cellules musculaires lisses** sont aussi directement sensibles à la PAM (Madhok et al., 2018).

La $PaCO_2$ agit sur le tonus des vaisseaux cérébraux, qui se dilatent elle est élevée (**hypercapnie**) (Ogoh and Tarumi, 2019).

Pour les branches de l'artère carotide interne (artères cérébrales moyenne et antérieure), une augmentation de la tension artérielle est compensée par une vasoconstriction (Avolio et al., 2018).

L'ensemble de ces mécanismes reste efficace pour une PAM comprise entre 60 et 150 mmHg.

Couplage neurovasculaire

Les artères, artérioles et capillaires cérébraux sont capables de s'adapter à la demande locale. Ce phénomène de **couplage neurovasculaire** est assuré par des communications étroites entre les neurones, la glie, les cellules musculaires lisses, les péricytes et les cellules endothéliales (Schaeffer and Iadecola, 2021). Lors du sommeil lent profond, les ondes cérébrales qui parcourent le cortex seraient à l'origine de pulsations de grande amplitude dans le LCR grâce à ce phénomène (Fultz et al., 2019).

Pulsatilité vasculaire

Le cœur propulse le sang dans le réseau vasculaire au rythme des systoles et diastoles. Ces variations périodiques de pression se traduisent par des **ondes** qui se propagent le long des vaisseaux. Grâce à leur composante élastique, les artères **amortissent** ces pulsations pour protéger les vaisseaux en aval (Cocciolone et al., 2018). Cependant, et contrairement à la plupart de la circulation systémique où le flux sanguin devient continu à partir des capillaires, **toute la vascularisation du SNC est parcourue par des ondes de pression** (O'Rourke and Safar, 2005).

La **rigidité vasculaire**, qui augmente avec la tension artérielle et avec l'âge, diminue la capacité des artères à amortir les ondes de pression. Cela se traduit par une **hypertension systolique** qui endommage la microcirculation (O'Rourke and Safar, 2005). De plus, le **stress mécanique** des cellules endothéliales favorise l'accumulation de peptide Aβ (Avolio et al., 2018; Golzan et al., 2017).

Barrière hémato-encéphalique

La majeure partie des vaisseaux sanguins de l'organisme sont plutôt perméables pour permettre les échanges entre le sang et les tissus, et dans certains organes comme le foie ou les poumons, les cellules endothéliales présentent une structure plus lâche, dite fenestrée. Cependant, la présence de composés potentiellement toxiques dans le sang a poussé vers l'établissement de **filtres sélectifs** pour protéger le SNC. Chez les tétrapodes, cette frontière est finement régulée au travers de la **barrière hémato-encéphalique (BHE)**, la **barrière sang-LCR** et la **barrière leptoméningée** (Abbott et al., 2006). La BHE en est l'archétype. Les échanges entre le sang et le SNC y sont restreints par la présence de **jonction serrées** entre les cellules endothéliales. À l'exception des petites molécules apolaires capables de diffuser au travers des membranes comme l'O_2 ou le glycérol, les échanges entre sang et tissu sont régulés par les **transporteurs** exprimés par l'endothélium. La **pinocytose** (passage transcellulaire par vésicules, aspécifique) est quasiment absente chez les cellules endothéliales du SNC. Enfin, elles expriment une variété d'**enzymes** capables de dégrader les composés potentiellement neurotoxiques (Engelhardt and Sorokin, 2009).

Controverse : La BHE comme site principal de production du LCR ?

La source du LCR n'a jamais fait l'objet d'un consensus absolu dans la communauté scientifique. Exemple récent, une équipe de cliniciens croates soutient que **le LCR serait produit par la BHE** et non par l'EPC (Oresković and Klarica, 2010). Ces déclarations, qui s'opposent à un corpus écrasant de preuves expérimentales, s'appuient sur une variété d'observations cliniques et précliniques.

Les auteurs relèvent notamment : 1) l'absence de sécrétion de LCR par l'EPC ; 2) une absence de gradient de pression entre système ventriculaire et espace sous-arachnoïdien ; 3) des échanges d'eau élevés au travers de la BHE (Bulat and Klarica, 2011; Oreškovič et al., 2017; Oresković and Klarica, 2010; Radoš et al., 2021).

Bien que ces observations puissent poser question, elles entrent en **contradiction directe avec le reste de la littérature** : 1) la production de LCR par l'EPC est appuyée depuis des décennies par de très nombreuses expériences ; 2) un flux net de fluide est observé du système ventriculaire vers l'espace sous-arachnoïdien par de nombreuses équipes, notamment en IRM ; 3) les échanges d'eau au travers de la BHE ne représentent pas une production nette de fluide car ce sont les transports d'ions qui en sont à l'origine et la BHE ne compte que très peu de tels transporteurs (Brinker et al., 2014; Damkier et al., 2016, 2013; Spector et al., 2015a).

Les disparités avec le reste de la communauté scientifique pourraient s'expliquer par des techniques inappropriées (Damkier et al., 2016), l'omission de travaux récents (Brinker et al., 2014) et des différences liées aux modèles utilisés (Spector et al., 2015a). Cette équipe réfractaire souligne toutefois le **besoin de modèles plus complets** sur les voies de production et d'élimination du LCR. Plus récemment, d'autres travaux ont suggéré que les **vaisseaux piaux**, dotés de transporteurs, pourraient contribuer à la formation d'une partie du LCR chez le rongeur (Li et al., 2020).

Résumé / *Abstract*

- Le SNC bénéficie d'**une des vascularisations des plus abondantes de l'organisme**. Celle-ci bénéficie de nombreuses **anastomoses** dont la plus importante est le polygone de Willis.
- Le flux sanguin du SNC est maintenu **constant** et parcouru d'**ondes de pressions** générées par les battements cardiaques
- Les vaisseaux cérébraux ajustent le flux sanguin en fonction des besoins locaux, il s'agit du **couplage neurovasculaire**.
- Le sang est séparé du tissu cérébral par un filtre sélectif, la **BHE**.
- Le sang est drainé hors de la cavité crânienne par des **sinus veineux**.

- The central nervous system is **higly vascularized**. Its circulation is protected by **anastomoses**, the most important being the Willis circle.
- The blood flow within the central nervous system is **constant**. **Pressure waves** generated by the heart beats travel along the vascular tree.
- The blood vessels adjust the blood flow to local needs, a phenomenon called **neurovascular coupling**.
- The **blood-brain barrier** is a selective filter protecting the brain from solutes in the blood.
- **Veinous sinuses** drains the blood out of the brain.

Système lymphatique

Le système lymphatique est un réseau de canaux et de ganglions présent dans la plupart des organes. En plus de son rôle de transport et de réserve pour les cellules immunitaires, le système lymphatique permet d'évacuer les exsudats filtrés au travers des vaisseaux sanguins (Breslin et al., 2018). Cependant, et malgré son activité métabolique intense, le SNC ne dispose pas d'un réseau lymphatique. L'imperméabilité de la BHE, qui limite le passage d'eau, ainsi que le statut immunitaire spécifique du SNC expliquent en grande partie cette divergence d'avec le reste de l'organisme. Malgré cela, le SNC est indirectement desservi par le réseau lymphatique cervical comme l'ont montré de nombreuses expériences où un traceur injecté dans le tissu cérébral est ensuite retrouvé dans les nœuds lymphatiques cervicaux (Földi et al., 1968).

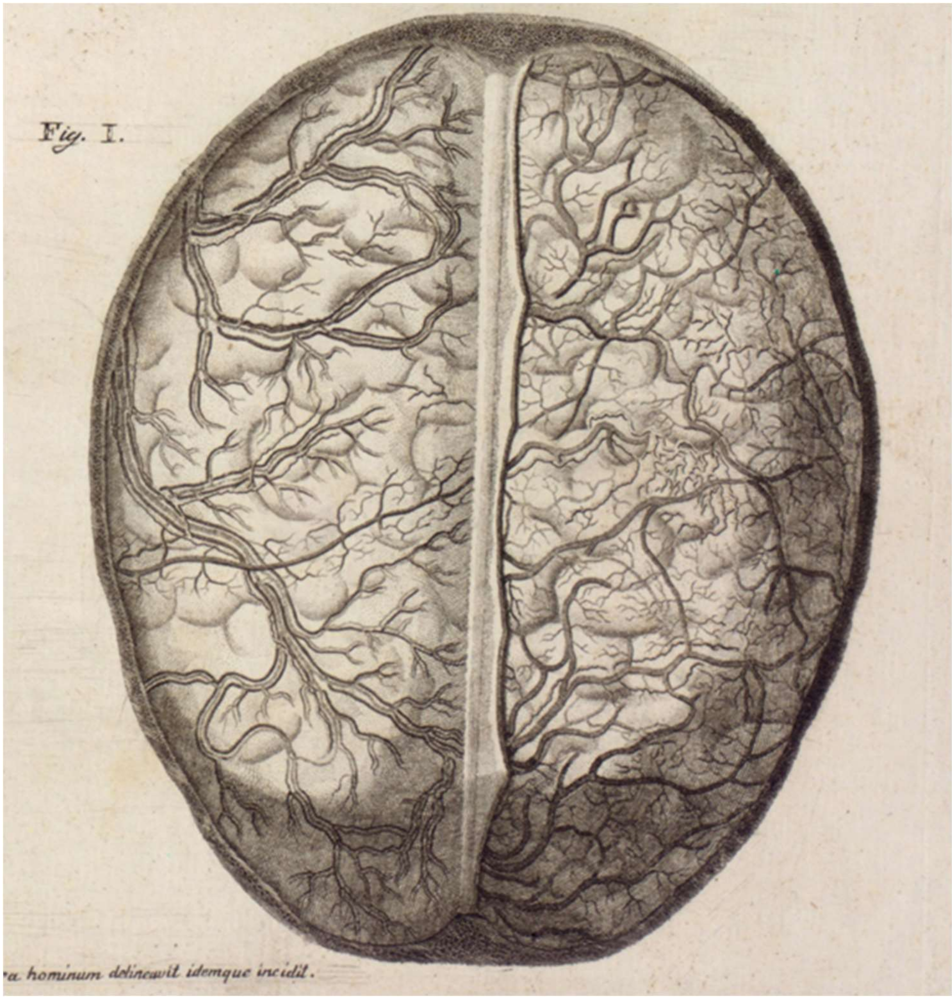

Figure 31 : Vaisseaux lymphatiques des méninges

Illustration tirée de *Vasorum lymphaticorum corporis humani historia et ichnographia*, ouvrage de Paolo Mascagni datant de 1787. Le réseau présenté ici est exagérément étendu et correspondrait à une condition pathologique, ce qui expliquerait que les contemporains de Paolo Mascagni n'aient pu reproduire son observation.

Généralités sur le système lymphatique

Contrairement au sang, qui parcourt une boucle de circulation alimentée par le cœur, la lymphe suit une **trajectoire en sens unique**, de sa formation à partir des exsudats tissulaires jusqu'à son drainage dans le système veineux. La circulation de la lymphe est **lente**, animée par les mouvements du corps et un **péristaltisme** dans les vaisseaux principaux. Huit à douze litres sont ainsi produit quotidiennement (Breslin et al., 2018).

Les vaisseaux lymphatiques initiaux, proches de la microcirculation sanguine, sont constitués d'une couche unique de **cellules endothéliales**. La lymphe se constitue à partir des **exsudats du tissu local** et sa composition est variable, notamment près de l'intestin où elle contribue à la **récupération des lipides**. Au fil de l'arborescence, les vaisseaux lymphatiques se dotent d'une **tunique musculaire lisse** péristaltique et de **valves** destinées à faciliter la progression de la lymphe (Breslin et al., 2018).

Le réseau lymphatique est émaillé de nœuds ou **ganglions** dont le plus gros est la rate. Les nœuds lymphatiques bénéficient d'une vascularisation importante et sont un site majeur pour la **surveillance immunitaire** de l'organisme (Willard-Mack, 2006).

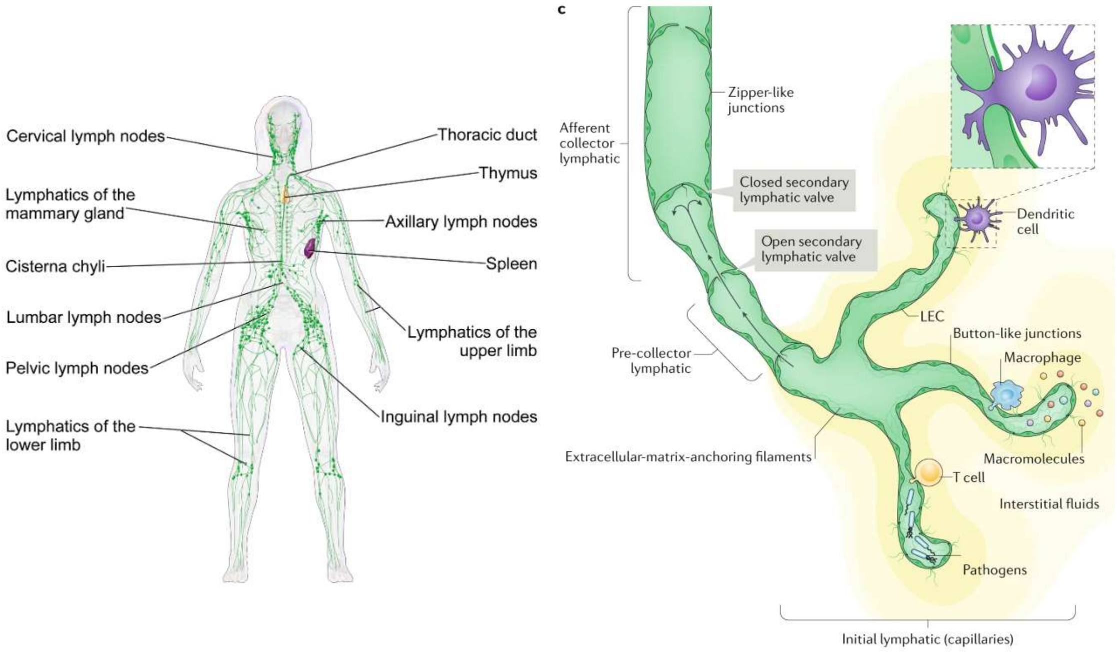

Figure 32 : Système lymphatique

Réseau lymphatique chez l'être humain (A). Structure des vaisseaux lymphatiques et interactions avec les cellules immunitaires (B). D'après Blausen Medical et adapté de Klaourakis et al., 2021.

Nœuds lymphatiques cervicaux

Sur les 800 nœuds lymphatiques de l'organisme, environ 300 se situent dans le cou. Ils peuvent être classés en au moins 6 groupes anatomiques selon leur localisation, leurs connections et les régions qu'ils desservent. Sur le côté du cou, les nœuds lymphatiques cervicaux forment un réseau en forme de triangle pointant vers le haut (**Figure 28**). Le bord antérieur constitue la **chaîne jugulaire interne, ou nœuds cervicaux profonds**, et draine notamment le visage, la bouche, la cavité nasale, le pharynx et les méninges (Koroulakis et al., 2021).

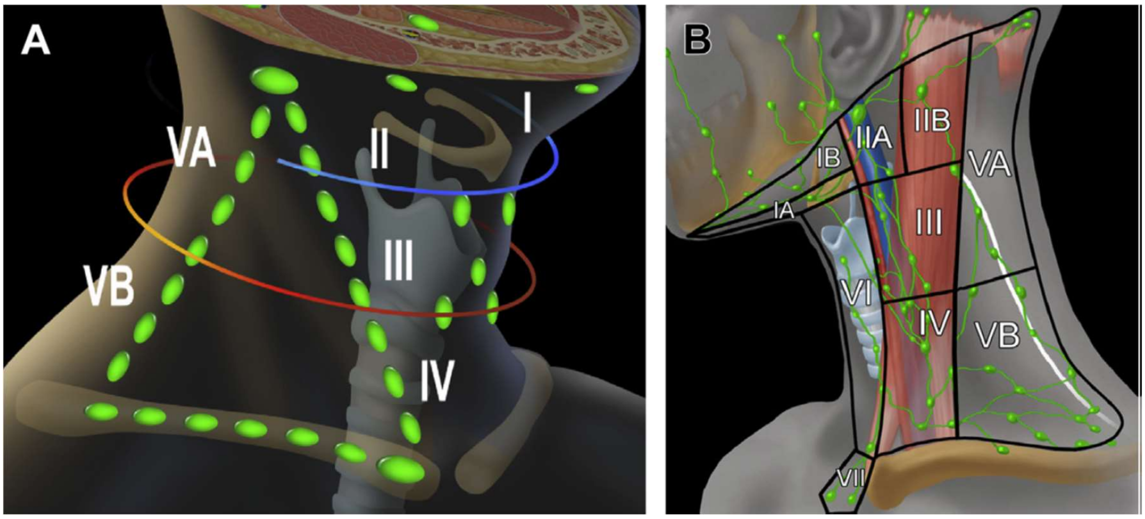

Figure 33 : Nœuds lymphatiques cervicaux

Représentation des groupes de nœuds lymphatiques cervicaux, dont les connections forment un triangle sur le côté du cou. Le bord antérieur (groupes II, III, IV) forme la chaîne jugulaire (nœuds cervicaux profonds) alors que le bord postérieur (Va, Vb) constitue la chaine spinale accessoire. Les deux chaînes sont unies à leur base par la chaîne cervicale transverse. D'après Eisenmenger et Wiggins III, 2015.

Réseau lymphatique méningé

Décrit dès le XVIIIème siècle, notamment par l'anatomiste italien Paolo Mascagni, le **réseau lymphatique méningé (RLM)** a été occulté par le dogme grandissant de l'absence de drainage lymphatique dans le cerveau. Quelques études sporadiques y font mention, jusqu'à sa redécouverte conjointe en 2015 par les équipes de Jonathan Kipnis et Kari Alitalo (Aspelund et al., 2015; Louveau et al., 2015). Depuis, de nombreuses études ont intégré le RLM comme un acteur majeur dans le drainage du LCR et la surveillance immunitaire du SNC.

Généralités

L'identification de "vrais" canaux lymphatiques est complexe et repose notamment sur l'utilisation croisée de **marqueurs** (Lyve1, podoplanine, Prox1, CD31) et la réponse à des **facteurs de croissance** (VEGF-C) (Louveau et al., 2015). D'abord décrit chez la souris, le RLM longe les sinus veineux mais aussi les artères majeures (Aspelund et al., 2015). Chez les primates dont les êtres humains, ce même schéma a pu être observé *in vivo* grâce au suivi d'agents de contraste en IRM (Absinta et al., 2017). Les vaisseaux lymphatiques méningés sont particulièrement abondants **le long du sinus veineux transverse**, où ils forment par endroit des zones plus ramifiées facilitant le passage du LCR (Papadopoulos et al., 2020). De plus, ils entretiendraient une relation privilégiée avec la **moelle osseuse du crâne** grâce à des canaux microscopiques au travers de l'os par lesquels transitent des cellules immunitaires (Herisson et al., 2018). A la base du crâne (notamment près du foramen jugulaire), les vaisseaux sont plus fins et ramifiés. Ils représentent chez le rongeur un des sites majeurs pour le drainage du LCR (Ahn et al., 2019). Il existe aussi un **RLM spinal** qui partage de nombreuses similitudes avec celui décrit dans l'encéphale (Antila et al., 2017).

Comme le système lymphatique périphérique dans le reste du corps, le RLM joue un rôle central dans la **surveillance immunitaire du SNC**. Des **cellules présentatrices d'antigènes** sont présentes dans les canaux latéraux du sinus sagittal transverse, et joueraient un rôle de médiatrices avec la moelle osseuse du crâne grâce à des canalicules au travers de l'os. Un système équivalent existerait dans la moelle des spondyles vertébraux (Cugurra et al., 2021).

Développement, plasticité et pathologie

Chez l'être humain et le rongeur, le système lymphatique se met en place dans la période prénatale. En revanche, le développement du RLM pourrait être plus tardif. Chez la souris, il se constitue pendant les premières semaines post-natales jusqu'à 1 mois (~adolescence). Le réseau lymphatique mature reste modulable, à l'instar des vaisseaux sanguins. La **lymphangiogenèse** dépend de l'action du facteur de croissance VEGF-C sur le récepteur VEGFR3 exprimé par les cellules de l'endothélium lymphatique (Antila et al., 2017).

Les canaux lymphatiques du RLM, dépourvus de musculature, sont particulièrement **vulnérables aux traumatismes**. Ainsi, la fonctionnalité du RLM est diminuée dès 2h après un traumatisme crânien chez la souris. Elle prend plusieurs semaines pour revenir à la normale grâce à la formation de nouveaux canaux et à l'élargissement des vaisseaux existants. Une augmentation de la PIC pendant quelques heures suffit à réduire l'efficacité du RLM (Bolte et al., 2020). Dans un modèle murin de sclérose en plaques, l'activation des lymphocytes et le développement de la pathologie sont ralentis chez les sujets privés de RLM, ce qui souligne son **rôle immunologique** (Louveau et al., 2018).

Dans un modèle murin d'AVC ischémique, des canalicules lymphatiques se développent au-dessus de la lésion (Yanev et al., 2020). Cette plasticité faciliterait la **résorption de l'œdème** post-ischémique, comme le suggère les lésions plus importantes observées chez un modèle murin déficient en VEGFR3 où le RLM est sous-développé (Yanev et al., 2020). Ce rôle de nettoyage est aussi retrouvé après une HSA (Chen et al., 2020).

Cependant, comme le système lymphatique périphérique, le RLM **perd en efficacité avec l'âge** (Da Mesquita et al., 2018). Du fait de sa capacité à éliminer les solutés dans le LCR, il a été étudié dans plusieurs modèles de la MA. Dans un modèle murin pro-amyloïde, des plaques apparaissent dans les méninges et sont aggravées en cas de perturbation du RLM. En revanche, stimuler la croissance du RLM compense en partie l'accumulation des plaques dans le tissu cérébral et les troubles cognitifs (Da Mesquita et al., 2018).

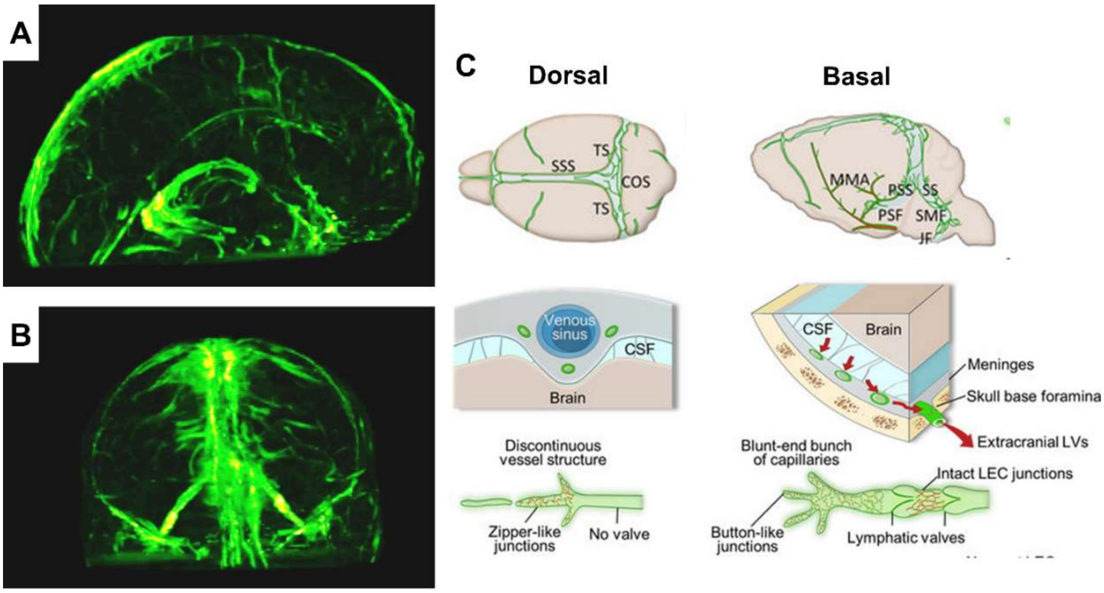

Figure 34 : Réseau lymphatique méningé

RLM vu en IRM chez un volontaire sain après administration d'un agent de contraste, projection 3D en vue latérale gauche (A) et antérieure (B). Structure des vaisseaux lymphatiques méningés dorsaux et basaux chez le rongeur (C). Adapté d'après Absinta et al., 2017, et Ahn et al., 2019.

Cas des autres tissus dépourvus de système lymphatique

En dehors du SNC, quelques tissus vascularisés ne disposent pas d'un réseau lymphatique propre, notamment l'os et l'œil.

Les **os** sont desservis par un réseau vasculaire étendu, mais ne semblent pas posséder de système lymphatique hors conditions pathologiques (lymphangiomes). Cependant, la diffusion de traceurs au travers du tissu osseux signe l'existence de systèmes jouant un rôle similaire, possiblement dans les espaces périvasculaires des **canaux de Volkmann** (canalicules permettant le passage des vaisseaux sanguins au travers de l'os) (Edwards et al., 2008).

Historiquement, la question d'un système lymphatique dans l'**œil** est sujette à débat (Breslin et al., 2018; Grüntzig and Hollmann, 2019). À la base de la cornée, le **canal de Schlemm** est un canal en forme d'anneau qui faciliterait le drainage de l'humeur aqueuse et présente certains marqueurs propres aux vaisseaux lymphatiques (Aspelund et al., 2014). Cette structure n'est cependant pas un vaisseau lymphatique à proprement parler (notamment, elle n'est pas connectée au reste du réseau lymphatique) et la présence de tels canaux dans l'œil reste à démontrer.

Résumé / *Abstract*

- Le système lymphatique est un **réseau de canaux et de nœuds** qui draine les **fluides excédentaires** vers la circulation veineuse.
- Le système lymphatique est présent dans l'ensemble de l'organisme, à l'exception notable du **SNC**, de l'**os** et de l'**œil**.
- Le **RLM** draine une partie du LCR vers les nœuds lymphatiques cervicaux profonds et assurent la surveillance immunitaire du SNC.
- Il existe une **communication entre FISC et système lymphatique**, mais elle reste à définir.

- The lymphatic system is a **network of channels and nodes** draining the **excess interstitial fluid** toward the veinous circulation.
- The lymphatic system expands over all the organism, with the notable exceptions of the **central nervous system**, the **bone** and the **eye**.
- The **meningeal lymphatics** drain a fraction of the cerebrospinal fluid to the deep cervical lymph nodes and play a role in the immune survey of the central nervous system.
- **The brain interstitial fluid communicates wtih the lymphatic system**, though the communication pathway is poorly understood.

Fluide interstitiel cérébral

L'espace extracellulaire représente un cinquième du volume cérébral, sous la forme d'un réseau complexe enveloppant neurones et cellules gliales. Entre les cellules, cet espace est occupé par une matrice extracellulaire ainsi que par le FISC (Hrabetova et al., 2018). Bien que les déplacements d'eau et de solutés soient restreints par l'encombrement extrême de ce milieu, il y existe des voies de moindre résistance le long des fibres nerveuses ainsi que des vaisseaux sanguins.

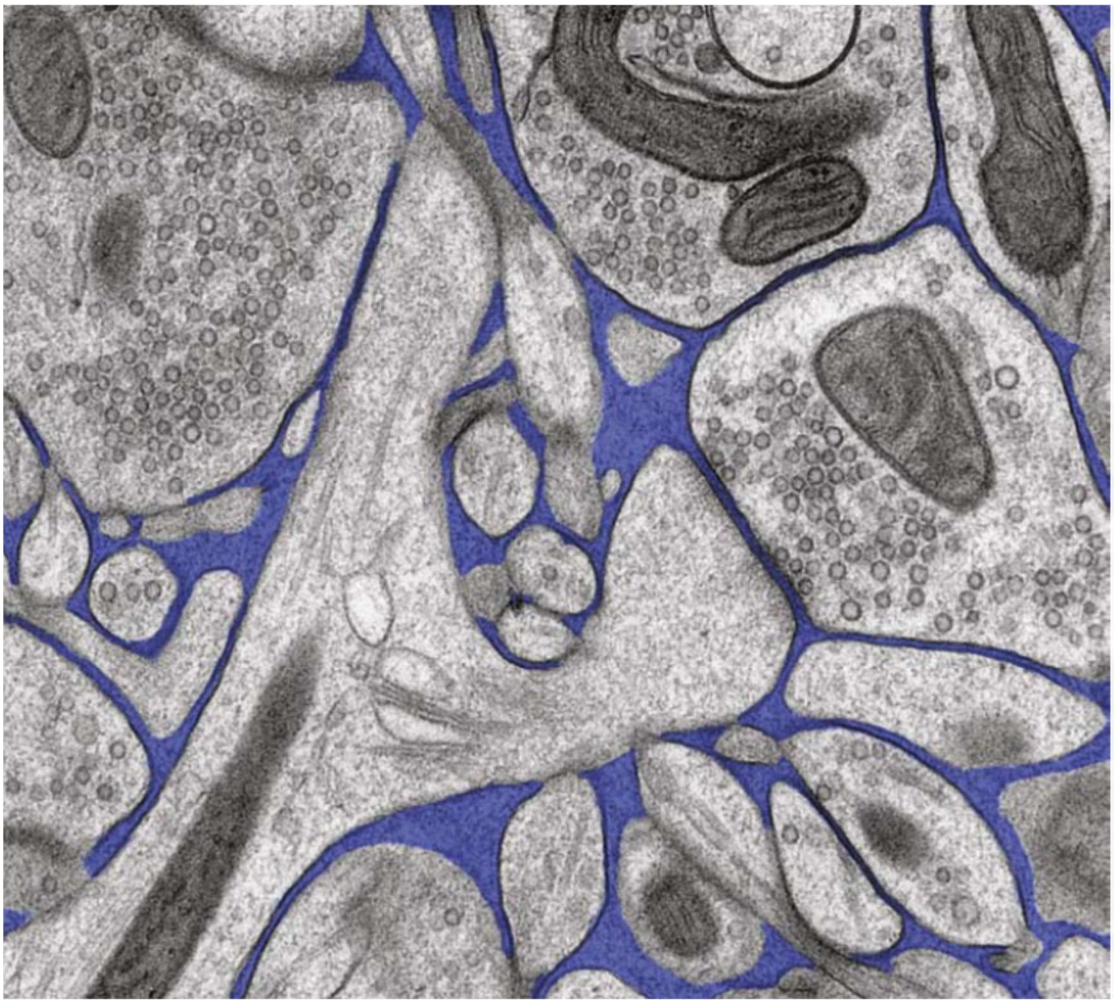

Figure 35 : Visualisation de l'espace interstitiel en microscopie électronique

Estimer le volume occupé par l'espace extracellulaire est complexe et dépend de la méthode de fixation employée. Ici, une coupe de tissu cryopréservée. Le FISC est représenté en bleu, entre les corps cellulaires (gris). Le côté de l'image mesure 5 µm. D'après Korogod et al., 2015.

Espace interstitiel du SNC

L'**espace interstitiel** représente environ 20% du volume cérébral. Il sépare les cellules d'environ 20 à 60 nm et est comblé par le FISC et la matrice extracellulaire (Sun and Sun, 2021).

Par rapport à la plupart des organes, la **matrice extracellulaire cérébrale** est relativement pauvre en collagène et fibronectine. Les hyaluronates, les protéoglycanes à base de chondroïtine sulfate (lecticans) et les ténascines y prédominent. Elle forme un support pour les cellules cérébrale et régule la croissance des axones. La matrice extracellulaire change de composition au cours du développement et permet entre autres la migration des cellules. Elle réagit à l'inflammation *via* des enzymes de dégradation ou des molécules structurelles sécrétés par les cellules gliales. Sa plasticité et son renouvellement sont assurés par des métalloendopeptidases, notamment la famille ADAMTS (*A Disintegrin And Metalloproteinase with Thrombospondin Motifs*). (Zimmermann and Dours-Zimmermann, 2008). Autour des neurones (et des nœuds de Ranvier), la matrice extracellulaire forme une enveloppe, le réseau périneuronal (*perineuronal net*) (Fawcett et al., 2019).

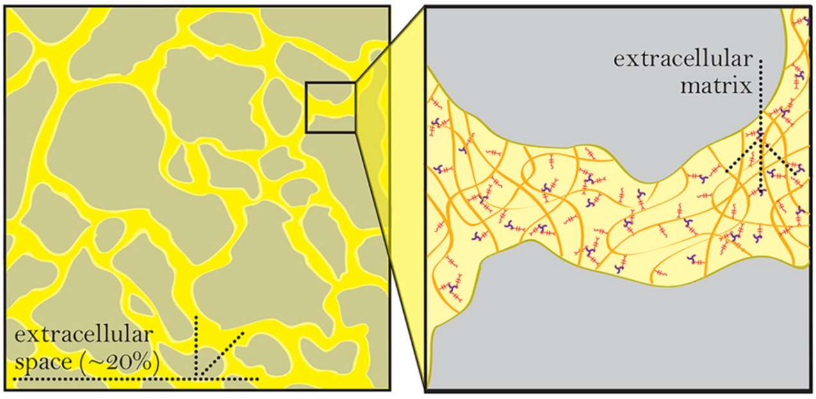

Figure 36 : Structure de l'espace interstitiel

L'espace interstitiel sépare les cellules et représente environ 20% du volume cérébral. Il est rempli de matrice extracellulaire et de FISC. D'après Odackal et al., 2017.

La composition du **FISC** dépend de la production des cellules environnantes et de son élimination. Elle varie selon l'activité cérébrale, par exemple pendant le sommeil (Ding et al., 2016). Des échanges entre le LCR et le FISC ont lieu au niveau de l'épendyme et à l'interface pie-mère/glie limitante, en particulier au niveau des **espaces périvasculaires**. Plusieurs études reposant sur l'injection de traceurs dans le tissu cérébral semblent indiquer une compartimentation dans les voies de drainage du FISC. Ainsi, le FISC du noyau caudé communique avec l'espace sous-arachnoïdien alors que celui du thalamus se dirige vers le cortex (Lei et al., 2017).

Le déplacement des molécules est largement entravé par l'**encombrement** de l'espace interstitiel. Les molécules d'eau s'y déplacent 80% moins rapidement que dans un milieu libre. La diffusion des macromolécules serait moins d'un millimètre par jour. Il existe cependant des **voies de moindre résistance** par exemple le long des fibres de matière blanche, mais la vitesse des solutés n'y excède pas 15 µm/s (Lei et al., 2017). Le drainage du FISC hors du SNC passe donc par d'autres voies plus rapides, comme le **drainage intramural périartériel (IPAD)** ou le **système glymphatique**, tous deux situés en périphérie des vaisseaux sanguins.

Péri- ou para- vasculaire ?

Les termes périvasculaire et paravasculaire sont souvent employés dans la littérature pour décrire le drainage des solutés qui se produit à la périphérie des vaisseaux (Bacyinski et al., 2017). Cependant, leur usage est compliqué par l'existence de deux modèles empruntant des voies proches mais distinctes : le drainage intramural périartériel (IPAD), qui concerne la membrane basale des capillaires et de la paroi artérielle ; et le système glymphatique qui concerne l'espace périvasculaire.
En fonction des articles, le drainage (ou voie) péri- ou para- vasculaire renvoie à l'un ou l'autre de ces modèles. Dans cette thèse, j'ai choisi pour des raisons de clarté de n'employer que le terme périvasculaire. **'Périvasculaire' renverra donc à la zone en continuité avec l'espace de Virchow-Robin, comprise entre la glie limitante et la paroi vasculaire**.

Drainage intramural périartériel (IPAD)

Malgré l'existence du RLM à proximité immédiate, le SNC ne dispose pas d'un système lymphatique dans son propre tissu. En revanche, il a été observé depuis des décennies que des traceurs injectés dans le parenchyme cérébral se retrouvent dans les **nœuds lymphatiques cervicaux** (Földi et al., 1968). Les mécanismes régissant le drainage du FISC dans le tissu cérébral restent flous, mais l'utilisation de traceurs a révélé des voies de moindre résistance le long des vaisseaux sanguins ou des fibres de substance blanche. Au début du XXIème siècle émerge l'idée qu'un **système actif**, mû par la pulsatilité vasculaire, emporterait les solutés hors du SNC via la membrane basale des artères : l'IPAD.

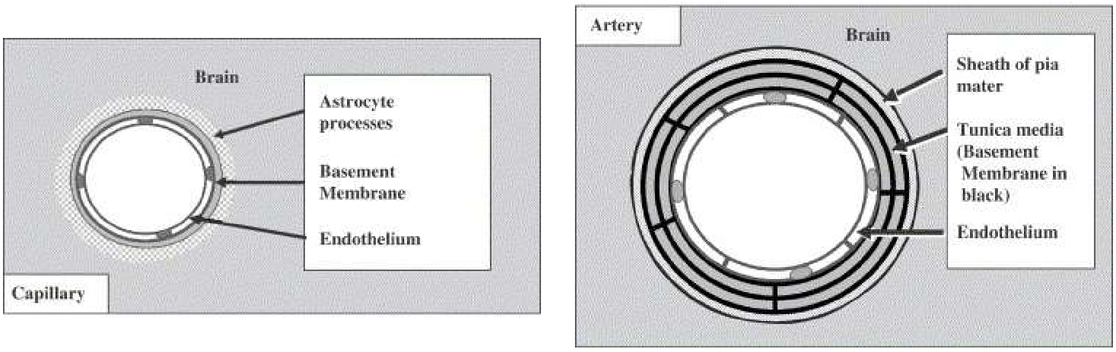

Figure 37 : Structure des parois vasculaires montrant la membrane basale

Capillaires et artères disposent de membranes basales qui permettraient le drainage du FISC hors du SNC. D'après Schley et al., 2006.

Membrane basale vasculaire

Les membranes basales exprimées par les astrocytes et les cellules endothéliales contribuent à la constitution de la BHE. Elles sont principalement constituées de laminine, de collagène de type IV, de nidogène et d'héparanes sulfate. Associés à la glie limitante, l'isoforme $\alpha 2$ de la laminine est retrouvée à la face interne des pieds astrocytaires (Thomsen et al., 2017). L'alpha-syntrophine, une molécule permettant l'ancrage de l'AQP4, y est également présente (Hoddevik et al., 2020). Les laminines de type $\alpha 4$ et $\alpha 5$ sont quant à elles à la face externe des cellules endothéliales (Thomsen et al., 2017).

La membrane basale est altérée dans les pathologies neurovasculaires. Ainsi, lors de l'AVC ischémique elle est dégradée par les MMP activées par l'inflammation cérébrale, alors qu'elle s'épaissit et accumule des plaques amyloïdes dans la maladie d'Alzheimer (Thomsen et al., 2017). L'ApoE ε4 est associée à une membrane basale enrichie en fibronectine par les astrocytes aux dépends de la laminine. Cette différence de composition favoriserait la formation des plaques amyloïdes dans la maladie d'Alzheimer et l'angiopathie amyloide cérébrale, un trait fortement lié au génotype ApoE ε4 (Keable et al., 2020).

L'**IPAD** a été proposé dès le début du XXIème siècle pour expliquer le **mouvement rétrograde** de solutés observée en microscopie dans la **paroi vasculaire** (Schley et al., 2006). Les traceurs injectés dans le parenchyme passent d'abord par les **membranes basales** des capillaires, puis des artères (mais pas des veines) et sont **éliminés du tissu cérébral en quelques heures**. Ce trajet est observé pour les solutés, alors que les microparticules sont évacuées par l'espace périvasculaire. La localisation des solutés du FISC dans la membrane basale pourrait être une des causes de l'accumulation de peptides Aβ dans la paroi vasculaire observée dans l'angiopathie amyloïde cérébrale (Carare et al., 2008).

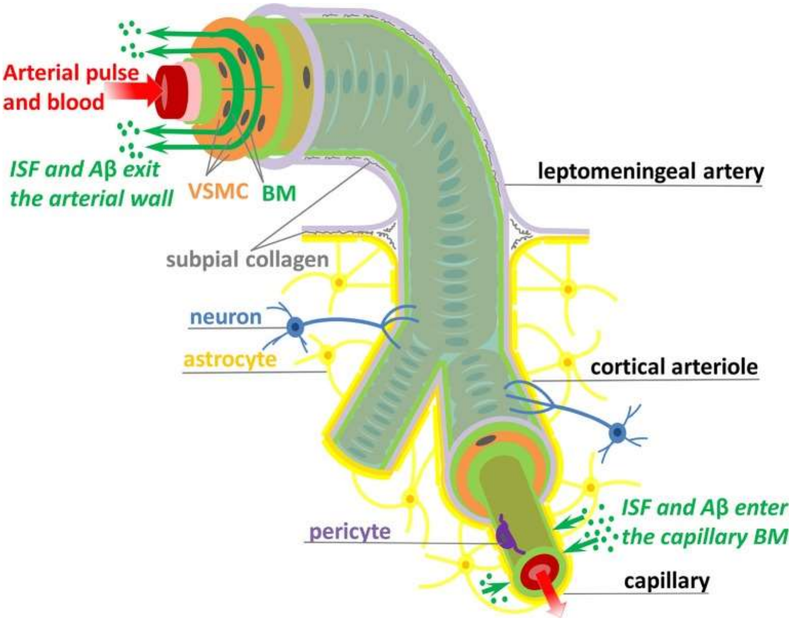

Figure 38 : Drainage intramural périartériel (IPAD)

Représentation des voies empruntés par les solutés du FISC le long de la membrane basale capillaire et artérielle. Les solutés remontent l'arbre vasculaire à contre-courant du flux sanguin. D'après Aldea et al., 2019.

Les mécanismes à l'origine de ce phénomène restent mal compris. Bien que la pulsatilité artérielle ait été intialement évoquée, son amplitude reste trop grande pour créer les gradients de pression nécessaire au déplacement des traceurs. De plus, la membrane basale, même dotée de valves, est un espace trop encombré pour permettre un tel déplacement (Diem et al., 2017; Faghih and Sharp, 2018). Plus récemment, un nouveau modèle tenant compte de ces limitations a été proposé et se base sur les **contractions synchronisés des différentes couches de cellules musculaires lisses** (Aldea et al., 2019).

Espaces périvasculaires

La description des **espaces périvasculaires (EPV)** remonte au XIXème siècle et est souvent attribuée aux anatomistes Rudolf Virchow et Charles Robin. Bien que de nombreuses équipes aient depuis exploré ces espaces de Virchow-Robin, le détail de leur anatomie ainsi que leurs fonctions restent sujet à débat (Hladky and Barrand, 2018; Wardlaw et al., 2020).

En **conditions physiologiques**, les EPV à l'entrée des grosses artères peuvent être **visibles en IRM** chez les êtres humains. Ils apparaissent comme des spots dans le tissu avec la même intensité que le LCR et ne sont normalement pas réhaussés par l'injection d'un agent de contraste dans le sang. Les EPV apparaissent au niveau des ganglions de la base (type I), du cortex (type II) ou dans le mésencéphale (type III). Ils sont souvent bilatéraux et leur taille excède rarement 5 mm. La prévalence d'**EPV dilatés** (> 5 mm) augmente avec l'âge et est associée à diverses pathologies dont la MA, les démences vasculaires (dont l'AAC) et les traumatismes crâniens. La taille des EPV peut parfois dépasser 1.5 cm (Rudie et al., 2018). Les mécanismes aboutissant à la dilatation des EPV restent mal connus. La présence de **facteurs inflammatoires** est souvent rapportée en périphérie des vaisseaux atteints ainsi qu'une **perméabilisation de la BHE** et une **perte de la réactivité de la paroi vasculaire** (Brown et al., 2018).

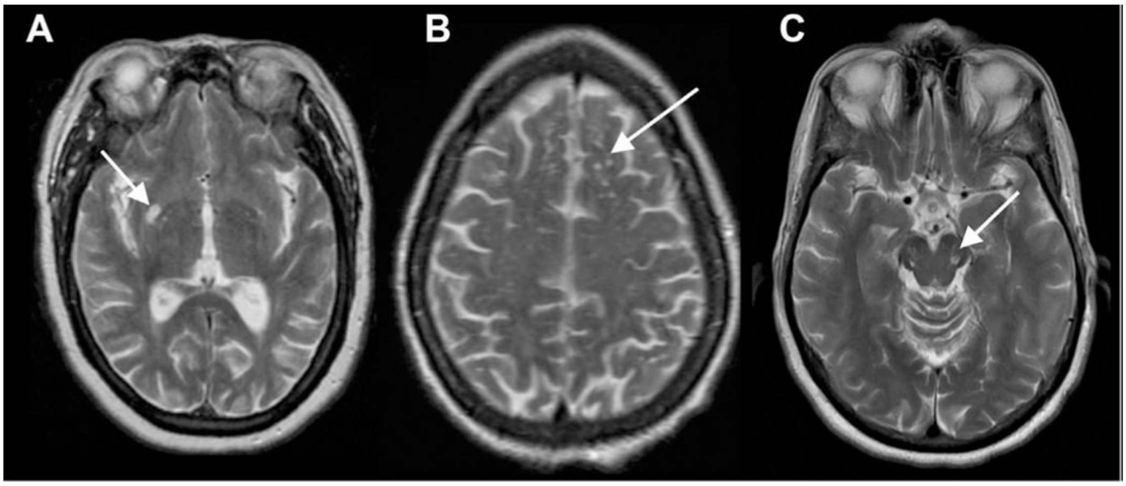

Figure 39 : Espaces périvasculaires vus en IRM

EPV couramment observés en IRM T2 (LCR en blanc) dans les ganglions de la base (A), dans la SB sous-corticale (B) ou dans le mésencéphale. D'après Rudie et al., 2018.

En périphérie des vaisseaux, la BHE est complétée par une couche formée par les pieds astrocytaires, la **glie limitante périvasculaire**. En plus des vaisseaux, cette membrane délimite l'ensemble du SNC à l'exception du système ventriculaire où elle est remplacée par l'épendyme. Les pieds astrocytaires sont unis par des jonctions gap et expriment fortement l'**AQP4**, polarisée vers le vaisseau. Cette expression pourrait permettre la redistribution de l'eau métabolique du FISC vers les espaces périvasculaires, où elle serait drainée vers l'espace sous-arachnoïdien (Abbott et al., 2006).

Des EPV sont également retrouvés en périphérie des **veinules et artérioles de la moelle épinière** (Lam et al., 2017).

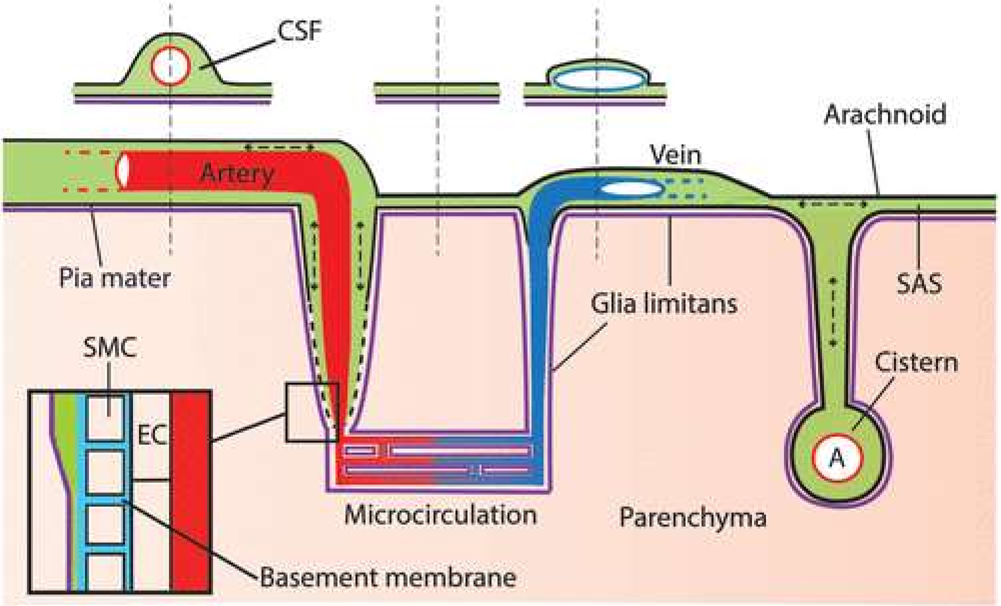

Figure 40 : Connections entre l'espace périvasculaire et le LCR

Schéma reprenant les connections entre les compartiments du LCR et des espaces périvasculaires. La pulsatilité artérielle facilite le brassage des fluides et accélère la dispersion des solutés. D'après Bedussi et al., 2017..

La maladie de Van der Knaap : une pathologie structurelle des espaces périvasculaires ?

La **maladie de Van der Knaap**, ou leucodystrophie mégalencéphalique avec kystes sous-corticaux (MLC), est un type rare de **leucodystrophie** (démyélinisation de la SB) se traduisant par une macrocéphalie précoce, l'apparition de **vacuoles** dans la SB et un déclin cognitif.

La MLC est causée par des mutations de **MLC1** ou de **GlialCAM**, deux protéines impliquées dans l'adhésion des pieds astrocytaires autour des vaisseaux.

Récemment, un modèle KO de MLC1 chez la souris a permis d'identifier de multiples anomalies dans la formation de l'**unité gliovasculaire**. En plus d'anomalies morphologiques des astrocytes et d'un défaut du couplage neurovasculaire (dans lequel les astrocytes jouent un rôle régulateur), le tissu cérébral présente une teneur en eau anormalement élevée et des échanges réduits avec le LCR. Ces travaux sont présentés dans les résultats de ce manuscrit : **Collaboration 1** (Gilbert et al., soumis).

Système glymphatique

Le **système glymphatique** est un modèle expliquant les **interactions LCR-FISC**, élaboré en 2012 par l'équipe de Maiken Nedergaard. Dans leur article fondateur, Iliff et collaborateurs proposent que le LCR serait **aspiré dans les espaces périartériels**, puis distribué dans le **parenchyme cérébral** grâce aux **AQP4** exprimées par les pieds astrocytaires. Le mélange LCR-FISC serait ensuite **drainé vers les espaces périveineux**, le long desquels il remonterait jusque dans l'espace sous-arachnoïdien, emportant sur sa route les métabolites solubles (Iliff et al., 2012).

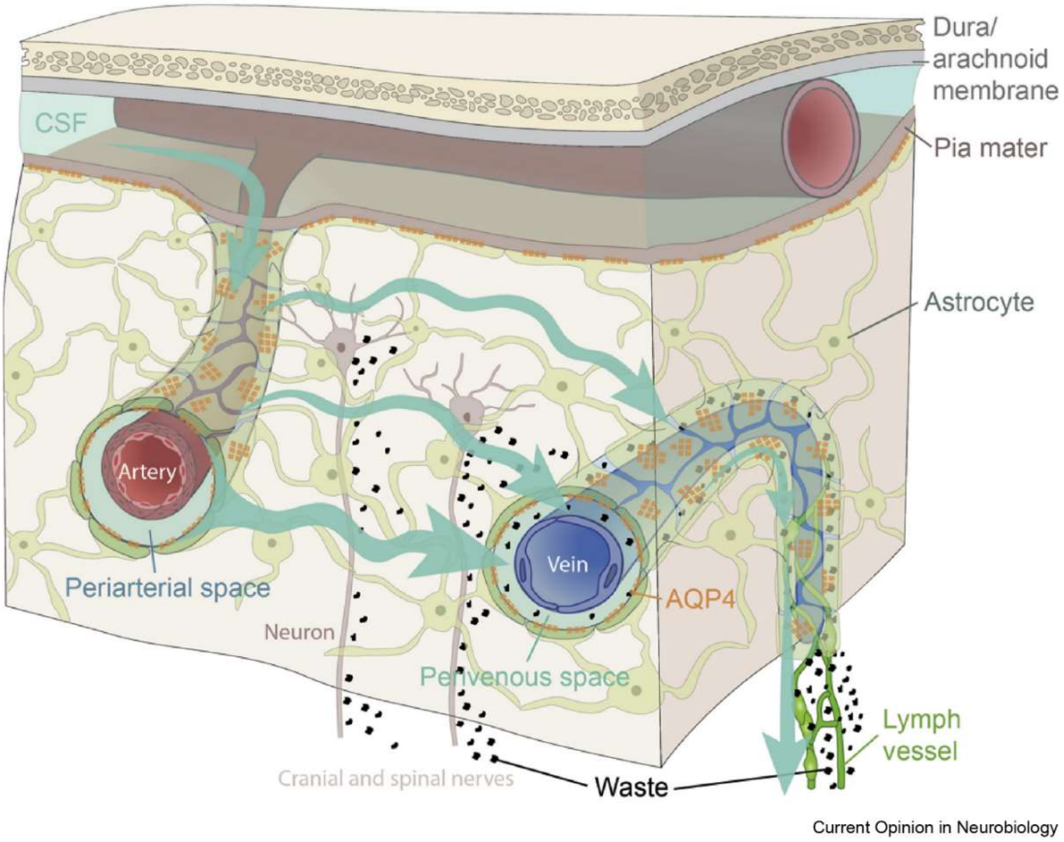

Figure 41 : Système glymphatique

Schéma présentant le flux de LCR dans les espaces artériels, le parenchyme puis les espaces périveineux. Le courant emporte les déchets hors du tissu cérébral. D'après Benveniste et Nedergaard, 2021

La théorie initiale s'est enrichie à mesure des expériences. En 2013, la même équipe propose la **pulsatilité artérielle** comme moteur du système glymphatique (Iliff et al., 2013b). L'**injection de traceurs dans le LCR** devient le *gold standard* pour la mesure de la fonctionnalité du système glymphatique et est rendue possible *in vivo* grâce à la microscopie 2-photons et à l'IRM rehaussée par agent de contraste (Iliff et al., 2013a). Une **régulation par le sommeil** (Xie et al., 2013) et l'**implication dans la MA** (Kress et al., 2014; Peng et al., 2016) sont avancées, à la base du triangle sommeil-Alzheimer-glymphatique qui servira de fer de lance à la vulgarisation de la théorie.

Malgré des **critiques précoces** sur l'hypothèse du flux convectif et le rôle des AQP4 (Brinker et al., 2014; Hladky and Barrand, 2014; Smith et al., 2015; Spector et al., 2015b), le système glymphatique est **rapidement adopté** par une partie de la communauté scientifique et décliné sur une **multitude de modèles** (*e.g.* AVC, diabète, hypertension). Grâce à l'IRM, les premières observations chez l'être humain sont réalisées à partir de 2015 (Eide and Ringstad, 2015).

Afin de répondre aux critiques, des méthodes de plus en plus élaborées voient le jour : simulations (Kiviniemi et al., 2016), mesures quantitatives du flux (Koundal et al., 2020; Ratner et al., 2017), suivi de microparticules (Mestre et al., 2018), systèmes avancés d'injection de traceurs (Raghunandan et al., 2021; Xavier et al., 2018) et optimisation des anesthésiques (Stanton et al., 2021). Mais la démultiplication des études sophistiquées ne parvient pas à étayer le cœur de la théorie : un flux convectif dans le parenchyme cérébral.

Au 1er septembre 2021, soit 9 ans après son introduction, le terme "*glymphatic*" comptabilise plus de 750 entrées sur Pubmed (dont 1/3 de *reviews*). À ce jour, la théorie initiale reste largement défendue par l'équipe de Maiken Nedergaard (Benveniste and Nedergaard, 2021; Mestre et al., 2020b) bien que ses failles soient de plus en plus évidentes (Faghih and Keith Sharp, 2021; Hladky and Barrand, 2018; Kaur et al., 2021).

Résumé / *Abstract*

- L'eapace interstitiel cérébral est un milieu **fortement encombré** mais où se trouvent des **voies de moindre résistance**.
- Le FISC se draine vers les **espaces périvasculaires**, qui eux-même communiquent avec le LCR dans l'espace sous-arachnoïdien
- Le **système glymphatique** est un modèle controversé proposant qu'un courant balaie le FISC et les déchets du métabolisme vers les EPV veineux.
- L'**IPAD** est une route alternative au travers de la membrane basale des artères et pourrait être un lien entre FISC et système lymphatique.

- The brain intercellular space is a **highly constrained** milieu with preferential, **lower resistance pathways**.
- The brain interstitial fluid drains toward the **perivascular spaces**, which communicates with the subarachnoid space.
- The **glymphatic system** is a controversed model which propose that a convective flow occurs across the parenchyma and drains the metabolic waste toward the perivascular spaces.
- The **intramural periarterial drainage** is an alternative pathway across the basal lamina in the media of arteries which could link together brain interstital fluid and lymphatics.

Imagerie par résonance magnétique

L'imagerie par résonance magnétique (IRM) est une méthode d'imagerie exploitant les propriétés du noyau atomique pour sonder la matière. Depuis sa mise au point dans les années 1970, l'IRM a été déclinée en une grande variété d'applications dont certaines utilisent des agents de contraste.

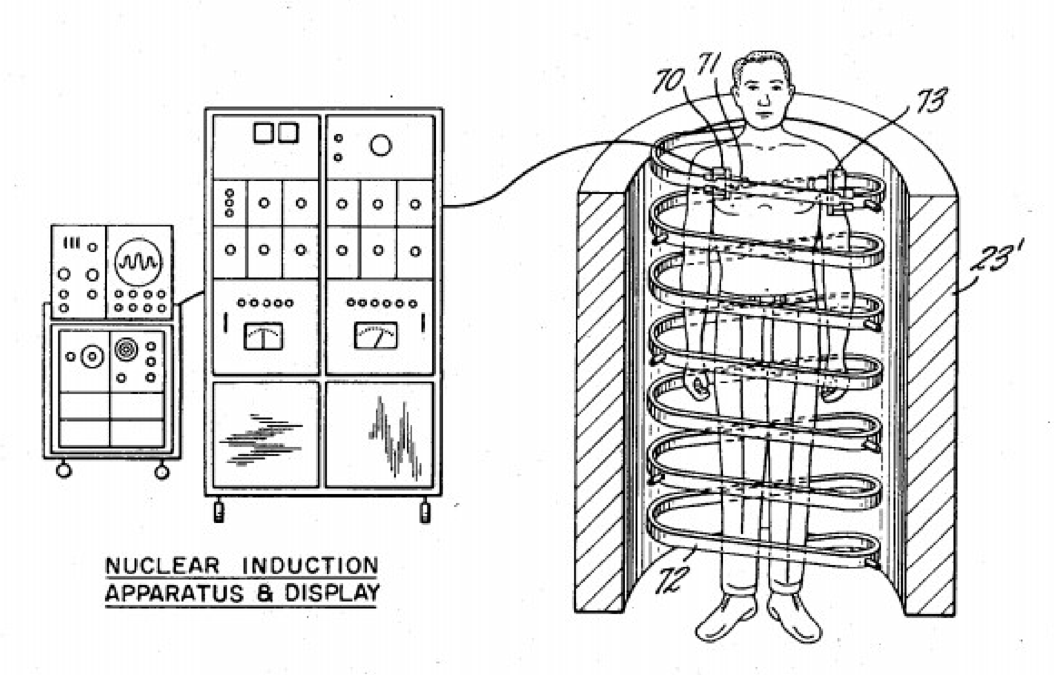

Figure 42 : Appareil d'imagerie par résonance magnétique

Le patient est placé dans un tunnel magnétique permettant de réaliser les acquisitions. Extrait du brevet déposé en 1974 par Raymond Damadian un des inventeurs de l'IRM. Le brevet couvre une application pour détecter les tumeurs.

De l'aimant à l'image

Pour référence, cf. mriquestions.com

La matière ordinaire est constituée d'atomes, eux-mêmes formés d'un noyau composé de neutrons et de protons autour duquel orbitent des électrons. Ces particules possèdent un moment magnétique, ou **spin**, défini par son orientation – un peu comme la Terre possède un champ magnétique défini par un axe Nord/Sud. Les spins des électrons sont à l'origine des propriétés magnétiques de la matière (la **susceptibilité magnétique**).

Le **diamagnétisme** est une forme universelle de magnétisme et se traduit par un effet répulsif des champs magnétiques. Cette force est généralement négligeable, mais peut être révélée par l'utilisation de champs magnétiques très élevés. Par exemple, un champ de 40 T est capable de faire léviter une grenouille (Simon and Geim, 2000). Le **paramagnétisme** n'est présent que chez certains matériaux, comme l'aluminium, l'oxygène ou l'oxyde de fer. Il correspond à une attraction faible par les champs magnétiques. Les matériaux **ferromagnétiques** (par exemple le fer, le nickel ou le cobalt) sont très sensibles aux champs magnétiques et même capables d'en garder le magnétisme, devenant ainsi des aimants. Enfin, le s**uperparamagnétisme** apparait dans les petites particules (dizaine de nm) de matériaux paramagnétiques et correspond à la fusion de leurs domaines paramagnétiques. Cela se traduit par une sensibilité plus importante aux champs magnétisme, mais sans la capacité de les conserver comme les matériaux ferromagnétiques. En plus de la susceptibilité magnétique intrinsèque à la matière, les champs magnétiques peuvent être induits par des **courants électriques**, par exemple dans les électro-aimants.

Il est possible de manipuler les spins grâce à des ondes électromagnétiques. Bien que les spins des électrons soient les plus réceptifs dans la matière, leur excitation requiert des micro-ondes, qui pénètrent mal les tissus organiques et peuvent les endommager en les chauffant. En revanche, les spins nucléaires sont excités par les ondes radio, plus pénétrantes et moins énergétiques. Le noyau atomique excitable le plus répandu dans le corps humain est celui de l'hydrogène, ou **proton (H^+)**, principalement sous forme d'**eau** (H_2O) et de lipides ($-CH_2-$). De ce fait, l'IRM utilisée en clinique est essentiellement une "**imagerie de l'eau**". À noter que d'autres noyaux (sodium, phosphore, carbone ^{13}C, xénon hyperpolarisé) voire les électrons eux-mêmes peuvent être exploités, mais leur utilisation est beaucoup plus rare.

L'IRM se base sur la résonance magnétique nucléaire pour créer des images en excitant le noyau atomique. Brièvement, l'application d'un **champ magnétique permanent B0** de quelques T force les spins de la matière à s'aligner sur les lignes de champ. Dans ces conditions, les noyaux sont ensuite excités par des ondes radio à une fréquence spécifique, la **fréquence de Larmor**. L'énergie accumulée par les spins se traduit par un mouvement de **précession** (bascule +

rotation du spin) synchronisé avec la fréquence d'excitation. Dès que l'excitation est interrompue, les spins vont se réaligner sur le champ principal B0.

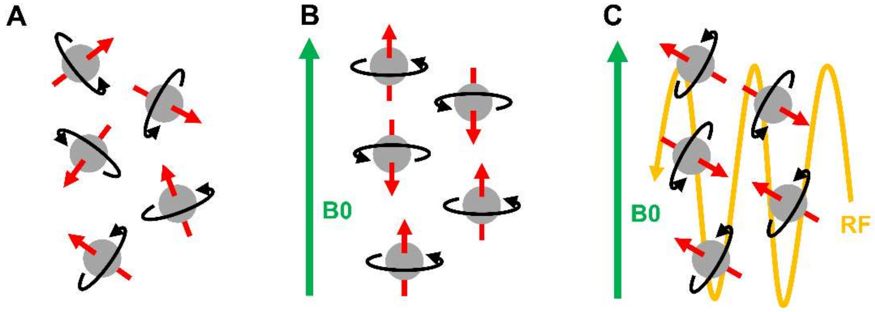

Figure 43 : Résonance magnétique nucléaire

Principe de la résonance magnétique nucléaire utilisée en IRM. Dans la matière organique, les spins (flèches rouges) ne sont normalement pas alignés (A). Mais lorsqu'un champ magnétique intense B0 est appliqué, les spins vont s'aligner selon les lignes de champ (B). Dans cet état, les spins peuvent être basculés par l'application d'une radiofréquence (RF) à la fréquence de Larmor (C). Si RF est interrompue, les spins se réalignent sur B0.

Deux phénomènes de relaxation se produisent alors : le ré-alignement des spins le long du champ principal B0, caractérisé par la constante temporelle **T1** correspondant à la récupération de 63% de la magnétisation initiale ; et la perte de la synchronicité de leur rotation, caractérisée par la constante temporelle **T2** correspondant à la perte de 63% de la magnétisation transverse induite par l'excitation. Les deux phénomènes sont affectés par les caractéristiques de la matière environnante, ce qui permet d'obtenir un **contraste** entre les différents types de tissus.

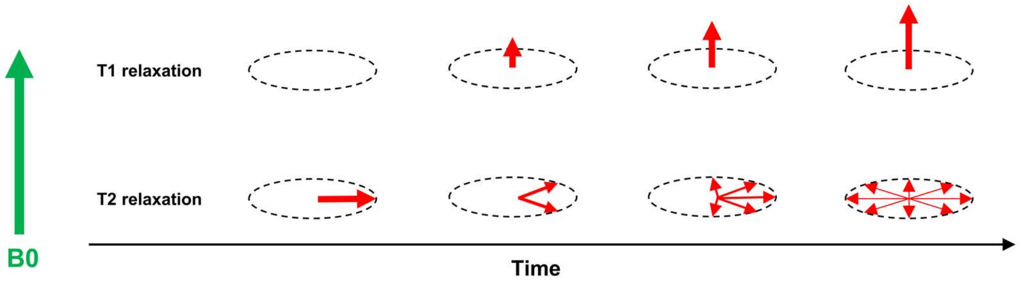

Figure 44 : Relaxation T1 et T2

Après leur bascule par l'onde radio, les spins vont se réaligner sur le champ principal B0 (relaxation T1) mais aussi perdre leur synchronisation (relaxation T2).

Cependant, les ondes et gradients employés pour exciter les spins interfèrent avec la réception du signal. L'**écho de spin** est une technique qui, grâce à une impulsion supplémentaire, permet de basculer les spins en cours de relaxation à 180°. Ce retournement se traduit par une reprise de la relaxation des spins mais en sens inverse, au cours duquel les spins vont temporairement récupérer la magnétisation imprimée par l'excitation initiale, mais en l'absence de celle-ci, ce qui autorise l'enregistrement du signal. Le **temps d'écho (TE)** correspond au temps laissé entre l'excitation et le moment où la bascule est réalisée. Certaines séquences comme l'imagerie rapide par échos refocalisés (RARE) utilisent plusieurs bascules à 180° pour maximiser le nombre

d'enregistrements à partir d'une seule excitation et accélérer la vitesse d'acquisition des images.
Le **temps de répétition (TR)** est le temps laissé entre deux excitations.
Le signal global obtenu en IRM (S) est décrit par l'équation suivante :

$$S = K.[H].\left(1 - e^{-TR/T1}\right).e^{-TE/T2}$$

, avec [H] la densité en protons et K un facteur d'échelle. En jouant sur TE et TR, il est possible de pondérer le signal obtenu davantage en T1 ou en T2.
L'enregistrement des relaxations T1 et T2 est réalisée grâce à des **antennes radio**. Le traitement du signal obtenu est complexe et ne sera pas détaillé dans cette introduction. Brièvement, le signal peut être obtenu pour une coupe entière grâce à un **codage en phase et en fréquence**. La position de la coupe est déterminée par un **gradient** dans l'intensité du champ B0 établi le long de l'imageur.

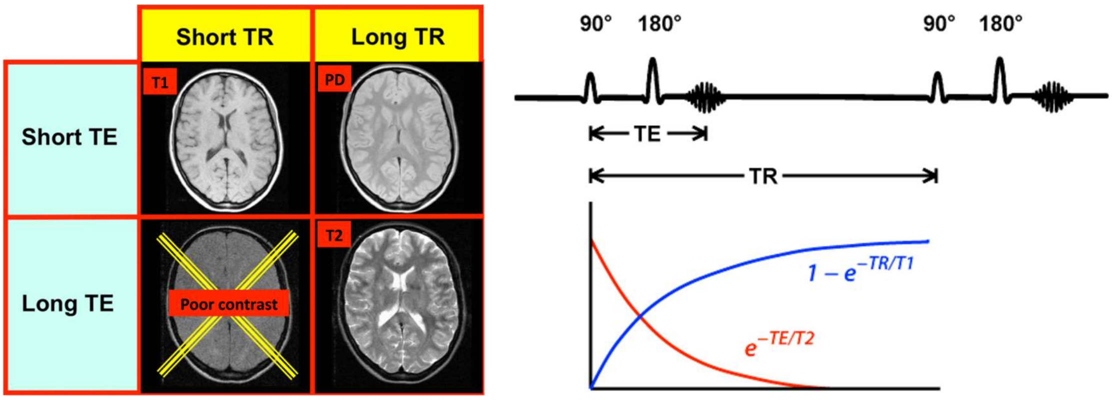

Figure 45 : Contrastes en IRM

Selon la durée du temps de relaxation (TR) et du temps d'excitation (TE), l'image obtenue sera davantage pondérée par la relaxation T1, T2, ou la densité de protons (PD). Les pondérations permettent de changer les contrastes entre les tissus. Illustrations tirées de mriquestions.com.

L'IRM a été développé à partir des années 1970 (d'abord sous le nom de "zeugmatographie"), notamment par Paul Lauterburg, Peter Mansfield et Raymond Damadian. Les deux premiers en seront récompensés par le prix Nobel de physiologie ou médecine en 2003.

Agents de contraste

Certains matériaux ont des propriétés magnétiques particulières qui leur valent d'être utilisés comme agents de contraste. À l'acquisition, ces propriétés se traduisent par une augmentation (**hypersignal** = blanc) ou une diminution (**hyposignal** = noir) du signal IRM par rapport au tissu de référence.

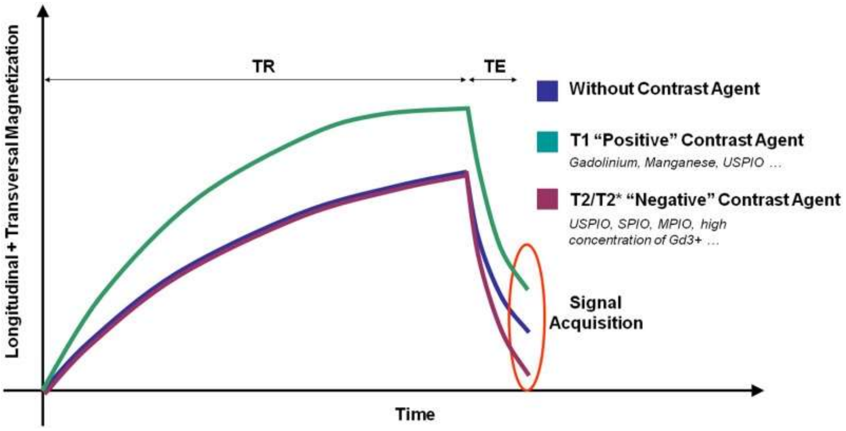

Figure 46 : Effets des agents de contraste sur les temps de relaxation

Les agents racourcissant le T1, comme le gadolinium, accélèrent la récupération de la magnétisation transversale et créent un hypersignal. Ceux qui racourcissent le T2, comme les dérivés de l'oxyde de fer, accélèrent la perte de magnétisation longitudinale et créent un hyposignal. D'après Gauberti et al., 2014.

Gadolinium

Le gadolinium (Gd) est un lanthanide (pseudo-métal appartenant aux terres rares) et l'élément présentant le plus fort effet **paramagnétique** à température ambiante. En solution, l'ion Gd^{3+} accélère considérablement la repousse T1 des molécules d'eau environnantes. Cependant, l'ion gadolinium libre est très toxique et les formes administrées en clinique sont en réalité liés à des chélateurs (pièges moléculaires). Plusieurs **chélates** ont été développés et possèdent différentes propriétés, comme la capacité à se lier à l'albumine sanguine (Ablavar®) ou un tropisme pour le foie (Multihance®). Les chélates macrocycliques comme le Dotarem® sont plus stables que ceux acycliques et leur utilisation est préférée en clinique (Kim et al., 2018).

En plus des composés utilisés en clinique, de nombreux autres agents ont été développés. Par exemple le GadoSpin D® a une structure en flocon (dendrimère) à laquelle sont rattachés 24 chélates cycliques. Le GadoSpin P® est une structure encore plus lourde (200 kDa) sous la forme d'un polymère groupant des centaines de chélates (Iliff et al., 2013a). Les chélates de gadolinium peuvent aussi être fixés à d'autres molécules comme des immunoglobulines (Pizzo et al., 2018).

Exemples d'agents de contraste à base de gadolinium utilisés en clinique				
Nom international	**Nom commercial**	**Chélateur**	**Classe**	**Usages (FDA)**
Gadoterate meglumine	Dotarem®	DOTA	Macrocyclique ionique hydrophile	Rupture BHE, anomalies vasculaires
Gadobutrol	Gadovist® / Gadavist®	BT-DO3A	Macrocyclique neutre	Rupture BHE, anomalies vasculaires
Gadoteridol	ProHance®	HP-DO3A	Macrocyclique neutre hydrophile	Anomalies vasculaires
Gadobenate dimeglumine	MultiHance®	BOPTA	Acyclique ionique lipophile	Rupture BHE, anomalies vasculaires, IRM hépatique
Gadopentetate meglumine	Magnevist®	DTPA	Acyclique ionique hydrophile	Anomalies vasculaires
Gadofosveset	Ablavar®	MS-325	Acyclique ionique	Angiographie
Gadodiamide	Omniscan®	DTPA-BMA	Acyclique neutre hydrophile	Anomalies vasculaires

Tableau 3 : Exemples d'agents de contraste à base de gadolinium utilisés en clinique

Les agents à base de gadolinium sont notamment utilisés en **IRM rehaussée par contraste dynamique (IRM-RCD)**. Dans cette technique, un bolus de gadolinium est injecté dans le sang et son passage dans le tissu est "filmé" grâce à une succession d'acquisitions rapides. L'augmentation de l'intensité de signal (le rehaussement) est alors dérivée en fonction du temps pour obtenir des paramètres pharmacocinétiques qui donnent des indications sur la structure et la perméabilité des vaisseaux (Khalifa et al., 2014).

Le rehaussement du signal IRM n'est cependant pas directement proportionnel à la quantité d'agent de contraste ajoutée dans le tissu. Pour réaliser cette quantification, la plupart des techniques exploitent l'effet du gadolinium sur le T1 de l'eau environnante : sa **relaxivité**. Connaissant cette constante et le T1 du tissu avant et après le passage du gadolinium, il est possible d'estimer la **concentration** de ce dernier. La relation est donnée par la formule :

$$r1.[C] = \frac{1}{T1_{post}} - \frac{1}{T1_{pre}}$$

, où r1 est la relaxivité T1, [C] la concentration de l'agent de contraste, et $T1_{pre}$ et $T1_{post}$ les T1 du tissu respectivement avant et après l'injection de gadolinium. La relaxivité dépend de l'agent de contraste et de l'environnement où est faite la mesure. Par exemple, la relaxivité du Dotarem® dans le sang humain à 37°C et pour un champ de 3T est : 3.43 $s^{-1}.mM^{-1}$ (Shen et al., 2015).

Les séquences IRM permettant l'imagerie quantitative du gadolinium se basent sur la **mesure du T1**. De très nombreuses techniques ont été développées dans ce but, la référence étant les séquences de type **récupération d'inversion (IRGRE)**. Mais leur relative lenteur a amené les cliniciens à préférer des séquences plus rapides au détriment de leur précision, par exemple les séquences à **angle de bascule variable (VFA-SPGR)** ou de type **Look-Locker** (Stikov et al., 2015).

L'IRM-RCD est particulièrement utile pour l'imagerie cérébrale. En effet, les chélates de gadolinium ne franchissent pas la BHE en conditions physiologiques. Cependant, celle-ci peut être altérée dans de nombreuses conditions (tumeurs, inflammation, maladie d'Alzheimer, vieillissement). Il est ainsi possible de quantifier le degré de **perméabilisation de la BHE** en mesurant le taux de passage du gadolinium dans le tissu cérébral (Chagnot et al., 2021).

L'injection de gadolinium dans le LCR permet aussi de réaliser l'imagerie du système ventriculaire et de l'espace sous-arachnoïdien (cisternographie) (Algin and Turkbey, 2013). Cependant, les injections de composés dans le LCR nécessitent un abord chirurgical particulier et sont réservées à des indications médicales strictes. Certains auteurs ont pu mettre à profit des images obtenues chez leurs patients pour étudier les échanges entre LCR-FISC chez l'être humain (Ringstad and Eide, 2020).

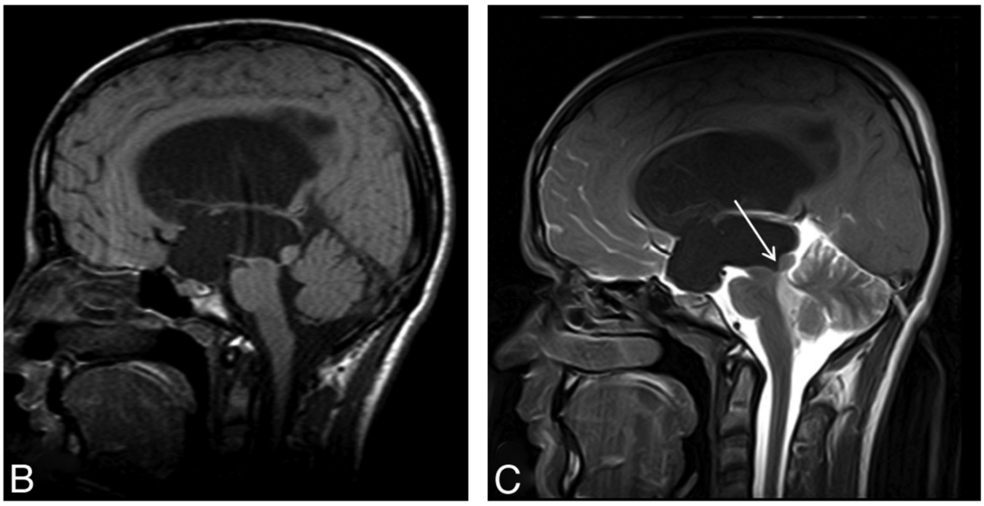

Figure 47 : Cisternographie

IRM T1 du système ventriculaire avant (B) et après (C) injection de gadolinium dans le LCR. Le rehaussement apparait en blanc et ne passe pas dans le système ventriculaire (en noir), révélant une obstruction due à une sténose de l'aqueduc (flèche) chez ce patient atteint d'hydrocéphalie. D'après Algin et Turkbey, 2013.

Oxyde de fer

Les oxydes de fer sont présents sous différentes formes. Parmi celles-ci, la magnétite (Fe_3O_4) est **ferrimagnétique**, une propriété connue et exploitée dès le Moyen-Âge pour la construction de boussoles. De nos jours, le magnétisme des oxydes de fer est utilisé dans des agents de contraste IRM, mais se révèle aussi en conditions pathologiques. Les dépôts de fer issus de saignements (**hémosidérine**) peuvent ainsi être observés en IRM T2* sous la forme de taches sombres (Cordonnier, 2010).

Les microparticules d'oxyde de fer (MPIO) ont des propriétés **superparamagnétiques** grâce auxquelles elles apparaissent 50 fois plus grandes que leur taille réelle (~1 µm). Ces particules peuvent être couplées à des anticorps et permettent de réaliser une imagerie moléculaire de la paroi vasculaire (par exemple pour tracer les marqueurs de l'inflammation). Elles sont visibles en imagerie T2* sous la forme de petits points noirs. Malgré leur potentiel clinique, les MPIO ne sont pas utilisables chez l'être humain car elles ne sont pas biodégradables (Gauberti et al., 2018).

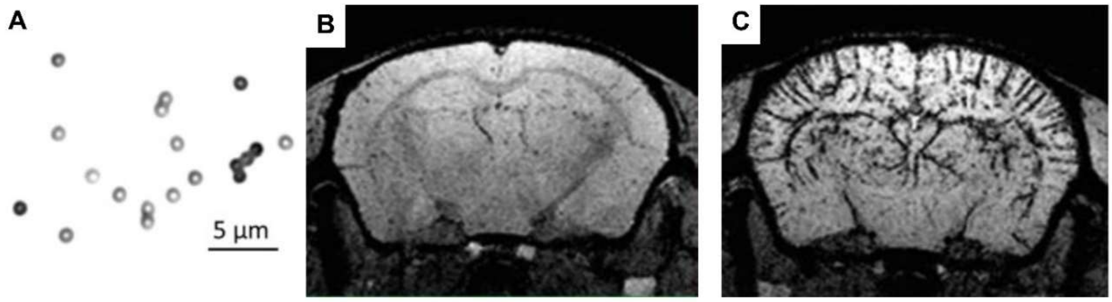

Figure 48 : IRM MPIO

MPIO vues en microscopie optique (A). Une fois couplées à des anticorps, les MPIO permettent de faire de l'imagerie moléculaire en IRM T2*. Par exemple, des MPIO couplées à des anticorps anti-VCAM (un marqueur endothélial de l'inflammation) vont se fixer à la paroi vasculaire en cas d'inflammation cérébrale (C). Chez un animal sain, elles ne se fixent pas et sont éliminées par le foie (B). D'après Gauberti et al., 2018.

Les **nanoparticules d'oxyde de fer (USPIO)** sont similaires aux MPIO mais plus petites d'un à deux ordres de grandeur. Le **ferumoxytol** est un médicament à base d'USPIO dont l'usage chez l'être humain a été approuvé par l'agence américaine du médicament (FDA ; *Food and Drug Administration*). Officiellement, le ferumoxytol sert à traiter les carences en fer mais est parfois utilisé comme agent de contraste, notamment pour l'**imagerie du système lymphatique**. En effet, les USPIO sont phagocytées par les cellules immunitaires qui se dirigent ensuite vers les ganglions. Cette propriété "lymphotropique" est notamment exploitée en cancérologie (Gkagkanasiou et al., 2016; Islam and Harisinghani, 2009). En plus de leurs propriétés en imagerie, les particules d'oxyde de fer peuvent être chauffées grâce au champ magnétique de l'IRM. Cet aspect a été exploré pour **détruire des tumeurs** (Maier-Hauff et al., 2007).

Dans l'organisme, certaines protéines possèdent des propriétés superparamagnétiques, comme la **ferritine** qui permet le stockage du fer. 24 unités de ferritine se combinent pour former une cage de 10 nm de diamètre (l'apoferritine) qui contient plusieurs milliers d'atomes de fer. Cette concentration exceptionnelle a amené certaines équipes à proposer des microparticules constituées d'agrégats de ferritine comme une **alternative biodégradable aux MPIO** (Charlton et al., 2016).

L'**hémoglobine** porte quatre atomes de fer qui lui permettent de transporter l'oxygène et sont à l'origine de la coloration rouge du sang. Leur état d'oxydation varie en fonction du taux d'O_2 et de CO_2. De manière intéressante, la consommation énergétique du tissu local cause la désaturation en oxygène du sang et modifie ses propriétés magnétiques. Ce **signal dépendant du taux d'oxygène dans le sang (BOLD)** est exploité en **IRM fonctionnelle** pour mesurer les variations de l'activité des régions cérébrales (Attwell and Iadecola, 2002).

Manganèse

Comme le gadolinium, le **manganèse** (Mn^{2+}) est un agent de contraste paramagnétique, mais ses effets sont plus faibles. Le manganèse est cependant capable de traverser la BHE et s'accumule dans les neurones, ce qui est utilisé en préclinique pour révéler la structure fine du tissu cérébral (Silva and Bock, 2008).

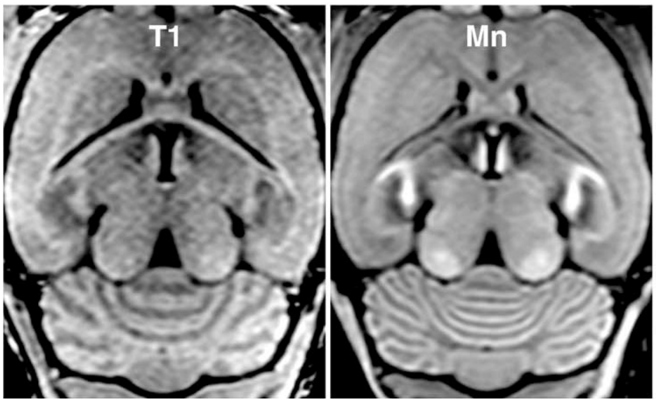

Figure 49 : IRM rehaussée au manganèse

Contraste pondéré T1 d'un cerveau de souris avant (T1) et trois jours après (Mn) injection de manganèse. Le manganèse s'est accumulé dans la substance grise dont il rehausse (blanchit) le signal. D'après Watanabe et al., 2010

Imagerie de diffusion

À l'échelle microscopique, les particules de matière sont animées de mouvements aléatoires en lien avec leur énergie thermique. Ainsi, des molécules d'eau à 20°C se déplacent à environ 600 $m.s^{-1}$. La trajectoire d'une particule individuelle est aléatoire du fait des collisions avec les autres molécules, un phénomène nommé **mouvement brownien**. La nature aléatoire du déplacement des particules tend à équilibrer leur concentration en tout point de l'espace.

La diffusion est un phénomène macroscopique issu de ce mouvement. Elle se traduit par l'homogénéisation des caractéristiques d'un milieu donné avec le temps (*e.g.* sucre dans un café, chaleur dans un objet). Ce phénomène est intrinsèquement lié à la notion d'**entropie**. La diffusion ne requiert aucun moteur autre que l'agitation thermique.

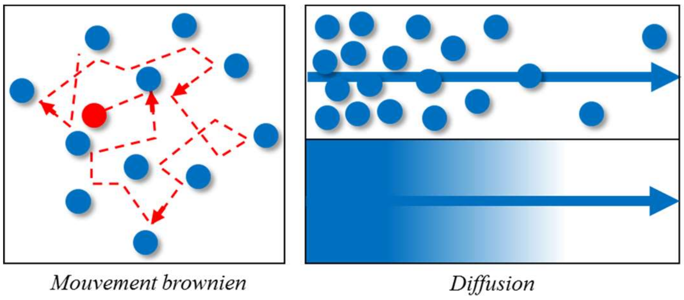

Figure 50 : Le mouvement brownien, base de la diffusion

La somme des mouvements imprévisibles des particules se traduit par le phénomène prévisible de la diffusion.

Restriction par les tissus

Ces mouvements microscopiques sont influencés par la **structure tissulaire** sous-jacente. En effet, le déplacement des molécules d'eau est restreint par les membranes cellulaires. Dans un milieu encombré (tissu), les déplacements des molécules d'eau couvriront un espace plus réduit que dans un milieu libre (LCR). De plus, le sens de déplacement des molécules peut indiquer la présence de fibres et permettre la reconstruction de leur réseau (**tractographie**). La résolution de l'IRM étant limitée à quelques dizaines de µm, le signal analysé résulte de la moyenne d'une importante population de molécules d'eau.

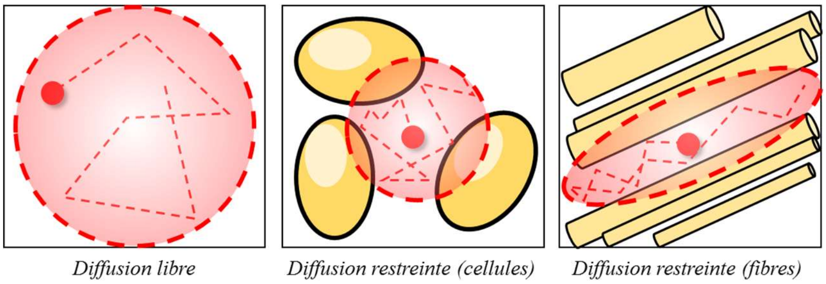

Figure 51 : Restriction de la trajectoire des molécules d'eau par le tissu

La moyenne des trajectoires possibles pour la molécule d'eau est représentée par un ellipsoïde. L'encombrement du milieu détermine le percours des molécules d'eau, i.e. le long des fibres nerveuses.

La répartition statistique des comportements des molécules d'eau de cette population peut être analysée, afin de séparer le signal global en plusieurs composantes. Dans le cas de l'analyse du **mouvement incohérent intravoxel (IVIM)**, un pool de diffusion rapide correspondant aux capillaires est séparé d'un pool de diffusion lente correspondant au reste du tissu. Quant aux analyses de **kurtosis**, elles permettent d'extraire un pool de diffusion 'statique'.

L'**imagerie de diffusion (DW-IRM)** exploite les propriétés d'encodage de l'imageur pour extraire ces informations. Brièvement, Pour un voxel donné, on peut ainsi tracer une courbe décrivant la perte de signal en fonction de la **b-value** (pondération en diffusion). En première approximation, cette courbe est une droite descendante (en échelle log) dont la pente est d'autant plus importante que la diffusion de l'eau est libre, c'est-à-dire que dans un liquide (*e.g.* le LCR) les molécules d'eau sortent rapidement du voxel puisque leurs déplacements ne sont pas contraints. A l'inverse, dans un tissu, les membranes cellulaires restreignent les déplacements de l'eau et réduisent *de facto* la perte de signal. La pente de cette droite est calculée en ne mesurant que 2-3 pondérations en diffusion (quelques minutes) et correspond au **coefficient de diffusion** apparent (ADC).

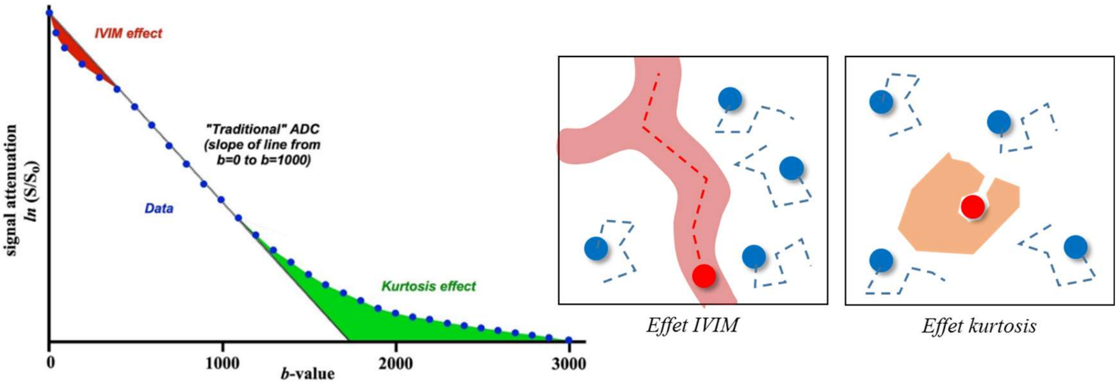

Effet IVIM

Effet kurtosis

http://www.mriquestions.com/ivim.html

Figure 52 : Courbe de perte du signal en IRM de diffusion

La perte du signal en fonction de la b-value (pondération en diffusion) forme une droite dont la pente est l'ADC. Dans le tissu, le signal de l'eau des capillaires est rapidement perdu en début de courbe (effet IVIM) ou est retenu par les interactions moléculaires avec le tissu (effet kurtosis). Illustration trouvée sur mriquestions.com.

Mais cette droite est une approximation d'une réalité bien plus complexe. Pour de faibles b-values, on peut parfois observer une diminution rapide du signal. C'est l'**effet IVIM** (IntraVoxel Incoherent Motion), qui correspond aux molécules d'eau des capillaires exclues très rapidement du voxel indépendamment de la diffusion. Les analyses IVIM se basent sur un modèle mathématique afin de séparer cette 'eau des capillaires' de 'l'eau des tissus'. Concrètement, il s'agit de séparer un pool de diffusion rapide, dont le **coefficient de pseudo-diffusion** est noté **D***, **du pool majoritaire de diffusion lente**, dont le **coefficient de diffusion** est noté **D**. L'influence relative, *i.e.* le ratio du 'volume' occupé par le pool rapide par rapport au 'volume' du pool lent est appelé **fraction de perfusion** et noté **fp**.

Pour des b-values élevées, la pente de la courbe s'adoucit. Cela signifie qu'il existe des molécules d'eau 'piégées' dans le voxel (par des interactions avec les protéines ou les membranes par ex.) et dont le signal ne disparaîtra pas même avec de très fortes pondérations en diffusion. Cette répartition statistique particulière est représentée par un paramètre nommé **kurtosis**. Plus ce paramètre est élevé, plus la fraction d'eau piégée au contact des membranes est importante. Cela décrit la complexité des tissus.

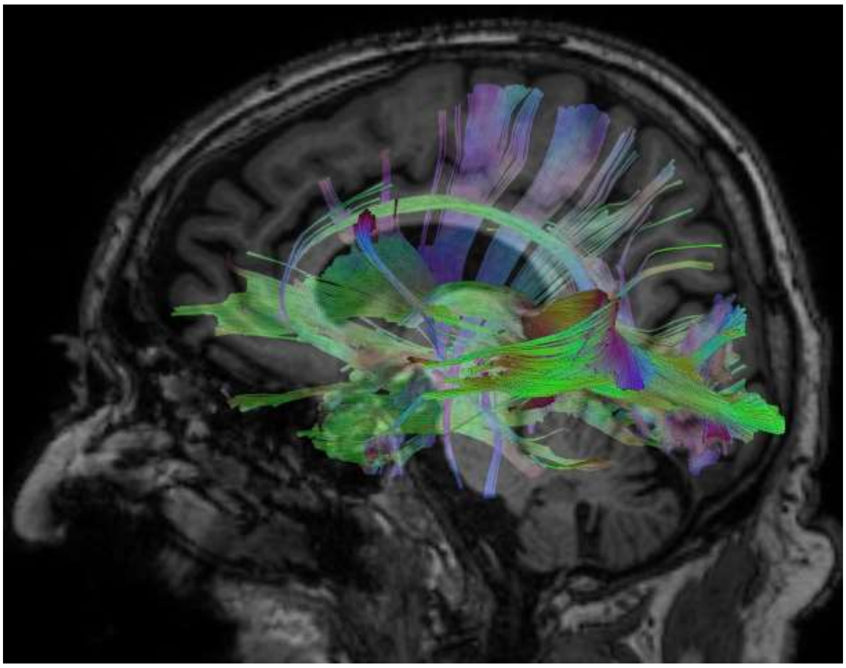

Figure 53 : Imagerie du tenseur de diffusion

L'IRM de diffusion permet de détermnier l'orientation des tractus de fibres. Ici, les fibres de l'hippocampe droit, superposées à une IRM anatomique T1 classique. La couleur permet de coder l'orientation en 3D. Image aimablement fournie par Jade Lasserve, 2021.

Résumé / *Abstract*

- L'**IRM** exploite des **champs magnétiques** intenses pour créer des coupes anatomiques *in vivo*. Le signal reçu dépend principalement des molécules d'**eau**.
- Les agents de contraste paramagnétiques comme le **gadolinium** peuvent être utilisés pour rehausser le signal de tissus comme le sang ou le LCR
- En **IRM de diffusion**, le mouvement des molécules d'eau est analysé de manière statistique pour révéler la **structure microscopique des tissus**.

- The **magnetic resonance imaging** relies on strong magnetic fields to analyze the tissues in vivo. The signal mostly depends on **water** molecules.
- Paramagnetic contrast agents such as **gadolinium** are used to enhance the signal of tissues such as blood or cerebrospinal fluid.
- **Diffusion-weighted magnetic resonance imaging** reveals the **microscopic structure of tissues** through the statistical analyse of the motion of water molecules.

Les maladies neurodégénératives, un problème de déchets ?

Maladie d'Alzheimer

Les peptides bêta-amyloïdes (Aβ) sont des molécules neurotoxiques produites par le métabolisme cérébral. Bien que plusieurs systèmes permettent leur élimination du SNC, les peptides Aβ s'accumulent avec le vieillissement et leur excès est associé à des pathologies telles que la maladie d'Alzheimer (MA) ou l'angiopathie amyloïde cérébrale (AAC). Plusieurs travaux récents suggèrent que les échanges LCR-FISC seraient impliqués dans la clairance des peptides Aβ hors du SNC et que l'altération de cette voie favoriserait l'émergence de pathologies neurodégénératives.

Cependant, l'hypothèse selon laquelle les peptides Aβ seraient le facteur causal des pathologies qui y sont associées est régulièrement remise en question. Les thérapies ciblant ces peptides n'ont, en effet, rencontré qu'un succès limité en clinique.

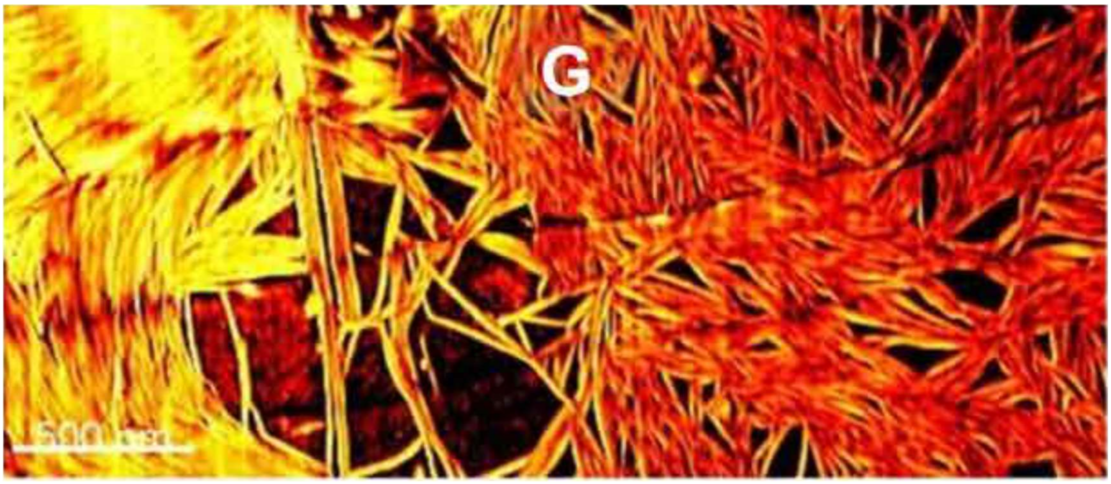

Figure 54 : Plaque amyloïde vue en microcopie à force atomique

Les peptides Aβ s'agrègent en microfibrilles avant de former des plaques. D'après Nirmalraj et al., 2020.

Epidémiologie et facteurs de risque

La MA est une **démence liée à l'âge** caractérisée par des troubles cognitifs et des pertes de mémoire. Elle est causée par une **neurodégénérescence** et la présence de **plaques amyloïdes** et de **neurofibrilles tau (NFT)** (Scheltens et al., 2021). La MA est la cause principale de démence (>70%). Elle affecte plus de 50 millions de personnes dans le monde, dont un million en France. Sa prévalence pourrait tripler d'ici 2050 du fait du vieillissement de la population (Alzheimer's Disease International, 2018). Le principal facteur de risque pour la MA est l'âge au-delà de 65 ans.

L'incidence de la MA est **plus élevée chez les femmes** qui représentent les deux tiers des patients. Il existe de plus des différences notables entre les sexes dans le développement de la maladie. Ainsi, les femmes sont sujettes à des formes plus sévères et tardives. Le taux d'hormones sexuelles (œstrogène ou testostérone) au cours de la vie jouerait un rôle protecteur contre la maladie (Pike, 2017). En plus du sexe, déterminé génétiquement et hormonalement, le genre en tant que rôle social contribue à expliquer les différences hommes/femmes par son influence sur le style de vie. Ainsi, les femmes ont un accès à l'éducation plus restreint que les hommes et une tendance moindre à pratiquer une activité physique, deux facteurs qui favorisent l'incidence de la MA (Mielke et al., 2014).

Une part significative du risque de développer la maladie est ainsi due à des **facteurs liés au mode de vie**. Ainsi, un rapport de 2020 de Livingston et collaborateurs estime que 12 paramètres modifiables sont responsables pour 40% du risque de démences. Pour lutter contre la maladie, les auteurs recommandent entre autres de limiter l'usage d'alcool et de tabac. Ils relèvent les traumatismes crâniens, l'hypertension, le diabète et l'obésité comme des facteurs de risque, alors que l'activité physique, sociale et cognitive sont des facteurs protecteurs (Livingston et al., 2020).

L'**origine ethnique** influence elle aussi le risque de développer la MA. Par exemple, aux Etats-Unis, les afro-américains ont un risque deux fois plus élevé de développer la maladie que les caucasiens. Bien que certains déterminants soient liés au fond génétique des populations (notamment pour les formes précoces, *cf.* (Chen and Panegyres, 2016)), là encore l'influence des facteurs sociaux (accès à l'éducation, comorbidités liées au mode de vie) reste primordiale (Weuve et al., 2018).

Plus de la moitié des facteurs de risque sont **génétiques**, notamment au travers de l'allèle ε4 de l'**apolipoprotéine E (APOE ε4)**, le second facteur le plus important après l'âge. Certaines mutations rares sur des gènes associés au métabolisme des peptides Aβ comme *APP*, *PSEN1* ou *PSEN2* sont à l'origine de formes familiales précoces de la maladie (Cacace et al., 2016).

Cas particulier, le **syndrome de Down** est fortement associé à la MA. Il s'agit d'un trouble génétique causé par une trisomie complète ou partielle du chromosome 21. C'est la cause la plus fréquente de déficience intellectuelle, qui affecte près de 6 millions de personnes dans le monde. Le syndrome de Down est associé à de nombreuses comorbidités, notamment cardiaques, mais aussi à un risque élevé de développer la maladie d'Alzheimer à un âge précoce (<40 ans). Ce risque accru est dû à une surexpression du gène de la protéine précurseure de l'amyloide (APP), porté par le chromosome 21 (Carmona-Iragui et al., 2019).

Aspects cliniques

Symptômes cliniques et évolution

La MA est une condition **évolutive**, marquée par des troubles cognitifs de plus en plus sévères. L'**échelle de Reisberg** propose sept stades gradués par ordre croissant à mesure du déclin cognitif (Reisberg et al., 1982).

Echelle de Reisberg pour la maladie d'Alzheimer (1982)	
Stade	**Observations cliniques**
1	Pas de déclin cognitif
2	Pertes de mémoire légères relevées par les patients
3	Les pertes de mémoire à court terme sont flagrantes, troubles de la concentration, anxiété modérée
4	Troubles de la concentration manifestes, oubli d'informations personnelles, émoussement affectif
5	Perte des repères dans le temps et l'espace, dépendance pour les tâches de la vie quotidienne
6	Perte du rythme jour/nuit, altération de la personnalité, incontinence
7	Perte quasi-totale du langage, dépendance pour l'alimentation et les soins du corps, troubles psychomoteurs sévères

Tableau 4 : Échelle de Reisberg pour la maladie d'Alzheimer

Bien qu'utile en pratique clinique, ce type d'échelle est insuffisant pour le diagnostic de la maladie, pour lequel l'imagerie et la mesure de biomarqueurs restent indispensables. En particulier, la MA a une phase prodromale dans laquelle les patients n'ont pas encore de symptômes mais peuvent présenter une atrophie cérébrale (Ten Kate et al., 2018).

La mort survient en moyenne six ans après le diagnostic initial (Rhodius-Meester et al., 2019). Les causes de décès sont liées aux troubles moteurs (dysphagie), mais aussi aux complications nosocomiales et à l'affaiblissement du système immunitaire (pneumonies) (Degerskär and Englund, 2020).

Traitements

Peu de traitements médicamenteux ont été validés contre les symptômes de la MA. Le **donepezil** est un inhibiteur de la cholinestérase visant à augmenter le taux d'acétylcholine, déficitaire chez les patients atteints de la MA. La **mémantine** est un inhibiteur non compétitif des récepteurs N-méthyl D-aspartate et vise à réduire l'excitotoxicité. Ces deux traitements sont souvent utilisés en association, mais leur bénéfice chez les patients reste modéré (Briggs et al., 2016).

Plusieurs essais cliniques se sont attaqués directement aux peptides Aβ, avec un succès limité. Certains ont testé l'efficacité d'inhibiteurs des sécrétases impliqués dans la sécrétion des peptides Aβ (**lanabecestat, verubecestat**), sans succès à ce jour (Briggs et al., 2016). En juin 2021 la *federal drug agency* (FDA) approuve l'utilisation d'un anticorps anti-amyloïde, l'**adacunamab**, pour le traitement de la MA (FDA, 2021) mais l'efficacité du traitement reste faible.

D'autres types d'intervention, comme la stimulation magnétique transcrânienne répétée (Chou et al., 2020), les thérapies basées sur le sommeil (Blackman et al., 2021), ou la méditation (Chételat et al., 2018) pourraient se révéler utiles pour alentir la progression de la maladie.

Diagnostic

La caractérisation de la MA se base sur trois éléments :

- **les plaques amyloïdes de peptide Aβ**
- **les NFT de protéine tau**
- **la neurodégénérescence ou atteinte neuronale**

En clinique, le diagnostic de la MA se base sur des symptômes prototypaux, confirmés par une analyse de biomarqueurs (Tau et Aβ) dans le LCR et par l'imagerie moléculaire, anatomique (perte de volume cérébral) et fonctionnelle (hypométabolisme) (Jack et al., 2018).

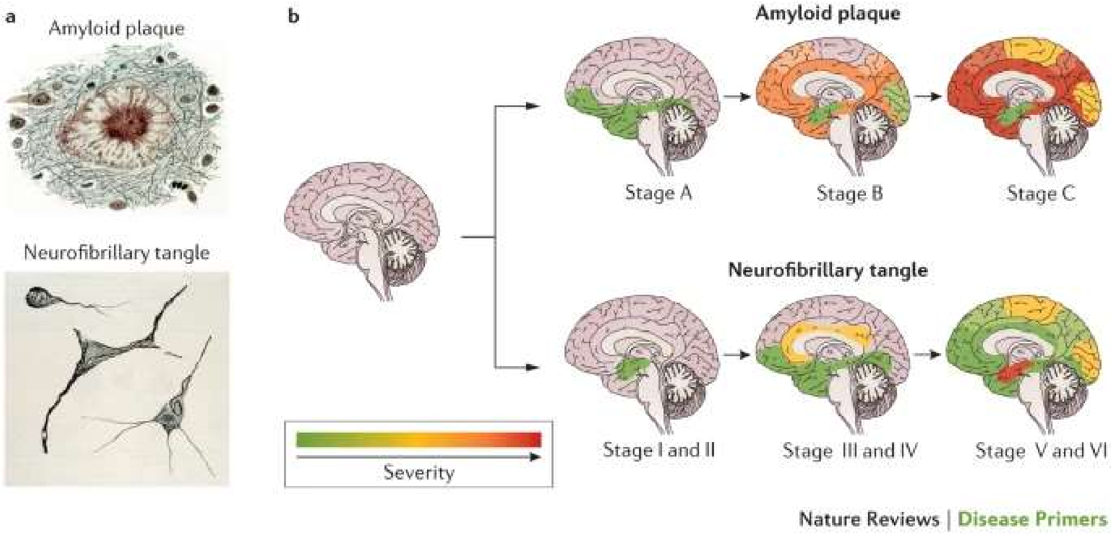

Figure 55 : L'évolution de la MA est liée aux fibrilles tau et aux plaques amyloïdes

Les stades A, B et C décrivent la progression des plaques amyloïdes, et les stades I à VI (stades de Braak) celle des NFT. D'après Masters etal., 2015.

Scores cognitifs

De nombreux scores cognitifs dédiés aux démences ont été exploités pour le diagnostic et le suivi de la MA, comme l'échelle de Reisberg précédemment mentionnée. **L'échelle d'évaluation clinique de la démence (CDR)** évalue les capacités du sujet dans six domaines (mémoire, orientation, résolution de problèmes, vie sociale, loisirs et soins personnels). Un score global est calculé à partir de ces items, de 0 (cognition normale) à 3 (démence sévère). Le ***mini-mental state examination*** **(MMSE)** est une autre échelle couramment utilisée car réalisable en une quinzaine de minutes. Le MMSE se base sur 30 questions, un score de 30 indiquant une cognition normale et 0 une démence sévère (Perneczky et al., 2006). En parallèle, le développement des **technologies numériques** a permis l'émergence d'une multitude de tests, complémentaires aux examens type 'papier-crayon'. Ainsi, l'utilisation de la réalité virtuelle, de capteurs de mouvement ou de l'apprentissage machine laissent entrevoir de nouvelles opportunités pour le dépistage précoce de la MA (Fernández Montenegro et al., 2020).

Les scores cognitifs permettent de détecter un **déficit cognitif léger (MCI)**, stade précurseur de la MA ou d'autres démences (Jongsiriyanyong and Limpawattana, 2018).

Biomarqueurs

L'analyse de marqueurs dans le LCR est souvent utilisée en premier lieu car moins chère que l'imagerie (Chételat et al., 2020). Elle se base sans s'y limiter sur les deux molécules signatures de la MA : les peptides Aβ et la protéine Tau. Le **peptide Aβ42** est une isoforme normalement minoritaire mais est le principal constituant des plaques amyloïdes. Ses taux dans le LCR et le plasma diminuent chez les patients atteints de la MA. Ils sont parfois exprimés sous forme de ratio avec **Aβ40,** la forme majoritaire, dont les taux ne changent pas avec la MA. Les peptides Aβ sont aussi retrouvés dans le LCR sous forme d'**oligomères**, mais leur corrélation avec la MA reste peu claire. Dans la MA, la protéine tau est présente sous une forme hyperphosphorylée, **p-tau**, qui s'agrège en fibrilles. La quantité totale de protéine Tau **t-tau** ainsi que p-tau sont toutes deux augmentées dans le LCR des patients atteints de la MA. D'autres marqueurs ont été mis en évidence dans la MA, qui révèlent des anomalies vasculaires, des troubles synaptiques, l'inflammation ou l'activation des cellules gliales (Molinuevo et al., 2018).

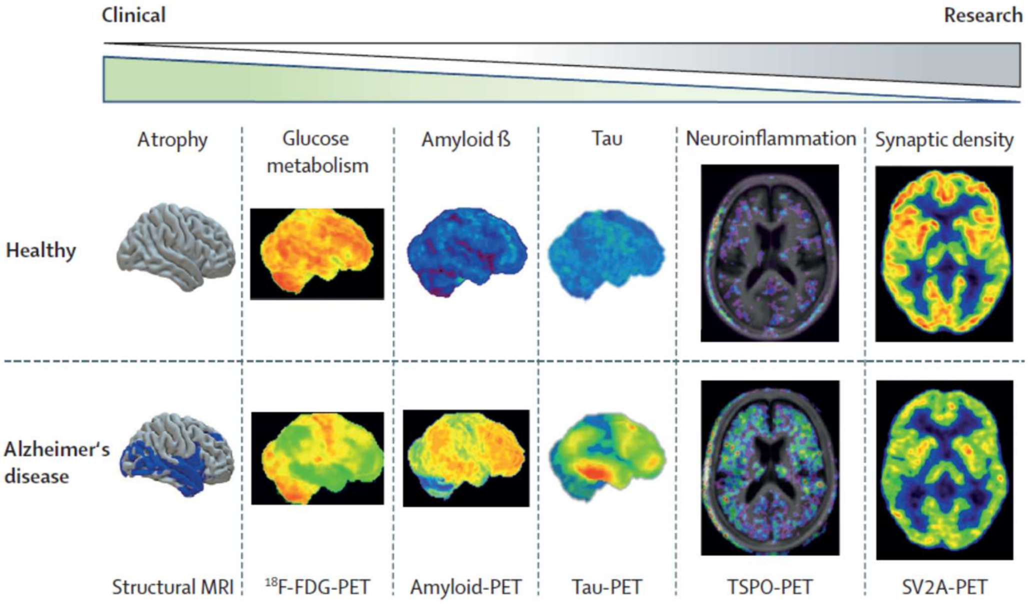

Figure 56 : Radiotraceurs utilisés en TEP pour l'imagerie de la MA

Compoaraison de plusieurs types d'imagerie entre des contrôles sains et des patients atteints de la MA. L'IRM structurelle reste la plus utilisée en clinique. TSPO : Translocator protein ; SV2A : Synaptic vesicle glycoprotein 2A. D'après Chételat et al., 2020.

Imagerie

La tomographie par émission de positons (TEP) exploite des traceurs radiomarqués pour l'étude et le diagnostic de la MA. En clinique, l'hypométabolisme et la présence de plaques amyloïdes sont les marqueurs les plus utilisés. Le fluorodéoxyglucose ^{18}F (^{18}F-FDG) est une molécule radiomarquée dont la structure imite le glucose, internalisé par les cellules ayant une forte demande énergétique (neurones, cellules cancéreuses). Dans la MA, il permet d'observer **l'hypométabolisme cérébral**. Le composé de Pittsburgh type B est le premier radiotraceur spécifique des plaques amyloïdes. D'autres ont été développés depuis, tels le ^{18}F-florbetapir. L'**imagerie amyloïde** est une des techniques les plus sensibles pour le diagnostic *ante mortem* de la MA (Chételat et al., 2020).

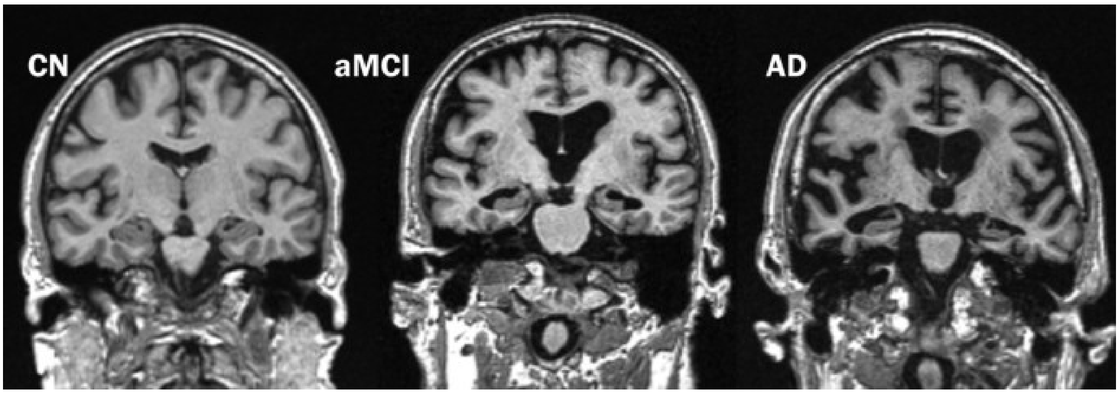

Figure 57 : Atrophie cérébrale dans la MA

IRM cérébral montrant l'atrophie cérébrale chez une personne atteinte de MCI avec amnésie (aMCI) et un patient atteint de la MA (AD) comparés à une personne âgée sans déficit cognitif (CN). D'après Vemuri et Jack, 2010.

L'IRM structurelle révèle plusieurs altérations cérébrales chez les patients atteints de MCI ou de la MA, notamment une **atrophie de la matière grise** (qui se traduit par des espaces de LCR plus important) et des **hypersignaux de la matière blanche** visibles en pondération T2 FLAIR. L'anatomie fine des régions les plus touchées, comme l'**hippocampe**, peuvent anticiper le développement de la maladie (de Flores et al., 2015). L'IRM pondérée en diffusion (DW-IRM) exploite le mouvement microscopique des molécules d'eau pour sonder la structure fine des tissus. Dans la MA, elle montre une **augmentation de l'ADC** ainsi qu'une **réduction de la FA**, causées par la désorganisation du tissu. L'ASL mesure la **diminution du CBF** observée dans la MA. L'IRMf permet quant à elle de visualiser la **perte de connectivité** (coordination) entre les régions cérébrales. Cas particulier, la spectroscopie par résonance magnétique est une technique voisine de l'IRM utilisée pour quantifier les métabolites dans le tissu cérébral. Dans la MA, sont observées une **diminution du N-acétyl-aspartate** et une **augmentation du myo-inositol** (Chandra et al., 2019). Enfin, l'IRM rehaussée par contraste dynamique (IRM-RCD) permet de montrer la **perméabilité accrue des vaisseaux** (Chagnot et al., 2021).

Le peptide bêta-amyloïde

Le terme ‘amyloïde’ (du latin *amylum* : amidon) a été employé dès 1845 par Rudolf Virchow pour décrire des anomalies tissulaires qu’il identifiait, à tort, à des dépôts d’amidon (Sipe and Cohen, 2000).

Les fibrilles amyloïdes sont des **assemblages stables de protéines homopolymères**, associées par des conformations en cross-β (Harrison et al., 2007). Elles sont impliquées dans divers mécanismes biologiques, par exemple en tant que forme de stockage pour les hormones pituitaires (Maji et al., 2009) ou comme antibactérien dans le sperme (Easterhoff et al., 2013).

Les plaques Aβ sont une forme neurotoxique, retrouvées dans une variété de pathologies incluant la MA. Les peptides Aβ, à l’origine de la formation de ces plaques, sont dérivés de la **protéine précurseure de l’amyloïde** (APP) (Hardy and Higgins, 1992).

Biosynthèse

L’APP est une protéine à un seul passage transmembranaire et présentant un large domaine extracellulaire. Elle est exprimée par les neurones excitateurs et les interneurones GABAergiques, en particulier dans le cortex et l’hippocampe. Une fois clivé par des sécrétases transmembranaires, le fragment libre de l’APP joue divers rôles neurotrophiques incluant la croissance axonale (Müller et al., 2017).

C’est lors de ce clivage que peuvent être libérés les peptides Aβ. **Trois sécrétases, α, β et γ**, interviennent dans la maturation de l’APP dans le réticulum endoplasmique et l’appareil de Golgi : la première étape est la séparation de la protéine APP libre, effectuée soit par l’α-sécrétase soit par la β-sécrétase. L’α-sécrétase et la β-sécrétase opèrent à des sites de clivage distincts : la première libère une forme de l’APP légèrement plus longue (APPsα) que la seconde (APPsβ). Puis, la γ-sécrétase clive la portion intracellulaire du fragment resté ancré à la membrane. Si le premier clivage a été réalisé par la β-sécrétase, le résidu transmembranaire est le peptide Aβ, capable de s’agréger en plaques. Le résidu libéré par la γ-sécrétase après clivage par l’α-sécrétase, p3, est quant à lui rapidement métabolisé (Müller et al., 2017).

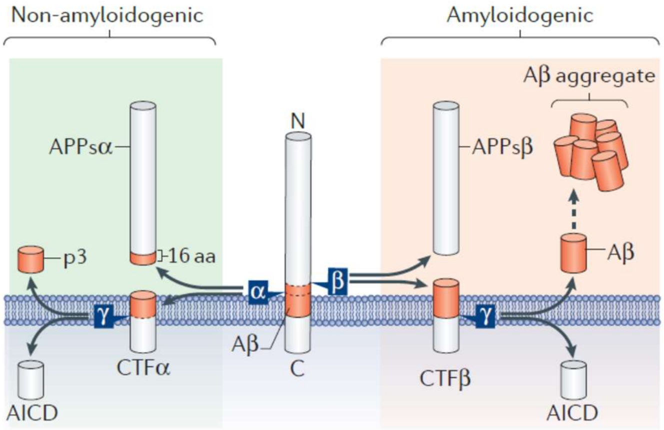

Figure 58 : Biosynthèse des peptides Aβ

Dans l'appareil de Golgi, l'APP (au centre) est clivable soit par l'α-sécrétase (à gauche), soit par la β-sécrétase (à droite). La γ-sécrétase ne libère de peptides Aβ que dans le second cas. D'après Müller et al., 2017.

Isoformes

Le clivage imparfait par la γ-sécrétase produit plusieurs isoformes du peptide Aβ, caractérisées par leur nombre de résidus. Les plus fréquentes sont les peptides **Aβ40** et **Aβ42**, toutes deux toxiques sous forme monomériques et capables de s'agréger. La forme Aβ40 est 5 à 7 fois plus abondante que Aβ42, mais cette dernière est plus toxique et amyloïdogène (Qiu et al., 2015). En plus des isoformes issues de la voie canonique, d'autres sont produites par des sites de clivages alternatifs ainsi que par des modifications post-traductionnelles (Roher et al., 2017).

L'assemblage des peptides produit plusieurs types de plaques ou de fibrilles ayant des propriétés distinctes, mais les formes solubles sont considérées comme les plus toxiques (Deshpande et al., 2006), en particulier le peptide Aβ42 (Qiu et al., 2015).

La toxicité des peptides Aβ s'exprime par divers mécanismes. Les plaques et les monomères possèdent des effets oxydants (Butterfield, 2002; Deshpande et al., 2006). Elles promeuvent aussi l'apoptose (mort cellulaire programmée) par l'activation des caspases (Gervais et al., 1999) et perturbent la régulation des fibrilles Tau, composant structurels des neurites (Hernández and Avila, 2008).

Récepteurs et transporteurs

Le **récepteur aux lipoprotéines de basse densité (LRP-1)** est un récepteur transmembranaire lourd (600 kDa) impliqué dans les phénomènes d'endocytose. Il intervient dans le métabolisme du cholestérol, associé à l'ApoE. LRP-1 est principalement exprimé par les cellules endothéliales et réalise le transfert des peptides Aβ vers le sang. La forme sLRP est un fragment clivé de LRP-1, présent dans le plasma et qui permet de retenir les peptides Aβ dans le sang jusqu'à leur élimination. 70% à 90% de l'Aβ sanguin est ainsi séquestré, un taux qui diminue chez les patients atteints de la MA (Deane et al., 2008). LRP-1 permet aussi l'endocytose et l'élimination de la p-tau (Rauch et al., 2020).

Le **récepteur aux produits finaux de glycation avancée (RAGE)** est un récepteur de la famille des immunoglobulines sensible à des motifs liés à des modifications post-traductionelles, en particulier des glycoprotéines. RAGE est impliqué dans les mécanismes inflammatoires et l'abondance de peptides Aβ capables de s'y lier pourraient contribuer à l'inflammation observée dans la MA. Dans la MA, l'expression de RAGE par les neurones diminue alors que celle dans les vaisseaux augmente. Cette expression vasculaire pourrait favoriser le retour des peptides Aβ du sang vers le tissu cérébral (Donahue et al., 2006).

Le **récepteur p75 aux neurotrophines (p75NTR)** est notamment exprimé par les neurones cholinergiques des noyaux de la base. La liaison des peptides Aβ à ce récepteur, puis leur internalisation, a été proposée comme une voie d'élimination, la perte de ces neurones cholinergiques étant liée à la MA. p75NTR est cependant impliqué dans la mort cellulaire, et une version plus probable du mécanisme suggère que les peptides Aβ causeraient la mort de ces neurones plutôt que d'être éliminés par eux (Qian et al., 2019).

Dégradation enzymatique

En complément de la clairance des peptides Aβ, il existe une grande variété d'enzymes capables de les dégrader (Miners et al., 2008).

La **plasmine** est une sérine protéase capable de cliver le peptide Aβ sur plusieurs sites. Impliquée dans la lyse du thrombus par action sur la fibrine, cette enzyme est présente sous une forme inactive, le plasminogène, activée par l'activateur tissulaire du plasminogène (tPA). *In vitro*, la présence de peptide Aβ induit la sécrétion de tPA par les neurones, et l'expression de tPA est plus élevée chez des modèles animaux présentant une charge amyloïde importante. Plasmine et tPA pourraient être impliqués dans une boucle de régulation des peptides Aβ (Miners et al., 2008; Mutimer et al., 2021).

Les **métalloprotéinases matricielles** (MMP) sont une famille d'endopeptidases dépendantes du zinc ou du calcium dont plusieurs sont sécrétées par les neurones et les cellules gliales. Les MMP-2, -3 et -9 sont capables de dégrader les peptides Aβ *in vitro*, et MMP-9 va jusqu'à dégrader les plaques amyloïdes. L'activité de ces enzymes est accrue dans les tissus de patients atteints de la MA (Miners et al., 2008).

La **néprilysine** est une métalloendopeptidase transmembranaire exprimée par les neurones à l'interface (pré et post) synaptique, ainsi que dans la media (couche musculaire lisse) et l'endothélium des vaisseaux corticaux et leptoméningés. L'expression de la néprilysine diminue avec l'âge et est réduite chez les porteurs de l'allèle APOE ε4 (Miners et al., 2008).

L'**insulysine** est une métalloendopeptidase cytosolique exprimée par les neurones, mais aussi par le foie, le muscle et le testicule. Une forme sécrétable existe également dans le LCR. L'expression de l'insulysine semble diminuer à mesure de la progression de la MA (Miners et al., 2008).

Les **enzymes de conversion de l'endothéline de type 1 et 2** sont des métalloendopeptidases transmembranaires exprimées par les cellules endothéliales et certains neurones corticaux. La diminution du taux de ces enzymes dans le LCR a été corrélée à la MA (Miners et al., 2008).

L'**enzyme de conversion de l'angiotensine** est une métalloprotéase largement exprimée par la vasculature dans l'ensemble du corps, où elle joue un rôle central dans la régulation de la tension artérielle. Elle est aussi retrouvée dans les neurones pyramidaux du cortex (Miners et al., 2008).

Cas de la protéine tau

La protéine tau est impliquée dans la régulation de la structure des microtubules, une part fondamentale de l’architecture de l’axone. Dans plusieurs pathologies (tauopathies), elle s’agrège en fibrilles neurotoxiques. Ces NFT sont une des signatures de la MA, mais aussi de la tauopathie primaire liée à l’âge (PART) ou de la maladie des grains argyrophiles (Wang and Mandelkow, 2016).

Au cours de son métabolisme, la protéine tau subit diverses modifications post-traductionnelles. En particulier, elle possède plus de 40 sites de phosphorylation. La forme hyperphosphorylée de la protéine tau (p-tau), pathologique, ne se lie plus aux microtubules et s’agrège en NFT (Meraz-Ríos et al., 2010; Wang and Mandelkow, 2016).

En dehors des formes familiales, causées par des mutations du gène de la protéine tau (*MAPT*), la pathogenèse des tauopathies reste mal connue. Comme pour les plaques amyloïdes, l’occurrence des NFT augmente avec l’âge. La PART se traduit pour les formes sévères par l’apparition d’une démence proche de la MA causée par l’accumulation des NFT (Crary et al., 2014). Dans la MA, il a été rapporté que les peptides Aβ promeuvent l’hyperphosphorylation de tau.

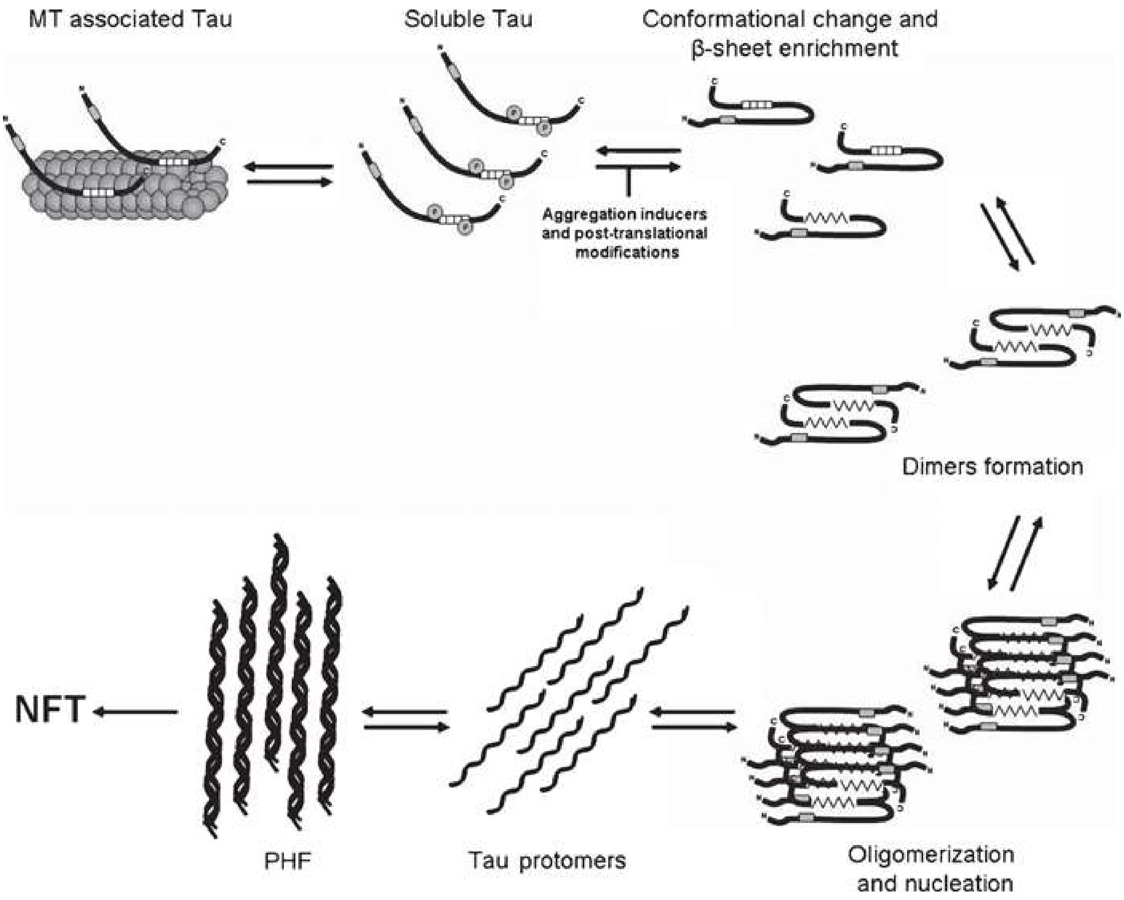

Figure 59 : Agrégation de la protéine tau en neurofibrilles

En conditions physiologiques, les protéines tau contribuent à la régulation des microtubules (MT) qui constituent la structure de l'axone. Elles sont régulées par plus de 40 sites de phosphorylation. Les formes hyperphosphorylées de tau s'agrèegent en oligomères avant de former des neurofibrilles (NFT) toxiques. D'après Meraz-Rios et al., 2010.

Angiopathie amyloïde cérébrale

L'angiopathie amyloïde cérébrale (AAC) est une vasculopathie fréquente chez la personne âgée et souvent associée à la MA. Elle affecte les petits vaisseaux cérébraux (<1 mm de diamètre). Elle se caractérise par une dégradation de la paroi des vaisseaux corrélée à la présence de plaques amyloïdes. En plus d'une perte de la perméabilité de la BHE, l'AAC se traduit par des épisodes hémorragiques et ischémiques. L'ensemble de ces phénomènes entraine la neurodégénérescence des tissus en périphérie des lésions et accroît les risques d'AVC (Cannistraro et al., 2019).

Epidémiologie

L'AAC se présente sous deux formes, sporadique et familiale. La **forme sporadique**, qui affecte surtout les personnes âgées, est la plus fréquente. Elle concerne 10 à 40% des plus de 65 ans et 80% des patients atteints de la MA. La proportion des formes modérées à sévères augmente avec l'âge, de 2.3% chez les 65-74 ans à plus de 12% chez les plus de 85 ans (Biffi and Greenberg, 2011). Les **formes familiales** sont rares mais affectent les patients plus tôt que la forme sporadique et sont généralement plus sévères.

Mécanismes et symptômes

Les peptides Aβ s'accumulent dans la media et l'adventice des artérioles et capillaires du cortex et des leptoméninges (Mutimer et al., 2021).

Ces **dépôts amyloïdes** peuvent dans un premier temps être asymptomatiques (50% des plus de 80 ans présentent de tels dépôts). Cependant, leur présence endommage la paroi vasculaire jusqu'à la survenue d'**hémorragies intraparenchymateuses**. Les dépôts amyloïdes peuvent également obstruer la lumière des vaisseaux et causer des ischémies incomplètes (Biffi and Greenberg, 2011).

La dégradation du tissu environnant se traduit par des hémorragies cérébrales, **des troubles cognitifs** et des épisodes neurologiques transitoires focaux (**épisodes amyloïdes**).

En clinique, la fragilisation de la paroi vasculaire causée par l'AAC limite l'emploi d'anticoagulants. Notamment, chez ces patients susceptibles aux AVC, l'utilisation d'agents fibrinolytiques comme le tPA est liée à un risque accru d'hémorragie intra-parenchymateuse (Charidimou et al., 2017b). Le développement de formes recombinantes de tPA pourrait réduire le risque de transformations hémorragiques chez ces patients (Anfray et al., 2021).

Imagerie et biomarqueurs

L'imagerie permet de révéler diverses altérations du tissu cérébral liées à l'AAC (Charidimou et al., 2017a). Des lésions hémorragiques peuvent être présentes sous la forme d'hémorragies lobaires, profondes ou sous-arachnoïdiennes. Les traces d'**hémorragies** passées persistent en sidérose (accumulation de fer). Des **lésions ischémiques** sont visibles dans la substance blanche (leukoarayose). Globalement, l'**atrophie cérébrale** se traduit par une augmentation de la taille des espaces de LCR (espace sous-arachnoïdien, ventricules) ainsi que par un élargissement des espaces périvasculaires (Wardlaw et al., 2013). Toutefois, le diagnostic de l'AAC ne se limite pas aux observations neurologiques et en imagerie car ces symptômes sont partagés avec d'autres vasculopathies comme l'artériopathie hypertensive (Charidimou et al., 2017a).

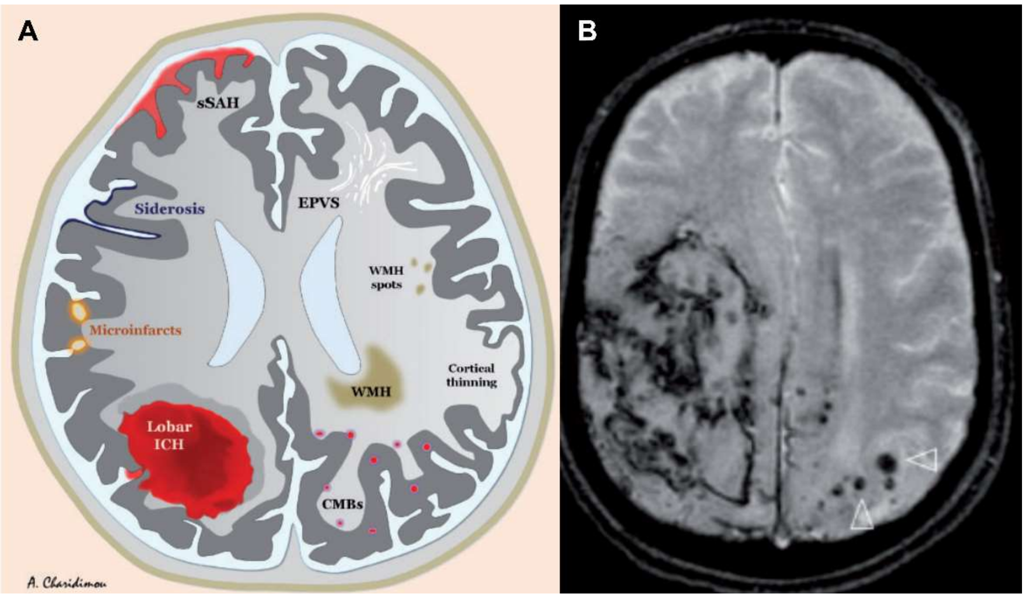

Figure 60: Caractéristiques de l'angiopathie amyloïde cérébrale en IRM

Schéma représentant les différentes altérations du tissu cérébral causées par l'AAC et visibles en IRM (A). IRM d'un patient montrant une hémorragie dans le lobe pariétal droit, le sang apparaît en noir (B). D'après Charidimou et al., 2017a)

Autres peptides liés à des pathologies neurodégénératives

En plus des peptides Aβ et de la p-tau, qui figurent en tête de proue des déchets neurotoxiques, de nombreuses protéines jouent des rôles similaires dans d'autres maladies neurodégénératives (Brundin et al., 2010). La dysfonction de leurs voies d'élimination, notamment par l'IPAD ou le système glymphatique, jouent un rôle majeur dans leur accumulation (Carare et al., 2013).

Alpha-synucléine

L'**alpha synucléine (α-syn)** est une protéine intracellulaire localisée dans les terminaisons présynaptiques. Dans certaines pathologies, elle s'agrège sous forme d'amas toxiques nommés **corps de Lewy** (Henderson et al., 2019).

Les maladies à corps de Lewy sont notamment représentées par la **maladie de Parkinson**, caractérisée par la perte des neurones dopaminergiques de la substance noire dans le mésencéphale. La maladie de Parkinson est la pathologie neurodégénérative la plus fréquente après la MA. Elle se traduit par des troubles croissants de la coordination motrice et, dans les stades tardifs, par l'apparition d'une démence. Il existe plusieurs **thérapies palliatives** visant à restaurer le taux de dopamine dont des médicaments et des neurostimulateurs (Henderson et al., 2019).

La maladie de Parkinson a été liée à divers facteurs, notamment à l'exposition aux produits phytosanitaires et à des mutations ou des duplications du gène de l'α-syn. La consommation de café et peut-être de tabac seraient des facteurs protecteurs (Delamarre and Meissner, 2017).

L'α-syn interviendrait dans le trafic vésiculaire. Elle subit un nombre important de modifications post-traductionnelles et ses voies de dégradations sont complexes. Ainsi, l'accumulation d'α-syn non dégradées par les lysosomes ou le système ubiquitine-protéasome pourrait déclencher leur agrégation (Rocha et al., 2018). L'α-syn partage des caractéristiques avec les prions par son mode de transmission dans le tissu nerveux (Henderson et al., 2019).

Protéine prion

La **protéine prion cellulaire (PrP^c)** est une glycoprotéine exprimée à la membrane de plusieurs tissus, notamment dans le cerveau. Ses rôles restent mal connus, possiblement liés au métabolisme du cuivre ou dans les interactions cellule-cellule. La PrP^c est la première **protéine infectieuse (prion)** à avoir été identifiée chez l'être humain (Liberski et al., 2019).

La PrP^c est impliquée dans plusieurs pathologies chez les êtres humains : maladie de Creutzfeld-Jakob, kuru ou insomnie fatale familiale. Dans ces pathologies, la PrP^c est retrouvée sous une conformation alternative, PrP^{sc}. La PrPsc s'agrège en fibrilles amyloïdes neurotoxiques et propage sa conformation anormale aux PrP^c (Sarnataro et al., 2017).

La **maladie de Creutzfeld-Jakob** est toujours **létale** et de progression **rapide** (quelques mois), caractérisée par des troubles psychomoteurs. Il n'existe **pas de traitement**. Les formes les plus fréquentes sont sporadiques ou génétiques, mais la maladie peut être transmise par des tissus contaminées.

Cas particulier, le ***kuru*** est une épidémie sporadique ayant ravagée la tribu des Fores en Nouvelle-Guinée. Le prion se transmettait grâce au **cannibalisme** rituel des défunts pratiqué par ce peuple (Liberski et al., 2019).

Autre exemple, l'**encéphalite spongiforme bovine** (maladie de la vache folle) est induite chez le bovin par introduction de tissus de conspécifiques (farines d'os) dans leur alimentation. Le prion a défrayé la chronique dans les années 1980 après plusieurs cas de **transmission chez les êtres humains** par consommation de viande contaminée (le prion résiste à la cuisson). Les cas rapportés présentaient des symptômes similaires à la maladie de Creutzfeldt-Jakob (Sitammagari and Masood, 2021).

L'**insomnie fatale familiale** est une maladie génétique autosomique dominante causée par une mutation du gène de la PrP^c. Elle se traduit par des troubles du sommeil sévères qui tuent en moins de deux ans (Llorens et al., 2017).

TDP-43

TDP-43 (*TAR DNA-binding protein* 43) est une protéine impliquée dans le métabolisme des acides ribonucléiques. Elle est présente sous forme d'amas dans le cerveau et la moelle épinière des patients atteints de **sclérose latérale amyotrophique (SLA)**.

La SLA, ou maladie de Charcot, est une maladie neurodégénérative d'évolution **fatale** causée par la **mort des neurones moteurs**. Elle se caractérise par une perte progressive de la motricité jusqu'à la mort des patients en 3 à 5 ans. La maladie reste relativement rare, avec une incidence annuelle de 5 / 100 000. La majorité des formes de SLA sont sporadiques, mais il existe des formes génétiques impliquant notamment le gène *TDP-43*.

TDP-43 est présente dans le noyau et le cytoplasme des neurones où elle intervient dans plusieurs étapes (transcription, traduction, transport, …) du métabolisme des ARN messagers. TDP-43 intervient sur 30% du transcriptome mais est incapable d'assurer sa fonction sous forme agrégée. Elle partage certains motifs avec la protéine prion et aurait les mêmes propriétés de transmission (Prasad et al., 2019).

Le cas intriguant des corps amylacés

Les corps amylacées sont des **amas extra- ou intra-cellulaires riches en glycoprotéines** observées dans les régions ventriculaires et sous-ventriculaires du cerveau âgé. Ces agrégats de 2 à 20 µm de diamètre possèdent une structure complexe et chaotique, incluant des fragments de membranes, des organelles et des fibrilles de GFAP dans une matrice d'amylopectine. La formation des corps amylacés a été observée dans le cytoplasme des **astrocytes**, où ils pourraient être issus d'une **accumulation de déchets** (Augé et al., 2019). Les corps amylacés 'matures' se localisent en **périphérie des vaisseaux** où ils seraient excrétés dans le LCR via l'espace périvasculaire (Navarro et al., 2018). Leurs rôles et leur métabolisme restent cependant largement inconnus.

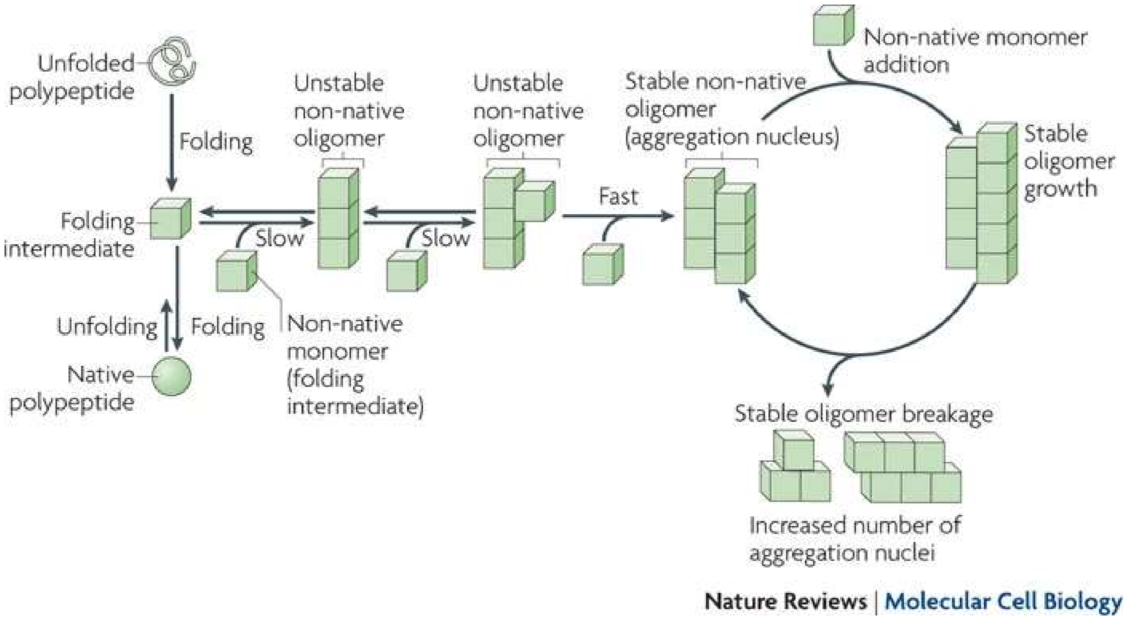

Figure 61 : Mécanismes d'agrégation des protéines

Le repliement de certaines protéines (Tau, PrP^c, α-syn, TDP-43, huntingtine) passe par des intermédiaires capables de s'agréger. Les oligomères gagnent en stabilité et croissent de plus en plus vite. Des fragments peuvent se détacher des oligomères stabilisés et promouvoir la formation de nouveaux noyaux d'agrégation. D'après Brundin et al., 2010.

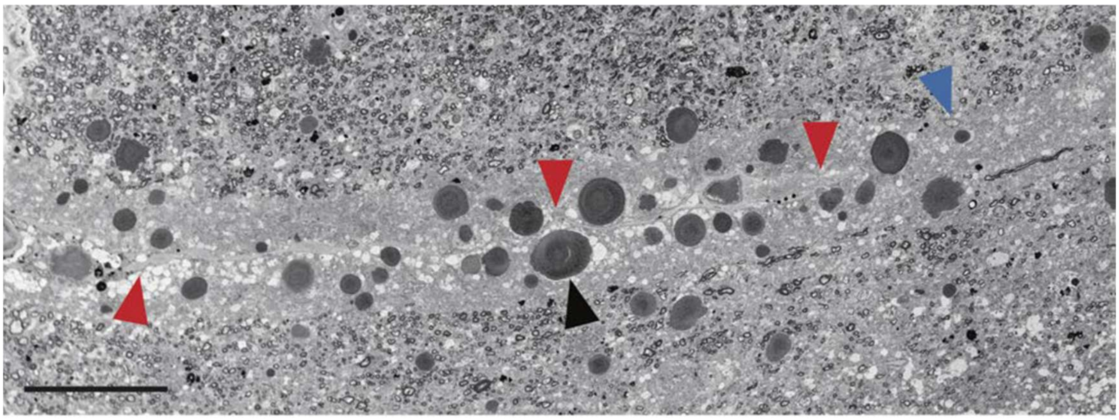

Figure 62 : Corps amylacés en périphérie d'un vaisseau sanguin

Les corps amylacés (flèche noire) sont localisés dans les pieds astrocytaires et dans l'espace périvasculaire autour d'un vaisseau (flèches rouges). La flèche bleue indique un noyau cellulaire, beaucoup plus petit. Barre d'échelle : 60 µm. Microscopie électronique d'une coupe de cerveau humain issue d'un patient âgé avec maladie de Parkinson. D'après Navarro et al., 2018.

Résumé / *Abstract*

- La **MA** est la cause principale de démence, liée à l'âge, au mode de vie et à certains facteurs génétiques. Les traitements actuels ne permettent pas de guérir la maladie.
- La MA se caractérise par une n**eurodégénérescence**, la présence de **plaques de peptides Aβ** et des **NFT de p-tau**.
- Les peptides Aβ sont des **déchets toxiques du métabolisme**. Les voies qui permettent leur élimination sont **moins efficaces avec l'âge**.
- D'**autres protéines** sont impliquées dans des **maladies neurodégénératives**, comme l'α-syn, la PrP^{sc} ou TDP-43.

- **Alzheimer's disease** is the leading cause of dementia. It is linked to aging, lifestyle and genetic factors. The available treatments cannot cure the disease.
- Alzheimer's disease is characterized by a **neurodegeneration**, the **accumulation of amyloid beta plaques** and **neurofibrillary tangles of hyperphosphoryled tau**.
- The amyloid beta peptides are **toxic metabolic waste** whose elimination pathways **lose in efficiency on aging**.
- **Other proteins** are implied in **neurodegenerative diseases**, such as synuclein alpha, prion protein and TDP-43.

OBJECTIFS

Introduction

Les échanges entre LCR et FISC font l'objet d'une attention croissante de la part de la communauté scientifique. En effet, des découvertes récentes mettent en lumière les espaces périvasculaires comme une voie alternative pour l'élimination des déchets du métabolisme cérébral. La perturbation de ces échanges peut résulter en une accumulation de déchets, un facteur de risque pour de nombreuses pathologies dont la maladie d'Alzheimer. Bien que de nombreuses approches ont été employées pour permettre l'observation des échanges LCR-FISC, peu sont applicables en clinique. En effet, la plupart des techniques reposent sur l'injection de traceurs dans le LCR ou dans le parenchyme cérébral. L'invasivité de ce type d'approche ne permet pas leur application dans des études sur la population générale.

Depuis son émergence dans les années 1950, l'IRM a été déclinée en une grande variété de techniques. Certaines méthodes ont permis de révéler *in vivo* chez l'être humain les échanges LCR-FISC mais se basent toujours sur une injection de traceurs et sont de ce fait soumises à indication médicale. En revanche, d'autres techniques telles que l'IRM de diffusion ne nécessitent pas d'agent de contraste et sont sensibles aux mouvements microscopiques de l'eau. **Les flux de liquides étant au cœur des échanges LCR-FISC, l'IRM de diffusion apparait comme un candidat valide pour mesurer ces échanges dans la population générale.**

Hypothèse

Ainsi, la question principale de ma thèse est de déterminer si l'IRM de diffusion peut déceler les altérations des échanges LCR-FISC. Pour valider cette hypothèse, j'ai exploité une séquence de diffusion multi-b sur une variété de modèles animaux connus pour présenter une altération des échanges LCR-FISC. En parallèle, et afin de confirmer l'atteinte des échanges LCR-FISC, j'ai injecté un agent de contraste paramagnétique chez ces animaux et suivi sa dispersion dans le parenchyme en IRM. J'ai ensuite évalué la corrélation entre les deux techniques.

La réponse à cette question a nécessité de compléter au préalable trois étapes de recherche :

Premier axe : Mise au point et validation des protocoles

L'objectif premier a consisté en la mise au point du protocole d'imagerie par résonance magnétique et en son application sur plusieurs modèles. Pour la séquence de diffusion, j'ai choisi de couvrir la majeure partie de la courbe de perte de signal au travers d'une séquence multi-b pour permettre une modélisation mixte IVIM-kurtosis. Concernant la séquence destinée à suivre la dispersion de l'agent de contraste, j'ai retenu une approche quantitative basée sur des cartes de T1 répétées dans le temps, laquelle a permis d'obtenir des cartes cinétiques de la dispersion de l'agent de contraste. Le vieillissement étant régulièrement présenté comme la cause la plus répandue d'une altération des échanges LCR-FISC, j'ai donc choisi d'appliquer mon protocole d'imagerie sur des animaux jeunes et âgés. Le rôle de l'AQP4 dans les échanges LCR-FISC est souvent présenté mais reste disputé. Pour complémenter mon étude par une approche pharmacologique, j'ai inclus un groupe d'animaux jeunes recevant une exposition aiguë au TGN-020, un inhibiteur des AQP4.

Deuxième axe : Comparaison de deux agents de contraste

En parallèle, et afin d'affiner mon modèle, j'ai testé un agent de contraste de poids supérieur à celui que j'utilisais et ai constaté que sa dispersion dans le parenchyme ne correspondait pas aux seules caractéristiques de diffusion. Mon hypothèse est qu'un effet 'tamis' au travers de l'espace interstitiel favorise le transport des composés de poids moyen dans les espaces périvasculaires. **La caractérisation des différences de dispersion entre les deux agents a été le second objectif de ma thèse et a fait l'objet d'un article actuellement en soumission.**

Troisième axe : Collaborations et travaux complémentaires

En plus des modèles animaux prévus dans le projet initial, j'ai exporté mes techniques d'imagerie et d'analyse vers d'autres conditions. Ainsi, j'ai évalué l'effet d'une exposition aux anesthésiques en période périnatale sur la fonctionnalité des échanges LCR-FISC chez l'adulte. Mes protocoles ont également contribué à la caractérisation d'un modèle de malacoleucodystrophie avec kystes chez la souris. J'ai aussi testé deux approches pharmacologiques ciblant la production de LCR : une exposition aiguë à l'acétazolamide, un inhibiteur de la sécrétion du LCR, ou une exposition chronique à la caféine, qui augmente la production de LCR. Enfin, je me suis intéressée au rôle du sommeil dans la régulation des échanges LCR-FISC, sujet à débat dans la littérature. **Cette mise à l'épreuve de mes protocoles au travers de collaborations sujettes à publications et de travaux annexes a constitué le troisième objectif de ma thèse.**

Quatrième axe : Réponse à l'hypothèse initiale

Le quatrième et dernier objectif de ma thèse est la réponse à ma question initiale, à savoir la capacité de l'IRM de diffusion à détecter des altérations des échanges LCR-FISC. J'ai pour cela exploité l'ensemble des données obtenues au cours des trois objectifs précédents. Les conclusions de ces corrélations sont mitigées. En effet, **bien que j'aie pu observer des variations significatives des paramètres de diffusion entre mes groupes expérimentaux, ces variations ne suivent pas les observations réalisées avec des agents de contraste.** Les causes de cette absence de corrélation sont explorées dans la discussion générale.

Autres observations

Au cours de mes travaux, j'ai pu faire plusieurs observations intrigantes que je n'ai pas eu l'occasion d'approfondir, tel un afflux de LCR post-mortem dans les espaces périvasculaires. De même, en fin de thèse j'ai pu entamer des mises à jour de mes protocoles sans avoir eu le temps de les exploiter pleinement. Les méthodes et résultats obtenus sont brièvement exposés dans la discussion générale et le détail de ces expériences présenté en annexe.

RÉSULTATS

Étude 1 : Dynamic Quantitative Contrast-Enhanced MRI of Large Paramagnetic Compound Reveals Impairment of Brain Solutes Transport in Aging Mice

Cet article sera prochainement soumis à Neuroimage

Résumé : Du développement embryonnaire au vieillissement, le LCR est un axe de transport pour une variétés de molécules, des facteurs trophiques comme le BDNF aux peptides Aβ impliqués dans la MA. Cependant, la plupart des études in vivo sur les échanges LCR-FISC ont utilisé des traceurs de poids moléculaires bien plus faibles (e.g. DOTA-Gd, DTPA-Gd). Dans cette étude, nous avons observé chez la souris des différences majeures dans la distribution de solutés au sein du tissu cérébral entre le DOTA-Gd (0.7 kDa) et un traceur plus lourd, le GadoSpin D (17 kDa). Notablement, le GadoSpin D présente une distribution plus homogène et des cinétiques plus rapide que le DOTA-Gd, contrairement à ce que prédirait le seul mécanisme de diffusion. De plus, la distribution du GadoSpin D est altérée par le vieillissement et l'inhibition des AQP4 bien plus que celle du DOTA-Gd.

Notre hypothèse est que la taille du GadoSpin D le restreint aux espaces périvasculaire et que celui-ci peut ainsi se répartir plus en profondeur dans le tissu cérébral. Le DOTA-Gd, plus léger, se dilue dans le tissu cérébral à proximité immédiate de son lieu d'injection et reste largement influencé par sa répartition initiale dans l'espace sous-arachnoïdien.

Cet "effet filtre" dans l'espace périvasculaire sous-tend l'existence de voies de circulation restrictives au sein du parenchyme cérébral et souligne l'importance de la taille des traceurs utilisés sur les conclusions des études antérieures.

Conclusions :

- Le poids des traceurs, et donc leur volume de distribution, est un contributeur majeur de leur dispersion dans le parenchyme cérébral.
- La répartition du traceur léger semble surtout liée aux caractéristiques de l'espace sous-arachnoïdien
- La répartition du traceur de poids moyen est davantage influencée par les espaces périvasculaires
- Le traceur de poids moyen discrimine mieux que le traceur léger les différences liées à l'âge ou causées par une inhibition des AQP4
- La distribution de molécules d'intérêt clinique (oligomères Aβ, facteurs trophique) serait mieux représentée par des traceurs de poids équivalent

Contribution : Dans cette étude dont je suis première autrice, j'ai contribué à la conception des expériences et les ai réalisées. J'ai également réalisé l'analyse des données et leur mise en forme, et ai contribué à la rédaction de la majeure partie de l'article.

DYNAMIC QUANTITATIVE CONTRAST-ENHANCED MRI OF LARGE PARAMAGNETIC COMPOUND REVEALS IMPAIRMENT OF BRAIN SOLUTES TRANSPORT IN AGING MICE

Audrey Chagnot[1], Mikael Naveau[2], Marina Rubio[1], Gael Chetelat[1]*, Maxime Gauberti[1,3]* and Denis Vivien[1,4]

*: *These co-authors have equally contributed.*

1. Normandie Univ, UNICAEN, INSERM, GIP Cyceron, Institut Blood and Brain @Caen-Normandie (BB@C), UMR-S U1237, Physiopathology and Imaging of Neurological Disorders (PhIND), Caen, FRANCE.

2. CNRS, UMR-S 3408, GIP Cyceron, Normandie Université, Caen, FRANCE.

3. CHU Caen, Department of Radiology, Caen University Hospital, Caen, FRANCE.

4. CHU Caen, Department of Clinical Research, Caen University Hospital, Caen, FRANCE.

Denis VIVIEN, PhD
INSERM UMR-S U1237 "Physiopathology and Imaging of Neurological Disorders", University Caen Normandie, GIP Cyceron, Institut Blood and Brain @ Caen-Normandie (BB@C), Bd Becquerel, BP5229, 14074 Caen, France.
Phone, fax and e-mail: +33 2 31 47 01 66, +33 2 31 47 02 22, vivien@cyceron.fr

Author Contributions: D.V. and M.G designed research, A.C. performed research, A.C., M.N. and GC analyzed data; and A.C., D.V., M.G., G.C. M.N. and M.R. wrote the paper.

Competing Interest Statement: The authors declare that the research was conducted in the absence of any commercial of financial relationships that could be construed as a potential conflict of interest.

Classification: BIOLOGICAL SCIENCES / Neuroscience

Keywords: Cerebrospinal fluid | Glymphatic | In vivo MR imaging | Aging | Aquaporin-IV

This PDF file includes:

Main Text
Figures 1 to 5

Abstract

Perivascular spaces are an exchange pathway between cerebrospinal fluid and brain interstitial fluid. Disruptions of these exchanges may lead to brain dysfunctions, but the precise mechanisms remain debated. *In vivo*, whole brain measurement of cerebrospinal fluid transport is usually performed by MRI after intracisternal injection of a low-molecular weight gadolinium chelate (such as DOTA-Gd, 0.7 kDa). However, the distribution of these compounds in the brain parenchyma is complex, since it depends both on intracranial cerebrospinal fluid bulk flow (e.g. the glymphatic system) and on free diffusion through permeable meningeal barriers and intercellular spaces. Consequently, intracisternal DOTA-Gd rapidly accumulates near subarachnoid space but did not penetrate much further into the brain. This distribution precludes precise measurement of CSF bulk flow in regions at a distance from the injection site such as the cortical areas. To overcome this limitation, we used GadoSpin D, a heavier gadolinium chelate (17 kDa). Unlike DOTA-Gd, GadoSpin D distributed throughout the brain without notable accumulation near subarachnoid space and presented faster kinetics in the parenchyma over the acquisition time (slope: -15.9% versus 26.8%), including a faster elimination rate. Moreover, GadoSpin D uptake into the parenchyma appeared strongly reduced by age (-78%) and by aquaporin-4 inhibition (-74%), and accumulated in the olfactory tracts in aged mice. While supporting the existence of a cerebrospinal fluid-dependent active transport for solutes in the brain parenchyma, a process impaired with age, our study also proposes a more relevant approach for measuring cerebrospinal fluid flows *in vivo*, with a potential for clinical translation.

Significance Statement

Perivascular spaces of the brain are a zone of exchanges for solutes between the cerebrospinal fluid and the brain. However, it is known that their efficiency is decreased in aging. Contrast-enhanced MRI was used to study the distribution of two tracers of different sizes in mice. The large tracer, GadoSpin D, 17 kDa, diffused homogeneously in brain tissues, in contrast to the small-sized tracer (DOTA-Gd, 0.7 kDa) which strongly impregnated the regions nearing CSF but failed to reach distant regions. This difference may be due to the smaller distribution volume of GadoSpin D, allowing its distribution further in the brain thanks to the perivascular spaces. Both Aquaporin-4 inhibition and aging impaired the diffusion of GadoSpin D.

Main Text

Introduction

Among other functions, the cerebrospinal fluid (CSF) drives solute transport. In adult humans, the CSF flows carries a variety of molecules such as neurotrophic factors, amyloid beta, leptin and immunoglobulins(1). The CSF is produced by the choroid plexus and the resulting pressure results in the CSF circulation, from the ventricular system to the subarachnoid space where the CSF is excreted by the arachnoid villi in the venous blood(2). While this view of the 'third circulation' is widely accepted, several reports suggest extended exchanges between the CSF and the brain interstitial fluid (bISF)(3–6).

Connections between the subarachnoid space and the bISF have been explored since the mid-20th century. Various experiments showed that tracers injected into brain parenchyma or CSF are drained into the cervical lymph nodes by paravascular pathways(3, 5–8). Indeed, vessels in brain benefit from multiple structural and anatomical adaptations in addition to the blood-brain barrier (BBB), including perivascular spaces (PVS), also known as Virchow-Robin spaces, for the largest vessels(9). These vessels are enwrapped into a membrane made of the astrocytic endfeet, the glia limitans, where the aquaporin-4 (AQP4) water channel is highly expressed toward the PVS.

While most brain solutes transit through the BBB, peri/paravascular routes might noticeably contribute to the transport of neurotrophic factors and immunoglobulins, which are secreted into the CSF by the choroid plexuses and do not cross easily the BBB(1). Elimination of brain wastes such as amyloid beta or hyperphosphorylated tau has been proposed to occur through arterial basement membranes(5, 10) and perivascular spaces(11). Accordingly, widely used CSF tracers such as dextran polyethylene glycols or magnetic resonance contrast agents cannot permeate through the BBB in physiological conditions and are mostly restrained to perivascular routes(12).

Alterations of CSF-bISF exchanges might be relevant in a variety of physiopathological conditions, including neurodegenerative diseases(13, 14), stroke (15–17), sleep (18, 19), hydrocephalus (20, 21), hypertension(22), development(23), cortical spreading depression(24), aging(25). surgical procedures with craniectomy(26, 27) or anesthesia(18, 28, 29) also likely alter CSF-bISF exchanges. The role of PVS in brain waste clearance has been studied since the late XXth century and led to a variety of models(4–6), the latest being the 'glymphatic' system standing for 'glial lymphatics'(3, 30–35).

Contrast-enhanced magnetic resonance imaging (CE-MRI) has allowed investigating *in vivo* the passage of contrast agents (CA) from the CSF to the parenchyma in a variety of species, conditions and developmental stages(16, 17, 22, 23, 28, 29, 36–38), including in humans(20, 39–43). However, most tracers used so far were small-sized molecules (Gd-DOTA; Gd-DTPA; ~1 kDa). A few papers observed highly restrained exchanges for heavy molecules (>100 kDa)(9, 37), but there is a general lack of MRI studies which investigated the distribution of medium-sized molecules.

Using an *in vivo* quantitative dynamic CE-MRI method in mice, we reveal in the present study the existence of routes between the CSF and deep parenchyma for medium size molecules (~17 kDa), which are dependent on aquaporin-4 and impaired with aging.

Results

Determination of respective contrast agent relaxivities

First, phantom experiments with saline (**Supplementary figure 1A**), DOTA-Gd (10 mM, 1 mM, 100 µM, 10 µM and 1 µM**, Supplementary figure 1B**) or GadoSpin D (2.5 mM, 1 mM, 100 µM, 10 µM and 1 µM, **Supplementary figure 1C**) were performed to measure their relaxivity. Values obtained at 7T were $r1 = 4.3\ s^{-1}.mM^{-1}$ for DOTA-Gd and $r1 = 4.9\ s^{-1}.mM^{-1}$ for GadoSpin D **(Supplementary figure 1D-E)**. T1 changes can be observed in-vivo, mostly due to partial volume effects between brain's mid T1 and CSF's high T1(44, 45). On anesthesia, the most salient feature that could lead to T1 alterations is hypercapnia and the subsequent vasoconstriction. Thus, during our *in vivo* experiments, we reduced the bias of hypercapnia by keeping mice at similar respiratory rates between groups and throughout all MRI acquisitions by precisely tuning levels of anesthetics (usually between 1.5 – 2% isoflurane) and corresponding controls were performed prior to CA injections **(Supplementary figure 1G, 1F)** with a reduction of T1 which was negligible.

Increased relative CSF volume in 18 months vs 2 months old mice

In order to evaluate CSF flux, we performed dynamic quantitative CE-MRI after intracisternal injection of CA (see methods section). To evaluate the CA concentrations within brain areas, we created MRI T1 maps of each mouse before and after CA injection. First, we compared the reference MRI T1 maps of 2 months (CTRL) (**Supplementary Figure 2A**) and 18 months (18M) (**Supplementary Figure 2B**) old mice. All maps were generated form single medial sagittal slices, allowing an overview on both brain tissues, subarachnoid spaces and ventricles. The brain sizes of mice were estimated using the surface occupied by the brain on these slices. We found that 18M mice had a significantly larger brain (+7.7% surface increase on medial sagittal slice) than their younger counterpart (**Supplementary Figure 2C**) (CTRL: 72.87 +/- 2.47 mm², n = 20; 18M: 78.49 +/- 5.6 mm², n = 20; $p < 0.001$, Student's T test). The CSF fraction was found to be 63% higher in 18M mice (**Supplementary Figure 2D**) (CTRL: 2.4 +/- 1.6 %, n = 20; 18M: 3.9 +/- 1.7 %, n = 20; $p = 0.006$, Student's T test). This increase in relative CSF volume is in agreement with previous observations in mice(46, 47) and coherent with our knowledge of brain atrophy with aging in humans(48). No difference was found in the MR T1 value of the brain tissue between CTRL and 18M mice (**Supplementary Figure 2F-K**).

Aging and AQP4 inhibition by TGN-020 reduce tracer intake into the parenchyma

Two MRI CA were used in this study: DOTA-Gd (0.7 kDa) and GadoSpin D (17 kDa). 1 µL of either DOTA-Gd or GadoSpin D was injected in the cisterna magna of mice over 1 minute to prevent increase of CSF pressure. 2 months controls (CRTL), 2 months receiving TGN-020 (TGN) and 18 months (18M) mice received CA injections before CE-MRI acquisition. The dispersion of CA was observed over 40 minutes, then the initial CA concentration, the mean CA concentration over the acquisition and the slope were measured for six regions of interest (ROIs), namely cerebellum, midbrain, thalamus, septal area, cortex and olfactory bulb. We observed that, while decreasing in all ROIs of CTRL mice with time after injection, the GadoSpin D concentrations were slowly, steadily increasing in aged mice throughout the time of the experiment (40 min.). But, GadoSpin D concentration at the first time point (i.e. 10 min post injection) was found to be significantly lower in most ROIs of 18M mice compared to CTRL (**Figure 3B**). The strongest differences were observed in the midbrain (**Figure 3C**), where mean GadoSpin D was 78% lower in 18M mice (**Figure 3D**) (CTRL: 0.018 +/- 0.0045, n = 9; 18M: 0.0039 +/- 0.0031, n = 9; p-value < 0.001, Mann-Whitney U test) while the slope increased with time (**Figure 3E**) (CTRL: -0.00019 +/- 0.00019, n = 9; 18M: 4.7E-5 +/- 8.9E-5, n = 9; p-value = 0.001, Mann-Whitney U test). We then tried to reproduce these observations in TGN mice. Interestingly, the GadoSpin D presented in TGN mice a pattern similar to 18M, i.e. a steadily increased concentrations in all ROIs with time, with the most salient differences exhibited in the midbrain (**Figure 3F**), where the mean GadoSpin D concentration over the acquisition was 74% lower in TGN-020 exposed mice (**Figure 3G**) (CTRL: 0.018 +/- 0.0045, n = 9; TGN: 0.0047 +/- 0.0028, n = 7; p-value < 0.001, Mann-Whitney U test) while the slope increased with time (**Figure 3H**) (CTRL: -0.00019 +/- 0.00019, n = 9; TGN: 9.8E-5 +/- 7.2E-5, n = 7; p-value < 0.001, Mann-Whitney U test). On the same time, only minor differences were observed with DOTA-Gd

(**Figure 2B**), with the notable exception of septal aera (**Figure 2C**), in which the mean DOTA-Gd concentration over the acquisition tended to be higher in 18M mice (**Figure 2D**) (CTRL: 0.079 +/- 0.069, n = 9; 18M: 0.14 +/- 0.068, n = 10; p-value = 0.079, Mann-Whitney U test) and significantly decreasing in time (**Figure 2E**) (CTRL: 2.17E-4 +/- 4.75E-4, n = 9; 18M: -0.0025 +/- 0.0027, n = 10; p-value = 0.004, Mann-Whitney U test), conversely to CTRL mice and to the other ROIs. In TGN mice, we observed an opposed tendency (**Figure 2F**). DOTA-Gd concentration seemed to be lower in septal area (**Figure 2G**), though no significant change has been found.

GadoSpin D concentration in the olfactory tracts is increased in aged mice but not in the TGN-020 exposed mice

The olfactory tracts (**Figure 4A**) are known since decades as a major outflow pathway for CSF to the lymphatic network in rodents(49). We then investigated whether changes could be observed on this ROI, thus reflecting alterations in the elimination of contrast agents. We normalized the concentration found in olfactory tracts by the concentration found in the nearest ROI, i.e. olfactory bulb (**Figure 4B-G**). This ratio was then compared between groups, for each agent. Interestingly, a significant increase of GadoSpin D concentration in the olfactory tracts of 18M mice was observed compared to CTRL (**Figure 4M**) (CTRL: 52.5 +/- 8.7%, n = 8; 18M: 72.2 +/- 5.4%, n = 6; p-value = 0.003, Mann-Whitney U test). This increase was not observed with DOTA-Gd (**Figure 4I**) (CTRL: 66.2 +/- 14.5%, n = 8; 18M: 72.2 +/- 5.4%, n = 8; p-value = 0.38, Mann-Whitney U test), neither in TGN mice (**resp. Figure 4K, 4O**) (CTRL DOTA-Gd: 66.2 +/- 14.5%, n = 8; TGN DOTA-Gd: 62.8 +/- 13.7%, n = 8; p-value = 0.72, Mann-Whitney U test), (CTRL GadoSpin D: 52.5 +/- 8.7%, n = 8; TGN GadoSpin D: 59.3 +/- 9.3%, n = 7; p-value = 0.23, Mann-Whitney U test). These data suggest either an increased elimination rate or retention in the olfactory tracts of medium size solutes in 18M mice, compared to CTRL.

Disparities between GadoSpin D and DOTA-Gd: a question of size?

Due to the different CA doses used, we expected that DOTA-Gd concentration in parenchyma would be larger than GadoSpin D. However, the GadoSpin D concentration at 10 minutes after injection was found to be nearly equal and possibly higher than DOTA-Gd in half of regions (**Figure 5C**), notably in cortex (DOTA-Gd: 0.0045 +/- 0.0043, n = 8; GadoSpin D: 0.0094 +/- 0.0059, n = 9; p-value = 0.046, Mann-Whitney U test) and thalamus (DOTA-Gd: 0.0051 +/- 0.0052, n = 9; GadoSpin D: 0.0096 +/- 0.0048, n = 9; p-value = 0.064, Mann-Whitney U test). The difference disappeared over the acquisition time (45 min.) (**Figure 5D**). Interestingly, we observed that GadoSpin D concentration was decreased in ROIs, while DOTA-Gd concentration was increased (**Figure 5E**). When comparing the normalized slope, i.e. slope normalized on area under curve (AUC), we found this difference to be significant (**Figure 5F**) (DOTA-Gd global slope: 26.8 +/- 23.8 %, n= 8; GadoSpin D global slope: -15.9 +/- 16.3 %, n = 9; p-value < 0.001, Mann-Whitney U test). We further observed that the repartition of GadoSpin D within the different brain areas was more homogeneous than of DOTA-Gd (**Figure 5A-B**). The first method we used was to compare the variance mean ratio over all ROIs, both for AUC and slope, and found that the dispersion of AUC (**Figure 6G**) and slope (**Figure 6H**) was lower for GadoSpin D than for DOTA-Gd (DOTA-Gd AUC dispersion: 0.21 +/- 0.18, n = 8; GadoSpin D AUC dispersion: 0.020 +/- 0.023 , n = 9 ; p-value < 0.001, Mann-Whitney U test) (DOTA-Gd slope dispersion: 0.022 +/- 0.027, n = 8; GadoSpin D slope dispersion: 0.0048+/- 0.0046, n = 9; p-value = 0.036, Mann-Whitney U test). A second method was to measure and compare the entropy. Entropy is a parameter that gives indications on ‘how well’ data approach to chaos, i.e. at the beginning of the experiment entropy should be fairly low as the CA is not yet mixed, but should increase with time as it is dispersed across the brain (**Figure 5I**). Shannon entropy was calculated based on histograms of voxel values for CA concentrations at each time point for the whole brain (**Figure 6J**). We found that, while global entropy was not different (**Figure 5K**) (DOT mean entropy: 68.5 +/- 12.2 %, n = 9; GSD mean entropy: 66.1 +/- 15.3 %, n = 10; p-value = 0.78, Mann-Whitney U test), its evolution over time was (**Figure 5L**). DOTA-Gd entropy was increased while GadoSpin D entropy was decreased (DOTA-Gd entropy slope: 11.5 +/- 6.5 %, n = 9; GadoSpin D entropy slope: -5.5 +/- 3.8 %, n = 10; p-value < 0.001, Mann-Whitney U test). At a first glance, part of these differences between the two CA behavior might be explained by the concentration used (i.e. 500 mM for DOTA-Gd and 25 mM for GadoSpin D). We hence hypothesized that the high concentration of

DOTA-Gd could be ‘saturating’ the intra-parenchymal CSF transport, and reproduced DOTA-Gd injection at a similar concentration than GadoSpin D (i.e. 25 mM). Interestingly, we observed that CA repartition was identical to higher-dose DOTA-Gd injection (**Supplementary Figure 2**), thus rejecting the ‘saturation’ hypothesis.

Discussion

Most in-vivo CE-MRI studies looking at the exchanges of tracers between CSF and bISF used small-sized contrast agents similar to DOTA-Gd (0.7 kDa)(16, 17, 19, 22, 23, 28, 36, 37, 39, 50). To our knowledge, no study has used medium-sized MRI CA such as GadoSpin D (17 kDa), which are comparable in molecular weight to molecules such as neutrophins or cytokines. One study used the heavy MRI CA GadoSpin P (200 kDa) but failed to observe its permeation in parenchyma, possibly due to the very high size of this agent(37), while another using Gd-DTPA labeled immunoglobulins (100 kDa) observed limited permeation into parenchyma, possibly thanks to specific transporters(9). Non-MRI studies used a wider variety of tracers, and usually found that the smaller the molecule, the best it is diffusion into the brain parenchyma(3, 51–54). However, in the present in-vivo study, we observed that GadoSpin D exhibited faster kinetics than DOTA-Gd, being more homogeneously distributed and present in regions such as the cortex where DOTA-Gd is just incoming. These results could emphasize that DOTA-Gd have a larger distribution volume, being distributed both in ISF and PVS while GadoSpin D is limited to the PVS. Glia limitans may hence play a filter role, allowing deep parenchymal distribution for medium-weight tracers only. An example of such filters can be found in elution columns, where pore sizes in gel beads retains the small molecules, while the larger compounds are pursuing their way around the beads. Dynamic differences between the two agents can be explained by the longer retention time of DOTA-Gd within the ISF.

Over the acquisition time in our present experiments (45 min.), GadoSpin D concentrations decreased in all the observed ROI of 2 months mice, but increased in the 18 months old mice. Initial (10 min.) repartition of GadoSpin D was found to be lower in aged mice, suggesting overall a slowdown of CSF-bISF solute exchanges due to age. A number of studies enforces potential explanations for this phenomenon, such as arterial wall rigidification, decrease of vasomotricity(55, 56) and loss of the AQP4 polarization(25). We further investigated this phenomenom by reproducing our experiments on young mice exposed to the AQP4 inhibitor TGN-020 and observed similar results than in old animals. AQP4 roles in brain are multiples, and its localization around perivascular spaces supports its implication in the gliovascular unit. AQP4 inhibition causes ADC increase(57) and astrocyte swelling(58, 59), the latter possibly coupled with a reduction in perivascular spaces(17, 24). In aged animals, both reduction of PVS and increase of subarachnoid spaces would affect GadoSpin D distribution volume and reduce its availability for passage into the brain parenchyma, while TGN-020 exposure, as possibly causing a brain volume increase, favorizes GadoSpin D distribution in the PVS over the reduced subarachnoid space.

The strongest difference we observed with DOTA-Gd was on its concentration in the septal area. Septal area is located nearly to an important anterior cisterna of CSF, and concentration of DOTA-Gd within this ROI may actually reflects its direct diffusion from the subarachnoid space. CSF spaces volume increases in aging, as revealed in our present study and in an abundant literature in both humans(48) and mice(46, 47). Enlarged subarachnoid spaces may explain our observation of a greater amount of DOTA-Gd in the ROIs near the anterior cisterna, with the hypothesis that large spaces favor a wider initial distribution of the contrast agent. Conversely, we observed a decrease of DOTA-Gd concentration in the septal area in TGN-020 mice, which can be explained with a similar mechanism as in aging. TGN-020 causes astrocytes swelling(58, 59), which might increase brain volume, hence reducing the subarachnoid space and preventing the DOTA-Gd from reaching a longer distance.

Olfactory tracts are a predominant CSF outflow pathway in rodents(49). Interestingly, we observed a significantly stronger presence of GadoSpin D in the olfactory tracts for 18 months mice compared to 2 months mice. Further, the lighter DOTA-Gd did not show accumulation in the olfactory tracts of 18 months mice, and TGN-020 exposure did not significantly influence its distribution in this area. Interestingly, aging and neuropathological dementias are often associated with olfactory loss(60), which accumulation of toxic metabolites in the nasal mucosa might contribute to explain. Translation of this observation from a species to another should however be tempered as olfactory nerves, while being a possible route for CSF drainage in humans, are not as preponderant as they are in rodents. Previous studies suggested that CSF elimination through olfactory tracts and nasal mucosa is reduced in aged mice, based on measure in neck ganglia(61).

Cerebrospinal fluid is now viewed as a major transport axis for a variety of solutes, ranging from amino-acids to whole cells. In this article, we show that transport of medium sized molecules was reduced with aging, potentially affecting the distribution of multiple signaling molecules (Leptin: 16 kDa; Insulin-like growth factor type 2: 7.5 kDa; Interferon type 1: 19.5 kDa; Brain-derived neurotrophic factor: 14 kDa)(1). Dissolution of amyloid plaques was often proposed as a potential treatment for Alzheimer’s disease, though these are resilient structures(62). Perivascular spaces are presented as a pathway for amyloid-beta clearance, thus preventing its aggregation into parenchyma(14). While amyloid-beta monomers weights 3 kDa, oligomeric forms exist in a variety of sizes (< 10 kDa to > 100 kDa)(63) and interestingly, higher levels of amyloid-beta oligomers in CSF is a strong biomarker for Alzheimer’s disease(64, 65). Comprehension of how oligomer size affects their transport in the perivascular spaces may lead to new approaches targeting an ‘ideal oligomer size’ for evacuation into the CSF. Another therapeutic implication for our study is convection enhanced delivery, which allows for drug distribution across the CSF without the limitations of BBB(66–69). In the design of compounds optimized for perivascular transport, molecular weight should be a critical question for further studies.

Limitations: This study was performed on anesthetized rodents after injection of a contrast agents into the CSF through cisterna magna. Most of previous studies were realized on anesthetized animal. However, it is well reported in the literature how physiological parameters such as repiratory frequency and vasomotricity act on CSF circulation(2, 70, 71) and are affected by anesthesia(18, 28, 29). In this study, we used isoflurane, which is known to reduce CSF circulation(28). Isoflurane is an inhibitor $GABA_A$, glycine and NMDA receptors(72). As a volatile agent with a fast turnover, it has to be administered continuously to maintain anesthesia, which allows for fine tuning of cardiorespiratory rates. Variability due to anesthesia has been controlled in our study by keeping all the animals at the same respiratory frequency during the MRI acquisitions.
Several studies observed similar solutes dispersion in primates(36), including humans(41–43, 50). However, absence of sulci in rodents is an important challenge. The folding of cortex in humans leads to an increased surface area, thus enhancing the exchanges with CSF. When scaled, interindividual variations can reach 20%(73). Though questioning, whether sulci and cortical folding could affect CSF solutes transport and exchanges remains unclear and cannot be investigated with our murine model.

Summary: In this study, quantitative dynamic CE-MRI was used on mice to investigate the influence of aging and AQP4 inhibition on tracers distribution in the CSF. While in agreement with previous studies, the findings differed dependently of the size of the contrast agents used. The important difference between the agents’ repartition emphasize how solutes transport across perivascular spaces can be related to molecular sizes. A variety of medium sized-molecules are found in the CSF, and the alteration of their transport through aging and AQP4 dysregulation may be linked to a wide range of human pathologies.

Materials and Methods

Animal preparation: Forty-three (43) young adult male C57bl6/J mice (20-30g, 8 weeks, Janvier, France) and twenty (20) old male C57bl/6J mice (30-40g, 18 months, Janvier, France) were used in this study. The animals were assigned to control group (CTRL, n=20, 8 weeks mice), TGN-020 group (TGN, n=20, 8 weeks mice) or old group (18M, n=20, 18 months mice). Each group was equally subdivided in two subgroups (i.e. n=10 and n=10) receiving either DOTA-Gd or GadoSpin D as contrast agent before MR imaging **(Figure 1A)**. 2 young adult mice were used as control for CA concentration and received a diluted solution of DOTA-Gd comparable to GadoSpin D (**Supplementary Figure 2**). One young adult mouse underwent T1-mapping MRI under anesthesia as control for T1 variations **(Supplementary Figure 1)**.

Ethical considerations and the 3R rule were accounted in this study accordingly to European and French standards. Mice were housed in standard polypropylene cages (22 x 37 x 19 cm, Charles River, L'Arbresle, France; 5 mice per cage) containing nesting material and cardboard tubes. These housing conditions were designed to meet animal welfare and to allow the expression of natural behaviors. The mice were maintained in a temperature and humidity-controlled room (12-hour light/dark cycle) and had free access to water and food (Animal care facilities: Centre Universitaire de Ressources Biologiques (CURB), Caen Normandy University, France; approval n° A14118015). Body weight was measured using a precision weighing scale (Kern PCB, Germany) before and during the surgery and imaging protocols. Anesthesia was induced with a 3 minutes exposure to isoflurane 5% in a 30%/70% O_2/NO_2 mix and maintained with isoflurane 2-3% during the surgery procedures. During the imaging session, anesthesia was reduced to 1% in pure O_2 to reduce perturbation of CSF flow by the anesthetics and hypercapnia. Ventilation frequency was monitored during imaging and kept at 80-100/min to reduce the variability due to anesthesia.

Exclusion: In 8 animals the CA was accidentally injected out of the intended injection site (cisterna magna). These animals were identified on MRI and were excluded, resulting in the following numbers in the experimental groups: DOTA-Gd/CTRL: n=9; DOTA-Gd/18M: n=10; DOTA-Gd/TGN: n=8; GadoSpin D/CTRL: n=9; GadoSpin D/18M: n=9; GadoSpin D/TGN: n=7.

AQP4 inhibition: All the animals in the TGN group (n=20) received an intraperitoneal injection of TGN-020 (N-1,3,4-Thiadiazol-2-yl-3-piridinecarboxamide, Bio-Techne®) at 100 mg/kg in 100 µL saline 1h before the intracisternal CA injection. TGN-020 is a specific inhibitor of AQP types I and IV whose usage have been shown to reduce CSF tracer transportation into the parenchyma.

Contrast agents: Two contrast agents of different sizes were used in this study, DOTA-Gd (0.7 kDa, Dotarem®, Guerbet®, France) and GadoSpin D® (17 kDa, Miltenyi Biotec®) **(Figure 1B)**. To prevent a brutal increase in CSF pressure and artefactual passage of CAs in the PVS, a volume of 1 µL, representing approximately 5% of the CSF volume of the mice, was slowly injected over 1 min. CAs were injected at their maximal concentration, i.e. 500 mM for the DOTA-Gd and 25 mM for the GadoSpin D. Two control animals received 25 mM of DOTA-Gd for comparison with GadoSpin D.

Intracisternal injection: After local shaving and lidocaine application, a dorsal midline neck incision was realized to expose the cisterna magna. An elongated glass micropipette loaded with the CA (either DOTA-Gd or GadoSpin D) was implanted in the cisterna magna, left in place for 1 min, then 1 µL of CA was injected over 1 min. A drop of superglue (Ethyl cyanoacrylate, Loctite®) was added over the puncture site, and the micropipette was left in place for 1 min more, then removed while the superglue instantly closed the hole, thus preventing extensive CSF leaks.

Magnetic resonance imaging: MRI was performed on a 7T Pharmascan MRI system (Bruker®, Germany) equipped with volume transmit and surface receive coils.

CA concentration was estimated using T1 maps before and after the intracisternal injection. The T1 map before injection was acquired at D-1, while the T1 maps after injection were acquired just after the surgery over 8 repetitions **(Figure 1A)**.

To estimate contrast agent concentration, T1 maps were computed before and after contrast injection from a FAIR RARE T1 mapping sequence with following parameters: TE = 5.3 ms; TR = 5000 ms;

FA = 90°; RARE factor = 4; 10 inversion times (TI) = 10 ms, 21 ms, 44 ms, 195 ms, 410 ms, 862 ms, 1811 ms, 3807 ms, 8000 ms; on a 64x64 single medio-sagittal slice with in-plan resolution = 0.3 x 0.3 mm and 0.8 mm thick; for a total duration of 4 min 25 s. A single acquisition was realized before contrast injection to map the reference T1, then 8 consecutive acquisitions were realized 10 minutes after contrast injection, allowing for a dynamic scan over 40 minutes.

Estimation of CSF volume fraction on T1 maps: T1 values allow an easy segmentation between brain tissue and CSF. In mice the T1 value of brain tissue is averaging 1.6 s, while being over 3 s in CSF. The planar resolution used (0.3x0.3 mm) did not allow precise manual segmentation due to partial volume effect, thus we estimated a CSF fraction based on thresholding of the T1 maps. After manual delineation of the brain area, voxels where T1 > 2.3 s were considered as mainly CSF. CSF fraction was estimated as the ratio of surface covered by mainly-CSF voxel over the whole brain surface measured on the medial-sagittal slice.

Estimation of CAs relaxivities: A phantom composed of tubes of CA at defined concentrations was used to estimate the relaxivities of DOTA-Gd and GadoSpin D on our MRI system. The same sequence as described upper was used on saline (**Supplementary Figure 1A**), 5 concentrations of DOTA-Gd (**Supplementary Figure 1B**) (10 mM, 1 mM, 100 µM, 10 µM and 1 µM) and 5 concentrations of GadoSpin D (**Supplementary Figure 1C**) (2.5 mM, 1 mM, 100 µM, 10 µM, 1 µM). A ROI was determined inside each tube and its T1 estimated. The relaxivity was estimated as the slope of 1/T1 = [CA] (**Supplementary Figure 1D-E**).

Estimation of CAs concentration: Registration and quantitative maps calculations were realized with home-made MATLAB code (MATLAB 2016b, the MathWorks, Inc., Natick, Massachussets, United States). Before calculation, the registration of images was realized independently for each animal, with the shortest TI (10 ms) as a reference, since it is the less affected by the T1 shortening due to CA injection. T1 maps were calculated for the reference acquisition, and CA concentration was estimated accordingly to the relaxivity constant determined previously, with the relation:

$$[CA].r1 = 1/T1_{post} - 1/T1_{pre}$$

, where [CA] is the CA concentration, r1 the T1 relaxivity constant, $T1_{post}$ the T1 of tissue measured after CA injection and $T1_{pre}$ the T1 of tissue before CA injection.

Representative T1 maps and the corresponding CA quantitative map are presented in **Supplementary Figure 3** for each experimental group.

Statistical analysis: The obtained CA maps where analyzed with FIJI. Concentration-time profiles where obtained from six ROIs on each CA map, viz. cerebellum, midbrain, thalamus, septal area, cortex and olfactory bulb. Both concentration at 10 min, mean CA concentration over the acquisition and concentration slope were extracted. Differences were evaluated between CTRL and 18M or CTRL and TGN for each ROI with the Mann-Whitney U test.

Entropy is defined as the degree of randomness in a given repartition. In this study, we computed Shannon entropy to indicate how well the CA was mixed and distributed across the brain.

Shannon entropy was computed from the voxel populations in whole brains at each time. Briefly, a 256 (2^8) bins histogram was formed from the image and the relative probability Pi of each value was estimated, then entropy H was obtained with the following formula:

$$H = -100.\Sigma(P_i.\log_2(P_i))/8$$

With this method, entropy is comprised between 0 % (minimal) and 100 % (maximal).

Mean entropy and entropy slope were compared using the Mann-Whitney U test.

Acknowledgments

We thank Carine Ali for her insightful comments. This work was supported by grants from the Ministère de l’Enseignement Supérieur et de la Recherche and INSERM (French National Institute for Health and Medical Research) (HCERES U1237-2017/2022) and by the special grant from the “Agence Nationale de la Recherche (ANR), MRGly ((ANR-17-CE37-0010)

.

References

1. R. Spector, S. Robert Snodgrass, C. E. Johanson, A balanced view of the cerebrospinal fluid composition and functions: Focus on adult humans. *Exp. Neurol.* **273**, 57–68 (2015).
2. M. E. Wagshul, P. K. Eide, J. R. Madsen, The pulsating brain: A review of experimental and clinical studies of intracranial pulsatility. *Fluids Barriers CNS* **8**, 5 (2011).
3. J. J. Iliff, *et al.*, A paravascular pathway facilitates CSF flow through the brain parenchyma and the clearance of interstitial solutes, including amyloid β. *Sci. Transl. Med.* **4**, 147ra111 (2012).
4. H. F. Cserr, Role of secretion and bulk flow of brain interstitial fluid in brain volume regulation. *Ann. N. Y. Acad. Sci.* **529**, 9–20 (1988).
5. R. O. Carare, *et al.*, Solutes, but not cells, drain from the brain parenchyma along basement membranes of capillaries and arteries: significance for cerebral amyloid angiopathy and neuroimmunology. *Neuropathol. Appl. Neurobiol.* **34**, 131–144 (2008).
6. M. Földi, B. Csillik, O. T. Zoltán, Lymphatic drainage of the brain. *Experientia* **24**, 1283–1287 (1968).
7. M. W. Bradbury, H. F. Cserr, R. J. Westrop, Drainage of cerebral interstitial fluid into deep cervical lymph of the rabbit. *Am. J. Physiol.* **240**, F329-336 (1981).
8. M. L. Rennels, T. F. Gregory, O. R. Blaumanis, K. Fujimoto, P. A. Grady, Evidence for a “paravascular” fluid circulation in the mammalian central nervous system, provided by the rapid distribution of tracer protein throughout the brain from the subarachnoid space. *Brain Res.* **326**, 47–63 (1985).
9. M. E. Pizzo, *et al.*, Intrathecal antibody distribution in the rat brain: surface diffusion, perivascular transport and osmotic enhancement of delivery. *J. Physiol.* **596**, 445–475 (2018).
10. J. Nimmo, *et al.*, Peri-arterial pathways for clearance of α-Synuclein and tau from the brain: Implications for the pathogenesis of dementias and for immunotherapy. *Alzheimers Dement. Diagn. Assess. Dis. Monit.* **12** (2020).
11. I. F. Harrison, *et al.*, Impaired glymphatic function and clearance of tau in an Alzheimer’s disease model. *Brain J. Neurol.* **143**, 2576–2593 (2020).
12. S. B. Hladky, M. A. Barrand, Elimination of substances from the brain parenchyma: efflux via perivascular pathways and via the blood–brain barrier. *Fluids Barriers CNS* **15** (2018).
13. R. O. Carare, C. A. Hawkes, M. Jeffrey, R. N. Kalaria, R. O. Weller, Review: cerebral amyloid angiopathy, prion angiopathy, CADASIL and the spectrum of protein elimination failure angiopathies (PEFA) in neurodegenerative disease with a focus on therapy. *Neuropathol. Appl. Neurobiol.* **39**, 593–611 (2013).
14. M. Nedergaard, S. A. Goldman, Glymphatic failure as a final common pathway to dementia. *Science* **370**, 50–56 (2020).
15. M. Arbel-Ornath, *et al.*, Interstitial fluid drainage is impaired in ischemic stroke and Alzheimer’s disease mouse models. *Acta Neuropathol. (Berl.)* **126**, 353–364 (2013).
16. T. Gaberel, *et al.*, Impaired glymphatic perfusion after strokes revealed by contrast-enhanced MRI: a new target for fibrinolysis? *Stroke* **45**, 3092–3096 (2014).
17. H. Mestre, *et al.*, Cerebrospinal fluid influx drives acute ischemic tissue swelling. *Science* **367** (2020).
18. L. Xie, *et al.*, Sleep drives metabolite clearance from the adult brain. *Science* **342**, 373–377 (2013).
19. X. Cai, *et al.*, Imaging the effect of the circadian light-dark cycle on the glymphatic system in awake rats. *Proc. Natl. Acad. Sci. U. S. A.* **117**, 668–676 (2020).
20. G. Ringstad, S. A. S. Vatnehol, P. K. Eide, Glymphatic MRI in idiopathic normal pressure hydrocephalus. *Brain J. Neurol.* **140**, 2691–2705 (2017).
21. B. C. Reeves, *et al.*, Glymphatic System Impairment in Alzheimer’s Disease and Idiopathic Normal Pressure Hydrocephalus. *Trends Mol. Med.* (2020) https:/doi.org/10.1016/j.molmed.2019.11.008.
22. K. N. Mortensen, *et al.*, Impaired Glymphatic Transport in Spontaneously Hypertensive Rats. *J. Neurosci. Off. J. Soc. Neurosci.* **39**, 6365–6377 (2019).
23. C. Di Palma, *et al.*, Cerebrospinal fluid flow increases from newborn to adult stages. *Dev. Neurobiol.* **78**, 851–858 (2018).
24. A. J. Schain, A. Melo-Carrillo, A. M. Strassman, R. Burstein, Cortical Spreading Depression Closes Paravascular Space and Impairs Glymphatic Flow: Implications for Migraine Headache. *J. Neurosci. Off. J. Soc. Neurosci.* **37**, 2904–2915 (2017).

25. B. T. Kress, *et al.*, Impairment of paravascular clearance pathways in the aging brain. *Ann. Neurol.* **76**, 845–861 (2014).
26. A. Borha, *et al.*, Cranioplasty Reverses Dysfunction of the Solutes Distribution in the Brain Parenchyma After Decompressive Craniectomy. *Neurosurgery* (2020) https:/doi.org/10.1093/neuros/nyaa028.
27. B. A. Plog, *et al.*, When the air hits your brain: Decreased arterial pulsatility after craniectomy leads to impaired glymphatic flow. *J. Neurosurg.*, 1–14 (2019).
28. C. Gakuba, *et al.*, General Anesthesia Inhibits the Activity of the “Glymphatic System.” *Theranostics* **8**, 710–722 (2018).
29. E. H. Stanton, *et al.*, Mapping of CSF transport using high spatiotemporal resolution dynamic contrast-enhanced MRI in mice: Effect of anesthesia. *Magn. Reson. Med.* **85**, 3326–3342 (2021).
30. A. J. Smith, A. S. Verkman, The “glymphatic” mechanism for solute clearance in Alzheimer’s disease: game changer or unproven speculation? *FASEB J. Off. Publ. Fed. Am. Soc. Exp. Biol.* **32**, 543–551 (2018).
31. N. A. Jessen, A. S. F. Munk, I. Lundgaard, M. Nedergaard, The Glymphatic System: A Beginner’s Guide. *Neurochem. Res.* **40**, 2583–2599 (2015).
32. S. B. Hladky, M. A. Barrand, Mechanisms of fluid movement into, through and out of the brain: evaluation of the evidence. *Fluids Barriers CNS* **11**, 26 (2014).
33. H. Mestre, Y. Mori, M. Nedergaard, The Brain’s Glymphatic System: Current Controversies. *Trends Neurosci.* **43**, 458–466 (2020).
34. M. Nedergaard, Neuroscience. Garbage truck of the brain. *Science* **340**, 1529–1530 (2013).
35. T. Brinker, E. Stopa, J. Morrison, P. Klinge, A new look at cerebrospinal fluid circulation. *Fluids Barriers CNS* **11**, 10 (2014).
36. R. Goulay, *et al.*, Subarachnoid Hemorrhage Severely Impairs Brain Parenchymal Cerebrospinal Fluid Circulation in Nonhuman Primate. *Stroke* **48**, 2301–2305 (2017).
37. J. J. Iliff, *et al.*, Brain-wide pathway for waste clearance captured by contrast-enhanced MRI. *J. Clin. Invest.* **123**, 1299–1309 (2013).
38. V. Ratner, *et al.*, Cerebrospinal and interstitial fluid transport via the glymphatic pathway modeled by optimal mass transport. *NeuroImage* **152**, 530–537 (2017).
39. G. Ringstad, *et al.*, Brain-wide glymphatic enhancement and clearance in humans assessed with MRI. *JCI Insight* **3** (2018).
40. C. S. Edeklev, *et al.*, Intrathecal Use of Gadobutrol for Glymphatic MR Imaging: Prospective Safety Study of 100 Patients. *AJNR Am. J. Neuroradiol.* **40**, 1257–1264 (2019).
41. P. K. Eide, S. A. S. Vatnehol, K. E. Emblem, G. Ringstad, Magnetic resonance imaging provides evidence of glymphatic drainage from human brain to cervical lymph nodes. *Sci. Rep.* **8**, 7194 (2018).
42. P. K. Eide, L. M. Valnes, A. H. Pripp, K.-A. Mardal, G. Ringstad, Delayed clearance of cerebrospinal fluid tracer from choroid plexus in idiopathic normal pressure hydrocephalus. *J. Cereb. Blood Flow Metab. Off. J. Int. Soc. Cereb. Blood Flow Metab.* **40**, 1849–1858 (2020).
43. P. K. Eide, G. Ringstad, In Vivo Imaging of Molecular Clearance From Human Entorhinal Cortex: A Possible Method for Preclinical Testing of Dementia. *Gerontol. Geriatr. Med.* **5**, 2333721419889739 (2019).
44. T. Jin, S.-G. Kim, Change of the cerebrospinal fluid volume during brain activation investigated by T1ρ-weighted fMRI. *NeuroImage* **51**, 1378–1383 (2010).
45. A. A. Bhogal, *et al.*, Quantitative T1 mapping under precisely controlled graded hyperoxia at 7T. *J. Cereb. Blood Flow Metab.* **37**, 1461–1469 (2017).
46. C.-C. V. Chen, Y.-Y. Tung, C. Chang, A lifespan MRI evaluation of ventricular enlargement in normal aging mice. *Neurobiol. Aging* **32**, 2299–2307 (2011).
47. E. N. Taylor, *et al.*, The brains of aged mice are characterized by altered tissue diffusion properties and cerebral microbleeds. *J. Transl. Med.* **18**, 277 (2020).
48. L. Pini, *et al.*, Brain atrophy in Alzheimer’s Disease and aging. *Ageing Res. Rev.* **30**, 25–48 (2016).
49. S. Kida, A. Pantazis, R. O. Weller, CSF drains directly from the subarachnoid space into nasal lymphatics in the rat. Anatomy, histology and immunological significance. *Neuropathol. Appl. Neurobiol.* **19**, 480–488 (1993).

50. P. K. Eide, G. Ringstad, MRI with intrathecal MRI gadolinium contrast medium administration: a possible method to assess glymphatic function in human brain. *Acta Radiol. Open* **4**, 2058460115609635 (2015).
51. A. J. Smith, X. Yao, J. A. Dix, B.-J. Jin, A. S. Verkman, Test of the "glymphatic" hypothesis demonstrates diffusive and aquaporin-4-independent solute transport in rodent brain parenchyma. *eLife* **6** (2017).
52. K. E. Holter, *et al.*, Interstitial solute transport in 3D reconstructed neuropil occurs by diffusion rather than bulk flow. *Proc. Natl. Acad. Sci. U. S. A.* **114**, 9894–9899 (2017).
53. C. Nicholson, S. Hrabětová, Brain Extracellular Space: The Final Frontier of Neuroscience. *Biophys. J.* **113**, 2133–2142 (2017).
54. O. Manouchehrian, M. Ramos, S. Bachiller, I. Lundgaard, T. Deierborg, Acute systemic LPS-exposure impairs perivascular CSF distribution in mice. *J. Neuroinflammation* **18**, 34 (2021).
55. P. Toth, S. Tarantini, A. Csiszar, Z. Ungvari, Functional vascular contributions to cognitive impairment and dementia: mechanisms and consequences of cerebral autoregulatory dysfunction, endothelial impairment, and neurovascular uncoupling in aging. *Am. J. Physiol. - Heart Circ. Physiol.* **312**, H1–H20 (2017).
56. Z. Ungvari, S. Tarantini, A. J. Donato, V. Galvan, A. Csiszar, Mechanisms of Vascular Aging. *Circ. Res.* **123**, 849–867 (2018).
57. C. Debacker, B. Djemai, L. Ciobanu, T. Tsurugizawa, D. Le Bihan, Diffusion MRI reveals in vivo and non-invasively changes in astrocyte function induced by an aquaporin-4 inhibitor. *PloS One* **15**, e0229702 (2020).
58. Y. Komaki, *et al.*, Differential effects of aquaporin-4 channel inhibition on BOLD fMRI and diffusion fMRI responses in mouse visual cortex. *PLoS ONE* **15** (2020).
59. T. Nakada, I. L. Kwee, H. Igarashi, Y. Suzuki, Aquaporin-4 Functionality and Virchow-Robin Space Water Dynamics: Physiological Model for Neurovascular Coupling and Glymphatic Flow. *Int. J. Mol. Sci.* **18** (2017).
60. C. Marin, *et al.*, Olfactory Dysfunction in Neurodegenerative Diseases. *Curr. Allergy Asthma Rep.* **18**, 42 (2018).
61. Q. Ma, B. V. Ineichen, M. Detmar, S. T. Proulx, Outflow of cerebrospinal fluid is predominantly through lymphatic vessels and is reduced in aged mice. *Nat. Commun.* **8**, 1434 (2017).
62. S. Gandy, F. L. Heppner, Breaking Up (Amyloid) Is Hard to Do. *PLoS Med.* **2** (2005).
63. M. Sakono, T. Zako, Amyloid oligomers: formation and toxicity of Abeta oligomers. *FEBS J.* **277**, 1348–1358 (2010).
64. C. M. Gao, *et al.*, Aβ40 oligomers identified as a potential biomarker for the diagnosis of Alzheimer's disease. *PloS One* **5**, e15725 (2010).
65. M. Hölttä, *et al.*, Evaluating amyloid-β oligomers in cerebrospinal fluid as a biomarker for Alzheimer's disease. *PloS One* **8**, e66381 (2013).
66. C. P. Foley, N. Nishimura, K. B. Neeves, C. B. Schaffer, W. L. Olbricht., Real-Time Imaging of Perivascular Transport of Nanoparticles During Convection Enhanced Delivery in the Rat Cortex. *Ann. Biomed. Eng.* **40**, 292–303 (2012).
67. W. M. Pardridge, CSF, blood-brain barrier, and brain drug delivery. *Expert Opin. Drug Deliv.* **13**, 963–975 (2016).
68. C. A. Stine, J. M. Munson, Convection-Enhanced Delivery: Connection to and Impact of Interstitial Fluid Flow. *Front. Oncol.* **9** (2019).
69. E. Vendel, V. Rottschäfer, E. C. M. de Lange, The need for mathematical modelling of spatial drug distribution within the brain. *Fluids Barriers CNS* **16**, 12 (2019).
70. S. Dreha-Kulaczewski, *et al.*, Inspiration is the major regulator of human CSF flow. *J. Neurosci. Off. J. Soc. Neurosci.* **35**, 2485–2491 (2015).
71. J. J. Iliff, *et al.*, Cerebral arterial pulsation drives paravascular CSF-interstitial fluid exchange in the murine brain. *J. Neurosci. Off. J. Soc. Neurosci.* **33**, 18190–18199 (2013).
72. T. F. Hawkley, M. Preston, C. V. Maani, "Isoflurane" in *StatPearls*, (StatPearls Publishing, 2021) (April 9, 2021).
73. R. Toro, *et al.*, Brain Size and Folding of the Human Cerebral Cortex. *Cereb. Cortex* **18**, 2352–2357 (2008).

Figures and Tables

Figure 1: Dispersion of two MRI contrast agents of different sizes after injection in the CSF

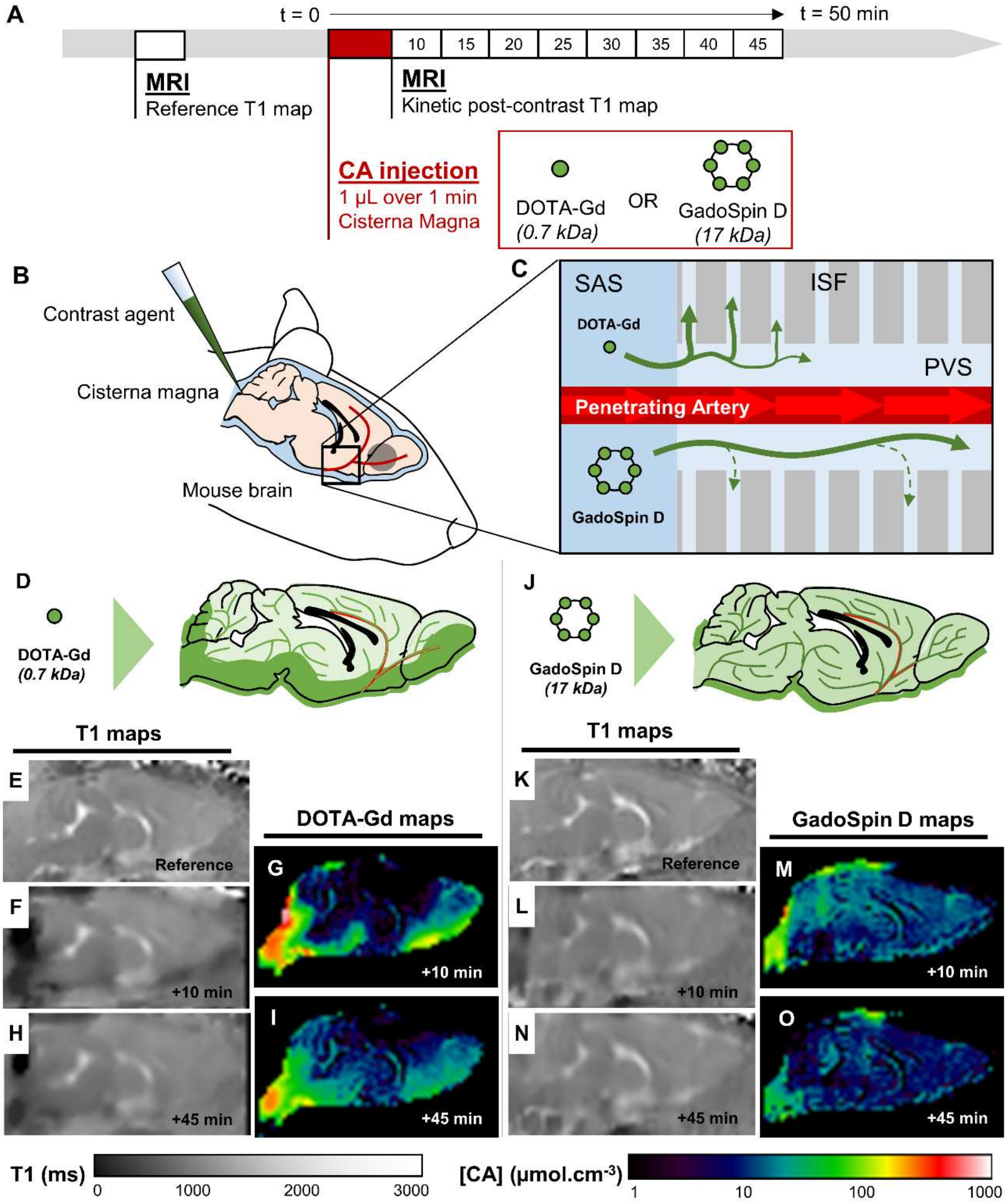

Figure 1. Dispersion of two MRI contrast agents of different sizes after injection in the CSF. To assess solute dispersion within mouse brain parenchyma, T1-mapping MRI were realized before and after CA injections in the CSF. After injection of either DOTA-Gd (0.7 kDa) or GadoSpin D (17 kDa), dynamic scans were acquired over 40 minutes (A). CA were injected in the cisterna magna, a CSF-filled space at the rear of mouse head (B). Our observations led us to hypothesize that small tracers permeate quickly into bISF, while medium-sized molecules are transported further along paravascular pathways (C). Shortly after injection, DOTA-Gd is mostly found along the basal SAS, and slowly progresses toward deeper parenchymal regions (D). In contrast, GadoSpin D was observed readily in deeper parenchymal regions such as cortex, with a more homogeneous repartition across brain and a faster elimination (J). CA concentration maps (G, I and M, G) were calculated from T1 maps (E,F,H and K,L,H). CA : Contrast Agent; CSF :

Cerebrospinal Fluid; ISF: Interstitial Fluid; MRI: Magnetic Resonance Imaging; SAS: Subarachnoid Space.

Figure 2: DOTA-Gd concentration in the septal area is increased in aged mice and reduced in TGN-20 exposed young mice

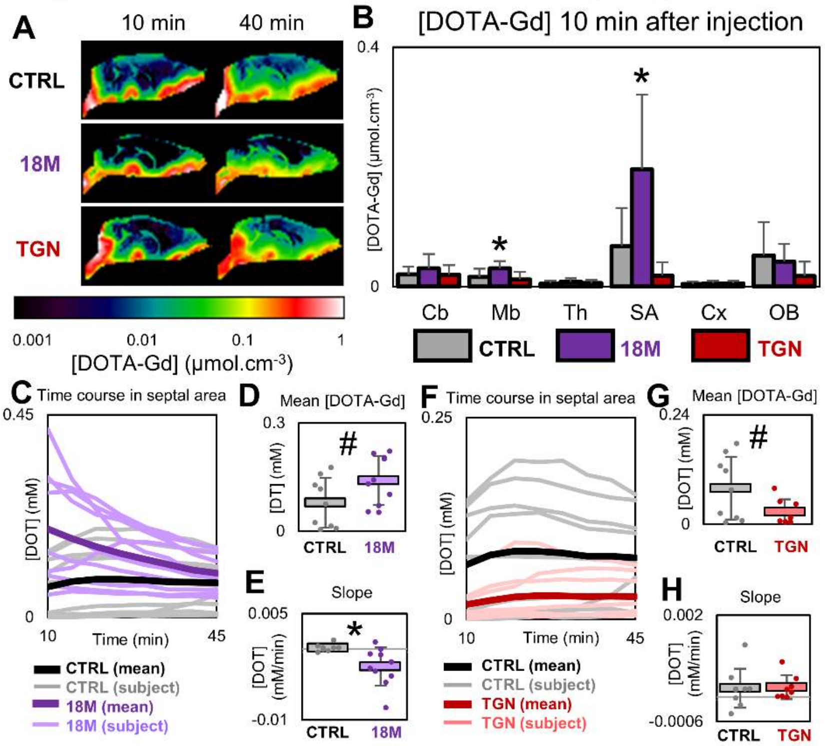

Figure 2. DOTA-Gd concentration in the septal aera is increased in aged mice and reduced in TGN-020 exposed young mice
DOTA-Gd concentrations profiles were observed in two conditions: aging and AQP-4 inhibition. Representative DOTA-Gd maps are displayed in (A). Comparison of DOTA-Gd concentrations at 10 min after injection show increased DOTA-Gd in the midbrain ($p = 0.028$, Mann-Whitney U test) and the septal area ($p = 0.028$, Mann-Whitney U test) of 18 months mice in comparison with control 2 months mice (B). Septal area appeared as the observed ROI exhibiting the most flagrant differences, with 18 months and TGN-020 exposed mice standing as two opposites when compared to the control 2 months mice (C, F). In 18 months mice, mean DOTA-Gd concentrations tended to be higher than in 2 months mice ($p = 0.079$, Mann-Whitney U test) while the slope was negative and significantly differed with younger counterpart ($p = 0.004$, Mann-Whitney U test). TGN-020 exposed mice showed a tendency toward decreased mean DOTA-Gd ($p = 0.139$, Mann-Whitney U test) but no slope difference with control mice.
18M: 18 months old mice; Cb: Cerebellum; CTRL: 2 months old control mice; Cx: Cortex; Mb: Midbrain; SA: OB: Olfactory Bulb; Septal Area; TGN: 2 months old TGN-020 exposed mice; Th: Thalamus.

p-value: 0.1 > # > 0.05 > * > 0.01

Figure 3: GadoSpin D kinetics are slowed in aged mice and TGN-020 exposed young mice

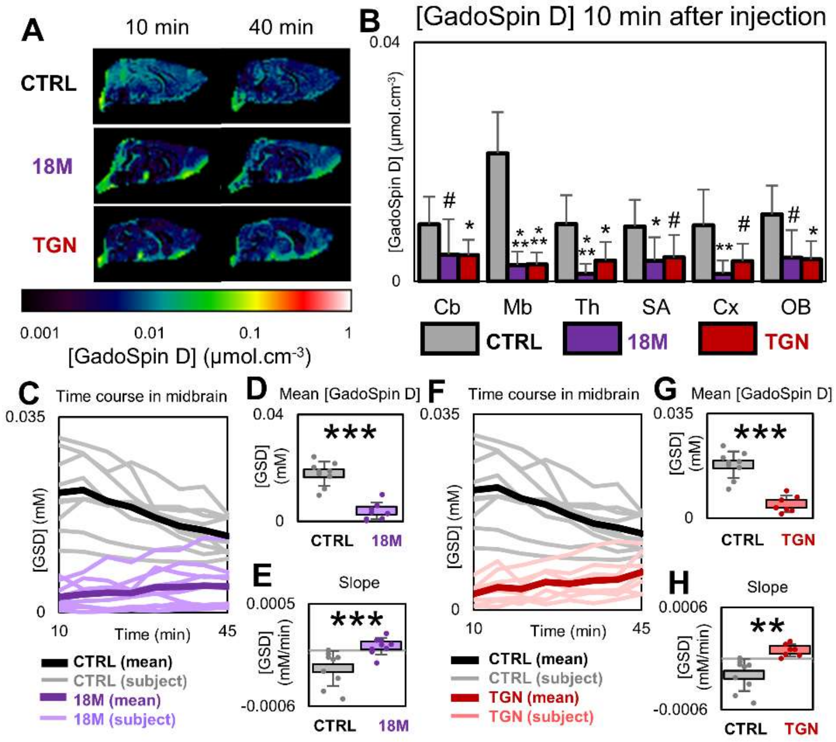

Figure 3. GadoSpin D kinetics are slowed in aged mice and TGN-020 exposed mice
GadoSpin D concentrations profile were observed in two conditions: aging and AQP-4 inhibition. Representative GadoSpin D maps are displayed in (A). Comparison of GadoSpin D concentrations at 10 min after injection show increased GadoSpin D in most regions of the control mice compared with 18 months and TGN-020 exposed mice, with the stronger differences in the midbrain ($p < 0.001$ and $p < 0.001$, respectively for CTRL vs 18M and CTRL vs TGN-020, Mann-Whitney U test) (B). In the midbrain, GadoSpin D exhibited a similar behavior in 18 months and TGN-020, opposed to control mice (C, F). Mean GadoSpin D concentrations were found to be significantly lower in both 18 months and TGN-020 exposed mice compared to controls ($p < 0.001$ and $p < 0.001$, respectively for CTRL vs 18M (D) and CTRL vs TGN-020 (G), Mann-Whitney U test), while concentrations slopes over time significantly increased ($p = 0.001$ and $p < 0.001$, respectively for CTRL vs 18M (E) and CTRL vs TGN-020 (H), Mann-Whitney U test).
18M: 18 months old mice; Cb: Cerebellum; CTRL: 2 months old control mice; Cx: Cortex; Mb: Midbrain; OB: Olfactory Bulb; SA: Septal Area; TGN: 2 months old TGN-020 exposed mice; Th: Thalamus.

p-value: 0.1 > # > 0.05 > * > 0.01 > ** > 0.001 > ***

Figure 4: Concentration of GadoSpin D in olfactory tracts increases in aged mice

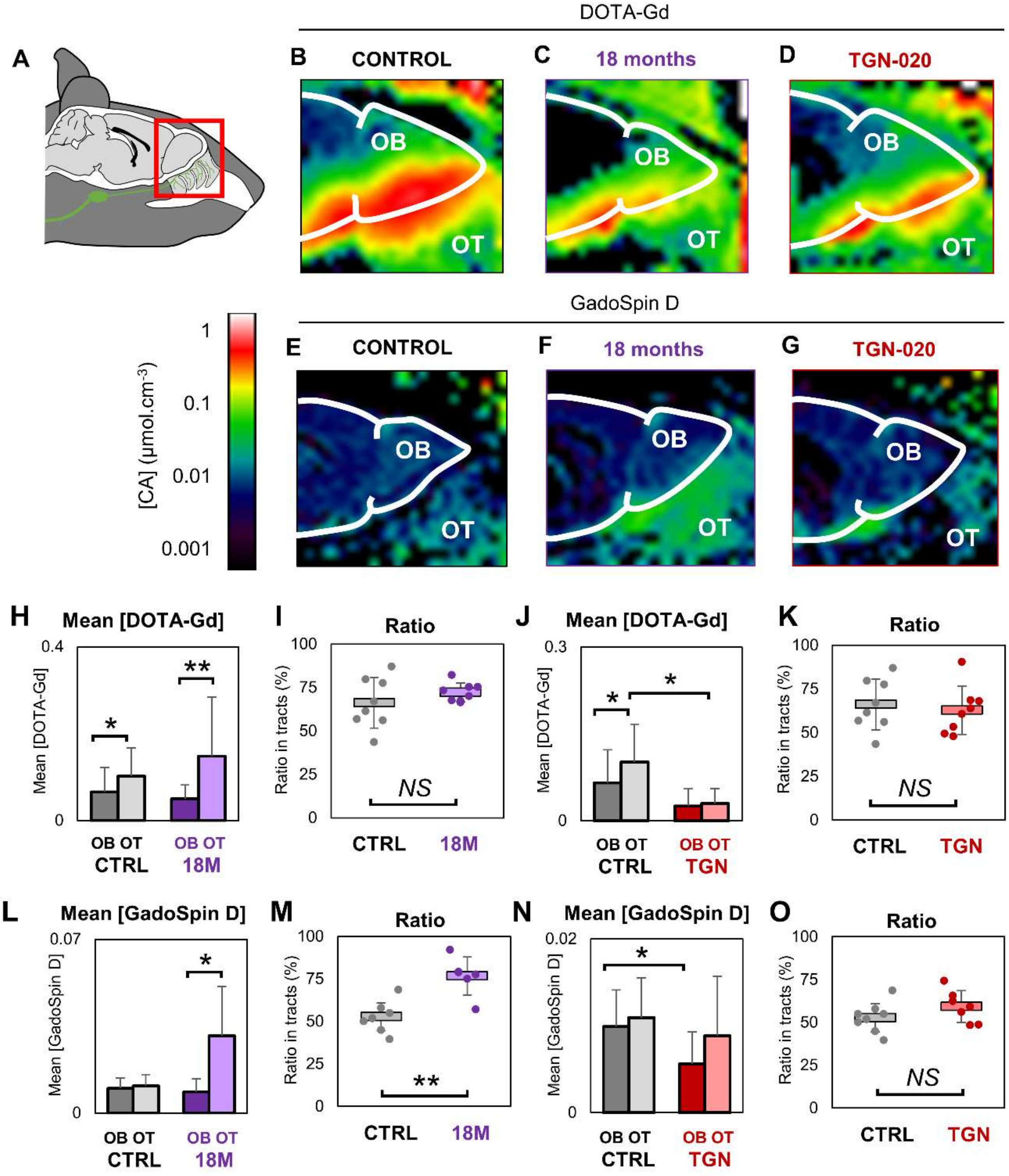

Figure 4. Concentration of GadoSpin D in olfactory tracts increases in aged mice
Olfactory tracts (A) are a predominant pathway for CSF outflow in rodents. Olfactory tracts and the nearest parenchymal ROI, olfactory bulb, are presented for representative mice from each group in (B-G). Higher CA concentrations than in olfactory bulb were measured in the olfactory tracts of control and 18 months mice with DOTA-Gd (H, J), but only in the 18 months mice with GadoSpin D (L). CA concentration was found to be lower in the olfactory tracts of TGN-020 exposed mice vs. to controls for DOTA-Gd (J), while it was lower in olfactory bulb of TGN-020 exposed mice vs. controls for GadoSpin D (N). A ratio was computed from olfactory tract and olfactory bulb concentrations: Ratio = OT/(OB+OT) to normalize the differences due to initial CA repartition in the SAS. 18 months mice exhibited an increased ratio, i.e. GadoSpin D accumulation in olfactory tracts, in regard to 2 months mice (M). These observations were not reproduced with DOTA-Gd, nor in TGN-020 exposed mice injected with Gadospin-D (I, K, O). 18M: 18 months old mice; CA: Contrast Agent; CTRL: 2 months old control mice; NS: Non Significant; OB: Olfactory Bulb; OT:

Olfactory Tract; TGN: 2 months old TGN-020 exposed mice. p-value: 0.05 > * > 0.01 > ** > 0.001 > ***

Figure 5: GadoSpin D penetrates into parenchyma deeper and faster than DOTA-Gd

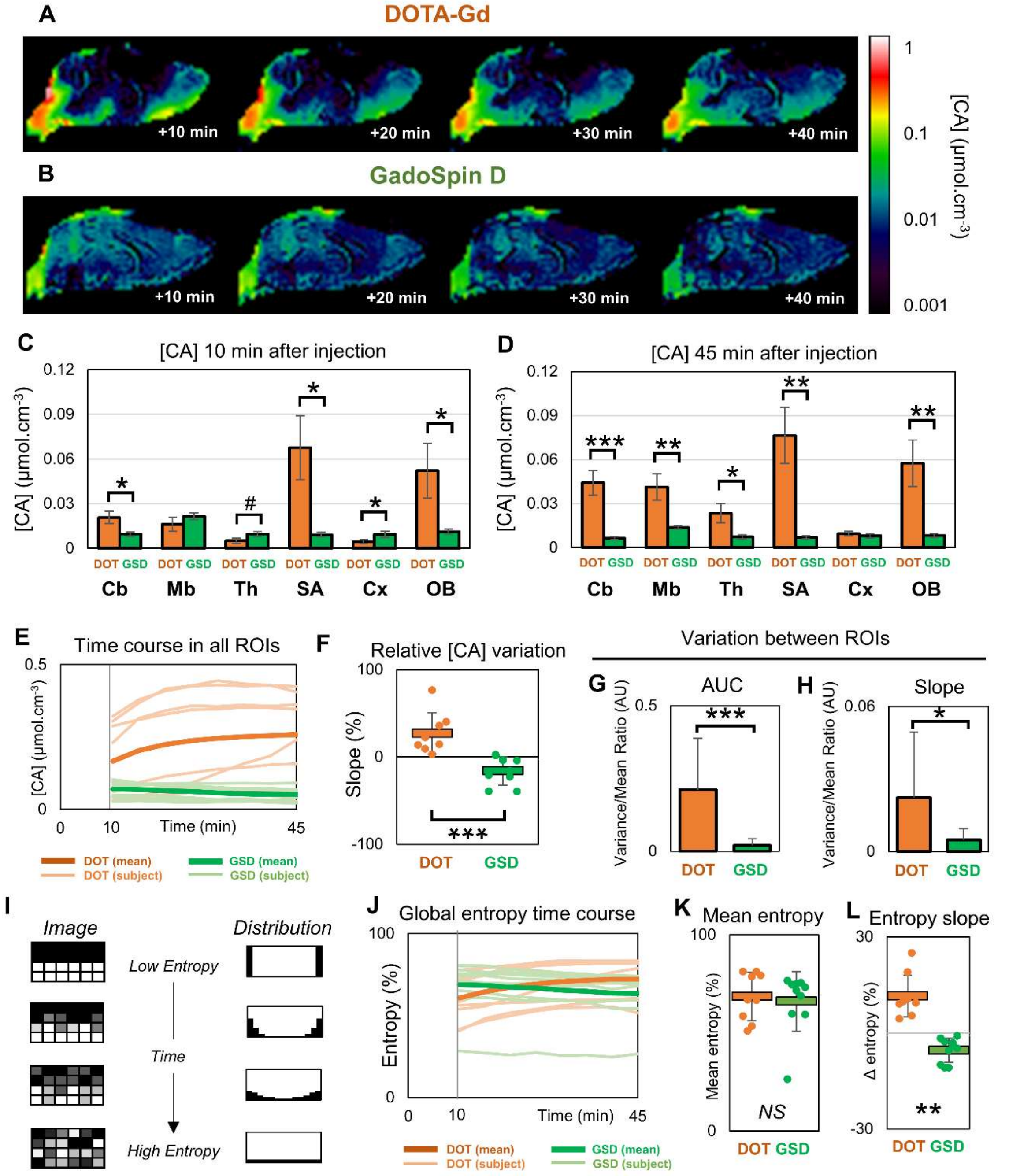

Figure 5. GadoSpin D penetrates into parenchyma deeper and faster than DOTA-Gd
DOTA-Gd and GadoSpin D exhibited different repartitions in tissues after injection in CSF. While DOTA-Gd appeared to be restricted to SAS and slowly diffused into the brain parenchyma (A), GadoSpin D distributed in the whole brain (B). Despite that GadoSpin D was used at a 20 times lower concentration that DOTA-Gd in our experiments, GadoSpin D intake appeared to be significantly higher in thalamus and cortex 10 minutes after injection (C). At 45 minutes, these differences disappeared and DOTA-Gd was found in higher levels than GadoSpin D in all ROIs (D). DOTA-Gd kinetics appeared as a slow CA accumulation in the whole brain, while GadoSpin D decreased steadily over the acquisition time (E), and the concentration slopes significantly differed between the 2 CAs (F). Due to its high concentration in the SAS, normalized variations across the

brain appeared to be higher for DOTA-Gd than for GadoSpin D, both for mean CA concentration (G) and slope (H). In a last analysis, we assessed the entropy of CAs distribution. Entropy is a reflect of chaos, and in our case, of how well a solution is mixed. Entropy always increase with time in a closed system (I). We observed opposite patterns between the two CAs, as entropy increased for DOTA-Gd while it decreased for GadoSpin D (J). Mean entropy did not differed (K), while slope was significantly lower for GadoSpin D (L). Negative entropy may here reflects the elimination of GadoSpin D, as the brain is not a closed system.

Cb: Cerebellum; Cx: Cortex; DOT: DOTA-Gd; GSD: GadoSpin D; Mb: Midbrain; NS: Non Significant; OB: Olfactory Bulb; SA: Septal Area; Th: Thalamus.

p-value: 0.1 > # > 0.05 > * > 0.01 > ** > 0.001 > ***

Supplementary figure 1: T1 and CA relaxivity calculation

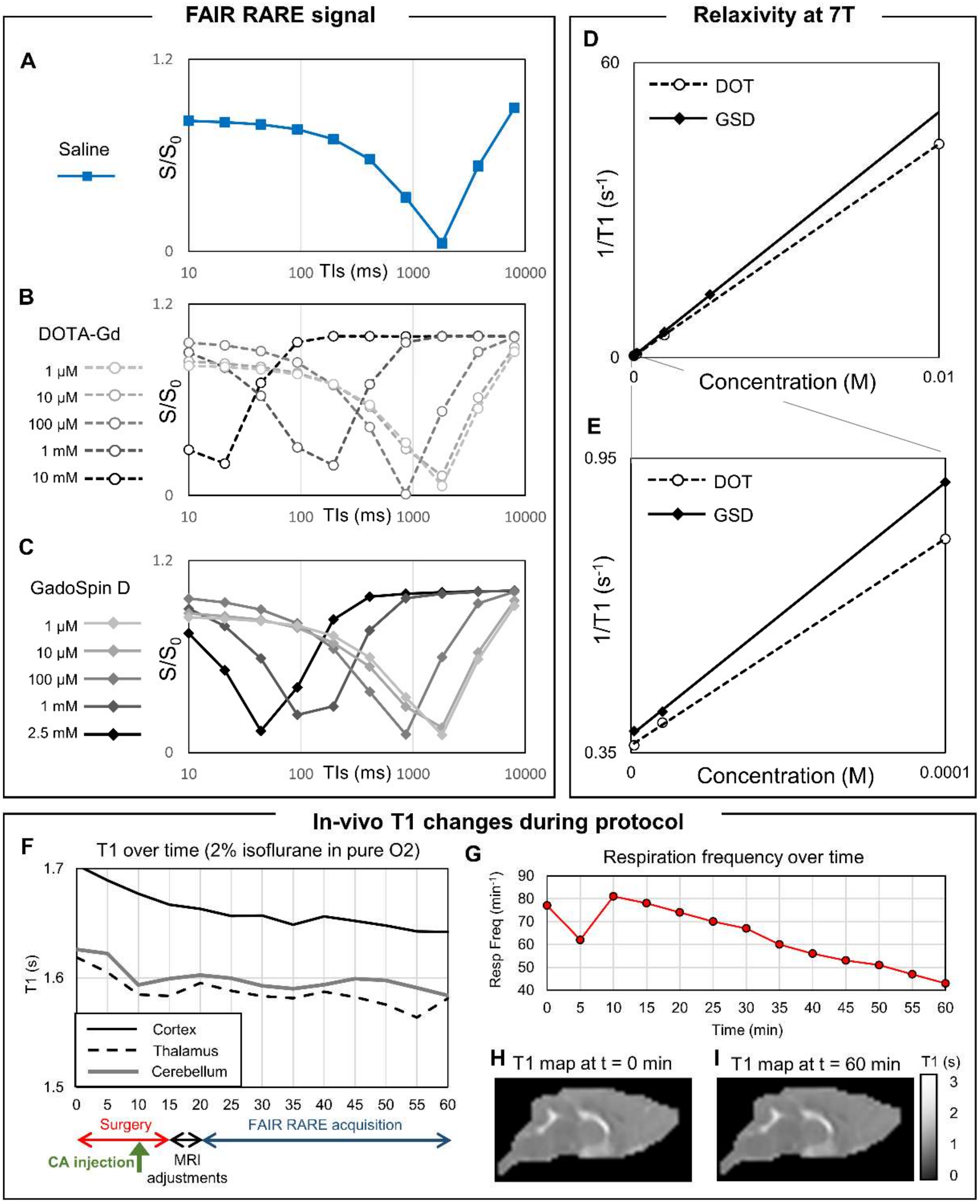

Supplementary figure 1. T1 and CA relaxivity calculation

A FAIR RARE sequence derived from Look-Locker sequence was used to measure T1. Signal recovery observed on a saline-filled phantom (A), DOTA-Gd dilutions in saline (B), GadoSpin D dilutions in saline (C). Relaxivity slopes (CA concentration = relaxivity . 1/T1) were computed for both DOTA-Gd and GadoSpin D (D,E). To asses wether T1 variation would occur on our protocol, we dynamically acquired the T1 over 1 hour (maximal experiment duration) on a test animal. Parenchymal T1 slightly decreased along the acquisition (F), possibly coupled with simultaneously decreasing respiratory frequency and increasing hypercapnia (G). Overall, T1 differences before (H) and after (I) the 1 hour anesthesia appeared to be negligible within our CA concentration calculation protocol.

CA: Contrast Agent; DOT: DOTA-Gd; DOTA: Dodecane Tetraacetic Acid ; FAIR: Flow sensitive Alternating Inversion Recovery; Gd: Gadolinium; GSD: GadoSpin D; MRI: Magnetic Resonance Imaging; RARE: Rapid Acquisition with Refocused Echoes; TI: Inversion Time

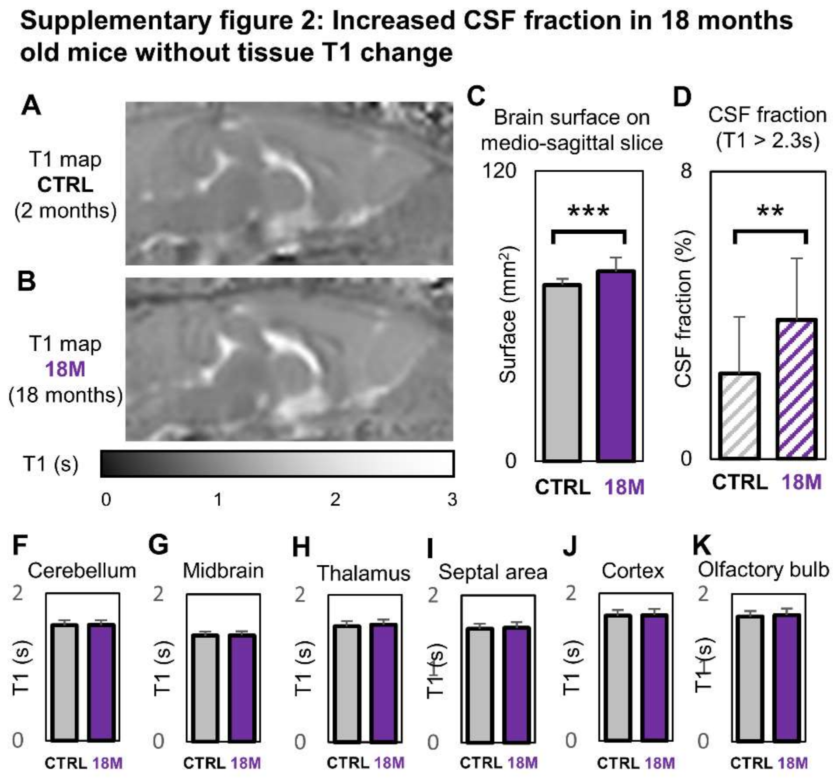

Supplementary figure 2. Increased brain size and CSF fraction in 18 months old mice without tissue T1 change

Reference T1 maps were used to estimate the brain size and the CSF fraction on 2 months (A) and 18 months (B) old mice. Brain size was found to be increased in 18 months mice (C, $p<0.001$, Student's T test), as well as CSF fraction (D, $p = 0.006$, Student's T test). In T1 maps, voxels where T1 > 2.3 s where considered as mostly CSF and used to calculate the CSF fraction. T1 measurements in cerebellum (F), midbrain (G), thalamus (H), septal area (I), cortex (J) and olfactory bulb (K) did not reveal significant difference between 2 months and 18 months old mice ($p = 0.542$, two-way ANOVA).
18M: 18 months old mice; CSF: Cerebrospinal Fluid; CTRL: 2 months old mice

Supplementary figure 3: T1 and [Gd] maps for representative mice

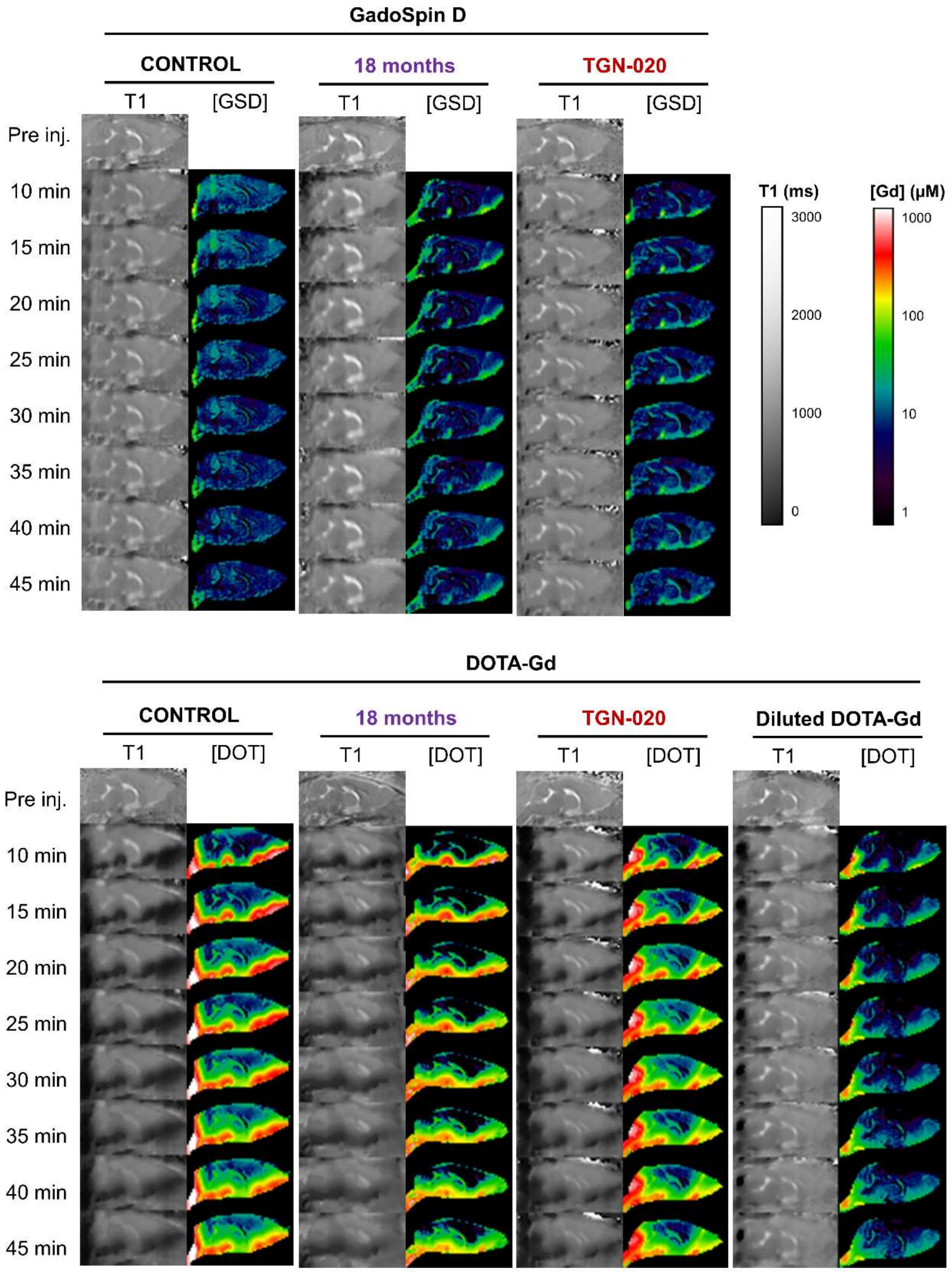

Supplementary figure 3. T1 and [Gd] maps for representative mice
T1 and CA concentration maps were computed for each group. 9 two-months control mice, 9 18-months mice and 7 two-month mice exposed to TGN-020 received 1µl of GadoSpin at 25 mM intracisternally. 9 two-months control mice, 10 18-months mice and 8 two-month mice exposed to TGN-020 received 1µl of DOTA-Gd at 500 mM intracisternally. Two additional mice received 1 µl of DOTA-Gd at 25 mM, allowing for a more direct comparison with GadoSpin.

CA: Contrast Agent; DOT: DOTA-Gd ; DOTA : Dodecane Tetraacetic Acid ; Gd : Gadolinium; GSD: GadoSpin D

Étude 2 : Cranioplasty Reverses Dysfunction of the Solutes Distribution in the Brain Parenchyma After Decompressive Craniectomy

Résumé : La craniectomie décompressive (CD) est une procédure chirurgicale réalisée pour parer à l'augmentation de la PIC causée par les oedèmes cérébraux. Il s'agit de retirer un volet crânien le temps que l'œdème se résorbe, ce qui peut durer quelques mois. Le volet crânien est replacé lors de la cranioplastie. Cependant, l'intégrité de la boîte crânienne est nécessaire à la mécanique complexe des jeux de pression à l'origine des oscillations dans le LCR.

Dans cette étude chez la souris, nous avons injecté un traceur (DOTA-Gd) dans le LCR afin de déterminer si la CD perturbe les échanges LCR-FISC et si la cranioplastie permet la récupération de la fonctionnalité de ces échanges.

Une CD se traduit par une diminution de la quantité de traceur atteignant l'extrémité antérieure de l'encéphale (bulbe olfactive). Cette réduction de la circulation du LCR est récupérée après une cranioplastie. De manière intéressante, la CD ne semble pas affecter différentiellement la pénétration du traceur entre les deux hémsphères alors qu'elle n'est réalisée que d'un côté, ce qui oriente vers un effet global.

Conclusions :

- La CD réduit la circulation globale du traceur dans l'espace sous-arachnoïdien
- La cranioplastie permet de récupérer une circulation normale du LCR

Contribution : Dans cette étude dont je suis deuxième autrice, j'ai contribué à l'analyse des données et à la rédaction d'une part sigificative de l'article.

RESEARCH—ANIMAL

Cranioplasty Reverses Dysfunction of the Solutes Distribution in the Brain Parenchyma After Decompressive Craniectomy

Alin Borha, MD, MSc[*‡]
Audrey Chagnot, MSc[*]
Romain Goulay, PhD[*]
Evelyne Emery, MD, PhD[*‡]
Denis Vivien, PhD[*§]
Thomas Gaberel, MD, PhD[*‡]

[*]Normandie Univ, UNICAEN, INSERM, U1237, PhIND "Physiopathology and Imaging of Neurological Disorders", Institut Blood and Brain @ Caen-Normandie, Cyceron, France; [‡]Department of Neurosurgery, Caen University Hospital, Avenue de la côte de Nacre, Caen, France; [§]Department of Clinical Research, Caen University Hospital, Avenue de la côte de Nacre, Caen, France

This material was previously presented as "The impact of decompressive craniectomy to the glymphatic system in mice". Research abstract. European Society of Pediatric Neurosurgery ESPN course on 28 February 2019 in Paris, France - oral presentation, plenary.

Correspondence:
Alin Borha, MD,
INSERM U919 "Serine protease and pathophysiology of the neurovascular unit",
University Caen Basse-Normandie,
GIP Cyceron, Bd Becquerel,
BP5229, 14074 Caen, France.
Email: alin_borha@hotmail.com

Received, August 23, 2019.
Accepted, December 28, 2019.

BACKGROUND: Solutes distribution by the intracranial cerebrospinal fluid (CSF) fluxes along perivascular spaces and through interstitial fluid (ISF) play a key role in the clearance of brain metabolites, with essential functions in maintaining brain homeostasis.

OBJECTIVE: To investigate the impact of decompressive craniectomy (DC) and cranioplasty (CP) on the efficacy of solutes distribution by the intracranial CSF and ISF flux.

METHODS: Mice were allocated in 3 groups: sham surgery, DC, and DC followed by CP. The solutes distribution in the brain parenchyma was assessed using T1 magnetic resonance imaging after injection of DOTA-Gadolinium in the cisterna magna. This evaluation was performed at an early time point following DC (after 2 d) and at a later time point (after 15 d). We evaluated the solutes distribution in the whole brain and in the region underneath the DC area.

RESULTS: Our results demonstrate that the global solutes distribution in the brain parenchyma is impaired after DC in mice, both at early and late time-points. However, there was no impact of DC on the solutes distribution just under the craniectomy. We then provide evidence that this impairment was reversed by CP.

CONCLUSION: The solute distribution in the brain parenchyma by the CSF and ISF is impaired by DC, a phenomenon reversed by CP.

KEY WORDS: Glymphatic system, Decompressive craniectomy, Cranioplasty, Magnetic resonance imaging

Neurosurgery 0:1–6, 2020 DOI:10.1093/neuros/nyaa028 www.neurosurgery-online.com

Decompressive craniectomy (DC) is a surgical procedure where a part of the skull bone is removed to relieve elevation of the intracranial pressure (ICP). When the brain edema has disappeared, usually a few months after DC, cranioplasty (CP) is realized, ie, the bone flap is replaced over the defect, essentially for safety and cosmetic reasons. Indications of DC include malignant ischemic stroke and post-traumatic refractory elevation of the ICP.[1,2] Still, its benefits are questioned in the early management of traumatic brain injuries or following intracerebral hemorrhages.[3,4] Interestingly, an immediate improvement of the patients' neurological status is often noted following CP, a phenomenon not fully understood.[5]

ABBREVITIONS: **CP,** cranioplasty; **CSF,** cerebrospinal fluid; **DC,** decompressive craniectomy; **ICP,** intracranial pressure; **ISF,** interstitial fluid; **MRI,** magnetic resonance imaging; **ROI,** regions of interest; **SI,** signal intensity

Recent description of meningeal lymphatic vessels and proposal of brain waste clearance models have changed our understanding of the phenomena underlying solutes pathways in the cerebrospinal fluid (CSF) and interstitial fluid (ISF) of the central nervous system.[6,7] The glymphatic (glial-lymphatic) system proposes that CSF fluxes along perivascular spaces and through interstitial spaces play a key role in the clearance of brain metabolites, with essential functions in maintaining brain homeostasis.

Here, we hypothesized that an alteration of the skull bone integrity induced by DC may impair the efficacy of the solutes distribution in the brain parenchyma, and that CP may restore its normal activity, explaining the benefit of CP on functional status.

This hypothesis was tested on a mouse model of DC and CP that we developed. The efficiency of the solutes distribution in the brain parenchyma was measured by using T1 magnetic resonance imaging (MRI) following intracisternal injection of DOTA-Gd.

METHODS

Animals

All the experiments were performed in male Swiss mice (35-40 g; CURB, Caen, France). All efforts were made to limit animal suffering as previously described.[8] None of the experimental procedures induced animal mortality. Experiments were carried out following the ARRIVE guidelines (www.nc3rs.org.uk) and in accordance with the European Communities Council Directive (86/609/EEC) regarding the care and use of animals for experimental procedures and were approved by the local ethical committee CENOMEXA 2 017 112 620 401 874_v4 (# 12 335) 24.05.2018.

"All the experiments were performed in mice anesthetized with isoflurane (2%) in 70%/30% NO2/O2. Body temperature was maintained at 37°C with a rectal temperature probe and homoeothermic heating pad. Mice received subcutaneous buprenorphine (0.05 mg/kg) at the time of the anesthesia and during the imaging procedure at when appropriate" as previously described.[8]

Experimental Design

A total of 36 mice were sorted in 6 experimental groups depending both on surgical conditions (sham surgery; DC; DC followed by CP) and delays after surgery for MRI evaluation (day 2; day 15) (Figure 1A).

Decompressive Craniectomy

DC was performed at day 0 as previously described.[9] While under general anesthesia, the mice were maintained using a stereotactic frame. The skull was exposed after longitudinal skin incision (Figure 1B). For the 24 mice undergoing DC, the skull bone over the right hemisphere was removed using a high-speed drill under continuous cooling with saline. Bone flaps with a size of 8 × 4 mm were obtained, with special attention paid to leave the dura mater intact, and not to expose the superior sagittal sinus. The bone flaps were conserved at −20°C under aseptic condition. The mice were allowed to recover once the wound was closed. For the 12 animals undergoing sham surgery, only the skin incision and wound closure were performed.

Cranioplasty

Half of the mice that undergone DC were randomly assigned to have CP 24 h later. Anesthesia and installation protocol were the same as those used for DC. After the wound was opened, the bone flap was thawed and put over the bone defect. The fixation of the bone flap was strengthened using bone cement (Fuji®, Japon) (Figure 1B). The mice were allowed to recover once the wound was closed.

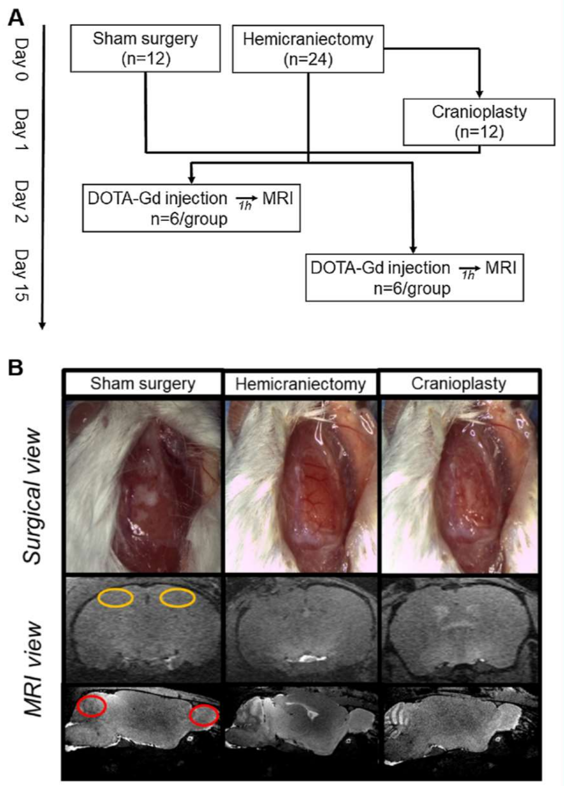

FIGURE 1. *Description of the method used.* **A**, *Flow chart of the study.* **B**, *On the upper part, macroscopic view of the surgical method used. Left = Sham Group: skin incision and skull exposure. Middle = Decompressive Craniectomy Group: a large bone flap has been removed, with the dura-mater left intact. Right = CP Group: Final view after replacement of the bone flap, which has been fixed using dental cement. On the lower part, description of the MRI method used to evaluate the intracranial CSF circulation. Representative T1-weighted images 60 min after Dotarem injection (DOTA-Gd) in CSF, revealing parenchymal enhancement corresponding to the intracranial CSF circulation. In yellow, on the coronal view, the ROI used to evaluate the local solutes distribution in the brain parenchyma just beneath the DC area. In red, on the sagittal view, the ROI used to evaluate the global solutes distribution in the brain parenchyma, defined as the ratio of the SI in the olfactory bulb/cerebellum.*

Intracisternal Injection of DOTA-Gd

Under general anesthesia, the mice were maintained using a stereotactic frame in a ventral position, with the head flexed about 45 to 50 degrees. A midline suboccipital incision was realized and the atlanto-occipital membrane was then gently dissected. One μL of DOTA-Gd (Gadoteric acid; Dotarem®, Guerbet, France), a T1-enhancing contrast agent, were injected over 1 min in the CSF through the cisterna magna using a pulled haematological glass micropipette as previously described.[9] The micropipette was left in place for 1 additional minute then the wound was closed. 1 h later, the animals undergone the MRI exam.

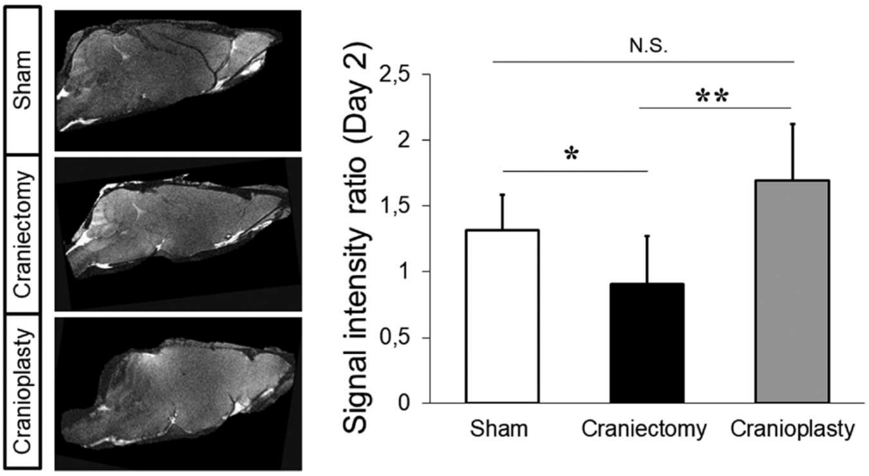

FIGURE 2. *Short term impact of DC and CP on the global solutes distribution in the brain parenchyma. Evaluation of the global solutes distribution in the brain parenchyma 2 d after the surgery. Representative sagittal T1-weighted images and corresponding quantification 1 h after Dotarem injection in sham, DC and CP mice (n = 6 per group). In sham mice, the enhancement of the olfactory bulb is normal, with a SI ratio of 1.316 ± 0.26. The SI ratio significantly decreases in the DC group (0.903 ± 0.43; ∗, P = .016 vs Sham group), and returns to its normal value after CP (n = 6; SI ratio 1.69 ± 0.36, ∗∗, P = .005 vs DC group).*

MRI Experiments

A 7T Pharmascan® MRI system (Bruker, Germany) equipped with surface coils was used (Figure 1B). High-resolution (78∗78∗150 μm) 3D T1-weighted imaging was performed with a Fast Low Angle Shot (FLASH) sequence with the following configuration: TR/TE 15/3.57 ms, flip angle = 25°, FoV = 20∗17∗14.4 mm, matrix = 256∗218∗96, leading to an acquisition time of 15 min.

MRI was performed 2 d after the initial surgery in the early evaluation groups or after 15 d in the late evaluation groups.

MRI Analysis

The signal intensity (SI) was measured using Image J 1.48 software (NIH) in regions of interest (ROI) in the right (ipsilateral) and left (contralateral) side of olfactory bulbs, cerebellum, and cortical region under the craniectomy area. Ratios between ROIs were used to assess DOTA-Gd distribution in the brain tissue.

Global distribution was estimated for each side with the ratio $SI_{Olfactory\ Bulb}/SI_{Cerebellum}$, with values from each hemisphere being meaned for the analysis (Figure 1B). Local distribution was estimated by comparing SI in the cortical regions just under the craniectomy area, with the ratio being $SI_{Ipsilateral\ Cortex}/SI_{Contralateral\ Cortex}$ (Figure 1B).

Statistics

"All statistical analyses were performed using Statistica (Softonic, Spain). The results are expressed as the mean ± SD. Statistical analyses were performed using the Kruskall-Wallis test, followed by *post hoc* comparison with the Mann-Whitney *U* test" as previously described.[10]

RESULTS

Decompressive Hemicraniectomy Impairs Global Cerebral Solutes Distribution

A contrast agent, DOTA-Gd, was injected in the CSF of the cisterna magna to evaluate at early (day 2) and late (day 15) time points how solutes distribution was affected by DC. Once injected, the contrast agent diffuses in the subarachnoid space while impregnating the parenchyma at the same time. We thus assumed that ratios based on the SI in parenchyma reflect solutes distribution.

Brain-wide (global) distribution was evaluated on a cranio-caudal axis with the mean ratio $SI_{Olfactory\ Bulb}/SI_{Cerebellum}$. At early evaluation (2 d after DC), this ratio was decreased in the DC group (SI ratio = 0.906) when compared to the sham group (SI ratio = 1.316) (n = 6 per group; *P* = .016; Figure 2), meaning that global solutes distribution was impaired as proportionally less DOTA-Gd reached the olfactory bulbs. This impairment remains consistent at late (day 15) evaluation with a SI ratio = 0.893 in DC group vs SI ratio = 1.336 in the Sham group (n = 6 per group; *P* = .025; Figure 3).

Local distribution was evaluated on the assumption that craniectomy may affect the underlying cerebral parenchyma. Solute distribution asymmetry was checked using the ratio $SI_{Ipsilateral\ Cortex}/SI_{Contralateral\ Cortex}$. SI was not found to be significantly different between the 2 hemispheres at any of the 2 time points, with SI ratio = 1.03 in early DC group vs 0.954 in

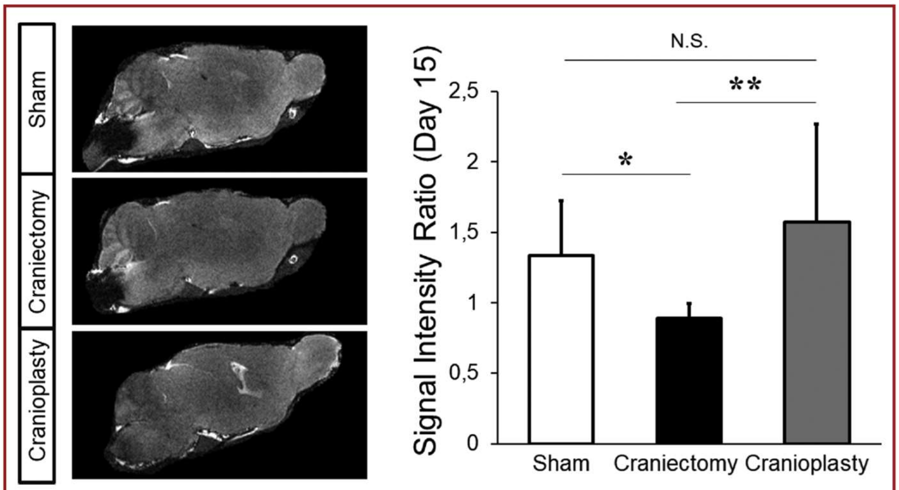

FIGURE 3. *Long term impact of DC and CP on the global solutes distribution in the brain parenchyma. Evaluation of the global solutes distribution in the brain parenchyma 15 d after the surgery. Representative sagittal T1-weighted images and corresponding quantification 1 h after Dotarem injection in sham, DC and CP mice (n = 6 per group). In sham mice, the enhancement of the olfactory bulb is normal, with a SI ratio of 1.336 ± 0.38. The SI ratio significantly decreases in the DC group (0.893 ± 0.1; *: P = .025 vs Sham group), and returns to its normal value after CP (1.578 ± 0.69; **: P = .002 vs DC group).*

early sham group (n = 6 per groups; *P* = .13; Figure 4) and SI ratio = 0.946 in late DC group and 0.916 in late sham group (n = 6 per groups; *P* = .93; Figure 5).

Cranioplasty Reverses the Impairment of the Global Solutes Distribution Caused by Decompressive Hemicraniectomy

As DC affects the topology and mechanical properties of the intracranial compartment, CP was hypothesized to allow recovering of normal solutes distribution by restoring the skull integrity.

At the early evaluation time (2 d after DC), global solutes distribution was not found to be significantly different in the sham (SI ratio = 1.31) and CP following DC (SI ratio = 1.69) groups (n = 6 per group; *P* = .092; Figure 2), though significant difference was found between CP following DC (SI ratio = 1.69) and DC (SI ratio = 0.906) (n = 6 per group; *P* = .005; Figure 2). The same observation was made in the late evaluation group, with CP following DC SI ratio = 1.578, no significant difference with sham (SI ratio = 1.337) (n = 6 per group; *P* = .59; Figure 3) and significant difference with DC (SI ratio = 0.893) (n = 6 per group; *P* = .002; Figure 3). This argues that CP following DC could reverse the impairment of global solutes distribution observed in the DC groups.

Furthermore, CP has no effect on local solutes distribution both at early (SI ratio = 0.996; n = 6 per group; *P* = .59 when compared with sham (SI ratio = 0.954) and *P* = .59 when compared with DC (SI ratio = 1.03; Figure 4) and late (CP SI ratio = 0.941; n = 6 per group; *P* = .81 when compared with sham (SI ratio = 0.916) and *P* = .93 when compared with DC (SI ratio = 0.946); Figure 5) time points.

DISCUSSION

The results obtained in this study in mice suggest that DC durably impairs the global solutes distribution within the brain parenchyma, without affecting the local solute distribution in the cortical area underneath the craniectomy site. Interestingly, we also demonstrate that this effect is prevented by CP.

Arterial pulsation was shown to contribute to water and solutes motion in the periarterial space.[11] Our results put in light the need of skull integrity for this phenomenon to be fully effective. When the skull integrity is altered as in DC, the decrease of ICP may be the explanatory cause of the reduced solutes distribution we observed. Reduction of ICP is a global phenomenon that occurs within the whole skull cavity, thus explaining the brain-wide effect we observed. Restoration of skull integrity with CP allows the recovering of a physiological ICP, thus reestablishing normal solutes distribution. Moreover, CP improves the blood perfusion of the brain, which may participate in CSF intracerebral flux recovery by increasing arterial pulsation.[12] These data may constitute an additional argument to perform CP as soon as possible, and underlined that further studies are needed in the field.

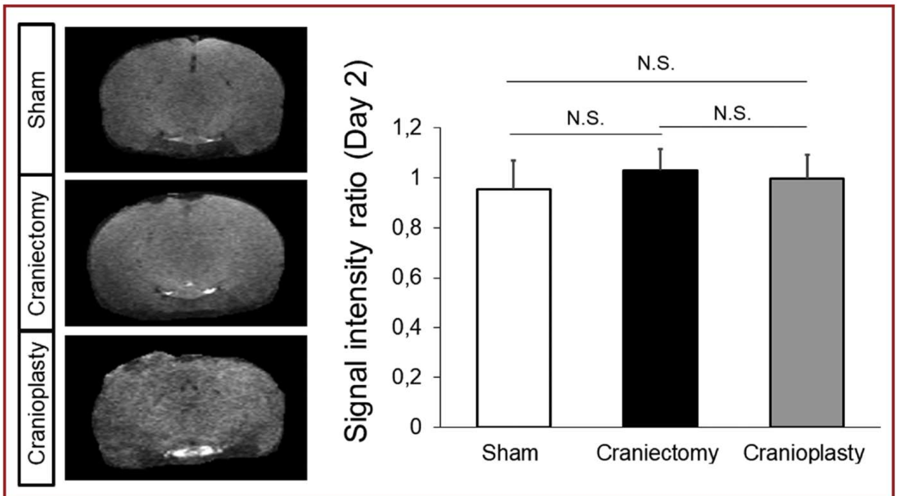

FIGURE 4. *Short term impact of DC and CP on the local solutes distribution in the brain parenchyma. Evaluation of the local solutes distribution in the brain parenchyma 2 d after the surgery. Representative coronal T1-weighted images and corresponding quantification 1 h after Dotarem injection in sham, DC and CP mice (n = 6 per group). In sham mice, the enhancement of brain is similar in both hemispheres, with a SI ratio of 0.954 ± 0.11. This is similar to the SI ratio observed in the DC group (1.03 ± 0.08; NS: P = .13 vs Sham group), and in the CP group (0.996 ± 0.09; NS; P = .59 sham vs CP, and P = .59, CP vs DC group).*

The functional improvement observed after CP should be partly attributed to the subsequent cerebral blood flow recovery.[5,12] Here, we suggest that the restoration of normal solutes distribution may as well contribute to this improvement. Indeed, patients with DC often show significant CSF physiology impairment which usually disappears after CP,[13] with an effective CSF flux needed to maintain brain homeostasis. Rupture of skull bone integrity and thus of normal solutes distribution could be responsible for secondary brain injuries. Consequently, in some indications such as subarachnoid hemorrhage or severe traumatic brain injury where the solutes distribution in the brain parenchyma is already impaired,[8,14] DC is shown to have disappointing results.[2,15]

Though, the use of an animal model limits the interpretation of our findings in humans. Mice were healthy with a normal ICP, in contrast to patients. Subsequently, we have not evaluated the neurological outcome, which is the gold standard for the evaluation in brain injured patients outcomes. Moreover, opening the dura mater, a common clinical practice, was not performed due to the fragility of the dura mater in mice. Also, mouse is a lissencephalic specie, and its brain physiology is possibly highly different from species with gyrencephalic brain, like human. This could limit the translation of our results to human pathology. Finally, the limited time window did not allowed extensive following as realized in humans. Giving the design of our study, it is particularly not possible to conclude about the impact of delayed CP, which is often the case in human pathology.

Interestingly, in agreement with our present in Vivo MRI study, a recent histological study by Plog et al[16] also proposed an impairment of the solutes distribution in the brain parenchyma occurring in both hemispheres after hemicraniectomy, a phenomenon reversed by CP. These authors have shown that this impairment was related to the decrease in vascular pulsatility and the microglial and inflammatory responses. Though this study gives several avenues to explain the impairment of solutes distribution in the brain parenchyma following DC, the small size of the craniectomy performed (2 × 2 mm) limits extrapolation in patients, where the removed bone flap size almost all the hemisphere, like we did in our present protocol.

We were also highly surprised by the fact that solutes distribution in the brain parenchyma was not different between the ipsi and contralateral side of the DC. We first hypothesized that the MRI method used to evaluate the solutes distribution was not enough sensitive. However, when solutes distribution in the parenchyma is studied through fluorescence microscopy, which might be more sensitive, the same solutes distribution was observed.[16] We hypothesized that the solutes distribution in the brain parenchyma is a global system relying on the ICP, which is usually the same in the whole skull cavity. Moreover, it seems that arterial pulsatility, which is one of the mechanisms driving brain solutes transport, is bilaterally impaired following a small unilateral craniectomy.[16] Further investigation in this field are probably needed.

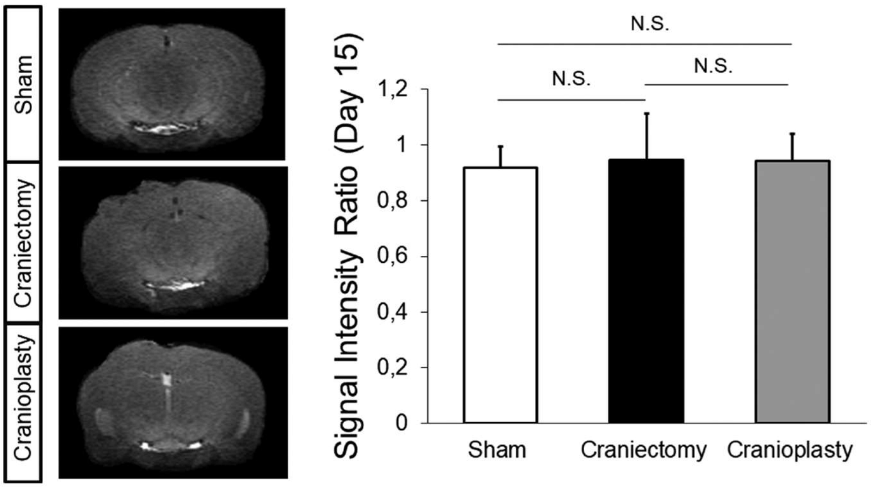

FIGURE 5. *Long term impact of DC and CP on the local solutes distribution in the brain parenchyma. Evaluation of the local solutes distribution in the brain parenchyma 15 d after the surgery. Representative coronal T1-weighted images and corresponding quantification 1 h after Dotarem injection in sham, DC and CP mice (n = 6 per group). In sham mice, the enhancement of the brain is similar in both hemispheres, with a SI ratio of 0.916 ± 0.07. This is similar to the SI ratio observed in the DC group (0.946 ± 0.16; NS: P = .93 vs Sham group), and in the CP group (0.941 ± 0.09; NS: P = .81 sham vs CP group; NS: P = .93, CP vs DC group).*

CONCLUSION

In conclusion, we demonstrate that the solutes distribution in the brain parenchyma by CSF and ISF is globally and durably impaired after DC in mouse, an effect reversed by CP.

Disclosures

This work was supported by the Institut National de la Santé Et de la Recherche Médicale. The authors have no personal, financial, or institutional interest in any of the drugs, materials, or devices described in this article.

REFERENCES

1. Vahedi K, Hofmeijer J, Juettler E, et al. DECIMAL, DESTINY, and HAMLET investigators. Early decompressive surgery in malignant infarction of the middle cerebral artery: a pooled analysis of three randomised controlled trials. *Lancet Neurol*. 2007;6(3):215-222.
2. Cooper DJ, Rosenfeld JV, Murray L, et al. DECRA Trial Investigators; Australian and New Zealand Intensive Care Society Clinical Trials Group. Decompressive craniectomy in diffuse traumatic brain injury. *N Engl J Med*. 2011;364(16):1493-1502.
3. Hutchinson PJ, Kolias AG, Timofeev IS, et al. RESCUEicp trial collaborators. trial of decompressive craniectomy for traumatic intracranial hypertension. *N Engl J Med*. 2016;375(12):1119-1130.
4. Fung C, Murek M, Z'Graggen WJ, et al. Decompressive hemicraniectomy in patients with supratentorial intracerebral hemorrhage. *Stroke*. 2012;43(12):3207-3211.
5. Bender A, Heulin S, Röhrer S, et al. Early CP may improve outcome in neurological patients with decompressive craniectomy. *Brain Inj*. 2013;27(9):1073-1079.
6. Iliff JJ, Wang M, Liao Y, et al. A paravascular pathway facilitates CSF flow through the brain parenchyma and the clearance of interstitial solutes, including amyloid beta. *Sci Trans Med*. 2012;4(147):147ra111.
7. Louveau A, Smirnov I, Keyes TJ, et al. Structural and functional features of central nervous system lymphatic vessels. *Nature*. 2015;523(7560):337-341.
8. Gaberel T, Gakuba C, Goulay R, et al. Impaired glymphatic perfusion after strokes revealed by contrast-enhanced MRI: a new target for fibrinolysis? *Stroke*. 2014;45(10):3092-3096.
9. Bühler D, Azghandi S, Schüller K, et al. Effect of decompressive craniectomy on outcome following subarachnoid hemorrhage in mice. *Stroke*. 2015;46(3):819-826.
10. Di Palma C, Goulay R, Chagnot S, et al. Cerebrospinal fluid flow increases from newborn to adult stages. *Dev Neurobiol*. 2018;78(9):851-858.
11. Iliff JJ, Wang M, Zeppenfeld DM, et al. Cerebral arterial pulsation drives paravascular CSF-interstitial fluid exchange in the murine brain. *J Neurosci*. 2013;33(33):18190-18199.
12. Winkler PA, Stummer W, Linke R, et al. Influence of CP on postural blood flow regulation, cerebrovascular reserve capacity, and cerebral glucose metabolism. *J Neurosurg*. 2000;93(1):53-61.
13. Nalbach SV, Ropper AE, Dunn IF, et al. Craniectomy-associated progressive Extra-Axial collections with treated hydrocephalus (CAPECTH): redefining a common complication of decompressive craniectomy. *J Clin Neurosci*. 2012;19(19):1222-1227.
14. Iliff JJ, Chen MJ, Plog BA, et al. Impairment of glymphatic pathway function promotes tau pathology after traumatic brain injury. *J Neurosci*. 2014;34(49):16180-16193.
15. D'Ambrosio AL, Sughrue ME, Yorgason JG, et al. Decompressive hemicraniectomy for poor-grade aneurysmal subarachnoid hemorrhage patients with associated intracerebral hemorrhage: clinical outcome and quality of life assessment. *Neurosurgery*. 2005;56(1):12-19.
16. Plog BA, Lou N, Pierre CA, et al. When the air hits your brain: decreased arterial pulsatility after craniectomy leading to impaired glymphatic flow. *J Neurosurg*. 2019;17:1-14 (doi:10.3171/2019.2.JNS182675).

Étude 3 : Cerebrospinal Fluid Flow increases from Newborn to Adult Stages

Résumé : Le LCR est une voie de transport pour de nombreuses molécules, y compris des facteurs essentiels au neurodéveloppement. Cette fonction est bien établie dans le système ventriculaire mais la maturation de la circulation du LCR en périphérie du SNC est mal connue. Cette dernière intervient notamment dans l'élimination de composés toxiques, et il est connu que le cerveau des nouveaux-nés est très vulnérable aux traumatismes. Dans cette étude, nous avons étudié grâce à l'injection de traceurs la maturation du flux de LCR chez le rongeur.

La quantité de traceur parvenant à l'extrémité antérieure (bulbe olfactif) du crâne est réduite chez le nouveau-né mais augmente progressivement jusqu'à 3 mois. La lame criblée étant une voie majeure du drainage du LCR chez le roneur, cela suggère une immaturité dans l'élimination des déchets par le LCR. De même, un traceur injecté dans le parenchyme est moins bien dispersé chez le rongeur nouveau-né. L'immaturité des voies de recyclage du FISC et du LCR chez le nouveau-né pourrait contribuer à l'accumulation de composés toxiques ou inflammatoires après un trauma et expliquer leur vulnérabilité. Plusieurs études suggèrent que le sommeil facilite le drainage des déchets hors du SNC, un phénomène qui pourrait expliquer les besoins en sommeil élevés des nouveaux-nés afin de compenser l'immaturité des flux de LCR.

Conclusions :

- Le flux de LCR est immature à la naissance chez le rongeur
- Le flux de LCR se développe jusqu'à l'âge adulte chez le rongeur (3 mois)
- La distribution d'un traceur injecté dans le parenchyme est réduite chez le rongeur nouveau-né
- L'immaturité des voies du LCR et du FISC pourrait être compensé par les besoins en sommeil des nouveaux nés

Contribution : Dans cette étude dont je suis troisième autrice, j'ai contribué à l'acquisition d'une partie des données IRM et NIRF et à leur analyse.

Cerebrospinal Fluid Flow Increases from Newborn to Adult Stages

**Camille Di Palma,[1,2†] Romain Goulay,[1†] Sebastien Chagnot,[1]
Sara Martinez De Lizarrondo,[1] Antoine Anfray,[1] Jean-Philippe Salaun,[1,3] Eric Maubert,[1]
Emmanuèle Lechapt-Zalcman,[4,6] Felipe Andreiuolo,[5] Clément Gakuba,[1,3]
Evelyne Emery,[1,2] Denis Vivien,[1,5] Maxime Gauberti,[1] Thomas Gaberel[1,2]**

[1] Normandie Université, UNICAEN, INSERM, UMR-S U1237, Physiopathology and Imaging of Neurological Disorders (PhIND), GIP Cyceron, Caen, 14000, France

[2] CHU Caen, Department of Neurosurgery, Caen University Hospital, Avenue de la Côte de Nacre, Caen, 14033, France

[3] CHU Caen, Department of Anesthesiology and Critical Care Medicine, Caen University Hospital, Avenue de la Côte de Nacre, Caen, 14033, France

[4] CHU Caen, Department of Pathology, Caen University Hospital, Avenue de la Côte de Nacre, Caen, 14033, France

[5] CHU Caen, Department of Clinical Research, Caen University Hospital, Avenue de la Côte de Nacre, Caen, 14033, France

[6] Department of Neuropathology, Sainte-Anne Hospital, rue Cabanis, Paris, 75674, France

Received 14 November 2017; revised 7 June 2018; accepted 10 June 2018

ABSTRACT: **Solute transport through the brain is of major importance for the clearance of toxic molecules and metabolites, and it plays key roles in the pathophysiology of the central nervous system. This solute transport notably depends on the cerebrospinal fluid (CSF) flow, which circulates in the subarachnoid spaces, the ventricles and the perivascular spaces. We hypothesized that the CSF flow may be different in the perinatal period compared to the adult period. Using *in vivo* magnetic resonance imaging (MRI) and near-infrared fluorescence imaging (NIRF), we assessed the dynamic of the CSF flow in rodents at different ages. By injecting a contrast agent into the CSF, we first used MRI to demonstrate that CSF flow gradually increases with age, with the adult pattern observed at P90. This observation was confirmed by NIRF, which revealed an increased CSF flow in P90 rats when compared with P4 rats not only at the surface of the brain but also deep in the brain structures. Lastly, we evaluated the exit routes of the CSF from the brain. We demonstrated that indocyanine green injected directly into the striatum spread throughout the parenchyma in adult rats, whereas it stayed at the injection point in P4 rats. Moreover, the ability of CSF to exit through the nasal mucosa was increased in the adult rodents. Our results provide evidence that the perinatal brain has nonoptimal CSF flow and exit and, thus, may**

Correspondence to: T. Gaberel, (thomas.gaberel@hotmail.fr) and D. Vivien (vivien@cyceron.fr).

[†] These authors equally participated in the drafting of the manuscript.

Contract grant sponsor: INSERM (French National Institute for Health and Medical Research), Equipe FRM N°DEQ20140329555 and the Regional Council of Lower Normandy. TG received a research grant from the Société Française de Neurochirurgie.

DOI 10.1002/dneu.22622

have impaired clean-up capacity. Develop Neurobiol 00: 000–000, 2018

Keywords: **blood brain barrier; brain development; cerebrospinal fluid; glymphatic system**

INTRODUCTION

Solute transport through the brain is of major importance for the clearance of toxic molecules and metabolites and also in the delivery of nutrients to brain cells (Hladky and Barrand, 2014). This solute transport through the brain notably depends on the cerebrospinal fluid (CSF) flow, which circulates in the ventricles, the subarachnoid spaces and the paravascular spaces (Rennels et al., 1985). During the last few years, there has been a major interest in the circulation of CSF and solutes in the brain parenchyma, which was described as a convective flow of CSF though the extra-cellular space from the para-arterial to the para-venous spaces (Iliff et al., 2012). This flow, named the glymphatic system, has been described as largely responsible for solute transport in the brain parenchyma (Iliff et al., 2012). It has been notably suggested that the glymphatic flow is dependent on Aquaporin-4 (AQP-4), a water canal membrane (Iliff et al., 2012). The glymphatic system's activity increases dramatically during sleep, suggesting a key role of sleep in brain waste clearance (Xie et al., 2013). In adults, the CSF flow could be involved in several pathological processes, including Alzheimer's disease (AD), chronic post-traumatic encephalopathy, ischemic stroke, and subarachnoid hemorrhage (Weller et al., 2009; Arbel-Ornath et al., 2013; Gaberel et al., 2014; Iliff et al., 2014). Of note, the glymphatic system hypothesis, in which solute transport through the brain parenchyma depends on the convective mechanism facilitated by AQP-4, has been recently challenged (Holter et al., 2017; Smith et al., 2017). It is clear, however, that solute transport through the brain exists and depends on diffusion in the parenchyma and convection in the CSF and the paravascular spaces (Rennels et al., 1985; Hladky and Barrand, 2014; Smith et al., 2017).

Based on the observations that babies spend much time sleeping and that immature brains are particularly sensitive to injury (Price et al, 2014; Licht et al., 2015), we hypothesized that the CSF flow may be different in the perinatal period compared to the adult period. Using magnetic resonance imaging (MRI) and near-infrared imaging (NIRF), we evaluated the CSF flow in newborns and in adult rodents.

MATERIALS AND METHODS

Animals

Experiments were performed in accordance with the European Communities Council Directive (86/609/EEC) regarding the care and use of animals for experimental procedures and were approved by the local ethical committee CENOMEXA. All efforts were made to limit animal suffering. None of the experimental procedures induced animal mortality. All experiments were performed following the ARRIVE guidelines (www.nc3rs.org.uk). Experiments were performed on Wistar rats or Swiss mice (CURB, Caen, France) at different ages: four days (P4 group), seven days (P7 group), 11 days (P11 group), 28 days (P28 group), and 90 days (P90 group). Rodents were anesthetized with isoflurane (2%) at 70%/30% N_2OO/O_2, and body temperature was maintained at 37°C.

Intracisternal Injection

The CSF circulation was assessed by MRI (7T, Bruker) or near-infrared fluorescence imaging (NIRF). For the intracisternal injection of the tracer, we used a pulled hematological glass micropipette surgically inserted into the cisterna magna. The tracer was then injected over one minute, the micropipette was left in place for 1 additional minute, and the wound was closed (Gaberel et al., 2014).

Intrastriatal Injection

To evaluate the possible exit routes of the CSF, intrastriatal injection of indocyanine green at a concentration of 2.5 mg/mL was performed. In P90 rats ($n = 4$), 2 µL of indocyanine green was injected at the following coordinates: AP +0.2 mm; LR +2.8 mm; and DV −5.3 mm from the bregma. In P4 rats ($n = 4$), 0.25 µL was injected at the following coordinates: AP +0.2 mm; LR +1.5 mm; and DV −2.8 mm from the bregma.

MRI Experiments

The CSF circulation was assessed by injecting DOTA-Gd (Dotarem) into the cisterna magna (Iliff et al., 2013; Gaberel et al., 2014). The volume of tracer injected was dependent on the animal's age and species: P4 rats received 0.5 µL, P7 rats received 1 µL, P11 received 1.25 µL, P28 received 3 µL and P90 received 4 µL ($n = 5$ per group). To make sure that the different volumes injected at different ages had no impact, we also injected P4 rats with the volume used in P90 rats ($n = 5$). For mice, P7 received 0.5 µL, and P28 received 1 µL. In the majority of the experiments

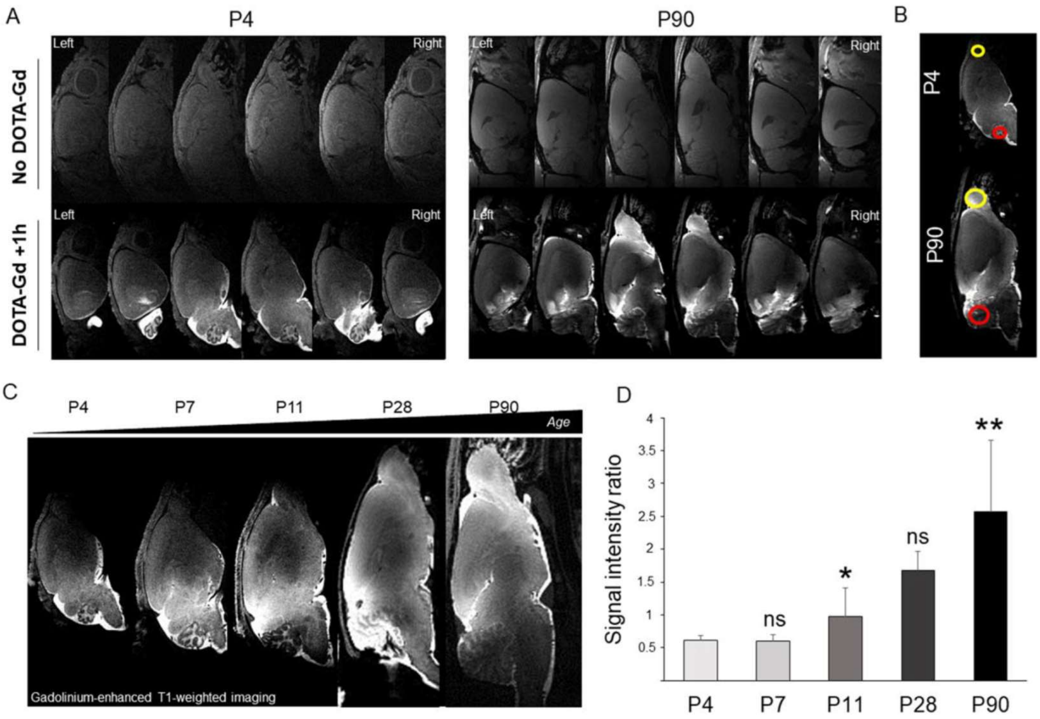

Figure 1 The CSF flow matures from birth to the adult age in rats. (**A**) The CSF circulation was evaluated by MRI in P4 rats (Left) and P90 rats (Right). The upper part shows an MRI acquisition without DOTA-Gd injection. The lower part shows an MRI acquisition after the DOTA-Gd injection. Rats received an injection of DOTA-Gd in the cisterna magna followed by MRI acquisition one hour later. In P4 rats, the gadolinium stayed in the posterior part of the brain, suggesting reduced CSF flow toward the anterior part of the brain. In P90 rats, the CSF clearly spread throughout the whole brain, suggesting an active CSF flow to the whole brain. (**B**) Representation of the two regions of interest (ROI) used to assess the CSF circulation: one was located in the olfactory bulb (yellow ROI), and the other, in the cerebellum (red ROI). The signal intensity (SI) was measured, and the SI ratio was defined as olfactory bulb SI/cerebellum SI. (**C**) Rats at different ages received an injection of DOTA-Gd in the CSF followed by MRI analyses. The parenchymal distribution of the DOTA-Gd increases in the anterior parts of the brain with age from birth to the adult age. (**D**) Corresponding quantification of the DOTA-Gd intensity in the olfactory bulb shows a clear increase from P4 to P90 ($n = 5$ per group). Mann-Whitney *U* test, $*P = 0.031$ versus P4, $**P = 0.007$ versus P4. [Color figure can be viewed at wileyonlinelibrary.com]

performed in this study, MRI analyses were performed one hour after the injection. Moreover, to ensure that there was no difference in the time course of DOTA-Gd circulation, we also performed MRI 30 minutes and 120 minutes after the DOTA-Gd injection in P4 and P90 rats ($n = 5$ per group). The signal intensity (SI) was measured using ImageJ 1.48 software (NIH) in three regions of interest (ROI): the cerebellum, the olfactory bulb and the ethmoid (Figs. 1B and 3C). The SI ratio was defined as the olfactory bulb SI/cerebellum SI and ethmoid SI/cerebellum SI. For each animal, the SI ratio was measured in each side, and the value used for the analysis was the mean of the right and left values.

Near-Infrared Fluorescence Experiments

The CSF circulation was also explored with NIRF experiments. Indocyanine green (Sigma Aldrich, USA), a fluorescent dye (MW= 774.96), was injected into the cisterna magna at a concentration of 25 mg/mL in P4 (0.25 μL) and P90 rats (2 μL) ($n = 5$ per group). Sixty minutes after the intracisternal injection, the rats were euthanized under anesthesia, and their brains were removed. *Ex vivo* NIRF images (excitation/emission= 600/700 nm, Biospace Photon Imager) of the ventral and dorsal parts of the brain were then taken. We also evaluated the penetration and the exit of the tracer by imaging brain coronal sections. The

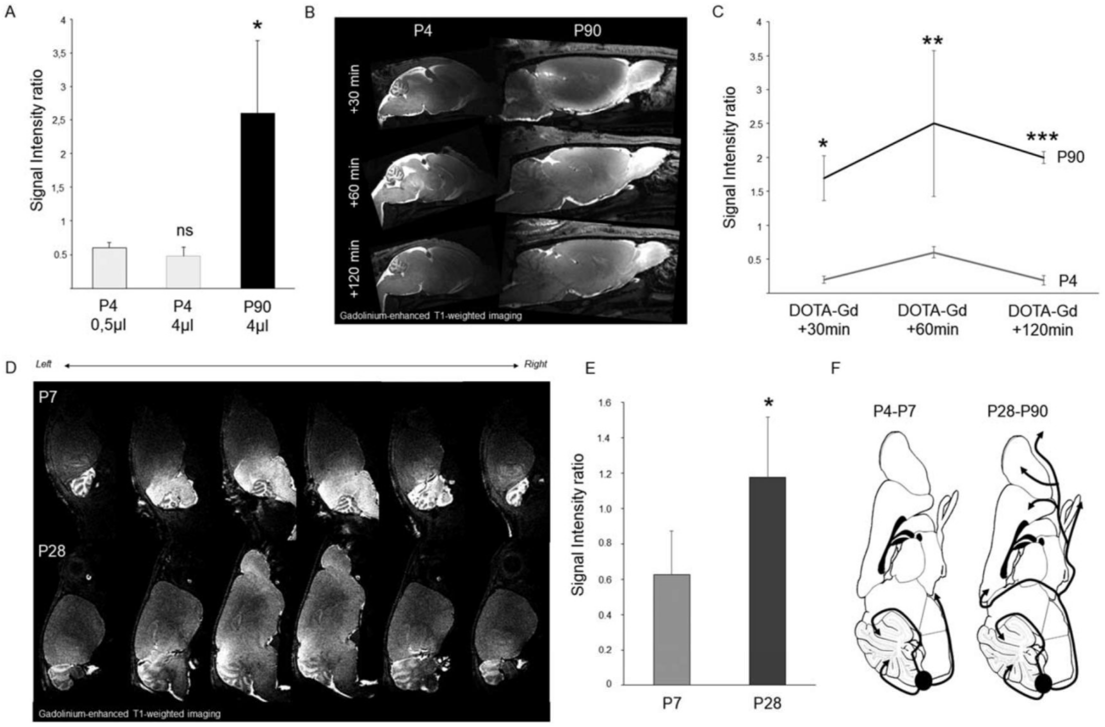

Figure 2 Impact of the volume of DOTA-Gd injected, the time of analyses after the injection of DOTA-Gd, and the species (mice *versus* rats) on the maturation of CSF flow. (**A**) The volume of DOTA-Gd injected in the CSF of P4 rats was increased to 4 µL as previously done in P90 rats. The SI ratio was similar among P4 rats receiving 0.5 µL and the ones receiving 4 µL, and the difference from P90 rats remained significant ($n = 5$ per group). Mann-Whitney *U* test, ns: $P = 0.19$ versus P4 0.5 µL, $^*P = 0.007$ versus P4 4 µL. (**B**) DOTA-Gd was injected in 5 P4 rats and 5 P90 rats, and MRI analyses were performed 30, 60, and 120 minutes after the injection. Representative pictures show a similar time course of DOTA-Gd circulation between the P4 and P90 rats. (**C**) Corresponding quantification confirmed the DOTA-Gd SI ratio at 60 min after the injection, and the ratios were higher at each time point in P90 rats when compared to P4 rats. Mann-Whitney *U* test, $^*P = 0.007$ versus P4, $^{**}P = 0.007$ versus P4, $^{***}P = 0.01$ versus P4. (**D**) The MRI analyses also confirmed an immaturity of the CSF flow in newborn mouse brains. (E) Corresponding quantifications in mice show an increase of DOTA-Gd diffusion from P7 to P28 ($n = 4$ per group). Mann-Whitney *U* test, $^*P = 0.025$ versus P7. (**F**) Schematic view of the CSF circulation in P4 and P90 rats.

analysis was performed using M3Vision 2.2.1 (Biospace Lab, France). Indocyanine green diffusion was measured using the ratio between the indocyanine green-positive area ($>2.5e^4$ counts per minute) and the total area of the brain.

Statistics

All statistical analyses were performed using Statistica (Softonic, Spain). The results are expressed as the mean ± SD. Statistical analyses were performed using the Kruskall-Wallis test, followed by *post hoc* comparison with the Mann-Whitney *U* test.

RESULTS

The CSF Flow Is Immature in Newborn Rodents

We first assessed the CSF circulation using MRI in rats of different ages after DOTA-gadolinium (DOTA-Gd) injections into the CSF. We assessed the distribution of DOTA-Gd within the brain, which reflects the CSF circulation[13]. At the adult age (post-natal day 90: P90), rats exhibited CSF flow that was qualitatively consistent with previous reports, i.e., penetrating the entire brain (Fig. 1A–B) (Iliff et al.,

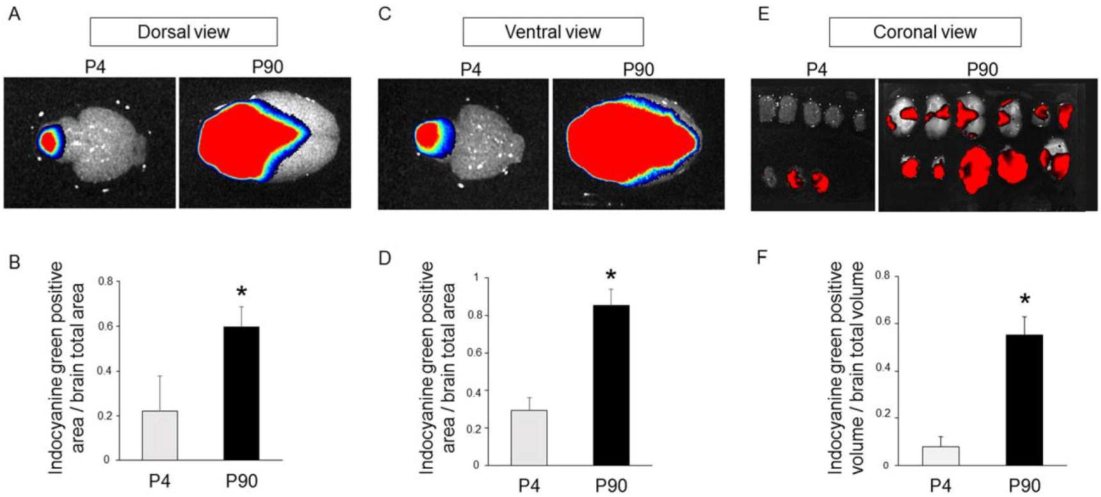

Figure 3 Immaturity of the parenchymal CSF circulation in the perinatal period was confirmed by NIRF experiments. (**A**) Representative *ex vivo* NIRF acquisition performed one hour after the injection of indocyanine green in the cisterna magna in P4 and P90 rats. Views are of the dorsal surface of the brains. In P4 rats, the dye stayed in the posterior part of the brain, whereas it spread throughout the whole brain in P90 rats. (**B**) Corresponding quantification: the ratio between the indocyanine green-positive area and the total area of the brain was measured ($n = 4$ per group). Mann-Whitney U test, *$P = 0.028$ versus P4. (**C**) The same representative *ex vivo* NIRF acquisition but with a view of the ventral surface of the brain. In P4 rats, the dye was only diffused in the posterior part of the brain, whereas it spread throughout the whole brain in P90 rats. (**D**) Corresponding quantification: the ratio between the indocyanine green-positive area and the total area of the brain was measured ($n = 4$ per group). Mann-Whitney U test, *$P = 0.028$ versus P4. (**E**) Representative *ex vivo* NIRF acquisition performed one hour after the injection of indocyanine green in the cisterna magna in P4 and P90 rats. Coronal views of the brains. In P4 rats, the dye stayed at the brain surface surrounding the injection point, whereas it can be revealed deeper in the brain structures in P90 rats. (**F**) The quantification was made by calculating the ratio between the volume of positive signal for indocyanine green and the total volume of the brain ($n = 4$ per group). Mann-Whitney U test, *$P = 0.028$ versus P4. [Color figure can be viewed at wileyonlinelibrary.com]

2013). In contrast, in newborn rats, the CSF penetrated the cerebellum but not the forebrain (Fig. 1A). This finding was particularly evident in very young animals (P4 and P7) (Fig. 1C). Thereafter, CSF circulation gradually increased with age, with the adult pattern observed at P90 (Fig. 1C). Corresponding quantification of the DOTA-Gd intensity in the olfactory bulb shows a clear increase from P4 to P90 ($n = 5$ per group, Fig. 1D).

To avoid a possible "artifact" due to the differential volumes of DOTA-Gd injected in the cisterna magna at P4 and P90 (Bedussi et al., 2017), we injected rats at P4 with the volume of DOTA-Gd used in the P90 rats (4 μL), and this did not affect the data obtained (Fig. 2A). We also evaluated the time course of DOTA-Gd circulation: in both P4 and P90 rats, the peak of the SI ratio was obtained 60 min after the DOTA-Gd injection, and the SI ratio in the P90 rats was higher than in the P4 rats 30 min, 60 min, and 120 min after DOTA-Gd injection (Fig. 2B,C).

We also confirmed our finding in another species: similar experiments performed in mice revealed the same CSF circulation maturation pattern (Fig. 2D,E).

To confirm the fact that CSF circulation is increase in adult rodents (Fig. 2F), we used NIRF after the injection of indocyanine green into the CSF. Consistent with the MRI findings, NIRF revealed an increased CSF circulation in P90 rats when compared with P4 rats not only at the surface of the brain but also deep in the brain structures ($n = 5$ per group, Fig. 3A–F).

Exit Routes of the CSF Increase in Adult Rodents

We then evaluated the possible exit routes of the CSF. First, we demonstrated that indocyanine green

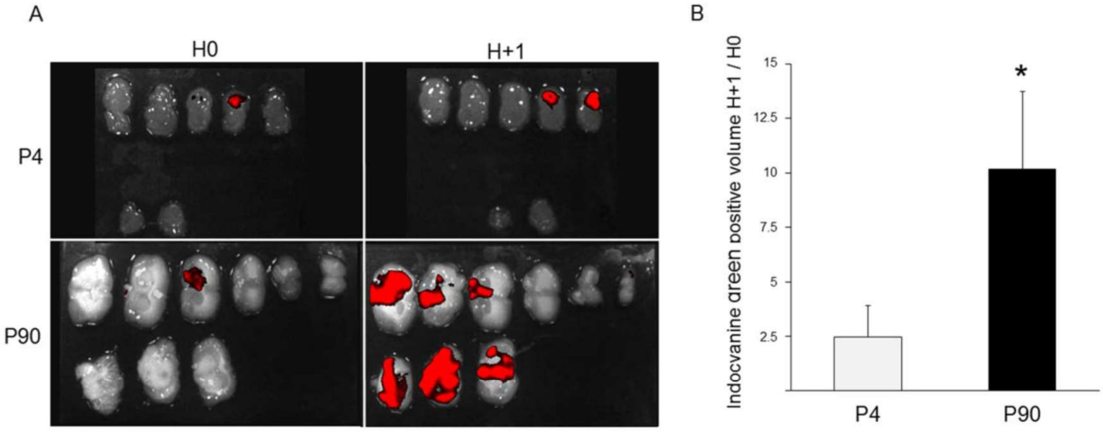

Figure 4 The intraparenchymal diffusion of indocyanine is increased in adult rats. **(A)** Representative *ex vivo* NIRF acquisition performed one hour after injection of indocyanine green in the striatum of P4 and P90 rats. Coronal views of the brains. In P4 rats, the dye surrounded the injection point, whereas it spread over a large part of the brain in P90 rats. **(B)** The quantification was made by calculating the ratio of the volume of positive signal for indocyanine green to the total volume of the brain ($n = 4$ per groups). Mann-Whitney U test, $^*P = 0.028$ versus P4. [Color figure can be viewed at wileyonlinelibrary.com]

injected directly into the striatum spread throughout the parenchyma in adult rats, but it stayed at the injection point in P4 rats ($n = 5$ per group, Fig. 4A,B).

Then, we evaluated the ability of CSF to exit through the nasal mucosa by measuring the SI of DOTA-Gd in the ethmoid 1 hour after its injection into the CSF. In P90 rats, the nasal mucosa was highly enhanced by DOTA-Gd, whereas no signal was identified in P4 rats, confirming that the exit routes of the CSF are immature in newborns (Fig. 5A,B).

DISCUSSION

These data suggest that the CSF flow and its exit from the brain increase during development.

CSF circulation and the blood-brain barrier share many cellular partners, including endothelial cells, astrocytic cells and the basal membrane (Iliff et al., 2012; Zhao et al., 2015; Morris et al., 2016); therefore, it is reasonable to note that the development of the CSF circulation is parallel to the development of the BBB. It starts at the embryonic phase and continues after birth, including organization of the astrocytic end-feet around vessels (Zhao et al., 2015). Accordingly, it is admitted that the perinatal immaturity of the BBB leads to an increased sensitivity to brain injuries (Licht et al., 2015). Here, we can postulate that the perinatal immaturity of CSF circulation, through its reported role in brain waste clearance (Iliff et al., 2012; Xie et al., 2013; Hladky and Barrand, 2014), may result in an inability of the young brain to clean up, increasing its susceptibility to injuries.

It has been reported that the CSF crosses the astrocytic end-feet to reach the brain interstitial space through a phenomenon dependent on AQP-4 (Iliff et al., 2012), even though this point has been debated (Smith et al., 2017). It is interesting to note, however, that AQP-4 expression and polarization has been shown to increase during development in rodents and humans (Wen et al, 1999; Gömöri et al., 2006). The progressive increase in the CSF circulation during the early life might depend on this maturation of AQP-4, even if other mechanisms could also be involved.

The CSF circulation evolution with age has previously been investigated but only in the elderly. Its activity dramatically decreases in old mice, a phenomenon related to the decrease in arterial pulsatility and to a loss of AQP-4 polarization on astrocytic end-feet (Kress et al., 2014). The authors concluded that this decrease in activity could explain the occurrence of neurodegenerative diseases in the elderly, such as Alzheimer's disease, due to an impaired clearance of amyloid-beta. This model does not, however, explain why Alzheimer's disease occurs in some people and not in others. Our results may

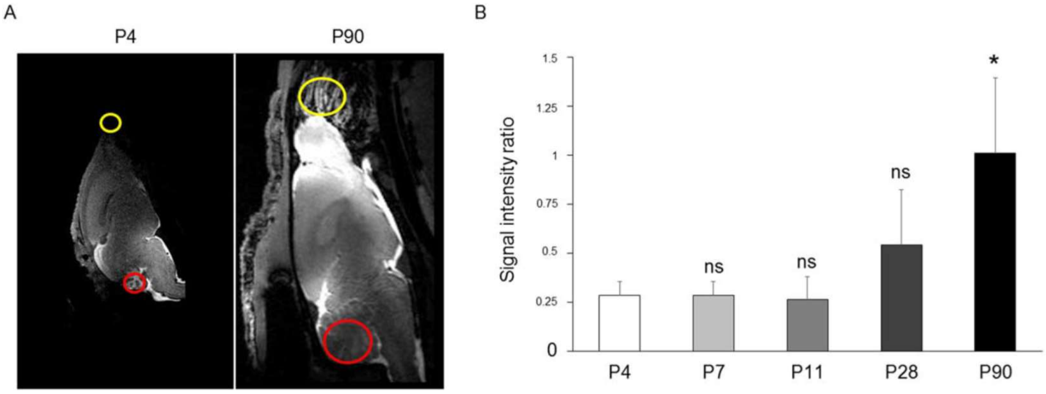

Figure 5 The exit routes of the CSF increased in the adult rats. (**A**) Rats at different ages received an injection of DOTA-Gd in the CSF followed by MRI analyses. The distribution of the DOTA-Gd in the ethmoid mucosa was then evaluated. In P90 rats, the mucosa was highly enhanced in P90 rats, whereas no DOTA-Gd was detected in the mucosa of P4 rats. (**B**) Corresponding quantification of the DOTA-Gd intensity in the nasal mucosa showed a clear increase from P4 to P90 ($n = 5$ per group). Mann-Whitney *U* test, $^*P = 0.007$ versus P4. [Color figure can be viewed at wileyonlinelibrary.com]

suggest that the impairment of CSF circulation development during the perinatal period may contribute to the inter-individual risk of AD, a hypothesis that we will address in a future study.

It is also interesting to note that glymphatic system activity has been reported to increase dramatically during sleep, suggesting a key role of sleep in brain waste clearance (Xie et al., 2013). Our observation that CSF circulation is immature in newborns may explain why babies spend more time sleeping than adults (Price et al., 2014).

Nevertheless, it is important to discuss certain limitations in the present work. First, the existence of a glymphatic system is still a matter of debate (Smith et al., 2017). There is evidence that CSF-ISF exchanges and waste clearance from the parenchyma may be achieved through other mechanisms, such as diffusion, rather than a bulk flow (Weller et al., 2009; Hladky and Barrand, 2014; Holter et al., 2017; Smith et al., 2017). Second, we did not monitor intracranial pressure during the intracisternal tracer injection, which may have modified the CSF circulation; however, our infusion rate was low (4 μL/min), with no significant elevation of the intracranial pressure expected (Bedussi et al., 2017). Additionally, some histological experiments following the injection of a fluorescent dye would have been beneficial to confirm our macroscopic observations and to differentiate between parenchymal circulation and pericerebral circulation of the CSF. Another limitation in the present work was that we did not provide data to demonstrate the hypersensitivity of newborn brains to injuries or any direct evidence that the immaturity of the parenchymal CSF circulation was an explanation for why babies tend to sleep longer than adults. Despite our efforts, we did not find any relevant experimental designs to address these questions.

CONFLICTS OF INTEREST/ DISCLOSURES

The authors declare no competing financial interests.

LITERATURE CITED

Arbel-Ornath M, Hudry E, Eikermann-Haerter K, Hou S, Gregory JL, Zhao L, Betensky RA, Frosch MP, Greenberg SM, Bacskai BJ. 2013. Interstitial fluid drainage is impaired in ischemic stroke and Alzheimer's disease mouse models. Acta Neuropathol 126:353–364.

Bedussi B, van der Wel NN, de Vos J, van Veen H, Siebes M, VanBavel E, Bakker EN. 2017. Paravascular channels, cisterns, and the subarachnoid space in the rat brain: A single compartment with preferential pathways. J Cereb Blood Flow Metab 37:1374–1385.

Gaberel T, Gakuba C, Goulay R, Martinez De Lizarrondo S, Hanouz JL, Emery E, Touze E, Vivien D, Gauberti M. 2014. Impaired glymphatic perfusion after strokes revealed by contrast-enhanced MRI: A new target for fibrinolysis?. Stroke 45:3092–3096.

Gömöri E, Pál J, Abrahám H, Vajda Z, Sulyok E, Seress L, Dóczi T. 2006. Fetal development of membrane water channel proteins aquaporin-1 and aquaporin-4 in the human brain. Int J Dev Neurosci 24:295–305.

Hladky SB, Barrand MA. 2014. Mechanisms of fluid movement into, through and out of the brain: Evaluation of the evidence. Fluids Barriers CNS 11:26.

Holter KE, Kehlet B, Devor A, Sejnowski TJ, Dale AM, Omholt SW, Ottersen OP, Nagelhus EA, Mardal KA, Pettersen KH. 2017. Interstitial solute transport in 3D reconstructed neuropil occurs by diffusion rather than bulk flow. Proc Natl Acad Sci U S A 114:9894–9899.

Iliff JJ, Wang M, Liao Y, Plogg BA, Peng W, Gundersen GA, Benveniste H, Vates GE, Deane R, Goldman SA, Nagelhus EA, Nedergaard M. 2012. A paravascular pathway facilitates CSF flow through the brain parenchyma and the clearance of interstitial solutes, including amyloid β. Sci Transl Med 4:147ra111.

Iliff JJ, Lee H, Yu M, Feng T, Logan J, Nedergaard M, Benveniste H. 2013. Brain-wide pathway for waste clearance captured by contrast-enhanced MRI. J Clin Invest 123:1299–1309.

Iliff JJ, Chen MJ, Plog BA, Zeppenfeld DM, Soltero M, Yang L, Singh I, Deane R, Nedergaard M. 2014. Impairment of glymphatic pathway function promotes tau pathology after traumatic brain injury. J Neurosci 34:16180–16193.

Kress BT, Iliff JJ, Xia M, Wang M, Wei HS, Zeppenfeld D, Xie L, Kang H, Xu Q, Liew JA, Plog BA, Ding F, Deane R, Nedergaard M. 2014. Impairment of paravascular clearance pathways in the aging brain. Ann Neurol 76:845–861.

Licht T, Dor-Wollman T, Ben-Zvi A, Rothe G, Keshet E. 2015. Vessel maturation schedule determines vulnerability to neuronal injuries of prematurity. J Clin Invest 125:1319–1328.

Morris AWJ, Sharp MM, Albargothy NJ, Fernandes R, Hawkes CA, Verma A, Weller RO, Carare RO. 2016. Vascular basement membranes as pathways for the passage of fluid into and out of the brain. Acta Neuropathol 131:725–736.

Price AMH, Brown JE, Bittman M, Wake M, Quach J, Hiscock H. 2014. Children's sleep patterns from 0 to 9 years: Australian population longitudinal study. Arch Dis Child 99:119–125.

Rennels ML, Gregory TF, Blaumanis OR, Fujimoto K, Grady PA. 1985. Evidence for a "paravascular" fluid circulation in the mammalian central nervous system, provided by the rapid distribution of tracer protein throughout the brain from the subarachnoid space. Brain Res 326:47–63.

Smith AJ, Yao X, Dix JA, Jin BJ, Verkman AS. 2017. Test of the 'glymphatic' hypothesis demonstrates diffusive and aquaporin-4-independent solute transport in rodent brain parenchyma. Elife 2017. 6:pii: e27679. doi: 10.7554/eLife.27679.

Weller RO, Djuanda E, Yow HY, Carare RO. 2009. Lymphatic drainage of the brain and the pathophysiology of neurological disease. Acta Neuropathol 117:1–14.

Wen H, Nagelhus EA, Amiry-Moghaddam M, Agre P, Ottersen OP, Nielsen S. 1999. Ontogeny of water transport in rat brain: Postnatal expression of the aquaporin-4 water channel. Eur J Neurosci 11:935–945.

Xie L, Kang H, Xu Q, Chen MJ, Liao Y, Thiyagarajan M, O'Donnell J, Christensen DJ, Nicholson C, Iliff JJ, Takano T, Deane R, Nedergaard M. 2013. Sleep drives metabolite clearance from the adult brain. Science 342: 373–377.

Zhao Z, Nelson AR, Betsholtz C, Zlokovic BV. 2015. Establishment and dysfunction of the blood-brain barrier. Cell 163:1064–1078.

Collaboration 1 : Megalencephalic leukoencephalopathy with subcortical cysts is a developmental disorder of the gliovascular unit

Cet article est en révision pour eLife

Résumé : La MLC, ou maladie de van der Knapp, est une pathologie génétique se traduisant par un défaut de mise en place de la glie limitante périvasculaire et un contenu en eau anormalement élevé dans le tissu cérébral. Elle est causée par des mutations de MLC1 ou de GlialCam, des protéines intervenant dans la mise en place de l'unité gliovasculaire. Dans cette étude réalisée en collaboration avec le groupe de Martine Cohen-Salmon, nous avons contribué à la caractérisation d'un modèle murin (MLC1KO) de cette maladie.

Nous avons retrouvé en IRM les caractéristiques principales de la MLC : une teneur en eau plus élevée et un cerveau plus gros, sans hydrocéphalie. Nous avons injecté un traceur dans le LCR afin d'évaluer la fonctionaité des échanges LCR-FISC, et observé d'une part une distribution réduite dans l'espace sous-aracbnoïdien, d'autre part une réduction de la dynamique des échanges LCR-FISC.

Le défaut de mise en place de la glie limitante chez ces animaux, confirmé par les autres expériences présentées dans cet article, pourrait favoriser l'accumulation de l'eau dans le tissu par manque d'une voie propre (les EPV) permettant son écoulement vers le LCR. L'absence d'EPV peut également expliquer la dispersion ralentie du traceur dans le tissu, et le gonflement du cerveau pourrait causer, par réduction de l'espace sous-arachnoïdien, une réduction du flux de LCR dans celui-ci.

Conclusions :

- Les MLC1KO présentent un défaut de mise en place de la glie limitante périvasculaire
- L'absence d'EPV fonctionnels favorise l'accumulation d'eau dans le tissu cérébral et perturbe les échanges LCR-FISC
- Le gonflement du cerveau causé par l'oedème empiète sur l'espace sous-arachnoïdien et perturbe la circulation du LCR

Contribution : Dans cette étude dont je suis quatrième autrice, j'ai réalisé l'acquisition et l'analyse des données IRM. J'ai aussi contribué à la rédaction des aspects méthodologiques et de la discussion concernant les résultats obtenus avec cette technique.

Megalencephalic leukoencephalopathy with subcortical cysts is a developmental disorder of the gliovascular unit

Alice Gilbert[1,2], **Xabier Elorza-Vidal**[1], **Armelle Rancillac**[3*], **Audrey Chagnot**[4*], **Mervé Yetim**[4*], **Vincent Hingot**[5], **Thomas Deffieux**[5], **Anne-Cécile Boulay**[1], **Rodrigo Alvear-Perez**[1], **Salvatore Cisternino**[6], **Sabrina Martin**[7], **Sonia Taib**[7], **Antoinette Gelot**[8], **Virginie Mignon**[9], **Maryline Favier**[10], **Isabelle Brunet**[7], **Xavier Declèves**[6, 11], **Mickael Tanter**[5], **Raul Estevez**[12, 13], **Denis Vivien**[4], **Bruno Saubaméa**[6, 9] and **Martine Cohen-Salmon**[1]

[1] Physiology and Physiopathology of the Gliovascular Unit Research Group, Center for Interdisciplinary Research in Biology (CIRB), College de France, CNRS Unité Mixte de Recherche 724, Inserm Unité 1050, Labex Memolife, Université PSL, 75005 Paris, France.

[2] École doctorale Cerveau Cognition Comportement "ED3C" N°158, Pierre and Marie Curie University, 75005 Paris, France.

[3] Neuroglial Interactions in Cerebral Physiopathology Research Group, Center for Interdisciplinary Research in Biology (CIRB), College de France, CNRS Unité Mixte de Recherche 724, INSERM Unité 1050, Labex Memolife, Université PSL, 75005 Paris, France.

[4] Normandie University, UNICAEN, Inserm, GIP Cyceron, Institut Blood and Brain @Caen-Normandie (BB@C), UMR-S U1237, Physiopathology and Imaging of Neurological Disorders (PhIND), 14014 Caen, France.

[5] Physics for Medicine Paris, Inserm U1273, CNRS UMR 8063, ESPCI Paris, PSL University, 75005 Paris, France.

[6] Université de Paris, Faculté de Santé, Inserm UMR-S 1144, 75015, Paris.

[7] Molecular control of the neurovascular development Research Group, Center for Interdisciplinary Research in Biology (CIRB), College de France, CNRS Unité Mixte de Recherche 724, Inserm Unité 1050, Labex Memolife, Université PSL, 75005 Paris, France.

[8] Service d'anatomie et cytologie pathologie de l'hôpital Armand Trousseau, 75012 Paris, France.

[9] Cellular and Molecular Imaging facility, US25 Inserm, UMS3612 CNRS, Faculty of Pharmacy, University of Paris, 75014 Paris, France.

[10] Plateforme HistIM Institut Cochin, 75014 Paris, France.

[11] Biologie du médicament et toxicologie, Assistance Publique – hôpitaux de Paris, APHP, Hôpital Cochin, 75014, Paris.

[12] Unitat de Fisiología, Departament de Ciències Fisiològiques, IDIBELL-Institute of Neurosciences, Universitat de Barcelona, L'Hospitalet de Llobregat, 08907 Barcelona, Spain.

[13] Centro de Investigación en Red de Enfermedades Raras (CIBERER), ISCIII, 08907 Barcelona, Spain.

* coauthors

Corresponding author: Martine Cohen-Salmon, Collège de France, Center for Interdisciplinary Research in Biology (CIRB), CNRS, UMR 7241, INSERM, U1050, 11 place Marcelin Berthelot, 75005 Paris, France. Tel: Tel: +33-144-271-242; E-mail: martine.cohen-salmon@college-de-france.fr

Abstract

Absence of the astrocyte-specific membrane protein MLC1 is responsible for megalencephalic leukoencephalopathy with subcortical cysts (MLC); this rare type of leukodystrophy is characterized by early-onset macrocephaly and progressive white matter vacuolation that lead to ataxia, spasticity, and cognitive decline. During postnatal development (from P5 to P15 in the mouse), MLC1 forms a membrane complex with GlialCAM (another astrocytic transmembrane protein) at the junctions between perivascular astrocytic processes (PvAPs, which along with blood vessels form the gliovascular unit (GVU)). We analyzed the GVU in the *Mlc1* knock-out mouse model of MLC. The absence of MLC1 led to an accumulation of fluid in the brain but did not modify the endothelial organization or the integrity of the blood-brain barrier. From P10 onward, the postnatal acquisition of vascular smooth muscle cell contractility was altered, resulting in a marked reduction in arterial perfusion and neurovascular coupling. These anomalies were correlated with alterations in astrocyte morphology, astrocyte polarity and the structural organization of the PvAP's perivascular coverage, and poor intraparenchymal circulation of the cerebrospinal fluid (CSF). Hence, MLC1 is required for the postnatal development and organization of PvAPs and controls vessel contractility and intraparenchymal interstitial fluid clearance. Our data suggest that (i) MLC is a developmental disorder of the GVU, and (ii) PvAP and VSMC maturation defects are primary events in the pathogenesis of MLC and therapeutic targets for this disease.

Keywords: Megalencephalic leukoencephalopathy with subcortical cysts; MLC1; Gliovascular unit; Development

Introduction

Megalencephalic leukoencephalopathy with subcortical cysts (MLC) is a rare type of leukodystrophy (OMIM 604004) mainly caused by mutations in the *MLC1* gene (MIM #605908) [1, 2]. Patients with MLC display early-onset macrocephaly and progressive white matter vacuolation, leading to slowly progressive ataxia, spasticity, and cognitive decline. Most mutations in *MLC1* result in the degradation of the encoded protein MLC1 [3, 2, 4], a membrane protein that is specifically expressed by the astrocytic lineage in the brain and present at high levels at the junctions between perivascular astrocytic processes (PvAPs) [5, 6]. At present, there is no cure for MLC - only symptomatic treatments and supportive care are available. Although the physiopathological mechanisms leading to MLC have not been characterized, the strong expression of MLC1 in PvAPs and other recent observations suggest that the protein has a role in gliovascular functions, in particular the regulation of ion/water homeostasis [7, 8, 5]. Indeed, MLC patients present widespread brain edema and swollen PvAPs [9, 10]. GlialCAM, another transmembrane protein forming a complex with MLC1 and responsible for its endoplasmic reticulum exit, is an auxiliary subunit of ClC-2, an inward rectifier chloride channel expressed in a subtype of astrocytes [11, 5, 10, 12, 13]. Recessive and dominant mutations in GlialCAM cause MLC subtypes MLC2A and MLC2B respectively [14]. *In vitro*, the MLC1/GlialCAM complex indirectly regulates other ion channels, such as TRPV4 and LRRC8 [15].

Despite the above observations, it is still not known whether and how MLC1 influences the physiology of the gliovascular unit (GVU, the functional interface comprising PvAPs and the brain vessels). We recently reported that MLC1 expression in mouse PvAPs starts around postnatal day (P)5 and that the MLC1/GlialCAM complexes in PvAPs form progressively from P5 to P15, with the protein deposits creating a meshwork between the astrocytes' perivascular membranes [16]. We also demonstrated that this postnatal period is a developmental window for the molecular maturation of brain endothelial cells (ECs), particularly with regard to their efflux properties and for the contractility of vascular smooth muscle cells (VSMCs) [16, 17]. Given that astrocytes are key regulators of cerebrovascular development and function (e.g. BBB integrity, immune quiescence and perivascular homeostasis, neurovascular coupling) [18-21], we hypothesized that the MLC1/GlialCAM complex might influence the postnatal differentiation of the vascular system.

Here, we characterized key aspects of the molecular and functional organization of the GVU in *Mlc1* KO mice, a preclinical model of MLC that recapitulates several important features of the disease and that can be used to examine the pathological cascade [5]. Our results revealed that MLC1 is a critical factor in the postnatal maturation and function of the GVU.

bioRxiv preprint doi: https://doi.org/10.1101/2021.05.17.444434; this version posted May 17, 2021. The copyright holder for this preprint (which was not certified by peer review) is the author/funder. All rights reserved. No reuse allowed without permission.

Materials and Methods

Animals

All animal experiments were carried out in compliance with the European Directive 2010/63/EU on the protection of animals used for scientific purposes and the guidelines issued by the French National Animal Care and Use Committee (reference: 2019021814073504 and 2019022113258393). *Mlc1* KO mice were maintained on a C57BL6 genetic background.

MVs purification

MVs were isolated from whole brain using selection filtration, as described previously [22]. We purified vessels that passed through 100 µm pores but not 20 µm pores [22]. Brain vessels from two animals were pooled for the 2-month sample, with 3 for P15 and 5 for P5.

Immunohistochemical analysis of brain slices

Mice were anesthetized with pentobarbital (600 mg/kg, i.p.) and killed by transcardiac perfusion with PBS/PFA 4%. The brain was removed and cut into 40-µm-thick sections using a Leitz (1400) cryomicrotome. Slices were immersed in the blocking solution (PBS/normal goat serum (NGS) 5%/Triton X-100 0.5%) for 1 h at room temperature (RT) and then incubated with primary antibodies (**Table S11**) diluted in the blocking solution 12 h at 4 °C. After 3 washes in PBS, slices were incubated for 2 h at RT with secondary antibodies and Hoechst dye, rinsed in PBS, and mounted in Fluormount G (Southern Biotech, Birmingham, AL).

Western blot

Proteins were extracted from one brain hemisphere or from purified MVs in 2% SDS (500 µl or 50µl per sample, respectively) with EDTA-free Complete Protease Inhibitor (Roche), sonicated three times at 20 Hz (Vibra cell VCX130) and centrifuged for 20 min at 10,000 g at 4 °C. Supernatants were heated in Laemmli loading buffer for 5 min at 56 °C. Proteins were extracted from one brain hemisphere per sample in 500 µL SDS 2%, under the same conditions. The protein content was measured using the Pierce 660 nm protein assay (Thermo Scientific, Waltham, MA, USA). Equal amounts of proteins were separated by denaturing electrophoresis on Mini-Protean TGX stain-free gels (Biorad) and then electrotransferred to nitrocellulose membranes using the Trans-blot Turbo Transfer

System (Biorad). Membranes were hybridized, as described previously [23]. The antibodies used in this study are listed in **Table S11**. Horseradish peroxidase activity was visualized using enhanced chemiluminescence in a Western Lightning Plus system (Perkin Elmer, Waltham, MA, USA). Chemiluminescent imaging was performed on a FUSION FX system (Vilber, South Korea). At least four independent samples were analyzed in each experiment. The level of chemiluminescence for each antibody was normalized against that of a stain-free membrane, or histone H3.

Quantitative RT-PCR

RNA was extracted using the Rneasy Lipid Tissue Mini Kit (Qiagen, Hilden, Germany). cDNA was then generated using the Superscript™ III Reverse Transcriptase Kit (Thermo Fisher). Differential levels of cDNA expression were measured using droplet digital PCR. Briefly, cDNA and primers (**Table S11**) were distributed into approximately 10,000 to 20,000 droplets. cDNAs were then PCR-amplified in a thermal cycler and read (as the number of positive and negative droplets) with a QX200 Droplet Digital PCR System (Biorad). The ratio for each tested gene was normalized against the total number of positive droplets for *Gapdh*.

In situ brain perfusion

Mice were anesthetized with ketamine-xylazine (140 and 8 mg/kg, respectively, i.p.), and a polyethylene catheter was inserted into the carotid veins. The heart was incised, and the perfusion was started immediately (flow rate: 2.5 mL/min) so as to completely replace the blood with Krebs carbonate-buffered physiological saline (128 mM NaCl, 24 mM $NaHCO_3$, 4.2 mM KCl, 2.4 mM NaH_2PO_4, 1.5 mM $CaCl_2$, 0.9 mM $MgCl_2$), 9 mM D-glucose) supplemented with [^{14}C] sucrose (0.3 µCi/mL) (Perkin Elmer Life Sciences, Courtaboeuf, France) as a marker of vascular integrity. The saline was bubbled with 95% O_2/5% CO_2 for pH control (7.4) and warmed to 37 °C. Perfusion was terminated after 120 sec by decapitating the mouse. The whole brain was removed from the skull and dissected out on a freezer pack. Brain hemisphere and two aliquots of perfusion fluid were placed in tared vials and weighed, digested with Solvable® (Perkin Elmer) and mixed with Ultima gold XR® (Perkin Elmer) for ^{14}C dpm counting (Tri-Carb®, Perkin Elmer). In some experiments, human serum albumin (40 g/L) (Vialebex®, Paris, France) was added to the perfusion fluid in order to increase the hydrostatic pressure (~180 mmHg) and create shear stress [23]. The brain [^{14}C]-sucrose vascular volume (Vv, in µL/g) was calculated from the distribution of the [^{14}C]-sucrose: $Vv = X_v/C_v$ where X_v (dpm/g) is the [^{14}C] sucrose concentration in the hemispheres and C_v (dpm/µL) is the [^{14}C] sucrose concentration in the perfusion fluid [24]. It should be noted that in mammals, the

bioRxiv preprint doi: https://doi.org/10.1101/2021.05.17.444434; this version posted May 17, 2021. The copyright holder for this preprint (which was not certified by peer review) is the author/funder. All rights reserved. No reuse allowed without permission.

very hydrophilic, low-molecular-weight (342 Da) disaccharide sucrose does not bind to plasma proteins and does not have a dedicated transporter. Accordingly, sucrose does not diffuse passively and thus serves as a marker of BBB integrity [25]. In this context, variations in sucrose's distribution volume in the brain solely reflect changes in the BBB's physical integrity.

VSMC responsiveness

Mice were rapidly decapitated, and the brains were quickly removed and placed in cold (~4 °C) artificial cerebrospinal fluid (aCSF) solution containing 119 mM NaCl, 2.5 mM KCl, 2.5 mM CaCl2, 26.2 mM NaHCO3, 1 mM NaH2PO4, 1.3 mM MgSO4, 11 mM D-glucose (pH = 7.35). Brains were constantly oxygenated with 95% O_2 –5% CO_2. Brain cortex slices (400 µm thick) were cut with a vibratome (VT2000S, Leica) and transferred to a constantly oxygenated (95% O_2–5% CO_2) holding chamber containing aCSF. Subsequently, individual slices were placed in a submerged recording chamber maintained at RT under an upright microscope (Zeiss) equipped with a CCD camera (Qimaging) and perfused at 2 ml/min with oxygenated aCSF. Only one vessel per slice was selected for measurements of vascular responsiveness, at the junction between layers I and II of the somatosensory cortex and with a well-defined luminal diameter (10–15 µm). An image was acquired every 30 s. Each recording started with the establishment of a control baseline for 5 min. Vessels with an unstable baseline (i.e. a change in diameter of more than 5%) were discarded from analysis. Vasoconstriction was induced by the application of the thromboxane A_2 receptor agonist U46619 (9,11-dideoxy-11a,9a- epoxymethanoprostaglandin F2α, 50 nM, Sigma) for 2 min. The signal was recorded until it had returned to the baseline.

Functional ultrasound

Two-month-old mice were anesthetized, and CBF responses to whisker stimulation were determined using fUS. The protocol is described in detail in [26]. Briefly, mice were intubated and mechanically ventilated (frequency: 120/min; Tidal volume:10 ml/kg) by maintaining anesthesia with 2% isoflurane in 70% N_2O/30% O_2. Mice were placed in a stereotaxic frame, and the head was shaved and cleaned with povidone-iodine. An incision was made along the midline head skin (to expose the skull), and lidocaine spray was applied to the head. Whiskers on the left side were cut to a length of one centimeter. Anesthesia was switched to a subcutaneous infusion of medetomidine (Domitor®, Pfizer, 0.1 mg/kg) and isoflurane, N_2O and O_2 were withdrawn 10 min later. So that the isoflurane could dissipate and the CBF could stabilization, the fUS measurements were initiated 20 min later. Ultrasound gel was applied between the ultrasound probe and the mouse's skull, to ensure good acoustic coupling.

The probe was positioned in the coronal plane, corresponding to the somatosensory barrel field cortex (S1bf; bregma -1.5 mm). Ultrafast acquisition was performed with an ultrasound sequence based on compounded plane wave transmission (11 angles from 10° to 10°, in increments of 2°), using a 15 MHz probe (Vermon, France; 100 µm x 100 µm in-plane pixels; slice thickness: 300 µm; elevation focus: 8 µm; frame rate: 500 Hz). The whiskers were mechanically stimulated three times for 30 s, interspaced with a 60 s rest period (total duration of the experiment: 300s). Using MATLAB (the MathWorks Inc., Natick, Massachussets, United States), we calculated the coefficient for the correlation between the normalized power Doppler (PD) intensity over time and a step function following the stimulation pattern. An activation map was reconstructed by selecting only pixels with a correlation coefficient above 0.2. The relative PD increase was quantified as the mean PD signal in the activated area.

Ultrasound localization microscopy

The acquisition and post processing steps for ultrasound localization microscopy were adapted from [27]. For each image, 100 µL of Sonovue microbubbles were injected into the tail vein. Blocks of 800 compounded frames (-5° 0° 5°) at 1 kHz were acquired for 800 ms and saved for 200 ms; this scheme was repeated for 180 s. A combination of a Butterworth high-pass filter (second order, 20 Hz) and a singular value decomposition filter (10 values) was used to separate microbubble echoes from tissue echoes. The microbubbles' centroid positions were localized using a weighted average algorithm. Microbubbles were tracked through consecutive frames using MathWorks (the MathWorks Inc., Natick, Massachussets, United States). The tracks were interpolated and smoothed using a 5-point sliding window, and redundant positions were removed. A density image was reconstructed on an 11 µm × 10 µm grid.

Magnetic resonance imaging

MRI was performed on a 7T Pharmascan MRI system (Bruker, Rheinstetten, Germany) equipped with volume transmit and surface receive coils and operated via Paravision® 6.0 software (Bruker, Rheinstetten, Germany). An anatomical T2-weighted acquisition was performed prior to contrast injection, with the following parameters: echo time (TE) = 40 ms; repetition time (TR) = 3500 ms; flip angle (FA) = 90°; averages = 2; number of echoes = 8; on a 256x256 sagittal matrix with 20 contiguous 0.5 mm thick slices (in-plan resolution = 0.07 x 0.07 mm) for a total duration of 2 min 41 s. The ADC was calculated from a multi-b diffusion-weighted echo planar imaging sequence, with following parameters: TE = 35 ms; TR = 2000 ms; FA = 90°; number of segments = 4; 16 b-values

= 20 s.mm^{-2}, 30 s.mm^{-2}, 40 s.mm^{-2}, 50 s.mm^{-2}, 75 s.mm^{-2}, 100 s.mm^{-2}, 150 s.mm^{-2}, 200 s.mm^{-2}, 300 s.mm^{-2}, 400 s.mm^{-2}, 500 s.mm^{-2}, 750 s.mm^{-2}, 1000 s.mm^{-2}, 1250 s.mm^{-2}, 1500 s.mm^{-2}, 2000 s.mm^{-2}; 12 directions; on a 128x40 sagittal matrix with 9 contiguous 1 mm thick slices (in-plan resolution: 0.15 x 0.15 mm), with use of a saturation band to remove the out-of-matrix signal, over a total duration of 25 min 45 s. The ADC acquisition was performed prior to contrast injection. To estimate the concentration of contrast agent, T1 maps before and after contrast injection were computed from a FAIR RARE (flow alternating inversion recovery, rapid acquisition with refocused echoes) acquisition derived from the Look-Locker T1 mapping sequence [28], with the following parameters: TE = 5.3 ms; TR = 5000 ms; FA = 90°; RARE factor = 4; 10 inversion times (TI) = 10 ms, 21 ms, 44 ms, 195 ms, 410 ms, 862 ms, 1811 ms, 3807 ms, 8000 ms; on a 64x64 single mediosagittal slice (in-plan resolution: 0.3 x 0.3 mm; thickness: 0.8 mm) for a total duration of 4 min 25 s. A single acquisition was performed before contrast injection (to map the reference T1), and 8 consecutive acquisitions were performed 10 minutes after contrast injection – providing dynamic data over 40 minutes.

Injection of contrast agent into the cerebrospinal fluid

1 µl of 500 mM DOTA-Gd (Dotarem®, Guerbet®, France) was injected over 1 minute into the CSF with a glass micropipette through the cisterna magna, as described previously [29]. Briefly, the mice were anesthetized with isoflurane (induction: 5%, maintenance: 2-3%) in 70% N_2O/30% O_2. The neck was shaved, and lidocaine was sprayed on for local analgesia. A vertical incision was performed, and the muscle planes were separated vertically upon reaching the cisterna magna. A micropipette formed from an elongated capillary glass tube and filled with 1 µL of DOTA-Gd was inserted into the cisterna magna. Before and after injection, one-minute pauses enabled the CSF pressure to normalize. Before micropipette removal, a drop of superglue was added to form a seal and prevent subsequent leakage of CSF. The incision was cleaned and then closed with 5.0 gauge surgical silk thread.

MRI analyses

T1 values, quantitative contrast measurements and ADC maps were calculated with in-house MATLAB code (R2021a, Natick, Massachusetts: the MathWorks Inc; 2020). Regions of interest were determined using the FIJI image analysis suite [30].

T1 maps were computed from the FAIR RARE data. Briefly, T1 was extracted after fitting the signal recovery equation:

$$M_t = M_0 . \exp\left(-t/_{T1}\right)$$

The contrast agent concentration [CA] was determined from the equation:

$$[CA].r1 = \frac{1}{T1_{post}} - \frac{1}{T1_{pre}}$$

where r1, $T1_{post}$ and $T1_{pre}$ were respectively the T1 relaxivity, the T1 value after contrast, and the T1 value before contrast. The ADC was calculated as the slope of the log of signal loss for the b-value, according to the following equation:

$$ADC = \frac{ln\left(\frac{S_0}{S_b}\right)}{b}$$

where b = 1000 s.mm^{-2}.

Tissue clearing and immunohistochemical staining

Mice were killed with pentobarbital (600 mg/kg, i.p.). Brains were removed and post-fixed in 4% paraformaldehyde (PFA) for 24 h at 4 °C and then assessed using the "immunolabeling-enabled three-dimensional imaging of solvent-cleared organs" technique [31]. The samples were first dehydrated with increasingly concentrated aqueous methanol solutions (MetOH: 20%, 40%, 60%, 80%, and twice 100%, for 1 h each) at RT and then incubated in 66% dichloromethane (DCM, Sigma Aldrich)/33% MetOH overnight. After 2 washes in 100% MetOH, brains were incubated in 5% H_2O_2/MetOH overnight at RT, rehydrated with increasingly dilute aqueous methanol solutions (80%, 60%, 40%, and 20%; 1h each). Before immunostaining, brains were permeabilized first for 2 x 1h at RT in 0.2% Triton X-100/PBS, for 24 h at 37 °C in 0.16% Triton X-100/2.3% glycine/20% DMSO/PBS, and then for 2 days at 37 °C in 0.16% Triton X-100/6% donkey serum/10% DMSO/PBS. Brains were incubated for 3 days at 37 °C with primary antibody diluted in a 0.2 Tween/1% heparin/3% donkey serum/5% DMSO/PBS solution, washed 5 times during 24h at 37 °C in 0.2% Tween20/1% heparin/PBS solution, incubated for 3 days at 37 °C with secondary antibody diluted in a 0.2 Tween/1% heparin/3% donkey serum/PBS solution, and another washed five times. The brain samples were then dehydrated again with a MetOH/H_2O series (20%, 40%, 60%, 80% and 100% for 1h each, and then 100% overnight) at RT. On the following day, brains were incubated for 3h in 66% DCM/33% MetOH and then twice for 15 min at RT in 100% DCM and lastly cleared overnight in dibenzyl ether.

The cleared tissues were imaged using a light sheet microscope and Inspector pro software (Lavision Biotec GmbH, Bielefeld, Germany). 3D reconstructions of the somatosensory cortex (a 400 µm-thick column for Pecam-1 and 500 to 750 µm for SMA) were visualized with Imaris software (Bitplane). The length and number of branch

bioRxiv preprint doi: https://doi.org/10.1101/2021.05.17.444434; this version posted May 17, 2021. The copyright holder for this preprint (which was not certified by peer review) is the author/funder. All rights reserved. No reuse allowed without permission.

points of Pecam-1- or SMA-immunolabeled brain vessels were quantified using the "Surface" and "Filament" tools in Imaris software (Oxford instruments, Oxford). Anastomoses were measured by eye.

Astrocyte morphology

Hippocampal slices were pictured using a 40X objective on a Zeiss Axio-observer Z1 with a motorized XYZ stage (Zeiss, Oberkochen, Germany). To analyze astrocyte ramifications, we adapted a previously described technique [32]. Using ImageJ software, 7 concentric circles at 5 µm intervals were drawn around each astrocyte on confocal Z-stack images. The number of intersections of GFAP-positive astrocytic processes with each circle was counted. We analyzed the astrocytes' orientation by adapting a previously described technique [33]. Using ImageJ software, a grid delimitating 100 μm^2 squares was drawn on confocal Z-stack images oriented with the PL or a vessel. The number of intersections of astrocytic GFAP positive processes with horizontal lines (i.e. processes perpendicular to the pyramidal layer or vessel, so-called axial processes) and vertical lines (i.e. processes parallel to the pyramidal layer or vessel, so-called lateral processes) were counted. The cell's polarity index was defined as the ratio between the axial processes and the lateral processes. A polarity index of 1 indicates no polarity, whereas a polarity index greater than 1 indicates preferentially perpendicular orientation toward the pyramidal layer or the vessel.

Electron microscopy

Mice were anesthetized with ketamine-xylazine (140 and 8 mg/kg, respectively, i.p.) and transcardially perfused with the fixative (2% paraformaldehyde, 3% glutaraldehyde, 3mM $CaCl_2$ in 0.1M cacodylate buffer pH 7.4) for 12 min. The brains were removed and left overnight at 4 °C in the same fixative. Brain fragments (0.3 x 1 x 1 mm^3) were postfixed first in 0.1M cacodylate buffer pH 7.4 + 1% OsO_4 for 1h at 4 °C and then in 1% aqueous uranyl acetate for 2h at RT. After dehydration in graded ethanol and then propylene oxide, the fragments were embedded in EPON resin (Electron Microscopy Sciences, Hatfield, PA). Ultrathin (80 nm) sections were prepared, stained with lead citrate and imaged in a Jeol 100S transmission electron microscope (Jeol, Croissy-sur-Seine, France) equipped with a 2k x 2k Orius 830 CCD camera (Roper Scientific, Evry, France).

Human tissue immunohistochemistry

Our study included specimens obtained from the brain collection "Hôpitaux Universitaires de l'Est Parisien – Neuropathologie du développement" (Biobank identification number BB-0033-00082). Informed consent was obtained for autopsy of the brain and histological examination. Our study included fetal brains obtained from

bioRxiv preprint doi: https://doi.org/10.1101/2021.05.17.444434; this version posted May 17, 2021. The copyright holder for this preprint (which was not certified by peer review) is the author/funder. All rights reserved. No reuse allowed without permission.

spontaneous or medical abortion that did not display any significant brain pathology. After removal, brains were fixed with formalin for 5–12 weeks. Macroscopic analysis was performed to select samples that where embedded in paraffin, sliced in 7 µm sections and stained with hematein for a first histological analysis. Immunohistochemical analyses were performed on coronal slices that included the temporal telencephalic parenchyma and hippocampus. They were dewaxed and rinsed before incubation in citrate buffer (pH 9.0). Expression of MLC1 on the sections was detected using the Bond Polymer Refine Detection Kit (Leica) with specific antibodies and an immunostaining system (Bond III, Leica). Images were acquired using a slide scanner (Lamina, Perkin Elmer). Staining was analyzed using QuPath [34]. A QuPath pixel classifier was trained to discriminate between DAB-positive spots and background areas. We selected a pixel classifier that used a random trees algorithm and four features: a Gaussian filter to select intensity, and the three structure tensor eigenvalues to select thin elongated objects. The classifier was trained on manually annotated MLC1 spots and the background area on one image per developmental stage. When the result was satisfactory, the pixel classifier was used to detect MLC1 in selected regions of interest.

Statistics

For all variables, the normality of data distribution was probed with using the Shapiro-Wilk test before the appropriate statistical test was chosen. Test names and sample sizes are indicated in the figure legends. Detailed results are presented in the supplementary tables.

bioRxiv preprint doi: https://doi.org/10.1101/2021.05.17.444434; this version posted May 17, 2021. The copyright holder for this preprint (which was not certified by peer review) is the author/funder. All rights reserved. No reuse allowed without permission.

Results

The absence of MLC1 results in accumulation of fluid in the brain but does not alter blood-brain barrier (BBB) integrity or the organization of the endothelial network

Astrocytes influence several properties of endothelial cells, such as BBB integrity [18-21]. We recently demonstrated that the postnatal maturation of the MLC1/GlialCAM complex in PvAPs from P5 to P15 coincides with the progressive increase in endothelium-specific proteins that contribute to BBB integrity, such as the tight junction protein claudin5 and the endothelial luminal ATP-binding cassette (ABC) efflux transporter P-glycoprotein (P-gP) - suggesting that PvAPs and the BBB mature in parallel [16, 17]. We therefore looked at whether the absence of MLC1 in the *Mlc1* KO mouse influenced postnatal endothelial maturation. To that end, we used qPCRs to characterize the expression of *Abcb1* (encoding P-gP) and *Cldn5* (encoding claudin5) on P5 and P15 and at 2 months (P60) on mRNAs extracted from whole brain microvessels (MVs) purified from WT and *Mlc1* KO animals [22] **(Fig. 1a; Table S1)**. In the WT, expression of all the analyzed mRNAs on P5 and P15 confirmed the progressive postnatal molecular maturation of endothelial cells (**Fig. 1a**). There were no differences between *Mlc1* KO mice and WT mice in this respect (**Fig. 1a**). Consistently, the protein levels of P-gP and claudin5 in purified MVs (on Western blots) were also similar in *Mlc1* KO and WT mice at all stages (**Fig. 1b; Table S2**). We next assessed BBB integrity in two-month-old *Mlc1* KO and WT mice. We first observed that the apparent diffusion coefficient (ADC, measured using MRI) was higher in *Mlc1* KO mice **(Fig. 1c; Fig. S1; Table S3).** Furthermore, the volume of the ventricles and the brain estimated from the anatomical T2-weighted MRI acquisition was larger in *Mlc1* KO mice than in WT mice **(Fig. S1c)**, although the relative ventricular volumes did not differ (**Fig. S1d**). These results reflected the previously described presence of fluid in the parenchyma in *Mlc1* KO mice [9]. However, this fluid accumulation was not related to leakage of the BBB. Indeed, the vascular volume measured by *in situ* brain perfusion of [^{14}C] sucrose (a marker of vascular space and integrity [24]) was the same in *Mlc1* KO and WT mice and so suggested that the BBB was not leaky **(Fig. 1d; Table S4) -** even in the shear stress conditions (increased hydrostatic pressure: 180 mmHg) produced by the addition of human serum albumin to the perfusate [23] (**Fig. 1d**). Lastly, we assessed the endothelium architecture by analyzing vessel length, branching and tortuosity in the whole cleared somatosensory cortex of 2-month-old WT and *Mlc1* KO immunolabeled for the endothelium-specific protein Pecam-1 (**Fig. 1e-h; Table S5**). There were no differences between WT and *Mlc1* KO mice with regard to these architectural parameters, either in the parenchymal (**Fig. 1e, f)** or pial vasculature at the cortical surface **(Fig. 1g, h)**.

bioRxiv preprint doi: https://doi.org/10.1101/2021.05.17.444434; this version posted May 17, 2021. The copyright holder for this preprint (which was not certified by peer review) is the author/funder. All rights reserved. No reuse allowed without permission.

Hence, the absence of MLC1 leads to fluid accumulation in the brain but has no obvious impact on the postnatal molecular maturation of ECs, BBB integrity, or endothelium architecture.

MLC1 is crucial for contractile maturation of VSMCs, arterial perfusion, and neurovascular coupling.

We recently showed that VSMCs mature postnatally, with the progressive acquisition of contractility from P5 onwards and the extension of the VSMC network [17]. Here, we investigated the VSMCs' status in *Mlc1* KO mice during postnatal development. We first used qPCRs to compare the mRNA expression of *Acta2* (encoding smooth muscle actin, SMA) in MVs purified from WT and *Mlc1* KO whole brain on P5 and P15 and at 2 months [22] **(Fig. 2a; Table S1).** We also measured the mRNA expression of *Atp1b1* (a VSMC-specific gene stably expressed during postnatal development) as a marker of VSMC density in purified MVs [35, 36]. In WT mice, the level of contractile-protein-encoding mRNAs rose progressively from P5 to P15, while the level of *Atp1b1* mRNA remained stable **(Fig. 2a)**. In *Mlc1* KO mice, however, *Acta2* was significantly downregulated between on P5 and P15, and *Atp1b1* levels were unchanged **(Fig. 2a)**. We next analyzed the protein levels of SMA in MVs purified from WT and *Mlc1* KO whole brain on P5 and P15 and at 2 months by Western blot (**Fig. 2b; Table S2**). A small decrease in SMA expression was found in *Mlc1* KO MVs from P15 onwards although it became significant only at 2 months. Moreover, at 2 months, additional bands of lower molecular weights (resembling a degradation pattern) were detected **(Fig. 2b)**. To determine whether the decrease in SMA expression and the putative increase in its degradation were related to VSMC degeneration, we used an immunofluorescence assay to detect SMA on 2-month-old WT and *Mlc1* KO whole cleared somatosensory cortices (**Fig. 2c-f**). No discontinuities in the labeling were detected in the parenchymal (**Fig. 2c, d**) or pial vasculature (at the cortical surface) (**Fig. 2e, f**). Moreover, the SMA-positive vessels' length, branching, tortuosity and number of anastomoses (analyzed only in pial vessels) were the same in *Mlc1* KO and WT mice (**Fig. 2c-f**). These findings indicate that the absence of MLC1 perturbs the developmental expression of SMA but does not affect the development of the vascular VSMC network.

To further assess the functional consequences of this molecular change, we compared the *ex vivo* contractility of VSMCs in brain slices obtained from *Mlc1* KO and WT mice on P5 and P15 and at 2 months (**Fig. 3a-c; Table S6**). We recorded the vasomotor changes in cortical arterioles upon exposure for 2 min to a thromboxane A_2 receptor agonist U46619 (9,11-dideoxy-11a,9a-epoxymethanoprostaglandin F2α, 5 nM), which acts directly on VSMCs to induce a reversible vasoconstriction. On P5, application of U46619 had a small effect on vessel diameter in both WT and *Mlc1* KO mice **(Fig. 3b, c)**. In contrast, a clear vasoconstriction was observed from P15 **(Fig. 3b, c)**. Strikingly, the amplitude and speed of vasoconstriction were significantly lower in *Mlc1* KO mice from P15 onwards (**Fig. 3b, c; Table S6**). These results indicate that the postnatal acquisition of contractility is impaired in the absence of MLC1.

Given this phenotype, we next hypothesized that arterial tonicity might be impaired in *Mlc1* KO mice. We first addressed this question by performing Ultrasound localization microscopy (ULM) *in vivo* imaging to reveal the brain vasculature at a microscopic resolution after intravenous microbubble injection (**Fig. 3d)**. *Mlc1* KO mice displayed significantly lower blood perfusion, which was suggestive of narrower penetrating arteries **(Fig. 3d; Table S7)**. Vasomotricity and cerebral blood flow (CBF) are tightly coupled to neuronal energy demand, in a process referred to as neurovascular coupling or functional hyperemia [37]. We then used functional Ultrasound (fUS) imaging to measure variations in CBF in the barrel cortex in response to whisker stimulation in 2-month-old WT and *Mlc1* KO mice [27, 38, 39] **(Fig. 3e; Table S7)**. The increase in CBF evoked by whisker stimulation was significantly smaller in *Mlc1* KO mice than in WT mice, indicating that neurovascular coupling was impaired in the KO mice **(Fig. 3e; Table S7)**.

In conclusion, the absence of MLC1 impairs the postnatal acquisition of contractile properties by VSMCs and impedes blood perfusion, vessel diameter and neurovascular coupling.

The absence of MLC1 alters the PvAPs' molecular maturation and perivascular cohesiveness.

We next characterized the PvAPs in *Mlc1* KO mice by focusing on membrane proteins known to be strongly expressed in these structures [18]: the water channel aquaporin 4 (Aqp4), the adhesion protein GlialCAM, and the gap junction protein connexin 43 (Cx43). We first used immunofluorescence to analyze the proteins' localization in PvAPs on brain sections on P5, P15 and at 2 months (**Fig. 4a**). Vessels were counterstained with isolectin B4. Interestingly, perivascular Aqp4, GlialCAM and Cx43 immunolabeling was almost undetectable (relative to WT) in *Mlc1* KO mice on P5 (**Fig. 4a**). In contrast, all proteins were detected normally in PvAPs from P15 onwards - with the exception of GlialCAM, which was not detected at any stage (as described previously [5]) (**Fig. 4a**). To further confirm and quantify these results, we assessed the levels of Cx43, GlialCAM and Aqp4 on Western blots of whole brain protein extracts on P5 and P15 and at 2 months (**Fig. 4b; Table S2**). In *Mlc1* KO mice, lower levels of all these proteins were observed but only on P5 (**Fig. 4b**). These data suggested that the molecular maturation of PvAPs is delayed in *Mlc1* KO mice.

We had demonstrated previously that PvAPs and the associated neuronal fibers remain attached to vessels during their mechanical purification (**Fig. 4e**) [22]. Surprisingly, Aqp4 levels were similar in whole brain extracts from 2-month-old WT and *Mlc1* KO mice but were significantly lower in extracts from *Mlc1* KO mechanically purified brain MVs (**Fig. 4c; Table S2**). The same was true for neurofilament protein M (NFM), a neuronal-specific intermediate filament protein present in neuronal fibers abutting PvAPs (**Fig. 4d**). NF-M was similarly present in whole brain extracts from WT and Mlc1 KO mice but was almost undetectable in 2-month-old *Mlc1* KO MVs (**Fig. 4d; Table S2**). These data suggested that the PvAPs and the associated neuronal fibers had detached from *Mlc1* KO brain vessels during the mechanical purification of MVs.

Taken as a whole, these results show that the absence of MLC1 delays the acquisition of Aqp4 and Cx43, disrupts (from P5 onwards) the membrane anchorage of GlialCAM, and reduces the cohesiveness of PvAPs at the vessel surface (**Fig. 4e**).

The absence of MLC1 alters astrocyte morphology and polarity, PvAP morphology, and perivascular coverage

Our results suggested that in the absence of MLC1, PvAPs may not adhere properly to the vessel surface. Since adhesion, cell morphology and polarity are interdependent, we hypothesized that the absence of MLC1 could perturb the astrocytes' morphology and polarity. We addressed this question by performing a Sholl analysis of glial fibrillary acid protein (GFAP)-immunolabeled astrocytic ramifications in the CA1 region of the hippocampus in 2-month-old mice (**Fig. 5a, b**). *Mlc1* KO astrocytes displayed a greater number of processes located between 15 to 25 µm from the soma (**Fig. 5b; Table S8**).

In the hippocampal stratum radiatum, GFAP-positive astrocytic processes are normally polarized perpendicular to the pyramidal cell layer (PL) [40]. We evaluated this preferential orientation and measured the polarity index, which corresponds to the ratio between parallel (axial) and perpendicular (lateral) crossing points between GFAP-positive processes and a grid oriented with the PL (**Fig. 5c, d**). We found that both *Mlc1* KO and WT astrocytes were equally well oriented, with a polarity index > 1 (**Fig. 5d; Table S8**). However, when taking hippocampal vessels as the reference (**Fig. 5e, f**), *Mlc1* KO astrocytes were abnormally oriented towards vessels in the axial plane (**Fig. 5e, f; Table S8).**

We next used transmission electron microscopy (TEM) to analyze the ultrastructural morphology of PvAPs in the cortex and hippocampus of 2-month-old WT and *Mlc1* KO mice, with a focus on vessels up to 10 µm in diameter (**Fig. 6**). In WT mice, endothelial cells were joined by tight junctions (TJs) and were totally covered by PvAPs, which themselves were joined by gap junctions. Astrocytes and endothelial cells were separated by a thin, homogeneous, regular basal lamina (BL) (**Fig. 6a**). In *Mlc1* KO mice, the endothelium appeared to be unaltered: normal tight junctions (TJ) and BL, and no accumulation of intracellular vesicles (**Fig. 6b**). However, the astrocytes' perivascular organization was drastically modified (**Fig. 6b-e**). We observed PvAPs surrounded by BL (**Fig. 6c**), or stacked on top of each other and joined by gigantic gap junction plaques, suggesting a loss of polarization (**Fig. 6d**). Some of the PvAPs interpenetrated each other (**Fig. S2b**). Astrocyte coverage was often discontinuous. In the free spaces, axons (recognizable by their microtubules) (**Fig. 6b, e**) and synapses (recognizable by the large number of vesicles in the presynaptic part and their electron dense postsynaptic density (**Fig. S2b**)) were found to be in direct contact with the endothelial BL. Accordingly, the percentage of MVs in which the endothelial BL was in direct contact with at least one neuronal process was higher in *Mlc1* KO mice than in WT mice (**Fig. 6f**). Despite the presence of these anomalies, no swelling was observed in *Mlc1* KO PvAPs vs. WT PvAPs (**Fig. 6b-e, g; Table S9**).

Taken as a whole, these results indicate that MLC1 is required for the astrocytes' morphology and polarity. Within the GVU, the absence of MLC1 greatly alters PvAPs' polarization, morphology and perivascular coverage.

The absence of MLC1 modifies the parenchymal circulation of cerebrospinal fluid

Several groups have reported a causal link between PvAP disorganization and impaired parenchymal CSF transport [41, 42]. We tested this hypothesis by observing (using T1-weighted MRI) the parenchymal distribution of DOTA-Gadolinium (Gd) injected in CSF through the cisterna magna in 2-month-old mice (**Fig. 7a**). Contrast-enhanced T1 mapping was used to quantify changes over time in the concentration of DOTA-Gd within the brain tissue. In line with the conventional models of CSF solute circulation, tracers injected into the cisterna magna dispersed into the arachnoid space and then entered the parenchyma through the perivascular spaces (**Fig. 7b**). As expected, a high concentration of DOTA-Gd was detected at the border of the brain as soon as 10 minutes after injection in both WT and *Mlc1* KO mice; this reflected the initial dispersion of contrast within the subarachnoid space. Forty-five minutes after injection, the brain tissue concentration rose as the DOTA-Gd penetrated into the parenchyma through the perivascular spaces (**Fig. 7c**). For both genotypes, the distribution of DOTA-Gd appeared to be in line with previous observations [43]. However, examination of the quantitative maps suggested that DOTA-Gd transport in the CSF was lower in *Mlc1* KO mice than in WT mice. We analyzed the time courses of DOTA-Gd dispersion in the cerebellum, midbrain, septal area, and cortex (**Fig. 7d-g**). As compared to the WT mice, the mean DOTA-Gd concentration was lower in the midbrain (**Fig. 7e**) and the slope was lower in the cerebellum, midbrain, and cortex in the *Mlc1* KO mice (**Fig. 7d, e, g**).

Thus, the absence of MLC1 impairs intraparenchymal circulation and clearance of CSF.

The absence of MLC1 impacts the development of astrocyte morphology, polarity and perivascular coverage.

MLC1 expression is a progressive process that starts in the mouse at P5 and completes at P15 [16]. In contrast, astrocyte ramification in the *stratum radiatum* increases greatly between P8 and P16 [40]. We therefore wondered whether the morphological and polarity defects observed in adult *Mlc1* KO astrocytes might be caused by an impairment development. Hence, we analyzed the morphology and orientation of GFAP-immunolabeled astrocytic processes on P10 and P15 [40] **(Fig. 8; Table S8)**. As observed at 2 months, *Mlc1* KO astrocytes had a larger number of processes at 10 to 25 µm from the soma (**Fig. 8a-d; Table S8**) and an abnormal axial orientation towards the hippocampal vessels on P10 and P15, relative to WT astrocytes **(Fig. 8 e-h; Table S8)**.

The time course of perivascular astrocyte coverage has not previously been described. Here, we used TEM to quantify the percentage of the perivascular diameter covered by PvAPs in *Mlc1* KO and WT cortex and hippocampus on P5, P10, P15 and at 2-months (**Fig. 9; Table S9**). On P5, the PvAPs covered about half of the vessel's circumference, and the WT and *Mlc1* KO samples did not differ significantly in this respect *(***Fig. 9b**). The perivascular astrocyte coverage increased dramatically between P5 and P15 and was almost complete on P15 in WT mice (**Fig. 9b**). In great contrast, however, *Mlc1* KO mice displayed a lower percentage of PvAP coverage from P10 onwards, and a large number of neuronal processes were inserted into the uncovered vascular areas (**Fig. 9a; Table S9)**.

MLC1 is therefore required for the development of astrocyte morphology and polarity. Our results demonstrated for the first time that the perivascular astrocyte coverage increases rapidly between P5 and P15. This process is impaired in *Mlc1* KO mice and results in incomplete perivascular PvAP coverage and direct contact between infiltrating neuronal processes and the endothelial basal lamina; the processes normally remain behind the perivascular astrocyte layer. MLC1 is therefore critical for the normal postnatal development of perivascular astrocyte coverage.

bioRxiv preprint doi: https://doi.org/10.1101/2021.05.17.444434; this version posted May 17, 2021. The copyright holder for this preprint (which was not certified by peer review) is the author/funder. All rights reserved. No reuse allowed without permission.

Discussion

MLC1 (the main gene involved in MLC) encodes an astrocyte-specific protein located in PvAPs, where it forms a junctional complex with GlialCAM. Our previous research showed that in the mouse, this complex forms progressively after birth (between P5 and P15) [16]. Our present work demonstrated that the P5-P15 time window is also important for the formation of perivascular astrocyte coverage. On P5, PvAPs covered only 50% of the vascular surface, and this coverage increased rapidly until completion on P15. The absence of MLC1 delays the PvAPs' molecular maturation, with a transient decrease in Aqp4 and Cx43 protein levels on P5. GlialCAM (whose anchorage in PvAP membranes depends on MLC1) is distributed diffusely, as described previously [5]. In the absence of MLC1, impairments in the PvAPs are observed from P10 onwards, with incomplete perivascular coverage and direct contact between neuronal components and the vessel wall. Remodeling of the gliovascular interface is accompanied by a loss of astrocyte polarity. Firstly, the astrocytes have a greater number of ramifications, which tend to project towards the blood vessels. Secondly, there are changes in the stacking and interpenetration of PvAPs, the presence of BL on their parenchymal side, and the loss of perivascular cohesiveness. Taken as a whole, these data demonstrate that MLC1 is crucial for the development of astrocyte polarity and perivascular coverage.

What impact, then, does the lack of MLC1 have on the gliovascular physiology? The incomplete perivascular astrocyte coverage, the abnormal astrocytic polarity, and the loss of PvAP cohesiveness probably alter the "barrier" formed by PvAPs around the vessels. In turn, this might greatly affect perivascular homeostasis and astrocyte signaling towards the vascular compartment [19, 44]. The astrocytes' perivascular organization is thought to be crucial for regulating the fluxes of CSF and interstitial fluid (ISF) into the parenchyma [45]. These alterations might therefore be directly linked to the loss of Gd drainage observed in *Mlc1* KO mice. Importantly, in the absence of BBB breakdown, impaired parenchymal circulation of CSF/ISF might (i) contribute to the fluid accumulation and megalencephaly observed in the *Mlc1* KO mouse model [9] and in patients with MLC [46], (ii) lead to the progressive accumulation of harmful molecules in the brain, and (iii) thus increase susceptibility to neural disorders [47].

Unlike skeletal or cardiac muscle, smooth muscle cells are not terminally differentiated; they are extremely plastic cells that are constantly integrating signals from their local environment and then expressing the appropriate patterns of genes. Smooth muscle cells undergo profound phenotypic changes in response to variations in the local environment [48, 49]. By perturbing perivascular homeostasis, the abnormal development of PvAPs in the absence of MLC1 might affect the postnatal acquisition of VSMCs' contractile properties and thus result in hypoperfusion and defective neurovascular coupling. This hypothesis is supported by the fact that perivascular astrocyte coverage, MLC1 expression [16] and VSMC contractile differentiation [17] develop concomitantly. Interestingly, deletion of astrocytic laminin γ1 was shown to lead to the loss of VSMC contractile proteins [50], which indicated a functional link between astrocytes and VSMCs. Our data now suggest that astrocytes have a critical role in the postnatal differentiation of contractile VSMCs. Alteration of VSMC contractility might influence brain perfusion and neurovascular coupling, which are critical for oxygen and nutrient delivery to neurons [37]; this impairment might compromise neuronal and cerebral functions.

In *Mlc1* KO mice, myelin vacuolation has been shown to develop only from 3 months onwards [9, 5]. Thus, PvAP and VSMC maturation defects might be primary events in the pathogenesis of MLC. The resulting defects in perivascular homeostasis and neurovascular coupling might then contribute to progressive intramyelinic edema. In an attempt to move closer to the context of MLC in humans, we used immunohistochemical techniques to analyze the development of perivascular expression of MLC1 in human cortical sections from 15 weeks of gestation (wg) to 17 years of age (**Fig. S3**). Interestingly, perivascular MLC1 was detected as early as 15 wg and remained stable thereafter. These results suggested that the MLC1/GlialCAM complex and the astrocyte's perivascular coverage are initiated prenatally, as already suggested by earlier observations of perivascular GFAP and AQP4 expression [51]. In the absence of MLC1, impaired PvAP formation might therefore occur *in utero* in individuals subsequently diagnosed with MLC. This impairment might deregulate perivascular homeostasis and then the postnatal differentiation of VSMC contractility.

In conclusion, we showed that the astrocyte-specific protein MLC1, which absence causes MLC, is critical for the postnatal development of perivascular astrocyte coverage, the acquisition of VSMC contractility, and parenchymal CFS/ISF efflux. Taken as a whole, these data indicate that MLC could be considered primarily as an early developmental disorder of the GVU. Moreover, our results shed light on the role of astrocytes in the postnatal the acquisition of VSMC contractility, a crucial component of neurovascular coupling in the brain. Our study illustrates how looking at physiopathological processes in a rare disease can enlighten important aspects of the brain's physiology.

Acknowledgements

We are grateful to the donors who support the charities and charitable foundations cited below. This work was funded by grants from the *Association Européenne contre les Leucodystrophies* (ELA, grant reference ELA2012-014C2B), the *Fondation pour la Recherche Médicale* (FRM, grant reference AJE20171039094) and the *Fondation Maladie Rares* (grant reference 20170603). A. Gilbert's PhD was funded by the FRM (grant reference: PLP20170939025p60) and ELA (grant reference: ELA2012-014C2B). The creation of the Center for Interdisciplinary Research in Biology (CIRB) was funded by the "Fondation Bettencourt Schueller". We thank Fawzi Boumezbeur, Aloïse Mabondzo, Corinne Blugeon, Laurent Jourdren and Stéphane Le Crom for helpful discussions. We thank Isabelle Bardou for her help writing ethical documents. We thank Louise Charpentier and Ines Masurel for their help analyzing astrocyte morphology and polarity. Lastly, we thank Virginie Mignon for help with the TEM analysis. Despite our efforts, our work has not received any funding from the French National Agency for Research (ANR).

References

1. Topcu M, Gartioux C, Ribierre F, Yalcinkaya C, Tokus E, Oztekin N, et al. Vacuoliting megalencephalic leukoencephalopathy with subcortical cysts, mapped to chromosome 22qtel. *Am J Hum Genet.* 2000;66(2):733-9.
2. Leegwater PA, Yuan BQ, van der Steen J, Mulders J, Konst AA, Boor PK, et al. Mutations of MLC1 (KIAA0027), encoding a putative membrane protein, cause megalencephalic leukoencephalopathy with subcortical cysts. *Am J Hum Genet.* 2001;68(4):831-8.
3. Duarri A, Teijido O, Lopez-Hernandez T, Scheper GC, Barriere H, Boor I, et al. Molecular pathogenesis of megalencephalic leukoencephalopathy with subcortical cysts: mutations in MLC1 cause folding defects. *Hum Mol Genet.* 2008;17(23):3728-39.
4. Lanciotti A, Brignone MS, Visentin S, De Nuccio C, Catacuzzeno L, Mallozzi C, et al. Megalencephalic leukoencephalopathy with subcortical cysts protein-1 regulates epidermal growth factor receptor signaling in astrocytes. *Hum Mol Genet.* 2016;25(8):1543-58.
5. Hoegg-Beiler MB, Sirisi S, Orozco IJ, Ferrer I, Hohensee S, Auberson M, et al. Disrupting MLC1 and GlialCAM and ClC-2 interactions in leukodystrophy entails glial chloride channel dysfunction. *Nat Commun.* 2014;5:3475.
6. Wang MX, Ray L, Tanaka KF, Iliff JJ, and Heys J. Varying perivascular astroglial endfoot dimensions along the vascular tree maintain perivascular-interstitial flux through the cortical mantle. *Glia.* 2020.
7. Ridder MC, Boor I, Lodder JC, Postma NL, Capdevila-Nortes X, Duarri A, et al. Megalencephalic leucoencephalopathy with cysts: defect in chloride currents and cell volume regulation. *Brain.* 2011;134(Pt 11):3342-54.
8. Capdevila-Nortes X, Lopez-Hernandez T, Apaja PM, Lopez de Heredia M, Sirisi S, Callejo G, et al. Insights into MLC pathogenesis: GlialCAM is an MLC1 chaperone required for proper activation of volume-regulated anion currents. *Hum Mol Genet.* 2013;22(21):4405-16.
9. Dubey M, Bugiani M, Ridder MC, Postma NL, Brouwers E, Polder E, et al. Mice with megalencephalic leukoencephalopathy with cysts: a developmental angle. *Ann Neurol.* 2015;77(1):114-31.
10. Bugiani M, Dubey M, Breur M, Postma NL, Dekker MP, Ter Braak T, et al. Megalencephalic leukoencephalopathy with cysts: the Glialcam-null mouse model. *Ann Clin Transl Neurol.* 2017;4(7):450-65.

11. Jeworutzki E, Lopez-Hernandez T, Capdevila-Nortes X, Sirisi S, Bengtsson L, Montolio M, et al. GlialCAM, a protein defective in a leukodystrophy, serves as a ClC-2 Cl(-) channel auxiliary subunit. *Neuron.* 2012;73(5):951-61.

12. Estevez R, Elorza-Vidal X, Gaitan-Penas H, Perez-Rius C, Armand-Ugon M, Alonso-Gardon M, et al. Megalencephalic leukoencephalopathy with subcortical cysts: A personal biochemical retrospective. *Eur J Med Genet.* 2018;61(1):50-60.

13. Benesova J, Rusnakova V, Honsa P, Pivonkova H, Dzamba D, Kubista M, et al. Distinct expression/function of potassium and chloride channels contributes to the diverse volume regulation in cortical astrocytes of GFAP/EGFP mice. *PLoS One.* 2012;7(1):e29725.

14. Elorza-Vidal X, Sirisi S, Gaitan-Penas H, Perez-Rius C, Alonso-Gardon M, Armand-Ugon M, et al. GlialCAM/MLC1 modulates LRRC8/VRAC currents in an indirect manner: Implications for megalencephalic leukoencephalopathy. *Neurobiol Dis.* 2018;119:88-99.

15. Gilbert A, Vidal XE, Estevez R, Cohen-Salmon M, and Boulay AC. Postnatal development of the astrocyte perivascular MLC1/GlialCAM complex defines a temporal window for the gliovascular unit maturation. *Brain Struct Funct.* 2019;224(3):1267-78.

16. Slaoui L, Gilbert A, Federici L, Rancillac A, Gelot A, Favier M, et al. In mice and humans, the brain's blood vessels mature postnatally to acquire barrier and contractile properties. *BioRXiv.* 2021.

17. Cohen-Salmon M, Slaoui L, Mazare N, Gilbert A, Oudart M, Alvear-Perez R, et al. Astrocytes in the regulation of cerebrovascular functions. *Glia.* 2021;69(4):817-41.

18. Boulay AC, Saubamea B, Decleves X, and Cohen-Salmon M. Purification of Mouse Brain Vessels. *J Vis Exp.* 2015;105(105).

19. Dagenais C, Rousselle C, Pollack GM, and Scherrmann JM. Development of an in situ mouse brain perfusion model and its application to mdr1a P-glycoprotein-deficient mice. *J Cereb Blood Flow Metab.* 2000;20(2):381-6.

20. Ezan P, Andre P, Cisternino S, Saubamea B, Boulay AC, Doutremer S, et al. Deletion of astroglial connexins weakens the blood-brain barrier. *J Cereb Blood Flow Metab.* 2012;32(8):1457-67.

21. Iadecola C. The Neurovascular Unit Coming of Age: A Journey through Neurovascular Coupling in Health and Disease. *Neuron.* 2017;96(1):17-42.

22. Hingot V, Brodin C, Lebrun F, Heiles B, Chagnot A, Yetim M, et al. Early Ultrafast Ultrasound Imaging of Cerebral Perfusion correlates with Ischemic Stroke outcomes and responses to treatment in Mice. *Theranostics.* 2020;10(17):7480-91.

23. Osmanski BF, Pezet S, Ricobaraza A, Lenkei Z, and Tanter M. Functional ultrasound imaging of intrinsic connectivity in the living rat brain with high spatiotemporal resolution. *Nat Commun.* 2014;5:5023.

24. Bertolo A, Nouhoum M, Cazzanelli S, Ferrier J, Mariani JC, Kliewer A, et al. Whole-Brain 3D Activation and Functional Connectivity Mapping in Mice using Transcranial Functional Ultrasound Imaging. *J Vis Exp.* 2021(168).

25. Hwang J, Vu HM, Kim MS, and Lim HH. Plasma membrane localization of MLC1 regulates cellular morphology and motility. *Mol Brain.* 2019;12(1):116.

26. Nixdorf-Bergweiler BE, Albrecht D, and Heinemann U. Developmental changes in the number, size, and orientation of GFAP-positive cells in the CA1 region of rat hippocampus. *Glia.* 1994;12(3):180-95.

27. Kress BT, Iliff JJ, Xia M, Wang M, Wei HS, Zeppenfeld D, et al. Impairment of paravascular clearance pathways in the aging brain. *Ann Neurol.* 2014;76(6):845-61.

28. Haj-Yasein NN, Jensen V, Ostby I, Omholt SW, Voipio J, Kaila K, et al. Aquaporin-4 regulates extracellular space volume dynamics during high-frequency synaptic stimulation: a gene deletion study in mouse hippocampus. *Glia.* 2012;60(6):867-74.

29. Iliff JJ, Lee H, Yu M, Feng T, Logan J, Nedergaard M, et al. Brain-wide pathway for waste clearance captured by contrast-enhanced MRI. *Journal of Clinical Investigation.* 2013;123(3):1299-309.

30. Abbott NJ, Ronnback L, and Hansson E. Astrocyte-endothelial interactions at the blood-brain barrier. *Nat Rev Neurosci.* 2006;7(1):41-53.

31. Yao LL, Hu JX, Li Q, Lee D, Ren X, Zhang JS, et al. Astrocytic neogenin/netrin-1 pathway promotes blood vessel homeostasis and function in mouse cortex. *J Clin Invest.* 2020;130(12):6490-509.

32. Abbott NJ, Pizzo ME, Preston JE, Janigro D, and Thorne RG. The role of brain barriers in fluid movement in the CNS: is there a 'glymphatic' system? *Acta Neuropathol.* 2018;135(3):387-407.

33. van der Knaap MS, Boor I, and Estevez R. Megalencephalic leukoencephalopathy with subcortical cysts: chronic white matter oedema due to a defect in brain ion and water homoeostasis. *Lancet Neurol.* 2012;11(11):973-85.

34. Rasmussen MK, Mestre H, and Nedergaard M. The glymphatic pathway in neurological disorders. *Lancet Neurol.* 2018;17(11):1016-24.

35. Owens GK. Regulation of differentiation of vascular smooth muscle cells. *Physiol Rev.* 1995;75(3):487-517.

36. Owens GK, Kumar MS, and Wamhoff BR. Molecular regulation of vascular smooth muscle cell differentiation in development and disease. *Physiol Rev.* 2004;84(3):767-801.

37. Chen ZL, Yao Y, Norris EH, Kruyer A, Jno-Charles O, Akhmerov A, et al. Ablation of astrocytic laminin impairs vascular smooth muscle cell function and leads to hemorrhagic stroke. *J Cell Biol.* 2013;202(2):381-95.

38. El-Khoury N, Braun A, Hu F, Pandey M, Nedergaard M, Lagamma EF, et al. Astrocyte end-feet in germinal matrix, cerebral cortex, and white matter in developing infants. *Pediatr Res.* 2006;59(5):673-9.

39. Takasato Y, Rapoport SI, and Smith QR. An in situ brain perfusion technique to study cerebrovascular transport in the rat. *Am J Physiol.* 1984;247(3 Pt 2):H484-93.

40. Anfray A, Drieu A, Hingot V, Hommet Y, Yetim M, Rubio M, et al. Circulating tPA contributes to neurovascular coupling by a mechanism involving the endothelial NMDA receptors. *J Cereb Blood Flow Metab.* 2019:271678X19883599.

41. Karlsson M, and Nordell B. Phantom and in vivo study of the Look-Locher T1 mapping method. *Magn Reson Imaging.* 1999;17(10):1481-8.

42. Gaberel T, Gakuba C, Goulay R, Martinez De Lizarrondo S, Hanouz JL, Emery E, et al. Impaired glymphatic perfusion after strokes revealed by contrast-enhanced MRI: a new target for fibrinolysis? *Stroke.* 2014;45(10):3092-6.

43. Schindelin J, Arganda-Carreras I, Frise E, Kaynig V, Longair M, Pietzsch T, et al. Fiji: an open-source platform for biological-image analysis. *Nat Methods.* 2012;9(7):676-82.

44. Renier N, Wu Z, Simon DJ, Yang J, Ariel P, and Tessier-Lavigne M. iDISCO: a simple, rapid method to immunolabel large tissue samples for volume imaging. *Cell.* 2014;159(4):896-910.

45. Pannasch U, Freche D, Dallerac G, Ghezali G, Escartin C, Ezan P, et al. Connexin 30 sets synaptic strength by controlling astroglial synapse invasion. *Nat Neurosci.* 2014;17(4):549-58.

46. Ghezali G, Calvo CF, Pillet LE, Llense F, Ezan P, Pannasch U, et al. Connexin 30 controls astroglial polarization during postnatal brain development. *Development.* 2018;145(4).

47. Bankhead P, Loughrey MB, Fernandez JA, Dombrowski Y, McArt DG, Dunne PD, et al. QuPath: Open source software for digital pathology image analysis. *Sci Rep.* 2017;7(1):16878.

Figure Legends

Fig. 1. The absence of MLC1 has no effect on BBB integrity or the organization of the endothelial network.

a mRNA expression (using qPCR) of *Abcb1* (encoding P-gP) and *Cldn5* (encoding claudin5) in MVs purified from WT and *Mlc1* KO whole brains on P5 and P15 and at 2 months (P60). Signals were normalized against *Gapdh*. Groups were compared using a two-tailed Mann-Whitney test. The data are presented as a Tukey box plot (n = 3 or 4 samples per genotype; mice per sample: 5 for P5; 3 for P15; 2 for P60)). Data are given in **Table S1**. **b** Western blot detection and analysis of P-gP and claudin5 in protein extracts from MVs purified from WT and *Mlc1* KO whole brains on P5 and P15 and at 2 months (P60). Signals were normalized against histone H3. Two-tailed Mann-Whitney test. The data are represented in a Tukey box plot (n = 4 or 5 sample per genotype; mice per sample: 5 for P5; 3 for P15; 2 for P60). Data are given in **Table S2**. **c** Apparent diffusion coefficient (ADC) values in the cortex of 2-month-old WT and *Mlc1* KO mice. Two-tailed Student's T test. The data are represented in a Tukey box plot (n = 7 mice per genotype). Data are given in **Table S3**. **d** BBB integrity, assessed by measuring the brain vascular volume (Vv, in µL/g) after *in situ* brain perfusion with [^{14}C]-sucrose and a normal hydrostatic vascular pressure (Albumin -; 120 mmHg) or an elevated hydrostatic vascular pressure (Albumin +; 180 mmHg) in 2-month-old WT (black) and *Mlc1* KO mice (red). Two-tailed Mann-Whitney test. The data are represented in a Tukey box plot (n = 8 WT and 9 *Mlc1* KO mice for Albumin -; n = 11 WT and 12 *Mlc1* KO mice for Albumin +). Data are given in **Table S4**. **e g** Representative 3D images of the endothelial architecture in cleared somatosensory cortex. Parenchymal (Z stack 320µm; scale bar: 100µm) **(e)** and pial **(g)** vessels (Z stack 50 µm; scale bar: 500µm) samples from 2-month-old WT and *Mlc1* KO mice, after immunolabeling for Pecam1. **f h** A comparative analysis of vessel length, branching and tortuosity in WT mice (black) and *Mlc1* KO mice (red) in the parenchymal cortex, normalized on sample volume **(f)** and cortical surface, normalized on sample surface **(h)**. One-tailed Mann-Whitney test. The data are represented in a Tukey box plot (n = 3 mice per genotype). Data are given in **Table S5**. *, $p \leq 0.05$, **, $p \leq 0.01$, ***, $p \leq 0.001$, and ns: not significant.

Fig. 2. MLC1 is crucial for the molecular maturation of VSMC contractility

a qPCR results for *Acta2* (encoding SMA) and *Atp1b1* in MVs purified from WT and *Mlc1* KO whole brains on P5 and P15 and at 2 months. Signals are normalized against *Gapdh*. Two-tailed Mann-Whitney test. The data are represented in a Tukey box plot (n = 3 to 5 samples per genotype; mice per sample: 5 for P5; 3 for P15; 2 for

P60)). Data are given in **Table S1**. **b** Western blot detection and analysis of SMA in protein extracts from MVs purified from WT and *Mlc1* KO whole brains on P5 and P15 and at 2 months (P60). Arrows indicate abnormally low SMA-positive bands. Signals were normalized against histone H3. Two-tailed Mann-Whitney test. The data are represented in a Tukey box plot (n = 4 or 5 samples per genotype; mice per sample: 5 for P5; 3 for P15; 2 for P60)). Data are given in **Table S2**. **c e** Representative 3D images of the VSMC arterial network in cleared somatosensory cortex. Parenchymal (Z stack 600 µm; scale bar: 100µm) **(c)** and pial vessels (Z stack 50 µm; scale bar: 500µm) **(e)** samples in 2-month-old WT and *Mlc1* KO mice after immunolabeling for SMA. **d f** Comparative analysis of arterial length, branching, tortuosity, and anastomosis in WT mice (black boxes) and *Mlc1* KO mice (red boxes) in the cortical parenchyma, normalized on sample volume (**d**) and at the cortical surface, normalized on sample surface (**f**). One-tailed Mann-Whitney test. The data are represented in a Tukey box plot (n = 3 mice per genotype). Data are given in **Table S5**. *, $p \leq 0.05$, **, $p \leq 0.01$, ***, $p \leq 0.001$, and ns: not significant.

Fig. 3. MLC1 is crucial for the postnatal acquisition of VSMC contractility, arterial diameter, and neurovascular coupling

a-c *Ex vivo* analysis of mean vascular constriction and dilation upon application of U46619 (50 nM) to somatosensory cortical slices from P5, P15 and 2-month-old WT mice (black traces) and *Mlc1* KO mice (red traces). **a** Representative infrared images of a cortical penetrating arteriole constriction in response to bath application of U46619 and dilation upon washing at P60. The vessel lumen is indicated by a dotted line. Scale bar: 10µm. **b** Contraction and dilation slopes on P5, P15 and P60. 0 min corresponds to the addition of U46619 to the recording chamber medium. The data are quoted as the mean ± SEM. **c** Analysis of the amplitude and slope of the contraction. Two-tailed Mann-Whitney test. The data are represented in a Tukey box plot (n = 13 vessels from WT and 13 *Mlc1* KO mice on P5; n = 9 vessels from WT and 12 *Mlc1* KO mice at P15; n = 8 vessels from WT and 11 *Mlc1* KO mice at P60; 3 mice per group). Data are given in **Table S6**. **d** *In vivo* ULM measurement of cortical arterial vessel diameter after intravenous microbubble injection in 2-month-old WT and *Mlc1* KO mice. **Left:** Schematic representation of the experiment; **Middle:** Cerebrovascular maps of WT and *Mlc1* KO mice, showing the arterial (red) and venous (blue) velocities in mm/s (scale bar: 0.15 cm); **Right:** Measurement of the penetrating arteries' diameter using ULM imaging of an injected microbubbles. The data are represented in a Tukey box plot. Two-tailed Mann–Whitney test (n=6 WT mice and *Mlc1* KO mice). Data are given in **Table S7**. **e** *In vivo* fUS analysis of CBF in the somatosensory cortex after whisker stimulation. **Left:** Schematic representation of the experiment (S1bf: bregma -1.5 mm, somatosensory barrel field cortex); **Middle:** fUS power doppler signal traces during whisker stimulation of 2-month-old WT mice (black) and *Mlc1* KO mice (red) mice; **Right:** Quantification of the normalized CBF variations. Two-tailed Mann–Whitney test. Curves in transparency correspond to the SEM (n=11 WT mice and 12 *Mlc1* KO mice). Data are given in **Table S7**. *, $p \leq 0.05$, **, $p \leq 0.01$, ***, $p \leq 0.001$, and ns: not significant.

Fig. 4. The absence of MLC1 alters the molecular maturation and adherence of PvAPs

a Representative confocal projection images of the immunofluorescent detection of GlialCAM, Aqp4 and Cx43 (red) on brain cortex sections from WT and *Mlc1* KO mice on P5, P15 and at 2 months. Vessels are stained with isolectin B4 (green) and nuclei are stained with Hoechst dye (blue). Scale bar: 20 µm. **b** Western blot detection and analysis of GlialCAM, Aqp4 and Cx43 in protein extracts from whole brains from WT and *Mlc1* KO mice on P5 and P15 and 2 months. **c** Western blot detection and analysis of Aqp4 in protein extracts from MVs purified from WT and *Mlc1* KO whole brains at 2 months (P60). **d** Western blot detection and analysis of NF-M in protein extracts from MVs purified from WT and *Mlc1* KO whole brains at 2 months (P60)**.** Signals were normalized against stain-free membranes. Two-tailed Mann-Whitney test. The data are represented in a Tukey box plot (for whole brain: n = 5 samples per genotype (one mouse per sample); for purified MVs: n = 5 samples per genotype (2 mice per sample). Data are given in **Table S2**. **e** Schematic interpretation of the data showed in (**c**) and (**d**). In *Mlc1* KO mice, the PvAPs (green) and neuronal associated fibers (red) are lost during the MV purification process (BL, yellow; mural cell, brown; EC, blue). MLC1 is represented by pink dots in WT. *, $p \leq 0.05$, **, $p \leq 0.01$, ***, $p \leq 0.001$, and ns: not significant.

Fig. 5. The absence of MLC1 alters astrocyte morphology and polarity

a A Sholl analysis of the ramification of hippocampal CA1 astrocytes immunolabeled for GFAP (black) in WT and *Mlc1* KO 2-month-old mice. Concentric circles are drawn starting from the astrocyte's soma. Scale bar: 20µm. **b** Quantitative analysis of the astrocyte's ramifications. Two-way ANOVA test followed by a Bonferroni *post hoc* test. Data are quoted as the median ± IQR (n=48 *Mlc1* KO cells; n=44 WT cells; n=3 mice per genotype). Data are given in **Table S8**. **c** Grid-baseline analysis of the orientation of the GFAP-immunolabeled astrocytic processes (white) toward the hippocampal pyramidal cell layer (PL) in WT and *Mlc1* KO 2-old-month mice. Nuclei are labeled with Hoechst dye (blue). Scale bar: 20µm. **d** Quantitative analysis of astrocyte process orientation toward the PL. The polarity index is the ratio between of axial GFAP contacts and lateral GFAP contacts. A polarity index of 1 means that there is no polarity. Two-tailed Mann-Whitney test. The data are represented in a Tukey box plot (n=52 *Mlc1* KO cells; n= 47 WT cells; 3 mice per genotype). Data are given in **Table S8**. **e** Grid-baseline analysis of the orientation of the GFAP immunolabeled astrocytic processes (white) toward vessels labeled with isolectin B4 (green) in WT and *Mlc1* KO 2-month-old mice. Nuclei are labeled with Hoechst dye (blue). Scale bar: 20µm. **f** Quantitative analysis of astrocyte process orientation toward vessels. The polarity index is the ratio between of axial GFAP contacts and lateral GFAP contacts. A polarity index of 1 means that there is no polarity. Two-tailed Mann-Whitney test. The data are represented in a Tukey box plot (n=41 *Mlc1* KO cells; n= 41 WT cells; 3 mice per genotype). Data are given in **Table S8**. *, $p \leq 0.05$, **, $p \leq 0.01$, ***, $p \leq 0.001$, and ns: not significant.

Fig. 6. The absence of MLC1 alters PvAP polarity and perivascular coverage

a-e Representative TEM images of the GVU in the hippocampus of 2-month-old WT and *Mlc1* KO mice (n=3 mice per genotype). Images are presented in pairs, with artificial colors in the lower panel: PvAPs in yellow; gap junctions in green; axons or synapses in red; mural cell in light blue; endothelial cells in dark blue; and TJs in purple. **a** In WT mice, PvAPs fully cover endothelial cells linked by a TJ and surrounded by a continuous basal lamina (BL). **b-e.** Data from *Mlc1* KO mice. **b** PvAPs are separated by an axon which contacts the endothelial BL (arrow head). **c** A PvAP is surrounded by the BL (arrow head). **d** Several PvAPs are stacked on the top of each other and are linked by extended gap junctions (arrow head). **e** PvAPs are separated by 4 axons that directly contact the vascular BL (arrow head). **f** Quantification of capillaries and venules contacted by neural processes (axons or synapses). T-test. The data are represented in a Tukey box plot (n=399 *Mlc1* KO cortical vessels; n=301 *Mlc1* KO hippocampal vessels; n=286 WT cortical vessels; n=287 WT hippocampal vessels; n=3 mice per genotype). **g** Percentage of vessels contacted by a normal PvAP (swelling 0), moderately swollen PvAP (swelling 1), or edematous PvAP (swelling 2) in hippocampus and cortex of 2-month-old mice. Two-tailed Mann-Whitney test . The data are represented in a Tukey box plot (n=399 *Mlc1* KO cortical vessels; n=301 *Mlc1* KO hippocampal vessels; n=286 WT cortical vessels; n=287 WT hippocampal vessels; n=3 mice per genotype). Data for (**f**) and (**g**) are given in **Table S9**. *, $p \leq 0.05$, **, $p \leq 0.01$, ***, $p \leq 0.001$, and ns: not significant.

Fig 7. Contrast-enhanced MRI reveals reduced tracer dispersion from the CSF to the parenchyma in *Mlc1* KO mice.

1 µL DOTA-Gd was injected into the mouse's CSF through the cisterna magna (**a**). After injection, the tracer disperses through the brain into the subarachnoid space before entering the deep parenchyma through the perivascular spaces (**b**). Quantitative contrast maps in WT and *Mlc1* KO mice, 10 and 45 minutes after contrast

bioRxiv preprint doi: https://doi.org/10.1101/2021.05.17.444434; this version posted May 17, 2021. The copyright holder for this preprint (which was not certified by peer review) is the author/funder. All rights reserved. No reuse allowed without permission.

injection (scale bar: 1cm) (**c**). Based on the dynamic acquisitions, the changes over time in contrast agent concentration were extracted, and the mean contrast concentration and the contrast slope were calculated for the cerebellum, midbrain, septal area, and cortex. Two-tailed Mann-Whitney test. The data are represented in a Tukey box plot (n = 9 per genotype (8 in the cortex)). Data are given in **Table S3**. *, p ≤ 0.05, **, p ≤ 0.01, ***, p ≤ 0.001, and ns: not significant.

Fig. 8. The absence of MLC1 alters the postnatal development of astrocyte morphology and polarity

a-d. A Sholl analysis of astrocyte ramification in WT and *Mlc1* KO mice on P10 (**a b**) and P15 (**c b**). Concentric circles are drawn, starting from the astrocyte's soma. Scale bar: 20µm. **b d** Quantitative analyses of astrocyte ramification on P10 (**a**) and P15 (**c**). Two-way ANOVA test followed by a Bonferroni *post hoc* test (P10: n=53 *Mlc1* KO cells; n=49 WT cells; n=3 mice per genotype; P15: n=51 *Mlc1* KO cells; n=50 WT cells; n=3 mice per genotype). Data are presented in **Table S8**. **e-h** Grid analysis of astrocyte polarity towards vessel in WT and *Mlc1* KO on P10 (**e**) and P15 (**g**). Scale bar: 20µm. **f-h** Quantitative analysis of astrocyte process orientation toward vessels on P10 (**f**) and P15 (**g**). The polarity index is the ratio between of axial GFAP contacts and lateral GFAP contacts. A polarity index of 1 means that there is no polarity. Two-tailed Mann-Whitney test. The data are represented in a Tukey box plot (P10: n=37 *Mlc1* KO cells; n=26 WT cells; n=3 mice per genotype; P15: n=48 *Mlc1* KO cells; n=46 WT cells; n=3 mice per genotype). Data are presented in **Table S8**. *, p ≤ 0.05, **, p ≤ 0.01, ***, p ≤ 0.001, and ns: not significant.

Fig. 9. The absence of MLC1 alters the postnatal development of astrocyte perivascular coverage

a Representative TEM images of the gliovascular interface in the cortex of WT and *Mlc1* KO mice on P10 and P15. Images are presented in pairs, with artificial colors in the lower panel: PvAPs in yellow; axons in red; TJs in purple; and endothelial cells in blue. **b** Percentage of the vessel diameter covered by PvAPs in the cortex of WT and *Mlc*1 KO mice on P5, P10, P15, and P60. Two-tailed Mann-Whitney test. The data are represented in a Tukey box plot (n = 46 vessels from WT mice and 68 *Mlc1* KO mice on P5, n=4 mice per genotype; n=121 vessels from WT mice and 81 *Mlc1* KO mice on P10, n=3 mice per genotype; n=207 vessels from WT mice and 144 *Mlc1* KO mice at P15, n=4 mice per genotype; n=143 vessels from WT mice and 134 *Mlc1* KO mice at P60, n=3 mice per genotype). Data are presented in **Table S9**. *, p ≤ 0.05, **, p ≤ 0.01, ***, p ≤ 0.001, and ns: not significant.

Supplementary information

Fig. S1 The absence of MLC1 causes overall brain swelling

Anatomical T2-weighted MRI (**a**); wich representative images of WT and KO mice are shown (**b**); was used to measure the brain volume (**c**) and the ventricles relative volume (**d**). The ADC was calculated for the midbrain (**E**), septal area (**F**), and thalamus (**G**). Two-tailed Student's T test. The data are represented in a Tukey box plot (n=7 mice per genotype). Data are presented in **Table S3.** *, $p \leq 0.05$, **, $p \leq 0.01$, ***, $p \leq 0.001$, and ns: not significant.

Fig. S2 Examples of changes in the architecture of GVU in 2-month-old *Mlc1* KO mice

a-c Representative TEM images of the GVU in the cortex of 2-month-old WT mice (**a**) and *Mlc1* KO mice (**b**) (n=3 mice per genotype). Images are presented in pairs, with artificial colors in the lower panel: PvAPs in yellow; gap junctions in green; synapse in orange; endothelial cells in dark blue; mural cell in light blue; and TJs in purple. **a** A WT sample showing continuous PvAP coverage around an endothelial cell. The PvAPs are linked by gap junctions **b** An *Mlc1* KO sample: **Left:** A synapse contacts the endothelial BL (arrowhead); **Middle:** A PvAP interdigitates into another PvAP and forms a large annular gap junction (arrowhead); **Right:** Stacked PvAPs surrounded by BL (arrowhead).

Fig. S3: Developmental perivascular expression of MLC1 in the human cortex

a-e Immunohistochemical analysis of MLC1 in the developing human cortex. **a-e** Representative images of MLC1-immunostained cortical slices (left) and a higher magnification image of the parenchyma in the boxed areas (right) at the prenatal stage (15 to 39 wg) (**a**); 0 to 1 year of age (B); 3 to 4 years of age (**c**); 10 to 13 years of age (D); 16 and 17 year of age (**e**). Scale bar: 100µm. MLC1 immunostaining (arrowheads) was revealed with DAB. **f.** DAB intensity was quantified and quoted as the mean ± SD. We applied the Kruskal-Wallis test (overall, in bold) and a one-tailed Mann-Whitney test (for comparing stages). The number of samples per developmental age was 5 for prenatal, 5 for 0-1 years, 4 for 3-4 years, 4 for 10-13 years, and 2 for 16-17 years. Data are presented in

Table S1 qPCRs data

Table S2 Western blot data

Table S3 MRI data

Table S4 *in situ* perfusion data

Table S5 Immunolabeling data

Table S6 *Ex vivo* VSMC contractility data

Table S7 ULM and fUS data

Table S8 Measurements of astrocyte morphology and polarity

Table S9 Electron microscopy data

Table S10 Immunohistochemistry data

Table S11 Resource table

Fig. 1

bioRxiv preprint doi: https://doi.org/10.1101/2021.05.17.444434; this version posted May 17, 2021. The copyright holder for this preprint (which was not certified by peer review) is the author/funder. All rights reserved. No reuse allowed without permission.

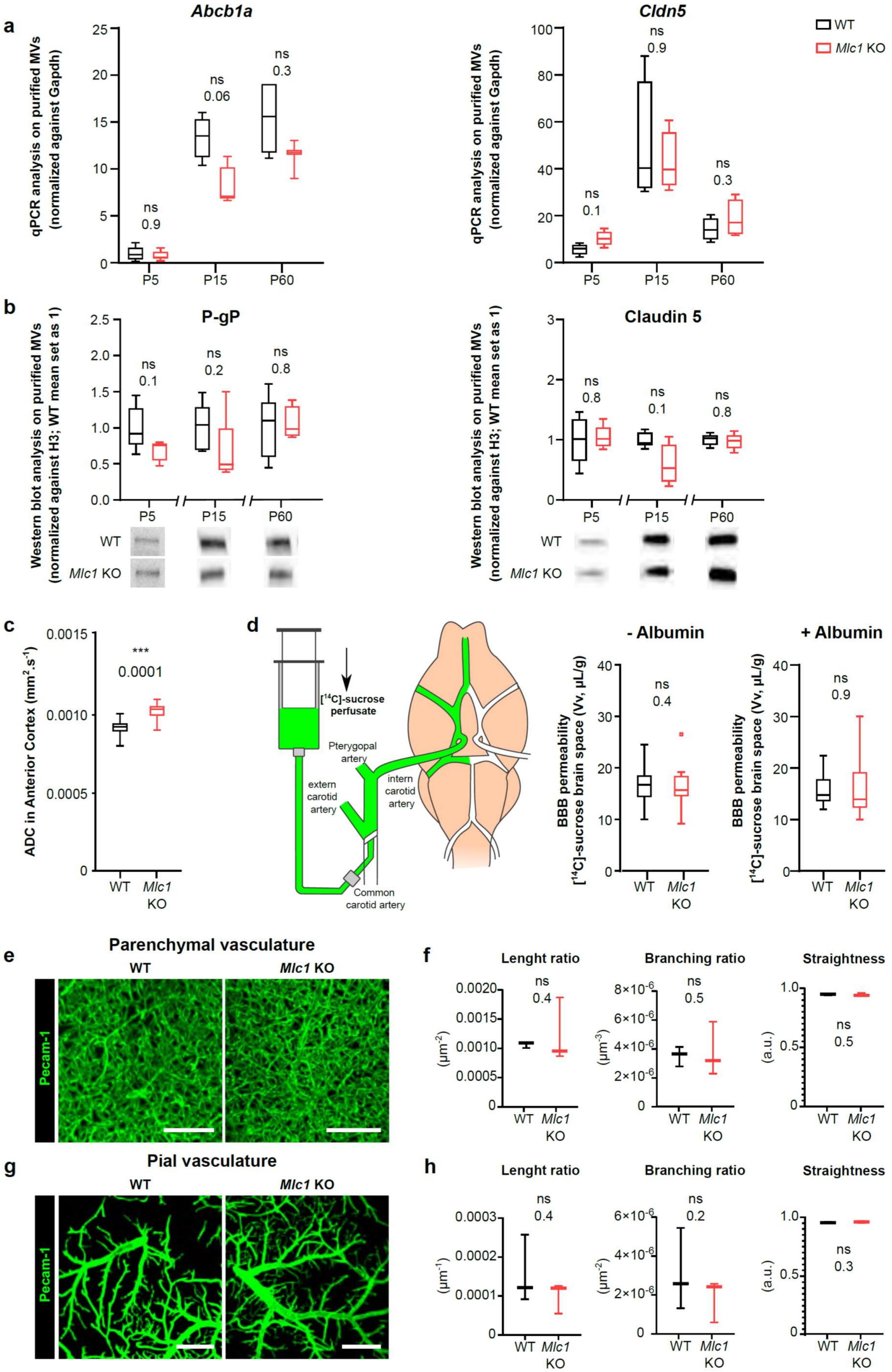

Fig. 2

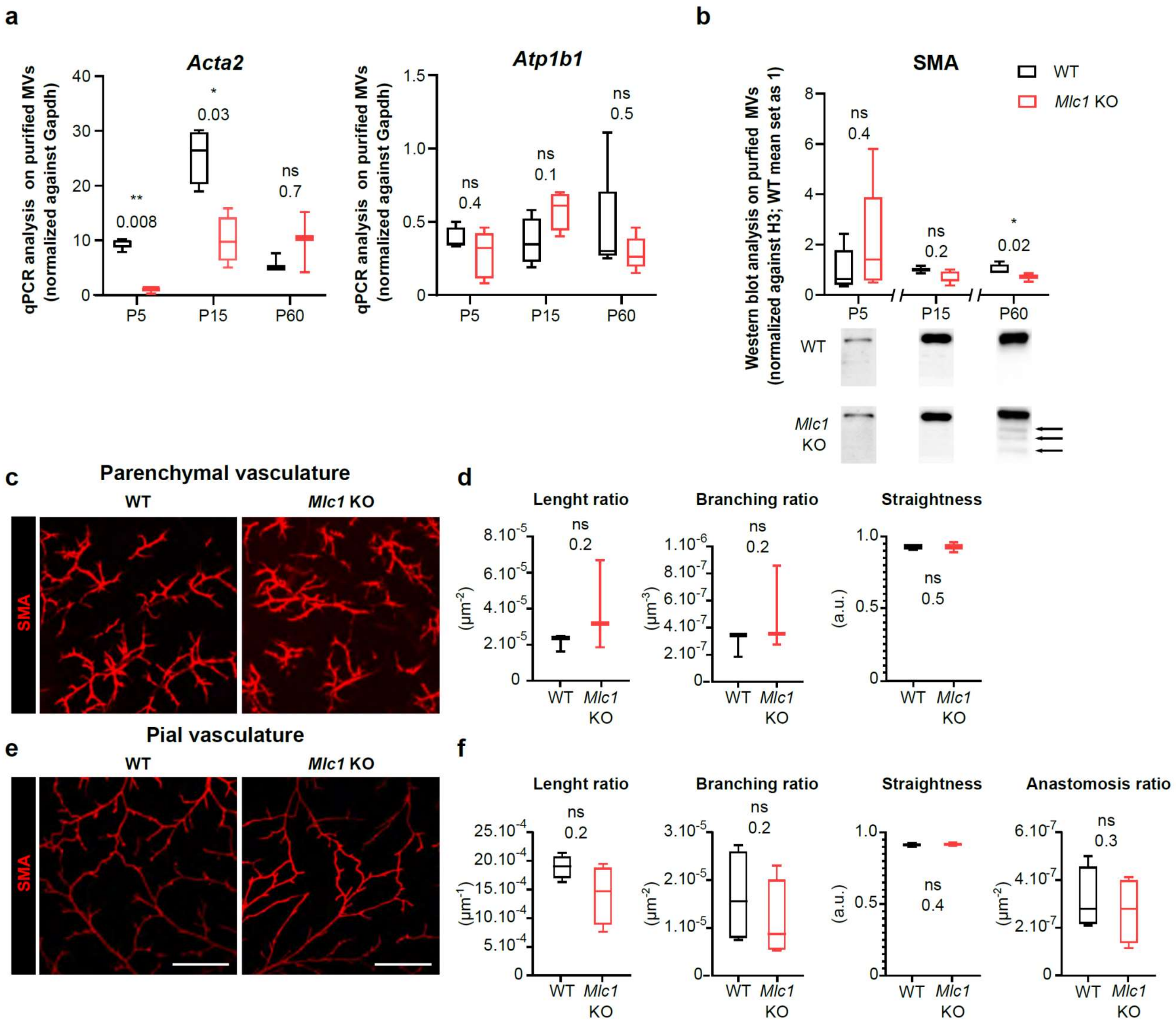
a
Acta2
qPCR analysis on purified MVs (normalized against Gapdh)
40
30
20
10
0
**
0.008
*
0.03
ns
0.7
P5
P15
P60
Atp1b1
qPCR analysis on purified MVs (normalized against Gapdh)
1.5
1.0
0.5
0
ns
0.4
ns
0.1
ns
0.5
P5
P15
P60
b
SMA
WT
Mlc1 KO
Western blot analysis on purified MVs (normalized against H3; WT mean set as 1)
8
6
4
2
0
ns
0.4
ns
0.2
*
0.02
P5
P15
P60
WT
Mlc1 KO
c
Parenchymal vasculature
WT
Mlc1 KO
SMA
d
Lenght ratio
(µm⁻²)
8.10⁻⁵
6.10⁻⁵
4.10⁻⁵
2.10⁻⁵
0
ns
0.2
WT
Mlc1 KO
Branching ratio
(µm⁻³)
1.10⁻⁶
8.10⁻⁷
6.10⁻⁷
4.10⁻⁷
2.10⁻⁷
0
ns
0.2
WT
Mlc1 KO
Straightness
(a.u.)
1.0
0.5
0
ns
0.5
WT
Mlc1 KO
e
Pial vasculature
WT
Mlc1 KO
SMA
f
Lenght ratio
(µm⁻¹)
25.10⁻⁴
20.10⁻⁴
15.10⁻⁴
10.10⁻⁴
5.10⁻⁴
0
ns
0.2
WT
Mlc1 KO
Branching ratio
(µm⁻²)
3.10⁻⁵
2.10⁻⁵
1.10⁻⁵
0
ns
0.2
WT
Mlc1 KO
Straightness
(a.u.)
1.0
0.5
0
ns
0.4
WT
Mlc1 KO
Anastomosis ratio
(µm⁻²)
6.10⁻⁷
4.10⁻⁷
2.10⁻⁷
0
ns
0.3
WT
Mlc1 KO

Fig. 3

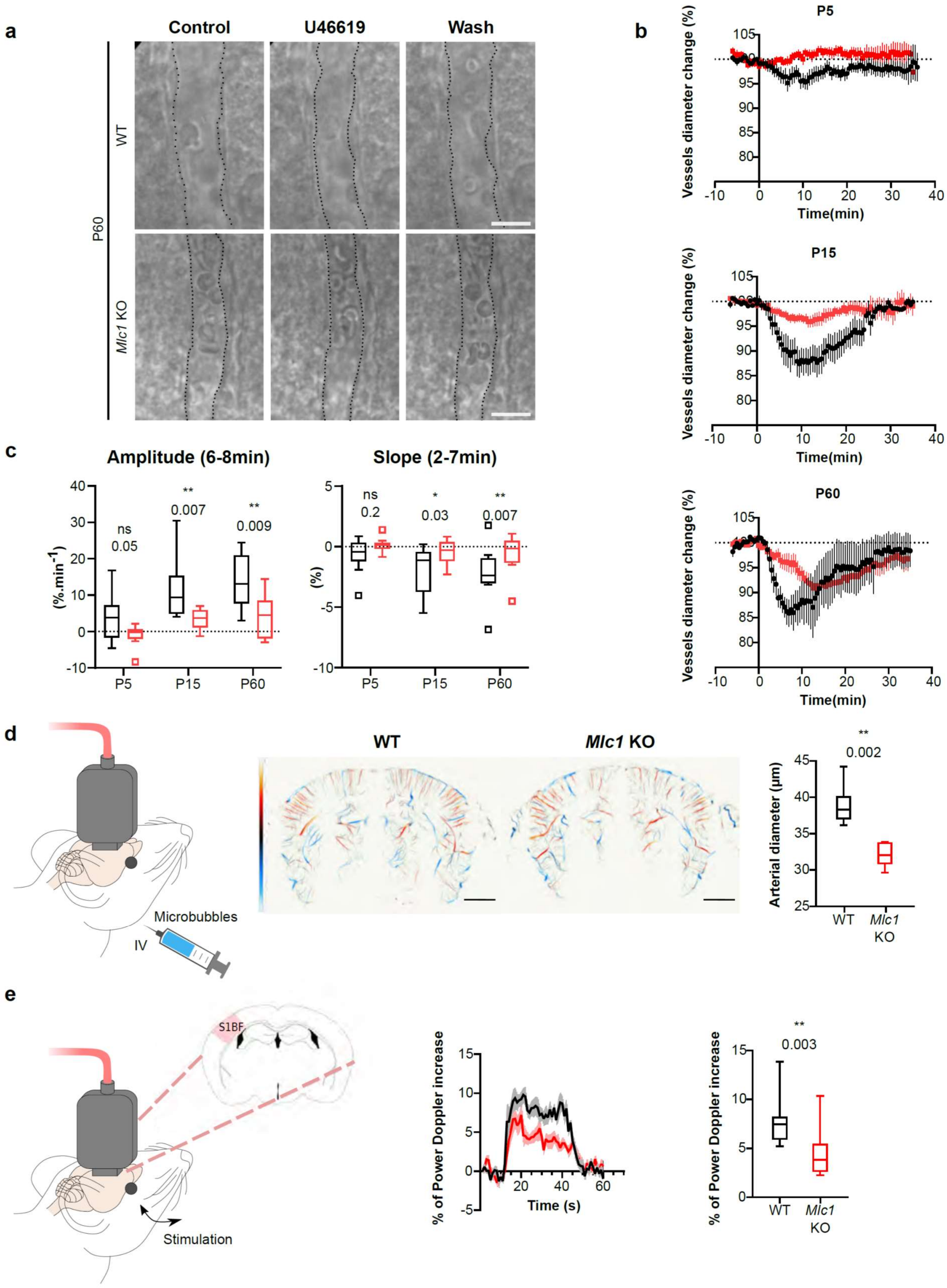
a
Control
U46619
Wash
P60
WT
Mlc1 KO
b
P5
P15
P60
Vessels diameter change (%)
105
100
95
90
85
80
-10
0
10
20
30
40
Time(min)
c
Amplitude (6-8min)
(%.min-1)
40
30
20
10
0
-10
ns
0.05
**
0.007
**
0.009
P5
P15
P60
Slope (2-7min)
(%)
5
0
-5
-10
ns
0.2
*
0.03
**
0.007
d
Microbubbles
IV
WT
Mlc1 KO
Arterial diameter (µm)
45
40
35
30
25
**
0.002
WT
Mlc1 KO
e
S1BF
Stimulation
% of Power Doppler increase
15
10
5
0
-5
20
40
60
Time (s)
**
0.003
WT
Mlc1 KO

Fig. 4

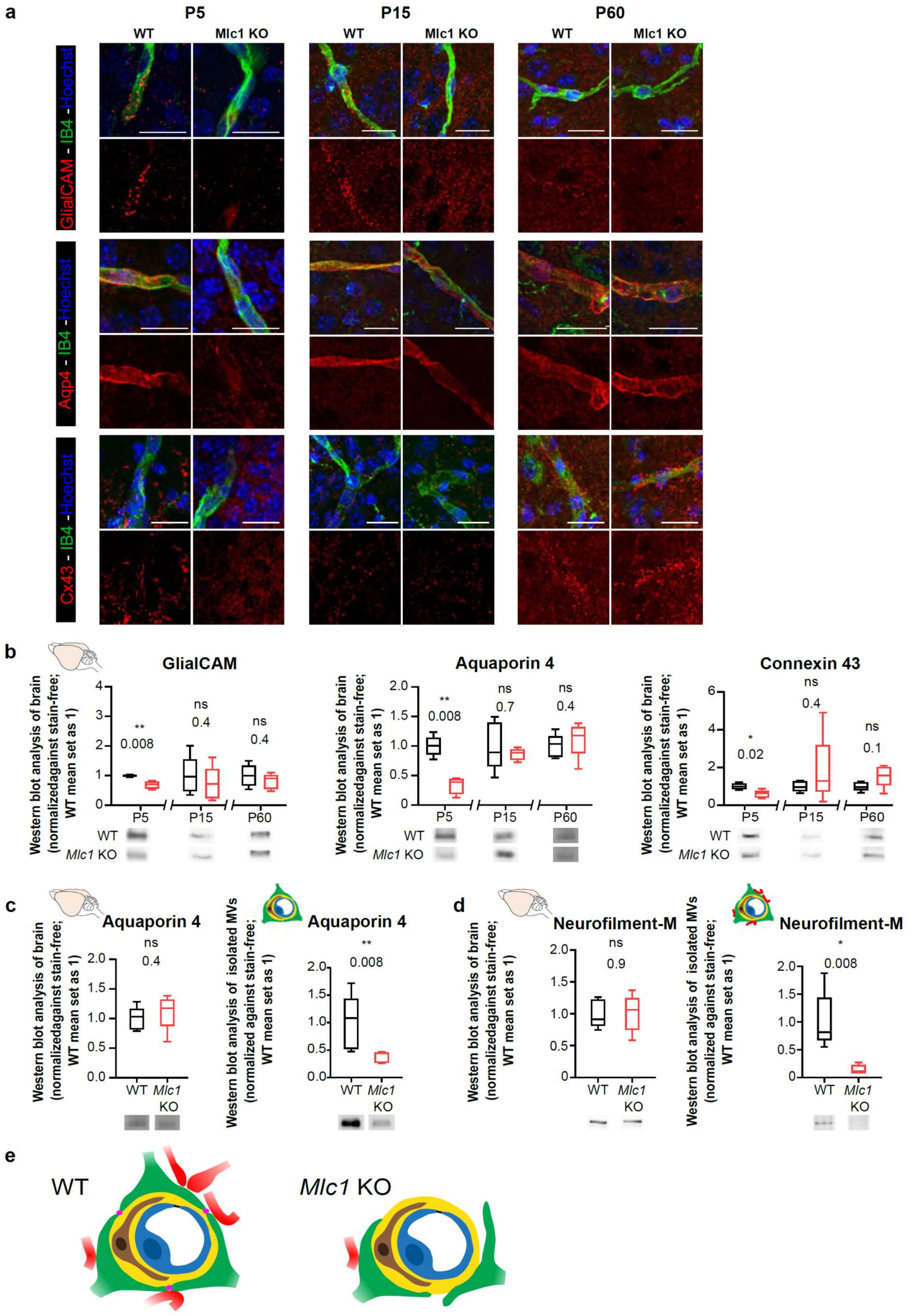
a
P5
P15
P60
WT
Mlc1 KO
GlialCAM - IB4 - Hoechst
Aqp4 - IB4 - Hoechst
Cx43 - IB4 - Hoechst
b
GlialCAM
Aquaporin 4
Connexin 43
Western blot analysis of brain (normalizedagainst stain-free; WT mean set as 1)
** 0.008
ns 0.4
ns 0.4
** 0.008
ns 0.7
ns 0.4
* 0.02
ns 0.4
ns 0.1
P5
P15
P60
WT
Mlc1 KO
c
Aquaporin 4
Western blot analysis of brain (normalizedagainst stain-free; WT mean set as 1)
ns 0.4
Western blot analysis of isolated MVs (normalized against stain-free; WT mean set as 1)
** 0.008
WT
Mlc1 KO
d
Neurofilment-M
Western blot analysis of brain (normalizedagainst stain-free; WT mean set as 1)
ns 0.9
Western blot analysis of isolated MVs (normalized against stain-free; WT mean set as 1)
* 0.008
e
WT
Mlc1 KO

Fig. 5

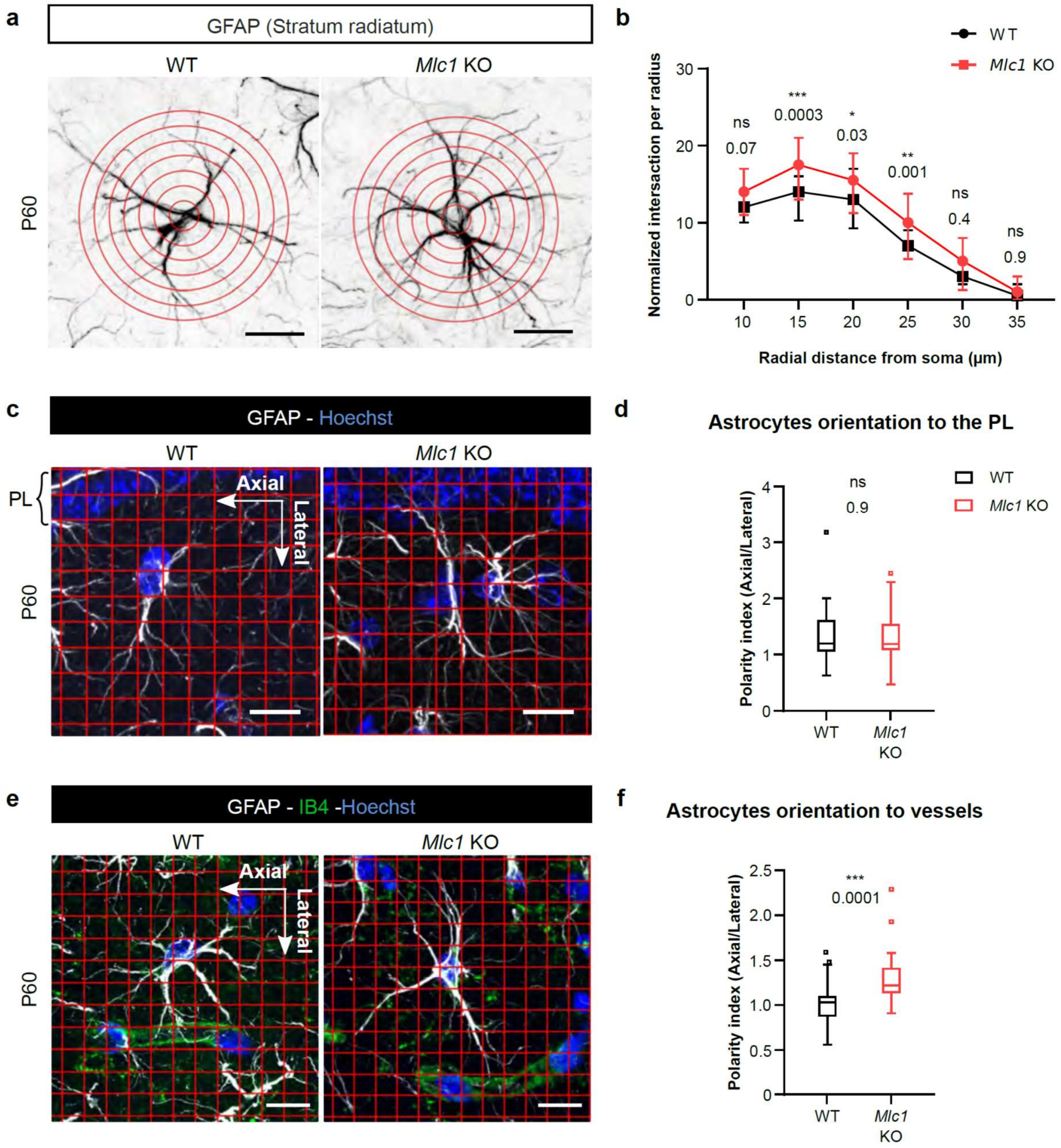
a
GFAP (Stratum radiatum)
WT
Mlc1 KO
P60
b
WT
Mlc1 KO
Normalized intersaction per radius
30
20
10
0
ns
0.07
***
0.0003
*
0.03
**
0.001
ns
0.4
ns
0.9
10
15
20
25
30
35
Radial distance from soma (µm)
c
GFAP - Hoechst
WT
Mlc1 KO
PL
Axial
Lateral
P60
d
Astrocytes orientation to the PL
Polarity index (Axial/Lateral)
4
3
2
1
0
ns
0.9
WT
Mlc1 KO
WT
Mlc1 KO
e
GFAP - IB4 -Hoechst
WT
Mlc1 KO
Axial
Lateral
P60
f
Astrocytes orientation to vessels
Polarity index (Axial/Lateral)
2.5
2.0
1.5
1.0
0.5
0
***
0.0001
WT
Mlc1 KO

Fig. 6

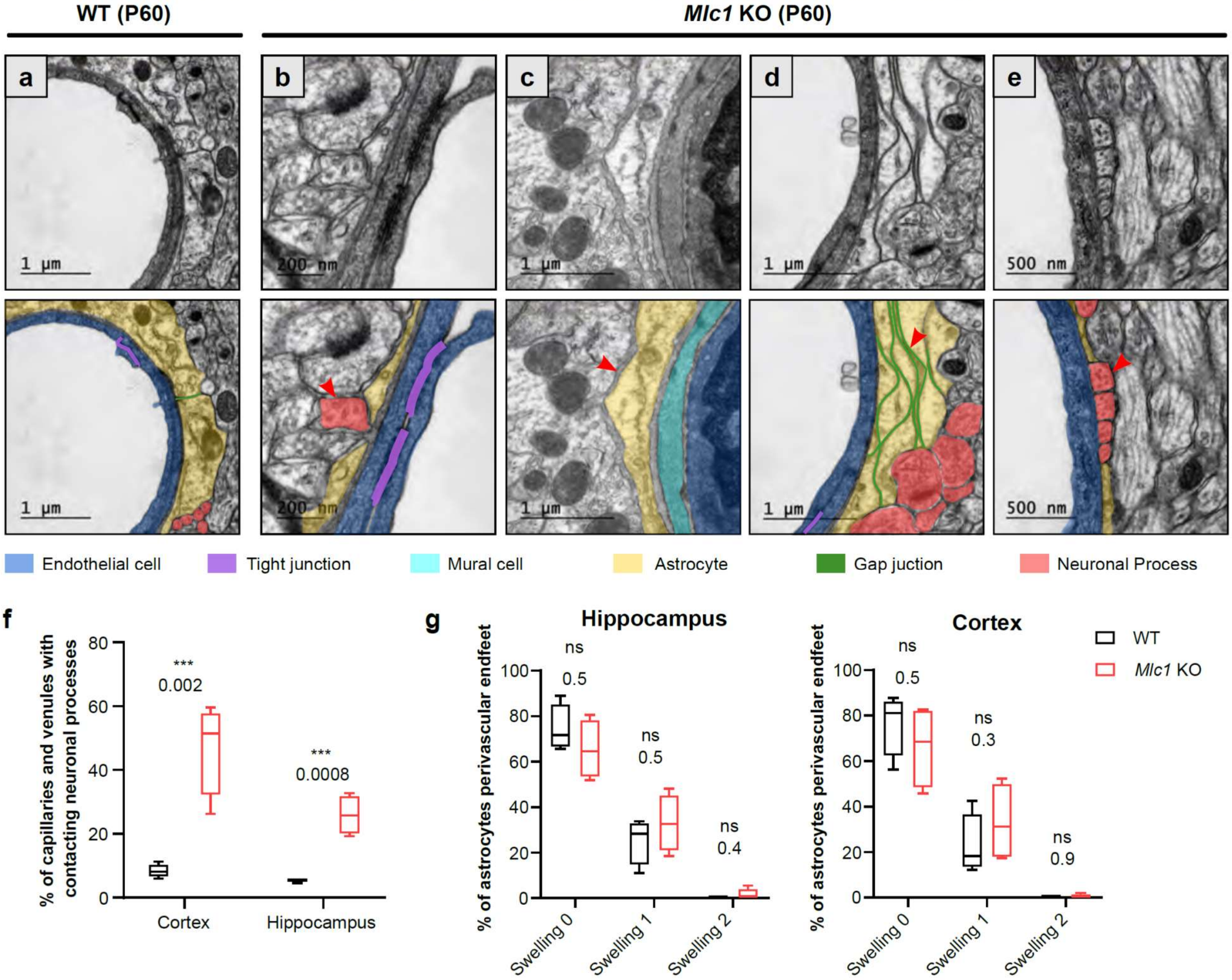
WT (P60)
Mlc1 KO (P60)
a
b
c
d
e
1 µm
200 nm
1 µm
1 µm
500 nm
1 µm
200 nm
1 µm
1 µm
500 nm
🟦 Endothelial cell
🟪 Tight junction
🟦 Mural cell
🟨 Astrocyte
🟩 Gap juction
🟥 Neuronal Process
f
% of capillaries and venules with contacting neuronal processes
80
60
40
20
0
***
0.002
***
0.0008
Cortex
Hippocampus
g
Hippocampus
% of astrocytes perivascular endfeet
100
80
60
40
20
0
ns
0.5
ns
0.5
ns
0.4
Swelling 0
Swelling 1
Swelling 2
Cortex
% of astrocytes perivascular endfeet
100
80
60
40
20
0
ns
0.5
ns
0.3
ns
0.9
Swelling 0
Swelling 1
Swelling 2
☐ WT
☐ *Mlc1* KO

Fig. 7

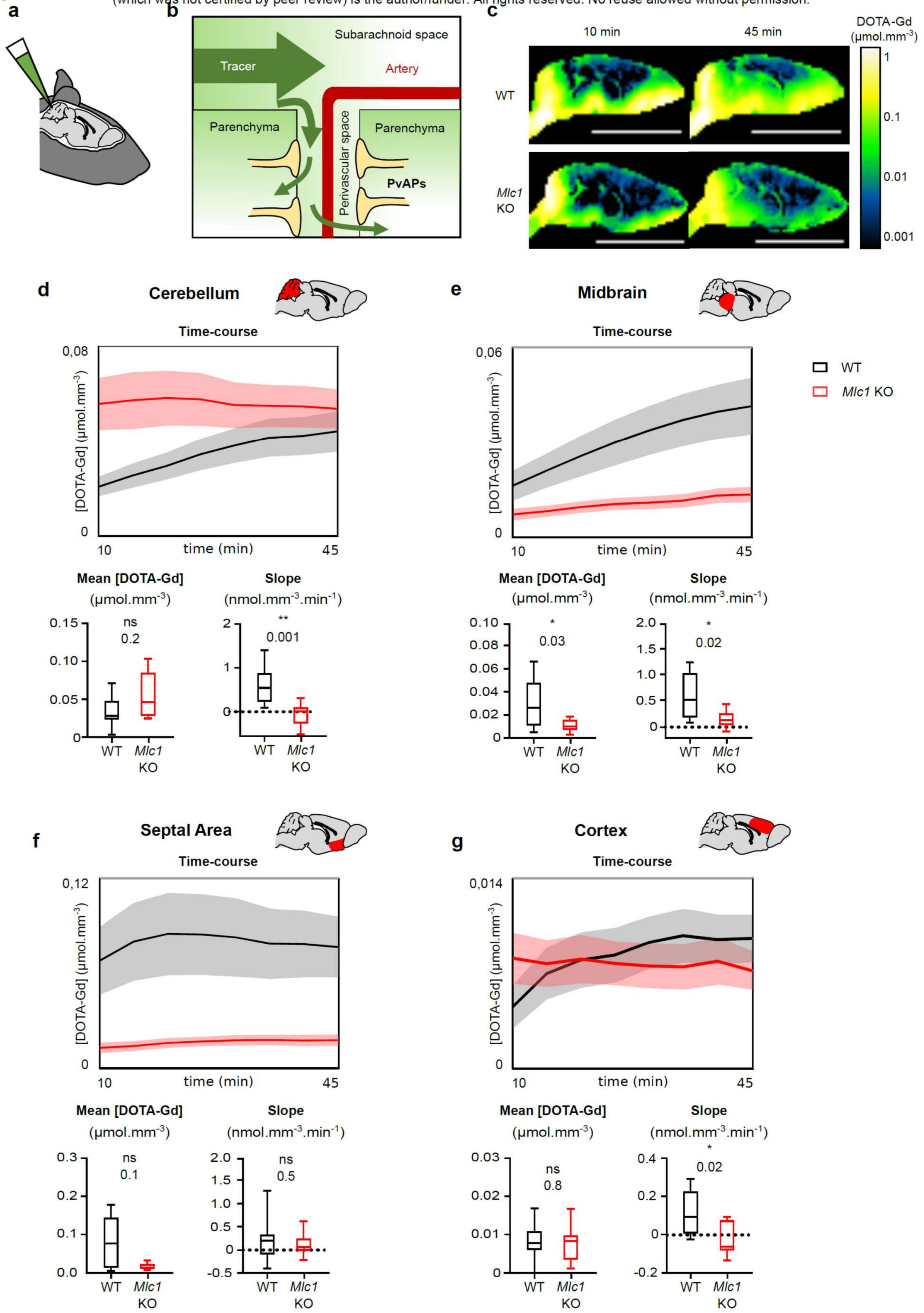
a
b
Subarachnoid space
Tracer
Artery
Parenchyma
Perivascular space
Parenchyma
PvAPs
c
10 min
45 min
DOTA-Gd
(µmol.mm-3)
WT
Mlc1 KO
1
0.1
0.01
0.001
d
Cerebellum
Time-course
0,08
0
[DOTA-Gd] (µmol.mm-3)
10
time (min)
45
Mean [DOTA-Gd]
(µmol.mm-3)
Slope
(nmol.mm-3.min-1)
0.15
0.10
0.05
0
ns
0.2
2
1
0
**
0.001
WT
Mlc1 KO
e
Midbrain
Time-course
0,06
0
10
time (min)
45
0.10
0.08
0.06
0.04
0.02
0
*
0.03
2.0
1.5
1.0
0.5
0
*
0.02
WT
Mlc1 KO
f
Septal Area
Time-course
0,12
0
10
time (min)
45
0.3
0.2
0.1
0.0
ns
0.1
2.0
1.5
1.0
0.5
0
-0.5
ns
0.5
g
Cortex
Time-course
0,014
0
10
time (min)
45
0.03
0.02
0.01
0
ns
0.8
0.4
0.2
0
-0.2
*
0.02

Fig. 8

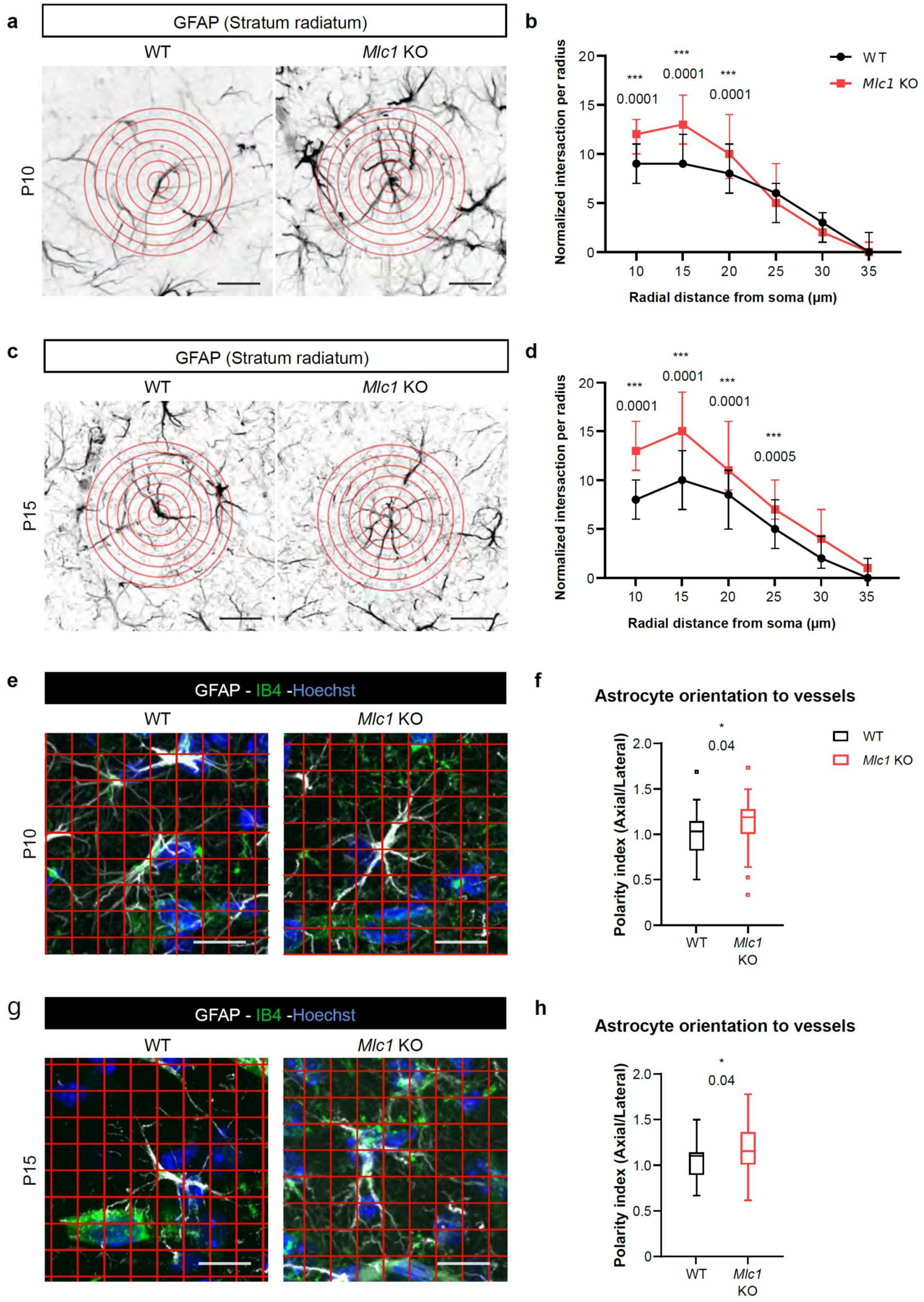
a
GFAP (Stratum radiatum)
WT
Mlc1 KO
P10
b
Normalized intersaction per radius
20
15
10
5
0
***
0.0001
***
0.0001
***
0.0001
WT
Mlc1 KO
10
15
20
25
30
35
Radial distance from soma (µm)
c
GFAP (Stratum radiatum)
WT
Mlc1 KO
P15
d
Normalized intersaction per radius
20
15
10
5
0
***
0.0001
***
0.0001
***
0.0001
***
0.0005
10
15
20
25
30
35
Radial distance from soma (µm)
e
GFAP - IB4 -Hoechst
WT
Mlc1 KO
P10
f
Astrocyte orientation to vessels
Polarity index (Axial/Lateral)
2.0
1.5
1.0
0.5
0
*
0.04
WT
Mlc1 KO
WT
Mlc1 KO
g
GFAP - IB4 -Hoechst
WT
Mlc1 KO
P15
h
Astrocyte orientation to vessels
Polarity index (Axial/Lateral)
2.0
1.5
1.0
0.5
0
*
0.04
WT
Mlc1 KO

Fig. 9

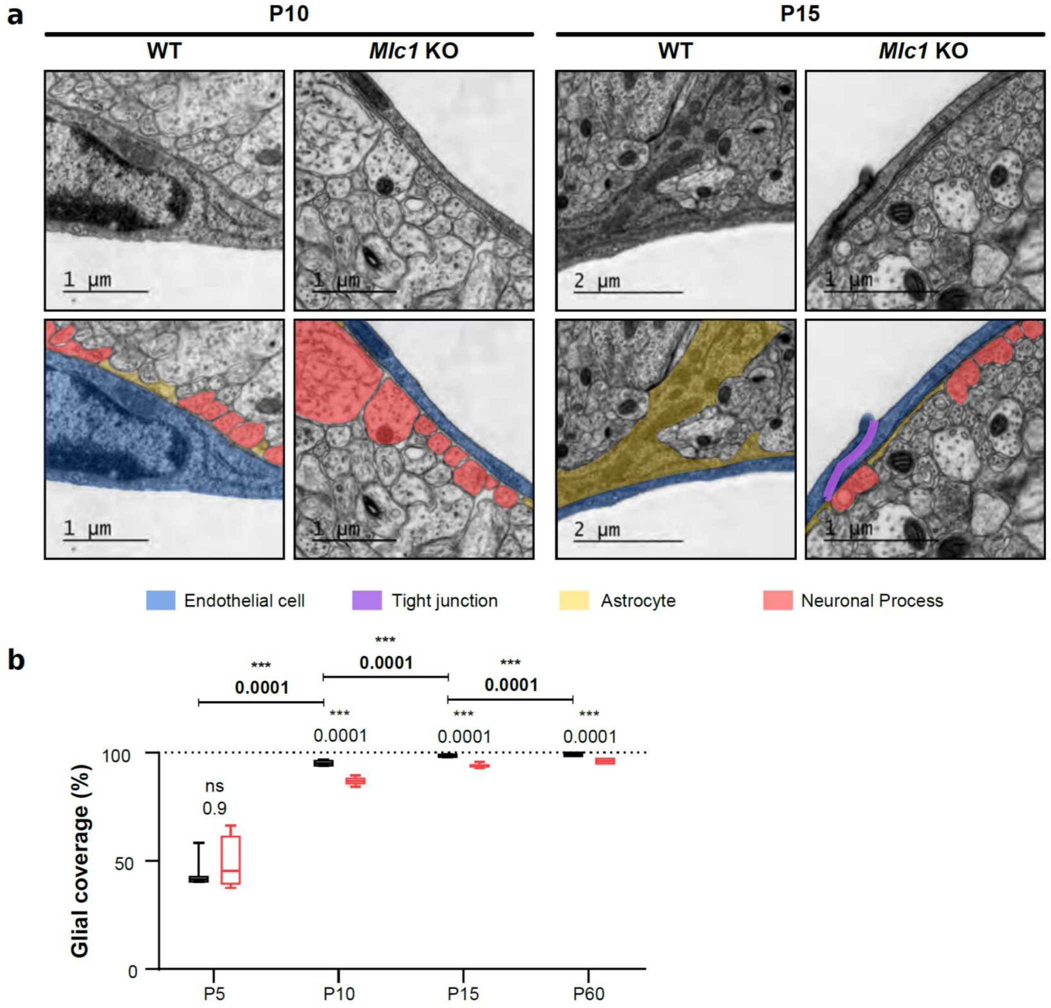
a
P10
P15
WT
Mlc1 KO
WT
Mlc1 KO
1 µm
1 µm
2 µm
1 µm
1 µm
1 µm
2 µm
1 µm
Endothelial cell
Tight junction
Astrocyte
Neuronal Process
b
***
0.0001
***
0.0001
***
0.0001
***
0.0001
***
0.0001
***
0.0001
ns
0.9
Glial coverage (%)
100
50
0
P5
P10
P15
P60

Collaboration 2 – Consequences of general anesthesia in infancy: convergent findings of independent rodent and human studies on long-term behavior and brain structures

Cet article sera prochainement soumis à Annals of Neurology

Résumé : Malgré des effets potentiellement délétères sur le neurodéveloppement, un enfant sur sept reçoit une anesthésie avant l'âge de trois ans dans les pays développés. Les résultats précliniques ne correspondent pas toujours avec les observations de cohortes pédiatriques et une approche trnaslationnelle exploitant l'imagerie est nécessaire.

Dans cette étude réalisée en collaboration avec le LaPsyDÉ, nous avons exploité rétrospectivement la cohorte pédiatrique APEX afin de déterminer si une anesthésie dans l'enfance avait une conséquence sur les scores comportementaux ou sur l'anatomie cérébrale. En parallèle, nous avons réalisé une série d'expositions aux anesthésiques sur des souris de 4 à 10 jours après leur naissance, puis réalisé des tests comportementaux ainsi que des expériences d'imagerie sur les mêmes animaux adultes.

Chez l'enfant comme chez la souris, nous avons montré une altération significative du comportement et de la structure cérébrale en lien avec l'exposition aux anesthésiques.

Conclusions :

- Chez le rongeur, l'exposition aux anesthésiques en période postnatale perturbe les comportements liés à la peur et l'anxiété. Une perte de volume dans la substance grise périacqueducale, zone liée à la peur, est également observée.
- Chez l'enfant, l'exposition aux anesthésiques est corrélée à un contrôle émotionel moindre ainsi qu'à une légère perte de volume dans le gyrus frontal inférieur droit.
- L'effet délétère des anesthésiques devrait davantage être pris en compte dans la pratique clinique pédiatrique et les chirurgies non vitales reculées à un âge où l'influence des anesthésiques est moindre.

Contribution : Dans cette étude dont je suis deuxième autrice, j'ai significativement contribué à l'analyse des résultats cliniques et précliniques et à leur mise en forme. J'ai aussi réalisé et analysé une expérience IRM avec injection de traceur chez la souris pour évaluer l'effet de l'anesthésie post-natale sur le développement des échanges LCR-FISC. Les résultats de cette expérience ont été négatifs et ne sont pas présentés dans cet article.

ORIGINAL INVESTIGATIONS

Full title: **Consequences of general anesthesia in infancy: convergent findings of independent rodent and human studies on long-term behavior and brain structure.**

Running head: **Pediatric anesthesia : lasting effects on brain.**

Authors : **Jean-Philippe Salaün[1,2], Audrey Chagnot[1], Arnaud Cachia[3,8], Nicolas Poirel[3,5,8], Valérie Datin-Dorrière[3,4,5], Cléo Dujarrier[1], Marine Rolland[1,2], Lisa Delalande[3], Pierre Gressens[6], Bernard Guillois[4], Olivier Houdé[3,5,8], Damien Levard[1], Clément Gakuba[1,2], Marine Moyon[3], Mikael Naveau[9], François Orliac[3,5], Gilles Orliaguet[10], Jean-Luc Hanouz[2,7], Véronique Agin[1], Grégoire Borst*[3,8], & Denis Vivien*[1,11].**

*These two authors contributed equally to the work.

Affiliations:

1. Normandie Univ, UNICAEN, INSERM, GIP Cyceron, Institut Blood and Brain @Caen-Normandie (BB@C), UMR-S U1237, Physiopathology and Imaging of Neurological Disorders (PhIND), Caen, France.

2. CHU Caen, Department of Anesthesiology and Critical Care Medicine, Caen University Hospital, Avenue de la Côte de Nacre, Caen, 14033, France.

3. Université de Paris, LaPsyDé, CNRS, 75005, Paris, France.

4. CHU Caen, Department of Neonatology, Caen University Hospital, Avenue de la Côte de Nacre, Caen, 14033, France.

5. GIP Cyceron, Caen, France.

6. Université de Paris, NeuroDiderot, INSERM, Paris, France.

7. EA 4650, Caen Normandy University, Unicaen, Esplanade de la Paix, CS 14 032, F-14000 Caen, France.

8. Institut Universitaire de France (IUF), Paris, France.

9. CNRS, UMR-S 3408, GIP Cyceron, Normandie Université, Caen, France.

10. Department of Pediatric Anesthesia and Intensive Care, Necker-Enfants Malades University Hospital, AP-HP. Centre - Université de Paris, France; Université de Paris, EA 7323 "Pharmacologie et évaluation des thérapeutiques chez l’enfant et la femme enceinte", 75006 Paris, France.

11. CHU Caen, Department of Clinical Research, Caen University Hospital, Avenue de la Côte de Nacre, Caen, 14033, France.

Correspondence to Jean-Philippe Salaün:

Department of Anesthesiology and Critical Care Medicine, Caen University Hospital, Avenue de la Côte de Nacre, Caen, 14033, France.

Phone number: +33644295087

Email ID: salaunjeanphilippe@gmail.com

Word and element counts:

- Title: 149 characters
- Running head: 48 characters
- Abstract: 250 words
- Introduction: 321 words
- Discussion: 1.444 words
- Body of the manuscript: 4.024
- Figures: 4
- Tables: 2

SUMMARY FOR SOCIAL MEDIA

Twitter: NA

Current knowledge of the topic: General anesthesia braintoxicity is a controversial issue.

Question addressed by the study: Does early exposure to general anesthesia impacts long-term behavior and brain structure in mice and humans?

What does this study add: This is the first translational study that suggests lasting effects of early life exposure to anesthetics on later emotional control behaviors and brain structures, both in rodents and humans.

Potential impact on the practice of neurology: These considerations should stimulate the development of less braintoxic anesthetic agents and to avoid early exposure to general anesthesia whenever it is possible.

ABSTRACT

Objective

One in seven children needs general anesthesia before three years old in Western countries. Braintoxicity of anesthetics issue is controversial. Our objective was to clarify whether exposure to general anesthesia of the developing brain could lead to lasting behavioral and structural brain changes.

Methods

A first study was performed in mice. The behaviors (fear conditioning, Y-Maze and actimetry) and brain anatomy (high-resolution Magnetic Resonance Imaging) of six to eight weeks old Swiss mice exposed or not to general anesthesia from 4 to 10 days-old were evaluated. A second study was a complementary analysis from the pre-existing APEX cohort to assess the replicability in humans of our data. The behaviors (Behavior Rating Inventory of Executive Function emotional control and working memory score, Backward Digit Span and Raven 36) and brain anatomy (high-resolution Magnetic Resonance Imaging) were compared in 102 children 9 to 10 years exposed or not to a single general anesthesia (surgery) during infancy.

Results

The animal study revealed chronic exacerbated fear behavior in the adult mice ($p= 0.03$) exposed to postnatal general anesthesia; this was associated with an atrophy of the periaqueductal grey matter ($p=0.046$). The study in humans revealed a lower emotional control ($p=0.05$) and an atrophy in the posterior part of the right inferior frontal gyrus ($p=0.019$) in the children who had been exposed to a single general anesthesia.

Interpretation

The preclinical and clinical findings of these independent studies suggest lasting effects of early life exposure to anesthetics on later emotional control behaviors and brain structures.

KEYWORDS

children; mouse; developing brain; general anesthesia; braintoxicity; pediatric anesthesia.

INTRODUCTION

The potential deleterious effects of anesthesia on the developing brain are mainly based on preclinical in vitro and in vivo studies in rodents and non-human primates Increasing preclinical in vitro and in vivo studies in rodents and non-human primates suggest that anesthesia *per se* has (deleterious or negative) effects on the developing brain [1,2,3]. These studies reported that early exposures to GABA or NMDA antagonists (i.e. the main receptors through which anesthesia modulate central nervous system activit) resulted in structural[4] and functional brain impairments including behavioral changes[5]. Consequently, the issue of The clinical relevance of general anesthetics (GA) braintoxicity in children was highlighted in the last decade but gathered less consistent proofs[6]. Some cohort studies reported an association between GA and impaired neurodevelopment[7–9] while others reported no effects of GA before the age of three years old [10–12]. Interestingly, parents reported changes in executive functions, behaviors or reading abilities in children who had undergone general anesthesia during infancy[11].

In one hand experimental preclinical studies are mandatory even though species differences preclude any clinical translation. On the other hand, it is ethically and practically impossible to design a randomized clinical study on the effect of GA on the developing human brain. Thus, at the present time, human cohort analysis remain the only way to examine the question raised.

In the present manuscript we have the opportunity to present the result of 1) an experimental study focused on behavioral and anatomical changes which occur following postnatal exposure to GA in mice, and 2) the analysis of data recorded an ongoing French cohort study of developing children (“APprentissages EXécutifs et cerveau chez les enfants d’âge scolaire”; APEX). Based on data from the APEX cohort the authors had access to behavior and magnetic resonance brain imaging (MRI) of 9-10 years old children exposed or not to a single GA for minor surgery during infancy (2007-2015).

The main objective of the preclinical study was to examine behavioral and structural brain changes in mice at a distance from exposure to postnatal general anesthesia. The main objective of the APEX data analysis was to examine long-term behavioral and structural brain imaging according to the exposure or not to general anesthesia in infancy. The secondary objectives of the APEX data analysis was to examine the relationship between (1) behavioral changes and structural brain abnormalities (2) the age of exposure to anesthesia and the magnitude of behavioral and structural brain changes.

METHODS

Study one: the mice model

Animals

Experiments were performed in 2018 on Swiss male mice (Janvier Labs, France) in accordance with the French ethical laws (Decree 2013-118, Approval n°8962) and the European Communities Council guidelines (2010/63/EU) (Animal care facilities: Centre Universitaire de Ressources Biologiques (CURB), Caen Normandy University, France; approval n° A14118015). Body weight was measured before behavioral evaluations. All behavioral tests were performed between 8AM-5PM in a room with dim illumination (6 lx) by an investigator blinded to group allocation. Two groups of animals: anesthesia-exposed mice (90 min per day exposure to an inspired concentration of isoflurane 1.3% = MAC 1.0, in 100% O2, from P4 to P10) and control mice (90 min per day exposure to 100% O2, from P4 to P10). Isoflurane was used as halogenated agent because (1) widely used in veterinary routine in rodents (2) our gas administration systems was not compatible with sevoflurane. The exposition occurred in a plastic box of 19x19x11.5cm with a fresh gas inlet on its lid, an aspiration on one of its sides and a humidification system. We decided to expose mice to repeated general anesthesia (7 times) to increase the probability to produce a visible effect. Behavioral experiments and then imaging were performed when the animals were 6-8 weeks old (see Table 1 for details).

Behavioral assessment

A range of behavioral tests were used for motor, emotional and cognitive functions assessment: actimetry[13], fear conditioning[14] and Y-maze[15].

Imaging

We used a 7T preclinical system (Bruker, Pharmascan, Advance III) to acquire a 3D isotropic T2 weighted image of the brain of each mouse (TR=13.5s, TE=48ms, RARE acceleration factor=8, matrix=90x90x90, isotropic resolution=0.2mm^3). The acquisitions were realized on mice anesthetized with isoflurane (1-2% in 100% O2) over 20 minutes. Deformation-Based Morphometry[16], and not Voxel-Based Morphometry (VBM), was used to analyze mouse brain anatomy as DBM overcome the VBM brain segmentation step, which is tedious with mouse.

Study two: the APEX cohort of children

Participants

The objective of the APEX study (2015-2019) was to test in healthy school-aged children (9-10 years old), the impact at the cognitive and neural levels of two types of executive training: a training targeting specifically the inhibitory control and a metacognitive training based on mindfulness meditation. All participants to this secondary analysis of the APEX cohort were tested in accordance with the national and international norms that govern the use of human research participants. It was approved by a French national ethic committee (IRB 2015-A00383-46, 21/05/2015) and carried out in line with the declaration of Helsinki (1964). We decided to include all participants (n=102) of the APEX cohort which were right-handed as determined by the Edinburgh Handedness Inventory[17], were born full-term, had normal or corrected-to-normal vision, had no history of neurological diseases and had no cerebral abnormalities. Parents or legal guardians gave written consent and all children agreed to participate at the APEX study. Thus, twenty-four children (nine males, mean±SD = 9.9±0.6 years, range = 9.1–11.0 years) who were exposed (between 2007-2015) to a single general anesthesia for non-urgent minor surgery when between 1-10 years-old (age at anesthesia: mean±SD = 4.0±2.3 years; 29% of patients were 3 years old and under, 54% were between 4 and 6 years old and 17% were over 6 years old; Fig. 1) constituted the GA-exposed group. Exposure to GA was determined by a standardized data collection completed by the children's parents. We unfortunately did not have any information on the nature and dosage of the drugs used during GA. The 78 children who had not been exposed to GA (35 males, mean±SD = 9.8±0.5 years, range = 9.0–10.9 years) constituted the control group.

Behavioral assessment

In order to achieve the most translational approach possible, we used the APEX cohort analysis of the backward digit span[18] task to assess working memory ability and the Raven's progressive matrices[19] to assess non-verbal intelligence. Emotional control and working memory in daily activities were assessed using the Behavior Rating Inventory of Executive Function (BRIEF) parent form[20].

Imaging

In the same way, we used the APEX cohort high-resolution isotropic 3T sagittal structural T1 MRI data (TE = 3.3; TR = 7.2; flip angle = 9; 1 x 1 x 1 mm) acquired at the Cyceron biomedical imaging platform (Archieva, Philips Medical System, The Netherlands). Local grey matter volumes were automatically assessed on the whole brain based on the standard voxel-based morphometry (VBM) approach[21]. Before the scans, children were familiarized with the MRI session noise in a fake MRI and were trained not to move during the acquisition. T1 MRI acquisitions were performed while they passively watched a mute cartoon on an MRI-compatible screen to reduce motion, provide a positive experience and decrease waiting times[22]. Local grey matter volumes were automatically assessed on the whole brain based on the standard voxel-based morphometry (VBM) approach using the Statistical Parametric Mapping software (SPM12) (http://www.fil.ion.ucl.ac.uk/spm/) and the Computational Anatomy Toolbox (CAT12) (http://www.neuro.uni-jena.de/cat/), a fully automatic, toolbox for performing robust and accurate VBM analyses. Of note, the we used the CAT12 (CAT12.6) toolbox which is optimized for the segmentation of brains of children (robust initial affine registration and sample-specific template based on a diffeomorphic image registration algorithm (DARTEL)[23].

Statistical Analysis

Data were analysed using the GraphPad Prism software (version 9.0). Preclinical and clinical statistical analyses were two-tailed (or otherwise mentioned).

Preclinical behavioral data

Analysis of the datasets via parametric approaches turned out to be inappropriate in some cases due to violation of normality (Shapiro-Wilk tests). Parametric or non-parametric approaches were used whenever appropriated. Behavioral performance was compared between groups using Unpaired Student's t-tests (Actimetry; Fear conditioning; Body Weight). Behavioral performance was compared within groups using Paired Student's t-tests (Y-maze: acquisition session). Friedman's tests were used in order to investigate effects of factors with three levels in a repeated measure setting (Y-maze: recall session). When an appropriate significant effect was detected by Friedman's tests, we performed post-hoc analysis using Dunn's Multiple Comparison Tests.

Preclinical imaging data

Using Advanced Normalization Tools (ANTs), an anatomical template of the control mice was built. Estimating the volumetric differences between the animals, the Jacobian determinant of the deformation field needed to warp the individuals to the template was used. Using SPM12, a second level of analysis was performed of these Jacobian determinant images to test morphological differences between groups. This second level analysis consist of voxel-wise T-tests corrected for the Family Wise Error rate (FWE).

Clinical behavioral data

Shapiro-Wilk analysis of the whole dataset revealed that the data followed a gaussian distribution, thus enabling the use of parametric tests. Behavioral performance was compared within groups using ANCOVA with the exposure age, monthly parental income as a proxy of socio-economic status, sex and birth weight as covariables.

Clinical imaging data

Voxelwise statistical analyses were performed on the whole brain using SPM12 software, within the General Linear Model (GLM) framework. Covariates were controlled for additive linear effects. No interaction with the covariates were entered in the linear model. Analyses were performed on the smoothed (8 mm) and modulated grey matter maps with gender, age, parental income as a proxy of socio-economic status, and weight at birth as matching variables. Individual grey matter volume of the VBM cluster was obtained using the Marsbar toolbox for SPM. All analyses were performed using a voxelwise threshold at $p < 0.05$, corrected for multiple testing using SPM12 Family Wise Error (FWE) method.

RESULTS

Study one: mice data

Exposure to GA did not impact the mice's food intake and body weight. No mortality was reported in either group of mice. Indeed, control and GA-exposed mice showed similar body weight at 6 weeks of life (control mice: weight (g) = 39.5±2.8; GA-exposed mice: weight = 39.7±2.7; mean difference = 0.2; *p* = 0.81). The spontaneous locomotor activity was measured using activity chambers. Control and GA-exposed mice showed similar horizontal locomotor activities (Fig. 3A; control mice: number of movements (nms) = 994±340; GA-exposed mice: nms= 1006±312; mean difference = 12; *p* = 0.91) and similar vertical activities (Fig. 3B; control mice: nms = 268±145; GA-exposed mice: nms= 263±108; mean difference = 5; *p*=0.9). These results indicate that postnatal GA did not influence locomotor activity during adulthood. We performed fear conditioning assays to estimate learning and reactions to aversive environmental stimuli. The percentage of freezing in both control and GA-exposed mice was similar during the acclimatizing period of the training (acquisition) session (Fig. 3C; control mice: freezing time (ft) = 32.87 sec±21.98; GA-exposed mice: ft = 28.67 sec±22.05; mean difference = 4.20; *p*=0.53). Moreover, all mice showed high levels of fear following the two aversive unconditioned stimuli and no group differences were detected (*p*=0.63). These results mean that the acquisition of fear was not impaired in adult mice exposed to GA during the postnatal period. Twenty-four hours and one month after the training session, contextual emotional memory was re-assessed with a significantly heightened freezing time in GA-exposed mice compared to controls (Fig. 3D; control mice: ft = 73.14±55.65 sec; GA-exposed mice: ft = 115.17±73.49 sec; mean difference = 42.03; *p* = 0.03). These results indicate that postnatal GA led to long-term emotional disorders characterized by the presence of pathological fear. Spatial cognitive abilities were also examined by using a place recognition task in a Y-maze. During the acquisition session, the total number of visits in the two free access arms of the Y-maze was similar in control and GA-exposed mice and both groups visited arm 1 as often as arm 2 (Fig. 3E and 3F; control mice: arm 1 vs arm 2, *p* = 0.44; GA-exposed mice: arm 1 vs arm 2, *p* = 0.07). During the recall session performed three hours later, GA-exposed and control mice visited significantly more often the new arm (Fig. 3G and 3H; control mice: Friedman test, *p*= 0.008, arm 1 vs new arm, *p* = 0.01, arm 2 vs new arm, *p* = 0.04; GA-exposed mice: Friedman test, *p*= 0.002, arm 1 vs new arm, *p* = 0.01; GA-exposed mice: arm 2 vs new arm, *p* = 0.01). These results demonstrate that postnatal GA does not influence spatial learning in adulthood. MRI Deformation based morphometry highlighted a volumetric difference between adult GA-exposed mice and non-exposed mice with a 11%

reduction in the volume of the periaqueductal grey matter (Fig. 2; peak-level two-tailed two-sample t-test, t=7.32, dof=15, *p-FWE* = 0.046).

Study two: the APEX cohort of children

Age (t(34.46) = 0.337, *p*=0.74), sex ratio ($X^2(1)$=0.527, *p*=0.47), monthly parental net income (t(36.207) = 0.168, *p*=0.87) and birth weight (t(48.09) = 0.836, *p*=0.41) did not differ between anesthesia-exposed and control groups (Table 2). The behavioral analyses revealed a significant difference in the average BRIEF emotional control score between GA-exposed children and control children (Fig. 4A; Mean±SD: 53±11 vs. 58±12 for control and GA-exposed groups, respectively, mean difference = 5; 95% confidence interval: -0.021 to 9.81; *p*= 0.05 (2-tailed) and *p*=0.025 one tailed). We found no difference between the two groups on the BRIEF working memory scores (Fig. 4B; 51±10 vs. 49±7 for the control and GA-exposed groups, respectively, mean difference = 2; 95% confidence interval: -5.83 to 3.31; *p*= 0.58), on the performance on the Raven's progressive matrices (Fig. 4C; 31.06±3.60 vs. 31.08±3.46 for the control and GA-exposed groups, respectively, mean difference = 0.02; 95% confidence interval: -1.54 to 1.65; *p*= 0.95) and on the Backward Digit Span performance (Fig. 4D; 3.91±1.02 vs. 3.875±1.12 for the control and GA exposed groups, respectively, mean difference = 0.035; 95% confidence interval: -0.53 to 0.42; *p*= 0.82). We did not observe any influence of age at the time of anesthesia on behavioral tests scores (BRIEF emotional control score: *p* = 0.64; BRIEF working memory score: *p* = 0.83; Raven's progressive matrices: *p* = 0.34; Backward Digit Span: *p* = 0.37; ANCOVA with sex, age of inclusion, parental income and birth weight as covariates). Given the difference in grey matter volumes observed in preclinical data between GA-exposed and control mice, we also conducted a whole brain Voxel based morphometry (VBM) analysis of the grey matter volume in both groups. The analysis revealed a lower grey matter volume in a single cluster (MNI coordinates x,y,z = [51;3;27]; height threshold: Z = 4.85, *p-FWE* = 0.019, corresponding to the posterior part of the right inferior frontal gyrus, BA9, 'aal' atlas) in the GA-exposed children compared to the control group (Fig. 4E, 4F, 4G, 4H). There was no difference in local white matter volume between the two groups even with uncorrected statistics (*p-uncorrected* < 0.05). Of note, exploratory analysis revealed that the BRIEF emotional control score - controlled for anesthesia exposure, gender, age, parental income, and weight at birth - was positively correlated with the volume of grey matter in the posterior part of the right inferior frontal gyrus (height threshold: Z = 2.65, *p-FWE* = 0.047, with small volume correction using a 10 x

10 x 10 mm search volume centered at [51;3;27]). The same analysis with the BRIEF working memory score did not yield any significant correlation (height threshold: Z = 1.70, *p-FWE* = 0.24, with the same small volume correction). In addition, exploratory analysis restricted to the GA-exposed children revealed that age at GA - controlled for gender, age, parental income, and weight at birth - was correlated positively with the volume of grey matter in the posterior part of the right inferior frontal gyrus (height threshold: Z = 2.94, *p-FWE* = 0.024, with the same small volume correction). These clinical data showed a lower emotional control and a reduced grey matter volume in the posterior part of the right inferior frontal gyrus in children subjected to a single general anesthesia between 1-10 years old.

DISCUSSION

There is a lack of translational studies[24], in particular about the possible brain toxicity of anesthesia that combine preclinical and clinical results[25] .

A translational study about anesthesia brain toxicity. Our preclinical study in mice revealed an atrophy of the periaqueductal grey matter in the GA-exposed group. The periaqueductal grey matter is a key component in context fear discrimination in mice[26] and has a major involvement in disease states including anxiety, panic disorder and depression[27]. These structural results are consistent with the chronic exacerbated fear observed in mice exposed to GA from P4-P10 in the postnatal period[28]. We had then the opportunity to perform a secondary analysis of the existing data of the APEX cohort of developing children (2015-2019) with the objective to assess the replicability of these results in rodents. The human data revealed that the GA-exposed children presented lower grey matter volumes in the posterior part of the right inferior frontal gyrus, the more pronounced the earlier the anesthesia. The right inferior frontal gyrus has a central role in the cognitive control, impulsivity and emotional regulation[29]. Reductions in the inferior frontal gyrus volume have been associated with impaired emotion functions, later depression and poor health outcomes[30,31]. These neuroimaging results, which are associated with impaired emotional control in GA-exposed children (no working memory and no general intelligence deficit were detected) argue for a potential brain toxicity of GA on this region of the developing brain[7]. By assessing not only general intelligence, but also emotional control and working memory, we have been able to uncover deficits induced by GA that were not reported in previous studies focusing only on general intelligence[10–12]. Interestingly, this behavioral result is consistent with a recent meta-analysis of the 3 main prospectively-assessed clinical studies (i.e., GAS, MASK, PANDA) about anesthesia-induced brain toxicity, which revealed an impaired BRIEF executive function global score (RR: 1.68 [95% CI 1.23-2.30]; *p*=0.001) in 841 children who had had a single exposure to GA[32].

Strengths. First, all humans were term born children free of confounding comorbidities undergoing only one minor non-urgent surgery[11]. Moreover, these children had no history of chronic pathologies- including neurological and cerebral abnormalities that could influence the interpretation of the results, in contrast to other studies[33]. In addition, human analyses were controlled for possible confounding factors influencing the developing brain constituted by a familial environment, including monthly parental income as a proxy of socio-economic status as covariate. The imbalance between the number of exposed (n=24) and unexposed participants to anesthesia (n=78) is the ratio of GA-exposed children within this particular pre-existing cohort. This ratio (here, 23.5%) is consistent with the prevalence of pediatric anesthesia in the general population. Indeed, it is admitted that 14.3% of children are exposed to general anesthesia before 3 years old[34]. The higher prevalence of anesthesia-exposed children in our sample is due to the fact that we also included children who were exposed to anesthesia beyond 3 years of age (Mean ± SD = 4.0±2.3 years). Our sample of children is thus representative of the general population which strengthens the findings of the present study. Second, the anatomical areas affected in mice and humans are both involved in emotional control[27,29]. In humans, a decreased grey matter volume was found only in one region of the brain. In fact, only that region showed a significant effect of anesthesia but exploratory analyses, using less stringent statistical thresholds, indicate a more widespread effect that is more visible in this region. Of note, this difference persisted after *FWE*-correction for multiple tests on the whole brain. Backeljauw's study has reported a grey matter decrease only in several voxels within a single region of interest (encompassing the thalamus and retrosplenial cortex)[7] and the correction for multiple comparisons was applied only to the voxels within the region of interest not for all the voxels of the brain (as in our study). The statistical method used in Backeljauw's study, also referred as small volume correction' (SVC), could possibly be associated with high false positive rates. Our study therefore provides the first evidence that exposure to GA in childhood can lead to local a grey matter atrophy localized in the right prefrontal gyrus which is more pronounced the earlier the exposure to anesthesia. The importance of timing of anesthesia exposure has already been highlighted in numerous studies dealing with anesthesia-related braintoxicity[37]. We speculate that the most likely mechanism to explain the atrophy detected in mice and children exposed to GA is the loss of GABAergic and glutamatergic neurons. Apoptosis is a mechanism that has been widely described in the literature on anesthesia-induced braintoxicity[5], and periaqueductal grey matter contains GABAergic interneurons[36] whose role in the effects of early anesthesia on the developing brain is pointed out by the recent preclinical scientific literature[37]. Another possible mechanism, although less described than apoptosis in the literature, is the role that neuroinflammation and microglial activation might play[38]. Indeed, microglia play central physiological roles during normal development in neuronal proliferation, programmed neuronal cell death, angiogenesis, synaptogenesis, and influencing oligodendroglial survival and maturation[39]. Moreover, the results of our two studies in mice and humans are consistent with non-human primate studies about anesthesia braintoxicity. On the one hand, at a behavioral level, it has been shown that repeated exposure to sevoflurane during the first month of life of non-human primates altered their emotional reactivity. On the other hand, some studies underlined the interest of a non-invasive neuroimaging evaluation of anesthesia impact on the developing brain by using Positron Emission Tomography to highlight an increased glial activation in monkeys exposed to sevoflurane during the first week of life[40].

Limitations and future research perspectives. Unfortunately, our human study is limited by a lack of clinical information about the drugs and doses during exposures to anesthetics. This is unfortunately often the case in retrospective studies (62% of the studies). In the present study, human anesthesia exposures were performed recently (2007-2015) in French hospitals for minor surgeries and most probably involved at least sevoflurane. Moreover, no perioperative anesthetic complications were reported in the health records of the GA-exposed children. The indications for all minor surgical procedures appear in Figure 1. Another limitation of the present study is that the GA-exposed children were exposed to GA at different ages. However, we note that in previous clinical studies about anesthesia-induced brain toxicity, ages at exposition to general anesthesia were not homogeneous either[41]. Indeed, children were exposed or not to GA in the first few months of life in the GAS study (< 60 weeks of post-conceptual age)[15] whereas children were exposed to anesthesia between 3-10 years in other studies[42]. Another limitation was that the mice underwent multiple exposures to approximate concentrations of isoflurane and that their vital signs could not be monitored for obvious technical reasons.

Future preclinical and clinical studies should also investigate to what extent detrimental effects of GA could be driven by side effects occurring during GA such as hypotension, hypocapnia, hypoxia, hyperoxia, or hypoglycemia[43]. We did not have access to these data in our human and animal studies. The NECTARINE prospective multicenter observational study has recently highlighted that it is very difficult to accurately monitor neonates and small infants[44], this is also very difficult in newborn mice. Moreover, data on intraoperative physiological homeostasis are often missing in human studies on the brain toxicity of anesthesia. This is the case of the two recent PANDA[13] and MASK[11] ambidirectional studies. Last, the small sample-size of the human study reflects the difficulty to conduct MRI brain imaging studies in young children. Nevertheless, we were able to show impacts on the developing brain of GA during childhood while controlling for a large number of external factors that are known to possibly interfere with our parameters of interest such as age, weight at birth, gender and parental net income. It is important to note that the BRIEF emotional scores of GA exposed children only marginally differed from those of the non-exposed children. Replication on a larger prospective sample of GA-exposed children is necessary.

In conclusion, we present the first translational study that analyzes both in mice and in humans the possible long-term behavioral and structural brain impact of childhood exposure to a single GA. This study is the result of a successful collaboration between a preclinical research team challenged by intriguing initial results in mice and a clinical neuropsychological research team that secondarily addressed the issue of anesthesia brain toxicity. These considerations should stimulate the development of less brain toxic anesthetic agents and better monitoring anesthesia parameters in children[45]. It would also be relevant to set up long-term monitoring of our cohort of children in order to establish whether or not people exposed to anesthesia in childhood are likely to develop psychiatric pathologies involving emotional control in adolescence or adulthood[46].

REFERENCES

1. Jevtovic-Todorovic V. Monkey business: the importance of mounting behavioural evidence for anaesthesia-induced developmental neurotoxicity. *Br J Anaesth*. 2018;120(4):617-619.

2. Stargatt R, Davidson AJ, Huang GH, et al. A cohort study of the incidence and risk factors for negative behavior changes in children after general anesthesia. *Paediatr Anaesth*. 2006;16(8):846-859.

3. Davidson AJ, Sun LS. Clinical Evidence for Any Effect of Anesthesia on the Developing Brain. *Anesthesiology*. 2018;128(4):840-853.

4. Ikonomidou C, Bosch F, Miksa M, et al. Blockade of NMDA receptors and apoptotic neurodegeneration in the developing brain. *Science*. 1999;283(5398):70-74.

5. Jevtovic-Todorovic V. Exposure of Developing Brain to General Anesthesia: What Is the Animal Evidence? *Anesthesiology*. 2018;128(4):832-839.

6. O'Leary JD, Warner DO. What do recent human studies tell us about the association between anaesthesia in young children and neurodevelopmental outcomes? *Br J Anaesth*. 2017;119(3):458-464.

7. Backeljauw B, Holland SK, Altaye M, Loepke AW. Cognition and Brain Structure Following Early Childhood Surgery With Anesthesia. *Pediatrics*. 2015;136(1):e1-12.

8. Hansen TG. Use of anaesthetics in young children: Consensus statement of the European Society of Anaesthesiology, the European Society for Paediatric Anaesthesiology, the European Association of Cardiothoracic Anaesthesiology and the European Safe Tots Anaesthesia Research Initiative. *Eur J Anaesthesiol*. 2017;34(6):327-328.

9. Wilder RT, Flick RP, Sprung J, et al. Early exposure to anesthesia and learning disabilities in a population-based birth cohort. *Anesthesiology*. 2009;110(4):796-804.

10. Sun LS, Li G, Miller TLK, et al. Association Between a Single General Anesthesia Exposure Before Age 36 Months and Neurocognitive Outcomes in Later Childhood. *JAMA*. 2016;315(21):2312-2320.

11. Warner DO, Zaccariello MJ, Katusic SK, et al. Neuropsychological and Behavioral Outcomes after Exposure of Young Children to Procedures Requiring General Anesthesia: The Mayo Anesthesia Safety in Kids (MASK) Study. *Anesthesiology*. 2018;129(1):89-105.

12. McCann ME, de Graaff JC, Dorris L, et al. Neurodevelopmental outcome at 5 years of age after general anaesthesia or awake-regional anaesthesia in infancy (GAS): an international, multicentre, randomised, controlled equivalence trial. *Lancet Lond Engl*. 2019;393(10172):664-677.

13. Mannara F, Radosevic M, Planagumà J, et al. Allosteric modulation of NMDA receptors prevents the antibody effects of patients with anti-NMDAR encephalitis. *Brain J Neurol*. 2020;143(9):2709-2720.

14. Chatterjee S, Angelakos CC, Bahl E, et al. The CBP KIX domain regulates long-term memory and circadian activity. *BMC Biol*. 2020;18(1):155.

15. Dellu F, Contarino A, Simon H, Koob GF, Gold LH. Genetic differences in response to novelty and spatial memory using a two-trial recognition task in mice. *Neurobiol Learn Mem*. 2000;73(1):31-48.

16. Chung MK, Worsley KJ, Paus T, et al. A unified statistical approach to deformation-based morphometry. *NeuroImage*. 2001;14(3):595-606.

17. Oldfield RC. The assessment and analysis of handedness: The Edinburgh inventory. *Neuropsychologia*. 1971;9(1):97-113.

18. Poirel N, Borst G, Simon G, et al. Number conservation is related to children's prefrontal inhibitory control: an fMRI study of a piagetian task. *PloS One*. 2012;7(7):e40802.

19. Raven J, Raven JC, Court JH. Manual for Raven's progressive matrices and vocabulary scales. Oxford, UK: Oxford Psychologists Press; 1998.

20. Baron IS. Behavior rating inventory of executive function. *Child Neuropsychol J Norm Abnorm Dev Child Adolesc*. 2000;6(3):235-238.

21. Ashburner J. Computational anatomy with the SPM software. *Magn Reson Imaging*. 2009;27(8):1163-1174.

22. Lemaire C, Moran GR, Swan H. Impact of audio/visual systems on pediatric sedation in magnetic resonance imaging. *J Magn Reson Imaging JMRI*. 2009;30(3):649-655.

23. Ashburner J. A fast diffeomorphic image registration algorithm. *NeuroImage*. 2007;38(1):95-113

24. Stratmann G, Lee J, Sall JW, et al. Effect of general anesthesia in infancy on long-term recognition memory in humans and rats. *Neuropsychopharmacol Off Publ Am Coll Neuropsychopharmacol*. 2014;39(10):2275-2287.

25. Salaün JP, Poirel N, Dahmani S, et al. Preventing the long-term effects of general anesthesia on the developing brain: how translational research can contribute. *Neuroscience*. Published online March 3, 2021.

26. Rozeske RR, Jercog D, Karalis N, et al. Prefrontal-Periaqueductal Gray-Projecting Neurons Mediate Context Fear Discrimination. *Neuron*. 2018;97(4):898-910.e6.

27. Ho YC, Lin TB, Hsieh MC, et al. Periaqueductal Gray Glutamatergic Transmission Governs Chronic Stress-Induced Depression. *Neuropsychopharmacol Off Publ Am Coll Neuropsychopharmacol*. 2018;43(2):302-312.

28. Satomoto M, Sun Z, Adachi YU, Makita K. Neonatal Sevoflurane Exposure Induces Adulthood Fear-induced Learning Disability and Decreases Glutamatergic Neurons in the Basolateral Amygdala. *J Neurosurg Anesthesiol*. 2018;30(1):59-64.

29. Zhang L, Li W, Wang L, et al. Altered functional connectivity of right inferior frontal gyrus subregions in bipolar disorder: a resting state fMRI study. *J Affect Disord*. 2020;272:58-65.

30. Luby JL, Barch D, Whalen D, Tillman R, Belden A. Association Between Early Life Adversity and Risk for Poor Emotional and Physical Health in Adolescence: A Putative Mechanistic Neurodevelopmental Pathway. *JAMA Pediatr*. 2017;171(12):1168-1175.

31. Janiri D, Moser DA, Doucet GE, et al. Shared Neural Phenotypes for Mood and Anxiety

Disorders: A Meta-analysis of 226 Task-Related Functional Imaging Studies. *JAMA Psychiatry*. 2020;77(2):172-179.

32. Ing C, Jackson WM, Zaccariello MJ, et al. Prospectively assessed neurodevelopmental outcomes in studies of anaesthetic neurotoxicity in children: a systematic review and meta-analysis. *Br J Anaesth*. 2021;126(2):433-444.

33. Andropoulos DB, Easley RB, Brady K, et al. Changing expectations for neurological outcomes after the neonatal arterial switch operation. *Ann Thorac Surg*. 2012;94(4):1250-1255; discussion 1255-1256.

34. Shi Y, Hu D, Rodgers EL, et al. Epidemiology of general anesthesia prior to age 3 in a population-based birth cohort. *Paediatr Anaesth*. 2018;28(6):513-519.

35. Wang X, Xu Z, Miao CH. Current clinical evidence on the effect of general anesthesia on neurodevelopment in children: an updated systematic review with meta-regression. *PloS One*. 2014;9(1):e85760.

36. Yin W, Mei L, Sun T, et al. A Central Amygdala-Ventrolateral Periaqueductal Gray Matter Pathway for Pain in a Mouse Model of Depression-like Behavior. *Anesthesiology*. 2020;132(5):1175-1196.

37. Vutskits L. Anaesthesia, neural activity, and brain development: interneurones in the spotlight. *Br J Anaesth*. 2021;126(6):1084-1085.

38. Gui L, Lei X, Zuo Z. Decrease of glial cell-derived neurotrophic factor contributes to anesthesia- and surgery-induced learning and memory dysfunction in neonatal rats. *J Mol Med Berl Ger*. 2017;95(4):369-379.

39. Baud O, Saint-Faust M. Neuroinflammation in the Developing Brain: Risk Factors, Involvement of Microglial Cells, and Implication for Early Anesthesia. *Anesth Analg*. 2019;128(4):718-725.

40. Zhang X, Liu S, Newport GD, et al. In Vivo Monitoring of Sevoflurane-induced Adverse Effects in Neonatal Nonhuman Primates Using Small-animal Positron Emission Tomography. *Anesthesiology*. 2016;125(1):133-146.

41. Foubert R, Devroe S, Foubert L, Van dee Velde M, Rex S. Anesthetic neurotoxicity in the pediatric population: a systematic review of the clinical evidence. *Acta Anaesth. Belg.* 2020;71:51-65.

42. Ing CH, DiMaggio CJ, Whitehouse AJO, et al. Neurodevelopmental outcomes after initial childhood anesthetic exposure between ages 3 and 10 years. *J Neurosurg Anesthesiol*. 2014;26(4):377-386.

43. Weiss M, Vutskits L, Hansen TG, Engelhardt T. Safe Anesthesia For Every Tot - The SAFETOTS initiative. *Curr Opin Anaesthesiol*. 2015;28(3):302-307.

44. Disma N, Veyckemans F, Virag K, et al. Morbidity and mortality after anaesthesia in early life: results of the European prospective multicentre observational study, neonate and children audit of anaesthesia practice in Europe (NECTARINE). *Br J Anaesth*. Published online March 31, 2021.

45. Marchesini V, Disma N. Anaesthetic neuroprotection in children: does it exist or is it all

just bad? *Curr Opin Anaesthesiol*. 2019;32(3):363-369.

46. Brumback TY, Worley M, Nguyen-Louie TT, Squeglia LM, Jacobus J, Tapert SF. Neural predictors of alcohol use and psychopathology symptoms in adolescents. *Dev Psychopathol*. 2016;28(4pt1):1209-1216.

FIGURES AND TABLE LEGENDS

p-value: * < 0.05; ** < 0.01; *** < 0.001.

Figure 1: Characteristics of the children exposed to anesthesia

Figure 1 : Characteristics of the children exposed to anesthesia

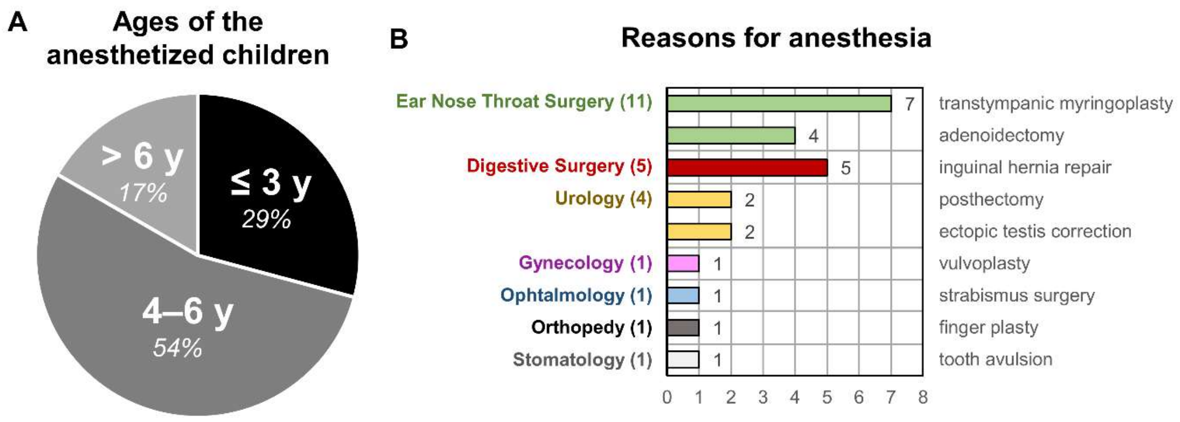

(A) Ages of the anesthetized children, (B) Reasons for anesthesia.

Figure 2: Preclinical imaging

Figure 2 : Preclinical imaging

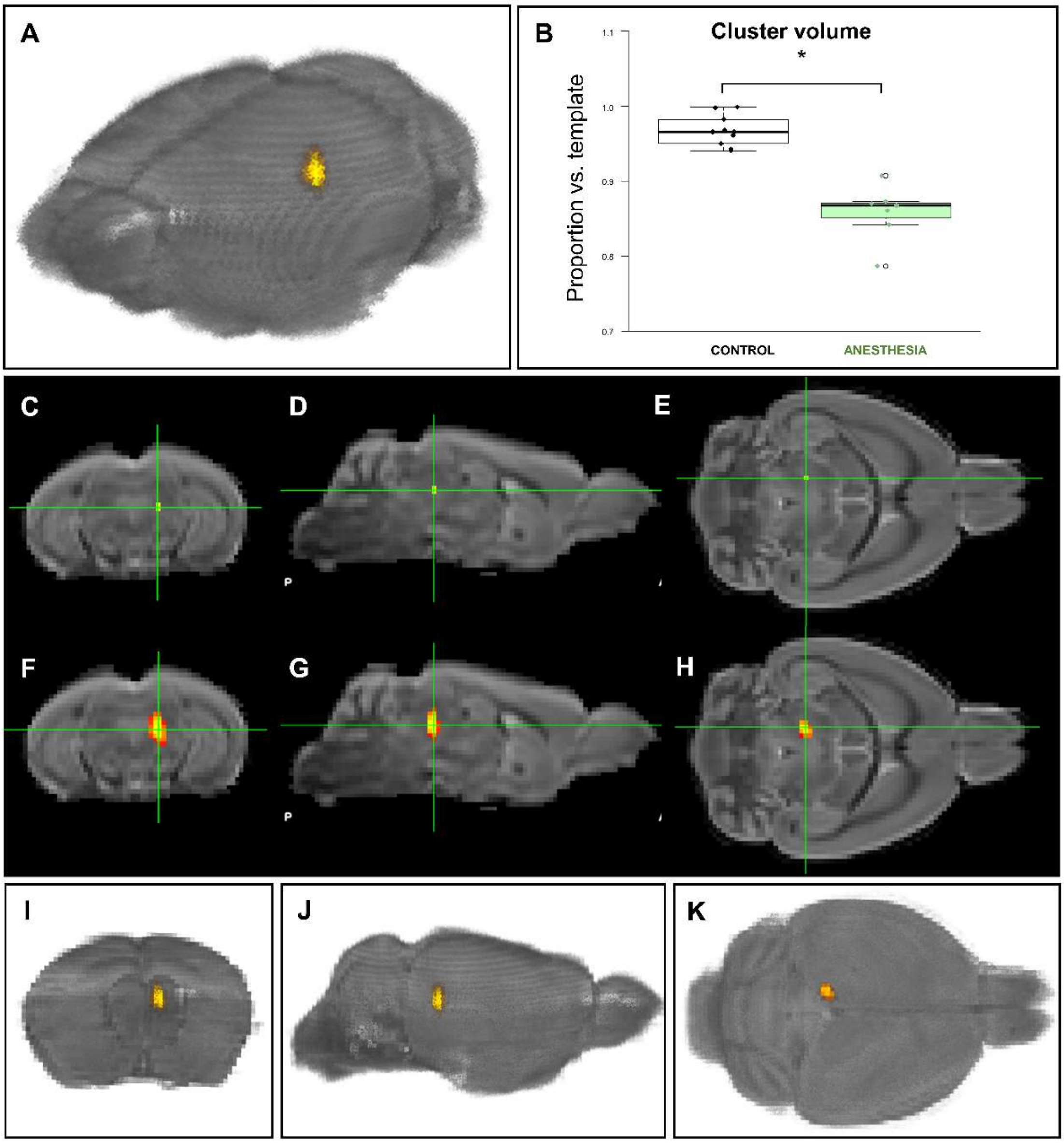

(A) For illustration purpose and ease of visualization, representation of the cluster (*uncorrected statistics*), showing an area covering the left periaqueductal grey matter.

(B) Proportion of grey matter is lower in general anesthetized mice vs. controls in the cluster.

(C,D,E) Orthogonal slices representing the position of the cluster (*FWE-correc*ted).

(F,G,H) Orthogonal slices representing the position of the extended cluster (*FWE-uncorrected*).

(I,J,K) 3D views of the extended cluster (*FWE-uncorrected*).

Figure 3: Preclinical behavioral testing

Figure 3 : Preclinical behavioral testing

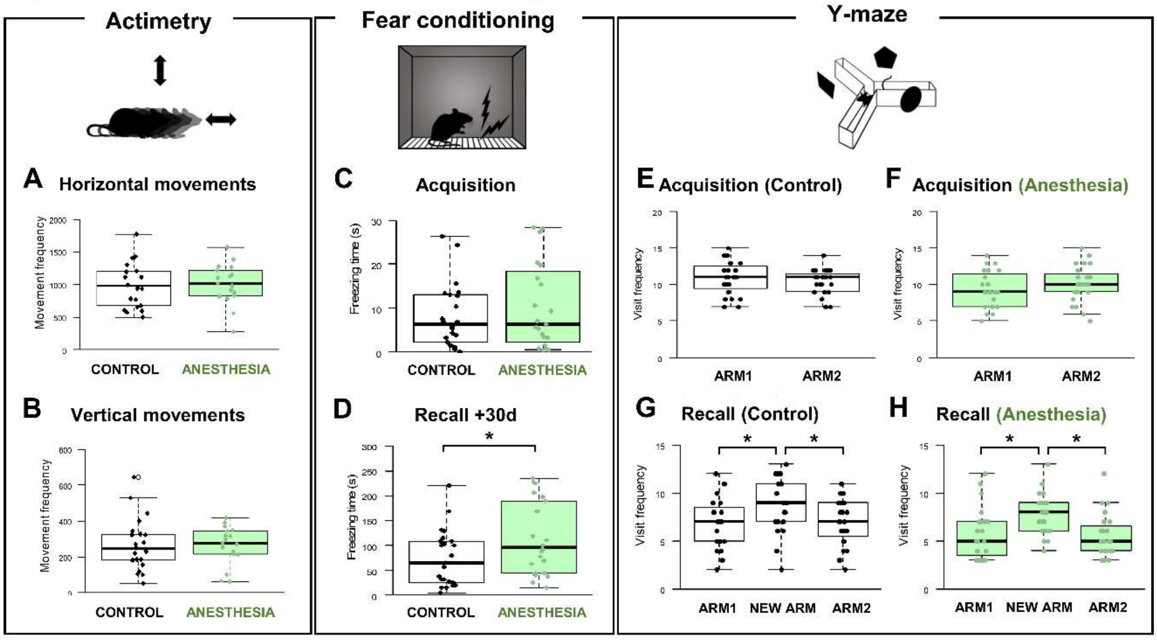

(A,B) Actimetry: horizontal (A) and vertical (B) spontaneous locomotor activity. No differences in horizontal or vertical movements were observed between control and general anesthesia-subjected mice (22 control and 17 anesthesia). Boxplots show distributions with black horizontal lines indicating the median, box margins denoting the lower and upper quartiles. Whiskers show the minimum and maximum values.

(C,D) Fear conditioning: acquisition (C) and recall (D) sessions. Freezing response at 30 days after acquisition is higher in general anesthesia-subjected mice (22 control and 22 anesthesia). * $P < 0.05$. Boxplots show distributions with black horizontal lines indicating the median, box margins denoting the lower and upper quartiles. Whiskers show the minimum and maximum values.

(E,F,G,H) Y-Maze: acquisition (E,F) and recall (G,H) sessions. Visit frequency in the new arm is higher than in familiar arms (1,2) at recall in both control and general anesthesia-subjected mice (24 control and 24 anesthesia). * $P < 0.05$. Boxplots show distributions with black horizontal lines indicating the median, box margins denoting the lower and upper quartiles. Whiskers show the minimum and maximum values.

Figure 4: Clinical imaging and behavioral testing

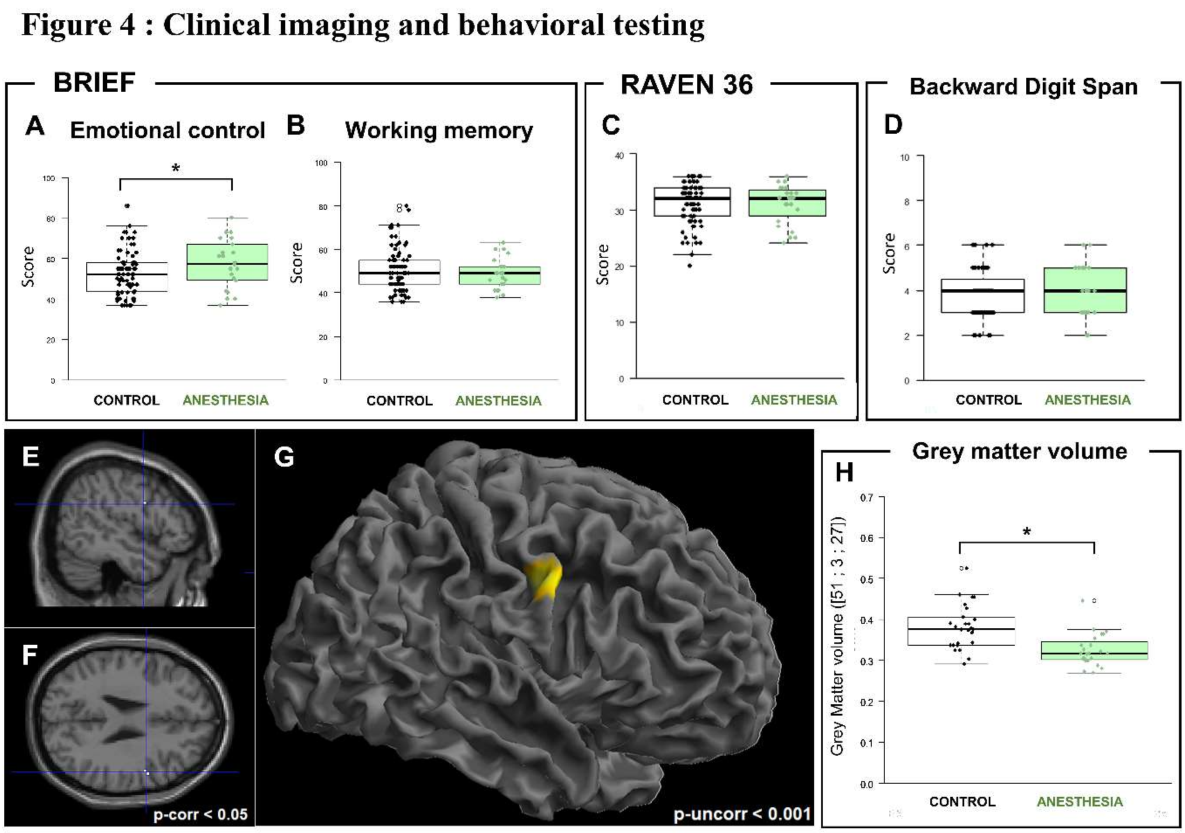

(A) Scores on the BRIEF emotional control scale is higher in children subjected to a single general anesthesia (*p-corrected* < 0.05; controlled for gender, age, parental income as a proxy of socio-economic status, and weight at birth) while scores on the BRIEF working memory scale (B), RAVEN36 (C), and backward digit span (D) did not differ between the groups.

(E, F) Lower local grey matter volume in children who were subjected to a single general anesthesia (*p-FWE* < 0.05; controlled for gender, age, parental income as a proxy of socio-economic status, and weight at birth).

(G) Three-dimensional rendering of the cortical surface and VBM cluster in the posterior part of the right inferior frontal gyrus (BA9) (voxel maximum: Talairach's x, y, z = [51;3;27]). For illustration purpose and ease of visualization, the cluster is represented with uncorrected statistics (*p-uncorrected* < 0.001).

(H) Grey matter volume in the VBM cluster located in the posterior part of the right inferior frontal gyrus is lower in children subjected to a single general anesthesia (*p-FWE* < 0.05; controlled for gender, age, parental income as a proxy of socio-economic status, and weight at birth).

Table 1: Number and age of mice used in the study.

Behavioral experiments		
Behavioral tests / Regimen of exposure	***noAG mice*** *(6 weeks)*	***AG mice*** *(6 weeks)*
Body Weight	n = 30	n = 29
Actimetry	n = 22	n = 17
Fear conditioning	n = 22	n = 22
Y-Maze	n = 24	n = 24
Imaging experiments		
Deformation-based Morphometry MRI	***noAG mice*** *(8 weeks)*	***AG mice*** *(8 weeks)*
	n = 10	n = 7

AG: Anesthesia-exposed mice; noAG: Control mice

Table 2: Human population characteristics.

		ANESTH *(n = 24)*	***CTRL*** *(n = 78)*	***P value***
Demography	***Age (y)***	9.9 (0.6)	9.8 (0.5)	0.74
	Male / Female ratio	9 / 15	35 / 43	0.47
	Birth weight (g)	3290 (377)	3369 (480)	0.41
	Monthly parental income (€)	3375 (647)	3400 (593)	0.87
	Age at anesthesia (y)	4.0 (2.3)	NA	/
Behavioral testing	***RAVEN36***	31 (3)	31 (4)	0.95
	Backward digit span	3.88 (1.12)	3.91 (1.02)	0.82
	BRIEF MDT	49 (7)	51 (10)	0.58
	BRIEF CE	58 (12)	53 (11)	**0.05**

POTENTIAL CONFLICTS OF INTEREST

The authors declare no competing interests.

FUNDING STATEMENT

This work was supported by the INSERM (French National Institute for Health and Medical Research), the French Ministry for Research and upper Education, the Caen-Normandy University, The Institute Blood and Brain @ Caen-Normandie (BB@C), European FEDER funds “Fonds Européens de Développement Economique et Régional Normandie” and the French National Research Agency (grant/award number: ANR-14-CE30-0014-01 APEX).

ACKNOWLEDGEMENTS

The authors thank the children who participated in the study and their families.

AUTHORS CONTRIBUTION

Jean-Philippe Salaün : conception and design of the study, acquisition and analysis of data, drafting a significant portion of the manuscript or figures

Audrey Chagnot : acquisition and analysis of data, drafting a significant portion of the manuscript or figures

Arnaud Cachia : conception and design of the study, drafting a significant portion of the manuscript or figures

Nicolas Poirel : conception and design of the study

Valérie Datin-Dorrière : acquisition and analysis of dat

Cléo Dujarrier : acquisition and analysis of data

Marine Rolland : drafting a significant portion of the manuscript or figures

Lisa Delalande : acquisition and analysis of data

Pierre Gressens : drafting a significant portion of the manuscript or figures

Bernard Guillois : conception and design of the study

Olivier Houdé : conception and design of the study

Damien Levard : acquisition and analysis of data

Clément Gakuba : drafting a significant portion of the manuscript or figures

Marine Moyon : acquisition and analysis of data

Mikael Naveau : acquisition and analysis of data

François Orliac : acquisition and analysis of data

Gilles Orliaguet : drafting a significant portion of the manuscript or figures

Jean-Luc Hanouz : drafting a significant portion of the manuscript or figures

Véronique Agin : acquisition and analysis of data, drafting a significant portion of the manuscript or figures

Grégoire Borst : conception and design of the study

Denis Vivien : conception and design of the study

DISCUSSION

Évolution des méthodes d'analyse des échanges LCR-FISC dans le laboratoire

Un des axes majeurs que j'ai poursuivi au long de ma thèse a été de faire évoluer nos méthodes d'imagerie du système glymphatique. Initialement, notre laboratoire s'est initialement intéressé au système glymphatique en l'intégrant à l'une de ses thématiques phares, l'AVC.
Brièvement, l'AVC est une des causes principales de décès dans le monde (5.5 millions par an). Les AVC ischémiques représentent 80% des AVC totaux et sont causés par une obstruction de la circulation cérébrale par un thrombus. La fibrinolyse est, avec la thrombectomie (extraction chirurgicale du thrombus), l'un des seuls traitements disponibles en clinique et doit être réalisée dans un délai très bref (4h30). À ce jour, le seul agent validé pour la fibrinolyse est le tPA, une sérine protéase endogène qui déclenche la lyse du thrombus par activation de la plasmine. Notre laboratoire s'est notamment illustré par la découverte du rôle neuromodulateur du tPA (Hébert et al., 2016) et par la proposition de formes présentant moins d'effets délétères que le tPA utilisé en clinique (Anfray et al., 2021). La seconde catégorie d'AVC est hémorragique, causée par la rupture de la paroi vasculaire et l'épanchement massif de sang dans l'espace sous-arachnoïdien. Une forme recombinante de tPA a été proposée par notre équipe pour favoriser la lyse et l'élimination des produits sanguins toxiques après l'hémorragie (Goulay et al., 2018).

Le premier article unissant les deux thèmes est publié en 2014 et porte sur les deux types d'AVC, réalisés dans plusieurs modèles murins (Gaberel et al., 2014). Dans cette étude, la fonctionnalité du système glymphatique est évaluée en IRM. Une première imagerie est réalisée, l'agent de contraste est injecté puis une seconde imagerie est réalisée une heure plus tard. Cette méthode a permis de retrouver les observations précédemment réalisées en IRM *in vivo* (Iliff et al., 2013a) et a montré notamment que : 1) l'agent de contraste, injecté dans la *cisterna magna*, ne parvenait pas à atteindre le bulbe olfactif après un AVC hémorragique ; et 2) l'agent de contraste pénètre plus difficilement la lésion 3h après un AVC ischémique, cette différence n'étant plus visible à 24h (Gaberel et al., 2014).

En 2018 sont publiés deux nouveaux articles exploitant la même méthode IRM (Di Palma et al., 2018; Gakuba et al., 2018). L'étude réalisée par Clément Gakuba et collaborateurs a porté sur l'effet des anesthésiques et la méthodologie IRM est identique à celle de l'article de 2014. Dans l'étude de Camille Di Palma et collaborateurs, dont je suis co-autrice (cf **Étude 3**), nous avons repris la méthode de l'article de 2014 mais, à la demande des reviewers, ajouté deux points supplémentaires (+30 min et +120 min) afin d'avoir une meilleure estimation de la cinétique de l'agent de contraste.

En 2019 est publié un article portant cette fois sur l'encéphalite autoimmune expérimentale (EAE), un modèle murin de SEP (Fournier et al., 2019). L'IRM est réalisée au niveau de la moelle et de l'encéphale, selon la méthodologie du papier de 2014. Si les animaux sujets à l'EAE présentent une diffusion restreinte de l'agent de contraste dans la moelle, aucune différence n'est observée dans le cerveau.

Une méthodologie dynamique a été employée dans un article portant sur l'AVC hémorragique chez le macaque (Goulay et al., 2018). Cette fois, l'imagerie est réalisée 20 minutes après l'injection d'agent de contraste et poursuivie sur environ deux heures, permettant l'acquisition dynamique de 25 images. Le volume de tissu rehaussé par l'agent de contraste est moindre chez les animaux ayant subi un AVC hémorragique.

Pendant ma thèse, j'ai été chargée d'approfondir ces techniques. Très rapidement, nous avons choisi une nouvelle séquence de type IRGRE (Inversion Recovery Gradient Echo) afin de pouvoir quantifier la concentration de l'agent de contraste (le détail de cette séquence est présenté dans l'**Étude 1**). De même, nous nous sommes orientés vers l'acquisition dynamique (IRM-RCD) afin de pouvoir modéliser les interactions LCR-FISC. Ces nouveaux protocoles ont nécessité l'élaboration d'outils à même de traiter nos images (quantification de l'agent de contraste, modélisation des échanges LCR-FISC) que j'ai développés en environnement MATLAB.

Le premier type de modèle auquel je me suis intéressée ont été les modèles pharmacocinétiques à deux compartiment (2CXM), mais la répartition de l'agent de contraste dans le LCR présentait une trop grande variabilité pour qu'ils soient exploitables. J'ai également évalué le modèle de Patlak (utilisé en IRM-RCD conventionelle), mais il s'est révélé insatisfaisant du fait de la circulation trop lente et inhomogène du LCR. Tenant compte de ces limitations, j'ai développé et testé un modèle mixte, considérant la concentration locale en agent de contraste, représentée par une équation pharmacocinétique, et en approximant son passage dans le tissu par la loi de diffusion de Fick. Ce modèle a montré une certaine efficacité par rapport à nos données *in vivo* et a permis d'établir des différences dans le coefficient de diffusion du traceur entre nos groupes. La relative complexité de ce modèle et son incapacité à modéliser le passage du GadoSpin D dans le tissu nous ont cependant poussé à abandonner son développement.

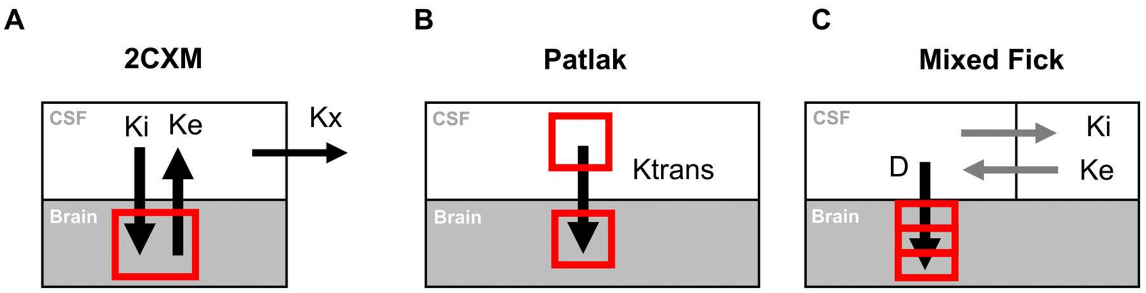

Figure 63 : Modèles d'échanges LCR-FISC

Schéma présentant trois des modèles candidats pour les interactions LCR-FISC que j'ai exploré au cours de ma thèse. Aucun de ces modèles n'a été retenu dans la suite de mes travaux.

Ces travaux de modélisation ont pris fin suite à la découverte des propriétés du GadoSpin D. Celui-ci permettait en effet une mesure simple de l'efficience des échanges LCR-FISC, qui s'est montrée plus robuste et efficace que les modèles basés sur le DOTA-Gd.

Une des limitations de la méthode IRGRE que nous avons choisie pour nos expériences est son temps d'acquisition. Vers la fin de ma thèse, je me suis intéessée à une méthode plus rapide, la VFA-SPGR. Cette dernière est moins précise que l'IRGRE mais sa rapidité en fait une des séquences les plus utilisées, notamment pour l'imagerie des échanges LCR-FISC (Lee et al., 2018). Bien que la séquence n'existe pas sur notre imageur, nous avons pu reproduire des images similaires. Les images que nous avons obtenues à ce jour restent bruitées et la concentration en gadolinium ne peut donc pas être estimée avec précision.

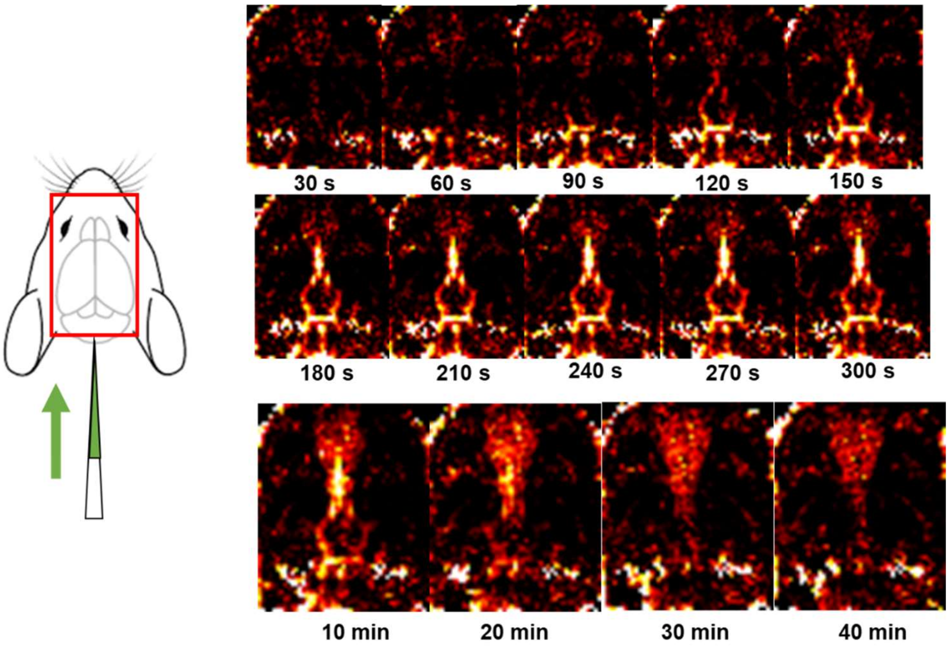

Figure 64 : Dispersion du GadoSpin D dans les EPV du polygone de Willis

Le GadoSpin D a été injecté dans la cisterna magna et parvient dans les espaces périvasculaires du polygone de Willis en à peine deux minutes. A plus long terme le contraste est principalement localisé dans les fosses nasales, une voie majeure d'excrétion du LCR chez le rongeur. Cartes de rehaussement (non quantitatives) obtenues grâce à notre séquence expérimentale 3D VFA-SPGR. Données personelles, 2021.

Un ‘effet filtre’ dans les espaces périvasculaires ?

Mes travaux sur l'IRM-RCD des échanges LCR-FISC m'ont amenée à tester différents agents de contraste. En effet, la grande majorité des études IRM utilisent des agents légers (DOTA-Gd, DTPA-Gd, < 1 kDa). Quelques études se sont intéressées à des agents plus lourds comme le GadoSpin P : 200 kDa (Iliff et al., 2013a) ou des immunoglobulines : 100 kDa (Pizzo et al., 2018), mais les agents de poids intermédiaire sont restés largement inexplorés.

Dans l'**Étude 1** présentée dans ce manuscrit, j'ai utilisé deux agents de contraste de poids différents : le DOTA-Gd, 0.7 kDa, et le GadoSpin D, 17 kDa.
La différence dans la répartition des agents nous a aussitôt frappés. Alors que le DOTA-Gd se répartit principalement en périphérie de l'espace sous-arachnoïdien de la base du crâne, le GadoSpin D pénètre rapidement (<10 minutes) et profondément le tissu cérébral.

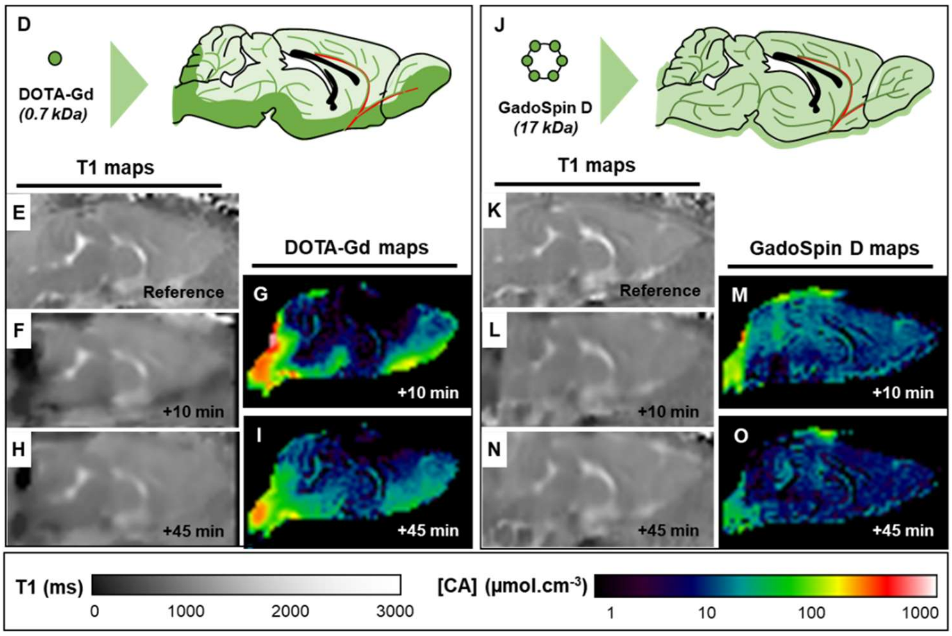

Figure 65 : La différence de répartition dans le tissu cérébral entre le DOTA-Gd et le GadoSpin D

Le GadoSpin D, plus lourd que le DOTA-Gd, se répartit pourtant plus uniformément. Figure extraite de l'**Étude 1**, 2021.

Cette différence est surprenante : en effet, les molécules légères diffusent plus rapidement (et donc plus loin) que les molécules lourdes, un phénomène déjà décrit en microscopie dans le parenchyme cérébral par Smith et collaborateurs (Smith et al., 2017). Les dextrans utilisés par ces auteurs ne pèsent cependant pas moins de 10 kDa, et leurs données peuvent donc ne pas s'appliquer à notre observation avec une molécule plus légère. Le même article montre par ailleur l'espace périvasculaire comme une voie de passage pour des composés présents dans le LCR jusqu'à 2000 kDa. Ce résultat est corroboré par un article en cours de révision utilisant du GadoSpin P (200 kDa) (Ray et al., 2021).

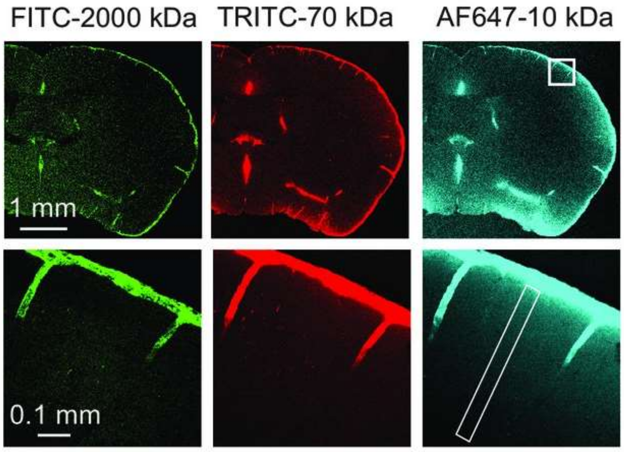

Figure 66 : La diffusion dans le parenchyme dépend de la taille des solutés, mais pas dans l'EPV

Vue d'une section de cortex de souris après injection de dextrans de différents poids moléculaires (10 kDa, 70 kDa et 2000 kDa). D'après Smith et al., 2017.

Notre théorie pour expliquer ces observations se base sur la différence du volume de distribution des deux traceurs que nous avons employé. Le DOTA-Gd, relativement léger, est ainsi capable de franchir la glie limitante et de se disperser dans l'espace interstitiel. En revanche, le GadoSpin D, plus lourd, reste principalement contraint dans l'espace sous-arachnoïdien et les EPV. Le deuxième effet à prendre en compte est la vitesse accélérée de dispersion dans l'EPV, un phénomène causé par la pulsatilité artérielle (Asgari et al., 2016; Iliff et al., 2013b). Bien que l'existence d'un flux convectif (directionnel) dans les EPV reste controversé, la pulsation des artères dans cet espace restreint permet un brassage oscillatoire du fluide et des solutés qui s'y trouvent. Le GadoSpin D, restreint à cet espace, bénéficierait donc davantage de cet effet que le DOTA-Gd qui se disperse très vite dans l'espace interstitiel proche. Globalement, le GadoSpin D, et peut-être d'autres macromolécules endogènes, seraient donc mieux dispersées dans le parenchyme que les petites molécules. Outre la BHE, ces dernières pourraient être préférentiellement drainées via l'IPAD.

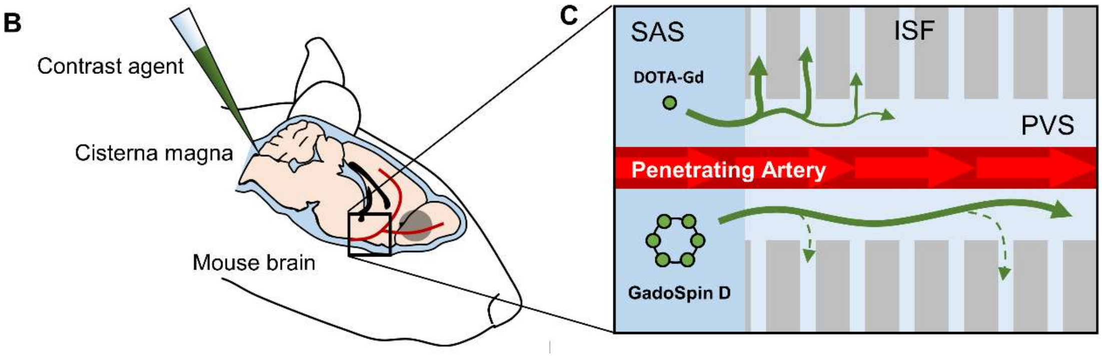

Figure 67 : Passage du GadoSpin D et du DOTA-Gd dans le tissu et l'EPV

L'effet filtre de la glie limitante pourrait expliquer que les gros composés se dispersent plus en profondeur que les petits. Figure extraite de l'étude 1 présentée dans ce manuscrit, 2021.

Pourquoi l'IRM de diffusion ne corrèle pas avec l'IRM-RCD

L'objectif principal de ma thèse a été d'établir une corrélation entre IRM de diffusion et IRM-RCD. Cependant, bien que cet objectif soit resté au cœur de notre effort de recherche, nous n'avons pu mettre en évidence une telle corrélation.

À la base de cet échec se trouvent les différences fondamentales entre les deux techniques utilisées. En effet, l'IRM de diffusion est une imagerie des mouvements **microscopiques** de l'**eau** dans le **tissu**, alors que l'IRM-RCD suit la dispersion **macroscopique** d'un **agent de contraste** injecté dans l'**espace sous-arachnoïdien**.

L'eau et les agents de contrastes (DOTA-Gd ou GadoSpin D) diffèrent par de nombreux aspects, en premier lieu leur mobilité dans le tissu. Si l'eau est capable de diffuser au travers de la BHE et dispose de ses propres canaux (aquaporines), il n'en est pas de même pour les agents de contraste. La dispersion de ces derniers dans le tissu est donc à rapprocher des métabolites ne pouvant franchir la BHE comme les ions (Hladky and Barrand, 2018).

En second lieu, l'échelle des phénomènes observés par chacune de ces imageries rend difficile leur corrélation. Alors que le signal en imagerie de diffusion peut être extrait voxel à voxel, la dispersion d'un traceur injecté dans le LCR ou le parenchyme est un phénomène à l'échelle de la boîte crânienne, et, dans le cadre de son injection dans le LCR, dépend fortement de son transport dans les espaces sous-arachnoïdiens, un facteur qui n'est aucunement mesuré par l'IRM de diffusion.

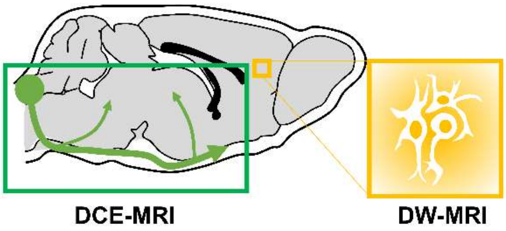

Figure 68 : Pourquoi l'IRM de diffusion ne corrèle pas avec l'IRM-RCD

L'objectif initial de ma thèse était de trouver un lien entre IRM de diffusion (DW-MRI) et IRM-RCD (DCE-MRI), pour que la première puisse remplacer la seconde en clinique. Je n'ai pu mener cet objectif à bien, une des causes étant que les deux types d'imagerie révèlent des phénomènes très différents.

Plus que le proxy que nous souhaitions en faire, l'IRM de diffusion s'est révélée complémentaire à l'IRM-RCD. Nous avons tiré parti de cet aspect dans la **Collaboration 1**.

Ce travail a porté sur la caractérisation d'un modèle murin de MLC (MLC1KO) développé par Martine Cohen-Salmon. La MCL est une pathologie dans laquelle les pieds astrocytaires ne forment pas d'EPV fonctionnels autour des vaisseaux, et se traduit entre autres par un œdème cérébral. L'IRM de diffusion nous a permis de montrer un ADC élevé dans le cerveau des animaux MLC1KO, ce qui correspond à l'œdème observé en pathologie humaine. Le volume cérébral des MLC1KO est également plus important, ce qui perturbe l'écoulement normal du LCR, ce qu'a révélé notre étude en IRM-RCD. Dans ce modèle, les deux imageries permettent de montrer des altérations dans le tissu cérébral et dans les flux de LCR, mais l'une ne peut remplacer l'autre.

Peut-on suivre le système glymphatique en IRM de diffusion ?

Un point important à questionner est la capacité de l'IRM de diffusion à déceler l'activité du système glymphatique. Au début de notre étude, nous avons supposé pouvoir observer directement cette activité. Les mouvements de fluide associés au système glymphatique que nous aurions pu détecter sont de deux types : le **flux périvasculaire**, et le **flux dans le tissu**.

L'existence d'un **flux oscillatoire périvasculaire** mû par la pulsatilité vasculaire fait généralement consensus. Cependant sa directionalité, l'un des piliers de la théorie glymphatique, est bien moins établie. En imagerie de diffusion, le flux périvasculaire a été visualisée par Harrisson et collaborateurs dans les EPV de la base du crâne chez le rat en imagerie de tenseur de diffusion (Harrison et al., 2018). Cependant, cette technique ne s'intéresse pas aux artères pénétrantes à proprement parler mais aux artères piales. D'autres études *in vivo* ont confirmé l'existence d'un flux oscillatoire et convectif dans ces dernières par le suivi de microparticules en imagerie biphotonique (Bedussi et al., 2018; Mestre et al., 2018).

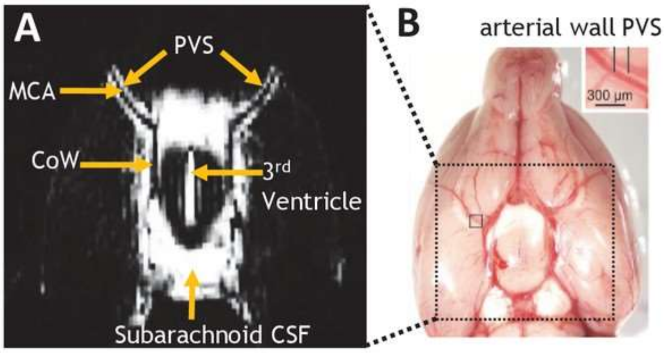

Figure 69 : IRM des EPV de la base du crâne chez le rat

Le flux oscillatoire de LCR dans les EPV (PVS) a été visualisé en imagerie du tenseur de diffusion. D'après Harrison et al., 2018.

Cette approche reste limitée par sa résolution aux EPV de gros diamètre. Au cours de ma thèse, nous nous sommes intéressés à une approche statistique similaire à l'IVIM. Brièvement, le modèle IVIM est capable de distinguer dans un voxel la part d'eau contenue dans les capillaires, dont le mouvement est rapide (pseudo-diffusion), à celle représentée par le tissu dont le mouvement plus lent est essentiellement de la diffusion (Bihan et al., 1988). Une possibilité que nous avons explorée est d'ajouter un troisième compartiment à ce modèle, correspondant aux espaces périvasculaires, et dont les molécules d'eau présenteraient une mobilité intermédiaire entre celles du sang et celles du tissu.

Cette solution ne s'est pas révélée viable car elle présentait un problème majeur : la quantité de signal provenant des EPV. La fraction corespondant aux EPV dans un voxel est difficile à estimer. D'après (Schain et al., 2017), l'aire de l'EPV sur une section de vaisseau est cinq fois inférieure à celle de l'artère et sept à huit fois inférieure à celle de la veine. Les EPV sont par ailleurs absents des capillaires, qui forment à eux seul la moitié du compartiment sanguin cérébral (Wilson, 2016). Le signal potentiellement exploitable en IRM de diffusion dans les EPV du tissu est ainsi au moins un ordre de grandeur au-dessous du signal du sang, lui-même un ordre de grandeur au-dessous de celui du tissu.

Une autre approche serait de s'intéresser au flux convectif dans le tissu, le second pilier de la théorie glymphatique (Iliff et al., 2012). Cette partie de la théorie est cependant fortement critiquée (Hladky and Barrand, 2018; Holter et al., 2017; Smith et al., 2017). Si un tel flux existait, il ne serait pas visible tel quel à l'échelle de nos méthodes d'imagerie – les distances artèrioles-veinules dans le tissu cérébral sont courtes, 200-300 µm selon (Holter et al., 2017) et fortement enchevêtrées (Reina-De La Torre et al., 1998). Un flux de FISC pourrait donc être isotropique et difficile à distinguer de la diffusion. Plusieurs études ont ainsi suggéré que l'ADC, un paramètre mesurant la diffusion générale dans le tissu, pourrait être corrélé à une activation du système glymphatique (Demiral et al., 2019; Komaki et al., 2020; Tuura et al., 2021). En pratique, l'ADC est modifié par une grande variété d'altérations tissulaires (fibrose, œdème) et ce manque de spécificité rend dificilement envisageable son exploitation clinique comme proxy de l'activité glymphatique.

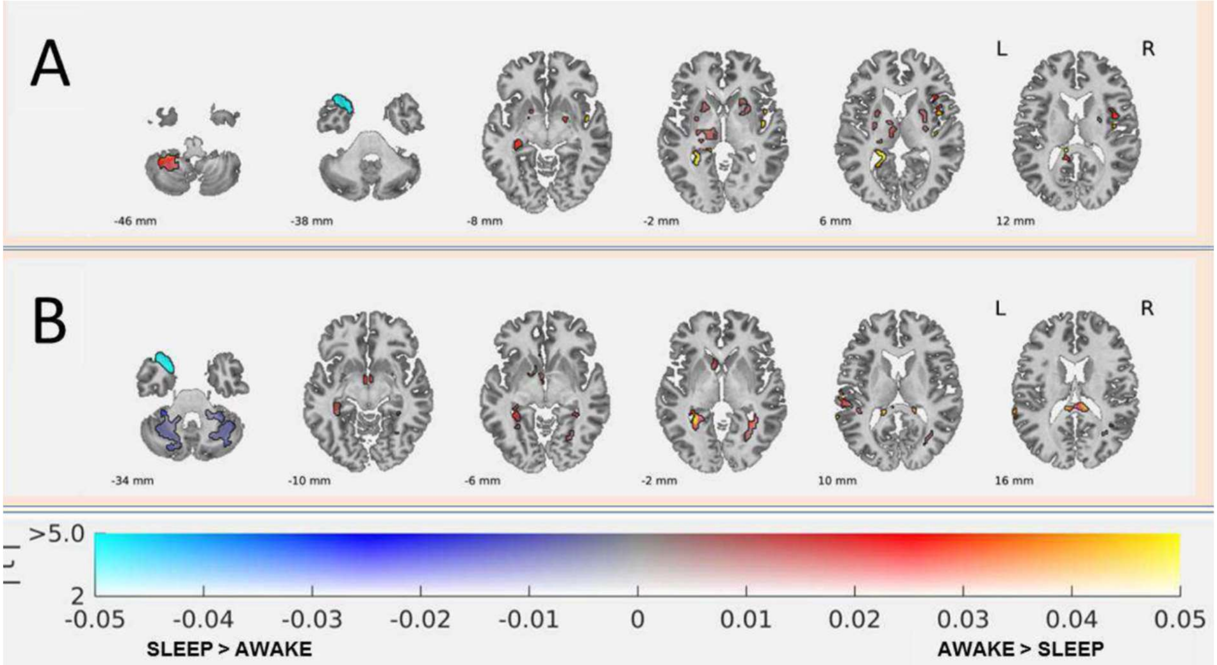

Figure 70 : Variations d'ADC observées entre la veille et le sommeil chez l'être humain

Le sommeil est régulièrement avancé comme un des activateurs du système glymphatique, et l'ADC est ici une technique proposée pour révéler son activité. L'ADC reste un paramètre peu spécifique, est son utilisation dans un contexte clinique reste peu envisageable. D'après Demiral et al., 2019.

Influence des anesthésiques sur la maturation des voies du LCR

Le LCR joue un rôle majeur lors du développement embryonnaire, où il permet le transport de facteurs trophiques le long de ce qui deviendra le système ventriculaire, i.e. le tube neural (Bueno et al., 2020). Ce flux est principalement réglé par le mouvement ciliaire des épendymocytes (Jiménez et al., 2014) et la dérégulation du système du LCR est liée à une variété de pathologies chez le nouveau-né, des TSA (Shen et al., 2017) aux hydrocéphalies (Kahle et al., 2016). Les anesthésiques, couramment utilisés en pratique clinique, sont reconnus comme des agents perturbant l'écoulement du LCR et son interaction avec le tissu cérébral (Gakuba et al., 2018; Hablitz et al., 2019; Stanton et al., 2021). Cependant, un enfant sur sept reçoit une anesthésie générale avant l'âge de trois ans (Shi et al., 2018).

Au cours de ma thèse, je me suis intéressée à la possible influence de l'anesthésie générale sur le développement des circuits du LCR chez la souris. Dans le cadre de la **Collaboration 2** présentée dans ce manuscrit et portée par Jean-Philippe Salaün, nous avons soumis des souriceaux à une exposition répétée à l'isoflurane, un analogue du sévoflurane utilisé en clinique. Nous avions précédemment montré dans notre équipe qu'une exposition aiguë à l'isoflurane diminue les échanges LCR-FISC (Gakuba et al., 2018). Les expositions ont été réalisées *in utero* ou en postnatal (P4-P10). Dans les deux cas, nous avons observé chez l'adulte des troubles comportementaux liés à la peur et à l'anxiété (les données *in utero* n'ont pas été retenues pour l'article). Pour les animaux exposés en période périnatale, une diminution de volume de la substance grise périacqueducale, impliquée dans la gestion de la peur, a également été observée (cette expérience n'a pas été menée sur les groupes *in utero*). Nous avons aussi évalué les échanges LCR-FISC en IRM-RCD après injection de DOTA-Gd dans le LCR. Cependant, cette expérience ne nous a pas permis de montrer de différences significatives entre les groupes exposés et non exposés. Ces résultats, qui ne pouvaient pas être reproduits chez l'enfant dans notre étude, n'ont pas été retenus pour l'article.

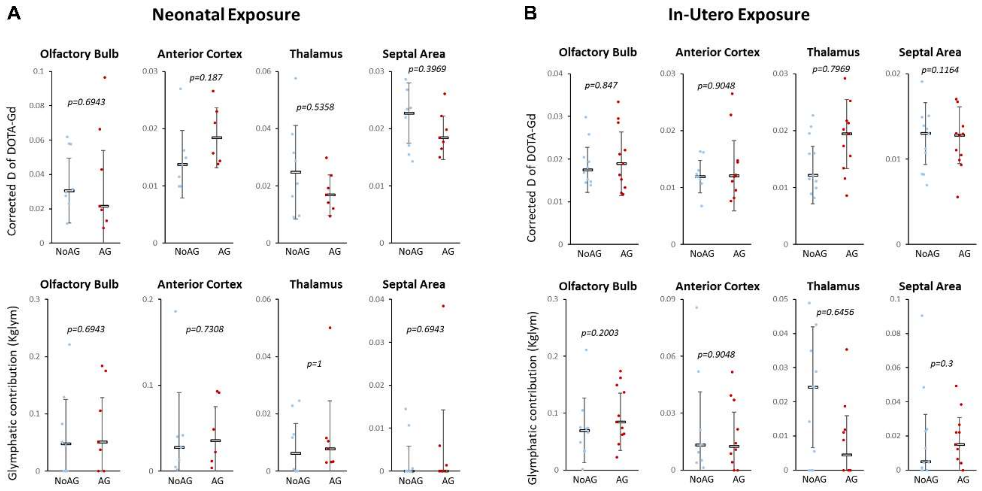

Figure 71 : L'exposition postnatale (isoflurane) à l'anesthésie ne perturbe pas les échanges LCR-FISC chez l'adulte

Comparaison entre groupes exposés (AG) ou non (noAG) à l'anesthésie. L'agent utilisé est le DOTA-Gd. Les valeurs exprimées sont issues du modèle corrigé pharmaco-Fick, qui a par la suite été abandonné. Figure réalisée à partir des données aimablement prêtées par Jean-Philippe Salaün, 2019.

Ultérieurement, nous avons réalisé des expériences en IRM-RCD chez des souris soumises cette fois à une exposition postnatale prolongée (4h30) à la kétamine. Cette expérience visait à modéliser les anesthésies prolongées chez les enfants en réanimation, chez lesquels ont été rapportés des troubles post-anesthésie (Manning et al., 2018). Dans cette étude dont les résultats sont détaillés dans la thèse de médecine de Marine Rolland, l'altération des comportements liés à l'anxiété est retrouvée, ce qui la rapproche des résultats de la Collaboration 2. En revanche, nous n'avons pu montrer de différence liée à l'exposition postnatale prolongée aux anesthésiques dans les échanges LCR-FISC, malgré l'utilisation du GadoSpin D potentiellement plus efficace que le DOTA-Gd. À noter toutefois que l'anesthésique employé ici, la kétamine, affecte moins les échanges LCR-FISC que l'isoflurane (Gakuba et al., 2018; Stanton et al., 2021).

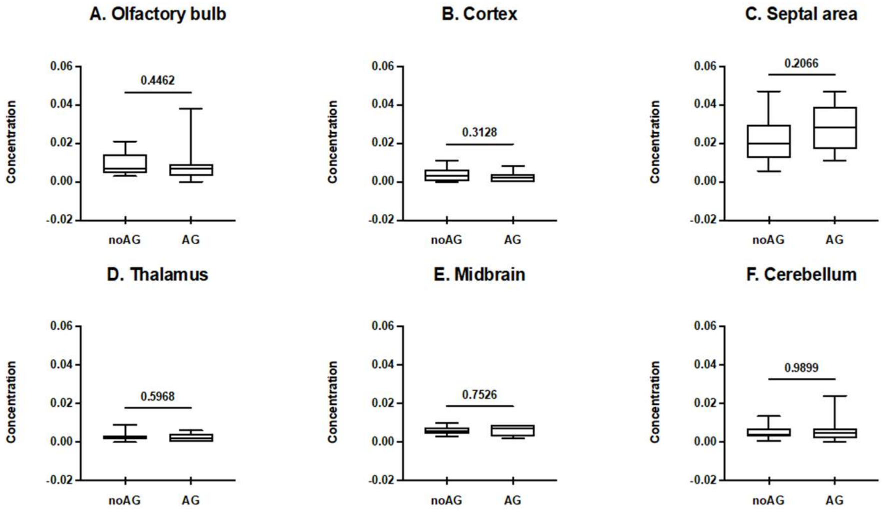

Figure 72 : L'exposition postnatale prolongée à l'anesthésie (kétamine) ne perturbe pas les échanges LCR-FISC chez l'adulte

Comparaison entre les groupes exposés à l'anesthésie (AG) ou contrôle (noAG). Les échanges LCR-FISC sont représentés par un ratio représentant l'évolution de la concentration en GadoSpin D dans le tissu sur 45 minutes. Figure aimablement prêtée par Marine Rolland, 2021.

Les anesthésiques agissent sur les échanges LCR-FISC à plusieurs niveaux (pulsatilité artérielle, PaCO2, ventilation, température corporelle, inhibition NMDA, etc…) (Hablitz et al., 2019; Stanton et al., 2021), mais leur effet sur le développement de ces échanges restent peu clairs. La mise en place des EPV dépend de la polarisation des pieds astrocytaires, un phénomène postnatal chez le rongeur et impliquant notamment MLC1, une protéine de jonction dont les mutations causent la MLC chez l'être humain et la souris (**Collaboration 1**). Les expériences que nous avons réalisé chez la souris suggère que, si les échanges LCR-FISC sont altérés lors d'une exposition aux anesthésiques (Gakuba et al., 2018), cette modification ne semble pas se répercuter sur le développement de ces échanges. En revanche, chez la souris comme chez l'enfant nous avons observé qu'une exposition précoce à l'anesthésie peut se traduire par des atteintes structurelles et cognitives (**Collaboration 2**). L'effet ou non d'une anesthésie sur le neurodéveloppement est encore débattue (Vutskits and Culley, 2019) et la recherche préclnique reste un acteur indispensable dans l'étude de cette question – *cf.* revue dans **Autres travaux 1** (Salaün et al., 2021).

Complément à la discussion de l'Étude 3

Dans l'article de Camille Di Palma et collaborateurs dont je suis coautrice (**Étude 3**) (Di Palma et al., 2018), nous nous sommes intéressés à la maturation des voies du LCR chez le rongeur. Des traceurs (indocyanine, 0.8 kDa ; ou DOTA-Gd, 0.7 kDa) ont été injectés dans le LCR au niveau de la *cisterna magna* ou dans le striatum, puis leur dispersion imagée en NIRF et en IRM.
Les résultats de l'article montrent sans équivoque que les flux de LCR et de FISC sont immatures chez le nouveau-né. La discussion tente de lier ces observations à une dysfonction du système glymphatique, un point auquel je souhaite apporter quelques précisions. En effet, de nombreux phénomènes autre que le système glymphatique peuvent agir sur la dispersion de l'agent de contraste au cours du développement, mais ils n'ont pas été abordés dans l'**Étude 3**.

En premier lieu, la dispersion du traceur dans l'espace sous-arachnoïdien, et dont la maturation est révélée par l'augmentation du ratio de contraste bulbe/cervelet, ne correspond pas au système glymphatique tel que décrit par (Iliff et al., 2012) mais aux voies sous-arachnoïdiennes du LCR. La géométrie de l'espace sous-arachnoïdien est complexe, délimitée par les méninges et dépend de multiples facteurs indépendants du système glymphatique. Dans la **Collaboration 1** et dans l'**Étude 1**, nous faisons ainsi le lien entre la dispersion de l'agent de contraste dans cet espace et une variation du volume cérébral, qu'il s'agisse d'une réduction liée à l'âge ou d'une augmentation causée par un œdème. Chez l'adulte, le crâne forme une boîte rigide permettant la transmission d'ondes de pression dans le LCR (Wagshul et al., 2011). Chez le nouveau-né humain comme murin, les os crâniens sont encore en cours de formation et séparés par des sutures souples (par exemple la fontanelle) (Bradley et al., 1996). L'intégrité de la boîte crânienne est essentielle à la circulation du LCR, tel que révélé par (Plog et al., 2019) et l'**Étude 2** dont je suis coautrice (Borha et al., 2020), mais cet aspect n'a pas été abordé dans l'**Étude 3**. Le RLM, autre voie d'élimination du LCR, a été décrit comme immature chez le nouveau-né (Antila et al., 2017). Notons enfin que l'une des voies canoniques d'élimination du LCR, les villosités arachnoïdiennes, ne sont présentes ni chez le rongeur, ni chez le nouveau-né humain (Proulx, 2021). Les mécanismes à l'œuvre sont encore peu étudiés mais ont une pertinence clinique. Chez la souris adulte, l'efflux du LCR se fait principalement par la lame criblée de l'ethmoïde, juste sous les bulbes olfactifs (Ma et al., 2017). Cette voie est réduite avec le vieillissement. D'autre part, chez l'être humain nouveau-né, un surplus de LCR extra-axial est corrélé au risque de TSA (Shen et al., 2017).

En second lieu, une des expériences réalisées dans l'article consiste en l'injection d'un traceur dans le parenchyme. Fait intéressant, cette voie a en réalité très peu été étudiée par les partisans du système glymphatique qui lui préfèrent une injection dans le LCR , mais elle trouve une pertinence nouvelle dans le cadre de l'IPAD. Brièvement, l'IPAD est une voie de drainage du FISC dans la media artérielle, principalement étudiée par injection de traceurs dans le parenchyme (Carare et al., 2008). L'expérience que nous avons réalisée suggère ainsi que l'IPAD, plutôt que le système glymphatique, est immature chez le nouveau-né.

Un influx périvasculaire de LCR après un arrêt cardiaque ?

J'ai pu au cours de ma thèse observer incidentalement la dispersion *post-mortem* d'un agent de contraste. Immédiatement après le décès de l'animal, l'agent de contraste injecté dans le LCR entre dans le parenchyme cérébral le long des espaces périvasculaires.

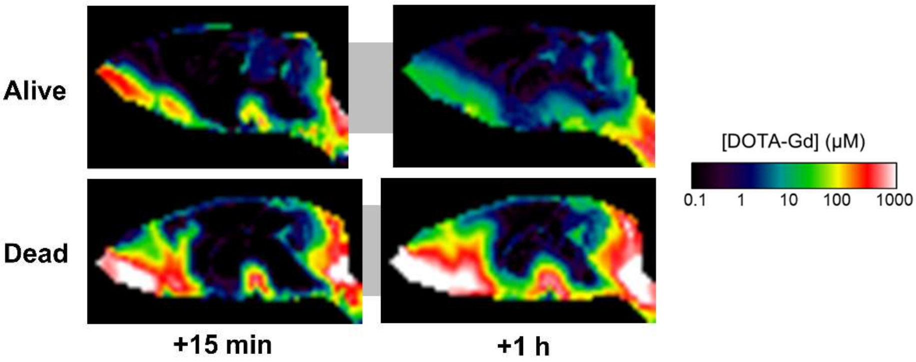

Figure 74 : Dispersion post-mortem de l'agent de contraste

L'agent de contraste (DOTA-Gd) injecté dans le LCR entre dans le tissu cérébral via les espaces périvasculaires chez un animal décédé. Images représentatives chez une souris vivante (Alive) et décédée (Dead) à 15 minutes et 1h après injection. Données personnelles, 2019.

Intrigués par le phénomène, nous avons pu le reproduire de manière contrôlée en coupant l'alimentation en O2 d'animaux anesthésiés en cours d'acquisition. En imagerie de diffusion, nous avons observé une diminution rapide de l'ADC, signalant l'apparition d'un œdème cytotoxique. Dans notre mini-étude, la mort est causée par un arrêt cardiorespiratoire. Au niveau tissulaire, l'interruption de la circulation sanguine s'apparente à celle observée dans la lésion ischémique provoquée par un AVC. En effet, dans leur article de 2020, Mestre et collaborateurs ont observé un phénomène similaire dans un modèle murin d'AVC (Mestre et al., 2020a). Selon ces auteurs, le flux de LCR est dû à la vasoconstriction des artères pénétrantes, causées par les dépolarisations envahissantes déclenchées par l'ischémie. Une observation semblable est rapportée par Schain et collaborateurs dans un modèle murin d'épilepsie (Schain et al., 2017).

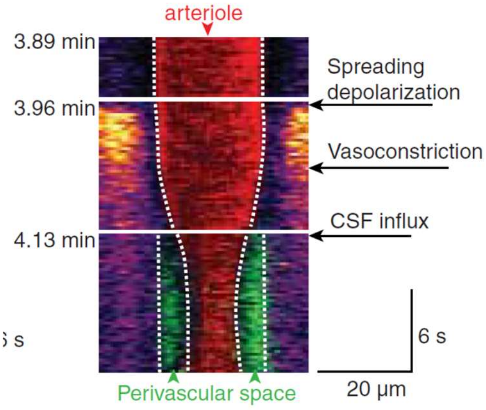

Figure 73 : Vasoconstriction et influx de LCR dans une lésion ischémique

Quelques minutes après l'arrêt de la circulation sanguine, des dépolarisations envahissantes se propagent dans le tissu cérébral. Ces dépolarisations entraînent la contraction des artérioles et un 'influx périvasculaire de LCR, qui contribue à la formation de l'œdème. Timelapse d'une section de vaisseau en imagerie biphotonique. D'après Mestre et al., 2020.

Une interruption générale de la circulation sanguine telle que dans notre modèle peut de plus se traduire par une redistribution du sang vers les régions basses du corps (*livor mortis*), et diminuer encore le volume sanguin dans l'espace périvasculaire. Ces phénomènes pourraient trouver une pertinence clinique dans l'arrêt cardiaque, fatal dans 90% des cas (Du et al., 2021; Gräsner and Bossaert, 2013).

Le problème des anesthésiques – vers des examens vigiles ?

La plupart des observations précliniques *in vivo* des échanges LCR-FISC, incluant celles présentées dans ce manuscrit, sont réalisées sous anesthésie. Cependant, il est établi que ces molécules perturbent le flux sanguin (Slupe and Kirsch, 2018), un des acteurs majeurs de ces échanges (Iliff et al., 2013b), ou agissent plus directement via leur activité neurodépressive (Hablitz et al., 2019). Seules quelques études ont pu réaliser l'imagerie d'animaux éveillés, par exemple en NIRF (Gakuba et al., 2018). L'IRM est une technique peu tolérante au mouvement, et lors d'acquisitions vigiles les animaux doivent être contentionnés.

Au laboratoire, nous avons développé une prothèse crânienne permettant de pratiquer un modèle d'ischémie sur animaux vigiles. À la fin de ma thèse, nous avons exploité ce système afin de réaliser une imagerie vigile des échanges LCR-FISC avec agent de contraste. Nous avons de plus adapté le protocole décrit par (Xavier et al., 2018) afin de réaliser l'injection du traceur lors des acqusitions grâce à une canule implantée dans la cisterna magna.

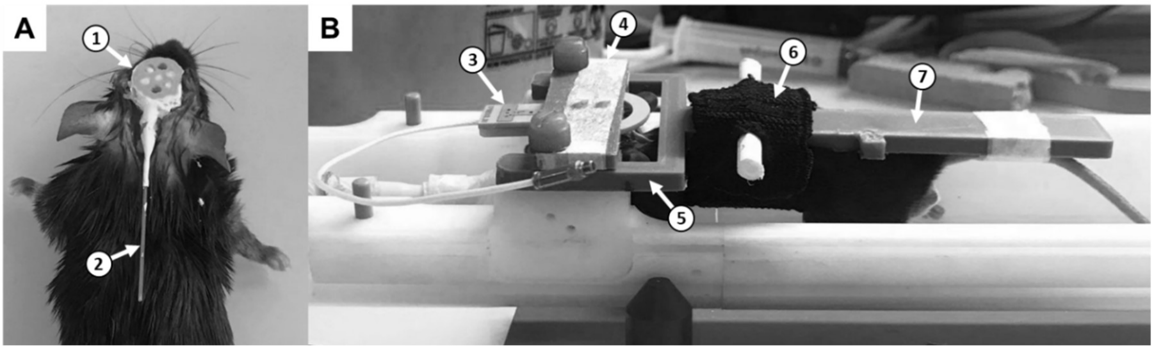

Figure 75 : Dispositif de contention pour IRM vigile

La souris est équipée d'une prothèse crânienne (1) permettant la fixation de la tête à la première pièce du dispositif de contention (4). Cette dernière est supportée par un cadre (5) prolongé par un bras (7) auquel le corps de la souris est attaché par un harnais (6). Une antenne de surface (3) permet de réaliser l'IRM et l'agent de contraste est injecté par une canule (2) implantée dans la cisterna magna. Photographies aimablement fournies par Quentin Gérard.

Nous comptons exploiter ce dispositif afin de réaliser l'IRM des échanges LCR-FISC sur un modèle d'AVC ischémique, dans la lignée d'études précédentes réalisées dans le laboratoire (Gaberel et al., 2014; Goulay et al., 2017). Le modèle utilisé repose sur la formation d'un caillot dans l'artère carotide interne à l'aide d'une application locale de chlorure de fer (de Lizarrondo et al., 2017).

L'examen vigile offre aussi l'opportunité d'étudier les mécanismes liés au sommeil. Dans leur article de 2013, Xie et collaborateurs ont en effet suggéré que le système glymphatique serait plus actif lors du sommeil (Xie et al., 2013), des résultats qui restent à confirmer (Cai et al., 2020; Gakuba et al., 2018). Une autre étude montre le lien entre oscillations de grande amplitude dans le LCR et sommeil lent profond (Fultz et al., 2019), lesquelles pourraient être liées à une plus grande diffusivité du tissu cérébral (Tuura et al., 2021).

Conclusion : y-a-t ’il un ‘système glymphatique’ ?

Le système glymphatique a été défini par l'équipe de Maiken Nedergaard comme un flux convectif de LCR, qui entre dans les espaces périartériels, traverse le tissu cérébral et arrive aux espaces périveineux en emportant à sa suite les déchets du métabolisme (Benveniste and Nedergaard, 2021; Iliff et al., 2012). Si le rôle des espaces périvasculaires en tant que carrefour entre le LCR et le FISC est largement reconnu, l'existence d'un flux convectif fait débat (Faghih and Keith Sharp, 2021; Hladky and Barrand, 2018; Smith and Verkman, 2018).

À titre personnel, je ne suis pas convaincue par l'hypothèse du système glymphatique. Si un flux directionnel a été montré le long des artères piales (Bedussi et al., 2018; Mestre et al., 2018), ce n'est le cas ni pour les artères pénétrantes, ni pour le tissu interstitiel (Smith et al., 2017). Par ailleurs, la mécanique invoquée pour expliquer son fonctionnement entre en conflit avec trop de constats bien établis dans la littérature (Faghih and Keith Sharp, 2021; Holter et al., 2017).
Dans cette discussion, nous n'entrerons pas dans les détails de la controverse, les observations réalisées au cours de cette thèse ne permettant en aucun cas de trancher la question. Remarquons cependant que nous observons bien un passage de l'agent de contraste dans le tissu. En particulier, ces échanges semblent plus rapides pour les molécules lourdes comme le GadoSpin D. Ces résultats évoquent, en continuité avec la littérature, l'existence dans le tissu cérébral d'axes d'échanges LCR-FISC rapides et à longue distance. Le travail présenté dans l'Étude 1 suggère de plus que ces voies sont sélectives à la taille des composés. Si les détails de leur fonctionnement et leurs interactions avec d'autres systèmes comme la BHE ou l'IPAD restent à définir, ce phénomène est bien tangible.

Plus viscéralement, un modèle n'a pas besoin d'être exact pour être utile. De nombreux paradigmes se sont succédés au cours de l'histoire du LCR : la théorie médiévale du *spiritus animalis* a ainsi été remplacée par le modèle contemporain de la "troisième circulation", lui-même mis à l'épreuve par la découverte du réseau lymphatique méningé. Chacune de ces compréhensions a donné un cadre conceptuel aux penseurs de son temps et permis l'élaboration et le raffinement de ses successeurs.
Le système glymphatique, issu d'observations *bona fide* liées à des théories antérieures (Cserr et al., 1977; Földi et al., 1968; Rennels et al., 1985), est lui aussi mis à l'épreuve. Ce modèle a cependant illuminé ce secteur de la recherche et a proposé un terme, *"glymphatic"*, repris par plus de 750 articles. Cette visibilité s'est traduite par l'étude des flux du LCR dans une grande variété de conditions et a permis le développement de méthodologies innovantes. Tout aussi important, elle a donné un cadre pour diffuser ces thématiques auprès du public et des décisionnaires. Par exemple, mes travaux de thèse ont été financés en partie par un crédit de l'Agence Nationale de la Recherche, pour un projet nommé *Magnetic Resonance Imaging of the Glymphatic System* (MRGly).

AUTRES TRAVAUX

Revue : Magnetic Resonance Imaging of Blood-Brain Barrier permeability in Dementia

Cette revue dont je suis première autrice a pour objet la perméabilisation de la BHE dans la démence, la maladie des petits vaisseaux et le vieillissement, observée en IRM-RCD. J'ai réalisé la recherche bibliographique, l'ai résumée dans les tableaux et la figure 3 et ai contribué à la rédaction d'une partie significative de l'article.

ARTICLE IN PRESS

NEUROSCIENCE

REVIEW

A. Chagnot et al. / Neuroscience xxx (2021) xxx–xxx

Magnetic Resonance Imaging of Blood–Brain Barrier permeability in Dementia

Audrey Chagnot, [a] **Samuel R. Barnes** [b] **and Axel Montagne** [c,d*]

[a] Normandie Université, UNICAEN, INSERM, UMR-S U1237, Physiopathology and Imaging of Neurological Disorders (PhIND), Institute Blood and Brain @ Caen-Normandie (BB@C), GIP Cyceron, Caen, France

[b] Department of Radiology, Loma Linda University, Loma Linda, CA, USA

[c] UK Dementia Research Institute, Edinburgh Medical School, University of Edinburgh, Edinburgh, UK

[d] Centre for Clinical Brain Sciences, University of Edinburgh, Edinburgh, UK

Abstract—Alzheimer's disease (AD) and cerebral small vessel disease (cSVD) are the two main causes of dementia with blood–brain barrier (BBB) breakdown being a common contributor. Recent advances in neuroimaging techniques offer new possibilities to understand how the brain functions in health and disease. This includes methods such as dynamic contrast-enhanced magnetic resonance imaging (DCE-MRI) which allows the detection of subtle regional changes in the BBB integrity. The purpose of this work is to provide a review on the recent DCE-MRI findings of subtle BBB leakage focusing on cSVD and AD, including both clinical and pre-clinical studies. Despite being widely used and well-established, we also highlight some of the DCE-MRI challenges and pitfalls faced in the context of dementia inherent to the subtle nature of BBB impairment.

This article is part of a Special Issue entitled: Brain imaging. **© 2021 IBRO. Published by Elsevier Ltd. All rights reserved.**

Key words: magnetic resonance imaging, blood-brain barrier, cerebral small vessel disease, Alzheimer's disease, dementia.

INTRODUCTION

Given its unique metabolic needs, the brain is one of the most highly perfused organs in the body with 400- and 0.4-mile-long vascular network in humans and mice, respectively (Begley and Brightman, 2003; Zlokovic, 2008; Montagne et al., 2017). This represents on average one mile of vessels per three grams of human brain tissue and for mice it is even denser, with one mile of vessels per one gram of brain tissue. All brain capillaries are constantly perfused, and it has been estimated that no neuron is more than 10–20 μm away from a capillary (Tsai et al., 2009), which implies that every neuron has its own capillary and thus demonstrates the critical relationship between the vascular and neuronal compartments. Importantly, there is increasing evidence supporting the involvement of brain vascular dysfunction in the early stages of brain disorders such as Alzheimer's disease (AD) (Montagne et al., 2015; Montagne et al., 2017; Montagne et al., 2020; van de Haar et al., 2016a; van de Haar et al., 2016b; Nation et al., 2019; Sweeney et al., 2019a) and cerebral small vessel disease (cSVD) (Zhang et al., 2017b; Wardlaw et al., 2019). Furthermore, it was recently discovered that vascular cells express at least 30 of the top 45 AD risk genes using single-nucleus RNA sequencing on human brain samples (Yang et al., 2021), suggesting that the brain vasculature may play a larger role in the pathogenesis of dementia than was originally thought. Vascular dysfunction can take many forms, involving different cell types comprising the neurovascular unit (NVU), and including disruption of the blood–brain barrier (BBB), which plays a vital role in maintaining brain functions. Many neuroimaging and biofluid biomarker studies, as well as neuropathological studies have revealed the importance of BBB breakdown in the development and progression of common dementias, as extensively reviewed elsewhere (Sweeney et al., 2018a; Sweeney et al., 2018b; Sweeney et al., 2019a)

The most advanced method for investigating quantitatively and regionally subtle BBB failure in the living human or rodent brain is dynamic contrast-

---

*Corresponding author. Address: UK Dementia Research Institute, Centre for Clinical Brain Sciences, The University of Edinburgh, Chancellor's Building, 49 Little France Crescent, Edinburgh EH16 4SB, UK.

E-mail address: axel.montagne@ed.ac.uk (A. Montagne).

Abbreviations: AD, Alzheimer's disease; ASL, arterial spin labeling; BBB, blood–brain barrier; cSVD, cerebral small vessel disease; DCE-MRI, dynamic contrast-enhanced magnetic resonance imaging; EPVS, enlarged perivascular spaces; GBCAs, gadolinium-based contrast agents; MCI, mild cognitive impairment; NVU, neurovascular unit; SPGR, spoiled gradient echo; SSS, superior sagittal sinus; VFA, variable flip angle; VTR, variable time repetition; WMH, white matter hyperintensities; Aβ, amyloid-β; APOE, apolipoprotein E; AQP4, aquaporin-4; BD, Binswanger's disease; CSF, cerebrospinal fluid; FLASH, fast low angle shot; Gd, gadolinium; GRE, gradient echo; MTL, medial temporal lobe; pTau, phosphorylated tau; RF, radiofrequency.

https://doi.org/10.1016/j.neuroscience.2021.08.003

0306-4522/© 2021 IBRO. Published by Elsevier Ltd. All rights reserved.

Please cite this article in press as: Chagnot A et al. Magnetic Resonance Imaging of Blood–Brain Barrier permeability in Dementia. Neuroscience (2021), https://doi.org/10.1016/j.neuroscience.2021.08.003

enhanced magnetic resonance imaging (DCE-MRI) using ~1 kDa paramagnetic gadolinium-based contrast agents (GBCAs). DCE-MRI method has become more and more available, and the field has now moved from the easily measured BBB damage in diseases with large permeability leaks (*e.g.*, brain tumors, multiple sclerosis, or strokes), to more subtle disruption in chronic vascular disease and dementia. The slow accumulation of GBCAs from the intravascular into the extracellular extravascular space of the brain can be measured to determine regional BBB permeability, often referred as the blood-to-brain transfer constant, K_{trans}. The low permeability is in the range of 10^{-4} to 10^{-3} min^{-1}, while permeability in tumors is at least an order of magnitude higher (*i.e.*, 10^{-2} min^{-1}). There are several mathematical models to compute K_{trans} that differ in complexity and assumptions under which they can be applied (Barnes et al., 2016). All the pre- and post-processing steps towards quantifying subtle BBB K_{trans} measurements from DCE-MRI datasets have been summarized elsewhere (Montagne et al., 2016; Raja et al., 2018; Thrippleton et al., 2019; Manning et al., 2021).

In this review, we briefly discuss the role of BBB in health and dementia with a focus on cSVD and AD. Next, we examine the recent DCE-MRI studies performed in both humans and animal models relevant to cSVD and AD pathologies. Finally, we comment on the DCE-MRI challenges and pitfalls from image acquisition to data analysis steps in the context of low-permeability applications.

Blood–Brain barrier in health and dementia

The primary role of the healthy BBB is to keep potentially toxic blood-derived components such as cells and pathogens out of the brain (Zlokovic, 2011; Sweeney et al., 2019b). At the same time, the BBB regulates the transport of molecules in-and-out of the brain and thus controls the chemical composition of the neuronal milieu which is essential for proper neuronal function (Zlokovic, 2011; Zhao et al., 2015; Sweeney et al., 2019b). The BBB comprises several components including endothelial cells, pericytes, basement membrane, astrocyte end feet, neuronal projections and surrounding glial cells, which altogether form the NVU (Fig. 1). Pericytes, embedded within the basement membrane, wrap around endothelial cells that line the BBB, followed by astrocytic end feet encircling them. The BBB links to neurons in a process called neurovascular coupling where alterations in local blood flow occur in response to changes in neuronal activity (Abbott et al., 2010). Other glial and immune cells such as oligodendrocytes, microglia and perivascular macrophages are also in close and sometimes direct contact with the other NVU components allowing for intimate crosstalk (Abbott et al., 2010; Procter et al., 2021). Brain endothelial cells possess a specialized genetic profile which confer the barriers' characteristic properties of limiting paracellular permeability (Pfau et al., 2021). Brain endothelial cells have indeed higher expression of junctional proteins such as adherens junctions (*e.g.*, VE-cadherin), tight junctions (*e.g.*, Occludin, Zonula Occludens-1, Claudin-5) and gap junctions, as detailed elsewhere (Stamatovic et al., 2016). Of note, tight junctions are important in limiting movement of small molecules (< 0.8 kDa) across the BBB (Nitta et al., 2003).

In recent years, there is a growing body of evidence for the contribution of BBB breakdown in the development and progression of common dementias such as AD and cSVD (Fig. 1), as comprehensively examined elsewhere (Sweeney et al., 2018b, 2019a; Wardlaw et al., 2019). Just to highlight a few, there is neuropathological evidence of BBB disruption in AD and cSVD brains as indicated by loss of pericyte coverage of the brain capillary wall as well as perivascular accumulation of blood-derived fibrin(ogen) (Halliday et al., 2016; McAleese et al., 2019). Strikingly, a large post-mortem study found that four out of five AD patients had signs of vascular pathology (Toledo et al., 2013). There are also biofluid biomarker studies providing further evidence of BBB damage being an important feature of dementia pathophysiology. For instance, increased levels of the most common biofluid marker of BBB breakdown, albumin quotient (Qalb), were found in AD (as reviewed in (Sweeney et al., 2019b)). Additionally, cerebrospinal fluid (CSF) levels of soluble platelet-derived growth factor receptor-β (sPDGFRβ), a marker of damaged pericytes (Montagne et al., 2015; Sweeney et al., 2020), were found increased with normal aging (Montagne et al., 2015) and markedly accelerated as cognition declined (Montagne et al., 2015; Montagne et al., 2020; Nation et al., 2019; Ding et al., 2020). Interestingly, CSF sPDGFRβ is significantly elevated in cognitively unimpaired individuals carrying the E4 variant of apolipoprotein E (APOE) *APOE4* (Montagne et al., 2020), the major genetic risk factor for AD, hinting that BBB disruption may be an early marker of cognitive dysfunction and could be considered as a possible driving factor leading to dementia. Besides neuropathological and biofluid biomarkers findings, there are now improved neuroimaging methods such as DCE-MRI which allows for quantifying subtle and local disruption of the BBB in the living human or rodent brain (Raja et al., 2018; Thrippleton et al., 2019). Here, we next summarize the most recent publications using DCE-MRI in the context of cSVD and AD, and applied in both clinical and pre-clinical settings.

DCE-MRI technique

DCE-MRI collects dynamic T1-weighted MRI images that can monitor the change in signal intensity over time. After the collection of some baseline images, a GBCA is injected, this increases the signal intensity proportional to the concentration of the contrast agent. The changes in signal intensity, along with a T1 map (typically measured right before the DCE scan), are used to calculate a quantitative concentration of contrast agent in the blood plasma (C_p) and in the brain tissue, the extracellular extravascular space (C_t). The transport between these two compartments can then be modeled mathematically to solve for various physiological parameters. The most commonly used model for BBB measurements, the Platlak model, has two parameters that are solved for: K_{trans}, a transfer constant from the

Please cite this article in press as: Chagnot A et al. Magnetic Resonance Imaging of Blood–Brain Barrier permeability in Dementia. Neuroscience (2021), https://doi.org/10.1016/j.neuroscience.2021.08.003

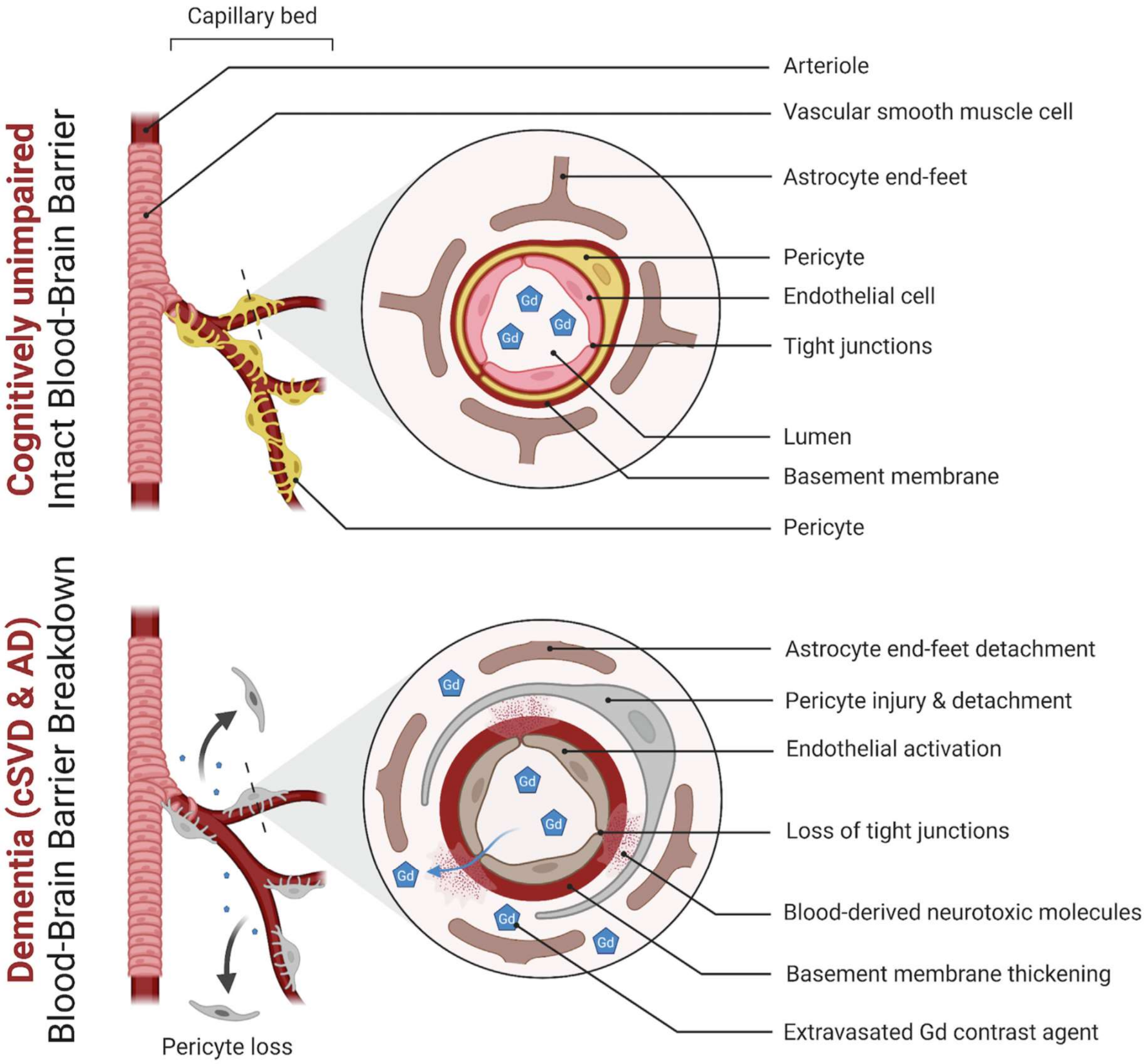

Fig. 1. Blood-brain barrier in health and dementia. A simplified neurovascular unit (NVU) diagram showing a healthy blood–brain barrier (BBB) with the interactive cellular network at the level of brain capillaries that comprises endothelial cells, pericytes, basal membrane, and astrocyte end-feet (*top panel*). In dementia, changes to endothelial cells and pericytes lead to loss of function and BBB breakdown with loss of tight junction proteins (*bottom panel*). Subtle extravasation of Gadolinium (Gd) contrast can be detected using dynamic contrast-enhanced magnetic resonance imaging (DCE-MRI) in both living cerebral small vessel disease (cSVD) and Alzheimer's disease (AD) participants. Subsequent damage then occurs to the surrounding brain cells such as astrocytes, neurons, and oligodendrocytes contributing to pathology and cognitive decline (Figure created using Biorender.com).

blood plasma to the extravascular extracellular space, and V_p, the volume of blood plasma (Fig. 2).

There are many different techniques to acquire T1-maps and T1-weighted MRI images. To our knowledge there has not been a thorough analysis of the tradeoffs or superiority of any given technique. The variety of techniques used is likely a significant source of variability across studies, a rigorous comparison and consolidation to recommended techniques would likely benefit the field. For the dynamic T1-weighted images, spoiled gradient echo (SPGR) is by far the most common sequence used, likely because it is the fastest technique. Fast low angle shot (FLASH), SPGR, fast SPGR (FSPGR), and gradient echo (GRE) are generally equivalent. Some papers utilized saturation recovery gradient echo sequences or spin echo sequences which are both somewhat slower but can still give high quality DCE images.

There were three main categories of T1-mapping techniques utilized by studies in this review. Variable flip angle (VFA) typically uses a SPGR sequence with identical parameters to the dynamic T1-weighted

Please cite this article in press as: Chagnot A et al. Magnetic Resonance Imaging of Blood–Brain Barrier permeability in Dementia. Neuroscience (2021), https://doi.org/10.1016/j.neuroscience.2021.08.003

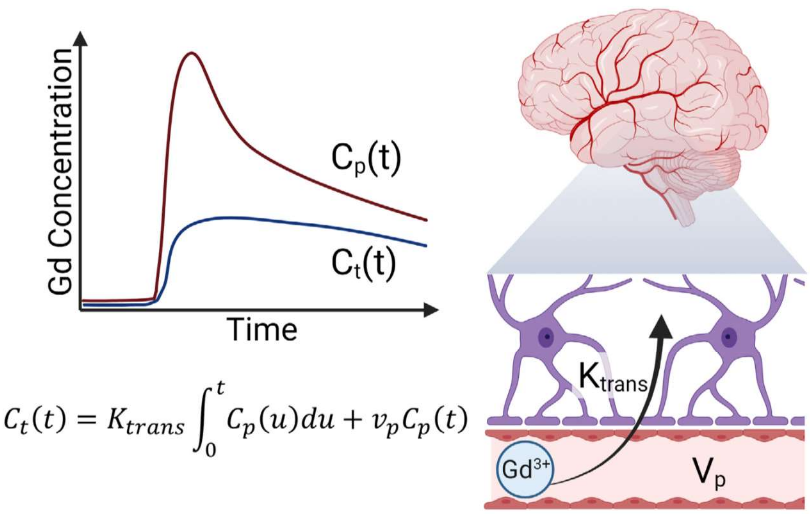

Fig. 2. DCE-MRI and BBB assessment. DCE-MRI is used to measure BBB integrity by measuring the concentration of gadolinium contrast agent over time in the blood plasma (C_p) and in the brain tissue (C_t). These measured concentrations are then used to calculate the blood-to-brain transfer coefficient (K_{trans}) and the blood volume (v_p) using the Patlak mathematical model (Figure created using Biorender.com).

acquisition. This is repeated generally three to seven times with different flip angles. This is a very fast technique for T1 mapping, and by utilizing the same sequence type and parameters as the dynamic T1-weighted scan, blood inflow effects and artifacts should be similar between the T1 mapping and dynamic sequence. Variable repetition time (VTR) techniques also use multiple image acquisitions but with different repetition times. These are usually a bit slower than VFA, may have different inflow effects across images, but are less sensitive to B1 inhomogeneity which can cause significant errors in VFA techniques. Finally, inversion recovery techniques such as TAPIR, fast T1 mApping sequence with Partial Inversion Recovery, were utilized in a few studies. These are generally a little slower but give high quality T1 maps.

EXPERIMENTAL PROCEDURES

Search sources and selection criteria

We reviewed the existing literature on DCE-MRI of subtle BBB permeability in aging, cSVD, and AD. The literature available on Pubmed was searched from January 1, 2015 to May 7, 2021. The following combinations of keywords were searched to be in the title, abstract and/or keywords of the article: (Dynamic contrast enhanced MRI) AND (small vessel disease): 30 results; (Dynamic contrast enhanced MRI) AND (Alzheimer's disease): 29 results; (Dynamic contrast enhanced MRI) AND (aging): 47 results; (Dynamic contrast enhanced MRI) AND (dementia): 32 results; (Dynamic contrast enhanced MRI) AND (cognition): 68 results. In total, 206 references were obtained.

Inclusion and exclusion criteria

After exclusion of 71 duplicates, a total of 135 references were obtained from the initial Pubmed search. Out of 135 references, 96 were rejected as they were out of scope. From the 39 remaining publications, 23 were clinical, 3 pre-clinical, 5 methodological recommendations, and 8 review articles. In addition, we included 11 recent DCE-MRI publications that fit the scope of our review but did not appear at the initial search. These include 6 clinical studies, 3 pre-clinical studies, and 2 additional reviews. In total, 50 papers were reviewed in this article. See flow diagram in Fig. 3. The main findings, sample characteristics, and protocol used in the clinical studies are detailed in Table 1 (cSVD; 11 publications) and Table 2 (normal aging, mild dementia, and AD; 14 publications), while pre-clinical studies are detailed in Table 3 (6 publications).

DCE-MRI in cSVD

Cerebral SVD covers a wide array of pathologies involving the dysfunction of the small vessels of the brain. Clinical manifestations include stroke, cognitive impairment, or gait disturbance. Many studies reported BBB impairment in cSVD patients, particularly in the white matter (WM) (Thrippleton et al., 2019). A growing number of neuroimaging studies have described subtle BBB breakdown in the living cSVD brain using DCE-MRI technique, as summarized in Table 1 and further discussed below.

White matter hyperintensities (WMH) are a common finding in the elderly population and a key feature of cSVD. While their pathogenesis remains yet unclear, BBB leakage is the most accepted hypothesis. In their 2017 article, Li et al. assessed the BBB permeability in a sample of 102 patients with low, medium, or high cSVD burden and found that global BBB permeability was associated with higher WMH burden (Li et al., 2017). The same year, Wardlaw's group also found a relationship between BBB permeability and WMH burden in a cohort of 201 cSVD patients (Wardlaw et al., 2017). Notably, they highlighted the fact that the healthy WM tissue surrounding WMH presented increased BBB permeability, suggesting that BBB disruption could precede further extensions of the WMH lesions. This result was recently confirmed by Kerkhofs et al. who demonstrated that BBB leakage nearing WMH is related to changes in WM diffusivity, an MRI-based diffusion marker of tissue degeneration possibly caused by local BBB damage (Kerkhofs et al., 2021). Furthermore, Wong et al. observed a negative correlation between

Please cite this article in press as: Chagnot A et al. Magnetic Resonance Imaging of Blood–Brain Barrier permeability in Dementia. Neuroscience (2021), https://doi.org/10.1016/j.neuroscience.2021.08.003

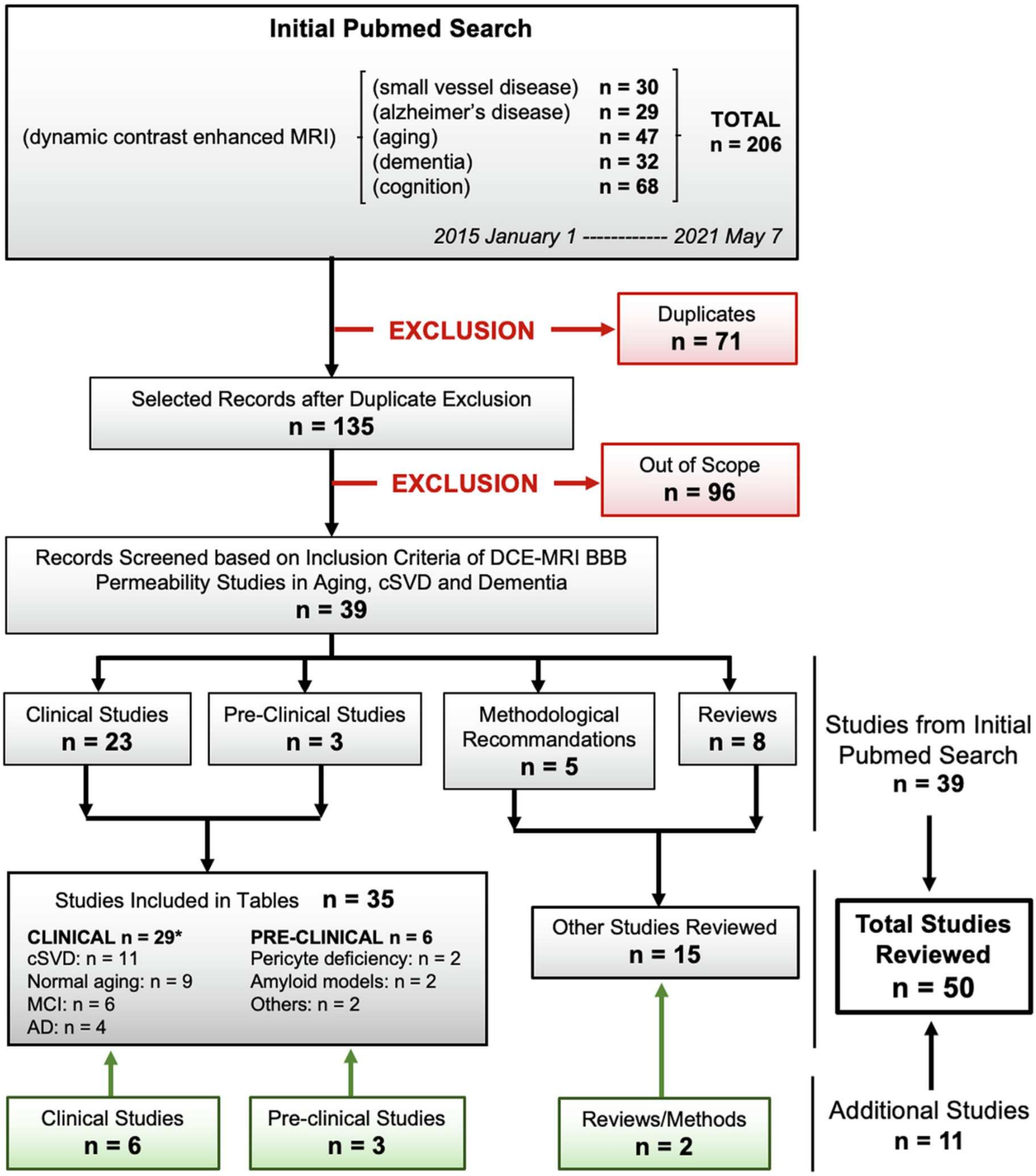

Fig. 3. Flow Diagram of literature search. Recent research articles and reviews (January 1, 2015–May 7, 2021) focusing on blood–brain barrier (BBB) permeability measured by dynamic contrast-enhanced magnetic resonance imaging (DCE-MRI) in normal aging, cerebral small vessel disease (cSVD) or Alzheimer's disease (AD) were recovered from Pubmed search. In addition to the 39 articles retrieved from the systematic search, 11 additional articles highly relevant to our focus were added (*green boxes*), leading to a total of 50 reviewed papers. Research articles were categorized into three tables: Tables 1 and 2 summarize DCE-MRI studies performed in cSVD participants (11 publications) and in the AD continuum [including normal aging, mild cognitive impairment (MCI), and AD participants] (14 publications), respectively; Table 3 summarizes pre-clinical DCE-MRI studies in animal models relevant to dementia (6 publications). **Some studies have occurrences for several conditions.*

cerebral blood flow (CBF) and BBB leakage in the tissue surrounding WMH in 27 cSVD patients (Wong et al., 2019).

DCE-based differences in BBB leakage due to normal aging and cSVD may be very subtle as illustrated by the work of Zhang et al. who did not observe a significant

Please cite this article in press as: Chagnot A et al. Magnetic Resonance Imaging of Blood–Brain Barrier permeability in Dementia. Neuroscience (2021), https://doi.org/10.1016/j.neuroscience.2021.08.003

Table 1. Dynamic contrast-enhanced MRI studies in cerebral small vessel disease

Study	Sample Size (Ct/Pt)	Mean Age (Ct/Pt)	DCE Protocol (FS/PS/TA)	CA/Dose (mmol/kg)	VIF	PK Model	Software	Average BBB K_{trans} (Ct/Pt; $\times 10^{-3}$ min^{-1})				Main Findings
								HC	NAWM	WMH	CGM	
Kerkhofs et al., 2021	NA/43	NA/68	3 T/DT-SRGRE/ 25 min	Gadovist (0.1)	SSS	Patlak	NK	NK	NA/ 0.17*	NA/ 0.18*	NA/ 0.11*	BBB leakage in the perilesional zone of WMH is related to WM degeneration
Shao et al., 2020	NA/16	NA/68	3 T/VFA-SPGR/16 min	Dotarem (0.1)	Carotid artery	Patlak	Rocketship	NA/ 0.76	NA/ 0.61	NK	NA/ 0.68	Patterns of BBB permeability for water (*Kw*) and Gd tracer (K_{trans}) are different
Uchida et al., 2020	21/21	46/51	3 T/VFA-SPGR/5min	Dotarem (0.1)	CCA	Patlak	In-house scripts (MATLAB)	0.78/ 0.89	NK	NK	NK	Iron leakage is associated with increased BBB permeability
Wong et al., 2019	NA/27	NA/69	3 T/DT-SRGRE/ 25 min	Gadovist (0.1)	SSS	Patlak	NK	NK	NA/ 0.19*	NA/ 0.20*	NK	Association between BBB impairment, WMH, and hypoperfusion
Li et al., 2018	31/68	NA/70	3 T/VFA-SPGR/NK	Gadolinium (0.1)	SSS	Patlak	nordicICE	NK	0.01/ 0.03	0.03/ 0.05	0.09/ 0.14	BBB leakage is associated with cSVD burden
Li et al., 2017	NA/102	NA/70	3 T/VFA-SPGR/NK	Gadolinium (0.1)	SSS	Patlak	nordicICE	NK	0.01/ 0.03	0.03/ 0.05	0.09/ 0.14	BBB leakage is associated with cSVD burden
Wardlaw et al., 2017	NA/201	NA/67	1.5 T/VFA-SPGR/24 min	Dotarem (0.1)	SSS	Linear mixed model	SAS 9.3	NK	NK	NK	NK	BBB leakage in NAWM nearing WMH predicts cognitive decline
Zhang et al., 2017a; Zhang et al., 2017b	40/80	69/70	3 T/DT-SRGRE/ 25 min	Gadovist (0.1)	SSS	Patlak	NK	NK	0.58*/ 0.53*	0.48*/ 0.47*	0.82*/ 0.79*	BBB leakage is associated with cSVD
Heye et al., 2016	NA/201	NA/66	1.5 T/VFA-SPGR/24 min	Dotarem (0.1)	SSS	Patlak	In-house scripts (MATLAB)	NK	NA/ 0.30	NA/ 0.40	NK	Patlak model is suited for evaluating subtle BBB leakage, but signal drift is limiting
Huisa et al., 2015	12/22	61/67	1.5 T-3 T/ TAPIR/20–28 min	Magnevist (NK)	SSS	Patlak	In-house scripts (MATLAB)	NK	NK	NK	NK	BBB permeability aeras fluctuates in Binswanger's disease
Rosenberg et al., 2015	NA/25	NA/66	1.5 T/TAPIR/ NK	Magnevist (NK)	NK	Patlak	NK	NK	NA/ 1.87*	NK	NK	BBB permeability is a predictor of Binswanger's disease

Abbreviations: BBB: Blood-Brain Barrier; CA: Contrast Agent; CCA: Common Carotid Artery; CGM: Cortical Gray Matter; cSVD: Cerebral Small Vessel Disease; Ct: Controls; DT-SRGRE: Dual-time SRGRE; FS: Field Strength; Gd: Gadolinium; HC: Hippocampus; Ki & K_{trans}: Blood-to-Brain Transfer Constant; Kw: Blood-to-Brain Water Exchange Rate; NAWM: Normal Appearing White Matter; NA: Not Applicable; NK: Not Known; PK: Pharmacokinetic; PS: Pulse Sequence; Pt: Patients; SPGR: Spoiled Gradient; SRGRE: Saturation Recovery Gradient Echo; SSS: Superior Sagittal Sinus; TA: Time Acquisition; TAPIR: fast T1 mApping sequence with Partial Inversion Recovery; VFA: Variable Flip Angle; VIF: Vascular Input Function; WMH: White Matter Hyperintensities.

*Denote Ki -> K_{trans} conversion using Ki = K_{trans}/[1-hematocrit] with hematocrit = 0.45.

Please cite this article in press as: Chagnot A et al. Magnetic Resonance Imaging of Blood–Brain Barrier permeability in Dementia. Neuroscience (2021), https://doi.org/10.1016/j.neuroscience.2021.08.003

Table 2. Dynamic contrast-enhanced MRI studies in Alzheimer's disease-continuum

	Study	Sample Size (Ct/Pt)	Mean Age (Ct/ Pt)	DCE Protocol (FS/PS/TA)	CA/Dose (mmol/kg)	VIF	PK Model	Software	Average BBB K_{trans} (Ct/Pt; $\times 10^{-3}$ min^{-1})				Main Findings
									HC	NAWM	WMH	CGM	
Normal aging	Ha et al., 2021	34/NA	65/NA	3 T/VFA-SPGR/ 10 min	Gadovist (0.1)	SSS	Patlak	nordicICE	0.56/NA	0.33/NA	NK	NK	Regional BBB K_{trans} differences exist in cognitively normal elderly adults
	Moon et al., 2021	75/NA	67/NA	3 T/GRE/ 10 min	Gadovist (1.0)	SSS	Patlak	nordicICE	NK	NK	NK	NK	Females are protected from early BBB breakdown in cortex
	Montagne et al., 2020	206#/NA	69/NA	3 T/VFA-SPGR/ 16 min	Dotarem (0.05)	ICA	Patlak	Rocketship	1.38/NA	1.90/NA	NK	1.43/NA	Increased BBB permeability in the MTL of cognitively unimpaired *APOE4* carriers
	Verheggen et al., 2020a	57/NA	66/NA	3 T/DT-SRGRE/ 25 min	Gadovist (0.1)	SSS	Patlak	In-house scripts (MATLAB)	NK	0.61E-3*/NA	NK	0.50E-3*/NA	Increased BBB permeability with aging
	Verheggen et al., 2020b	57/NA	66/NA	3 T/DT-SRGRE/ 25 min	Gadovist (0.1)	SSS	Patlak	In-house scripts (MATLAB)	0.94E-3*/NA	0.61E-3*/NA	NK	0.50E-3*/NA	BBB leakage is associated with memory decline in normal aging
	Li et al., 2019	109/NA	70/NA	3 T/VFA-SPGR/NK	Gadolinium (0.1)	SSS	Patlak	nordicICE	NK	0.03/NA	NK	NK	Increased BBB permeability correlates with BG-EPVS
	Montagne et al., 2019	46/NA	69/NA	3 T/VFA-SPGR/ 16 min	Multihance (0.05) / Dotarem (0.05)	CCA	Patlak	Rocketship	1.12/NA	NK	NK	NK	Increased hippocampal BBB permeability with normal aging
	Montagne et al., 2015	24/NA	63/NA	3 T/VFA-SPGR/ 16 min	Multihance (0.05)	CCA	Patlak	Rocketship	1.18/NA	2.06/NA	NK	1.26/NA	BBB breakdown starts in HC
MCI	Li et al., 2021	21/26	67/71	3 T/VFA-SPGR/NK	Gadolinium (0.1)	SSS	Patlak	nordicICE	NK	0.02/ 0.03	0.03/ 0.06	0.09/ 0.16	Increased BBB permeability in WMH is linked to CI
	Freeze et al.,2020	32/34	72/69	3 T/DT-SRGRE/ 25 min	Gadovist (0.1)	SSS	Patlak	In-house scripts (MATLAB)	0.40E-3*/ 0.16E-3*	0.67E-3*/ 1.03E-3*	0.69E-3*/ 0.72E-3*	0.54E-3*/ 0.47E-3*	Increased BBB permeability in WMH is linked to CI
	Montagne et al., 2020	206/39	69/72	3 T/VFA-3D-VIBE/ 16 min	Dotarem (0.05)	CCA	Patlak	Rocketship	1.38/ 1.69	1.90/ 2.13	NK	1.43/ 1.42	Accelerated BBB breakdown in the MTL of *APOE4* carriers
	Montagne et al., 2019	40/12	74/75	3 T/VFA-SPGR/ 16 min	Multihance (0.05) / Dotarem (0.05)	CCA	Patlak	Rocketship	1.36/ 1.70	NK	NK	NK	Increased hippocampal BBB permeability in MCI
	Nation et al., 2019	42/20	74/73	3 T/VFA-SPGR/ 16 min	Multihance (0.05) / Dotarem (0.05)	CCA	Patlak	Rocketship	1.38/ 1.67	2.23/ 2.39	NK	1.32/ 1.35	Increased hippocampal BBB permeability in MCI independent of amyloid and tau pathology
	Montagne et al., 2015	18/21	73/72	3 T/VFA-SPGR/ 16 min	Multihance (0.05)	CCA	Patlak	Rocketship	1.28/ 1.64	2.19/ 2.30	NK	1.29/ 1.38	BBB breakdown starts in HC and may contribute to CI
AD	Freeze et al., 2020	32/14	72/72	3 T/DT-SRGRE/ 25 min	Gadovist (0.1)	SSS	Patlak	In-house scripts (MATLAB)	0.40E-3*/ 0.25E-3*	0.67E-3*/ 0.44E-3*	0.69E-3*/ 0.56E-3*	0.54E-3*/ 0.41E-3*	Increased BBB permeability is related to cSVD severity in AD patients

(continued on next page)

Please cite this article in press as: Chagnot A et al. Magnetic Resonance Imaging of Blood–Brain Barrier permeability in Dementia. Neuroscience (2021), https://doi.org/10.1016/j.neuroscience.2021.08.003

Table 2 (*continued*)

Study	Sample Size (Ct/Pt)	Mean Age (Ct/ Pt)	DCE Protocol (FS/PS/TA)	CA/Dose (mmol/kg)	VIF	PK Model	Software	Average BBB K_{trans} (Ct/Pt; $\times 10^{-3}$ min^{-1})				Main Findings
								HC	NAWM	WMH	CGM	
Van de Haar et al., 2017	17/7	76/74	3 T/DT-SRGRE/ 25 min	Gadovist (0.1)	SSS	Patlak	In-house scripts (MATLAB)	NK	0.04*/ 0.04*‡	NK	4.00E-3*/ 0.057*‡	Global BBB leakage in patients with early AD that is associated with cognitive decline
Van de Haar et al., 2016a	17/7	76/74	3 T/DT-SRGRE/ 25 min	Gadovist (0.1)	SSS	Patlak	In-house scripts (MATLAB)	NK	0.04/ 0.04‡	0.03/ 0.06‡	4.00E-3/0.05‡	Brain-wide increased BBB permeability in AD patients is associated with CI
Van de Haar et al., 2016b	16/7	76/75	3 T/DT-SRGRE/ 25 min	Gadovist (0.1)	SSS	Patlak	In-house scripts (MATLAB)	NK	NK	NK	0.18/ 0.27‡	AD patients show increased BBB permeability in cortex

Abbreviations: AD: Alzheimer's Disease; APOE4: Apolipoprotein E4; BG-EPVS: Enlarged Perivascular Spaces in the Basal Ganglia; BBB: Blood-Brain Barrier; CA: Contrast Agent; CCA: Common Carotid Artery; CDR: Clinical Dementia Rating; CGM: Cortical Gray Matter; CI: Cognitive Impairment; cSVD: Cerebral Small Vessel Disease; Ct: Controls; DT-SRGRE: Dual-time SRGRE; FS: Field Strength; FSPGR: Fast SPGR; GRE: Gradient Echo; HC: Hippocampus; ICA: Internal Carotid Artery; Ki & K_{trans}: Blood-to-Brain Transfer Constant; MCI: Mild Cognitive Impairment; MTL: Median Temporal Lobe; NAWM: Normal Appearing White Matter; NA: Not Applicable; NK: Not Known; PK: Pharmacokinetic; PS: Pulse Sequence; Pt: patients; sPDGFRβ: Soluble Platelet-Derived Growth Factor Receptor β; SPGR: Spoiled Gradient; SRGRE: Saturation Recovery Gradient Echo; SSS: Superior Sagittal Sinus; TA: Time Acquisition; VFA: Variable Flip Angle; VIBE: Volumetric Interpolated Breath-Hold; VIF: Vascular Input Function; WMH: White Matter Hyperintensities.

Table 3. Dynamic contrast-enhanced MRI studies in animal models relevant to dementia

	Study	Model (species)	Sample Size (Ct/Tg)	Age (months)	DCE Protocol (FS/PS/TA)	CA/Dose (mmol/kg)	VIF	PK Model	Software	Average BBB K_{trans} (Ct/Tg; $^{-}10^{-3}$ min^{-1})				Main Findings
										HC	CTX	THAL	CC	
Pericyte deficiency	Nikolakopoulou et al., 2019	Pericyte-Cre-DTR (mouse)	5/6	2–3	7 T/VFA-FLASH/ 15 min	Magnevist (0.5)	CCA	Patlak	Rocketship	$0.59^{\#}$/ $1.13^{\#}$	$0.68^{\#}$/ $1.23^{\#}$	NK	NK	Increased BBB permeability after pericyte ablation
	Montagne et al., 2018	*Pdgfrb*$^{F7/F7}$ (mouse)	5–7/5–7	1–1.5, 3–4, 9–12	7 T/ VTR-FLASH/ 35 min	Magnevist (0.5)	CCA	Patlak	Rocketship	NK	NK	NK	0.60/ 0.86, 0.58/ 1.05, 0.70/1.22	Increased BBB permeability in pericyte-depleted WM regions
Amyloid models	Dickie et al., 2021	TgF344-AD (rat)	16/13, 5/7, 7/8	13, 18, 21	7 T/VFA-SPGR/ 10 min	Dotarem (0.5)	SSS	Patlak	R	NK	NK	NK	NK	AD genotype did not lead to K_{trans} changes, but higher water permeability (*Kw*) was observed
	Montagne et al., 2021	5xFAD; TR-APOE3/4 (mouse)	12–14 FAD-/ 13–16 FAD+	18–24	7 T/VFA-FLASH/ 25 min	Gd-DTPA (BioPAL) (0.5)	CCA	Patlak	Rocketship	0.68/ $0.98^{\$}$	0.69/ $0.91^{\$}$	NK	NK	Increased BBB permeability in *APOE4* AD mice, independent of amyloid pathology
Others	Wang et al., 2018	SHR (rat)	5/5	17	7 T/Spin Echo/ 35 min	Magnevist (0.2)	NK	Extended Tofts	DCE@urLAB	8.40/ 31.60	5.20/ 30.20	NK	NK	Increased BBB permeability and Aβ accumulation in HC and CTX of SHR rats
	Xu et al., 2017	Diabetes (rhesus monkey)	6/5	13 years	3 T/ SRGRE/ 10 min	MultiHance (0.1)	SSS	Extended Tofts	DCE@urLAB	3.32/ 7.91	3.27/ 8.11	3.30/ 7.47	NK	Increased BBB permeability in diabetic monkeys

Abbreviations: Aβ: Amyloid-beta; AD: Alzheimer's Disease; APOE4: Apolipoprotein E4; BBB: Blood-Brain Barrier; CA: Contrast Agent; CCA: Common Carotid Artery; cSVD: Cerebral Small Vessel Disease; Ct: Controls; CTX: Cortex; DTR: Diphtheria Toxin Receptor; DT-SRGRE: Dual-time SRGRE; FAD: Familial Alzheimer's Disease; FLASH: Fast Low Angle Shot; FS: Field Strength; HC: Hippocampus; Ki & K_{trans}: Blood-to-Brain Transfer Constant; Kw: Blood-to-Brain Water Exchange Rate; NK: Not Known; Pdgfrb: Platelet-Derived Growth Factor Receptor b; PK: Pharmacokinetic; PS: Pulse Sequence; SHR: Spontaneously Hypertensive Rat; SPGR: Spoiled Gradient; SRGRE: Saturation Recovery Gradient Echo; SSS: Superior Sagittal Sinus; TA: Time Acquisition; Tg: Transgenic Animals; TR: Targeted Replacement; THAL: Thalamus; VFA: Variable Flip Angle; VIF: Vascular Input Function; VTR: Variable Time Repetition.

*Denote Ki -> K_{trans} conversion using Ki = K_{trans}/[1-hematocrit] with hematocrit = 0.45; $^{\#}$Denotes all cognitively normal (CDR = 0) participants; ‡MCI and AD groups combined.

$^{\#}$ BBB K_{trans} values from 15 days post Diphtheria Toxin treatment.

$^{\$}$ BBB K_{trans} values from TR-APOE4;5xFAD (Tg) vs TR-APOE3;5xFAD (Ct) mice.

Please cite this article in press as: Chagnot A et al. Magnetic Resonance Imaging of Blood–Brain Barrier permeability in Dementia. Neuroscience (2021), https://doi.org/10.1016/j.neuroscience.2021.08.003

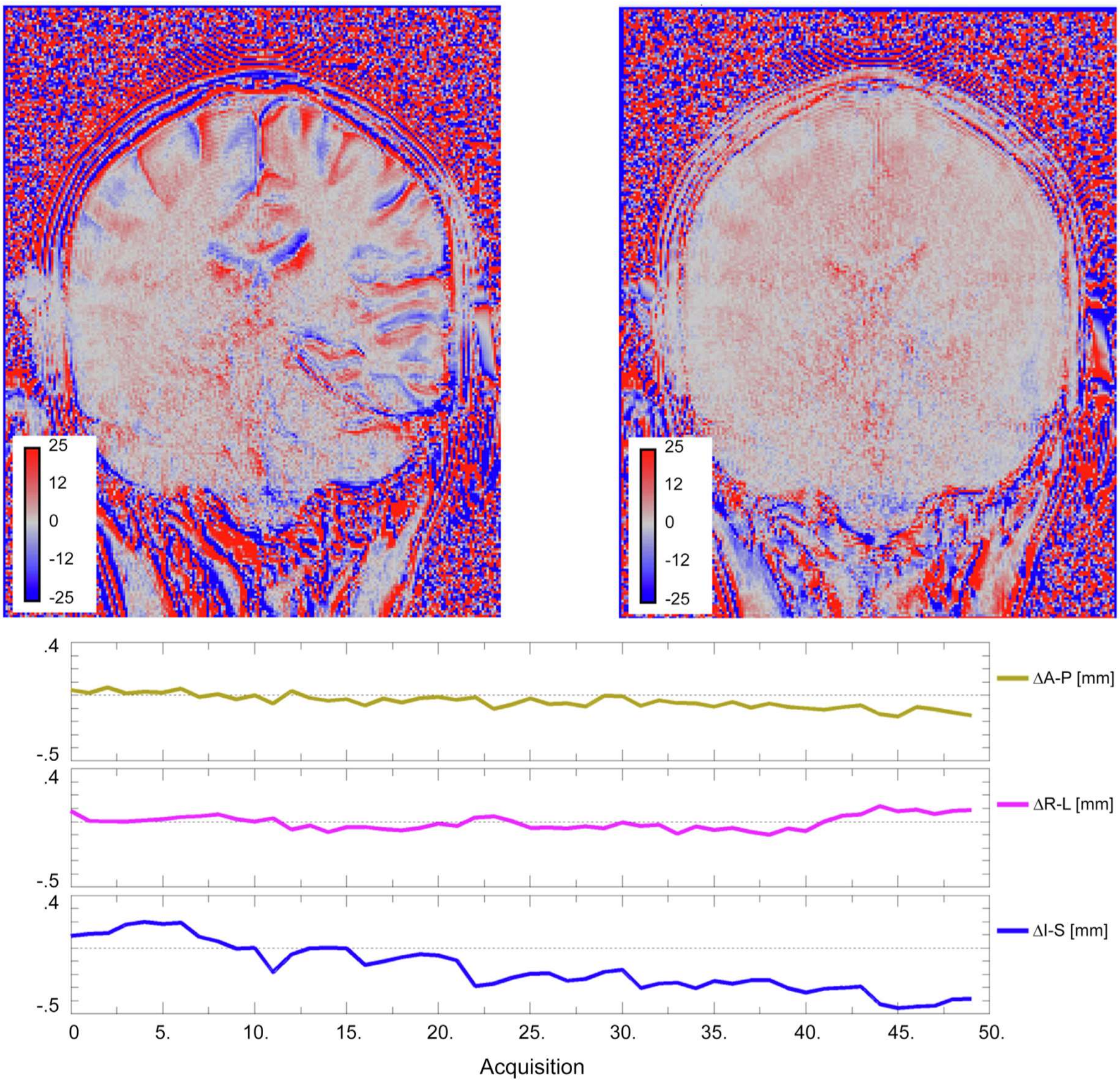

Fig. 4. Dynamic contrast-enhanced magnetic resonance imaging and motion correction. Dynamic contrast-enhanced (DCE) protocol acquisition without contract injection shows percent signal change calculated from a linear fit over time (*top images*). *Left* image is the 'without motion correction' and shows signal changes up to 25%, particularly at cerebrospinal fluid (CSF)-tissue interface, due to small motions of subjects' head. *Right* image is the same dataset after motion correction, which shows almost all signal change is eliminated. *Bottom* graphs show calculated brain motion relative to the first image along the three principal axis (A-P, anterior-posterior; R-L, right-left; I-S, inferior-superior). Even < 0.5 mm of motion can induce significant signal changes (Images courtesy of SRB).

difference in BBB leakage rate (Zhang et al., 2017a). However, leakage extent was found to be higher in cSVD patients. Also, Binswanger's disease (BD) belongs to the cSVD spectrum and is characterized by an extensive involvement of WM and impairment of executive functions. Differentiating BD from other cSVD-related conditions is often difficult; hence, Rosenberg et al. aimed to define more specific biomarkers. Among these, WM BBB permeability was found to be increased in BD patients compared to a combined group of patients having multiple infarcts, mixed AD/vascular cognitive impairment (vCI), or leukoaraiosis (Huisa et al., 2015; Rosenberg et al., 2015).

A known consequence of BBB disruption is the increasing occurrence of microbleeds (Wardlaw et al., 2019). Uchida et al. successfully correlated iron accumulation detected by quantitative susceptibility mapping MRI to local BBB leakage in patients with Cerebral Autosomal Dominant Arteriopathy with Subcortical Infarcts and Leukoencephalopathy (CADASIL), emphasizing how

Please cite this article in press as: Chagnot A et al. Magnetic Resonance Imaging of Blood–Brain Barrier permeability in Dementia. Neuroscience (2021), https://doi.org/10.1016/j.neuroscience.2021.08.003

alternate imaging techniques could support DCE-MRI findings (Uchida et al., 2020). Another alternate method would be to measure vessel density, diameter, and size from the R2 and R2* relaxation rates upon GBCA injection (Choi et al., 2020)

In a cohort of older subjects at risk for cSVD, Shao et al. compared DCE-MRI to an arterial spin labeling (ASL)-based technique allowing measurement of water permeability across the BBB (Shao et al., 2020). Interestingly, they found only few correlations between K_{trans} and *kw*, suggesting that the mechanisms regulating the permeability of water or contrast agents across the BBB are likely to be different.

DCE-MRI in the AD-continuum

The vascular contribution to AD pathophysiology is increasingly recognized. As such, BBB breakdown is considered an important player in the development and progression of the most common cause of dementia (Sweeney et al., 2018a; Sweeney et al., 2018b; Sweeney et al., 2019a). Thus, it is not surprising to see a growing number of DCE-MRI studies performed in the normal aging to AD spectrum, as reviewed in Table 2 and examined hereafter.

Normal aging

In 2015, Montagne et al. first showed an age-dependent BBB leakage starting in the hippocampus in a cohort of 24 healthy individuals ranging from 23 to 91 years of age (Montagne et al., 2015), which was further confirmed in a larger cohort of 46 cognitively unimpaired participants (Montagne et al., 2019). Another group also observed that global BBB impairment was correlated with age (Verheggen et al., 2020a) and cognitive decline (Verheggen et al., 2020b) in a sample of 57 healthy elderly individuals. Interestingly, Moon et al. investigated gender-related differences in BBB permeability in a sample of 75 elderly patients (51 females). They showed that while women are better protected than men with regards to age-related BBB disruption thanks to the protective effect of estrogens, they are also more sensitive to late BBB disruption in the occipital cortex, where the estrogen receptor is more expressed (Moon et al., 2021). Another recent DCE study spotted subtle differences between brain regions in a cohort of 35 cognitively normal elderly participants, with the lowest and highest K_{trans} values in the frontal and occipital WM, respectively (Ha et al., 2021). Of note, no differences between left and right hemispheres were detected. Finally, enlarged perivascular spaces (EPVS) are a common finding in normal aging, and highly increased EPVS load is a feature of both cSVD and AD. In a sample of 109 middle-aged to elderly participants, Li et al. found that BBB leakage and EPVS burden were associated in the basal ganglia (Li et al., 2019).

Mild dementia

Although regional BBB leakage seems to occur during normal aging, Montagne et al. also reported that hippocampal BBB disruption worsened as participants' cognition declined (Montagne et al., 2015; Montagne et al., 2019). A following study from the same group observed a local increase of BBB permeability in the medial temporal lobe (MTL) (including the hippocampi and parahippocampal gyri) of 42 patients with mild cognitive impairment (MCI) compared to 20 age-matched cognitively unimpaired controls (Nation et al., 2019). Interestingly, the authors demonstrated that MTL vascular leakage is an independent, early biomarker of cognitive impairment unrelated to amyloid-β (Aβ) and tau pathology, as the positivity for the respective CSF biomarkers $A\beta_{42}$ and phosphorylated tau (pTau) did not affect the results.

Recently, the same authors questioned the relation between *APOE4* genotype and BBB permeability in a cohort of 245 elderly MCI and cognitively unimpaired participants (Montagne et al., 2020). Increased BBB permeability in the MTL was confirmed in MCI and further accelerated in *APOE4* carriers. Interestingly, cognitively unimpaired individuals carrying *APOE4* had substantially higher MTL BBB K_{trans} values compared non-carriers (Montagne et al., 2020), supporting the involvement of BBB dysfunction early in the course of AD.

A study by Li et al. showed that BBB leakage in WMH was significantly higher in vascular MCI individuals, an uncommon condition where the sole cause for cognitive impairment is vascular pathology, when compared to age- and sex-matched healthy controls (Li et al., 2021). Additionally, Freeze et al. investigated the link between BBB leakage, WMH, and processing speed in a cohort of 80 elderly participants, including 34 MCI as well as 14 AD patients (Freeze et al., 2020). The authors found an association between increased BBB permeability in WMH and cognitive impairment suggesting that local BBB breakdown may trigger WM lesions which could then explain the reduction in information processing speed (Freeze et al., 2020).

Alzheimer's disease

In their AD cohort, Freeze et al. found that BBB disruption throughout the whole brain was associated with cSVD severity, independently of cognitive status (Freeze et al., 2020). The group of Backes recently studied BBB dysfunction in AD using DCE-MRI method. For instance, they confirmed the relationship between BBB disruption and early AD in a cohort of 33 elderly, whom 9 presented MCI and 7 AD diagnosis. Indeed, AD patients showed increased BBB leakage in the whole brain, which worsened with cognitive impairment (van de Haar et al., 2016a). In a follow-up study, the same authors also observed a general decrease in CBF in the gray matter of early AD patients, which correlated with increased BBB leakage in a cohort of 14 MCI/AD and 16 age-matched controls (van de Haar et al., 2016b; van de Haar et al., 2017).

DCE-MRI in pre-clinical models relevant to dementia

As MRI is becoming more accessible, DCE method is also increasingly applied in a variety of rodent models that are relevant to dementia (see Table 3).

Please cite this article in press as: Chagnot A et al. Magnetic Resonance Imaging of Blood–Brain Barrier permeability in Dementia. Neuroscience (2021), https://doi.org/10.1016/j.neuroscience.2021.08.003

Pericyte deficiency

Pericytes are a major component of the BBB, especially at the capillary level where the smooth muscle layers are lacking (Procter et al., 2021). Pericytes wrap around endothelial cells that line the BBB, and their dysfunction is thought to play a critical role in aggravating dementia (Sweeney et al., 2019b; Uemura et al., 2020). Analyses of post-mortem brains and CSF samples provided substantial evidence supporting early pericyte loss in AD (Baloyannis and Baloyannis, 2012; Sagare et al., 2013; Sengillo et al., 2013; Miners et al., 2018), mild dementia (Montagne et al., 2015, 2020; Nation et al., 2019), stroke (Yemisci et al., 2009; Hall et al., 2014), and cSVD (Ghosh et al., 2015; Montagne et al., 2018). Using DCE-MRI in a chronic mouse model of pericyte deficiency, Montagne et al. reported a global and age-dependent increase in BBB permeability with the highest K_{trans} values found in WM structures (Montagne et al., 2018). Also, they observed CBF reduction and EPVS in the WM of young pericyte-deficient mice, which are common findings in the aged brain (Montagne et al., 2018). In another model of acute pericyte ablation, the same group reported a substantial circulatory failure with acute BBB disruption and reduced CBF in the cortex and hippocampus, followed by rapid neuronal loss (Nikolakopoulou et al., 2019). These pre-clinical results emphasize the role of pericytes in BBB homeostasis and promote the use of DCE-MRI to detect subtle BBB changes in the living rodent brains.

Amyloid models

Although several studies found increased BBB permeability to gadolinium contrast agent in rodent models of AD (Montagne et al., 2017), Dickie et al. failed to observe BBB K_{trans} changes in old TgF344-AD rats compared to wildtype controls but did find an increase in water permeability (Dickie et al., 2021). It suggests that old TgF344-AD rats do not develop BBB breakdown with loss of tight junction proteins as one would assume, but rather show an increase in water exchange rate that is facilitated by dedicated water channel, predominantly aquaporin-4 (AQP4) in astrocytes and aquaporin-1 (AQP1) in endothelial and mural cells. Of note, it is important to clarify that Kw and K_{trans} are measuring two very different processes, one being the water exchange rate across the BBB and the other one the BBB permeability to gadolinium contrast (Shao et al., 2020).

As shown in humans carrying *APOE4* (Montagne et al., 2020), the same group found that, compared to *APOE3*, *APOE4* accelerates BBB breakdown, loss of CBF, neuronal loss, and behavioral deficits independently of Aβ using aged *APOE* knock-in mice crossed with *5xFAD* mice (Montagne et al., 2021). Such results support that BBB disruption may occur earlier than anticipated in AD and be an early contributor to the pathogenesis of the disease, thus emphasizing the need for appropriate methods to detect subtle BBB leakage in humans.

Vascular risk factors

Several conditions related to lifestyle are associated with BBB disruption. Wang et al. found a sharp increase of BBB K_{trans} measured in the cortex and hippocampus of aged spontaneously hypertensive rats compared with controls (Wang et al., 2018). Similarly, diabetes increased BBB leakage in the cortex, hippocampus, and thalamus of aged rhesus monkeys (Xu et al., 2017). While BBB disruption occurring due to normal aging cannot be prevented, moderating the lifestyle factors known to affect vessel wall integrity could delay the occurrence of clinical consequences.

DCE-MRI challenges and pitfalls in dementia

The small amounts of leakage that occur in cSVD and AD bring the inherent difficulty of detecting and quantifying very small signal changes in DCE-MRI. This is a significant technical challenge, but steady progress is being made in identifying and mitigating the various challenges. Here we highlight some of the principal challenges that can prevent accurate data. For a more thorough review of the technical challenges, recommended acquisition, and processing steps, see the recent review by (Thrippleton et al., 2019).

Motion

Patient motion is a significant concern over the course of a 10–20-minute DCE acquisition. Even small changes in head position can cause changes in tissue type in a given voxel, particularly at parenchyma-CSF boundaries. These changes show up as gradual increases or decreases in signal intensity. This will bias measured K_{trans} values higher or lower, even causing K_{trans} to have negative values. Fig. 4 shows an example of a measured percent signal change over 12 min DCE acquisition without any contrast injection, so the expected signal change is zero. Images are shown with and without motion correction co-registration algorithms, and show signal changes up to 25% near CSF boundaries. These changes occur even though there is minimal motion (<0.5 mm of displacement in any direction) but are almost entirely corrected with co-registration. Motion correction with co-registration is recommended for all DCE studies (Thrippleton et al., 2019), and more recent publications have demonstrated errors in fit parameters of $>200\%$ in some voxels including many negative K_{trans} values from even low motion that are almost entirely corrected with co-registration (Bernal et al., 2021). We have found co-registration is more effective when a brain mask is applied first, as scalp motion can be independent of brain motion and DCE measurements in the scalp are usually of little interest.

Signal drift

Small amounts of signal intensity drift over time can be a significant source of error as they can be comparable to the amount of signal intensity change from the contrast

Please cite this article in press as: Chagnot A et al. Magnetic Resonance Imaging of Blood–Brain Barrier permeability in Dementia. Neuroscience (2021), https://doi.org/10.1016/j.neuroscience.2021.08.003

agent (Barnes et al., 2016). A frequent cause of signal drift is temperature changes of the MRI hardware and electronics. In animal acquisitions this can be caused by thermal support systems for the animal (particularly blowing warm air into the bore), and care should be taken to achieve a steady temperature and not make adjustments for the entirety of the acquisition. In humans, newer wide bore systems (70 cm bore diameter) are more susceptible to heat transfer from the gradients, and gradient heavy sequences (such as diffusion tensor imaging) can potentially cause heating and signal drift after they are run (as the gradients cool). Signal drift is very system-dependent and therefore it is recommended to acquire some datasets without contrast injection to evaluate any signal drift on the scanner that will be used. If signal drift is a problem on a particular system, it can be monitored and corrected to some extent with constant signal intensity phantom added to the field of view (Barnes et al., 2016; Thrippleton et al., 2019). This is usually a water tube dopped with a small amount of gadolinium contrast agent. Care should be taken to make sure the phantom is large enough that the signal can be reliably measured, so small movements are not mistaken for signal drift.

Vascular Input function

The measurement of the vascular input function is a critical step that can have a large effect on the final K_{trans} values. It can be challenging to make accurate measurements for a variety of reasons including: motion artifacts of the flowing blood, small size of vessels causing partial volume errors, inflow of fresh blood that has seen few radiofrequency (RF) pulses and hasn't reached steady state, and insufficient temporal resolution to accurately measure the first pass of the contrast bolus. While each of these can be a source of considerable error, most can be minimized by simple acquisition choices. A coronal acquisition, measuring in the superior sagittal sinus (SSS), and a slow contrast agent injection (greater than the temporal resolution) generally gives good results. The coronal acquisition exposes the blood to many RF pulses ensuring it will reach steady state, as the 2D excitation slab will extend through the neck, and possibly to the heart depending on the angle of the slab (Thrippleton et al., 2019). Measuring in the SSS minimizes the flow speed and associated artifacts compared to arterial measurements. The blood in the SSS has also been exposed to more RF pulses traveling through the brain, so is more likely to achieve steady state. The SSS is also relatively large and stationary so will minimize partial volume errors. The venous measurements have been shown to be very similar to arterial measurements and are largely just shifted by 5–7 s (Sourbron et al., 2009; Foottit et al., 2010). For acquisitions with temporal resolution greater than 7 seconds there will be little measurable difference. Finally, injecting the contrast agent over a longer duration will minimize errors in measuring the first pass of a bolus injection (Manning et al., 2021).

CONCLUSION

DCE-MRI underlined the occurrence of local, subtle, and progressive BBB leakage in aging. One of the plausible causal links to cognitive impairment and dementia is through the passage of blood-derived neurotoxic compounds from the blood to brain tissues, causing progressive damage in strategic regions such as the WM and medial temporal lobe. The integrity of the BBB depends on the cohesion of all its components, especially at the capillary level which represents the largest surface for blood contact. Pericytes are found on the whole vascular tree and are key actors in the regulation of vasomotricity and BBB permeability. *APOE4* genotype leads to faster BBB disruption, which could prevent waste removal and trigger amyloid-related pathologies such as AD. Inter-regional differences, as well as gender-related differences in the development of BBB disruption may lead to a more precise interpretation of the experimental results. Pre-clinical transgenic models, as well as clinical cohorts, have helped to connect vascular aging to cognitive impairment and led to important insights on the physiology and disease processes. However, detecting earlier stages of BBB breakdown is challenging and may require additional technical innovations in DCE-MRI acquisition and processing techniques. Alternate methods evaluating the water permeability of the BBB does not necessarily correlate with DCE-MRI, thus emphasizing the complexity of the exchanges occurring across the BBB and the need for additional studies to understand these mechanisms.

ACKNOWLEDGEMENTS

Audrey Chagnot is supported by grants from the Ministère de l'Enseignement Supérieur et de la Recherche and INSERM (French National Institute for Health and Medical Research) (HCERES U1237-2017/2022) and by the special grant from the Agence Nationale de la Recherche (ANR), MRGly (ANR-17-CE37-0010). Samuel R Barnes is supported by a GRASP award from Loma Linda University and National Institute of Aging 2R44AG059478-03. Axel Montagne is supported by UK Dementia Research Institute which receives its funding from DRI Ltd, funded by the Medical Research Council, Alzheimer's Society and Alzheimer Research UK. We also thank Michael G Harrington for careful reading of the manuscript. Figs. 1 and 2 were created using BioRender.com (Toronto, Canada).

REFERENCES

Abbott NJ, Patabendige AAK, Dolman DEM, Yusof SR, Begley DJ (2010) Structure and function of the blood-brain barrier. Neurobiol Dis 37(1):13–25.

Baloyannis SJ, Baloyannis IS (2012) The vascular factor in Alzheimer's disease: a study in Golgi technique and electron microscopy. J Neurol Sci 322(1-2):117–121.

Barnes SR, Ng TSC, Montagne A, Law M, Zlokovic BV, Jacobs RE (2016) Optimal acquisition and modeling parameters for accurate

Please cite this article in press as: Chagnot A et al. Magnetic Resonance Imaging of Blood–Brain Barrier permeability in Dementia. Neuroscience (2021), https://doi.org/10.1016/j.neuroscience.2021.08.003

assessment of low Ktrans blood-brain barrier permeability using dynamic contrast-enhanced MRI. Magn Reson Med 75 (5):1967–1977.

Begley DJ, Brightman MW (2003) Structural and functional aspects of the blood-brain barrier. Prog Drug Res Fortschritte Arzneimittelforschung Progres Rech Pharm 61:39–78.

Bernal J, Valdés-Hernández MdC, Escudero J, Heye AK, Sakka E, Armitage PA, Makin S, Touyz RM, Wardlaw JM, Thrippleton MJ (2021) A four-dimensional computational model of dynamic contrast-enhanced magnetic resonance imaging measurement of subtle blood-brain barrier leakage. NeuroImage 230:117786.

Choi H-I, Ryu C-W, Kim S, Rhee HY, Jahng G-H (2020) Changes in microvascular morphology in subcortical vascular dementia: a study of vessel size magnetic resonance imaging. Front Neurol 11:545450.

Dickie BR, Boutin H, Parker GJM, Parkes LM (2021) Alzheimer's disease pathology is associated with earlier alterations to blood-brain barrier water permeability compared with healthy ageing in TgF344-AD rats. NMR Biomed:e4510.

Ding H, Liu X, Li X, Wen M, Li Ya, Han Y, Huang L, Liu M, Zeng H (2020) Hypercapnia exacerbates the disruption of the blood-brain barrier by inducing interleukin-1β overproduction in the blood of hypoxemic adult rats. Int J Mol Med 46(2):762–772.

Foottit C, Cron GO, Hogan MJ, Nguyen TB, Cameron I (2010) Determination of the venous output function from MR signal phase: feasibility for quantitative DCE-MRI in human brain. Magn Reson Med 63(3):772–781.

Freeze WM, Jacobs HIL, de Jong JJ, Verheggen ICM, Gronenschild EHBM, Palm WM, Hoff EI, Wardlaw JM, Jansen JFA, Verhey FR, Backes WH (2020) White matter hyperintensities mediate the association between blood-brain barrier leakage and information processing speed. Neurobiol Aging 85:113–122.

Ghosh M, Balbi M, Hellal F, Dichgans M, Lindauer U, Plesnila N (2015) Pericytes are involved in the pathogenesis of cerebral autosomal dominant arteriopathy with subcortical infarcts and leukoencephalopathy. Ann Neurol 78(6):887–900.

Ha IH, Lim C, Kim Y, Moon Y, Han SH, Moon WJ (2021) Regional differences in blood-brain barrier permeability in cognitively normal elderly subjects: a dynamic contrast-enhanced MRI-based study. Korean J Radiol.

Hall CN, Reynell C, Gesslein B, Hamilton NB, Mishra A, Sutherland BA, O'Farrell FM, Buchan AM, Lauritzen M, Attwell D (2014) Capillary pericytes regulate cerebral blood flow in health and disease. Nature 508(7494):55–60.

Halliday MR, Rege SV, Ma Q, Zhao Z, Miller CA, Winkler EA, Zlokovic BV (2016) Accelerated pericyte degeneration and blood-brain barrier breakdown in apolipoprotein E4 carriers with Alzheimer's disease. J Cereb Blood Flow Metab Off J Int Soc Cereb Blood Flow Metab 36(1):216–227.

Heye AK, Thrippleton MJ, Armitage PA, Valdés Hernández MDC, Makin SD, Glatz A, Sakka E, Wardlaw JM (2016) Tracer kinetic modelling for DCE-MRI quantification of subtle blood-brain barrier permeability. Neuroimage 125:446–455.

Huisa BN, Caprihan A, Thompson J, Prestopnik J, Qualls CR, Rosenberg GA (2015) Long-term blood-brain barrier permeability changes in binswanger disease. Stroke 46(9):2413–2418.

Kerkhofs D, Wong SM, Zhang E, Staals J, Jansen JFA, van Oostenbrugge RJ, Backes WH (2021) Baseline blood-brain barrier leakage and longitudinal microstructural tissue damage in the periphery of white matter hyperintensities. Neurology 96: e2192–e2200.

Li M, Li Y, Zuo L, Hu W, Jiang T (2021) Increase of blood-brain barrier leakage is related to cognitive decline in vascular mild cognitive impairment. BMC Neurol 21:159.

Li Y, Li M, Yang L, Qin W, Yang S, Yuan J, Jiang T, Hu W (2019) The relationship between blood-brain barrier permeability and enlarged perivascular spaces: a cross-sectional study. Clin Interv Aging 14:871–878.

Li Y, Li M, Zuo L, Shi Q, Qin W, Yang L, Jiang T, Hu W (2018) Compromised blood-brain barrier integrity is associated with total magnetic resonance imaging burden of cerebral small vessel disease. Front Neurol 9:221.

Li Y, Li M, Zhang X, Shi Q, Yang S, Fan H, Qin W, Yang L, Yuan J, Jiang T, Hu W (2017) Higher blood-brain barrier permeability is associated with higher white matter hyperintensities burden. J Neurol 264(7):1474–1481.

Manning C, Stringer M, Dickie B, Clancy U, Valdés Hernandez MC, Wiseman SJ, Garcia DJ, Sakka E, Backes WH, Ingrisch M, Chappell F, Doubal F, Buckley C, Parkes LM, Parker GJM, Marshall I, Wardlaw JM, Thrippleton MJ (2021) Sources of systematic error in DCE-MRI estimation of low-level blood-brain barrier leakage. Magn Reson Med.

McAleese KE, Graham S, Dey M, Walker L, Erskine D, Johnson M, Johnston E, Thomas AJ, McKeith IG, DeCarli C, Attems J (2019) Extravascular fibrinogen in the white matter of Alzheimer's disease and normal aged brains: implications for fibrinogen as a biomarker for Alzheimer's disease. Brain Pathol Zurich Switz 29 (3):414–424.

Miners JS, Schulz I, Love S (2018) Differing associations between Aβ accumulation, hypoperfusion, blood-brain barrier dysfunction and loss of PDGFRB pericyte marker in the precuneus and parietal white matter in Alzheimer's disease. J Cereb Blood Flow Metab Off J Int Soc Cereb Blood Flow Metab 38(1):103–115.

Montagne A, Nikolakopoulou AM, Zhao Z, Sagare AP, Si G, Lazic D, Barnes SR, Daianu M, Ramanathan A, Go A, Lawson EJ, Wang Y, Mack WJ, Thompson PM, Schneider JA, Varkey J, Langen R, Mullins E, Jacobs RE, Zlokovic BV (2018) Pericyte degeneration causes white matter dysfunction in the mouse central nervous system. Nat Med 24(3):326–337.

Montagne A, Nation DA, Sagare AP, Barisano G, Sweeney MD, Chakhoyan A, Pachicano M, Joe E, Nelson AR, D'Orazio LM, Buennagel DP, Harrington MG, Benzinger TLS, Fagan AM, Ringman JM, Schneider LS, Morris JC, Reiman EM, Caselli RJ, Chui HC, TCW J, Chen Y, Pa J, Conti PS, Law M, Toga AW, Zlokovic BV (2020) APOE4 leads to blood-brain barrier dysfunction predicting cognitive decline. Nature 581(7806):71–76.

Montagne A, Barnes S, Sweeney M, Halliday M, Sagare A, Zhao Z, Toga A, Jacobs R, Liu C, Amezcua L, Harrington M, Chui H, Law M, Zlokovic B (2015) Blood-brain barrier breakdown in the aging human hippocampus. Neuron 85(2):296–302.

Montagne A, Huuskonen MT, Rajagopal G, Sweeney MD, Nation DA, Sepehrband F, D'Orazio LM, Harrington MG, Chui HC, Law M, Toga AW, Zlokovic BV (2019) Undetectable gadolinium brain retention in individuals with an age-dependent blood-brain barrier breakdown in the hippocampus and mild cognitive impairment. Alzheimers Dement J Alzheimers Assoc 15(12):1568–1575.

Montagne A, Nation DA, Pa J, Sweeney MD, Toga AW, Zlokovic BV (2016) Brain imaging of neurovascular dysfunction in Alzheimer's disease. Acta Neuropathol (Berl) 131(5):687–707.

Montagne A, Nikolakopoulou AM, Huuskonen MT, Sagare AP, Lawson EJ, Lazic D, Rege SV, Grond A, Zuniga E, Barnes SR, Prince J, Sagare M, Hsu CJ, LaDu MJ, Jacobs RE, Zlokovic BV (2021) APOE4 accelerates advanced stage vascular and neurodegenrative disorder in old Alzheimer's mice via cyclophilin A independently of amyloid-β. Nat. Aging..

Montagne A, Zhao Z, Zlokovic BV (2017) Alzheimer's disease: A matter of blood-brain barrier dysfunction? J Exp Med 214:3151–3169.

Moon Y, Lim C, Kim Y, Moon W-J (2021) Sex-related differences in regional blood-brain barrier integrity in non-demented elderly subjects. Int J Mol Sci 22.

Nation DA, Sweeney MD, Montagne A, Sagare AP, D'Orazio LM, Pachicano M, Sepehrband F, Nelson AR, Buennagel DP, Harrington MG, Benzinger TLS, Fagan AM, Ringman JM, Schneider LS, Morris JC, Chui HC, Law M, Toga AW, Zlokovic BV (2019) Blood-brain barrier breakdown is an early biomarker of human cognitive dysfunction. Nat Med 25(2):270–276.

Nikolakopoulou AM, Montagne A, Kisler K, Dai Z, Wang Y, Huuskonen MT, Sagare AP, Lazic D, Sweeney MD, Kong P, Wang M, Owens NC, Lawson EJ, Xie X, Zhao Z, Zlokovic BV

Please cite this article in press as: Chagnot A et al. Magnetic Resonance Imaging of Blood–Brain Barrier permeability in Dementia. Neuroscience (2021), https://doi.org/10.1016/j.neuroscience.2021.08.003

(2019) Pericyte loss leads to circulatory failure and pleiotrophin depletion causing neuron loss. Nat Neurosci 22(7):1089–1098.

Nitta T, Hata M, Gotoh S, Seo Y, Sasaki H, Hashimoto N, Furuse M, Tsukita S (2003) Size-selective loosening of the blood-brain barrier in claudin-5-deficient mice. J Cell Biol 161:653–660.

Pfau SJ, Langen UH, Fisher TM, Prakash I, Nagpurwala F, Lozoya RA, Lee W-CA, Wu Z, Gu C (2021) Vascular and perivascular cell profiling reveals the molecular and cellular bases of blood-brain barrier heterogeneity. bioRxiv:2021.04.26.441465.

Procter T, Williams A, Montagne A (2021) Interplay between brain pericytes and endothelial cells in dementia. Am J Pathol.

Raja R, Rosenberg GA, Caprihan A (2018) MRI measurements of Blood-Brain Barrier function in dementia: A review of recent studies. Neuropharmacology 134:259–271.

Rosenberg GA, Prestopnik J, Adair JC, Huisa BN, Knoefel J, Caprihan A, Gasparovic C, Thompson J, Erhardt EB, Schrader R (2015) Validation of biomarkers in subcortical ischaemic vascular disease of the Binswanger type: approach to targeted treatment trials. J Neurol Neurosurg Psychiatry 86 (12):1324–1330.

Sagare AP, Bell RD, Zhao Z, Ma Q, Winkler EA, Ramanathan A, Zlokovic BV (2013) Pericyte loss influences Alzheimer-like neurodegeneration in mice. Nat Commun 4:2932.

Sengillo JD, Winkler EA, Walker CT, Sullivan JS, Johnson M, Zlokovic BV (2013) Deficiency in mural vascular cells coincides with blood-brain barrier disruption in Alzheimer's disease. Brain Pathol Zurich Switz 23(3):303–310.

Shao X, Jann K, Ma SJ, Yan L, Montagne A, Ringman JM, Zlokovic BV, Wang DJJ (2020) Comparison between blood-brain barrier water exchange rate and permeability to gadolinium-based contrast agent in an elderly cohort. Front Neurosci 14 571480.

Sourbron S, Heilmann M, Biffar A, Walczak C, Vautier J, Volk A, Peller M (2009) Bolus-tracking MRI with a simultaneous T1- and T2*-measurement. Magn Reson Med 62:672–681.

Stamatovic SM, Johnson AM, Keep RF, Andjelkovic AV (2016) Junctional proteins of the blood-brain barrier: New insights into function and dysfunction. Tissue Barriers 4(1):e1154641. https://doi.org/10.1080/21688370.2016.1154641.

Sweeney MD et al (2019a) Vascular dysfunction-The disregarded partner of Alzheimer's disease. Alzheimers Dement J Alzheimers Assoc 15:158–167.

Sweeney MD, Kisler K, Montagne A, Toga AW, Zlokovic BV (2018a) The role of brain vasculature in neurodegenerative disorders. Nat Neurosci 21:1318–1331.

Sweeney MD, Sagare AP, Pachicano M, Harrington MG, Joe E, Chui HC, Schneider LS, Montagne A, Ringman JM, Fagan AM, Morris JC, Pa J, Nation DA, Toga AW, Zlokovic BV (2020) A novel sensitive assay for detection of a biomarker of pericyte injury in cerebrospinal fluid. Alzheimers Dement J Alzheimers Assoc 16 (6):821–830.

Sweeney MD, Sagare AP, Zlokovic BV (2018b) Blood-brain barrier breakdown in Alzheimer disease and other neurodegenerative disorders. Nat Rev Neurol 14:133–150.

Sweeney MD, Zhao Z, Montagne A, Nelson AR, Zlokovic BV (2019b) Blood-Brain Barrier: From Physiology to Disease and Back. Physiol Rev 99:21–78.

Thrippleton MJ, Backes WH, Sourbron S, Ingrisch M, van Osch MJP, Dichgans M, Fazekas F, Ropele S, Frayne R, van Oostenbrugge RJ, Smith EE, Wardlaw JM (2019) Quantifying blood-brain barrier leakage in small vessel disease: Review and consensus recommendations. Alzheimers Dement J Alzheimers Assoc 15 (6):840–858.

Toledo JB, Arnold SE, Raible K, Brettschneider J, Xie SX, Grossman M, Monsell SE, Kukull WA, Trojanowski JQ (2013) Contribution of cerebrovascular disease in autopsy confirmed neurodegenerative disease cases in the National Alzheimer's Coordinating Centre. Brain J Neurol 136:2697–2706.

Tsai PS, Kaufhold JP, Blinder P, Friedman B, Drew PJ, Karten HJ, Lyden PD, Kleinfeld D (2009) Correlations of neuronal and microvascular densities in murine cortex revealed by direct counting and colocalization of nuclei and vessels. J Neurosci 29 (46):14553–14570.

Uchida Y, Kan H, Sakurai K, Arai N, Inui S, Kobayashi S, Kato D, Ueki Y, Matsukawa N (2020) Iron leakage owing to blood-brain barrier disruption in small vessel disease CADASIL. Neurology 95: e1188–e1198.

Uemura MT, Maki T, Ihara M, Lee VMY, Trojanowski JQ (2020) Brain microvascular pericytes in vascular cognitive impairment and dementia. Front Aging Neurosci 12:80.

van de Haar HJ, Burgmans S, Jansen JFA, van Osch MJP, van Buchem MA, Muller M, Hofman PAM, Verhey FRJ, Backes WH (2016a) Blood-Brain Barrier Leakage in Patients with Early Alzheimer Disease. Radiology 281:527–535.

van de Haar HJ, Jansen JFA, Jeukens CRLPN, Burgmans S, van Buchem MA, Muller M, Hofman PAM, Verhey FRJ, van Osch MJP, Backes WH (2017) Subtle blood-brain barrier leakage rate and spatial extent: Considerations for dynamic contrast-enhanced MRI. Med Phys 44:4112–4125.

van de Haar HJ, Jansen JFA, van Osch MJP, van Buchem MA, Muller M, Wong SM, Hofman PAM, Burgmans S, Verhey FRJ, Backes WH (2016b) Neurovascular unit impairment in early Alzheimer's disease measured with magnetic resonance imaging. Neurobiol Aging 45:190–196.

Verheggen ICM, de Jong JJA, van Boxtel MPJ, Gronenschild EHBM, Palm WM, Postma AA, Jansen JFA, Verhey FRJ, Backes WH (2020a) Increase in blood-brain barrier leakage in healthy, older adults. GeroScience.

Verheggen ICM, de Jong JJA, van Boxtel MPJ, Postma AA, Jansen JFA, Verhey FRJ, Backes WH (2020b) Imaging the role of blood-brain barrier disruption in normal cognitive ageing. GeroScience 42:1751–1764.

Wang Y, Zhang R, Tao C, Xu Z, Chen W, Wang C, Song Li, Zheng J, Gao F (2018) Blood-brain barrier disruption and perivascular beta-amyloid accumulation in the brain of aged rats with spontaneous hypertension: evaluation with dynamic contrast-enhanced magnetic resonance imaging. Korean J Radiol 19 (3):498–507.

Wardlaw JM, Makin SJ, Valdés Hernández MC, Armitage PA, Heye AK, Chappell FM, Muñoz-Maniega S, Sakka E, Shuler K, Dennis MS, Thrippleton MJ (2017) Blood-brain barrier failure as a core mechanism in cerebral small vessel disease and dementia: evidence from a cohort study. Alzheimers Dement 13(6):634–643.

Wardlaw JM, Smith C, Dichgans M (2019) Small vessel disease: mechanisms and clinical implications. Lancet Neurol 18 (7):684–696.

Wong SM, Jansen JFA, Zhang CE, Hoff EI, Staals J, van Oostenbrugge RJ, Backes WH (2019) Blood-brain barrier impairment and hypoperfusion are linked in cerebral small vessel disease. Neurology 92(15):e1669–e1677.

Xu Z, Zeng W, Sun J, Chen W, Zhang R, Yang Z, Yao Z, Wang L, Song L, Chen Y, Zhang Y, Wang C, Gong L, Wu B, Wang T, Zheng J, Gao F (2017) The quantification of blood-brain barrier disruption using dynamic contrast-enhanced magnetic resonance imaging in aging rhesus monkeys with spontaneous type 2 diabetes mellitus. NeuroImage 158:480–487.

Yang AC et al. (2021) A human brain vascular atlas reveals diverse cell mediators of Alzheimer's disease risk. bioRxiv:2021.04.26.441262.

Yemisci M, Gursoy-Ozdemir Y, Vural A, Can A, Topalkara K, Dalkara T (2009) Pericyte contraction induced by oxidative-nitrative stress impairs capillary reflow despite successful opening of an occluded cerebral artery. Nat Med 15(9):1031–1037.

Zhang CE, Wong SM, van de Haar HJ, Staals J, Jansen JFA, Jeukens CRLPN, Hofman PAM, van Oostenbrugge RJ, Backes WH (2017a) Blood-brain barrier leakage is more widespread in patients with cerebral small vessel disease. Neurology 88:426–432.

Zhang Y, Kim MS, Jia B, Yan J, Zuniga-Hertz JP, Han C, Cai D (2017b) Hypothalamic stem cells control ageing speed partly through exosomal miRNAs. Nature 548:52–57.

Please cite this article in press as: Chagnot A et al. Magnetic Resonance Imaging of Blood–Brain Barrier permeability in Dementia. Neuroscience (2021), https://doi.org/10.1016/j.neuroscience.2021.08.003

Zhao Z, Nelson AR, Betsholtz C, Zlokovic BV (2015) Establishment and dysfunction of the blood-brain barrier. Cell 163(5):1064–1078.

Zlokovic BV (2008) The blood-brain barrier in health and chronic neurodegenerative disorders. Neuron 57(2):178–201.

Zlokovic BV (2011) Neurovascular pathways to neurodegeneration in Alzheimer's disease and other disorders. Nat Rev Neurosci 12(12):723–738.

(Received 15 June 2021, Accepted 5 August 2021)
(Available online xxxx)//

Please cite this article in press as: Chagnot A et al. Magnetic Resonance Imaging of Blood–Brain Barrier permeability in Dementia. Neuroscience (2021), https://doi.org/10.1016/j.neuroscience.2021.08.003

Autres travaux 1 : Preventing the Long-term Effects of General Anesthesia on the Developing Brain : How Translational Research can Contribute

Cette revue dont je suis quatrième autrice est dans la continuité de la collaboration 2 présentée dans les résultats. Elle souligne le besoin d'études translationelles dans la recherche pédiatrique, en particulier sur l'effet des anesthésiques. J'ai contribué à la mise en forme du manuscrit et ai créé la figure.

NEUROSCIENCE

INTERNATIONAL BRAIN IBRO RESEARCH ORGANIZATION

NEUROSCIENCE FOREFRONT REVIEW

J.-P. Salaün et al. / Neuroscience 461 (2021) 172–179

Preventing the Long-term Effects of General Anesthesia on the Developing Brain: How Translational Research can Contribute

Jean-Philippe Salaün, [a,b*] **Nicolas Poirel,** [c,d] **Souhayl Dahmani,** [e,f,g] **Audrey Chagnot,** [b] **Clément Gakuba,** [a,b] **Carine Ali,** [b] **Jean-Louis Gérard,** [a] **Jean-Luc Hanouz,** [a†] **Gilles Orliaguet** [h,i†] **and Denis Vivien** [b,j†]

[a] *Department of Anesthesiology and Critical Care Medicine, Caen University Hospital, Avenue de la Côte de Nacre, Caen 14033, France*

[b] *Normandie Université, UNICAEN, INSERM, UMR-S U1237, Physiopathology and Imaging of Neurological Disorders (PhIND), Institute Blood and Brain @ Caen-Normandie (BB@C), GIP Cyceron, Caen 14000, France*

[c] *Université de Paris, LaPsyDÉ, CNRS, F-75005 Paris, France*

[d] *Institut Universitaire de France (IUF), Paris, France*

[e] *Department of Anesthesia and Intensive Care, Robert Debre University Hospital, Paris, France*

[f] *Paris Diderot University, 10 Avenue de Verdun, 75010 Paris, France*

[g] *DHU PROTECT, INSERM U1141, Robert Debre University Hospital, Paris, France*

[h] *Department of Pediatric Anesthesia and Intensive Care, Necker-Enfants Malades University Hospital, AP-HP. Centre – Université de Paris, France*

[i] *EA 7323 Université de Paris "Pharmacologie et évaluation des thérapeutiques chez l'enfant et la femme enceinte", Paris, France*

[j] *Department of Clinical Research, Caen University Hospital, Avenue de la Côte de Nacre, Caen 14033, France*

Abstract—In 2017, the Food and Drug Administration published a safety recommendation to limit the exposure to general anesthesia as much as possible below the age of three. Indeed, several preclinical and clinical studies have questioned the possible toxicity of general anesthesia on the developing brain. Since then, recent clinical studies tried to mitigate this alarming issue. What is true, what is false? Contrary to some perceptions, the debate is not over yet. Only stronger translational research will allow scientists to provide concrete answers to this public health issue. In this review, we will provide and discuss the more recent data in this field, including the point of view of preclinical researchers, neuropsychologists and pediatric anesthesiologists. Through translational research, preclinical researchers have more than ever a role to play to better understand and identify long-term effects of general anesthesia for pediatric surgery on brain development in order to minimize it. © 2021 IBRO. Published by Elsevier Ltd. All rights reserved.

Key words: children, developing brain, general anesthesia, translational research, neurotoxicity.

INTRODUCTION

Each year, millions of children require surgery. One out of seven children is subjected to general anesthesia before three years old in western countries (Shi et al., 2018). General anesthesia for pediatric surgery is a safe procedure with a low risk of immediate complications (Habre et al., 2017). However, preclinical studies have shown that exposure to general anesthesia during the early stages of the developing brain- *in utero* or in the early infancy- could lead to structural and functional brain abnormalities, as well as cognitive and behavioral disorders (Jevtovic-Todorovic, 2018). From a neurochemical aspect, cerebral consequences are conceptually possible, as most anesthetic agents exert their hypnotic effect through their agonist activity on GABA receptors or their antagonist activity on NDMA receptors, which are critical in neurodevelopmental processes. These preclinical considerations rightfully opened the debate on the possible neurotoxicity of general anesthesia in children and have been the driving force behind several retrospective clinical studies. In this context, in 2017 the Food And Drug Administration (FDA) issued a warning that repeated or prolonged general anesthesia in children younger than 3 years old should be performed with caution (Andropoulos and Greene, 2017). Following this recommendation, recent clinical studies have provided reassuring evidence of the safety of anesthesia in children. Yet, the debate is not over.

---

*Correspondence to: J.-P. Salaün, Department of Anesthesiology and Critical Care Medicine, Caen University Hospital, Avenue de la Côte de Nacre, Caen 14033, France.
E-mail address: salaunjeanphilippe@gmail.com (J.-P. Salaün).

[†] These authors contributed equally to the work.

Abbreviations: EDI, Early Development Index; FDA, Food and Drug Administration; TNF, tumor necrosis factor.

https://doi.org/10.1016/j.neuroscience.2021.02.029
0306-4522/

After pointing out the limits of first preclinical and retrospective clinical studies, we will discuss the most recent data of the literature, including the points of views of preclinical researchers, neuropsychologists and anesthesiologists. While the latest major clinical studies on this topic seem to minimize the impact of general anesthesia on the developing brain, and thus convey a reassuring message to practitioners and the population, their data should be considered with caution. It is likely that the answer to the enigmatic question of long-term effects of general anesthesia on the developing brain lies in an improved translational research in which preclinical researchers will play a key role. At the end of this literature review, we will therefore propose the outline of an original translational study in mice and human which could strongly contribute to providing answers to this major issue.

GENERAL ANESTHESIA FOR CHILDHOOD SURGERY: A RECURRING PHENOMENON

Recent epidemiological data have shown a high incidence of general anesthesia in childhood (Shi et al., 2018). No previous study directly measured the incidence of receiving procedures requiring general anesthesia in a population of children. Thus, among a 20,922 American children cohort, 3120 (14.9%) underwent at least one general anesthesia before age 3. There is no gender difference in the incidence of general anesthesia in childhood. Seven hundred and twenty-three children (3.5%) had at least one subsequent procedure. The first procedure occurred in the first year of life in 1208 (39.0%) children. The most common classification of first procedure received was otorhinolaryngologic surgery (44.9%). Estimated gestational age < 32 weeks and low birth weight were independently associated with receiving repeated anesthesia. Eight hundred and twenty children (3.9%) had a single prolonged exposure above 3 h, multiple exposures prior to age 3, or both. This means that approximately 1 in 4 children who received general anesthesia fall within the high-risk category as defined by the recent FDA warning whose aim was to define the high-risk categories of neurotoxicity of general anesthesia during childhood established on the basis of the underlying described literature.

PRECLINICAL AND RETROSPECTIVE CLINICAL STUDIES HAVE OPENED THE DEBATE ON THE LONG-TERM EFFECTS OF GENERAL ANESTHESIA ON THE DEVELOPING BRAIN

Preclinical studies

During the last 20 years, most of the commonly used anesthetic drugs, either injected intravenously or inhaled, have been reported to interfere with the developing brain (Marchesini and Disma, 2019). Preclinical research on the potential toxicity of general anesthesia on the developing brain started at the end of the 20th century with Ikonomidou study (Ikonomidou et al., 1999). After administering an NMDA antagonist (MK801) to young rats (postnatal days 3, 7, 14, 21) and to pregnant rats (embryonic stage 17, 19, 21), examination of the brain at 24 h by TUNEL (terminal deoxynucleotidyl transferase- mediated dUTP nick-end labeling) revealed a large apoptotic degeneration in the developing brain, both after those prenatal or postanal blockades. This supported the hypothesis that anesthetic agents – some of which act on NMDA receptors – could possibly impair the development of the brain. That's why, in 2003, Todorovic and colleagues administered a combination of anesthetic agents (midazolam, nitrous oxide and isoflurane) for a 6-hour anesthesia in 7-d-old young rats (Jevtovic-Todorovic et al., 2003). Immuno-histological analysis for activate caspase-3, highlighted extensive apoptotic neurodegeneration in the developing brain. But these findings were all the more worrying that it was also noted – thanks to behavioral analysis at subsequent ages – an impairment of spatial reference memory on postnatal days 32 and 131 and, moreover, a spatial working memory impairment at postnatal day 53. This was one of the seminal studies that suggested that in addition to a structural impact on the developing brain, general anesthesia could lead to long-term behavioral changes (Mintz et al., 2013).

These results in rodents have been confirmed in nonhuman primate studies. Within a population of 24 socially reared rhesus macaques, was examined how exposure to either single or multiple early postnatal isoflurane affected a set of behavioral tasks (Coleman et al., 2017). Young animals were exposed to 5 h of isoflurane 0.7–1.5 vol% once (postnatal day 5) or three times (postnatal days 6, 9 and 12). Reflex development and anxiety were evaluated using standardized tests over a time period of one year. Macaques were weaned and housed indoors with other subjects. Animals which has been exposed to repeated isoflurane anesthesia appeared to have significantly lower basic motor reflex after 1 month and demonstrated an exacerbated anxiety and affiliative/appeasement behavior at 1 year as compared to those exposed only once to isoflurane. In fact, no significant behavioral alteration was observed following a single exposure to isoflurane. Behavioral tasks of Rhesus monkeys after general anesthesia were also evaluated in other studies. Animals of both sexes underwent either 3 times repeated 4 h exposures to anesthesia with sevoflurane or brief repeated maternal separations (controls) at 6, 14 and 28 days postnatal (Raper et al., 2015). Depth of anesthesia was adjusted based on reaction to calibrated pressure stimulus. Throughout the experiment, monkeys remained close to their mother, forming large social groups, excepted for overnight observations after each anesthetic and control procedure. When reaching 6 months of age, each monkey was measured on the human intruder test, a testing paradigm for emotional reactivity in nonhuman primates. Anxiety behaviors were significantly more frequent in monkeys that had been exposed to anesthetics than in controls animals.

The possibility that exposure to general anesthesia induces neuroinflammation in the developing brain has also been explored. Repeated exposure of young mice to sevoflurane anesthesia for 2 h on 3 consecutive days induced a marked increase in interleukine-6 and tumor necrosis factor (TNF) protein levels in the brain, and also led to decreased activity of the AKT-glycogen synthase kinase 3β (GSK 3β) signaling pathway in these animals (Shen et al., 2013; Zhang et al., 2014). Altogether, these preclinical investigations suggest a wide range of deleterious impacts of general anesthesia on the developing brain, including the commonly used anesthetic drugs and possible structural and morphologic changes and functional or behavioral impairments (Vutskits and Xie, 2016; Jevtovic-Todorovic, 2018). However, although these preclinical studies have raised the major issue of the neurotoxicity of general anesthesia on developing brain, their conclusions cannot be directly transposed to clinical practice. Indeed, discrepancies between species is a major limitation including correspondences of the different stages of cerebral development. Furthermore, preclinical studies consist in exposition to anesthetic agents without any surgical procedure or control of systemic blood pressure and oxygenation. Yet, the preclinical literature justifies the need to investigate whether changes in behavior or social development also occur in the clinical setting.

Retrospective clinical studies

Most of the clinical studies regarding the effects of general anesthesia on developing brain have a retrospective design. Although some studies suggested an association between surgery during childhood and either a lower academic performance or increased risks of behavioral disorders, other have not identified such associations. In a cohort of 188,557 children (28,366 children who underwent surgery before 5–6 years and 55,910 unexposed children), O'Leary et al. showed an association between surgery in early life and children performances at entry to primary school measured by the Early Development Index (EDI) (O'Leary et al., 2016). Early developmental vulnerability was higher in the exposed group (25.6%) when compared to the unexposed control group (25.0%). However, the overall magnitude of the risk was small (adjusted odds ratio, 1.05; 95% CI 1.01–1.08). In another population-based cohort (116 multiply exposed, 457 singly exposed and 463 unexposed children) multiple – but not single – exposures to anesthesia before 3 years of age resulted in higher frequency of learning disabilities and attention-deficit/ hyperactivity disorder up to age 18 years (hazard ratio for learning disabilities: 2.17; 95% CI 1.32–3.59) (Hu et al., 2017). Single exposure resulted in only a slight decline in reading and language achievement but not in cognitive functions. Thus, even if several clinical studies are in favor of a repercussion of general anesthesia for pediatric surgery on brain development, others are not. Indeed, in a retrospective matched-cohort study (Ko et al., 2015) including 114,435 children among whom 5197 were exposed to general anesthesia and surgery before the age of 2 years, there appeared to be no difference in the frequency of autistic disorder between the exposed group (0.96%) and the unexposed control group (0.89%) ($p = 0.62$). The hazard ratio of exposure to general anesthesia and surgery was 0.93 (95% CI 0.57–1.53) post adjustment for potential cofounders. Remarkably, age at the time of the first exposure appeared to have no influence on the risk of autistic disorder.

What could explain such discrepancies between clinical studies? Among other, these retrospective clinical studies differ in the number and duration of exposures, the delay between exposures to anesthesia and neurodevelopmental evaluations, the mode of data retrieval (diagnostic codes in database (Ko et al., 2015) or parental interrogations (Bong et al., 2013)), the age of anesthesia (Flick et al., 2011), and the regimen of anesthetic agents administered (halothane versus sevoflurane etc.). In addition, there are three different categories of outcomes. Some studies focused on academic performances evaluated by national educational achievement test (results and nonattainment scores) and teachers rating of cognitive problems (Hansen et al., 2011) whereas other investigated clinical outcomes such as learning disabilities (Sprung et al., 2009), behavior disorders (Hu et al., 2017) or neuropsychological tests (de Heer et al., 2017). Discrepancies could also be explained by the presence of confounding factors, including the personal medical history of patients (prematurity (DiMaggio et al., 2009), birth weight, visual or hearing impairment) or the socioeconomic and educational contexts (parental age, lone-parent family, parental income).

Despite solid clinical confirmations, preclinical and retrospective clinical studies have brought enough elements leading the Food and Drug Administration (FDA) to issue a warning in 2016 that repeated or prolonged use of general anesthesia in children younger than 3 years old should be performed with caution. These label changes were applied to some of the most commonly used anesthetic and sedative drugs from 2017 (Research, 2019). Thus, an exhaustive list of general anesthetic and sedation drugs concerned has been established by the FDA including anesthetic and sedation drugs that block N-methyl-D-aspartate receptors and/or potentiate gamma-aminobutyric acid activity. No specific medication has been shown to be safer than any other. A disturbing fact is that approximately 1 in 7 children in the United States is exposed to anesthetic agents before age 3 years, and 1 in 4 of these children is considered to be at highest risk of anesthesia-related neurotoxicity by the FDA (Shi et al., 2018). This recommendation was likely written as a matter of urgency, to provide an answer to the public on the major public health issue which is the toxicity of general anesthesia on the developing brain. Indeed, only clinical studies with a higher level of evidence could settle this debate. This is what recent clinical studies have tried to achieve.

EVEN IF RECENT CLINICAL STUDIES WITH A HIGHER LEVEL OF EVIDENCE HAVE PROVIDED A REASSURING MESSAGE FOR PRACTITIONERS AND THE PUBLIC, THE DEBATE IS NOT OVER.

Although recent clinical studies provide reassuring evidence for practitioners and the general population (Sun et al., 2016; Warner et al., 2018a, 2018b; McCann et al., 2019), their conclusions should be considered with caution. In particular, behavioral assessment used in these studies presented several limitations for interpreting the results and for concluding that exposure to procedures requiring general anesthesia before 3 years of age is not associated with cognitive consequences. Indeed, these studies proposed traditional measures of intelligence (e.g., IQ measures such as the Wechsler Abbreviated, or Preschool and Primary, Scale of Intelligence), provide information regarding other cognitive abilities such as attention and executive functions (using the Behavior Rating Inventory of Executive Function, BRIEF), and found a lack of impact of anesthesia on both IQ measures and BRIEF scores. Nevertheless, it should be note that BRIEF scores are extracted from parents' responses to a questionnaire: BRIEF scores did not reflect children cognitive abilities *per se*. A more fine-grained analysis from experimental tasks, performed by children themselves, will thus be necessary in future work to confirm that anesthesia had actually no impact on cognitive abilities. In particular, precise estimations of executive functions assessment seem essential, according to developmental psychology evidence suggesting that executive functions and self-control played a key role in childhood, for predicting physical health (Moffitt et al., 2011) and future academic performances (Duckworth and Seligman, 2005). As a matter of fact, IQ measures and BRIEF questionnaires are thus probably not sufficient to assess the potential detrimental impact of anesthesia on cognitive abilities in children. This is in agreement with statements from children's parents who reported increased problems related to executive function, behavior or even reading abilities (Warner et al., 2018a, 2018b). Moreover, even if it has been suggested that children IQ seemed predictive of later school abilities (Batty et al., 2006), recent work evidenced that fundamental school abilities are also strongly linked to executive functions (Viarouge et al., 2019). One could argue that executive functions were already assessed in previous studies that aimed at investigating the impact of anesthesia in children, thanks for instance to the Trail Making or the Wisconsin card sort tests (Warner et al., 2018a, 2018b). Unfortunately, these executive tests mainly evaluated cognitive flexibility process and did not provide indication regarding other executive functions, such as inhibitory control (see Diamond, 2013, for a recent discussion about executive functions (Diamond, 2013)). Given the importance of inhibitory control in daily life situations (Borst et al., 2015) and for school performances (Diamond et al., 2007), future work will be necessary to further investigate the consequences of anesthesia on this essential cognitive function, using for instance Stroop task that precisely allow its assessment (Poirel et al., 2021). Finally, another issue concerns the lack of brain imaging data associated with behavioral measures collected in children. Indeed, outcomes from recent studies have to be interpreted cautiously because findings cannot directly demonstrate causality between brain morphometry (or brain functioning) variations due to anesthesia and behavioral assessment. Given that no behavioral differences were found between groups in these studies (Sun et al., 2016; Warner et al., 2018a, 2018b; McCann et al., 2019) one could hypothesize that long-term anesthesia consequences should be associated with more subtle and specific pattern of injury between brain modifications and cognitive outcomes. Consequently, multimodal exploration each child, with both behavioral and brain imaging data, seems a necessary area of future study.

PANDA, MASK and GAS studies all have delivered a reassuring message about the effects of general anesthesia on the developing brain. A history of single or repeated exposure to general anesthesia before the age of 3 years would not alter the primary outcomes of these studies measuring general intelligence (Vutskits and Culley, 2019). As a consequence, the FDA recommendation has not been approved by several European societies, in particular the European Society of Anesthesiology and the European Society For Pediatric Anesthesiology. However, these studies do not definitively close the question of the cerebral toxicity of anesthesia in young children, particularly because their neurodevelopmental evaluation is insufficient. Thus, one could say it is only the end of the beginning (Warner et al., 2018a, 2018b). The time has come to turn again to preclinical research.

PRECLINICAL RESEARCH WILL ALWAYS BE A MAJOR ACTOR IN RESEARCH ON THE TOXICITY OF GENERAL ANESTHESIA

We can go further in research about anesthesia neurotoxicity. Indeed, if expert opinion is divided over the applicability of first preclinical studies to humans, the interpretation of how recent clinical studies should influence clinical practice is still unclear (Hansen, 2017). Further high-quality multidisciplinary research is required to clarify and, if necessary, mitigate risks of anesthesia neurotoxicity (Disma et al., 2018). It will necessarily involve preclinical research.

Role of basic science

Many issues regarding the long-term effects of general anesthesia on the developing brain are not yet resolved. Difficulty lies in the fact that the molecular, cellular and systemic events implicated in the maintenance of anesthetic states overlap with the mechanisms that lead to the sustained effect of anesthetic agents on neuronal structure and function. Only preclinical research could identify which mechanisms are implicated in neurotoxicity so as to open up avenues for neuroprotective strategies (Marchesini and Disma, 2019). Moreover, knowledge of how structural changes induced by anesthetic agents causes behavioral impairment is unclear. Otherwise, we do not understand why the increased vulnerability of central nervous system structures to anesthetic agents depend or not to region-specific time windows during brain development. Finally, mechanisms underlying the physiological context-dependent effect of aesthetic agents on morphologic and functional changes in the brain also need to be explored (Jevtovic-Todorovic, 2018). *In vitro* and *in vivo* models could elucidate such issues.

The major role of translational research

Clinicians have often criticized the difficulty in translating preclinical conclusions into clinical practice (Todd, 2004). A strong effort should be made in this area. An effort that will open up new fields of preclinical research such as defining original neuroimaging and biological markers of anesthesia neurotoxicity. One of the flaws in preclinical research is the inadequate monitoring or physiological parameters in laboratory animals when compared with human-anesthesia management. Indeed, because of their size, appropriate hemodynamic monitoring in rodents is a challenging tasks especially in early postnatal period (Vutskits and Patel, 2014). This is a major issue because disturbance of systemic homeostasis contributes to anesthesia-induced neurotoxicity both in the young and in the old brain (Planel et al., 2007). This is why the concept of SAFETOTS recently emerged in pediatric anesthesia clinical practice (Weiss et al., 2015). The SAFETOTS initiative has enabled to list perioperative causes for cerebral morbidity in young children during the perioperative period. The concept of the 10-N quality pediatric anesthesia takes the form of a quality checklist of factors that anesthesiologists must know and control during the perioperative period: No fear, Normovolemia, Normotension, Normocardia, Normoxemia, Normocapnia, Normonatremia, Normoglycemia, Normothermia, No pain. SAFETOTS are all factors whose preclinical research can allow us to determine the importance in the supposed toxicity of general anesthesia. Thus, future experimental studies will require improvements in quality and reproducibility adhering to the appropriate conduct and reporting guidelines (Kilkenny et al., 2010) and tend to use as much as possible physiological monitoring during general anesthesia. Another flaw identified in preclinical studies relates to the drug-exposure times in rodent pups when compared with those in human context. That is why studies using non-human primates are interesting in the experimental field of research about toxicity of general anesthesia. Indeed, they more closely resemble human physiology and pathophysiology, especially during early development (Wang and Slikker, 2008). Behavioral studies have also shown that well-trained non-human primates can perform certain tasks with comparable accuracy to children, supporting their extrapolation to humans (Paule et al., 2011). Another difficulty is that most experiments were performed in the absence of surgery or other painful stimuli, a situation rarely encountered in humans. This is an important issue because painful stimuli themselves can trigger pathological morpho-functional plasticity in the neonatal brain (Koch and Fitzgerald, 2013). Neurodevelopmental assessment after a surgery carried out under exclusive locoregional anesthesia (Baldi et al., 2007) in animals could make it possible to measure the extent to which surgical stimulation contributes (or not) to brain impairment after surgery under general anesthesia during childhood. This type of study could also position locoregional anesthesia as a major tool in a multimodal strategy to reduce the neurodevelopmental impact of general anesthesia. Moreover, surgery-related inflammation and painful stimuli may both impair central nervous system function. Future preclinical studies will have to study the impact of the pain of surgery on neurodevelopment while proposing the most translational models possible. If when it comes to the long-term effects of general anesthesia during the infancy, it is necessary to consider as much about the impact of the surgical stimulus as the effects of the anesthetic agent used, it is also necessary to take into account the structural impact of environmental stimuli on brain. For example, a multimodal neuroimaging study assessed the consequences of psychological trauma due to World Trade Center attacks (Ganzel et al., 2008). More than 3 years after September 11th, the adults most exposed to the attack presented a reduced grey matter volume versus a control group notably in the amygdala, hippocampus and insula. When elucidating the mechanism underlying long-term effects of anesthetic exposures on neurodevelopment, it will also be necessary to causally link structural changes observed in immature brains immediately following exposure with long-term cognitive consequences. This will require the identification of biological or neuroimaging biomarkers so as to detect biological or imaging signature of general anesthesia neurotoxicity (Fig. 1). The question is not whether general anesthesia should be used or not in younger patients, but the challenge is more to offer safer children care during surgery which we think will be the least neurotoxic possible. One of the most important issues is to determine whether all anesthetic agents currently used have comparable risks for toxicity (Vutskits and Xie, 2016). Experimental data are controversial regarding this issue. These works will be of great translational importance because they could guide future human trials so as to find the safest drug combinations in clinical practice.

AN ORIGINAL TRANSLATIONAL STUDY TO CONTRIBUTE TO THE ANESTHESIA NEUROTOXICITY DEBATE

Future translational studies will be necessary to further examine if a general anesthesia exposure is associated (or not) with impaired neurocognitive development and abnormal behavior in later childhood. Here we propose an original translational study which would take place in two phases: a preclinical phase and a clinical phase. Initially, mice – animals whose brain development is substantially shorter that human (weeks as opposed to years) and well documented in the literature (Dobbing and Sands, 1979) – could be repeatedly exposed to general anesthesia with isoflurane in the postnatal period. Indeed, halogenated anesthetic agents are the most commonly used class of hypnotic agents in pediatric anesthesia. Due to the specific metabolism of rodents, a repeatedly expose mice to general anesthesia to get a greater chance to reveal any effects. These mice would be compared to a control group not exposed to postnatal general anesthesia at an age corresponding to adolescence (4 weeks of life). This evaluation should include both behavioral testing and in high-definition neuroimaging (for example, Magnetic Resonance Imaging) in order to develop a mechanistic approach to possible exacerbated behavioral disorder. The behavioral approach

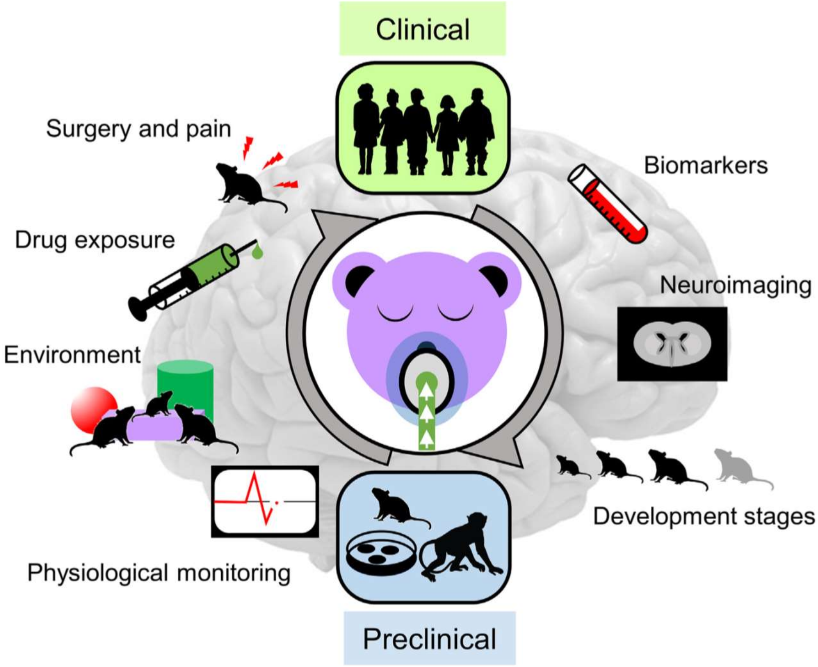

Fig. 1. Translational research is the key to improve research about anesthesiainduced neurotoxicity. The future of research about the long-term effects of anesthesia on the developing brain will necessarily involve translational findings. The development of tools to highlight the impact of general anesthesia for pediatric surgery will be possible thanks to preclinical research. This must require the control of a number of factors to reinforce the translational nature of the results.

would ideally be multimodal and would allow us to explore several domains such as locomotor activity, anxiety, contextual emotional memory and working memory. In a second stage, a mirroring study should be carried out in humans. Thus, two groups of children would be compared during adolescence in terms of behavior (experimental tasks performed by children themselves and hetero-evaluations) and neuroimaging according to their antecedents or not of general anesthesia in childhood. Behavioral testing would focus not on measures of general intelligence but on cognitive domains considered to be disturbed in mice anesthetized during the preclinical phase of the study. It should be noted that attention will have to be paid to biases in the clinical phase of the study, such as the socio-economic educational context (Farah, 2017) but also co-morbidities which could influence neurodevelopment, notably a history of prematurity (Ream and Lehwald, 2018). Particular attention should also be paid to intra-operative anesthetic data, as intraoperative management through the maintenance of physiological homeostasis (Weiss et al., 2015) which is a key factor in long-term neurological outcome (Marchesini and Disma, 2019). The application of this kind of experimental design will investigate if a direct causality between long term anesthesia, developing brain and cognitive abilities in children is present or not.

If recent clinical studies have put the risk of cerebral toxicity of general anesthesia in young children into perspective and take a step back from the FDA recommendation that advises against anesthesia before the age of 3, debate about general anesthesia on developing brain is not over. The potential for adverse neurodevelopmental effects of general anesthesia clearly remains a complex issue. Preclinical research offers key opportunities in removing these grey areas in this field of research. It has to go through improving preclinical models so as to strengthen link between laboratory and clinical practice. Indeed, it is now only through stronger translational research that safer anesthetic techniques will be identified for a better care of our children who will have to be operated.

REFERENCES

Andropoulos DB, Greene MF (2017) Anesthesia and developing brains – implications of the FDA warning. N Engl J Med 376:905–907.

Baldi C, Bettinelli S, Grossi P, Fausto A, Sardanelli F, Cavalloro F, Allegri M, Braschi A (2007) Ultrasound guidance for locoregional anesthesia: a review. Minerva Anestesiol 73:587–593.

Batty GD, Der G, Macintyre S, Deary IJ (2006) Does IQ explain socioeconomic inequalities in health? Evidence from a population-based cohort study in the west of Scotland. BMJ 332:580–584.

Bong CL, Allen JC, Kim JTS (2013) The effects of exposure to general anesthesia in infancy on academic performance at age 12. Anesth Analg 117:1419–1428.

Borst G, Aïte A, Houdé O (2015) Inhibition of misleading heuristics as a core mechanism for typical cognitive development: evidence from behavioral and brain-imaging studies. Dev Med Child Neurol 57(Suppl 2):21–25.

Coleman K, Robertson ND, Dissen GA, Neuringer MD, Martin LD, Cuzon Carslon VC, Kroenke C, Fair D, et al. (2017) Isoflurane anesthesia has long-term consequences on motor and behavioral development in infant rhesus macaques. Anesthesiology 126:74–84.

Diamond A (2013) Executive functions. Annu Rev Psychol 64:135–168.

Diamond A, Barnett WS, Thomas J, Munro S (2007) Preschool program improves cognitive control. Science 318:1387–1388.

DiMaggio C, Sun LS, Kakavouli A, Byrne MW, Li G (2009) A retrospective cohort study of the association of anesthesia and hernia repair surgery with behavioral and developmental disorders in young children. J Neurosurg Anesthesiol 21:286–291.

Disma N, O'Leary JD, Loepke AW, Brambrink AM, Becke K, Clausen NG, De Graaf JC, Liu F, et al. (2018) Anesthesia and the developing brain: a way forward for laboratory and clinical research. Paediatr Anaesth 28:758–763.

Dobbing J, Sands J (1979) Comparative aspects of the brain growth spurt. Early Hum Dev 3:79–83.

Duckworth AL, Seligman MEP (2005) Self-discipline outdoes IQ in predicting academic performance of adolescents. Psychol Sci 16:939–944.

Farah MJ (2017) The neuroscience of socioeconomic status: correlates, causes, and consequences. Neuron 96:56–71.

Flick RP, Katusic SK, Colligan RC, Wilder RT, Voigt RG, Olson RD, Sprung J, Weaver AL, et al. (2011) Cognitive and behavioral outcomes after early exposure to anesthesia and surgery. Pediatrics 128:e1053–1061.

Ganzel BL, Kim P, Glover GH, Temple E (2008) Resilience after 9/11: multimodal neuroimaging evidence for stress-related change in the healthy adult brain. NeuroImage 40:788–795.

Habre W, Disma N, Virag K, Becke K, Hansen TG, Jöhr M, Leva B, Morton NS, et al. (2017) Incidence of severe critical events in pediatric anesthesia (APRICOT): a prospective multicentre observational study in 261 hospitals in Europe. Lancet Respir Med 5:412–425.

Hansen TG (2017) Use of anesthetics in young children: consensus statement of the European Society of Anesthesiology, the European Society for Pediatric Anesthesiology, the European Association of Cardiothoracic Anesthesiology and the European Safe Tots Anesthesia Research Initiative. Eur J Anaesthesiol 34:327–328.

Hansen TG, Pedersen JK, Henneberg SW, Pedersen DA, Murray JC, Morton NS, Christensen K (2011) Academic performance in adolescence after inguinal hernia repair in infancy: a nationwide cohort study. Anesthesiology 114:1076–1085.

de Heer IJ, Tiemeier H, Hoeks SE, Weber F (2017) Intelligence quotient scores at the age of 6 years in children anaesthetised before the age of 5 years. Anesthesia 72:57–62.

Hu D, Flick RP, Zaccariello MJ, Colligan RC, Katusic SK, Schroeder DR, Hanson AC, Buenvenida SL, et al. (2017) Association between exposure of young children to procedures requiring general anesthesia and learning and behavioral outcomes in a population-based birth cohort. Anesthesiology 127:227–240.

Ikonomidou C, Bosch F, Miksa M, Bittigau P, Vöckler J, Dikranian K, Tenkova TI, Stefovska V, et al. (1999) Blockade of NMDA receptors and apoptotic neurodegeneration in the developing brain. Science 283:70–74.

Jevtovic-Todorovic V (2018) Exposure of developing brain to general anesthesia: what is the animal evidence? Anesthesiology 128:832–839.

Jevtovic-Todorovic V, Hartman RE, Izumi Y, Benshoff ND, Dikranian K, Zorumski CR, Olney JW, Wozniak DF (2003) Early exposure to common anesthetic agents causes widespread neurodegeneration in the developing rat brain and persistent learning deficits. J Neurosci 23:876–882.

Kilkenny C, Brown WJ, Cuthill IC, Emerson M, Altman DG (2010) Improving bioscience research reporting: the ARRIVE guidelines for reporting animal research. PLoS Biol 8 e1000412.

Ko WR, Huang JY, Chiang YC, Nfor ON, Ko PC, Jan SR, Lung CC, Chang HC, et al. (2015) Risk of autistic disorder after exposure to general anesthesia and surgery: a nationwide, retrospective matched cohort study. Eur J Anaesthesiol 32:303–310.

Koch SC, Fitzgerald M (2013) Activity-dependent development of tactile and nociceptive spinal cord circuits. Ann N Y Acad Sci 1279:97–102.

Marchesini V, Disma N (2019) Anesthetic neuroprotection in children: does it exist or is it all just bad? Curr Opin Anaesthesiol 32:363–369.

McCann ME, de Graaf JC, Dorris L, Disma N, Withington D, Bell G, Grobler A, Stargatt R, et al. (2019) Neurodevelopmental outcome at 5 years of age after general anesthesia or awake-regional anesthesia in infancy (GAS): an international, multicentre, randomised, controlled equivalence trial. Lancet Lond Engl 393:664–677.

Mintz CD, Barrett KMS, Smith SC, Benson DL, Harrison NL (2013) Anesthetics interfere with axon guidance in developing mouse neocortical neurons in vitro via a γ-aminobutyric acid type A receptor mechanism. Anesthesiology 118:825–833.

Moffitt TE, Arseneault L, Belsky D, Dickson N, Hancox RJ, Harrington H, et al. A gradient of childhood self-control p.

O'Leary JD, Anus M, Duku E, Wijeysundera D, To T, Li P, Maynes JT, Crawford MW. A population-based study evaluating the association between surgery in early life and child development at primary school entry. Anesthesiology 2016;125, 272–279.

Paule MG, Li M, Allen RR, Liu F, Hotchkiss C, Hanig JP, Patterson TA, Slikker Jr W, et al. (2011) Ketamine anesthesia during the first week of life can cause long-lasting cognitive deficits in rhesus monkeys. Neurotoxicol Teratol 33:220–230.

Planel E, Richter KEG, Nolan CE, Finley JE, Liu L, Wen Y, Krishnamurthy P, Herman M, et al. Anesthesia leads to tau hyperphosphorylation through inhibition of phosphatase activity by hypothermia. J Neurosci 2007;27, 3090–309.

Poirel N, Borst G, Simon G, Rossi S, Cassotti M, Pineau A, Houdé O (2021) Number conservation is related to children's prefrontal inhibitory control: an fMRI study of a piagetian task. PLoS ONE 7 e40802.

Raper J, Alvarado MC, Murphy KL, Baxter MG (2015) Multiple anesthetic exposure in infant monkeys alters emotional reactivity to an acute stressor. Anesthesiology 123:1084–1092.

Ream MA, Lehwald L (2018) Neurologic consequences of preterm birth. Curr Neurol Neurosci Rep 18:48.

Research C. for DE and FDA Drug Safety Communication: FDA review results in new warnings about using general anesthetics and sedation drugs in young children and pregnant women. FDA 2019.

Shen X, Dong Y, Xu Z, Wang H, Miao C, Soriano SG, Sun D, Baxter MG, et al. (2013) Selective anesthesia-induced neuroinflammation in developing mouse brain and cognitive impairment. Anesthesiology 118:502–515.

Shi Y, Hu D, Rodgers EL, Katusic SK, Gleich SJ, Hanson AC, Schroeder DR, Flick RP, et al. (2018) Epidemiology of general anesthesia prior to age 3 in a population-based birth cohort. Paediatr Anaesth 28:513–519.

Sprung J, Flick RP, Wilder RT, Katusic SK, Pike TL, Dingli M, Gleich SJ, Schroeder DR, et al. (2009) Anesthesia for cesarean delivery and learning disabilities in a population-based birth cohort. Anesthesiology 111:302–310.

Sun LS, Li G, Miller TLK, Salorio C, Byrne MW, Bellinger DC, Ing C, Park R, et al. (2016) Association between a single general anesthesia exposure before age 36 months and neurocognitive outcomes in later childhood. JAMA 315:2312–2320.

Todd MM (2004) Anesthetic neurotoxicity: the collision between laboratory neuroscience and clinical medicine. Anesthesiology 101:272–273.

Viarouge A, Houdé O, Borst G (2019) Evidence for the role of inhibition in numerical comparison: a negative priming study in 7- to 8-year-olds and adults. J Exp Child Psychol 186:131–141.

Vutskits L, Culley DJ (2019) GAS, PANDA, and MASK: no evidence of clinical anesthetic neurotoxicity! Anesthesiology 131:762–764.

Vutskits L, Patel P (2014) Pushing the standards forward: in-depth monitoring of physiological parameters in anesthetized neonatal mice. Anesth Analg 119:1029–1031.

Vutskits L, Xie Z (2016) Lasting impact of general anesthesia on the brain: mechanisms and relevance. Nat Rev Neurosci 17:705–717.

Wang C, Slikker W (2008) Strategies and experimental models for evaluating anesthetics: effects on the developing nervous system. Anesth Analg 106:1643–1658.

Warner DO, Shi Y, Flick RP (2018a) Anesthesia and neurodevelopment in children: perhaps the end of the beginning. Anesthesiology 128:700–703.

Warner DO, Zaccariello MJ, Katusic SK, Schroeder DR, Hanson AC, Schulte P, Buenvenida SL, Gleich SJ, et al. (2018b) Neuropsychological and behavioral outcomes after exposure of young children to procedures requiring general anesthesia: The Mayo Anesthesia Safety in Kids (MASK) Study. Anesthesiology 129:89–105.

Weiss M, Vutskit L, Hansen TG, Engelhardt T (2015) Safe Anesthesia For Every Tot – The SAFETOTS initiative. Curr Opin Anaesthesiol 28:302–307.

Zhang L, Zhang J, Dong Y, Swain CA, Zhang Y, Xie Z (2014) The potential dual effects of sevoflurane on AKT/GSK3β signaling pathway. Med Gas Res 4:5.

(Received 21 October 2020, Accepted 24 February 2021)
(Available online 4 March 2021)

Autres travaux 2 : Early Ultrafast Ultrasound Imaging of Cerebral Perfusion correlates with Ischemic Stroke outcomes and responses to treatment in Mice

Dans cet article dont je suis cinquième autrice, nous avons utilisé l'imagerie ultrason ultrarapide (fUS) chez un modèle d'AVC ischémique chez la souris.

Au début de ma thèse, j'ai réalisé plusieurs expériences en fUS sur un modèle murin d'anévrisme. L'objectif était de déclencher la rupture de l'anévrisme par une impulsion d'ultrasons, puis de visualiser l'hémorragie en fUS. Faute de temps, je n'ai pu poursuivre ces expériences (qui ne font pas l'objet de cet article) mais ai néanmoins contribué à la mise en pace de l'imagerie fUS dans notre laboratoire.

IVYSPRING
INTERNATIONAL PUBLISHER

Theranostics

2020; 10(17): 7480-7491. doi: 10.7150/thno.44233

Research Paper

Early Ultrafast Ultrasound Imaging of Cerebral Perfusion correlates with Ischemic Stroke outcomes and responses to treatment in Mice

Vincent Hingot[1†], Camille Brodin[2†], Florent Lebrun[2,5], Baptiste Heiles[1], Audrey Chagnot[2], Mervé Yetim[2], Maxime Gauberti[3], Cyrille Orset[2], Mickael Tanter[1], Olivier Couture[1], Thomas Deffieux[1‡], Denis Vivien[2,4‡]✉

1. Institute Physics for Medicine Paris, Inserm U1273, ESPCI Paris, CNRS FRE 2031, PSL University.
2. Normandie Univ, UNICAEN, INSERM, GIP Cyceron, Institut Blood and Brain @Caen-Normandie (BB@C), UMR-S U1237, Physiopathology and Imaging of Neurological Disorders (PhIND), Caen, France.
3. CHU Caen, Department of radiology, Caen University Hospital, Avenue de la Côte de Nacre, Caen, France.
4. CHU Caen, Department of Clinical Research, Caen University Hospital, Avenue de la Côte de Nacre, Caen, France.
5. STROK@LLIANCE, ETAP-Lab, 2 rue des Rochambelles, Caen, France

[†]These co-first authors equally contributed to this work.

[‡]These co-last authors equally contributed to this work.

✉ Corresponding author: Denis VIVIEN, PhD, INSERM UMR-S U1237 "Physiopathology and Imaging of Neurological Disorders", University Caen Normandie, GIP Cyceron, Institut Blood and Brain @ Caen-Normandie (BB@C), Bd Becquerel, BP5229, 14074 Caen, France. Phone: +33 2 31 47 01 66; Fax: +33 2 31 47 02 22; E-mail: vivien@cyceron.fr.

Received: 2020.01.23; Accepted: 2020.04.28; Published: 2020.06.12

Abstract

In the field of ischemic cerebral injury, precise characterization of neurovascular hemodynamic is required to select candidates for reperfusion treatments. It is thus admitted that advanced imaging-based approaches would be able to better diagnose and prognose those patients and would contribute to better clinical care. Current imaging modalities like MRI allow a precise diagnostic of cerebral injury but suffer from limited availability and transportability. The recently developed ultrafast ultrasound could be a powerful tool to perform emergency imaging and long term follow-up of cerebral perfusion, which could, in combination with MRI, improve imaging solutions for neuroradiologists.

Methods: In this study, in a model of *in situ* thromboembolic stroke in mice, we compared a control group of non-treated mice (N=10) with a group receiving the gold standard pharmacological stroke therapy (N=9). We combined the established tool of magnetic resonance imaging (7T MRI) with two innovative ultrafast ultrasound methods, ultrafast Doppler and Ultrasound Localization Microscopy, to image the cerebral blood volumes at early and late times after stroke onset and compare with the formation of ischemic lesions.

Results: Our study shows that ultrafast ultrasound can be used through the mouse skull to monitor cerebral perfusion during ischemic stroke. In our data, the monitoring of the reperfusion following thrombolytic within the first 2 h post stroke onset matches ischemic lesions measured 24 h. Moreover, similar results can be made with Ultrasound Localization Microscopy which could make it applicable to human patients in the future.

Conclusion: We thus provide the proof of concept that in a mouse model of thromboembolic stroke with an intact skull, early ultrafast ultrasound can be indicative of responses to treatment and cerebral tissue fates following stroke. It brings new tools to study ischemic stroke in preclinical models and is the first step prior translation to the clinical settings.

Key words: Ischemic stroke; Thrombolysis; Ultrasound Imaging; Ultrasound Localization Microscopy; Outcome

Introduction

Cerebral arterial recanalization and tissue reperfusion are the major prognostic factors of good functional outcomes following ischemic stroke. The only FDA approved pharmacological treatment of stroke remains thrombolytic therapy, using recombinant tissue plasminogen activator (rtPA), with a therapeutic window of 4.5 h after stroke onset [1]. The Extend clinical trial suggests the safe use of rtPA alone, even 9 h after stroke onset [2]. The overall acute recanalization rate after rtPA treatment is below 35 %, with its efficacy affected by the time to treatment, poor collaterals, clot localization and the size of thrombi [3, 4]. This efficacy is dramatically improved when combined with endovascular thrombectomy (EVT) when treated within 6-24 h of the onset of symptoms [5, 6].

The main imaging techniques dedicated to brain hemodynamics are positron emission tomography (PET), single photon emission computed tomography (SPECT), Xenon-enhanced computed tomography (XeCT), dynamic perfusion computed tomography (PCT), MRI dynamic susceptibility contrast (DSC), arterial spin labeling (ASL) and transcranial Doppler ultrasonography (TCD). Finer estimation of cerebral perfusion can be obtained in Perfusion Weighted Imaging (PWI) but requires the injection of MR contrast agents and only provide one reading [7]. Currently, there are no tools that could be performed at bedside (as TCD), repeatable (as ASL), provides quantitative measurement (as PET and XeCT) and measures multiple perfusion parameters (as PCT) [8,9]. The recent development of ultrafast ultrasound and progresses in probe technologies combined all these criteria in a unique system [10]. Unlike optical methods that are used for cerebral perfusion imaging, ultrasound allows the imaging in depth in living tissues. Specifically, ultrafast Doppler allows the monitoring of subtle Cerebral Blood Volume (CBV) changes without contrast agents and led to the development of the ultrasound analog of functional MRI (fMRI): functional Ultrasound (fUS) [11-16]. Ultrafast ultrasound also allows the detection of injected intravascular microbubbles, a clinical ultrasound contrast agent, and led to the development of Ultrasound Localization Microscopy (ULM) [17-20] which, unlike ultrafast Doppler, may allow transcranial imaging in adults patients [21,22]. In this study, we demonstrate that both modalities are adapted to the study of stroke in a mouse model, with ultrafast Doppler producing longitudinal monitoring and ULM proving an increased sensitivity and definition, two criteria which are mandatory for clinical applicability.

In preclinical studies where the skull was removed, ultrafast Doppler have been showed to detect vessels with flow as slow as 1 $mm.s^{-1}$ with a 100 µm precision whereas ULM detected vessels under 1 $mm.s^{-1}$ with a 10 µm resolution. In this study, the skull was kept intact and image quality was degraded but still enabled quality imaging of cerebral perfusion. Our present work demonstrates in an intact skull setup with a clinically relevant model of Middle Cerebral Artery (MCA) occlusion [23-25] that ultrafast Doppler and ULM can provide characterization of cerebral perfusion during an ischemic episode and follow-up in mice. The potential of ULM for transcranial imaging in human patients might allow the imaging of cerebral perfusion very early after stroke onset and possible improvement in medical care.

Materials and Methods

Animals

Experiments were performed on swiss male mice (35-40 g; Janvier Labs, France, 8-10 weeks old) in accordance with French ethical laws (Decree 2013-118) and European Communities Council guidelines (2010/63/EU).

Middle Cerebral Artery occlusion in the thromboembolic model

Micropipettes were filled with 1 µL of purified murine alpha thrombin (1 UI = 0.05 mg; Stago BNL). The pipettes were introduced in the lumen of the MCA and murine thrombin was slowly injected to form a fibrin clot. Micropipettes were left in place for 10 min to stabilize the clot.

Tissue-Type Plasminogen Activator induced thrombolysis

To induce thrombolysis, 10 mice received intravenous injection of 200 µL of rtPA (10 mg/kg, Actilyse), 10% as a bolus and 90% as an infusion for 40 min at a steady rate of 4.5 µL/min. A control group of 10 mice was injected with saline under similar conditions. One animal was excluded from the rtPA group due to poor sterotactic fixing.

Ultrafast ultrasound

Acquisitions were performed on an ultrafast scanner (Verasonics, 128 channels, 62.5 MHz sampling rate) with Neuroscan live acquisition software (ART Inserm U1273 & Iconeus; Paris, France) with a custom ultrasound probe (15 MHz, 0.11 mm pitch, 128 elements, 14 mm width, Vermon, France) which enables a 110 µm x 100 µm in plane resolution at a depth of 10 mm. The probe was mounted on 4 motors (3 translation + 1 rotation, Pi, Germany). A schematic of the setup can be found in Figure 1A. As both stereotactic frame and motorization system were fixed to the table, a common coordinate system was set so each animal could be imaged later in similar configuration. In this study, the coordinate system is (z, x, y) with z the axial axis, x the lateral axis and y the elevation axis as shown in Figure 1A. The coordinate system was adapted to match stereotactic coordinates by taking a reference on the antero-posterior axis at the vertical plane under the Bregma suture β=0.

Ultrafast Doppler

200 compounded frames (11 angles between -10°: 10°) were acquired at 500 Hz. Singular Value Decomposition filters were used (removal of the 60 first singular values) to separate blood signal from tissues and summed to produce a power Doppler image [26-30]. Between two images, a 1.2 s pause was added to let the motor move to the next slice. 24 coronal planes were imaged every 0.3 mm to reconstruct a 10 mm × 14 mm × 8 mm volume between β+2 mm and β-6 mm with an in plane resolution of 110 µm × 100 µm and a step of 300 µm every 40 s (Figure 1B).

Temporal profiles

Two regions of interest were defined on the body of the MCA and on the hypoperfused part of the cortex. The mean Doppler intensity in the ROI was calculated at each time to produce temporal profiles proportional to cerebral blood volumes in the ROI. The profiles were normalized on the basis of pre-occlusion levels.

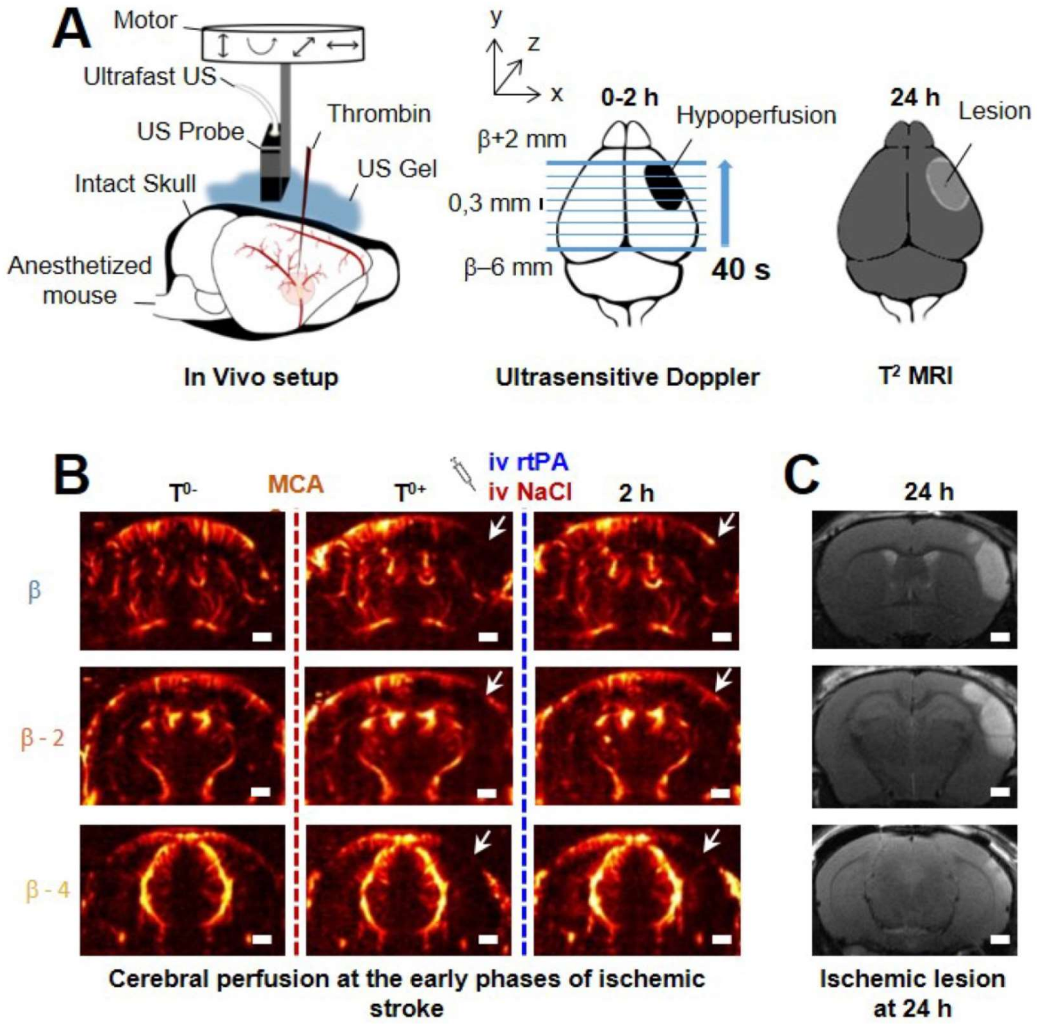

Figure 1. Transcranial ultrafast ultrasound imaging to monitor cerebral perfusion before, during and after stroke A. Experimental setup with an ultrasound probe connected to an ultrafast ultrasound acquisition system (Inserm Accelerator of Technological Research) and mounted on a 4 axis-motor for 3D scanning over the whole mice brain by steps of 0.3 mm. A volume over the whole brain is reconstructed every 40 s. Ultrafast Ultrasound monitors cerebral perfusion during the early phase of the ischemic episode, before, during and after onset, including treatment with the gold standard recombinant-tPA (rtPA). At 24 h MRI reveals the final ischemic lesion. **B**. Ultrafast Doppler reveals hypoperfusion in the ipsilateral cortices subjected to thrombin injection (clot formation) in the middle cerebral artery (MCA) and reperfusion of the corresponding territory after injection of the thrombolytic, rtPA. **C**. Registration and comparison with MRI reveal tight relationships between cerebral perfusions at the early phase of stroke and the final lesion volumes. Scale bar 1 mm.

Ultrasound Localization Microscopy

To perform ULM, acquisition and post processing steps were adapted from the reference methods [17-20]. For each image, 100 µL of Sonovue microbubbles were injected in the tail vein. Blocks of 800 compounded frames (-5° 0° 5°) at 1 kHz were acquired for 800 ms and saved for 200 ms and this scheme repeated for 180 s. A combination of Butterworth high pass filter (second order, 20 Hz) and SVD filters (removal of the 10 first singular values) were used to separate microbubbles echoes from tissues. Microbubbles centroid positions were localized using a weighted average algorithm. Microbubbles were tracked through consecutive frames using *simpletracker* (Mathworks). Tracks were interpolated and smoothed using a sliding window of 5 points and cleaned from redundant positions. A density image was reconstructed on an 11 µm × 10 µm grid.

Magnetic Resonance Imaging

Acquisitions were performed on a 7T Brucker system. T2-weighted images were acquired using a multislice multiecho sequence: TE/TR 33 ms/2500 ms and reconstructed with a 0.7 mm × 0.7 mm × 0.5 mm resolution. Lesions were manually segmented on T2 acquisitions. MRI and ultrafast Doppler volumes were registered on anatomical similarities using *imregister* (Mathworks), an intensity-based function for multimodal registration. As the coordinate system was the same for ultrafast Doppler and ULM, the volumetric registration used for ultrafast Doppler was applied to ULM to ensure registration with MRI. Segmentation of ischemic lesion was performed manually and blind to ultrasound images.

Quantifications and statistical analyses

To account for tissue swelling due to the edema, a first correction factor had to be calculated for every mouse. On T_2 MRI images, the distance between the skull and the corpus callosum was measured on both hemisphere of the mouse brain. Because skull thickness increases at the front of the head, ultrasound imaging in the most anterior parts of the head suffered from stronger wave attenuation. Consequentially, the contrast and sensitivity to the vasculature was strongly impaired and meaningful analysis could not be performed reliably after β+1.5 mm. As lesions spread up to β+3 mm, the parts between β+1.5 mm and β+3 mm were not included in lesion quantifications in the analysis in Figure 5 under the mention adjusted volume of lesion.

Quantifications are expressed as mean ± std (Figure 5A and 5B). Statistical analysis was performed using GraphPad®. We first assessed normal distribution of all samples by Shapiro-Wilk tests. In the panels A, B and E unpaired two-tailed t tests were performed. Pearson correlation tests were used for panels C and D. Sidak's multiple comparisons tests were used to assess multiple comparisons in panel F. Differences were considered statistically significant for a probability value $p < 0.05$.

Ultrafast ultrasound TICI score

In human, the TICI score is used to describe the perfusion following stroke [34,35]. We adapted a TICI-like score for ultrafast Doppler. The scoring was estimated by an operator from a combination of markers: recanalisation and reperfusion profiles reaching 50% or pre-occlusion levels, and the presence of significant remaining hypoperfused volumes at 2 h. Grade 0: No Recanalisation. Grade 1: Recanalisation but no Reperfusion Grade 2: Recanalisation and partial reperfusion. Grade 3: Complete recanalisation and reperfusion.

Results

Transcranial ultrafast ultrasound monitors hypoperfusion following thromboembolic stroke

On ultrafast Doppler, the body of the MCA can be observed on a coronal slice over 1 mm. Directly after thromboembolic occlusion of the MCA (Figure 1A), blood flow in the artery is completely blocked and the appearance of a large hypoperfused area can be observed in the ipsilateral cortex to the occluded MCA and spreading between β -3 mm and β -4 mm (Figure 1B). In the lateral part of the cortex, fed by the MCA, the blood supply is completely stopped. The most central part of the cortex, fed by the Anterior Cerebral Artery (ACA) is sometimes subjected to small and rapid changes in cerebral blood volumes (CBVs). During the 2 h following MCAo and rtPA treatment, restoration of perfusion can be assessed. At 24 h post-stroke onset and treatment, T_2 weighted MRI reveals areas with high water content corresponding to the ischemic lesion (Figure 1C). The edema as seen on T_2 MRI is known to correlate with tissue damage seen by histopathological staining [23,24]. Moreover, the edema only appears several hours after the stroke onset which makes it ineffective to image tissue damage during the early phase of stroke (Figure S1).

Without rtPA treatment, the ischemic lesion is the hypoperfused volume measured early in ultrafast ultrasound

In the control group, 10 mice were injected with saline 20 min after MCAo, corresponding to the sham of the rtPA-treated group (Figure 2B). Variations in ultrafast Doppler before and after occlusion exhibit hypoperfusion in the corresponding ipsilateral cortices (Figure 2B). Additionally, differences in ultrafast Doppler between post-occlusion time and 2 h after the stroke onset is displayed in Figure 2C and reveal the absence of any reperfusion. After identification of the MCA on ultrafast Doppler image, recanalization profiles were plotted and exhibited the absence of recanalization for saline treated mice (Figure 2D). Deep in the tissues fed by the MCA, no reperfusion was observed in any of the mice (Figure 2E). Profiles directly after MCAo can be reconstructed and reveal a peak around β-1 mm and spreading between β-4 mm and further than β+3 mm (Figure 2F). Total measured volumes at risk were 16 mm^3 ± 3 mm^3. Similar measurements were performed 2 h post MCAo and show little evolutions and hypoperfused volumes stayed similar within the margin of error (Figure 2G). Infarct areas on T_2 weighted MRI reveal lesion spreading between β-5 mm and β+3 mm with a peak also around β-1 mm and co-localization with the hypoperfused areas (Figure 2H). To account for late edema and ultrasound blindness between β+1 mm and β+3 mm, two corrections were made to the volume of lesions with adjusted volumes of 17 mm^3 ± 3 mm^3 (24 mm^3 ± 5 mm^3 without correction). This represents a 6% difference between ultrasound and MRI. In these conditions, the lesions measured by MRI at 24 h appear to be the totality of the hypoperfused volumes measured by ultrafast Doppler at 2 h post stroke onset. This hypothesis was validated in a supplementary group of 5 mice in which the MCA has been permanently occluded through electrocoagulation thus allowing neither recanalization nor reperfusion of the tissue (Figure S2). As expected, no reperfusion was observed, and similar hypoperfused volumes were observed in ultrafast Doppler imaging together with similar ischemic lesions on T_2 weighted MRI. The volumes at risk were 19 mm^3 ± 3 mm^3 while the volumes of lesion were 18 mm^3 ± 5 mm^3 (24 mm^3 ± 7 mm^3 before adjustments). This represents a 5 % difference between ultrasound and MRI.

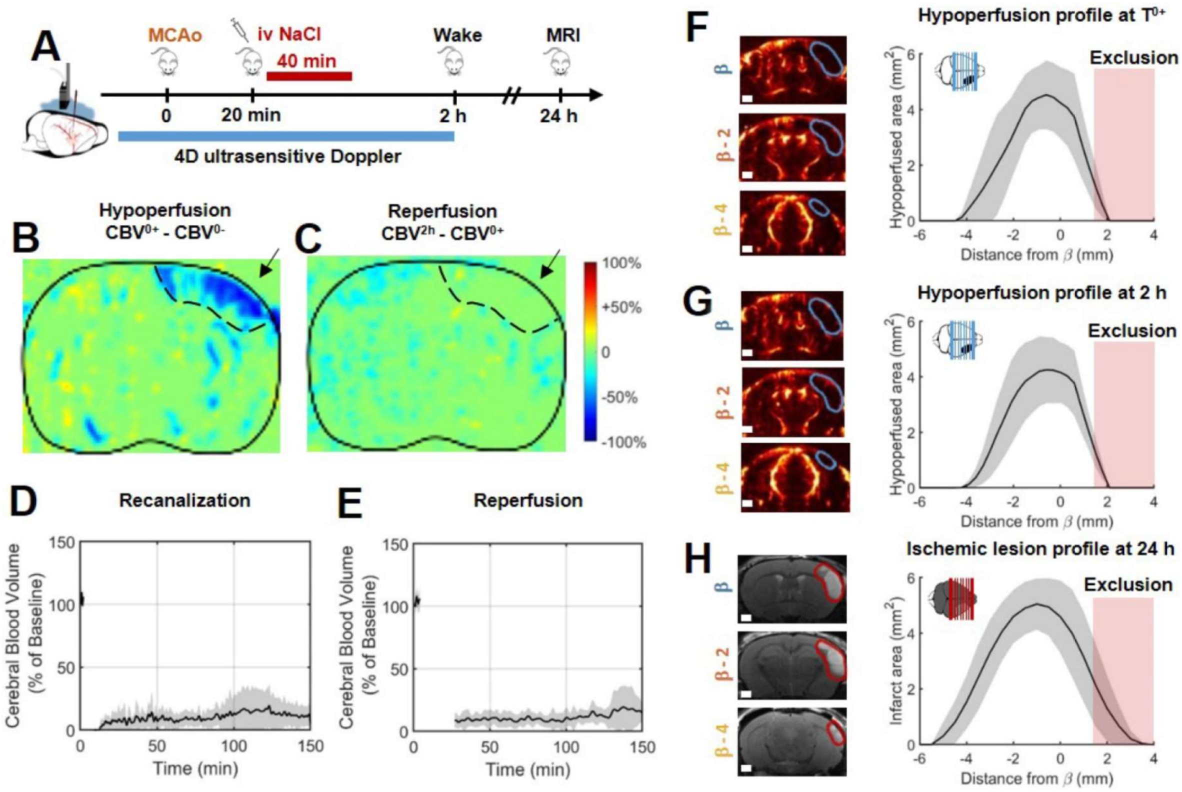

Figure 2. **In the absence of treatment, the final volume of lesion corresponds to the early hypoperfused area. A**. Experimental timeline for ultrasound monitoring of cerebral blood volumes after MCAo and comparison with MRI. **B**. Differences between ultrafast Doppler imaging performed before and after occlusion of the middle cerebral artery (MCAo) reveal hypoperfusion in the corresponding ipsilateral cortices. **C**. Differences between ultrafast Doppler imaging just after MCAo and 2 h later show no sign of reperfusion in the corresponding ipsilateral cortices. **D**. Monitoring of blood flows in the MCA on ultrafast Ultrasound over β+1 mm shows permanent occlusion with no clear recanalization occurring during the first 2 h. **E**. Monitoring of cerebral perfusion in the hypoperfused volume shows no sign of reperfusion. **F**. Patterns of hypoperfusions directly after MCAo reveal large hypoperfused volumes in the cortex. **G**. Patterns of hypoperfusions 2 h after MCAo reveal similar hypoperfused volumes. **H**. Patterns of the final ischemic lesions measured at 24 h after MCAo revealed by T_2 MRI.

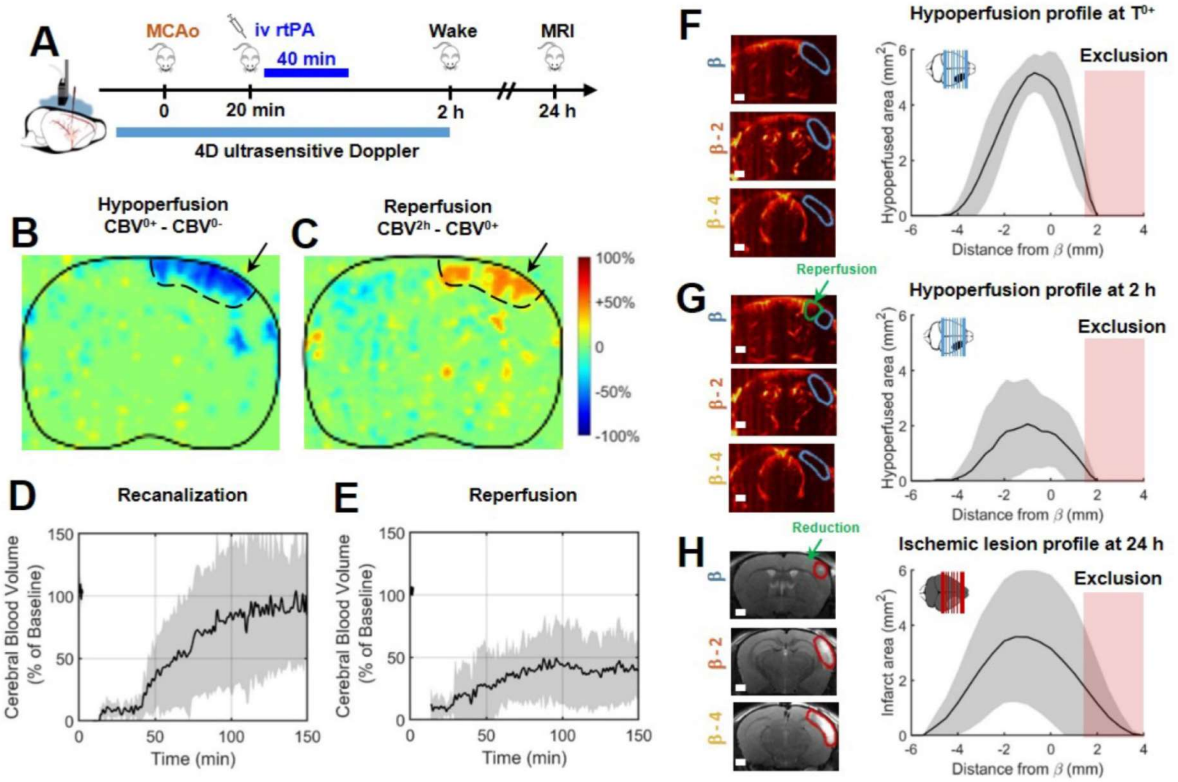

Figure 3. Early injection of rtPA causes arterial recanalization, tissue reperfusion and reduces the volume of lesion. A. Differences between ultrafast Doppler before and after MCAo reveal hypoperfusion in the corresponding ipsilateral cortices. **B**. Differences between ultrafast Doppler just after MCAo and 2 h later show reperfusion in the hypoperfused part of the corresponding cortices. **C**. Corresponding MRIs reveal the formation of smaller lesions. **D**. Monitoring of flows in the MCA on ultrafast ultrasound images over β+1 mm shows rapid and effective recanalization. **E**. Monitoring of cerebral perfusion in the hypoperfused volumes show some tissue reperfusions. **F**. Patterns of hypoperfusions directly after MCAo revealed by ultrafast ultrasound imaging. **G**. Patterns of hypoperfusions 2 h after MCAo revealed by ultrafast ultrasound imaging. **H**. Patterns of the ischemic lesions 24 h after MCAo revealed by MRI in rtPA treated animals.

rtPA induces recanalization and reperfusion can be monitored transcranially with ultrafast ultrasound

In a group of 9 mice, the gold standard fibrinolytic treatment, rtPA was injected intravenously 20 min after occlusion of the MCA, 10 % in bolus and 90 % in infusion as in clinic (Figure 3A). The differences of ultrafast Doppler images from before and after MCAo exhibit the hypoperfusion in the ipsilateral cortices (Figure 3B) whereas the differences between just after occlusion and 2 h after this time display the reperfused areas (Figure 3C). The monitoring of the recanalization of the body of the MCA reveals an overall improvement in arterial recanalization (Figure 3D). Although tissue reperfusion can be observed, it does not appear as effective as arterial recanalization (Figure 3E). The areas at risk in ultrafast Doppler were measured as previously (sham control group, Figure 2) directly after MCAo (before rtPA treatment) and reveal the same behaviors, a peak around β-1 mm and spreading between β-4 mm and further than β+1 mm with total hypoperfused volumes of 17 mm^3 ± 3 mm^3 (Figure 3F). 2 h post MCAo however, the action of rtPA treatment can be quantified as the hypoperfused volumes are reduced to 7 mm^3 ± 7 mm^3 (Figure 3G). In agreement with recanalization-reperfusion of the ischemic brain tissue, revealed by a rescue of the CBV, the final infarct areas on T$_2$ weighted MRI at 24 h are 11 mm^3 ± 3 mm^3 (14 mm^3 ± 11 mm^3 before adjustment), (Figure 3H) i.e. reduced by 30 % of the lesion volumes compared to the initially identified areas at risk measured before rtPA treatment. There remains a 30 % difference between ultrasound and MRI which highlights the fact that although they are reperfused, some tissues can still be infarcted. The variability in the response to rtPA treatment comes from the thromboembolic model and is rather representative of what happens in human patients. This variability of behaviors can be more finely observed with ultrafast ultrasound.

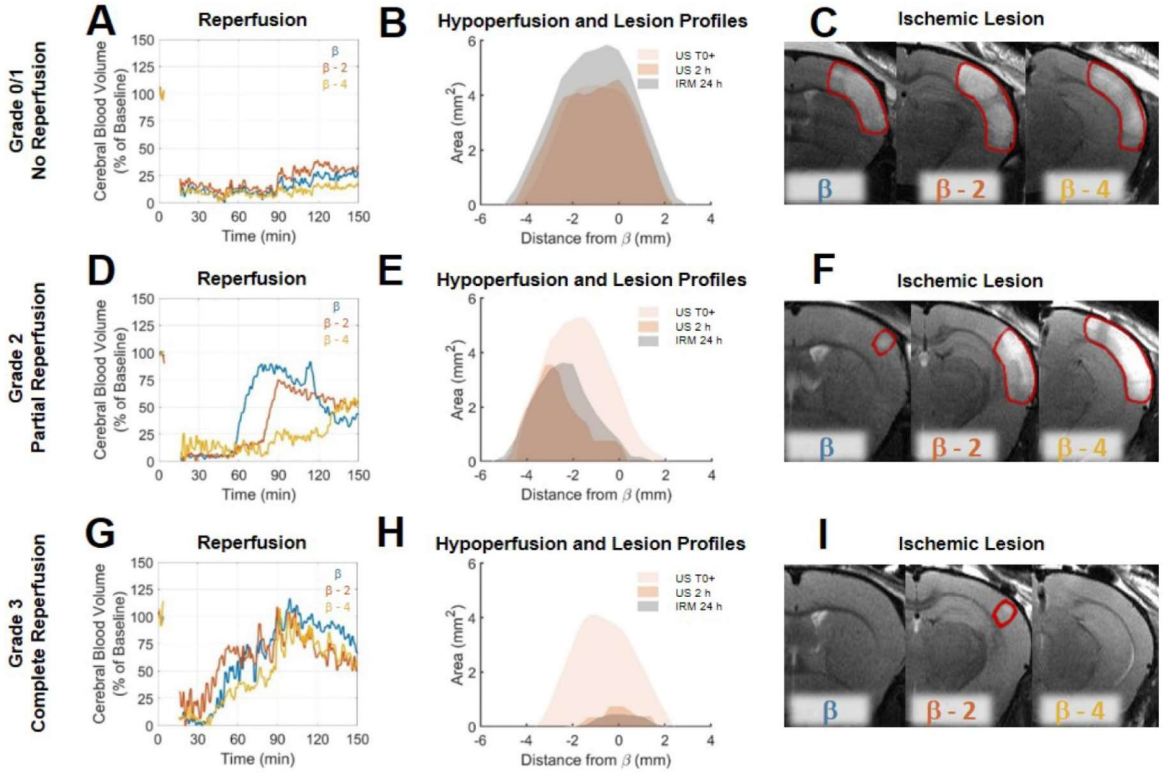

Figure 4. Differences in reperfusion patterns revealed by ultrafast ultrasound imaging correspond to the formation of ischemic lesions. A. For a typical Grade 0/1 mouse, the reperfusion curves in three different parts of the hypoperfused areas show no reperfusion. B. Hypoperfused profiles immediately post MCAo and after 2 h show no significant evolution of the formation of the ischemic lesions co-localized with hypoperfusions. C. Ischemic lesions on the corresponding areas. D. For a typical Grade 2 mouse, the reperfusion curves in three different parts of the hypoperfused areas show inhomogeneous reperfusions. E. Hypoperfused profiles immediately post MCAo and after 2 h show significant evolutions of the formation of the ischemic lesions co-localized with the remaining hypoperfusions at 2h. F. Ischemic lesions on the corresponding areas. G. For a typical Grade 3 mouse, the reperfusion curves in three different parts of the hypoperfused areas show early and effective reperfusions. H. Hypoperfused profiles immediately post MCAo and after 2 h show significant reductions of hypoperfusions associated with the formation of reduced ischemic lesions. I. Ischemic lesions on the corresponding areas.

Transcranial ultrafast ultrasound allows a fine spatiotemporal follow-up of the cerebral blood volumes following stroke and treatment

Analysis of individual animals of the rtPA treated group, unmasks fine correspondence between reperfusion patterns and volumes of lesion. In two animals, some degree of arterial recanalization was observed without any tissue reperfusion. In two other animals, complete tissue reperfusions were achieved. In the other animals, recanalization was followed by some form of incomplete reperfusions. To highlight these differences and how ultrafast ultrasound can be used to understand lesion formation, reperfusion profiles were reconstructed in three different coronal planes to explore spatial temporal differences in reperfusion. To standardize the analysis of reperfusion, a grading system similar to the clinical TICI grading system [31,32] (Thrombolysis In Cerebral Ischemia) from 0 to 3 was used to describe the reperfusion, 0 being no recanalization, 1 being recanalization but no reperfusion, 2 being a partial reperfusion and 3 being a complete reperfusion. This scoring was performed based on the ultrafast Doppler images. On Figure 4 are given three examples of mice with different reperfusion patterns. The first mouse showed little arterial recanalization and no tissue reperfusion corresponding to a TICI grade of 1. The whole hypoperfused volume directly after MCAo remains hypoperfused for the duration of the experiment as shown by reperfusion curves at β (in blue), β-2 (in red) and β-4 (in yellow) (Figure 4A). The hypoperfusion profiles show no significant evolution 2 h after MCAo and the lesion is the entire hypoperfused volume (Figure 4B). MRI reveals a large lesion over the hypoperfused areas (Figure 4C). The second mouse showed good arterial recanalization but inhomogeneous tissue reperfusion corresponding to a TICI grade of 2. Some parts of the hypoperfused volume directly after MCAo are reperfused within the first 2 h as shown by reperfusion curves at β, β-2 mm and β-4 mm (Figure 4D). The hypoperfusion profiles show significant reduction 2 h after MCAo and the lesion matches the remaining hypoperfused volume (Figure 4E). MRI reveals the inhomogeneity of the lesion (Figure 4F). The third mouse showed good arterial recanalization and good tissue reperfusion corresponding to a TICI grade of 3. All the hypoperfused volume directly after MCAo is reperfused within the first 2 h as shown by reperfusion curves at β, β-2 mm and β-4 mm (Figure 4G). The hypoperfusion profiles show a complete reduction 2 h after MCAo and the absence of lesion (Figure 4H). MRI reveals the absence of lesion (Figure 4I). Eventually, the prediction ability of ultrafast ultrasound can be tested on all the animals.

Transcranial ultrafast ultrasound at 2 h predicts responses to thrombolytic treatment and final outcomes

The effect of rtPA in this model reduces the lesion by more than 30 % (P=0.032) (Figure 5A). The saving of tissue caused by early reperfusion can be observed in rtPA animals (P=0.0206) (Figure 5B). To represent the link between hypoperfusion and the formation of a lesion, the adjusted volumes of lesion can be plotted as a function of the volumes at risk defined as the hypoperfusion directly after the occlusion of the MCA (Figure 5C). For the control group, the outcome of the stroke can be predicted since, after adjustments, all points align along the diagonal (R^2=0.8273, p=0.0003). This means that when no early reperfusion is observed, the final volumes of lesion are the whole volumes at risk measured by using CBV only, just after stroke onset. For animals receiving rtPA, the volumes of lesion are reduced compared to the volumes at risk, meaning that tissue areas were effectively saved (R^2=0.4001, p=0.0675). The size of the lesion depends on two factors: the initial size of the hypoperfused zone and the efficiency of the reperfusion. When plotting the adjusted volumes of lesion as a function of the hypoperfusion at 2 h after stroke onset (control and treated groups) (Figure 5D), all points align around the diagonal (NaCl: R^2=0.8186, p=0.0003) (rtPA: R^2=0.4438, p=0.05) with a strong correlation, even in the rtPA group with a large variability of outcome. This means that in both cases, the volumes of lesion are the hypoperfused volumes measured at 2 h using CBV only.

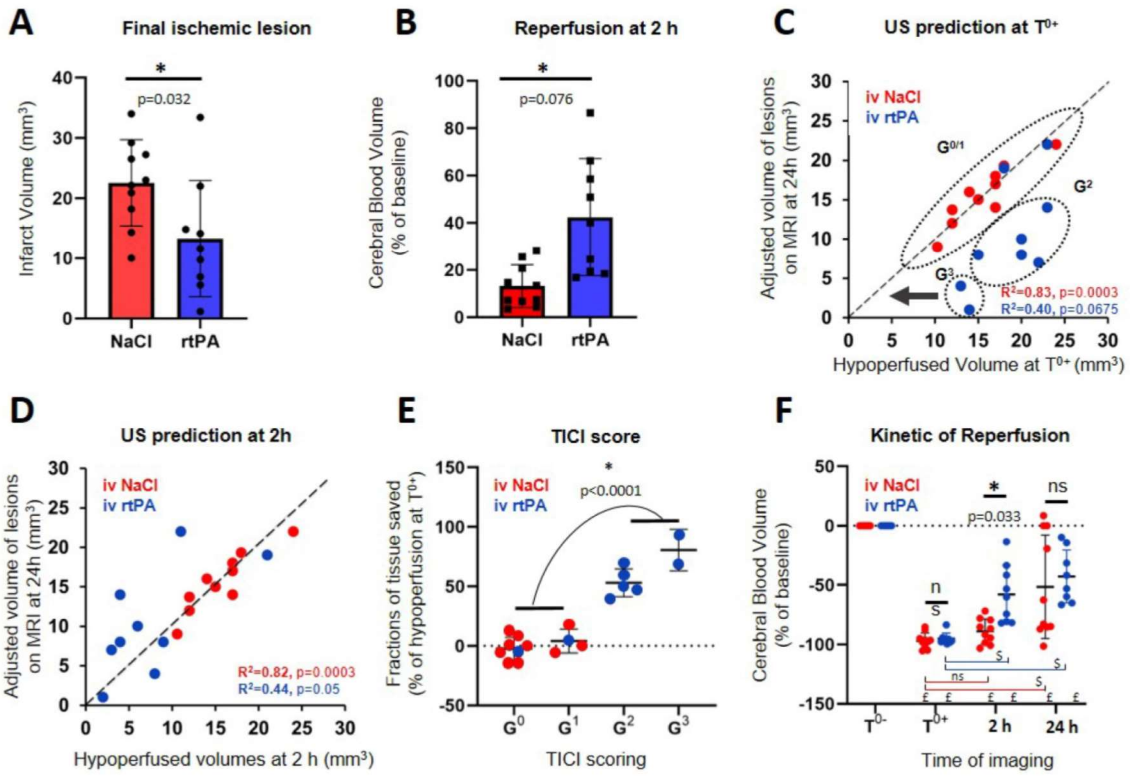

Figure 5. Prediction of lesions and responses to treatment based on early Transcranial ultrafast Doppler imaging. A, B, E = Unpaired t test Two-tailed (n=10; 9); C, D = Pearson correlation (n=10; 9); F = Sidak's multiple comparisons test (n=10; 9), *Intergroup differences; $ Intragroup differences; £ significant compared to T^{0-}. **A.** Final ischemic lesions determined at 24 h indicate reduction of lesions in animals treated with rtPA. **B.** State of reperfusion 2 h after MCAo shows improved reperfusions in the rtPA treated group. **C.** Directly after MCAo, the hypoperfused volume in ultrafast Doppler imaging is a marker of final ischemic lesion volumes for the NaCl treated animals (red) with the lesions that correspond to the complete hypoperfused volumes, aligned around the diagonal. For the rtPA treated group (blue), the lesions are smaller than the volumes at risk defined directly after occlusion because of effective tissue reperfusions. **D.** After rtPA treatment, the remaining hypoperfused volumes are predictive of the final lesion volumes in both groups. **E.** Effectiveness of the prediction of lesions based on reperfusion using the ultrafast ultrasound based TICI score. **F.** Evolutions of perfusions in the volumes at risk at the early time after stroke onset (0 and 2 h) and at 24 h show that after a therapeutic window of 2 h, perfusion is no longer predictive of the lesion.

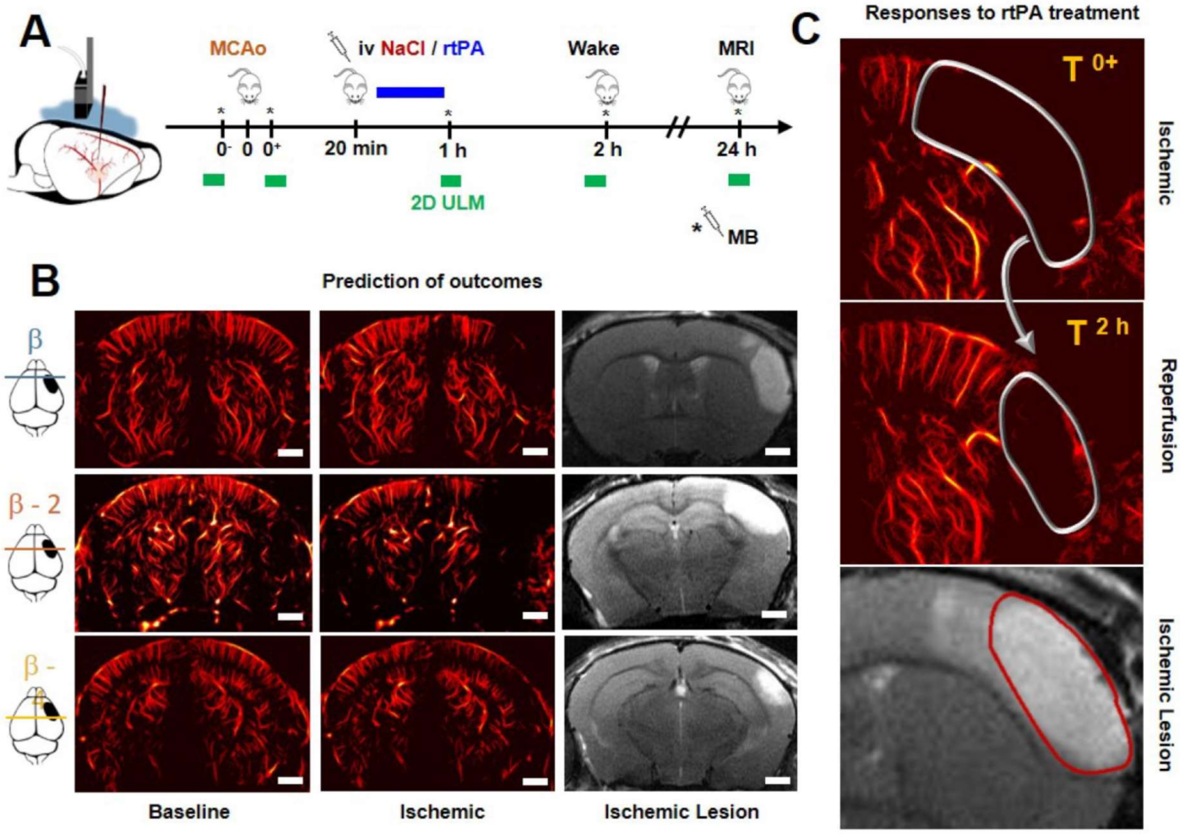

Figure 6. Predicting the outcomes and evaluating responses to treatment with transcranial ULM. A. Timeline for ULM acquisitions. **B.** For mice treated with NaCl, a large lesion can be seen in ULM just after ischemia and very little reperfusion can be observed 2 h after the onset. In ultrafast Doppler, the hypoperfused area is the infarcted lesion seen in MRI. **C.** On rtPA treated mice, the reperfusion can be evaluated with ULM and predicts the formation of the lesion. Scale bar 1 mm.

However, this representation does not consider the quality of the reperfusion in saving tissues. All mice in the control group are attributed a TICI score of 0 or 1, meaning that no reperfusion was ever observed. Four mice in the rtPA treated group were attributed TICI scores of 0 or 1 meaning that thrombolysis was not effective enough to reperfuse the tissues. In these conditions, the prognostic of lesions is similar to the control saline group. Six mice in the rtPA group were attributed TICI scores of 2 or 3, meaning that reperfusions were achieved. In these conditions, the lesions were reduced compared to the volumes at risk and compared to the control group, implying that the better the reperfusion is, the more tissues are saved. Using the ultrafast Doppler based TICI grading system, we can represent how much tissue was effectively saved by an early and effective reperfusion compared to the initial areas at risk measured by CBV (Figure 5E). It is no surprise that for grades 0 and 1, no tissue is saved. On the contrary, major improvements can be observed for mice with grade 2 and 3 with preservation of more than half of the tissue ($P<0.0001$). All animals were imaged again at 24 h. Some reperfusion 24 h after the onset of the stroke is observed in both the saline and rtPA groups, with an improved reperfusion for the rtPA treated animals when measured at 2 h ($p=0.033$) (Figure 5F).

Transcranial Ultrasound Localization Microscopy to image hypoperfusion

In four mice in each group, ULM was performed in a single coronal plane at particular times, just before and after occlusion of the MCA, 1 and 2 h later and again after 24 h (Figure 6A). On the given examples in Figure 6B, although there is still shadowing by the skull, ULM can be performed and reveals the vasculature with enhanced spatial resolution and sensitivity. ULM reveals the localization and extent of the hypoperfusion. 24 h after the onset of the stroke, we can compare the lesions seen in T_2 weighted MRI with the hypoperfused areas. The given examples in Figure 6B, shows the formation of a large lesion. The hypoperfused area is large to begin with, and the injection of NaCl does not induce efficient reperfusion. 2 h after the onset of the ischemia, only a small area is reperfused, which we can easily identify as saved on the corresponding T_2 image. The given example in Figure 6C shows the formation of a reduced lesion after rtPA treatment and reperfusion. These examples give an idea of how ULM could be used to image the hypoperfused areas and monitor the response to treatment.

Discussion

An important goal to improve stroke therapy is to identify how the lesion will extend with time, whether the patient will respond to treatment and ultimately to predict the functional outcome. To address these important questions, neurologists and neuroradiologists use a combination of prediction tools with the severity of stroke, its location, age, previous risk factors and comorbid disease (such as high blood pressure, diabetes, etc.) as key factors. Despite all these criteria, their answer remains most often very evasive and is usually postponed until the evolution of permanent neurological deficits. An early biomarker to accurately identify salvageable tissues and to predict functional outcome after stroke is, therefore, mandatory [33] and could be met with the assistance of neuroimaging techniques [34].

In our study, we demonstrate that ultrafast Doppler and Ultrasound Localization Microscopy can be relevant neuroimaging modalities for stroke. We show here that early assessment of the cerebral perfusion using *in vivo* ultrafast Doppler brain imaging, when performed early after stroke onset (here 2 h in rodents) is indicative of final lesion volumes measured by MRI at 24 h. We also demonstrate, that when performed just after thrombolytic treatment (rtPA-induced fibrinolysis), the methodology can be used to monitor the treatment efficacy.

Ultrafast Doppler for functional imaging was demonstrated in different animal models [11–14] and in clinical settings: in newborns [15] or intraoperatively [16]. In the context of stroke, it was first investigated in 2012 [35] and recent works confirmed its relevance [36,37], but not in a model of thromboembolic stroke as it occurs in clinic and without considering prognostic and/or responses to the gold standard treatment. However, the translation of results to human should always be done carefully, especially in the context of stroke. Indeed, all strategies identified so far to save the brain excepted rtPA treatment have failed in the clinic, mainly because of poor animal modeling. The model of stroke we have used here [23,24] is relevant with the actual clinical setting [25,38]. Moreover, ultrasound imaging of the early phases following stroke was also performed with optical contrast using photoacoustic imaging but in a simpler mouse model of photo thrombose and filament induced MCA occlusion [39]. Unlike ultrafast Doppler and ULM, photoacoustic imaging is sensitive to oxygen saturation in tissue and not blood volumes but can nonetheless provide similar results in terms of temporal dynamics and formation of lesion [40]. Although its translation to human patients might be severely limited by the strong absorption of light through the skull, photoacoustic can be complementary with ultrafast Doppler and ULM for preclinical studies to provide both cerebral blood volume and tissue oxygenation in tissues with different sets of sensitivity and resolutions.

Similarly, the translation of ultrasound imaging methods to human has always been a challenge because of a strong attenuation by the skull bone. As demonstrated previously, ultrafast Doppler can be performed through the fontanel [15] and could thus contribute to the diagnosis of stroke in babies. However, there are clear limitations about the possibility to use ultrafast ultrasound in adult due to strong aberrations and absorptions by the skull bone. The more recent improvements of both contrast and resolution of ULM may allow transcranial imaging [21,22], all the more so than microbubbles are commonly used in human as contrast agent for ultrasound imaging (Sonovue, Bracco), and in particular in MCA infarction to improve the signal to noise ratio [41]. This is a major point considering the recent report made by the Food and Drug Administration (FDA) about a Safety Announcement related to gadolinium-based contrast agents (GBCAs) administered for MRIs [42]. Nonetheless, the quality of the imaging through the skull will be critical to determine the quality of the readings, as there is a priori no way to distinguish ischemic from shadowed areas.

A proper clinical trial has yet to demonstrate the ability of ULM to provide quality reading through the human skull. The clinical use of ULM in this context could be performed through the temporal window, and would benefit from the extension of the field of view from 2D to 3D to access large areas of the brain which may reduce the dependency of the imaging procedure to the operator and allow the detection of scattered lesion. It may also enable the estimation of quantitative biomarkers of vascular suffering over large areas of the brain. Such extension is envisioned to become possible in the next years with the advent of piezocomposite 2D Matrix Arrays or Capacitive Micromachined Ultrasonic Transducers (CMUT) technologies and development of 3D ultrafast ultrasound modalities [43-45].

The possibility to have access to an easy to use, cheap, operator independent and transportable machine to image cerebral perfusion would undoubtedly increase the number of patients eligible for treatment, with the possibility to use this imaging method in the ambulance. Although recanalization is associated with rapid clinical improvement in some patients, for others despite recanalization, they show delayed or impaired reperfusion. Ideal patient selection for thrombolysis alone or combined to thrombectomy should therefore not be based on therapeutic windows but rather on perfusion imaging to determine "a signature" of response to treatments. In addition, such type of monitoring could be very useful for long term recording of recovery and to prevent and treat recurrent stroke.

In conclusion, we provide here, in a relevant model of thromboembolic stroke model in mice with rtPA treatment, the demonstration that ultrafast ultrasound *in vivo* imaging can be used in the context of stroke to diagnose ischemic injury, to prognose outcomes and responses to treatment, in an early time frame after stroke onset.

Supplementary Material

Supplementary figures and tables. http://www.thno.org/v10p7480s1.pdf

Acknowledgments

This work was supported by Agence Nationale de la Recherche (ANR), within the project ANR Predic, the European Research Council under the European Union Horizon H2020 programme/ERC Consolidator grant agreement No 772786-ResolveStroke, the RHU project Marvelous (16-RHUS-0009), the LABEX WIFI (Laboratory of Excellence ANR -10 -LABX -24) within the French Program "Investments for the Future" under reference ANR -10 - IDEX -0001 -02 PSL* and performed with the technical and scientific support of the INSERM Accelerator of Technological Research in Biomedical Ultrasound and the institute Blood and Brain @ Caen-Normandie (BB@C).

Author contributions

All authors designed the research, V.H., C.B. and C.O. did the experiments, V.H., C.B., T.D., M.T. and D.V. analyzed the data, T.D. developed parts of the sequence, acquisition and processing software, VH, B.H. and O.C. developed the algorithms for ULM, all the authors discussed the results and wrote the paper.

Disclosure

O.C. and M.T. are depositor of the patent /FR2011/052810. T.D. and M.T. are cofounder of Iconeus.

Competing Interests

The authors have declared that no competing interest exists.

References

1. Zivin J, Fisher M, DeGirolami U, Hemenway C, Stashak J. Tissue plasminogen activator reduces neurological damage after cerebral embolism. Science. 1985; 230: 1289–92.
2. Campbell BCV, Ma H, Ringleb PA, Parsons MW, Churilov L, Bendszus M, et al. Extending thrombolysis to 4·5–9 h and wake-up stroke using perfusion imaging: a systematic review and meta-analysis of individual patient data. Lancet. 2019; 394: 139-147.
3. Berkhemer OA, Fransen PSS, Beumer D, van der Berg LA, Lingsma HF, Yoo AJ, et al. A Randomized Trial of Intraarterial Treatment for Acute Ischemic Stroke. N Engl J Med. 2015; 372: 11–20.
4. Coutinho JM, Liebeskind DS, Slater LA, Nogueira RG, Clark W, Davalos A, et al. Combined Intravenous Thrombolysis and Thrombectomy vs Thrombectomy Alone for Acute Ischemic Stroke: A Pooled Analysis of the SWIFT and STAR Studies. JAMA Neurol. 2017; 74: 268-274.
5. Nogueira RG, Jadhav AP, Haussen DC, Bonafe A, Budzik RF, Bhuva P, et al. Thrombectomy 6 to 24 h after Stroke with a Mismatch between Deficit and Infarct. N Engl J Med. 2018; 378: 11–21.
6. Thiebaut AM, Gauberti M, Martinez De Lizarrondo S, Vivien D, Yepes M, Roussel BD. The role of plasminogen activators in stroke treatment: fibrinolysis and beyond. Lancet Neurol. 2018; 17: 1121–1132.
7. Shen Q, Duong T. Magnetic resonance imaging of cerebral blood flow in animal stroke models. Brain Circ. 2016; 2:20-27.
8. Wintermark M, Sesay M, Barbier M, Borbely K, Dillon WP, Eastwood JD, et al. Comparative Overview of Brain Perfusion Imaging Techniques. Stroke. 2005; 36:e83-99
9. Essig M, Shiroishi MS, Nguyen TB, Saake M, Provenzale JM, Enterline D, et al. Perfusion MRI: The Five Most Frequently Asked Technical Questions. AJR Am J Roentgenol. 2013; 200:24–34.
10. Tanter M, Fink M. Ultrafast imaging in biomedical ultrasound. IEEE Trans Ultrason Ferroelectr Freq Control. 2014; 61: 102–119.
11. Deffieux T, Demene C, Pernot M, Tanter M. Functional ultrasound neuroimaging: a review of the preclinical and clinical state of the art. Curr Opin Neurobiol. 2018; 50:128–135.
12. Mace E, Montaldo G, Cohen I, Baulac M, Fink M, Tanter M. Functional ultrasound imaging of the brain. Nat Methods. 2011; 8: 662–4.
13. Demene C, Tiran E, Sieu LA, Bergel A, Gennisson JL, Pernot M, et al. 4D microvascular imaging based on ultrafast Doppler tomography. NeuroImage. 2016; 127: 472–483.
14. Tiran E, Ferrier J, Deffieux T, Genisson JL, Pezet S, Lenkei Z, et al. Transcranial Functional Ultrasound Imaging in Freely Moving Awake Mice and Anesthetized Young Rats without Contrast Agent. Ultrasound Med Biol. 2017; 43: 1679–1689.
15. Demene C, Baranger J, Bernal M, Delanoe C, Auvin S, Biran V, et al. Functional ultrasound imaging of brain activity in human newborns. Sci Transl Med. 2017; 9(411).
16. Imbault M, Chauvet D, Gennisson JL, Capelle L, Tanter M. Intraoperative Functional Ultrasound Imaging of Human Brain Activity. Sci Rep. 2017; 7: 7304.
17. Errico C, Pierre J, Pezet S, Dessailly Y, Lekei Z, Couture O, et al. Ultrafast ultrasound localization microscopy for deep super-resolution vascular imaging. Nature. 2015; 527(7579): 499–502.
18. Couture O, Hingot V, Heiles B, Muleki-Seya P, Tanter M. Ultrasound Localization Microscopy and Super-Resolution: A State of the Art. IEEE Trans Ultrason Ferroelectr Freq Control. 2018; 65: 1304–1320.
19. Hingot V, Errico C, Heiles B, Rahal L, Tanter M, Couture O. Microvascular flow dictates the compromise between spatial resolution and acquisition time in Ultrasound Localization Microscopy. Sci Rep. 2019; 9: 2456.
20. Heiles B, Correia M, Hingot V, Pernot M, Provost J Tanter M, et al. Ultrafast 3D Ultrasound Localization Microscopy using a 32×32 Matrix Array. IEEE Trans Med Imaging. 2019; 38: 2005-2015.
21. O'Reilly MA, Hynynen K. A super-resolution ultrasound method for brain vascular mapping. Med Phys. 2013; 40: 110701.
22. Soulioti De, Espíndola D, Dayton PA, Pinton GF. Super-Resolution Imaging Through the Human Skull. IEEE Trans Ultrason Ferroelectr Freq Control. 2020; 67: 25-36.
23. Orset C, Haelenwyn B, Allan SM, Ansar S, Sampos F, Cho TH, et al. Efficacy of Alteplase in a Mouse Model of Acute Ischemic Stroke: A Retrospective Pooled Analysis. Stroke. 2016; 47: 1312–1318.
24. Orset C, Macrez R, Young AR, Panthou D, Angles-Cano E, Maubert E, et al. Mouse Model of In Situ Thromboembolic Stroke and Reperfusion. Stroke. 2007; 38: 2771–2778.
25. Llovera G, Hofmann K, Roth S, Salas-Perdomo A, Ferrer-Ferrer M, Perego C, et al. Results of a preclinical randomized controlled multicenter trial (pRCT): Anti-CD49d treatment for acute brain ischemia. Sci Transl Med. 2015; 7(299): 299ra121.

26. Demene C, Deffieux T, Pernot M, Osmanski BF, Gennisson JL, Sieu LA, et al. Spatiotemporal Clutter Filtering of Ultrafast Ultrasound Data Highly Increases Doppler and fUltrasound Sensitivity. IEEE Trans Med Imaging. 2015; 34: 2271-85.
27. Baranger J, Arnal B, Perren F, Baud O, Tanter M, Demene C. Adaptive Spatiotemporal SVD Clutter Filtering for Ultrafast Doppler Imaging Using Similarity of Spatial Singular Vectors. IEEE Trans Med Imaging. 2018; 37: 1574–1586.
28. Shung KK, Sigelmann R, Reid JM. Scattering of ultrasound by blood. IEEE Trans Biomed Eng. 1976; 23: 460–467.
29. Cloutier G, Qin Z. Ultrasound backscattering from non-aggregating and aggregating erythrocytes--a review. Biorheology. 1997; 34: 443–470.
30. Bercoff J, Montaldo G, Loupas T, Savery D, Meziere F, Find M, et al. Ultrafast compound Doppler imaging: providing full blood flow characterization. IEEE Trans Ultrason Ferroelectr Freq Control. 2011; 58: 134–147.
31. Zaidat OO, Lazzaro MA, Liebeskind DS, Janjua N, Wechsler L, Nogueira RG, et al. Revascularization grading in endovascular acute ischemic stroke therapy. Neurology. 2012; 79: S110–S116.
32. Zerna C, Thomalla G, Campbell BCV, Rha JH, Hill MD. Current practice and future directions in the diagnosis and acute treatment of ischaemic stroke. Lancet. 2018; 392: 1247–1256.
33. Stinear CM. Prediction of motor recovery after stroke: advances in biomarkers. Lancet Neurol. 2017; 16: 826–836.
34. Thomalla G, Gerloff C. Acute imaging for evidence-based treatment of ischemic stroke. Curr Opin Neurol. 2019; 32: 521-529.
35. Martin A, Mace E, Boisgard R, Montaldo G, Theze B, Tanter M, et al. Imaging of perfusion, angiogenesis, and tissue elasticity after stroke. J Cereb Blood Flow Metab. 2012; 32: 1496–1507.
36. Brunner C, Isabel C, Martin A, Dussaux C, Savoye A, Emmrich J, et al. Mapping the dynamics of brain perfusion using functional ultrasound in a rat model of transient middle cerebral artery occlusion. J Cereb Blood Flow Metab. 2017; 37: 263–276.
37. Brunner C, Korostelev M, Raja S, Montaldo G, Urban A, Baron JC. Evidence from functional ultrasound imaging of enhanced contralesional microvascular response to somatosensory stimulation in acute middle cerebral artery occlusion/reperfusion in rats: A marker of ultra-early network reorganization? J Cereb Blood Flow Metab. 2018; 38: 1690–1700.
38. Martinez de Lizarrondo S, Gakuba C, Herbig BA, Repesse Y, Ali C, Denis CV, et al. Potent Thrombolytic Effect of N -Acetylcysteine on Arterial Thrombi. Circulation. 2017; 136: 646–660.
39. Lv J, Shi L, Jingde Z, Fei D, Zhiyou W, Ronghe C, et al. In vivo photoacoustic imaging dynamically monitors the structural and functional changes of ischemic stroke at a very early stage. Theranostics. 2020; 10:816-828.
40. Cao R, Li J, Kharel Y, Zhang C, Morris E, Santos WL, et al. Photoacoustic microscopy reveals the hemodynamic basis of sphingosine 1-phosphate-induced neuroprotection against ischemic stroke. Theranostics. 2018; 8:6111-6120.
41. Seidel G, Meyer-Wiethe K, Berdien G, Hollstein D, Toth D, Aach T. Ultrasound Perfusion Imaging in Acute Middle Cerebral Artery Infarction Predicts Outcome. Stroke. 2004; 35:1107-1111.
42. Levine D, McDonald RJ, Kressel HY. Gadolinium Retention After Contrast-Enhanced MRI. JAMA. 2018; 320:1853.
43. Provost J, Papadacci C, Arango JE, Imbault M, Fink M, Genisson JL, et al. 3D ultrafast ultrasound imaging in vivo. Phys Med Biol. 2014; 59: L1–L13.
44. Provost J, Papadacci C, Demene C, Gennisson JL, Tanter M, Pernot M. 3-D ultrafast Doppler imaging applied to the noninvasive mapping of blood vessels in vivo. IEEE Trans Ultrason Ferroelectr Freq Control. 2015; 62: 1467–1472.
45. Rabut C, Correia M, Finel V, Pezet S, Pernot M, Deffieux T, et al. 4D functional ultrasound imaging of whole brain activity in rodents. Nat Methods. 2019; 16: 994–997.

RÉFÉRENCES

- A -

Abbott, N.J., Rönnbäck, L., Hansson, E., 2006. Astrocyte–endothelial interactions at the blood–brain barrier. Nat. Rev. Neurosci. 7, 41–53. https://doi.org/10.1038/nrn1824

Abir-Awan, M., Kitchen, P., Salman, M.M., Conner, M.T., Conner, A.C., Bill, R.M., 2019. Inhibitors of Mammalian Aquaporin Water Channels. Int. J. Mol. Sci. 20. https://doi.org/10.3390/ijms20071589

Aboitiz, F., Montiel, J.F., 2021. The Enigmatic Reissner's Fiber and the Origin of Chordates. Front. Neuroanat. 15, 703835. https://doi.org/10.3389/fnana.2021.703835

Absinta, M., Ha, S.-K., Nair, G., Sati, P., Luciano, N.J., Palisoc, M., Louveau, A., Zaghloul, K.A., Pittaluga, S., Kipnis, J., Reich, D.S., 2017. Human and nonhuman primate meninges harbor lymphatic vessels that can be visualized noninvasively by MRI. eLife 6. https://doi.org/10.7554/eLife.29738

Adeeb, N., Deep, A., Griessenauer, C.J., Mortazavi, M.M., Watanabe, K., Loukas, M., Tubbs, R.S., Cohen-Gadol, A.A., 2013a. The intracranial arachnoid mater : a comprehensive review of its history, anatomy, imaging, and pathology. Childs Nerv. Syst. ChNS Off. J. Int. Soc. Pediatr. Neurosurg. 29, 17–33. https://doi.org/10.1007/s00381-012-1910-x

Adeeb, N., Mortazavi, M.M., Deep, A., Griessenauer, C.J., Watanabe, K., Shoja, M.M., Loukas, M., Tubbs, R.S., 2013b. The pia mater: a comprehensive review of literature. Childs Nerv. Syst. ChNS Off. J. Int. Soc. Pediatr. Neurosurg. 29, 1803–1810. https://doi.org/10.1007/s00381-013-2044-5

Adeeb, N., Mortazavi, M.M., Tubbs, R.S., Cohen-Gadol, A.A., 2012. The cranial dura mater: a review of its history, embryology, and anatomy. Childs Nerv. Syst. 28, 827–837. https://doi.org/10.1007/s00381-012-1744-6

Agre, P., 2004. Aquaporin Water Channels. Biosci. Rep. 24, 127–163. https://doi.org/10.1007/s10540-005-2577-2

Ahn, J.H., Cho, H., Kim, J.-H., Kim, S.H., Ham, J.-S., Park, I., Suh, S.H., Hong, S.P., Song, J.-H., Hong, Y.-K., Jeong, Y., Park, S.-H., Koh, G.Y., 2019. Meningeal lymphatic vessels at the skull base drain cerebrospinal fluid. Nature 572, 62–66. https://doi.org/10.1038/s41586-019-1419-5

Aldea, R., Weller, R.O., Wilcock, D.M., Carare, R.O., Richardson, G., 2019. Cerebrovascular Smooth Muscle Cells as the Drivers of Intramural Periarterial Drainage of the Brain. Front. Aging Neurosci. 11, 1. https://doi.org/10.3389/fnagi.2019.00001

Algin, O., Turkbey, B., 2013. Intrathecal Gadolinium-Enhanced MR Cisternography: A Comprehensive Review. AJNR Am. J. Neuroradiol. 34, 14–22. https://doi.org/10.3174/ajnr.A2899

Alt, K.W., Jeunesse, C., Buitrago-Téllez, C.H., Wächter, R., Boës, E., Pichler, S.L., 1997. Evidence for stone age cranial surgery. Nature 387, 360–360. https://doi.org/10.1038/387360a0

Anderson, B.W., Kortz, M.W., Al Kharazi, K.A., 2021. Anatomy, Head and Neck, Skull, in: StatPearls. StatPearls Publishing, Treasure Island (FL).

Anfray, A., Brodin, C., Drieu, A., Potzeha, F., Dalarun, B., Agin, V., Vivien, D., Orset, C., 2021. Single- and two- chain tissue type plasminogen activator treatments differentially influence cerebral recovery after stroke. Exp. Neurol. 338, 113606. https://doi.org/10.1016/j.expneurol.2021.113606

Antila, S., Karaman, S., Nurmi, H., Airavaara, M., Voutilainen, M.H., Mathivet, T., Chilov, D., Li, Z., Koppinen, T., Park, J.-H., Fang, S., Aspelund, A., Saarma, M., Eichmann, A., Thomas, J.-L., Alitalo, K., 2017. Development and plasticity of meningeal lymphatic vessels. J. Exp. Med. 214, 3645–3667. https://doi.org/10.1084/jem.20170391

Asgari, M., de Zélicourt, D., Kurtcuoglu, V., 2016. Glymphatic solute transport does not require bulk flow. Sci. Rep. 6, 38635. https://doi.org/10.1038/srep38635

Aspelund, A., Antila, S., Proulx, S.T., Karlsen, T.V., Karaman, S., Detmar, M., Wiig, H., Alitalo, K., 2015. A dural lymphatic vascular system that drains brain interstitial fluid and macromolecules. J. Exp. Med. 212, 991–999. https://doi.org/10.1084/jem.20142290

Aspelund, A., Tammela, T., Antila, S., Nurmi, H., Leppänen, V.-M., Zarkada, G., Stanczuk, L., Francois, M., Mäkinen, T., Saharinen, P., Immonen, I., Alitalo, K., 2014. The Schlemm's canal is a VEGF-C/VEGFR-3–responsive lymphatic-like vessel. J. Clin. Invest. 124, 3975–3986. https://doi.org/10.1172/JCI75395

Atkinson, A.J., 2017. Intracerebroventricular drug administration. Transl. Clin. Pharmacol. 25, 117–124. https://doi.org/10.12793/tcp.2017.25.3.117

Attwell, D., Iadecola, C., 2002. The neural basis of functional brain imaging signals. Trends Neurosci. 25, 621–625. https://doi.org/10.1016/S0166-2236(02)02264-6

Augé, E., Bechmann, I., Llor, N., Vilaplana, J., Krueger, M., Pelegrí, C., 2019. Corpora amylacea in human hippocampal brain tissue are intracellular bodies that exhibit a homogeneous distribution of neo-epitopes. Sci. Rep. 9, 2063. https://doi.org/10.1038/s41598-018-38010-7

Avolio, A., Kim, M.O., Adji, A., Gangoda, S., Avadhanam, B., Tan, I., Butlin, M., 2018. Cerebral Haemodynamics: Effects of Systemic Arterial Pulsatile Function and Hypertension. Curr. Hypertens. Rep. 20, 20. https://doi.org/10.1007/s11906-018-0822-x

- B -

Bacyinski, A., Xu, M., Wang, W., Hu, J., 2017. The Paravascular Pathway for Brain Waste Clearance: Current Understanding, Significance and Controversy. Front. Neuroanat. 11, 101. https://doi.org/10.3389/fnana.2017.00101

Badaut, J., Fukuda, A.M., Jullienne, A., Petry, K.G., 2014. Aquaporin and brain diseases. Biochim. Biophys. Acta 1840, 1554–1565. https://doi.org/10.1016/j.bbagen.2013.10.032

BAHNEY, J., VON BARTHELD, C.S., 2018. The Cellular Composition and Glia-Neuron Ratio in the Spinal Cord of a Human and a Non-Human Primate: Comparison with other Species and Brain Regions. Anat. Rec. Hoboken NJ 2007 301, 697–710. https://doi.org/10.1002/ar.23728

Bedussi, B., Almasian, M., de Vos, J., VanBavel, E., Bakker, E.N., 2018. Paravascular spaces at the brain surface: Low resistance pathways for cerebrospinal fluid flow. J. Cereb. Blood Flow Metab. Off. J. Int. Soc. Cereb. Blood Flow Metab. 38, 719–726. https://doi.org/10.1177/0271678X17737984

Benveniste, H., Nedergaard, M., 2021. Cerebral small vessel disease: A glymphopathy? Curr. Opin. Neurobiol. 72, 15–21. https://doi.org/10.1016/j.conb.2021.07.006

Biffi, A., Greenberg, S.M., 2011. Cerebral amyloid angiopathy: a systematic review. J. Clin. Neurol. Seoul Korea 7, 1–9. https://doi.org/10.3988/jcn.2011.7.1.1

Bihan, D.L., Breton, E., Lallemand, D., Aubin, M.L., Vignaud, J., Laval-Jeantet, M., 1988. Separation of diffusion and perfusion in intravoxel incoherent motion MR imaging. Radiology. https://doi.org/10.1148/radiology.168.2.3393671

Blackman, J., Swirski, M., Clynes, J., Harding, S., Leng, Y., Coulthard, E., 2021. Pharmacological and non-pharmacological interventions to enhance sleep in mild cognitive impairment and mild Alzheimer's disease: A systematic review. J. Sleep Res. 30, e13229. https://doi.org/10.1111/jsr.13229

Böhm, U.L., Prendergast, A., Djenoune, L., Nunes Figueiredo, S., Gomez, J., Stokes, C., Kaiser, S., Suster, M., Kawakami, K., Charpentier, M., Concordet, J.-P., Rio, J.-P., Del Bene, F., Wyart, C., 2016. CSF-contacting neurons regulate locomotion by relaying mechanical stimuli to spinal circuits. Nat. Commun. 7, 10866. https://doi.org/10.1038/ncomms10866

Bolte, A.C., Dutta, A.B., Hurt, M.E., Smirnov, I., Kovacs, M.A., McKee, C.A., Ennerfelt, H.E., Shapiro, D., Nguyen, B.H., Frost, E.L., Lammert, C.R., Kipnis, J., Lukens, J.R., 2020. Meningeal lymphatic dysfunction exacerbates traumatic brain injury pathogenesis. Nat. Commun. 11, 4524. https://doi.org/10.1038/s41467-020-18113-4

Borha, A., Chagnot, A., Goulay, R., Emery, E., Vivien, D., Gaberel, T., 2020. Cranioplasty Reverses Dysfunction of the Solutes Distribution in the Brain Parenchyma After Decompressive Craniectomy. Neurosurgery. https://doi.org/10.1093/neuros/nyaa028

Bradley, J.P., Levine, J.P., Roth, D.A., McCarthy, J.G., Longaker, M.T., 1996. Studies in cranial suture biology: IV. Temporal sequence of posterior frontal cranial suture fusion in the mouse. Plast. Reconstr. Surg. 98, 1039–1045. https://doi.org/10.1097/00006534-199611000-00018

Bradley, K.C., 1970. Cerebrospinal fluid pressure. J. Neurol. Neurosurg. Psychiatry 33, 387–397. https://doi.org/10.1136/jnnp.33.3.387

Breslin, J.W., Yang, Y., Scallan, J.P., Sweat, R.S., Adderley, S.P., Murfee, W.L., 2018. Lymphatic Vessel Network Structure and Physiology. Compr. Physiol. 9, 207–299. https://doi.org/10.1002/cphy.c180015

Briggs, R., Kennelly, S.P., O'Neill, D., 2016. Drug treatments in Alzheimer's disease. Clin. Med. 16, 247–253. https://doi.org/10.7861/clinmedicine.16-3-247

Brinker, T., Stopa, E., Morrison, J., Klinge, P., 2014. A new look at cerebrospinal fluid circulation. Fluids Barriers CNS 11, 10. https://doi.org/10.1186/2045-8118-11-10

Brown, R., Benveniste, H., Black, S.E., Charpak, S., Dichgans, M., Joutel, A., Nedergaard, M., Smith, K.J., Zlokovic, B.V., Wardlaw, J.M., 2018. Understanding the role of the perivascular space in cerebral small vessel disease. Cardiovasc. Res. 114, 1462–1473. https://doi.org/10.1093/cvr/cvy113

Brozici, M., Zwan, A. van der, Hillen, B., 2003. Anatomy and Functionality of Leptomeningeal Anastomoses. Stroke. https://doi.org/10.1161/01.STR.0000095791.85737.65

Brundin, P., Melki, R., Kopito, R., 2010. Prion-like transmission of protein aggregates in neurodegenerative diseases. Nat. Rev. Mol. Cell Biol. 11, 301–307. https://doi.org/10.1038/nrm2873

Bucchieri, F., Farina, F., Zummo, G., Cappello, F., 2015. Lymphatic vessels of the dura mater: a new discovery? J. Anat. 227, 702–703. https://doi.org/10.1111/joa.12381

Bueno, D., Parvas, M., Nabiuni, M., Miyan, J., 2020. Embryonic cerebrospinal fluid formation and regulation. Semin. Cell Dev. Biol. 102, 3–12. https://doi.org/10.1016/j.semcdb.2019.09.006

Bulat, M., Klarica, M., 2011. Recent insights into a new hydrodynamics of the cerebrospinal fluid. Brain Res. Rev. 65, 99–112. https://doi.org/10.1016/j.brainresrev.2010.08.002

Butterfield, D.A., 2002. Amyloid beta-peptide (1-42)-induced oxidative stress and neurotoxicity: implications for neurodegeneration in Alzheimer's disease brain. A review. Free Radic. Res. 36, 1307–1313. https://doi.org/10.1080/1071576021000049890

- C -

Cacace, R., Sleegers, K., Van Broeckhoven, C., 2016. Molecular genetics of early-onset Alzheimer's disease revisited. Alzheimers Dement. 12, 733–748. https://doi.org/10.1016/j.jalz.2016.01.012

Cai, X., Qiao, J., Kulkarni, P., Harding, I.C., Ebong, E., Ferris, C.F., 2020. Imaging the effect of the circadian light-dark cycle on the glymphatic system in awake rats. Proc. Natl. Acad. Sci. U. S. A. 117, 668–676. https://doi.org/10.1073/pnas.1914017117

Cannistraro, R.J., Badi, M., Eidelman, B.H., Dickson, D.W., Middlebrooks, E.H., Meschia, J.F., 2019. CNS small vessel disease. Neurology 92, 1146–1156. https://doi.org/10.1212/WNL.0000000000007654

Carare, R.O., Bernardes-Silva, M., Newman, T.A., Page, A.M., Nicoll, J. a. R., Perry, V.H., Weller, R.O., 2008. Solutes, but not cells, drain from the brain parenchyma along basement membranes of capillaries and arteries: significance for cerebral amyloid angiopathy and neuroimmunology. Neuropathol. Appl. Neurobiol. 34, 131–144. https://doi.org/10.1111/j.1365-2990.2007.00926.x

Carare, R.O., Hawkes, C.A., Jeffrey, M., Kalaria, R.N., Weller, R.O., 2013. Review: cerebral amyloid angiopathy, prion angiopathy, CADASIL and the spectrum of protein elimination failure angiopathies (PEFA) in neurodegenerative disease with a focus on therapy. Neuropathol. Appl. Neurobiol. 39, 593–611. https://doi.org/10.1111/nan.12042

Carmona-Iragui, M., Videla, L., Lleó, A., Fortea, J., 2019. Down syndrome, Alzheimer disease, and cerebral amyloid angiopathy: The complex triangle of brain amyloidosis. Dev. Neurobiol. 79, 716–737. https://doi.org/10.1002/dneu.22709

Chagnot, A., Barnes, S.R., Montagne, A., 2021. Magnetic Resonance Imaging of Blood-Brain Barrier win Dementia. Neuroscience S0306-4522(21)00402–4. https://doi.org/10.1016/j.neuroscience.2021.08.003

Chandra, A., Dervenoulas, G., Politis, M., Alzheimer's Disease Neuroimaging Initiative, 2019. Magnetic resonance imaging in Alzheimer's disease and mild cognitive impairment. J. Neurol. 266, 1293–1302. https://doi.org/10.1007/s00415-018-9016-3

Charidimou, A., Boulouis, G., Gurol, M.E., Ayata, C., Bacskai, B.J., Frosch, M.P., Viswanathan, A., Greenberg, S.M., 2017a. Emerging concepts in sporadic cerebral amyloid angiopathy. Brain 140, 1829–1850. https://doi.org/10.1093/brain/awx047

Charidimou, A., Turc, G., Oppenheim, C., Yan, S., Scheitz, J.F., Erdur, H., Klinger-Gratz, P.P., El-Koussy, M., Takahashi, W., Moriya, Y., Wilson, D., Kidwell, C.S., Saver, J.L., Sallem, A., Moulin, S., Edjlali-Goujon, M., Thijs, V., Fox, Z., Shoamanesh, A., Albers, G.W., Mattle, H.P., Benavente, O.R., Jäger, H.R., Ambler, G., Aoki, J., Baron, J.-C., Kimura, K., Kakuda, W., Takizawa, S., Jung, S., Nolte, C.H., Lou, M., Cordonnier, C., Werring, D.J., 2017b. Microbleeds, Cerebral Hemorrhage, and Functional Outcome After Stroke Thrombolysis. Stroke 48, 2084–2090. https://doi.org/10.1161/STROKEAHA.116.012992

Charlton, J., Pearl, V., Denotti, A., Lee, J., Swaminathan, S., Scindia, Y., Charlton, N., Baldelomar, E., Beeman, S., Bennett, K., 2016. Biocompatibility of ferritin-based nanoparticles as targeted MRI contrast agents. Nanomedicine Nanotechnol. Biol. Med. 12, 1735–1745. https://doi.org/10.1016/j.nano.2016.03.007

Chazen, J.L., Dyke, J.P., Holt, R.W., Horky, L., Pauplis, R.A., Hesterman, J.Y., Mozley, D.P., Verma, A., 2017. Automated segmentation of MR imaging to determine normative central nervous system cerebrospinal fluid volumes in healthy volunteers. Clin. Imaging 43, 132–135. https://doi.org/10.1016/j.clinimag.2017.02.007

Chen, H.-Y., Panegyres, P.K., 2016. The Role of Ethnicity in Alzheimer's Disease: Findings From The C-PATH Online Data Repository. J. Alzheimers Dis. JAD 51, 515–523. https://doi.org/10.3233/JAD-151089

Chen, J., Wang, L., Xu, H., Xing, L., Zhuang, Z., Zheng, Y., Li, X., Wang, C., Chen, S., Guo, Z., Liang, Q., Wang, Y., 2020. Meningeal lymphatics clear erythrocytes that arise from subarachnoid hemorrhage. Nat. Commun. 11, 3159. https://doi.org/10.1038/s41467-020-16851-z

Chételat, G., Arbizu, J., Barthel, H., Garibotto, V., Law, I., Morbelli, S., van de Giessen, E., Agosta, F., Barkhof, F., Brooks, D.J., Carrillo, M.C., Dubois, B., Fjell, A.M., Frisoni, G.B., Hansson, O., Herholz, K., Hutton, B.F., Jack, C.R., Lammertsma, A.A., Landau, S.M., Minoshima, S., Nobili, F., Nordberg, A., Ossenkoppele, R., Oyen, W.J.G., Perani, D., Rabinovici, G.D., Scheltens, P., Villemagne, V.L., Zetterberg, H., Drzezga, A., 2020. Amyloid-PET and 18F-FDG-PET in the diagnostic investigation of Alzheimer's disease and other dementias. Lancet Neurol. 19, 951–962. https://doi.org/10.1016/S1474-4422(20)30314-8

Chételat, G., Lutz, A., Arenaza-Urquijo, E., Collette, F., Klimecki, O., Marchant, N., 2018. Why could meditation practice help promote mental health and well-being in aging? Alzheimers Res. Ther. 10, 57. https://doi.org/10.1186/s13195-018-0388-5

Chou, Y., That, V.T., Sundman, M., 2020. A Systematic Review and Meta-Analysis of rTMS Effects on Cognitive Enhancement in Mild Cognitive Impairment and Alzheimer's Disease. Neurobiol. Aging 86, 1–10. https://doi.org/10.1016/j.neurobiolaging.2019.08.020

Cipolla, M.J., 2009. The Cerebral Circulation. Morgan & Claypool Life Sciences.

Cocciolone, A.J., Hawes, J.Z., Staiculescu, M.C., Johnson, E.O., Murshed, M., Wagenseil, J.E., 2018. Elastin, arterial mechanics, and cardiovascular disease. Am. J. Physiol. - Heart Circ. Physiol. 315, H189–H205. https://doi.org/10.1152/ajpheart.00087.2018

Cordonnier, C., 2010. Brain microbleeds. Pract. Neurol. 10, 94–100. https://doi.org/10.1136/jnnp.2010.206086

Crary, J.F., Trojanowski, J.Q., Schneider, J.A., Abisambra, J.F., Abner, E.L., Alafuzoff, I., Arnold, S.E., Attems, J., Beach, T.G., Bigio, E.H., Cairns, N.J., Dickson, D.W., Gearing, M., Grinberg, L.T., Hof, P.R., Hyman, B.T., Jellinger, K., Jicha, G.A., Kovacs, G.G., Knopman, D.S., Kofler, J., Kukull, W.A., Mackenzie, I.R., Masliah, E., McKee, A., Montine, T.J., Murray, M.E., Neltner, J.H., Santa-Maria, I., Seeley, W.W., Serrano-Pozo, A., Shelanski, M.L., Stein, T., Takao, M., Thal, D.R., Toledo, J.B., Troncoso, J.C., Vonsattel, J.P., White, C.L., Wisniewski, T., Woltjer, R.L., Yamada, M., Nelson, P.T., 2014. Primary age-related tauopathy (PART): a common pathology associated with human aging. Acta Neuropathol. (Berl.) 128, 755–766. https://doi.org/10.1007/s00401-014-1349-0

Cserr, H.F., Cooper, D.N., Milhorat, T.H., 1977. Flow of cerebral interstitial fluid as indicated by the removal of extracellular markers from rat caudate nucleus. Exp. Eye Res. 25 Suppl, 461–473. https://doi.org/10.1016/s0014-4835(77)80041-9

Cugurra, A., Mamuladze, T., Rustenhoven, J., Dykstra, T., Beroshvili, G., Greenberg, Z.J., Baker, W., Papadopoulos, Z., Drieu, A., Blackburn, S., Kanamori, M., Brioschi, S., Herz, J., Schuettpelz, L.G., Colonna, M., Smirnov, I., Kipnis, J., 2021. Skull and vertebral bone marrow are myeloid cell reservoirs for the meninges and CNS parenchyma. Science eabf7844. https://doi.org/10.1126/science.abf7844

Cui, J., Xu, H., Lehtinen, M.K., 2021. Macrophages on the margin: choroid plexus immune responses. Trends Neurosci. https://doi.org/10.1016/j.tins.2021.07.002

- D -

Da Mesquita, S., Louveau, A., Vaccari, A., Smirnov, I., Cornelison, R.C., Kingsmore, K.M., Contarino, C., Onengut-Gumuscu, S., Farber, E., Raper, D., Viar, K.E., Powell, R.D., Baker, W., Dabhi, N., Bai, R., Cao, R., Hu, S., Rich, S.S., Munson, J.M., Lopes, M.B., Overall, C.C., Acton, S.T., Kipnis, J., 2018. Functional aspects of meningeal lymphatics in ageing and Alzheimer's disease. Nature 560, 185–191. https://doi.org/10.1038/s41586-018-0368-8

Damkier, H.H., Brown, P.D., Praetorius, J., 2016. Reply to Orešković et al. Physiol. Rev. 96, 1663–1664. https://doi.org/10.1152/physrev.00020.2016

Damkier, H.H., Brown, P.D., Praetorius, J., 2013. Cerebrospinal fluid secretion by the choroid plexus. Physiol. Rev. 93, 1847–1892. https://doi.org/10.1152/physrev.00004.2013

de Bellis, M., Cibelli, A., Mola, M.G., Pisani, F., Barile, B., Mastrodonato, M., Banitalebi, S., Amiry-Moghaddam, M., Abbrescia, P., Frigeri, A., Svelto, M., Nicchia, G.P., 2021. Orthogonal arrays of particle assembly are essential for normal aquaporin-4 expression level in the brain. Glia 69, 473–488. https://doi.org/10.1002/glia.23909

de Flores, R., La Joie, R., Chételat, G., 2015. Structural imaging of hippocampal subfields in healthy aging and Alzheimer's disease. Neuroscience 309, 29–50. https://doi.org/10.1016/j.neuroscience.2015.08.033

de Lizarrondo, S.M., Gakuba, C., Herbig, B.A., Repessé, Y., Ali, C., Denis, C.V., Lenting, P.J., Touzé, E., Diamond, S.L., Vivien, D., Gauberti, M., 2017. Potent thrombolytic effect of N-Acetylcysteine on arterial thrombi. Circulation 136, 646–660. https://doi.org/10.1161/CIRCULATIONAHA.117.027290

Deane, R., Sagare, A., Zlokovic, B.V., 2008. The role of the cell surface LRP and soluble LRP in blood-brain barrier Abeta clearance in Alzheimer's disease. Curr. Pharm. Des. 14, 1601–1605. https://doi.org/10.2174/138161208784705487

Degerskär, A.N.W., Englund, E.M., 2020. Cause of death in autopsy-confirmed dementia disorders. Eur. J. Neurol. 27, 2415–2421. https://doi.org/10.1111/ene.14450

Del Bigio, M.R., 2010. Ependymal cells: biology and pathology. Acta Neuropathol. (Berl.) 119, 55–73. https://doi.org/10.1007/s00401-009-0624-y

Delamarre, A., Meissner, W.G., 2017. Epidemiology, environmental risk factors and genetics of Parkinson's disease. Presse Medicale Paris Fr. 1983 46, 175–181. https://doi.org/10.1016/j.lpm.2017.01.001

Delion, M., Dinomais, M., Mercier, P., 2017. Arteries and Veins of the Cerebellum. Cerebellum Lond. Engl. 16, 880–912. https://doi.org/10.1007/s12311-016-0828-3

Demiral, Ş.B., Tomasi, D., Sarlls, J., Lee, H., Wiers, C.E., Zehra, A., Srivastava, T., Ke, K., Shokri-Kojori, E., Freeman, C.R., Lindgren, E., Ramirez, V., Miller, G., Bandettini, P., Horovitz, S., Wang, G.-J., Benveniste, H., Volkow, N.D., 2019. Apparent diffusion coefficient changes in human brain during sleep - Does it inform on the existence of a glymphatic system? NeuroImage 185, 263–273. https://doi.org/10.1016/j.neuroimage.2018.10.043

Deshpande, A., Mina, E., Glabe, C., Busciglio, J., 2006. Different Conformations of Amyloid β Induce Neurotoxicity by Distinct Mechanisms in Human Cortical Neurons. J. Neurosci. 26, 6011–6018. https://doi.org/10.1523/JNEUROSCI.1189-06.2006

Di Palma, C., Goulay, R., Chagnot, S., Martinez De Lizarrondo, S., Anfray, A., Salaun, J.-P., Maubert, E., Lechapt-Zalcman, E., Andreiuolo, F., Gakuba, C., Emery, E., Vivien, D., Gauberti, M., Gaberel, T., 2018. Cerebrospinal fluid flow increases from newborn to adult stages. Dev. Neurobiol. 78, 851–858. https://doi.org/10.1002/dneu.22622

Diem, A.K., MacGregor Sharp, M., Gatherer, M., Bressloff, N.W., Carare, R.O., Richardson, G., 2017. Arterial Pulsations cannot Drive Intramural Periarterial Drainage: Significance for Aβ Drainage. Front. Neurosci. 11. https://doi.org/10.3389/fnins.2017.00475

Ding, F., O'Donnell, J., Xu, Q., Kang, N., Goldman, N., Nedergaard, M., 2016. Changes in the composition of brain interstitial ions control the sleep-wake cycle. Science 352, 550–555. https://doi.org/10.1126/science.aad4821

Donahue, J.E., Flaherty, S.L., Johanson, C.E., Duncan, J.A., Silverberg, G.D., Miller, M.C., Tavares, R., Yang, W., Wu, Q., Sabo, E., Hovanesian, V., Stopa, E.G., 2006. RAGE, LRP-1, and amyloid-beta protein in Alzheimer's disease. Acta Neuropathol. (Berl.) 112, 405–415. https://doi.org/10.1007/s00401-006-0115-3

Dreha-Kulaczewski, S., Joseph, A.A., Merboldt, K.-D., Ludwig, H.-C., Gärtner, J., Frahm, J., 2015. Inspiration is the major regulator of human CSF flow. J. Neurosci. Off. J. Soc. Neurosci. 35, 2485–2491. https://doi.org/10.1523/JNEUROSCI.3246-14.2015

Du, T., Mestre, H., Kress, B.T., Liu, G., Sweeney, A.M., Samson, A.J., Rasmussen, M.K., Mortensen, K.N., Bork, P.A.R., Peng, W., Olveda, G.E., Bashford, L., Toro, E.R., Tithof, J., Kelley, D.H., Thomas, J.H., Hjorth, P.G., Martens, E.A., Mehta, R.I., Hirase, H., Mori, Y., Nedergaard, M., 2021. Cerebrospinal fluid is a significant fluid source for anoxic cerebral oedema. Brain J. Neurol. awab293. https://doi.org/10.1093/brain/awab293

- E -

Easterhoff, D., Ontiveros, F., Brooks, L.R., Kim, Y., Ross, B., Silva, J.N., Olsen, J.S., Feng, C., Hardy, D.J., Dunman, P.M., Dewhurst, S., 2013. Semen-derived enhancer of viral infection (SEVI) binds bacteria, enhances bacterial phagocytosis by macrophages, and can protect against vaginal infection by a sexually transmitted bacterial pathogen. Antimicrob. Agents Chemother. 57, 2443–2450. https://doi.org/10.1128/AAC.02464-12

Edwards, J.R., Williams, K., Kindblom, L.G., Meis-Kindblom, J.M., Hogendoorn, P.C.W., Hughes, D., Forsyth, R.G., Jackson, D., Athanasou, N.A., 2008. Lymphatics and bone. Hum. Pathol. 39, 49–55. https://doi.org/10.1016/j.humpath.2007.04.022

Eide, P.K., Ringstad, G., 2021. Cerebrospinal fluid egress to human parasagittal dura and the impact of sleep deprivation. Brain Res. 1772, 147669. https://doi.org/10.1016/j.brainres.2021.147669

Eide, P.K., Ringstad, G., 2015. MRI with intrathecal MRI gadolinium contrast medium administration: a possible method to assess glymphatic function in human brain. Acta Radiol. Open 4, 2058460115609635. https://doi.org/10.1177/2058460115609635

Ellis, D.Z., Nathanson, J.A., Sweadner, K.J., 2000. Carbachol inhibits Na(+)-K(+)-ATPase activity in choroid plexus via stimulation of the NO/cGMP pathway. Am. J. Physiol. Cell Physiol. 279, C1685-1693. https://doi.org/10.1152/ajpcell.2000.279.6.C1685

Engelhardt, B., 2021. Private immune protection at the border of the central nervous system. Nature 596, 38–40. https://doi.org/10.1038/d41586-021-01962-4

Engelhardt, B., Carare, R.O., Bechmann, I., Flügel, A., Laman, J.D., Weller, R.O., 2016. Vascular, glial, and lymphatic immune gateways of the central nervous system. Acta Neuropathol. (Berl.) 132, 317–338. https://doi.org/10.1007/s00401-016-1606-5

Engelhardt, B., Sorokin, L., 2009. The blood-brain and the blood-cerebrospinal fluid barriers: function and dysfunction. Semin. Immunopathol. 31, 497–511. https://doi.org/10.1007/s00281-009-0177-0

Engelhardt, B., Vajkoczy, P., Weller, R.O., 2017. The movers and shapers in immune privilege of the CNS. Nat. Immunol. 18, 123–131. https://doi.org/10.1038/ni.3666

- F -

Faghih, M.M., Keith Sharp, M., 2021. Mechanisms of tracer transport in cerebral perivascular spaces. J. Biomech. 118, 110278. https://doi.org/10.1016/j.jbiomech.2021.110278

Faghih, M.M., Sharp, M.K., 2018. Is bulk flow plausible in perivascular, paravascular and paravenous channels? Fluids Barriers CNS 15. https://doi.org/10.1186/s12987-018-0103-8

Faraco, G., Park, L., Anrather, J., Iadecola, C., 2017. Brain perivascular macrophages: characterization and functional roles in health and disease. J. Mol. Med. Berl. Ger. 95, 1143–1152. https://doi.org/10.1007/s00109-017-1573-x

Faraco, G., Sugiyama, Y., Lane, D., Garcia-Bonilla, L., Chang, H., Santisteban, M.M., Racchumi, G., Murphy, M., Van Rooijen, N., Anrather, J., Iadecola, C., 2016. Perivascular macrophages mediate the neurovascular and cognitive dysfunction associated with hypertension. J. Clin. Invest. 126, 4674–4689. https://doi.org/10.1172/JCI86950

Farquhar-Smith, P., Chapman, S., 2012. Neuraxial (epidural and intrathecal) opioids for intractable pain. Br. J. Pain 6, 25–35. https://doi.org/10.1177/2049463712439256

Fawcett, J.W., Oohashi, T., Pizzorusso, T., 2019. The roles of perineuronal nets and the perinodal extracellular matrix in neuronal function. Nat. Rev. Neurosci. 20, 451–465. https://doi.org/10.1038/s41583-019-0196-3

Fernández Montenegro, J.M., Villarini, B., Angelopoulou, A., Kapetanios, E., Garcia-Rodriguez, J., Argyriou, V., 2020. A Survey of Alzheimer's Disease Early Diagnosis Methods for Cognitive Assessment. Sensors 20, 7292. https://doi.org/10.3390/s20247292

Földi, M., Csillik, B., Zoltán, O.T., 1968. Lymphatic drainage of the brain. Experientia 24, 1283–1287. https://doi.org/10.1007/bf02146675

Fournier, A.P., Gauberti, M., Quenault, A., Vivien, D., Macrez, R., Docagne, F., 2019. Reduced spinal cord parenchymal cerebrospinal fluid circulation in experimental autoimmune encephalomyelitis. J. Cereb. Blood Flow Metab. 39, 1258–1265. https://doi.org/10.1177/0271678X18754732

Fultz, N.E., Bonmassar, G., Setsompop, K., Stickgold, R.A., Rosen, B.R., Polimeni, J.R., Lewis, L.D., 2019. Coupled electrophysiological, hemodynamic, and cerebrospinal fluid oscillations in human sleep. Science 366, 628–631. https://doi.org/10.1126/science.aax5440

- G -

Gaberel, T., Gakuba, C., Goulay, R., Martinez De Lizarrondo, S., Hanouz, J.-L., Emery, E., Touze, E., Vivien, D., Gauberti, M., 2014. Impaired glymphatic perfusion after strokes revealed by contrast-enhanced MRI: a new target for fibrinolysis? Stroke 45, 3092–3096. https://doi.org/10.1161/STROKEAHA.114.006617

Gakuba, C., Gaberel, T., Goursaud, S., Bourges, J., Di Palma, C., Quenault, A., Martinez de Lizarrondo, S., Vivien, D., Gauberti, M., 2018. General Anesthesia Inhibits the Activity of the "Glymphatic System." Theranostics 8, 710–722. https://doi.org/10.7150/thno.19154

Gauberti, M., Fournier, A.P., Vivien, D., Martinez de Lizarrondo, S., 2018. Molecular Magnetic Resonance Imaging (mMRI). Methods Mol. Biol. Clifton NJ 1718, 315–327. https://doi.org/10.1007/978-1-4939-7531-0_19

Gervais, F.G., Xu, D., Robertson, G.S., Vaillancourt, J.P., Zhu, Y., Huang, J., LeBlanc, A., Smith, D., Rigby, M., Shearman, M.S., Clarke, E.E., Zheng, H., Van Der Ploeg, L.H., Ruffolo, S.C., Thornberry, N.A., Xanthoudakis, S., Zamboni, R.J., Roy, S., Nicholson, D.W., 1999. Involvement of caspases in proteolytic cleavage of Alzheimer's amyloid-beta precursor protein and amyloidogenic A beta peptide formation. Cell 97, 395–406. https://doi.org/10.1016/s0092-8674(00)80748-5

Gkagkanasiou, M., Ploussi, A., Gazouli, M., Efstathopoulos, E.P., 2016. USPIO-Enhanced MRI Neuroimaging: A Review. J. Neuroimaging Off. J. Am. Soc. Neuroimaging 26, 161–168. https://doi.org/10.1111/jon.12318

Golzan, S.M., Goozee, K., Georgevsky, D., Avolio, A., Chatterjee, P., Shen, K., Gupta, V., Chung, R., Savage, G., Orr, C.F., Martins, R.N., Graham, S.L., 2017. Retinal vascular and structural changes are associated with amyloid burden in the elderly: ophthalmic biomarkers of preclinical Alzheimer's disease. Alzheimers Res. Ther. 9, 13. https://doi.org/10.1186/s13195-017-0239-9

Goulay, R., Flament, J., Gauberti, M., Naveau, M., Pasquet, N., Gakuba, C., Emery, E., Hantraye, P., Vivien, D., Aron-Badin, R., Gaberel, T., 2017. Subarachnoid Hemorrhage Severely Impairs Brain Parenchymal Cerebrospinal Fluid Circulation in Nonhuman Primate. Stroke 48, 2301–2305. https://doi.org/10.1161/STROKEAHA.117.017014

Goulay, R., Naveau, M., Gaberel, T., Vivien, D., Parcq, J., 2018. Optimized tPA: A non-neurotoxic fibrinolytic agent for the drainage of intracerebral hemorrhages. J. Cereb. Blood Flow Metab. Off. J. Int. Soc. Cereb. Blood Flow Metab. 38, 1180–1189. https://doi.org/10.1177/0271678X17719180

Gräsner, J.-T., Bossaert, L., 2013. Epidemiology and management of cardiac arrest: What registries are revealing. Best Pract. Res. Clin. Anaesthesiol., Saving 100,000 Lives Each Year in Europe 27, 293–306. https://doi.org/10.1016/j.bpa.2013.07.008

Greene, N.D.E., Copp, A.J., 2014. Neural Tube Defects. Annu. Rev. Neurosci. 37, 221–242. https://doi.org/10.1146/annurev-neuro-062012-170354

Grüntzig, J., Hollmann, F., 2019. Lymphatic vessels of the eye – old questions – new insights. Ann. Anat. - Anat. Anz. 221, 1–16. https://doi.org/10.1016/j.aanat.2018.08.004

- H -

Hablitz, L.M., Vinitsky, H.S., Sun, Q., Stæger, F.F., Sigurdsson, B., Mortensen, K.N., Lilius, T.O., Nedergaard, M., 2019. Increased glymphatic influx is correlated with high EEG delta power and low heart rate in mice under anesthesia. Sci. Adv. 5, eaav5447. https://doi.org/10.1126/sciadv.aav5447

Hardy, J.A., Higgins, G.A., 1992. Alzheimer's disease: the amyloid cascade hypothesis. Science 256, 184–185. https://doi.org/10.1126/science.1566067

Harrison, I.F., Siow, B., Akilo, A.B., Evans, P.G., Ismail, O., Ohene, Y., Nahavandi, P., Thomas, D.L., Lythgoe, M.F., Wells, J.A., 2018. Non-invasive imaging of CSF-mediated brain clearance pathways via assessment of perivascular fluid movement with diffusion tensor MRI. eLife 7. https://doi.org/10.7554/eLife.34028

Harrison, R.S., Sharpe, P.C., Singh, Y., Fairlie, D.P., 2007. Amyloid peptides and proteins in review. Rev. Physiol. Biochem. Pharmacol. 159, 1–77. https://doi.org/10.1007/112_2007_0701

Hébert, M., Lesept, F., Vivien, D., Macrez, R., 2016. The story of an exceptional serine protease, tissue-type plasminogen activator (tPA). Rev. Neurol. (Paris) 172, 186–197. https://doi.org/10.1016/j.neurol.2015.10.002

Heiss, W.D., Graf, R., 1994. The ischemic penumbra. Curr. Opin. Neurol. 7, 11–19. https://doi.org/10.1097/00019052-199402000-00004

Henderson, M.X., Trojanowski, J.Q., Lee, V.M.-Y., 2019. alpha-Synuclein Pathology in Parkinson's Disease and Related alpha-Synucleinopathies. Neurosci. Lett. 709, 134316. https://doi.org/10.1016/j.neulet.2019.134316

Herbowski, L., 2013. The Maze of the Cerebrospinal Fluid Discovery. Anat. Res. Int. 2013. https://doi.org/10.1155/2013/596027

Herisson, F., Frodermann, V., Courties, G., Rohde, D., Sun, Y., Vandoorne, K., Wojtkiewicz, G.R., Masson, G.S., Vinegoni, C., Kim, J., Kim, D.-E., Weissleder, R., Swirski, F.K., Moskowitz, M.A., Nahrendorf, M., 2018. Direct vascular channels connect skull bone marrow and the brain surface enabling myeloid cell migration. Nat. Neurosci. 21, 1209–1217. https://doi.org/10.1038/s41593-018-0213-2

Hernández, F., Avila, J., 2008. The role of glycogen synthase kinase 3 in the early stages of Alzheimers' disease. FEBS Lett. 582, 3848–3854. https://doi.org/10.1016/j.febslet.2008.10.026

Hladky, S.B., Barrand, M.A., 2018. Elimination of substances from the brain parenchyma: efflux via perivascular pathways and via the blood–brain barrier. Fluids Barriers CNS 15. https://doi.org/10.1186/s12987-018-0113-6

Hladky, S.B., Barrand, M.A., 2014. Mechanisms of fluid movement into, through and out of the brain: evaluation of the evidence. Fluids Barriers CNS 11, 26. https://doi.org/10.1186/2045-8118-11-26

Hoddevik, E.H., Rao, S.B., Zahl, S., Boldt, H.B., Ottersen, O.P., Amiry-Moghaddam, M., 2020. Organisation of extracellular matrix proteins laminin and agrin in pericapillary basal laminae in mouse brain. Brain Struct. Funct. 225, 805–816. https://doi.org/10.1007/s00429-020-02036-3

Holter, K.E., Kehlet, B., Devor, A., Sejnowski, T.J., Dale, A.M., Omholt, S.W., Ottersen, O.P., Nagelhus, E.A., Mardal, K.-A., Pettersen, K.H., 2017. Interstitial solute transport in 3D reconstructed neuropil occurs by diffusion rather than bulk flow. Proc. Natl. Acad. Sci. U. S. A. 114, 9894–9899. https://doi.org/10.1073/pnas.1706942114

Hrabetova, S., Cognet, L., Rusakov, D.A., Nägerl, U.V., 2018. Unveiling the Extracellular Space of the Brain: From Super-resolved Microstructure to In Vivo Function. J. Neurosci. 38, 9355–9363. https://doi.org/10.1523/JNEUROSCI.1664-18.2018

Huber, V.J., Tsujita, M., Nakada, T., 2009. Identification of aquaporin 4 inhibitors using in vitro and in silico methods. Bioorg. Med. Chem. 17, 411–417. https://doi.org/10.1016/j.bmc.2007.12.040

Huda, S., Whittam, D., Bhojak, M., Chamberlain, J., Noonan, C., Jacob, A., Kneen, R., 2019. Neuromyelitis optica spectrum disorders. Clin. Med. 19, 169–176. https://doi.org/10.7861/clinmedicine.19-2-169

- I -

Iliff, J.J., Lee, H., Yu, M., Feng, T., Logan, J., Nedergaard, M., Benveniste, H., 2013a. Brain-wide pathway for waste clearance captured by contrast-enhanced MRI. J. Clin. Invest. 123, 1299–1309. https://doi.org/10.1172/JCI67677

Iliff, J.J., Wang, M., Liao, Y., Plogg, B.A., Peng, W., Gundersen, G.A., Benveniste, H., Vates, G.E., Deane, R., Goldman, S.A., Nagelhus, E.A., Nedergaard, M., 2012. A paravascular pathway facilitates CSF flow through the brain parenchyma and the clearance of interstitial solutes, including amyloid β. Sci. Transl. Med. 4, 147ra111. https://doi.org/10.1126/scitranslmed.3003748

Iliff, J.J., Wang, M., Zeppenfeld, D.M., Venkataraman, A., Plog, B.A., Liao, Y., Deane, R., Nedergaard, M., 2013b. Cerebral arterial pulsation drives paravascular CSF-interstitial fluid exchange in the murine brain. J. Neurosci. Off. J. Soc. Neurosci. 33, 18190–18199. https://doi.org/10.1523/JNEUROSCI.1592-13.2013

Islam, T., Harisinghani, M.G., 2009. Overview of nanoparticle use in cancer imaging. Cancer Biomark. Sect. Dis. Markers 5, 61–67. https://doi.org/10.3233/CBM-2009-0578

- J -

Jack, C.R., Bennett, D.A., Blennow, K., Carrillo, M.C., Dunn, B., Haeberlein, S.B., Holtzman, D.M., Jagust, W., Jessen, F., Karlawish, J., Liu, E., Molinuevo, J.L., Montine, T., Phelps, C., Rankin, K.P., Rowe, C.C., Scheltens, P., Siemers, E., Snyder, H.M., Sperling, R., 2018. NIA-AA Research Framework: Toward a biological definition of Alzheimer’s disease. Alzheimers Dement. J. Alzheimers Assoc. 14, 535–562. https://doi.org/10.1016/j.jalz.2018.02.018

Jalalvand, E., Robertson, B., Tostivint, H., Löw, P., Wallén, P., Grillner, S., 2018. Cerebrospinal Fluid-Contacting Neurons Sense pH Changes and Motion in the Hypothalamus. J. Neurosci. Off. J. Soc. Neurosci. 38, 7713–7724. https://doi.org/10.1523/JNEUROSCI.3359-17.2018

Jiménez, A.J., Domínguez-Pinos, M.-D., Guerra, M.M., Fernández-Llebrez, P., Pérez-Fígares, J.-M., 2014. Structure and function of the ependymal barrier and diseases associated with ependyma disruption. Tissue Barriers 2, e28426. https://doi.org/10.4161/tisb.28426

Jongsiriyanyong, S., Limpawattana, P., 2018. Mild Cognitive Impairment in Clinical Practice: A Review Article. Am. J. Alzheimers Dis. Dementias® 33, 500–507. https://doi.org/10.1177/1533317518791401

- K -

Kahle, K.T., Kulkarni, A.V., Limbrick, D.D., Warf, B.C., 2016. Hydrocephalus in children. The Lancet 387, 788–799. https://doi.org/10.1016/S0140-6736(15)60694-8

Kaur, C., Rathnasamy, G., Ling, E.-A., 2016. The Choroid Plexus in Healthy and Diseased Brain. J. Neuropathol. Exp. Neurol. 75, 198–213. https://doi.org/10.1093/jnen/nlv030

Kaur, J., Fahmy, L.M., Davoodi-Bojd, E., Zhang, L., Ding, G., Hu, J., Zhang, Z., Chopp, M., Jiang, Q., 2021. Waste Clearance in the Brain. Front. Neuroanat. 15, 665803. https://doi.org/10.3389/fnana.2021.665803

Keable, A., O’Neill, R., MacGregor Sharp, M., Gatherer, M., Yuen, H.M., Johnston, D.A., Weller, R.O., Carare, R.O., 2020. ApoE4 Astrocytes Secrete Basement Membranes Rich in Fibronectin and Poor in Laminin Compared to ApoE3 Astrocytes. Int. J. Mol. Sci. 21, 4371. https://doi.org/10.3390/ijms21124371

Khalifa, F., Soliman, A., El-Baz, A., El-Ghar, M.A., El-Diasty, T., Gimel’farb, G., Ouseph, R., Dwyer, A.C., 2014. Models and methods for analyzing DCE-MRI: A review. Med. Phys. 41, 124301. https://doi.org/10.1118/1.4898202

Kiecker, C., 2018. The origins of the circumventricular organs. J. Anat. 232, 540–553. https://doi.org/10.1111/joa.12771

Kiliç, T., Akakin, A., 2008. Anatomy of cerebral veins and sinuses. Front. Neurol. Neurosci. 23, 4–15. https://doi.org/10.1159/000111256

Kim, H.-K., Lee, G.H., Chang, Y., 2018. Gadolinium as an MRI contrast agent. Future Med. Chem. 10, 639–661. https://doi.org/10.4155/fmc-2017-0215

Kiviniemi, V., Wang, X., Korhonen, V., Keinänen, T., Tuovinen, T., Autio, J., LeVan, P., Keilholz, S., Zang, Y.-F., Hennig, J., Nedergaard, M., 2016. Ultra-fast magnetic resonance encephalography of physiological brain activity - Glymphatic pulsation mechanisms? J. Cereb. Blood Flow Metab. Off. J. Int. Soc. Cereb. Blood Flow Metab. 36, 1033–1045. https://doi.org/10.1177/0271678X15622047

Kivisäkk, P., Mahad, D.J., Callahan, M.K., Trebst, C., Tucky, B., Wei, T., Wu, L., Baekkevold, E.S., Lassmann, H., Staugaitis, S.M., Campbell, J.J., Ransohoff, R.M., 2003. Human cerebrospinal fluid central memory CD4+ T cells: Evidence for trafficking through choroid plexus and meninges via P-selectin. Proc. Natl. Acad. Sci. U. S. A. 100, 8389–8394. https://doi.org/10.1073/pnas.1433000100

Komaki, Y., Debacker, C., Djemai, B., Ciobanu, L., Tsurugizawa, T., Bihan, D.L., 2020. Differential effects of aquaporin-4 channel inhibition on BOLD fMRI and diffusion fMRI responses in mouse visual cortex. PLoS ONE 15. https://doi.org/10.1371/journal.pone.0228759

Koroulakis, A., Jamal, Z., Agarwal, M., 2021. Anatomy, Head and Neck, Lymph Nodes, in: StatPearls. StatPearls Publishing, Treasure Island (FL).

Koundal, S., Elkin, R., Nadeem, S., Xue, Y., Constantinou, S., Sanggaard, S., Liu, X., Monte, B., Xu, F., Van Nostrand, W., Nedergaard, M., Lee, H., Wardlaw, J., Benveniste, H., Tannenbaum, A., 2020. Optimal Mass Transport with Lagrangian Workflow Reveals Advective and Diffusion Driven Solute Transport in the Glymphatic System. Sci. Rep. 10, 1990. https://doi.org/10.1038/s41598-020-59045-9

Kress, B.T., Iliff, J.J., Xia, M., Wang, M., Wei, H.S., Zeppenfeld, D., Xie, L., Kang, H., Xu, Q., Liew, J.A., Plog, B.A., Ding, F., Deane, R., Nedergaard, M., 2014. Impairment of paravascular clearance pathways in the aging brain. Ann. Neurol. 76, 845–861. https://doi.org/10.1002/ana.24271

- L -

Lam, M.A., Hemley, S.J., Najafi, E., Vella, N.G.F., Bilston, L.E., Stoodley, M.A., 2017. The ultrastructure of spinal cord perivascular spaces: Implications for the circulation of cerebrospinal fluid. Sci. Rep. 7, 12924. https://doi.org/10.1038/s41598-017-13455-4

le Gros Clark, W.E., 1920. On the Pacchionian Bodies. J. Anat. 55, 40–48.

Lee, H., Mortensen, K., Sanggaard, S., Koch, P., Brunner, H., Quistorff, B., Nedergaard, M., Benveniste, H., 2018. Quantitative Gd-DOTA uptake from cerebrospinal fluid into rat brain using 3D VFA-SPGR at 9.4T. Magn. Reson. Med. 79, 1568–1578. https://doi.org/10.1002/mrm.26779

Lei, Y., Han, H., Yuan, F., Javeed, A., Zhao, Y., 2017. The brain interstitial system: Anatomy, modeling, in vivo measurement, and applications. Prog. Neurobiol. 157, 230–246. https://doi.org/10.1016/j.pneurobio.2015.12.007

Levard, D., Buendia, I., Lanquetin, A., Glavan, M., Vivien, D., Rubio, M., 2021. Filling the gaps on stroke research: Focus on inflammation and immunity. Brain. Behav. Immun. 91, 649–667. https://doi.org/10.1016/j.bbi.2020.09.025

Li, Q., Aalling, N.N., Förstera, B., Ertürk, A., Nedergaard, M., Møllgård, K., Xavier, A.L.R., 2020. Aquaporin 1 and the Na+/K+/2Cl- cotransporter 1 are present in the leptomeningeal vasculature of the adult rodent central nervous system. Fluids Barriers CNS 17, 15. https://doi.org/10.1186/s12987-020-0176-z

Li, X., Kong, H., Wu, W., Xiao, M., Sun, X., Hu, G., 2009. Aquaporin-4 maintains ependymal integrity in adult mice. Neuroscience 162, 67–77. https://doi.org/10.1016/j.neuroscience.2009.04.044

Liberski, P.P., Gajos, A., Sikorska, B., Lindenbaum, S., 2019. Kuru, the First Human Prion Disease. Viruses 11, 232. https://doi.org/10.3390/v11030232

Liu, X., Zhang, Z., Guo, W., Burnstock, G., He, C., Xiang, Z., 2013. The Superficial Glia Limitans of Mouse and Monkey Brain and Spinal Cord. Anat. Rec. 296, 995–1007. https://doi.org/10.1002/ar.22717

Livingston, G., Huntley, J., Sommerlad, A., Ames, D., Ballard, C., Banerjee, S., Brayne, C., Burns, A., Cohen-Mansfield, J., Cooper, C., Costafreda, S.G., Dias, A., Fox, N., Gitlin, L.N., Howard, R., Kales, H.C., Kivimäki, M., Larson, E.B., Ogunniyi, A., Orgeta, V., Ritchie, K., Rockwood, K., Sampson, E.L., Samus, Q., Schneider, L.S., Selbæk, G., Teri, L., Mukadam, N., 2020. Dementia prevention, intervention, and care: 2020 report of the Lancet Commission. The Lancet 396, 413–446. https://doi.org/10.1016/S0140-6736(20)30367-6

Llorens, F., Zarranz, J.-J., Fischer, A., Zerr, I., Ferrer, I., 2017. Fatal Familial Insomnia: Clinical Aspects and Molecular Alterations. Curr. Neurol. Neurosci. Rep. 17, 30. https://doi.org/10.1007/s11910-017-0743-0

Louveau, A., Herz, J., Alme, M.N., Salvador, A.F., Dong, M.Q., Viar, K.E., Herod, S.G., Knopp, J., Setliff, J.C., Lupi, A.L., Da Mesquita, S., Frost, E.L., Gaultier, A., Harris, T.H., Cao, R., Hu, S., Lukens, J.R., Smirnov, I., Overall, C.C., Oliver, G., Kipnis, J., 2018. CNS lymphatic drainage and neuroinflammation are regulated by meningeal lymphatic vasculature. Nat. Neurosci. 21, 1380–1391. https://doi.org/10.1038/s41593-018-0227-9

Louveau, A., Smirnov, I., Keyes, T.J., Eccles, J.D., Rouhani, S.J., Peske, J.D., Derecki, N.C., Castle, D., Mandell, J.W., Lee, K.S., Harris, T.H., Kipnis, J., 2015. Structural and functional features of central nervous system lymphatic vessels. Nature 523, 337–341. https://doi.org/10.1038/nature14432

Ludwig, H.C., Dreha-Kulaczewski, S., Bock, H.C., 2021. Neurofluids-Deep inspiration, cilia and preloading of the astrocytic network. J. Neurosci. Res. https://doi.org/10.1002/jnr.24935

Lun, M.P., Monuki, E.S., Lehtinen, M.K., 2015. Development and functions of the choroid plexus-cerebrospinal fluid system. Nat. Rev. Neurosci. 16, 445–457. https://doi.org/10.1038/nrn3921

- M -

Ma, Q., Decker, Y., Müller, A., Ineichen, B.V., Proulx, S.T., 2019. Clearance of cerebrospinal fluid from the sacral spine through lymphatic vessels. J. Exp. Med. 216, 2492–2502. https://doi.org/10.1084/jem.20190351

Ma, Q., Ineichen, B.V., Detmar, M., Proulx, S.T., 2017. Outflow of cerebrospinal fluid is predominantly through lymphatic vessels and is reduced in aged mice. Nat. Commun. 8, 1434. https://doi.org/10.1038/s41467-017-01484-6

Madhok, D.Y., Vitt, J.R., Nguyen, A.T., 2018. Overview of Neurovascular Physiology. Curr. Neurol. Neurosci. Rep. 18, 99. https://doi.org/10.1007/s11910-018-0905-8

Magnaes, B., 1976. Body position and cerebrospinal fluid pressure: Part 2: Clinical studies on orthostatic pressure and the hydrostatic indifferent point. J. Neurosurg. 44, 698–705. https://doi.org/10.3171/jns.1976.44.6.0698

Maier-Hauff, K., Rothe, R., Scholz, R., Gneveckow, U., Wust, P., Thiesen, B., Feussner, A., von Deimling, A., Waldoefner, N., Felix, R., Jordan, A., 2007. Intracranial thermotherapy using magnetic nanoparticles combined with external beam radiotherapy: results of a feasibility study on patients with glioblastoma multiforme. J. Neurooncol. 81, 53–60. https://doi.org/10.1007/s11060-006-9195-0

Maji, S.K., Perrin, M.H., Sawaya, M.R., Jessberger, S., Vadodaria, K., Rissman, R.A., Singru, P.S., Nilsson, K.P.R., Simon, R., Schubert, D., Eisenberg, D., Rivier, J., Sawchenko, P., Vale, W., Riek, R., 2009. Functional amyloids as natural storage of peptide hormones in pituitary secretory granules. Science 325, 328–332. https://doi.org/10.1126/science.1173155

Manning, J.C., Pinto, N.P., Rennick, J.E., Colville, G., Curley, M.A.Q., 2018. Conceptualizing Post Intensive Care Syndrome in Children-The PICS-p Framework. Pediatr. Crit. Care Med. J. Soc. Crit. Care Med. World Fed. Pediatr. Intensive Crit. Care Soc. 19, 298–300. https://doi.org/10.1097/PCC.0000000000001476

Marshall-Goebel, K., Damani, R., Bershad, E.M., 2019. Brain Physiological Response and Adaptation During Spaceflight. Neurosurgery 85, E815–E821. https://doi.org/10.1093/neuros/nyz203

Mehta, A.M., Sonabend, A.M., Bruce, J.N., 2017. Convection-Enhanced Delivery. Neurotherapeutics 14, 358–371. https://doi.org/10.1007/s13311-017-0520-4

Meraz-Ríos, M.A., Lira-De León, K.I., Campos-Peña, V., De Anda-Hernández, M.A., Mena-López, R., 2010. Tau oligomers and aggregation in Alzheimer's disease. J. Neurochem. 112, 1353–1367. https://doi.org/10.1111/j.1471-4159.2009.06511.x

Mestre, H., Du, T., Sweeney, A.M., Liu, G., Samson, A.J., Peng, W., Mortensen, K.N., Stæger, F.F., Bork, P.A.R., Bashford, L., Toro, E.R., Tithof, J., Kelley, D.H., Thomas, J.H., Hjorth, P.G., Martens, E.A., Mehta, R.I., Solis, O., Blinder, P., Kleinfeld, D., Hirase, H., Mori, Y., Nedergaard, M., 2020a. Cerebrospinal fluid influx drives acute ischemic tissue swelling. Science 367. https://doi.org/10.1126/science.aax7171

Mestre, H., Mori, Y., Nedergaard, M., 2020b. The Brain's Glymphatic System: Current Controversies. Trends Neurosci. 43, 458–466. https://doi.org/10.1016/j.tins.2020.04.003

Mestre, H., Tithof, J., Du, T., Song, W., Peng, W., Sweeney, A.M., Olveda, G., Thomas, J.H., Nedergaard, M., Kelley, D.H., 2018. Flow of cerebrospinal fluid is driven by arterial pulsations and is reduced in hypertension. Nat. Commun. 9, 4878. https://doi.org/10.1038/s41467-018-07318-3

Mielke, M.M., Vemuri, P., Rocca, W.A., 2014. Clinical epidemiology of Alzheimer's disease: assessing sex and gender differences. Clin. Epidemiol. 6, 37–48. https://doi.org/10.2147/CLEP.S37929

Miners, J.S., Baig, S., Palmer, J., Palmer, L.E., Kehoe, P.G., Love, S., 2008. SYMPOSIUM: Clearance of Aβ from the Brain in Alzheimer's Disease: Aβ-Degrading Enzymes in Alzheimer's Disease. Brain Pathol. 18, 240–252. https://doi.org/10.1111/j.1750-3639.2008.00132.x

Mitchell, H.H., Hamilton, T.S., Steggerda, F.R., Bean, H.W., 1945. THE CHEMICAL COMPOSITION OF THE ADULT HUMAN BODY AND ITS BEARING ON THE BIOCHEMISTRY OF GROWTH. J. Biol. Chem. 158, 625–637. https://doi.org/10.1016/S0021-9258(19)51339-4

Molinuevo, J.L., Ayton, S., Batrla, R., Bednar, M.M., Bittner, T., Cummings, J., Fagan, A.M., Hampel, H., Mielke, M.M., Mikulskis, A., O'Bryant, S., Scheltens, P., Sevigny, J., Shaw, L.M., Soares, H.D., Tong, G., Trojanowski, J.Q., Zetterberg, H., Blennow, K., 2018. Current state of Alzheimer's fluid biomarkers. Acta Neuropathol. (Berl.) 136, 821–853. https://doi.org/10.1007/s00401-018-1932-x

Moskowitz, M.A., Lo, E.H., Iadecola, C., 2010. The science of stroke: mechanisms in search of treatments. Neuron 67, 181–198. https://doi.org/10.1016/j.neuron.2010.07.002

Müller, U.C., Deller, T., Korte, M., 2017. Not just amyloid: physiological functions of the amyloid precursor protein family. Nat. Rev. Neurosci. 18, 281–298. https://doi.org/10.1038/nrn.2017.29

Mutimer, C.A., Keragala, C.B., Markus, H.S., Werring, D.J., Cloud, G.C., Medcalf, R.L., 2021. Cerebral Amyloid Angiopathy and the Fibrinolytic System: Is Plasmin a Therapeutic Target? Stroke. https://doi.org/10.1161/STROKEAHA.120.033107

- N -

Nagelhus, E.A., Ottersen, O.P., 2013. Physiological Roles of Aquaporin-4 in Brain. Physiol. Rev. 93, 1543–1562. https://doi.org/10.1152/physrev.00011.2013

Navarro, P.P., Genoud, C., Castaño-Díez, D., Graff-Meyer, A., Lewis, A.J., de Gier, Y., Lauer, M.E., Britschgi, M., Bohrmann, B., Frank, S., Hench, J., Schweighauser, G., Rozemuller, A.J.M., van de Berg, W.D.J., Stahlberg, H., Shahmoradian, S.H., 2018. Cerebral Corpora amylacea are dense membranous labyrinths containing structurally preserved cell organelles. Sci. Rep. 8, 18046. https://doi.org/10.1038/s41598-018-36223-4

Nilsson, C., Ståhlberg, F., Thomsen, C., Henriksen, O., Herning, M., Owman, C., 1992. Circadian variation in human cerebrospinal fluid production measured by magnetic resonance imaging. Am. J. Physiol. 262, R20-24. https://doi.org/10.1152/ajpregu.1992.262.1.R20

Norris, G.T., Kipnis, J., 2019. Immune cells and CNS physiology: Microglia and beyond. J. Exp. Med. 216, 60–70. https://doi.org/10.1084/jem.20180199

- O -

Ogoh, S., Tarumi, T., 2019. Cerebral blood flow regulation and cognitive function: a role of arterial baroreflex function. J. Physiol. Sci. 69, 813–823. https://doi.org/10.1007/s12576-019-00704-6

Oresković, D., Klarica, M., 2010. The formation of cerebrospinal fluid: nearly a hundred years of interpretations and misinterpretations. Brain Res. Rev. 64, 241–262. https://doi.org/10.1016/j.brainresrev.2010.04.006

Orešković, D., Radoš, M., Klarica, M., 2017. Role of choroid plexus in cerebrospinal fluid hydrodynamics. Neuroscience 354, 69–87. https://doi.org/10.1016/j.neuroscience.2017.04.025

O'Rourke, M.F., Safar, M.E., 2005. Relationship Between Aortic Stiffening and Microvascular Disease in Brain and Kidney. Hypertension 46, 200–204. https://doi.org/10.1161/01.HYP.0000168052.00426.65

- P -

Papadopoulos, Z., Herz, J., Kipnis, J., 2020. Meningeal Lymphatics: From Anatomy to Central Nervous System Immune Surveillance. J. Immunol. 204, 286–293. https://doi.org/10.4049/jimmunol.1900838

Peng, W., Achariyar, T.M., Li, B., Liao, Y., Mestre, H., Hitomi, E., Regan, S., Kasper, T., Peng, S., Ding, F., Benveniste, H., Nedergaard, M., Deane, R., 2016. Suppression of glymphatic fluid transport in a mouse model of Alzheimer's disease. Neurobiol. Dis. 93, 215–225. https://doi.org/10.1016/j.nbd.2016.05.015

Perneczky, R., Wagenpfeil, S., Komossa, K., Grimmer, T., Diehl, J., Kurz, A., 2006. Mapping Scores Onto Stages: Mini-Mental State Examination and Clinical Dementia Rating. Am. J. Geriatr. Psychiatry 14, 139–144. https://doi.org/10.1097/01.JGP.0000192478.82189.a8

Pike, C.J., 2017. Sex and the development of Alzheimer's disease. J. Neurosci. Res. 95, 671–680. https://doi.org/10.1002/jnr.23827

Pizzo, M.E., Wolak, D.J., Kumar, N.N., Brunette, E., Brunnquell, C.L., Hannocks, M., Abbott, N.J., Meyerand, M.E., Sorokin, L., Stanimirovic, D.B., Thorne, R.G., 2018. Intrathecal antibody distribution in the rat brain: surface diffusion, perivascular transport and osmotic enhancement of delivery. J. Physiol. 596, 445–475. https://doi.org/10.1113/JP275105

Plog, B.A., Lou, N., Pierre, C.A., Cove, A., Kenney, H.M., Hitomi, E., Kang, H., Iliff, J.J., Zeppenfeld, D.M., Nedergaard, M., Vates, G.E., 2019. When the air hits your brain: Decreased arterial pulsatility after craniectomy leads to impaired glymphatic flow. J. Neurosurg. 1–14. https://doi.org/10.3171/2019.2.JNS182675

Prasad, A., Bharathi, V., Sivalingam, V., Girdhar, A., Patel, B.K., 2019. Molecular Mechanisms of TDP-43 Misfolding and Pathology in Amyotrophic Lateral Sclerosis. Front. Mol. Neurosci. 12, 25. https://doi.org/10.3389/fnmol.2019.00025

Prinz, M., Jung, S., Priller, J., 2019. Microglia Biology: One Century of Evolving Concepts. Cell 179, 292–311. https://doi.org/10.1016/j.cell.2019.08.053

Prinz, M., Masuda, T., Wheeler, M.A., Quintana, F.J., 2021. Microglia and Central Nervous System-Associated Macrophages-From Origin to Disease Modulation. Annu. Rev. Immunol. 39, 251–277. https://doi.org/10.1146/annurev-immunol-093019-110159

Prinz, M., Priller, J., 2014. Microglia and brain macrophages in the molecular age: from origin to neuropsychiatric disease. Nat. Rev. Neurosci. 15, 300–312. https://doi.org/10.1038/nrn3722

Proulx, S.T., 2021. Cerebrospinal fluid outflow: a review of the historical and contemporary evidence for arachnoid villi, perineural routes, and dural lymphatics. Cell. Mol. Life Sci. 78, 2429–2457. https://doi.org/10.1007/s00018-020-03706-5

Purves, D., Augustine, G.J., Fitzpatrick, D., Katz, L.C., LaMantia, A.-S., McNamara, J.O., Williams, S.M., 2001. The Blood Supply of the Brain and Spinal Cord. Neurosci. 2nd Ed.

- Q -

Qian, L., Milne, M.R., Shepheard, S., Rogers, M.-L., Medeiros, R., Coulson, E.J., 2019. Removal of p75 Neurotrophin Receptor Expression from Cholinergic Basal Forebrain Neurons Reduces Amyloid-β Plaque Deposition and Cognitive Impairment in Aged APP/PS1 Mice. Mol. Neurobiol. 56, 4639–4652. https://doi.org/10.1007/s12035-018-1404-2

Qiu, T., Liu, Q., Chen, Y.-X., Zhao, Y.-F., Li, Y.-M., 2015. Aβ42 and Aβ40: similarities and differences. J. Pept. Sci. 21, 522–529. https://doi.org/10.1002/psc.2789

Quintela, T., Albuquerque, T., Lundkvist, G., Carmine Belin, A., Talhada, D., Gonçalves, I., Carro, E., Santos, C.R.A., 2018. The choroid plexus harbors a circadian oscillator modulated by estrogens. Chronobiol. Int. 35, 270–279. https://doi.org/10.1080/07420528.2017.1400978

Quirk, J.D., Bretthorst, G.L., Duong, T.Q., Snyder, A.Z., Springer, C.S., Ackerman, J.J.H., Neil, J.J., 2003. Equilibrium water exchange between the intra- and extracellular spaces of mammalian brain. Magn. Reson. Med. 50, 493–499. https://doi.org/10.1002/mrm.10565

- R -

Radoš, M., Živko, M., Periša, A., Orešković, D., Klarica, M., 2021. No Arachnoid Granulations-No Problems: Number, Size, and Distribution of Arachnoid Granulations From Birth to 80 Years of Age. Front. Aging Neurosci. 13, 698865. https://doi.org/10.3389/fnagi.2021.698865

Raghunandan, A., Ladron-de-Guevara, A., Tithof, J., Mestre, H., Du, T., Nedergaard, M., Thomas, J.H., Kelley, D.H., 2021. Bulk flow of cerebrospinal fluid observed in periarterial spaces is not an artifact of injection. eLife 10, e65958. https://doi.org/10.7554/eLife.65958

Ratner, V., Gao, Y., Lee, H., Elkin, R., Nedergaard, M., Benveniste, H., Tannenbaum, A., 2017. Cerebrospinal and interstitial fluid transport via the glymphatic pathway modeled by optimal mass transport. NeuroImage 152, 530–537. https://doi.org/10.1016/j.neuroimage.2017.03.021

Rauch, J.N., Luna, G., Guzman, E., Audouard, M., Challis, C., Sibih, Y.E., Leshuk, C., Hernandez, I., Wegmann, S., Hyman, B.T., Gradinaru, V., Kampmann, M., Kosik, K.S., 2020. LRP1 is a master regulator of tau uptake and spread. Nature 580, 381–385. https://doi.org/10.1038/s41586-020-2156-5

Ray, L.A., Pike, M., Simon, M., Iliff, J.J., Heys, J.J., 2021. Quantitative Analysis of Macroscopic Solute Transport in the Murine Brain. https://doi.org/10.21203/rs.3.rs-806107/v1

Reina-De La Torre, F., Rodriguez-Baeza, A., Sahuquillo-Barris, J., 1998. Morphological characteristics and distribution pattern of the arterial vessels in human cerebral cortex: a scanning electron microscope study. Anat. Rec. 251, 87–96. https://doi.org/10.1002/(SICI)1097-0185(199805)251:1<87::AID-AR14>3.0.CO;2-7

Reisberg, B., Ferris, S.H., de Leon, M.J., Crook, T., 1982. The Global Deterioration Scale for assessment of primary degenerative dementia. Am. J. Psychiatry 139, 1136–1139. https://doi.org/10.1176/ajp.139.9.1136

Rennels, M.L., Gregory, T.F., Blaumanis, O.R., Fujimoto, K., Grady, P.A., 1985. Evidence for a “paravascular” fluid circulation in the mammalian central nervous system, provided by the rapid distribution of tracer protein throughout the brain from the subarachnoid space. Brain Res. 326, 47–63. https://doi.org/10.1016/0006-8993(85)91383-6

Rhodius-Meester, H.F.M., Tijms, B.M., Lemstra, A.W., Prins, N.D., Pijnenburg, Y.A.L., Bouwman, F., Scheltens, P., Flier, W.M. van der, 2019. Survival in memory clinic cohort is short, even in young-onset dementia. J. Neurol. Neurosurg. Psychiatry 90, 726–728. https://doi.org/10.1136/jnnp-2018-318820

Ringstad, G., Eide, P.K., 2020. Cerebrospinal fluid tracer efflux to parasagittal dura in humans. Nat. Commun. 11. https://doi.org/10.1038/s41467-019-14195-x

Roher, A.E., Kokjohn, T.A., Clarke, S.G., Sierks, M.R., Maarouf, C.L., Serrano, G.E., Sabbagh, M.S., Beach, T.G., 2017. APP/Aβ Structural Diversity and Alzheimer’s Disease Pathogenesis. Neurochem. Int. 110, 1–13. https://doi.org/10.1016/j.neuint.2017.08.007

Rojas, S., Ortega, M., Rodríguez-Baeza, A., 2021. Anatomical study of the pial arterial network in human spinal cords. Clin. Anat. N. Y. N 34, 596–604. https://doi.org/10.1002/ca.23622

Rosner, J., Reddy, V., Lui, F., 2021. Neuroanatomy, Circle of Willis, in: StatPearls. StatPearls Publishing, Treasure Island (FL).

Rudie, J.D., Rauschecker, A.M., Nabavizadeh, S.A., Mohan, S., 2018. Neuroimaging of Dilated Perivascular Spaces: From Benign and Pathologic Causes to Mimics. J. Neuroimaging Off. J. Am. Soc. Neuroimaging 28, 139–149. https://doi.org/10.1111/jon.12493

- S -

Saboori, P., 2021. Subarachnoid space trabeculae architecture. Clin. Anat. 34, 40–50. https://doi.org/10.1002/ca.23635

Salaün, J.-P., Poirel, N., Dahmani, S., Chagnot, A., Gakuba, C., Ali, C., Gérard, J.-L., Hanouz, J.-L., Orliaguet, G., Vivien, D., 2021. Preventing the Long-term Effects of General Anesthesia on the Developing Brain: How Translational Research can Contribute. Neuroscience 461, 172–179. https://doi.org/10.1016/j.neuroscience.2021.02.029

Sarnataro, D., Pepe, A., Zurzolo, C., 2017. Chapter Three - Cell Biology of Prion Protein, in: Legname, G., Vanni, S. (Eds.), Progress in Molecular Biology and Translational Science, Prion Protein. Academic Press, pp. 57–82. https://doi.org/10.1016/bs.pmbts.2017.06.018

Schaeffer, S., Iadecola, C., 2021. Revisiting the neurovascular unit. Nat. Neurosci. 1–12. https://doi.org/10.1038/s41593-021-00904-7

Schain, A.J., Melo-Carrillo, A., Strassman, A.M., Burstein, R., 2017. Cortical Spreading Depression Closes Paravascular Space and Impairs Glymphatic Flow: Implications for Migraine Headache. J. Neurosci. Off. J. Soc. Neurosci. 37, 2904–2915. https://doi.org/10.1523/JNEUROSCI.3390-16.2017

Schaller, B., Graf, R., 2005. Different compartments of intracranial pressure and its relationship to cerebral blood flow. J. Trauma 59, 1521–1531. https://doi.org/10.1097/01.ta.0000197402.20180.6b

Scheltens, P., De Strooper, B., Kivipelto, M., Holstege, H., Chételat, G., Teunissen, C.E., Cummings, J., van der Flier, W.M., 2021. Alzheimer's disease. The Lancet 397, 1577–1590. https://doi.org/10.1016/S0140-6736(20)32205-4

Schley, D., Carare-Nnadi, R., Please, C.P., Perry, V.H., Weller, R.O., 2006. Mechanisms to explain the reverse perivascular transport of solutes out of the brain. J. Theor. Biol. 238, 962–974. https://doi.org/10.1016/j.jtbi.2005.07.005

Schwerk, C., Tenenbaum, T., Kim, K.S., Schroten, H., 2015. The choroid plexus—a multi-role player during infectious diseases of the CNS. Front. Cell. Neurosci. 9, 80. https://doi.org/10.3389/fncel.2015.00080

Shen, M.D., Kim, S.H., McKinstry, R.C., Gu, H., Hazlett, H.C., Nordahl, C.W., Emerson, R.W., Shaw, D., Elison, J.T., Swanson, M.R., Fonov, V.S., Gerig, G., Dager, S.R., Botteron, K.N., Paterson, S., Schultz, R.T., Evans, A.C., Estes, A.M., Zwaigenbaum, L., Styner, M.A., Amaral, D.G., Piven, J., 2017. Increased Extra-axial Cerebrospinal Fluid in High-Risk Infants who Later Develop Autism. Biol. Psychiatry 82, 186–193. https://doi.org/10.1016/j.biopsych.2017.02.1095

Shen, Y., Goerner, F.L., Snyder, C., Morelli, J.N., Hao, D., Hu, D., Li, X., Runge, V.M., 2015. T1 relaxivities of gadolinium-based magnetic resonance contrast agents in human whole blood at 1.5, 3, and 7 T. Invest. Radiol. 50, 330–338. https://doi.org/10.1097/RLI.0000000000000132

Shi, Y., Hu, D., Rodgers, E.L., Katusic, S.K., Gleich, S.J., Hanson, A.C., Schroeder, D.R., Flick, R.P., Warner, D.O., 2018. Epidemiology of general anesthesia prior to age 3 in a population-based birth cohort. Paediatr. Anaesth. 28, 513–519. https://doi.org/10.1111/pan.13359

Shipley, F.B., Dani, N., Xu, H., Deister, C., Cui, J., Head, J.P., Sadegh, C., Fame, R.M., Shannon, M.L., Flores, V.I., Kishkovich, T., Jang, E., Klein, E.M., Goldey, G.J., He, K., Zhang, Y., Holtzman, M.J., Kirchhausen, T., Wyart, C., Moore, C.I., Andermann, M.L., Lehtinen, M.K., 2020. Tracking Calcium Dynamics and Immune Surveillance at the Choroid Plexus Blood-Cerebrospinal Fluid Interface. Neuron 108, 623-639.e10. https://doi.org/10.1016/j.neuron.2020.08.024

Shook, B.A., Lennington, J.B., Acabchuk, R.L., Halling, M., Sun, Y., Peters, J., Wu, Q., Mahajan, A., Fellows, D.W., Conover, J.C., 2014. Ventriculomegaly associated with ependymal gliosis and declines in barrier integrity in the aging human and mouse brain. Aging Cell 13, 340–350. https://doi.org/10.1111/acel.12184

Silva, A.C., Bock, N.A., 2008. Manganese-Enhanced MRI: An Exceptional Tool in Translational Neuroimaging. Schizophr. Bull. 34, 595–604. https://doi.org/10.1093/schbul/sbn056

Simon, M.D., Geim, A.K., 2000. Diamagnetic levitation: Flying frogs and floating magnets (invited). J. Appl. Phys. 87, 6200–6204. https://doi.org/10.1063/1.372654

Sipe, J.D., Cohen, A.S., 2000. Review: History of the Amyloid Fibril. J. Struct. Biol. 130, 88–98. https://doi.org/10.1006/jsbi.2000.4221

Sitammagari, K.K., Masood, W., 2021. Creutzfeldt Jakob Disease, in: StatPearls. StatPearls Publishing, Treasure Island (FL).

Siyahhan, B., Knobloch, V., de Zélicourt, D., Asgari, M., Schmid Daners, M., Poulikakos, D., Kurtcuoglu, V., 2014. Flow induced by ependymal cilia dominates near-wall cerebrospinal fluid dynamics in the lateral ventricles. J. R. Soc. Interface 11, 20131189. https://doi.org/10.1098/rsif.2013.1189

Slupe, A.M., Kirsch, J.R., 2018. Effects of anesthesia on cerebral blood flow, metabolism, and neuroprotection. J. Cereb. Blood Flow Metab. 38, 2192–2208. https://doi.org/10.1177/0271678X18789273

Smith, A.J., Jin, B.-J., Verkman, A.S., 2015. Muddying the water in brain edema? Trends Neurosci. 38, 331–332. https://doi.org/10.1016/j.tins.2015.04.006

Smith, A.J., Verkman, A.S., 2018. The "glymphatic" mechanism for solute clearance in Alzheimer's disease: game changer or unproven speculation? FASEB J. Off. Publ. Fed. Am. Soc. Exp. Biol. 32, 543–551. https://doi.org/10.1096/fj.201700999

Smith, A.J., Yao, X., Dix, J.A., Jin, B.-J., Verkman, A.S., 2017. Test of the "glymphatic" hypothesis demonstrates diffusive and aquaporin-4-independent solute transport in rodent brain parenchyma. eLife 6. https://doi.org/10.7554/eLife.27679

Solár, P., Zamani, A., Kubíčková, L., Dubový, P., Joukal, M., 2020. Choroid plexus and the blood–cerebrospinal fluid barrier in disease. Fluids Barriers CNS 17. https://doi.org/10.1186/s12987-020-00196-2

Song, S.-Y., Zhai, X.-M., Shan, C.-J., Lu, L.-L., Hong, J., Cao, J.-L., Zhang, L.-C., 2020. A Special Cranial Nucleus (CSF-Contacting Nucleus) in Primates. Front. Neuroanat. 14, 53. https://doi.org/10.3389/fnana.2020.00053

Spector, R., Keep, R.F., Robert Snodgrass, S., Smith, Q.R., Johanson, C.E., 2015a. A balanced view of choroid plexus structure and function: Focus on adult humans. Exp. Neurol. 267, 78–86. https://doi.org/10.1016/j.expneurol.2015.02.032

Spector, R., Robert Snodgrass, S., Johanson, C.E., 2015b. A balanced view of the cerebrospinal fluid composition and functions: Focus on adult humans. Exp. Neurol. 273, 57–68. https://doi.org/10.1016/j.expneurol.2015.07.027

Stanton, E.H., Persson, N.D.Å., Gomolka, R.S., Lilius, T., Sigurðsson, B., Lee, H., Xavier, A.L.R., Benveniste, H., Nedergaard, M., Mori, Y., 2021. Mapping of CSF transport using high spatiotemporal resolution dynamic contrast-enhanced MRI in mice: Effect of anesthesia. Magn. Reson. Med. 85, 3326–3342. https://doi.org/10.1002/mrm.28645

Stikov, N., Boudreau, M., Levesque, I.R., Tardif, C.L., Barral, J.K., Pike, G.B., 2015. On the accuracy of T1 mapping: searching for common ground. Magn. Reson. Med. 73, 514–522. https://doi.org/10.1002/mrm.25135

Strazielle, N., Ghersi-Egea, J.F., 2000. Choroid plexus in the central nervous system: biology and physiopathology. J. Neuropathol. Exp. Neurol. 59, 561–574. https://doi.org/10.1093/jnen/59.7.561

Sun, Y., Sun, X., 2021. Exploring the interstitial system in the brain: the last mile of drug delivery. Rev. Neurosci. 32, 363–377. https://doi.org/10.1515/revneuro-2020-0057

- T -

Tatu, L., Moulin, T., Vuillier, F., Bogousslavsky, J., 2012. Arterial territories of the human brain. Front. Neurol. Neurosci. 30, 99–110. https://doi.org/10.1159/000333602

Ten Kate, M., Dicks, E., Visser, P.J., van der Flier, W.M., Teunissen, C.E., Barkhof, F., Scheltens, P., Tijms, B.M., Alzheimer’s Disease Neuroimaging Initiative, 2018. Atrophy subtypes in prodromal Alzheimer’s disease are associated with cognitive decline. Brain J. Neurol. 141, 3443–3456. https://doi.org/10.1093/brain/awy264

Thomsen, M.S., Routhe, L.J., Moos, T., 2017. The vascular basement membrane in the healthy and pathological brain. J. Cereb. Blood Flow Metab. 37, 3300–3317. https://doi.org/10.1177/0271678X17722436

Tuura, R.O., Volk, C., Callaghan, F., Jaramillo, V., Huber, R., 2021. Sleep-related and diurnal effects on brain diffusivity and cerebrospinal fluid flow. NeuroImage 118420. https://doi.org/10.1016/j.neuroimage.2021.118420

- V -

Vasvári, G., Reisch, R., Patonay, L., 2005. Surgical anatomy of the cribriform plate and adjacent areas. Minim. Invasive Neurosurg. MIN 48, 25–33. https://doi.org/10.1055/s-2004-830180

Verkman, A.S., 2012. Aquaporins in Clinical Medicine. Annu. Rev. Med. 63, 303–316. https://doi.org/10.1146/annurev-med-043010-193843

Vinje, V., Ringstad, G., Lindstrøm, E.K., Valnes, L.M., Rognes, M.E., Eide, P.K., Mardal, K.-A., 2019. Respiratory influence on cerebrospinal fluid flow – a computational study based on long-term intracranial pressure measurements. Sci. Rep. 9, 9732. https://doi.org/10.1038/s41598-019-46055-5

von Bartheld, C.S., Bahney, J., Herculano-Houzel, S., 2016. The Search for True Numbers of Neurons and Glial Cells in the Human Brain: A Review of 150 Years of Cell Counting. J. Comp. Neurol. 524, 3865–3895. https://doi.org/10.1002/cne.24040

Vutskits, L., Culley, D.J., 2019. GAS, PANDA, and MASK: No Evidence of Clinical Anesthetic Neurotoxicity! Anesthesiology 131, 762–764. https://doi.org/10.1097/ALN.0000000000002863

- W -

Wagshul, M.E., Eide, P.K., Madsen, J.R., 2011. The pulsating brain: A review of experimental and clinical studies of intracranial pulsatility. Fluids Barriers CNS 8, 5. https://doi.org/10.1186/2045-8118-8-5

Wang, Y., Mandelkow, E., 2016. Tau in physiology and pathology. Nat. Rev. Neurosci. 17, 22–35. https://doi.org/10.1038/nrn.2015.1

Wardlaw, J.M., Benveniste, H., Nedergaard, M., Zlokovic, B.V., Mestre, H., Lee, H., Doubal, F.N., Brown, R., Ramirez, J., MacIntosh, B.J., Tannenbaum, A., Ballerini, L., Rungta, R.L., Boido, D., Sweeney, M., Montagne, A., Charpak, S., Joutel, A., Smith, K.J., Black, S.E., 2020. Perivascular spaces in the brain: anatomy, physiology and pathology. Nat. Rev. Neurol. 16, 137–153. https://doi.org/10.1038/s41582-020-0312-z

Wardlaw, J.M., Smith, E.E., Biessels, G.J., Cordonnier, C., Fazekas, F., Frayne, R., Lindley, R.I., O’Brien, J.T., Barkhof, F., Benavente, O.R., Black, S.E., Brayne, C., Breteler, M., Chabriat, H., DeCarli, C., de Leeuw, F.-E., Doubal, F., Duering, M., Fox, N.C., Greenberg, S., Hachinski, V., Kilimann, I., Mok, V., Oostenbrugge, R. van, Pantoni, L., Speck, O., Stephan, B.C.M., Teipel, S., Viswanathan, A., Werring, D., Chen, C., Smith, C., van Buchem, M., Norrving, B., Gorelick, P.B., Dichgans, M., 2013. Neuroimaging standards for research into small vessel disease and its contribution to ageing and neurodegeneration. Lancet Neurol. 12, 822–838. https://doi.org/10.1016/S1474-4422(13)70124-8

Weuve, J., Barnes, L.L., Mendes de Leon, C.F., Rajan, K.B., Beck, T., Aggarwal, N.T., Hebert, L.E., Bennett, D.A., Wilson, R.S., Evans, D.A., 2018. Cognitive aging in black and white Americans: Cognition, cognitive decline, and incidence of Alzheimer disease dementia. Epidemiol. Camb. Mass 29, 151–159. https://doi.org/10.1097/EDE.0000000000000747

Whish, S., Dziegielewska, K.M., Møllgård, K., Noor, N.M., Liddelow, S.A., Habgood, M.D., Richardson, S.J., Saunders, N.R., 2015. The inner CSF-brain barrier: developmentally controlled access to the brain via intercellular junctions. Front. Neurosci. 9, 16. https://doi.org/10.3389/fnins.2015.00016

WILKIE, K.P., NAGRA, G., JOHNSTON, M., 2012. A MATHEMATICAL ANALYSIS OF PHYSIOLOGICAL AND MOLECULAR MECHANISMS THAT MODULATE PRESSURE GRADIENTS AND FACILITATE VENTRICULAR EXPANSION IN HYDROCEPHALUS. Int. J. Numer. Anal. Model. Ser. B 316, 65–81.

Willard-Mack, C.L., 2006. Normal Structure, Function, and Histology of Lymph Nodes. Toxicol. Pathol. 34, 409–424. https://doi.org/10.1080/01926230600867727

Wilson, M.H., 2016. Monro-Kellie 2.0: The dynamic vascular and venous pathophysiological components of intracranial pressure. J. Cereb. Blood Flow Metab. Off. J. Int. Soc. Cereb. Blood Flow Metab. 36, 1338–1350. https://doi.org/10.1177/0271678X16648711

- X -

Xavier, A.L.R., Hauglund, N.L., von Holstein-Rathlou, S., Li, Q., Sanggaard, S., Lou, N., Lundgaard, I., Nedergaard, M., 2018. Cannula Implantation into the Cisterna Magna of Rodents. J. Vis. Exp. JoVE. https://doi.org/10.3791/57378

Xian-guang, H., Aldridge, R.J., Siveter, David J., Siveter, Derek J., Xiang-hong, F., 2002. New evidence on the anatomy and phylogeny of the earliest vertebrates. Proc. Biol. Sci. 269, 1865–1869. https://doi.org/10.1098/rspb.2002.2104

Xie, L., Kang, H., Xu, Q., Chen, M.J., Liao, Y., Thiyagarajan, M., O’Donnell, J., Christensen, D.J., Nicholson, C., Iliff, J.J., Takano, T., Deane, R., Nedergaard, M., 2013. Sleep drives metabolite clearance from the adult brain. Science 342, 373–377. https://doi.org/10.1126/science.1241224

- Y -

Yanev, P., Poinsatte, K., Hominick, D., Khurana, N., Zuurbier, K.R., Berndt, M., Plautz, E.J., Dellinger, M.T., Stowe, A.M., 2020. Impaired meningeal lymphatic vessel development worsens stroke outcome. J. Cereb. Blood Flow Metab. 40, 263–275. https://doi.org/10.1177/0271678X18822921

- Z -

Zamboni, M., Santopolo, G., Frisén, J., 2020. Induction of Leptomeningeal Cells Modification Via Intracisternal Injection. J. Vis. Exp. JoVE. https://doi.org/10.3791/61009

Zimmermann, D.R., Dours-Zimmermann, M.T., 2008. Extracellular matrix of the central nervous system: from neglect to challenge. Histochem. Cell Biol. 130, 635–653. https://doi.org/10.1007/s00418-008-0485-9

Zou, W., Pu, T., Feng, W., Lu, M., Zheng, Y., Du, R., Xiao, M., Hu, G., 2019. Blocking meningeal lymphatic drainage aggravates Parkinson’s disease-like pathology in mice overexpressing mutated α-synuclein. Transl. Neurodegener. 8, 7. https://doi.org/10.1186/s40035-019-0147-y

Les échanges entre liquide céphalo-rachidien et parenchyme cérébral – observations in vivo par imagerie par résonance magnétique et implications dans le développement, le vieillissement et la pathologie

Audrey Chagnot, 2021

Résumé

Le liquide céphalo-rachidien (LCR) baigne l'ensemble du système nerveux central. En plus de son rôle protecteur, le LCR transporte des nutriments, des facteurs trophiques et des déchets qu'il échange avec le fluide interstitiel cérébral (FISC). Situés en périphérie des vaisseaux, les espaces périvasculaires offrent un accès au LCR vers la profondeur du tissu cérébral. Depuis une décennie, l'hypothèse d'un flux de liquide emportant les déchets du métabolisme vers ces espaces est avancée sous le nom de système glymphatique. Bien que ce modèle reste controversé, l'altération des échanges LCR-FISC a été montrée dans diverses pathologies dont la maladie d'Alzheimer, une démence liée à l'accumulation de plaques amyloïdes.

L'imagerie par résonance magnétique (IRM) permet d'observer in vivo la circulation du LCR et a montré chez l'être humain les échanges LCR-FISC. Cependant, l'utilisation d'agents de contraste restreint son exploitation clinique. Moins invasive, l'IRM de diffusion se base sur le mouvement des molécules d'eau et pourrait remplacer l'IRM rehaussée par agent de contraste pour l'exploration des échanges LCR-FISC.

Au cours de ma thèse, j'ai exploité deux techniques d'IRM (diffusion ou agent de contraste) pour explorer les échanges LCR-FISC chez la souris. Mes travaux soulignent la complémentarité de ces techniques et l'importance des traceurs utilisés dans des modèles de développement, de pathologie et de vieillissement.

Mots-clés : IRM | liquide céphalo-rachidien | glymphatique | développement | maladie d'Alzheimer

Abstract

The central nervous system is bathed in the cerebrospinal fluid (CSF). In addition to its protective role, the CSF carries nutrients, trophic factors and metabolic waste that are exchanged with the interstitial fluid of the brain (bISF). Around the vessels, the perivascular spaces give to the CSF an access toward the deep brain tissues. Since a decade, the 'glymphatic system' hypothesis has been advanced as a convective flow draining the metabolic waste to the perivascular spaces. While this model remains disputed, the CSF-bISF exchanges dysfunctions in a variety of pathologies including the Alzheimer's disease, a dementia related to the accumulation of amyloid plaques.

Magnetic resonance imaging (MRI) allows in vivo observations of the CSF circulation and shown the CSF-bISF exchnages in humans. However, the necessity of contrast agents restricts its clinical use. Diffusion-weighted MRI is a alternative, contrast agent-free technique exploiting the motion of water molecules and could replace contrast-enhanced MRI to investigate the CSF-bISF exchanges.

During my thesis, I used two MRI techniques (diffusion-weighted or contrast agent enhanced) to explore the CSF-bISF exchanges in mouse. My works emphasize the complementarity of these techniques and the importance of tracers in several models of development, pathology and aging.

Keywords : MRI | cerebrospinal fluid | glymphatic | development | Alzheimer's disease